MASSEY UNIVERSITY
TE KUNENGA KI PŪREHUROA
UNIVERSITY OF NEW ZEALAND

The Theory of Diffusionless Phase Transitions in Elemental Solids

A thesis presented in partial fulfillment of the requirements for the degree of

Doctor of Philosophy

in
Chemistry

at Massey University, Albany,
New Zealand

Andrés Eduardo Robles-Navarro

2026

Acknowledgments

After these three years of journey, many new things learned are kept in my mind, but also people that deserve to be mentioned here. First of all, thanks to Peter for giving me the opportunity to work and learn from him here at Massey University, even though it took a long wait to start due to the pandemic situation before. It is hard to live at interesting times, as someone said. Also thanks to Vesna, who helped me from the very first moment I arrived to New Zealand and with all the administrative work to start my PhD journey. This would have been many times harder without her aid. Thanks to my co-supervisor Shaun Cooper for his support throughout this project, particularly in strengthening the mathematical foundations of this thesis. During this time I also met some quite nice people who supported me and also had many great conversations. Odile and Catia, for the work we did together and the interesting lunch conversations. Cannot say lunch without mentioning my lunch buddy Seona, of course. Also a big thanks to Kimberley for your support during the last stage of this journey. Angy, for reminding me not forget the Latino vibe while living here, and to everyone else I have met on these three years. Finally, thanks to the Sir Neil Waters Foundation in Massey University for financing my studies.

Abstract

Although phase transitions in the solid state have been described with the aid of phenomenological theories and molecular dynamics or Monte Carlo simulations, a microscopic framework that treats both crystallography and the energy landscape on equal grounds is still missing. This thesis aims to establish the basis of the theory of diffusionless phase transitions by relating different crystal structures, lattices and non-lattices, described by few parameters through the use of accurate density functional approximations and exact lattice sums. The methods described here, together with the use of fast converging series of modified Bessel functions of the second kind, allow to treat general lattice sums for cubical and hexagonal lattices equivalently during the transformation, as well as to calculate the lattice parameters, cohesive and zero-point vibrational energies, bulk moduli, and entropy to computer precision for systems obeying inverse-power potentials. Furthermore, the relative stability of the infinitely many Barlow packings is assessed, showing that a linear relation between the free energies of the packings explains why only a few of these structures are actually observed in nature.

Contents

List of Figures

List of Tables

List of Publications

1. A. Robles-Navarro, P. Jerabek, P. Schwerdtfeger. "Tipping the balance between the bcc and fcc phase within the alkali and coinage metal groups". *Angewandte Chemie International Edition*, **2024**, *63(1)*: e202313679.

2. S. Cooper, A. Robles-Navarro, O. R. Smits, and P. Schwerdtfeger. "From hard to soft dense sphere packings: The cohesive energy of Barlow structures using exact lattice summations for a general Lennard-Jones potential". *The Journal of Physical Chemistry Letters*, **2024**, *15(32)*: 8387–8392.

3. A. Robles-Navarro, S. Cooper, O. R. Smits, P. Schwerdtfeger. "Exploring the mechanism of phase transitions between the hexagonal close-packed and the cuboidal structures". *The Journal of Physical Chemistry C*, **2025**, *129(17)*: 8389–8394.

4. S. Cooper, A. Robles-Navarro, O. R. Smits, P. Schwerdtfeger. "The theory of Barlow packings: Basic properties and cohesive energies from exact lattice summations within the sticky hard-sphere model". *The Journal of Chemical Physics*, **2025**, *162(1)*: 014105.

5. A. Robles-Navarro, S. Cooper, A. A. Buchheit, J. K. Busse, A. Burrows, O. Smits, P. Schwerdtfeger. "Exact lattice summations for Lennard-Jones potentials coupled to a three-body Axilrod–Teller–Muto term applied to cuboidal phase transitions". *The Journal of Chemical Physics*, **2025**, *163(9)*: 094104.

6. A. Robles-Navarro, S. Cooper, A. W. Hauser, F. Zehetmair, O. Smits, P. Schwerdtfeger. "Lattice Instabilities Along the Transformation from Hexagonal to Cuboidal Structures in Hard-and Soft-Sphere Models". *Physical Review B*, **2026**, *113*, 024116.

7. A. Robles-Navarro, P. Schwerdtfeger. "Accurate Relativistic Density Functional Calculations for the Solid-State of Metallic Francium" *Physical Chemistry Chemical Physics*, **2026**, Advance Article.

8. A. Robles-Navarro, S. Cooper, A. Travesset, P. Schwerdtfeger. "The Theory of Barlow Packings: Application to Lennard-Jones Solids and Metallic Lithium". *In preparation*

Chapter 1

Introduction

The structure of matter has fascinated philosophers and scientists for millennia with by far the greatest progress made only during the last few centuries. Tracing the origins back to the Ancient Greece, Plato's theory of elements associated with well-known regular polyhedra intended to explain many properties of matter such as chemical reactions, the physical variety of matter, melting and freezing.[1,2] This was a starting point for the philosophical basis of an atomic theory. However, the first opposite viewpoint was made by Aristotle, who argued that only two of the regular polyhedra would not create a void in space, something "incompatible with reality", therefore rejecting Plato's four-element atomic hypothesis.[3,4] Nevertheless, Aristotle was wrong because regular tetrahedra cannot tile the space without voids, an error that persisted for almost 2000 years.[4] In fact, the only regular polyhedron that can fill the space without any gaps is the cube or distorted versions of it, leading to the so-called Bravais lattices in crystallography. It is worth mentioning that 3-dimensional space can also be tiled by other polyhedra such as triangular and hexagonal prisms, parallelepipeds, and other types of space-filling polyhedra.[5,6]

These geometrical concepts developed were not simply an abstract reasoning without connection to reality. As it was known from antiquity, many minerals are known to adopt polyhedral forms, for example the pyrite (iron disulfide, FeS_2), diamond (a carbon allotrope) and quartz (made of silicon dioxide, SiO_2). The last case is of special historical importance since different geometrical structures of quartz are known and, indeed, is due to this mineral that the word "crystal" became widespread in scientific research,[7] although the modern concept of a crystal would appear not too long ago.

One of the first recorded attempts to understand the microscopic structure of objects in terms of geometry was done by Kepler in his publication *De nive sexangula* in 1611.[8] The central idea was to understand why snowflakes have a six-fold symmetry, like an hexagon, by assuming they are composed of tiny pellets that stack to form a macroscopic structure. However, he was unable to explain the snowflake's symmetry. Nonetheless, this effort was not futile: it

settled a conjecture that would wait for around four hundred years to be proven, namely, that a special type of sphere packing (now known as the cubic-close packed structure) is the optimal in three-dimensions.[9] The computer-assisted proof of Kepler's conjecture was carried out only very recently by the mathematician Hales.[10,11] A far more challenging problem put forward by Hilbert in 1900 is building up of space from congruent polyhedra and remains unsolved (Hilbert's 18th problem).[12]

The influence of Kepler's work was in line with the crescent popularity of atomism by the hand of Robert Boyle and further influenced Robert Hooke to state that "all crystalline forms could be explained by a few basic packing arrangements of spherical atoms".[4,13] Following the same train of thought, it is natural to ask whether the microscopic structure of solid matter can be explained by either sphere or polyhedral packing. The advent of quantum mechanics and the discovery of X-ray diffraction would help in giving an answer to this issue and now one naively could say that both sphere and polyhedron packing can be correct to some extent.[1]

On the one hand, Niels Steensen would discover the First Law of Crystallography in 1669, namely, the constancy of interfacial angles, later generalized by Jean-Baptiste L. Romé de l'Isle in 1783.[4] The very next year, René Just Häuy would continue the work on crystals to settle down the Second Law (that can be associated with Miller indices) and Third Law of Crystallography (regarding the symmetries of crystals). In his work, he thought of crystals made of tiny parallelepipeds stacked in a way that resembles the macroscopic structure, following certain relations between angles and planes found empirically.[13–17]

The increasing popularity of the atomic theory at the beginnings of the 19th century, mainly influenced by Dalton's theory, revived the interest in sphere packings as the fundamental structure of matter. One of the greatest advances was made by William Barlow at the end of the same century, when he developed a sphere-packing theory describing the nature of some crystals and also discovered the hexagonal close-packed structures.[18–20] Barlow's work even influenced William Bragg's work on X-ray diffraction, which later would support the ideas of Barlow about the structure of alkali halide crystals with experimental evidence.[21–23]

Nowadays, it is well-known that atoms in a solid stay primarily at fixed positions[24,25], besides vibrations and distortion (and internal rotations in the case of plastic crystals[26] or orientational glasses[27]). A special type of solids are crystals, which are characterized by an ordered arrangement of atoms. This situation can be idealized by the mathematical concept of a lattice in the following way: each atom occupies a certain position in the lattice, such that there is a repeating pattern that extends over the space infinitely (translational symmetry).[25] Naturally, there is no infinite perfect crystal in nature, but the much larger extension of a macroscopic solid compared to the atomic distances makes this approximation plausible. An

[1] For completeness, it is worth noting that R. G. Boscovich in the 18th century proposed that, instead of spherical or polyhedral atoms with a given volume, there were a set of points balanced by attractive and repulsive forces, a concept related to a lattice of interacting point particles.[13]

essential concept in lattice theory is that of the fundamental domain (or region)[28], which comes from dividing the space into equal polyhedra (D-dimensional parallelepipeds). This could be seen as one point in favor of polyhedral packing.

Now, from quantum mechanics, it is also well-known that atoms with valence electrons in s states and filled or half-filled p, d, f, or g orbitals are spherically symmetric.[29] In other cases, the bonding with other atoms could pose the picture of a spherical atomic core (nucleus plus non-valence electrons) immersed in a sea of interacting electrons, keeping the whole structure together. This is, in fact, one of the first ideas to microscopically explain the structure and properties of metals, developed by Paul Drude in 1900.[30,31] This model has proven to be very useful and thus can be extrapolated to the idea of atoms embedded in a lattice as spheres being packed in a certain regular way. Point in favor of sphere packing, settling the draw.

But not everything is about packing; a first principles explanation of the properties of a crystalline solid also requires the joint work of quantum mechanics and statistical mechanics. In principle, solving the Schrödinger (or Dirac) equation yields the desired result or prediction, however, the enormous number of degrees of freedom in a macroscopic sample makes the task impossible to solve in a normal time of a human lifespan. Therefore, it is common practice to resort on interatomic model potentials to describe ground states, elastic properties, and phase transitions, among other properties.[32] Nonetheless, this does not mean that a full quantum mechanical treatment is ruled out, since there exist a variety of techniques and models that approximate reasonably well to experimental data.[33]

Sometimes, however, it is not possible to obtain experimental data with enough accuracy, thus the only form to understand phenomena is through computational methods, either *ab initio* or using interatomic model potentials. This can happen when describing some phase transition problems, due to the small energy differences. In particular, one could think about solid-solid phase transitions as a good example of problems that remain poorly understood. The experimental techniques in solid-state physics do not allow to directly follow the entire transformation process and thus the mechanisms are usually inferred through certain geometric relations between different phases[34,35] (when it is possible to synthesize and isolate them) or by monitoring a physical property during the whole process.[36]

One of the difficulties lies in the fact that no real crystal is perfect, without vacancies, dislocations, or impurities. Therefore, the exact transformation path is perturbed by changes in the energy hypersurface driving the transition between two or more phases,[37] an issue that can be problematic near transition states or critical temperatures. Fortunately, the formation of the initial and final structures while changing the conditions is still possible, although the mechanism and driving forces can be hindered to experiment. This difficulty is also strongly tied to the nucleation mechanism that depict the actual transformation in a real system.[38]

The different crystal structures that an element or compound can adopt under certain conditions are often referred to as polymorphs.[39–41] Despite of having the same composition,

each polymorph has its own physical, chemical, mechanical and optical properties. The study of polymorphic transitions has a high relevance in both academic and industrial applications like the prediction of solid-state structures of a compound when crystallizing, the manufacture of steels and shape-memory alloys, and the development of pharmaceuticals. The latter case is of particular interest to general public, since there have been cases where the polymorphism of a medication can affect the bioavailability of the drug,[42,43] or in the specific case of enantiomorphism where the toxicity of one enantiomer can cause serious adverse effects to human health.[44]

Understanding the kinetics of a solid-to-solid phase transformation is a complex task, since there are many factors that can affect the initial steps of the process. For example, the freezing of water is a first-order phase transition that is driven by thermal fluctuations,[45] however, there are systems, like certain shape-memory alloys, in which these effects do not play any role during the transformation.[36] A broader classification of these phase transitions is according to the kinetics of the transformation: when atoms move over long distances it is referred as a diffusive phase transition[46,47] (observed in crystallization from the melt in metals[48–50] and water[51,52], polymorphic transformations in molecular solids[53], certain kinds of graphite-diamond conversions[54] and the devitrification of glasses[55]), otherwise it is called a diffusionless phase transition.[56]

An archetypical example of solid-solid transformations that can involve both types of phase transitions is the hardening of steel.[57,58] There is evidence that since the Iron Age it was known that crucial processes for hardening steel involve the heating and quenching of the alloy,[59] that is, rapidly cooling it after applying enough heat (usually over 1000°C). It was not until the 17th and 18th centuries that scientists developed microscopy methods that revealed the formation of microstructures in iron and steel[60], as well as discovering the existence of carbon in steel[61] and how influences the physical properties of the alloy. Subsequently, and with the aid of the thermodynamics developed by Gibbs around the same time, a phase diagram of the iron-carbon system would be sketched in which several phases in the solid state are recognized.[62]

The polymorphism of pure iron becomes evident when studying its cooling curve at ambient pressure. Starting from the melt above 1536°C, the first crystal structure encountered is δ-Fe (a body-centered cubic lattice), which transforms into γ-Fe (a face-centered cubic lattice) at 1392°C. Upon further cooling, another transformation back to a body-centered cubic lattice occurs at 911°C, reaching a form called β-Fe, a paramagnetic solid. A further phase transition happens at 769°C to α-Fe, where iron becomes magnetic while keeping the same crystal structure[2] as β-Fe.[64]

The case of steel, however, is more complex than that of pure iron due to the additional

[2]Strictly speaking, the α-Fe phase is a body-centered tetragonal structure due to Joule magnetostriction, however the distortion from a cubic structure is so small[63] that can be neglected and α-Fe is usually treated as a body-centered cubic structure.

carbon atoms, which do not exceed the 2% in mass content.[65] A small amount of carbon can make steel crystallize from the melt directly into the face-centered cubic structure (γ-Fe), where carbon atoms are embedded in the center of the cubic unit cell; a phase called austenite.[66] Upon cooling, there is a γ-α transformation of iron[67], where carbon atoms are hardly soluble within the cubic unit cells. When the cooling process is slow, the steel reaches a phase with an almost carbon-free iron lattice called ferrite,[65,66] however a rapid cooling (quenching) of the steel produces a tetragonally distorted body-centered structure called martensite,[68–70] which traps the carbon atoms within the unit cells.

The γ-α transformation described above is diffusive when obtaining ferrite by slow cooling, but diffusionless to get the martensite structure. This latter process is often called a martensitic transformation and it has been shown that it is not unique to iron or steel.[71] Other solids can also undergo martensitic transformations, for example, the transition from a face-centered cubic crystal to an hexagonal close-packed structure in cobalt[71–73] and the different phases of lithium when varying temperature and pressure.[74–79] Furthermore, a new class of materials discovered in the 1950s, known as shape-memory alloys[80–83], can undergo reversible martensitic transformations.[84–87]

Although there is a vast collection of materials that can exhibit martensitic transformations, the underlying mechanisms are still on debate and no general microscopic theory describing them is known. Some attempts include the use phenomenological theories using the relations between the parent and product phases[88–90], the Landau theory of phase transitions and phase-field models,[91–93] however, they heavily rely on parameters and no direct explanation of energetics along crystallography is provided. There are also attempts using molecular dynamics or Monte Carlo simulations and density functional theory that overcome this problem,[94–101] however, they can be computationally expensive and the limited system size and time scales could affect the accuracy of the calculation, considering that the energy differences between two phases could be beyond the accuracy that many density functional approximations can offer.

The lack of a precise mechanism of transformation between two or more crystal phases makes difficult the transferability of the predictions of parametrized or ideal models to new materials, since there are evidence of metals deviating substantially from ideal behavior.[102,103] Moreover, ideal models of sphere packing cannot describe properly the properties of a system of interacting atoms. Real systems involve van der Waals interactions and other quantum effects that can play a fundamental role in the geometries and stabilities of different packings, for example, in determining the most stable structure for rare gas solids[104] and the different structures found in Group 2 metals[105–107]. Although many descriptions of Lennard-Jones systems in hexagonal and cubical close-packed structures have been reported,[108–110]there is still gaps to fill, for example the more general Barlow packings which have maximal packing density.[18] There are uncountable infinite Barlow packings, however they are extremely rare

in nature, except for the cubical and hexagonal close-packed structures. There is currently no explanation for this.

The use of interatomic potentials together with lattice theory has extended the understanding of sphere packings in three dimensions through lattice sums.[28,111] The first realization of the connection between crystal lattices and number theory was by Lennard-Jones and Ingham[112], who related inverse power potentials to the so-called Epstein zeta functions[113], an extension of the better known Riemann zeta function.[114] They realized that the calculation of the sum over all lattice points in a crystal, the lattice sum, by a direct method can be troublesome due to the convergence of the terms towards lattice constant. This is why they developed a fast converging Bessel function expansion for cubic crystals, opening a new area within solid-state calculations.

One of the first highly accurate calculations of lattice sums was done by Madelung for three-dimensional ionic solids.[115] He demonstrated that the lattice sum in an ionic rock-salt structure is conditionally convergent and can be performed with the aid of Bessel functions. Furthermore, the same method has been successfully applied for other ionic crystals in different lattices,[116–118] but other highly accurate methods for more general lattice summations have been developed. For example, Ewald's method to treat long-range interactions.[119,120] Later, another procedure was developed by Glasser[121–123] and Zucker[124] through the use of Jacobi's theta functions[125].

All these developments have helped in evaluating the cohesive energy or the lattice energy of a solid structure, however, the treatment of solid-solid phase transitions through exact lattice sums has not been attempted yet for general crystal lattices. Exceptions are the cuboidal transformation from bcc to fcc.[126,127] A more general treatment, that includes lattices of different symmetries and even non-lattice structures still remains to be made.

The main objective of this thesis is therefore to develop a microscopic theory of diffusionless phase transitions through lattice sum techniques. From this, we gain important insights which allows for further first principles method simulations of several types of materials, specially elemental metals. The methodology proposed here is designed to deal explicitly with the behavior of individual atoms during the transformation and therefore create a highly accurate energy profile around the stable and metastable crystal structures of a material using density functional theory. The tools developed here are also applied to ideal Lennard-Jones systems coupled to three-body forces, due to the availability of analytical formulas to calculate the thermodynamic properties of a crystal from exact lattice sums. This also represents a challenge, since the evaluation of lattice sums by direct summation can converge very slowly depending on the type of potential used, therefore fast converging series are employed to expand the known lattice sums. Furthermore, a complete description of the structural and thermodynamic properties of ideal Barlow packings is presented here.

Chapter 2

Theoretical Background

The first step in understanding solid-solid phase transitions is the correct structural and quantum theoretical description of matter in the solid state. From the two broad categories of solids, crystalline and amorphous, the focus of this work will be on the description of ideal crystals (with no vacancies or defects) through model interaction potentials and density functional theory, as detailed in the following sections. This chapter contains a brief summary of the theoretical background required in order to provide a solid basis of the methods selected and to standardize the notation used in this work. More information can be found in the relevant chapters.

2.1 The Crystal Lattice

Among the different types of solids, crystals possess the characteristic feature of a highly ordered structure where atoms are located at certain positions determined by the symmetry of the crystal.[25,128,129] This idea is the starting point of a mathematical description of crystals called lattice theory. Since the atomic distances are much smaller than the actual size of the solid they form, a first idealization is to consider the entire crystal as an infinite three-dimensional array of atoms placed at specific locations. In mathematical terms, the lattice is isomorphic to $\mathbb{Z}^3$. If the system displays periodicity in the atomic positions, then the geometric structure formed is called a lattice.

For a D-dimensional lattice, any point that can be represented by the lattice vector

$$\mathbf{L}(\boldsymbol{\ell}) = \sum_{i=1}^{D} \ell_i \mathbf{a}_i, \tag{2.1}$$

where $\{\mathbf{a}_i\}, \mathbf{a}_i \in \mathbb{R}^D$ is the set of basis vectors of the lattice and $\ell_i \in \mathbb{Z}$, is called a lattice site. In three dimensions, the parallelepiped formed by the basis vectors define the fundamental region[28] of the lattice, also called the unit cell[130]. If just one atom is in the unit cell, then it

is called a primitive cell, which is the smallest possible unit cell, and all the coefficients ℓ_i are integers. Otherwise, it is termed as the conventional unit cell[130] and needs additional vectors to describe all the atomic positions.

For a given lattice, the set of basis vectors is not unique, however the volume of the fundamental region is uniquely determined by the lattice up to a scaling factor. This volume, Ω, can be calculated from the basis vectors by forming the generator matrix,

$$\boldsymbol{B} = \begin{pmatrix} \mathbf{a}_1^\top \\ \mathbf{a}_2^\top \\ \mathbf{a}_3^\top \end{pmatrix} = \begin{pmatrix} a_{11} & a_{12} & a_{13} \\ a_{21} & a_{22} & a_{23} \\ a_{31} & a_{32} & a_{33} \end{pmatrix} \tag{2.2}$$

and then calculate its determinant, $\Omega = |\det \boldsymbol{B}|$. By placing $\mathbf{a}_1$ onto the x-axis and $\mathbf{a}_2$ into the (x, y)-plane, the B-matrix can be brought into a triangular form. If the generator matrix is not a square matrix (i.e. for a subspace of a D-dimensional lattice), then we cannot follow this procedure. Hence, it is more convenient to define the (positive definite) Gram matrix of the lattice by,

$$\boldsymbol{G} = \boldsymbol{B}\boldsymbol{B}^\top \tag{2.3}$$

which is always a square matrix whose entries are the inner products $\mathbf{a}_i \cdot \mathbf{a}_j$. Then the volume of the fundamental region can be written as[28]

$$\Omega = \sqrt{\det \boldsymbol{G}} \tag{2.4}$$

Two lattices are congruent if there is a matrix $\boldsymbol{U}$ with determinant ± 1 such that the following relation holds for their Gram matrices[28,131]

$$\boldsymbol{G}' = k^2 \boldsymbol{U}\boldsymbol{G}\boldsymbol{U}^\top \tag{2.5}$$

where k is a non-zero constant. This relation makes clear the validity of the previous statement about the volume of the fundamental region: it is uniquely determined by the lattice type up to a constant $k > 0$, $\Omega = \sqrt{\det \boldsymbol{G}'} = k\sqrt{\det \boldsymbol{G}}$.

2.1.1 Packing of Spheres

Having the structure of the lattice, the following question arises: how do we place the atoms into a unit cell? From a chemistry or physics point of view, this is not a trivial question because it depends on the electronic structure of the atoms and their bonding properties, however one can follow a naive approach and think of atoms as non-overlapping touching (or kissing) hard spheres. In the case of elemental solids (one atom type), all spheres are equivalent. In general, the most efficient way to fill a D-dimensional space with equal spheres is known as the sphere

packing problem,[28] where efficiency means maximum occupation of the available space.

To account for this, we can define the packing density in a D-dimensional lattice as

$$\rho = \frac{\text{volume of one } D\text{-sphere}}{\text{volume of the fundamental region}} = \frac{\pi^{D/2} r^D}{\Gamma\left(\frac{D}{2}+1\right)\sqrt{\det \boldsymbol{G}}} \tag{2.6}$$

where r is the radius of the D-sphere, and Γ is the well known Gamma function. As an example in two dimensions, the area of the fundamental region of a square lattice is $2r^2$ and that of the hexagonal lattice is $\sqrt{12}r^2$, hence the packing densities are approximately 0.7854 and 0.9069, respectively.[28] Furthermore, it has been shown that the hexagonal lattice has maximum packing density in two dimensions.[132] An example structure resembling this 2-dimensional lattice can be found in the individual sheets of graphene, as observed through transmission electron microscopy.[133] The extension of this problem to three or higher dimensions is not trivial. In three dimensions the problem is called the Kepler conjecture,[134,135] which states that the maximum packing density is found in the cubical and hexagonal close-packed structures, with a value of

$$\rho = \frac{\pi}{\sqrt{18}} \approx 0.74048 \tag{2.7}$$

This problem was established by Kepler in 1611 and its formal proof, making it a theorem now, was given by Thomas Hales[10] and officially accepted in 2017.[11]

As the name implies, a close-packed structure is the most compact arrangement of equal spheres in space, either in a lattice or non-lattice arrangement. Regarding the crystal structure of elemental solids, at standard conditions of temperature and pressure, most of the elements adopt either a cubical close-packed (ccp) structure or an hexagonal one (hcp). However, many of them also take non-close-packed forms, being the body centered cubic lattice the most common alternative.[136,137] Furthermore, with varying conditions of temperature and pressure, more complex structures can be found.[74–77,79,136] A complete explanation of the crystal structures adopted by all elements in the Periodic Table is not available yet, however some insights from electronic structure and lattice dynamics will be given in later chapters.

The hexagonal and cubical close-packed structures of hard spheres are also examples of strictly jammed packings[138,139], defined as any packing that resists any internal motion and any boundary-preserving deformation, that is, where true mechanical rigidity is found.[139] In general, jammed packings are important for understanding the mechanical properties of solids[140], some soft matter phenomena[141], and even in biology[142,143], but they are more about geometry and mechanical motion, rather than thermodynamics.

They can be divided into 3 categories: locally jammed (resists particle displacements), collectively jammed (has network rigidity), and strictly jammed.[138] The latter type can be understood in terms of a packing with positive-definite elastic constants and positive phonon frequencies in the first Brillouin zone. Most elements of the Periodic Table at 0 K possess

these properties, hence they are strictly jammed. Nonetheless, any system presenting lattice instabilities or soft phonon modes under certain conditions could be only locally and/or collectively jammed. Furthermore, non-close-packed structures like the simple cubic and body-centered cubic lattices are only locally and collectively jammed, since a shear deformation of the whole lattice will destabilize the packing.[138]

2.1.2 Bravais Lattices

From the packings mentioned in the previous section, the only one that does not fulfill the lattice vector definition in Eq. (2.1) is the hcp structure. All the others mentioned are part of the cubic crystal system, which is the one where the unit cell is simply a cube and it comes in three different flavors: the simple cubic (sc), the body-centered cubic (bcc), and the face-centered cubic (fcc, which is equivalent to the ccp structure). The simple cubic, shown in Fig. 2.1a, has all sides of the cube of equal length, all the angles are 90°, and just one atom placed at the vertex of the cube. In the bcc structure (Fig. 2.1b), there is one atom at each corner and another in the center of the cube. Similarly, in the fcc structure, there is one atom at each corner and one atom at the center of each face of the cube (Fig. 2.1c). On the other hand, there is the hcp structure, which can be viewed as an hexagonal lattice with one atom at each vertex and three atoms in the center, see Fig. 2.1d. In the hexagonal lattice, the height of the cell is different from the length of the sides at the bottom and top faces, whose angles between the lattice positions are 120°. The ideal hcp structure has a c/a ratio equal to $\sqrt{8/3}$ and the atoms at the center are at a distance of $c/2$ from the bottom and top hexagonal faces.

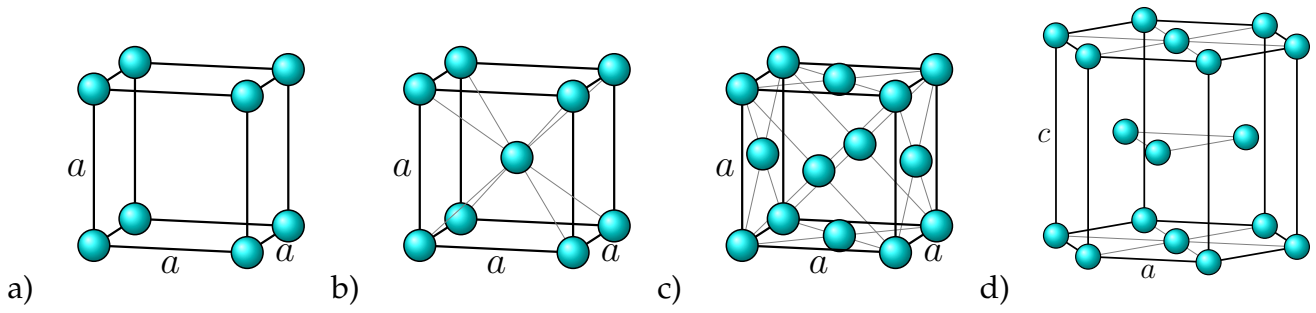

Figure 2.1: Four examples of crystal structures: a) sc, b) bcc, c) fcc, d) hcp.

More generally, it is possible to build all the non-equivalent lattices in D dimensions by considering their symmetries with respect to rigid transformations such as translations, rotations, reflections, inversions, among others. All these symmetries can form a point group in the Euclidean space, however, not all point groups known, for example, for molecules are useful when dealing with crystals. In fact, the crystallographic point group has to be compatible with the translational symmetry of the crystal and there is a further constraint in the rotational symmetry given by the well-known crystallographic restriction theorem[144], which states that

only one-, two-, three-, four-, and six-fold rotations are allowed in three dimensions (thus so-called quasi-crystals do not belong to the common class of periodic lattices, but they are still isomorphic to $\mathbb{Z}^3$). The consequence of this is that only 32 crystallographic point groups exist.[144]

The lattice vectors in Eq. (2.1) also form a group of infinite order called the translation group of the lattice, whose symmetry operations are defined by the set of basis vectors $\{\mathbf{a}_i\}$. The 32 crystallographic point groups are compatible with the translation group, however, some of them are subgroups of other crystallographic point groups among the 32 mentioned. Hence, a crystal can only be represented by the point group with the largest amount of symmetries of the lattice, called the holosymmetric[144,145] point group of the crystal. This further reduces the number of relevant point groups to 7 holosymmetric point groups: O_h, D_{6h}, D_{3d}, D_{4h}, D_{2h}, C_{2h} and C_i. They are often referred as the seven crystal systems in three dimensions, where the cubic system mentioned before belongs to the O_h point group.

Furthermore, it is possible to keep adding lattice points to the seven crystal systems without altering the holosymmetric point group and maintaining the same translational symmetry. This process is called the centering of a lattice.[144] When the lattice has no additional points, it is called a primitive lattice, otherwise it is a body-centered, face-centered or base-centered lattice. This procedure creates seven new lattices in three dimensions that, when added to the seven primitive lattices, form a set called the Bravais lattices.

A clear and visually appealing way to define the 14 Bravais lattices is starting from the most asymmetric one and then add restrictions to the lattice parameters, such as the length of the sides and angles between the basis vectors. This also helps to visualize the symmetries involved in the definition of the Bravais lattices. To begin with, the most asymmetric of the Bravais lattices is called the triclinic lattice (C_i), whose basis vectors are

$$\begin{aligned}
\mathbf{a}_1^a &= a\,(1,0,0)^\top \\
\mathbf{a}_2^a &= a\gamma_1\,(\cos\theta_1, \sin\theta_1, 0)^\top \\
\mathbf{a}_3^a &= a\gamma_2 \left(\cos\theta_3, \left[\frac{\cos\theta_2 - \cos\theta_3\cos\theta_1}{\sin\theta_1}\right], \sqrt{1-\cos^2\theta_3 - \left[\frac{\cos\theta_2 - \cos\theta_3\cos\theta_1}{\sin\theta_1}\right]^2}\right)^\top
\end{aligned} \tag{2.8}$$

where $\theta_1 = \angle(\mathbf{a}_1, \mathbf{a}_2)$, $\theta_2 = \angle(\mathbf{a}_2, \mathbf{a}_3)$, $\theta_3 = \angle(\mathbf{a}_1, \mathbf{a}_3)$, $\gamma_1 = \frac{b}{a}$, $\gamma_2 = \frac{c}{a}$, and the superscript a means anorthic, which is another way to call the triclinic lattice. The first constraint to make that keeps the lattice structure is to set $\theta_1 = \theta_2 = 90^\circ$ such that the basis vectors become

$$\mathbf{a}_1^{mP} = a(1,0,0)^\top, \qquad \mathbf{a}_2^{mP} = a\gamma_1\,(0,1,0)^\top, \qquad \mathbf{a}_3^{mP} = a\gamma_2\left(\cos\theta_3, 0, \sqrt{1-\cos^2\theta_3}\right)^\top \tag{2.9}$$

This set of vectors define the primitive monoclinic (C_{2h}) unit cell, which can also be

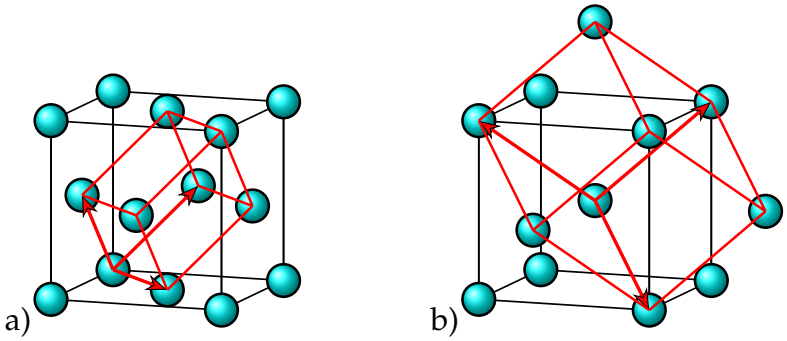

Figure 2.2: Primitive unit cell (in red) of a) fcc, and b) bcc.

base-centered. A further restriction on the angles would be $\theta_1 = \theta_2 = \theta_3 = 90°$, in which case the three vectors are perpendicular and only the side lengths are different, forming the orthorhombic lattice (D_{2h}). This lattice allows the three types of centering, hence there are four Bravais lattices that are orthorhombic. The next constraint is to set $b = a$ while having all vectors perpendicular to each other, forming the tetragonal lattice (D_{4h}), whose unit cell is a simple rectangular prism in its primitive form and also allows a body-centered structure.

Another lattice structure can be made from the tetragonal by allowing $\theta_1 = 120°$, while keeping $\theta_2 = \theta_3 = 90°$ and $b = a$. This is the hexagonal lattice (D_{6h}) with basis vectors

$$\mathbf{a}_1^h = a(1,0,0)^\top, \qquad \mathbf{a}_2^h = a\,(\cos\theta_1, \sin\theta_1, 0)^\top, \qquad \mathbf{a}_3^h = a\,(0,0,\gamma_2)^\top \tag{2.10}$$

The hexagonal lattice does not allow centering and it is closely related to the rhombohedral lattice (D_{3d}) in which $c = b = a$ and $\theta_1 = \theta_2 = \theta_3 \neq 90°$. For the last three Bravais lattices, all angles are 90° and all side lengths are equal, such that the basis vectors of the primitive cubic are

$$\mathbf{a}_1^{cP} = a(1,0,0)^\top, \qquad \mathbf{a}_2^{cP} = a\,(0,1,0)^\top, \qquad \mathbf{a}_3^{cP} = a\,(0,0,1)^\top \tag{2.11}$$

This crystal system has a O_h symmetry and can also be found as a body-centered structure and face-centered structure. These are the 14 Bravais lattices in three dimensions. Even though the process of centering adds a new lattice point, all centered lattices can also be described by a primitive unit cell. For example, the primitive cells for fcc and bcc are shown in red in Figure 2.2.

Nevertheless, it is possible to find crystal structures that cannot be simply described by a Bravais lattice. This is the case of the hcp structure shown in Figure 2.1d, where the central atoms are in positions that do not belong to the D_{6h} group. In these cases, one must set up a conventional cell with additional (shift) vectors that point towards the extra atoms, such that

$$\mathbf{r}_j(\boldsymbol{\ell}) = \mathbf{L}_j(\boldsymbol{\ell}) + \boldsymbol{\tau}_j \tag{2.12}$$

is the atomic position of atom j, $\boldsymbol{\ell}$ is the integer vector defining the Bravais lattice translations, and $\boldsymbol{\tau}_j$ is the fractional basis vector for the other atoms in the unit cell with all its components within $[0, 1)$. Since the 14 Bravais lattices can also be described by Equation (2.12), the choice of their unit cell is, therefore, not restricted to primitive cells. However, when doing solid-state electronic structure calculations, it is usually preferred to work with a primitive unit cell, when available, since it is the smallest cell that follows the translational invariance of the Hamiltonian.

2.1.3 Barlow Packings

An important class of crystals that cannot, in general, be described by a single Bravais lattice are close-packed structures. Many elemental solids in the Periodic Table adopt these kind of structures and the observation that this also can happen in binary solids led Barlow to the discovery of the hexagonal close-packed structure together with the cubical close-packed one,[18–20] later identified as the fcc lattice. Both structures are the densest packings in three dimensions. However Barlow himself[20], and Melmore later[146], mentioned that some mixtures of hcp and ccp/fcc can also have maximal packing density.

Conway and Sloane showed that strictly jammed packings of spheres in three dimensions at maximal density (Barlow packings) can also be obtained by a 3-coloring of A_1, which is an integer lattice in one dimension, provided some additional restrictions.[147] This means that if we assign three colors or labels to the points in A_1, namely (A, B, C), and enforce consecutive labels to be different, then a Barlow packing can be built where each label represents a hexagonal layer closely-packed to the adjacent layers. Note that each layer can only be hexagonal since it is the densest packing in two dimensions and the three different layers are related by a translation of the hexagonal center, such that the spheres sit in one of the three types of holes in the adjacent layers. Therefore, the stacking sequence given by allowed combinations of A, B, and C fully determines the Barlow packing. For example, hcp has the stacking sequence $ABABAB\ldots$ continued to infinity, while fcc is $ABCABC\ldots$.

At this point, one has to differentiate between periodic and aperiodic Barlow packings. If a sequence is infinite, then the packing is aperiodic, resembling a structure with randomly stacked hexagonal layers. A periodic Barlow packing with a finite stacking sequence is more relevant for the solid state community due to translational symmetry, i.e., a periodic Barlow packing is a perfect crystal. With the exemption of fcc, a periodic Barlow packing cannot be described by a single lattice vector as defined in Equation (2.1), therefore one needs to extend the concept of a lattice to a n-lattice (or multilattice), where n lattice points are within the fundamental region of the n-lattice.[148] Hence, any point in a D-dimensional n-lattice is given by

$$\mathbf{L}^k(\boldsymbol{\ell}, \{\mathbf{v}_k\}) = \sum_{i=1}^{D} \ell_i \mathbf{a}_i + \mathbf{v}_k, \qquad k = 1, \ldots, n \tag{2.13}$$

where $\{\mathbf{a}_i\}$ is the set of lattice basis vectors, $\{\mathbf{v}_k\}$ is the minimal set of required shift vectors with $\mathbf{v}_1 = \mathbf{0}$, and $\ell_i \in \mathbb{Z}$. In this sense, we can say that fcc is a 1-lattice, hcp is a 2-lattice, and a more complex Barlow packing sequences like $ABAC\ldots$ is a 4-lattice. A more detailed definition for a periodic Barlow packing will be presented in later chapters.

2.1.4 Reciprocal Lattice and First Brillouin Zone

The description of n-lattices so far has been done in real space, but this picture can also be complemented by a description in a dual (or reciprocal) space. This is specially useful when describing the physical properties of periodic arrangements of atoms, such as a Bravais lattice or a Barlow packing. In a n-lattice, the reciprocal space is defined by the underlying Bravais lattice, since the shift vectors do not change the translational symmetry or the unit cell volume of the n-lattice. Therefore, the reciprocal lattice vectors $\mathbf{b}_i$ satisfy

$$\mathbf{b}_i \cdot \mathbf{a}_j = 2\pi\delta_{ij} \tag{2.14}$$

where δ_{ij} is the Kronecker delta and the 2π factor is a convention used in physics such that plane waves can be written simply as $e^{\mathbf{i}\mathbf{k}\cdot\mathbf{r}}$. From the set of vectors $\{\mathbf{b}_i\}$, a reciprocal lattice vector in three dimensions is given by

$$\mathbf{G}(\boldsymbol{\ell}) = \ell_1\mathbf{b}_1 + \ell_2\mathbf{b}_2 + \ell_3\mathbf{b}_3 \tag{2.15}$$

with $\ell_i \in \mathbb{Z}$. For example, we can think of a simple cubic lattice with side a whose reciprocal lattice is another simple cubic with side length equal to $2\pi/a$; the dual lattice of fcc is a bcc lattice of side $4\pi/a$; and the dual of an hexagonal lattice with sides a and c is also an hexagonal lattice rotated by 30° with sides $4\pi/\sqrt{3}a$ and $2\pi/c$.[25]

Since the reciprocal lattice is also a lattice, one can choose a unit cell to form it by translational symmetry from a basis set $\{\mathbf{b}_i\}$. A particularly convenient choice of unit cell that preserves the point symmetries of the lattice is known as the Wigner-Seitz unit cell, however, when working in reciprocal space, its name changes to the first Brillouin zone (1BZ).[25,128,129] This type of unit cell contains only non-equivalent points of space around a lattice site, hence it is a primitive cell and it is independent of the basis vectors used. In other words, the Wigner-Seitz cell and the 1BZ are unique to a lattice and its reciprocal, respectively.

Two points in a lattice will be equivalent if their difference is a lattice vector. For example, $\mathbf{k}_1$ and $\mathbf{k}_2$ are equivalent if $\mathbf{k}_2 - \mathbf{k}_1 = \mathbf{G}(\boldsymbol{\ell})$. This means that a simple way to construct 1BZ is to connect a lattice point to its nearest neighbors by reciprocal lattice vectors and take the perpendicular planes that bisect them. These planes are the boundaries of the first Brillouin zone. In some lattices, however, nearest-neighbor bisectors alone may not create a closed surface, but one can also take the planes bisecting the reciprocal lattice vectors toward next

nearest-neighbors, thus completing the construction of the 1BZ.

Historically, the first Brillouin zone can be traced back to the work of M. J. O. Strutt on vibrations of a string with a periodic mass distribution,[149] which showed that waves in periodic systems possess a band-like spectra, identifying a region of interest for the solutions of the Mathieu-type differential equation posed. Later, L. Brillouin[150] explicitly applied the Wigner-Seitz construction of the unit cell in reciprocal space to the study of Bragg reflection, energy band formation, and wave propagation in solids, establishing the modern definition of the Brillouin zone.

2.2 Quantum Theory of Solids

A complete first-principles understanding of crystalline solids comes, naturally, from the quantum theory. Unfortunately, the exact solution of the many-body problem in quantum mechanics is not possible in general, thus we need to rely on some approximations that are valid in many cases of interest and also will enrich conceptually the theory of the solid state.

2.2.1 The Born-Oppenheimer Approximation and Bloch's Theorem

Let us start by setting up the full many-body time-independent Schrödinger equation for a system composed of N electrons and M positive nuclei with charges Z_α, where $\alpha, \beta, \ldots$ will designate nuclei, can be written, in atomic units, as

$$\hat{\mathcal{H}}\Psi(\mathbf{x},\mathbf{R}) = \left[\hat{\mathcal{T}}_e(\mathbf{r}) + \hat{\mathcal{T}}_n(\mathbf{R}) + \hat{\mathcal{U}}_{ee}(\mathbf{r}) + \hat{\mathcal{U}}_{nn}(\mathbf{R}) + \hat{\mathcal{U}}_{en}(\mathbf{r},\mathbf{R})\right]\Psi(\mathbf{x},\mathbf{R}) = E\Psi(\mathbf{x},\mathbf{R}) \tag{2.16}$$

where E is the total energy of the system, $\mathbf{x}$ denotes all electronic (spatial, $\mathbf{r}$, and spin, σ) coordinates and $\mathbf{R}$ all nuclei coordinates. The first two terms are the kinetic energy operators for the electrons and the nuclei,

$$\hat{\mathcal{T}}_e(\mathbf{r}) = -\sum_i^N \frac{\nabla^2_{\mathbf{r}_i}}{2} \qquad \text{and} \qquad \hat{\mathcal{T}}_n(\mathbf{R}) = -\sum_\alpha^M \frac{\nabla^2_{\mathbf{R}_\alpha}}{2M_\alpha}, \tag{2.17}$$

respectively. The third and fourth term are the electron-electron and nucleus-nucleus repulsion Coulomb potential operators between each one of its species in the system,

$$\hat{\mathcal{U}}_{ee}(\mathbf{r}) = \frac{1}{2}\sum_i^N \sum_{j\neq i}^N \frac{1}{|\mathbf{r}_j - \mathbf{r}_i|} \qquad \text{and} \qquad \hat{\mathcal{U}}_{nn}(\mathbf{R}) = \frac{1}{2}\sum_\alpha^M \sum_{\beta\neq\alpha}^M \frac{Z_\alpha Z_\beta}{|\mathbf{R}_\beta - \mathbf{R}_\alpha|} \tag{2.18}$$

respectively. The last term is, of course, the electron-nucleus attraction potential energy operator,

$$\hat{\mathcal{U}}_{en}(\mathbf{r},\mathbf{R}) = -\sum_{\alpha}^{M}\sum_{i}^{N}\frac{Z_\alpha}{|\mathbf{r}_i - \mathbf{R}_\alpha|} \tag{2.19}$$

The problem of solving Eq. (2.16) quickly becomes intractable when just increasing the number of electrons. A first simplification comes from the expansion of the total wavefunction into an orthonormal set of eigenfunctions $\Psi_i(\mathbf{x};\mathbf{R})$, such that

$$\Psi(\mathbf{x},\mathbf{R}) = \sum_{i}^{\infty}\chi_i(\mathbf{R})\Psi_i(\mathbf{x};\mathbf{R}) \tag{2.20}$$

where the coefficients $\chi_i(\mathbf{R})$ are functions of the nuclear coordinates only. Consequently, the Schrödinger equation for the nuclear motion becomes

$$\left[\nabla^2_{\mathbf{R}} + E_j(\mathbf{R}) - \sum_{i}^{\infty}\sum_{\alpha}^{M}\frac{1}{2M_\alpha}\left\{2\left\langle\Psi_j\left|\nabla_{\mathbf{R}_\alpha}\right|\Psi_i\right\rangle\nabla_{\mathbf{R}_\alpha} + \left\langle\Psi_j\left|\nabla^2_{\mathbf{R}_\alpha}\right|\Psi_i\right\rangle\right\}\right]\chi_j(\mathbf{R}) = E\chi_j(\mathbf{R}) \tag{2.21}$$

The terms inside the curly brackets are called the first and second-order non-adiabatic coupling elements, however, if we are only interested in the ground state of the system, then the non-adiabatic terms can usually be neglected. Thus, the resulting equation,

$$\left[\nabla^2_{\mathbf{R}} + E_j(\mathbf{R})\right]\chi_j(\mathbf{R}) = E\chi_j(\mathbf{R}), \tag{2.22}$$

is to be interpreted as the nuclei moving on a potential energy surface (PES) in which the potential at every point, $E_j(\mathbf{R})$, is defined by solving the electronic Schrödinger equation

$$\hat{\mathcal{H}}_e(\mathbf{r};\mathbf{R})\Psi_i(\mathbf{x};\mathbf{R}) = E_i(\mathbf{R})\Psi_i(\mathbf{x};\mathbf{R}), \qquad i = 1,2,\ldots \tag{2.23}$$

where $\hat{\mathcal{H}}_e = \hat{\mathcal{T}}_e + \hat{\mathcal{U}}_{ee} + \hat{\mathcal{U}}_{en} + \hat{\mathcal{U}}_{nn}$ is the electronic Hamiltonian. This procedure of simplification is called the Born-Oppenheimer approximation[151,152] and it is commonly described as neglecting the kinetic energy of the nuclei due to them being much heavier than electrons ($M_\alpha \gg 1$).

The second step is to find the energies $E_i(\mathbf{R})$ that define the potential energy surface for the nuclei. However, the electronic problem is still extremely difficult to solve without relying on approximations. In this case, the interaction between the electrons is very important, and it is not possible to neglect this term. Nonetheless, there are some models in which the electrons can be treated as independent, but moving under the influence of a mean-field generated by all the other electrons. Two such approximations are known as Hartree-Fock theory and density functional theory; the latter being described in the next section.

In a single-particle approximation, some special features can be found in the Hamiltonian when treating atoms embedded in a lattice. First of all, the translational symmetry of the lattice is inherited to the Hamiltonian through the terms including the positions of the nuclei. Consequently, $\hat{\mathcal{H}}_e$ commutes with all translation operators of the lattice. This implies that the wavefunction of a single particle in a periodic potential becomes

$$\psi_{n\mathbf{k}}(\mathbf{r}) = e^{i\mathbf{k}\cdot\mathbf{r}} u_{n\mathbf{k}}(\mathbf{r}) \tag{2.24}$$

This is the Bloch theorem,[153] where $u_{n\mathbf{k}}$ is a periodic function, n the set of quantum numbers describing the particle and $\mathbf{k}$ can be defined from the constraint on the wavefunction to remain unchanged under any lattice translation, $\hat{\mathcal{T}}_{\mathbf{L}}$. This restriction is equivalent to state that $\mathbf{k}\cdot\mathbf{L} = 2\pi\eta_i$ with $\eta_i \in \mathbb{Z}$ and $i = 1, 2, 3$. Therefore, the vector $\mathbf{k}$ is a reciprocal lattice vector given by

$$\mathbf{k} = \sum_i^3 \frac{2\pi\eta_i}{\ell_i}\mathbf{b}_i \tag{2.25}$$

The following relation holds due to Bloch's theorem: $\psi_{n,\mathbf{k}} = \psi_{n,\mathbf{k}+\mathbf{G}}$, where $\mathbf{G}$ is an arbitrary reciprocal lattice vector of the lattice $\mathscr{L}$. This means that each $\mathbf{k}$ vector within the first Brillouin zone corresponds to different solutions of the Schrödinger equation (if non-degeneracy is assumed).[128]

2.2.2 Kohn-Sham Density Functional Theory

To extract all the potential usefulness of the Bloch theorem, we need a single-particle approach to solve the many-electron problem. One of the most successful methods is density functional theory (DFT), whose foundation was provided by the celebrated Hohenberg-Kohn theorems which shows the one-to-one correspondence between the electron density and the potential generated by the nuclei, thus determining all ground-state properties from just a function of 3 variables.[154]

However, practical applications of DFT became apparent only after the introduction of the Kohn-Sham scheme (KS).[155] This method relies on the use of a non-interacting auxiliary system of particles through one-particle functions which has (in principle) exactly the same one-particle density as the real system, but with the particles moving under the influence of an effective potential which includes all the interactions and correlation of motion between the interacting particles of the real system. Since the wavefunction of a non-interacting system can be written in terms of a Slater determinant, the KS-DFT approach offers an orbital model of atoms and molecules, which extends to solids as electronic bands.[128] Hence, the central

problem is to solve the Kohn-Sham equations

$$\left[-\frac{\nabla^2}{2} + v_{eff}[\rho(\mathbf{r})]\right] \varphi_n(\mathbf{r}) = \varepsilon_n \varphi_n(\mathbf{r}) \tag{2.26}$$

to find the energy eigenvalues, ε_n, and the orbitals, $\varphi_n(\mathbf{r})$. The one-particle density of the system is related to the orbitals through

$$\rho(\mathbf{r}) = \sum_i^N \sum_\sigma |\varphi_i(\mathbf{r}, \sigma)|^2 \tag{2.27}$$

where σ denotes spin coordinates. Note that the effective potential in Eq. (2.26) also depends on the density, therefore the KS equations must be solved self-consistently. The problem, however, is to find the exact form of v_{eff}. The separate contributions to the effective potential are simply terms regarding the electron-nuclei (v_{ne}) and electron-electron interactions, where the latter is divided into two terms: the Hartree potential, v_H, and the exchange-correlation potential, v_{xc}:

$$v_{eff}(\mathbf{r}) = v_{ne}(\mathbf{r}) + \underbrace{\int \frac{\rho(\mathbf{r}')}{|\mathbf{r}' - \mathbf{r}|}\, \mathrm{d}\mathbf{r}'}_{V_H(\mathbf{r})} + v_{xc}(\mathbf{r}) \tag{2.28}$$

Both v_{ne} and v_H potentials can be readily calculated by standard methods, however the exchange-correlation potential is troublesome and some approximations, discussed briefly in the next chapter, are needed. This is one of the main problems to be solved in KS-DFT and the complication is that there is no systematic approach to improve the functional apart from the approximations mentioned. Despite this difficulty, KS-DFT has proved its value by becoming one of the most widely used methods for ab-initio calculations in physics and chemistry.[156,157] This is due to the fact that highly accurate wave-function based quantum chemical methods used commonly for atoms and molecules, such as configuration interaction theory, coupled-cluster theory or the perturbative treatment of electron correlation, cannot be so easily applied to the solid state because of its exorbitant computational costs and divergency problems when the band gap closes (metallic systems).[158]

2.2.3 Relativistic Effects in Solids

Historically, relativistic corrections to the electronic structure of matter were not considered important before the decade of 1970, when Desclaux and Pyykkö demonstrated that the orbital energies (in a Hartree-Fock picture) for transition metal compounds can be heavily influenced by relativistic effects.[159] The only relativistic correction considered to be important was spin-orbit coupling in optical spectra of solid state compounds.[160] However, some hints that

this is not the case were given as early as 1940[161], and later proven by the work of Christiansen and Seraphin.[162]

In an orbital picture of the electronic structure of atoms, relativistic effects make s and, to a lesser extent, $p_{1/2}$ electrons more tightly bound (direct relativistic effect), whereas $p_{3/2}$, d and f electrons become more loosely bound than the non-relativistic counterparts (indirect relativistic effect).[163,164]. When moving from atoms to solids, those effects can play a fundamental role in describing optical properties or phase transitions. For example, band structure calculations on gold show that the excitation energy lies in the middle of the visible range due to relativistic effects, giving gold its characteristic yellow color.[165] Likewise, the melting point of mercury is severely affected when including relativity, making it liquid at room temperature.[166] Even in lead compounds, usually found in car batteries, relativistic effects are important since they explain much of the voltage obtained from the lead-acid-battery reaction.[167]

Actual calculations including relativistic effects can be approximated by neglecting the spin-orbit coupling. This is termed as the scalar relativistic approximation[168] and includes all corrections to the kinetic and potential energies due to the finite speed of light and retardation of the interactions.[169] Spin-orbit coupling, as it names indicates, can be an important factor when discussing the magnetic properties of materials, which appears due to the total angular momentum of the atoms, or in electronic spectra obtained from band structure calculations. Such effects can often be treated perturbatively as they are often suppressed by the intermolecular interactions.

2.3 Interatomic Potentials

After establishing the mathematical theory of lattices for crystalline solids and the quantum theory that governs the electron motion for the atoms in the lattice, the next step is to approximately describe the effective interactions between atoms in the solid, such that they give rise to a reasonably accurate description of physical properties. While Kohn-Sham DFT or more accurate wavefunction methods provide ab initio interatomic forces from the electronic ground state at a given nuclei configuration, it is common practice relying on empirical functions designed to reproduce the essential physical aspects of chemical bonding.

The concept of interatomic force is, strictly speaking, loosely defined since there is not a unique way of decomposing a quantum many-body system into interacting subsystems. Although we can think of a molecule or solid made out of atoms, when they are bonded they become part of an entire correlated system of electrons and nuclei which strongly interact, making the notion of an atom in a molecule or solid relatively vague. Nonetheless, some partition schemes can be devised to gain insight in the bonding properties of a material, for example, Bader's atoms-in-molecules[170–172], Mulliken[173–177] or Löwdin[178,179] population analyses, among many others.

2.3.1 The Many-Body Expansion of the Total Energy

Within the Born-Oppenheimer approximation, this idea of partitioning an entire quantum system becomes more powerful: the electronic degrees of freedom generate the effective PES, parametrized by the nuclear coordinates, $E_j(\mathbf{R})$, that governs nuclear dynamics. Hence, the interatomic potential is an approximation to the Born-Oppenheimer ground-state energy as a function of the nuclear configuration. This is still a highly complex many-body function, $E_j(\mathbf{R})$ with $\mathbf{R} \equiv \{\mathbf{R}_1, \ldots, \mathbf{R}_M\}$, containing many-body interactions of all orders. One way to think of this is to partition the energy as a finite expansion of the type[180–182]

$$E(\{\mathbf{R}\}) = \sum_i E_1(\mathbf{R}_i) + \sum_{i<j} E_2(\mathbf{R}_i, \mathbf{R}_j) + \sum_{i<j<k} E_3(\mathbf{R}_i, \mathbf{R}_j, \mathbf{R}_k) + \ldots \tag{2.29}$$

where E_1 is the energy of the isolated subsystems, E_2 the pair interaction energy, E_3 represents three-body interactions, and so on. For a system of M atoms, this expansion goes up to M-body interactions, and its convergence is problematic for strongly interacting systems such as metals due to the ambiguity of defining the quantum states of all subsystems,[183,184] however it has proven to work well for van der Waals systems, hydrogen-bonded, and aqueous ionic clusters.[183,185,186]

Although the expansion in Equation (2.29) is exact, it is common practice to work with truncated expansions, exchanging accuracy for computational cost. This is specially useful for systems where the leading contributions to cohesion and ground-state geometries are two- and three-body interactions, such as van der Waals solids and hydrogen-bonded and aqueous ionic clusters, as mentioned before.[183,185,186] In such cases, the higher-order terms become much smaller in magnitude and hence they can be neglected. Before 1960, it was assumed that three-body interactions could also be neglected, but the work by Axilrod, Teller, and Muto demonstrated that they can contribute significantly to the stability of the solid phase.[187–190]

Since, in the absence of external fields, the two-body term depends only on the internuclear distance, $E_2 = E_2(|\mathbf{R}_j - \mathbf{R}_i|)$, the forces on each atom are additive, unlike higher-order terms, which depend on the geometry of multiple atoms simultaneously. It has been found that structural and thermodynamical properties of some rare-gas solids are well represented by two-body potentials only, even at high pressures and in the liquid state,[191] however, non-additive forces are needed to accurately reproduce internal energies, enthalpy, and pressure.[104,108,192,193] Thus, one can use experimental data and reliable two-body potentials to calculate the extent of non-additive forces in solids.

Two main approaches can be taken in order to design reliable two-body potentials: 1) generating an effective pair potential that reproduces structural and thermodynamical properties, and 2) using a true pair potential that accurately reproduces the second virial coefficient. The first approach is more extensively used, even though a potential designed to

work in the bulk may be inaccurate for surfaces, liquids, and gases. For the second approach, one can use Mayer's cluster expansion[194–197] to relate the virial coefficients to two-, three-, and many-body interactions. For example, the second virial coefficient for two spherical molecules as a function of the temperature T is

$$B_2(T) = -\frac{1}{2}\int_0^\infty 4\pi r^2 \left[e^{-\beta\phi_2(r)} - 1\right] \, \mathrm{d}r \tag{2.30}$$

where $\beta = 1/k_B T$, k_B is the Boltzmann constant, and $\phi_2(r)$ is a two-body potential as a function of the interatomic distance r. Although it seems that a pair potential could be reconstructed from experimental data on $B_2(T)$ alone, it has been shown that this is only possible if the potential is monotonic.[198] A remedy for this is assuming an analytical form for $\phi_2(r)$ with few adjustable parameters and fit the function to $B_2(T)$. In principle, knowledge of higher-order virial coefficients would help quantifying many-body effects, however the convergence of the virial expansion can be problematic due to the existence of phase transitions.[199]

An effective two-body, or empirical, potential with parameters fitted to experimental data may incorporate part of the many-body contributions to the total energy of the system, limiting its transferability to other phases[32] or predictability of properties outside the fitting region. However, the analytical form of an empirical potential can be useful to obtain insight on the physical forces that are acting in the system. For example, the repulsion at short distances and attraction at long distances. Indeed, by using perturbation theory, London showed that long-range forces between atoms with closed valence shells yield an additive interaction proportional to R^{-6}, with R the interatomic distance.[200]

2.3.2 Model Interaction Potentials

At distances greater than the dimensions of the molecules involved, the electrostatic energy of two interacting molecules can be expanded as a series in powers of $1/R$, known as the multipole expansion.[201] The terms describing multipole-multipole interactions are well-known from classical electrodynamics,[202] however, when considering two interacting quantum systems, the delocalization and overlap between the charge distributions is non-negligible even at long-distances. Therefore, it is necessary to consider polarization (induction and dispersion) and exchange interactions. Retardation[203–205] and magnetic[206,207] interactions can also play a role in some systems. It has been shown, using perturbation theory to second order, that the multipole expansion for the dispersion energy can be written as a series[180]

$$E_{\mathrm{disp}} = -\sum_{n=6}^{\infty} \frac{C_n}{R^n} \tag{2.31}$$

where C_n are called dispersion coefficients. For interactions between atoms, the leading term, $n = 6$, is related to dipole-dipole interactions, the $n = 8$ term are for dipole-quadrupole interactions and $n = 10$ accounts for quadrupole-quadrupole and dipole-octupole interactions. When it comes to molecules, odd powers may also be involved.

The case of exchange interactions is more complicated since it depends on the nature of the interacting subsystems. It has been found[208] that for two closed-shell atoms, the exchange interaction can be approximated by the exponentially decaying repulsive term $Ae^{-\alpha R}$, with parameters A and α. On the other hand, for atoms with an open shell, the exchange energy can be negative, contributing to the attraction that forms a covalent bond. Nonetheless, in the short-range, the force between two atoms is strongly repulsive due to the Pauli exclusion principle and strong nuclear repulsion.

The simplest model for the interaction between atoms of the same type that consider the short-range repulsion is the hard-sphere model,

$$\phi_{\mathrm{HS}}(R) = \begin{cases} \infty & \text{if } R \leq r_0 \\ 0 & \text{if } R > r_0 \end{cases} \tag{2.32}$$

where r_0 is the radius of the hard sphere. This leads, for example, to a volume corrected ideal gas equation. A modification of this model can include a rectangular well of depth ε and width σ,[209,210] which in the limit of no width becomes a sticky hard-sphere model, also called a kissing hard-sphere.[211] Although the hard-sphere model can give some qualitatively sound results,[212–215] a physically more appealing model includes the attraction from the dispersion interaction at large distances while keeping the hard-core. This is the Sutherland potential,[216]

$$\phi_{\mathrm{Su}}(R) = \begin{cases} \infty & \text{if } R \leq r_0 \\ \frac{C_6}{R^6} & \text{if } R > r_0 \end{cases} \tag{2.33}$$

that has been found to be in reasonable agreement with experimental data of the second virial coefficient.[217]

A better approach is to introduce a "softer" repulsive term that varies with the internuclear distance. One of the earliest examples that has had great success in molecular simulations is the so-called Mie-Grüneisen potential (also called general Lennard-Jones potential)[218,219],

$$\phi_{\mathrm{MG}}(R) = \frac{A_n}{R^n} - \frac{B_m}{R^m} \tag{2.34}$$

where A_n and B_n are parameters to be determined. One of the most widely used form of this potential is the Lennard-Jones (LJ) potential with $n = 12$ and $m = 6$,[220,221] incorporating the dipole-dipole term of dispersion in its attractive part and a repulsive term that was

originally introduced due to computational convenience.[180] For a historical account on the Lennard-Jones potential see Schwerdtfeger and Wales.[222] If the minimum of the potential is fixed to match the diatomic equilibrium distance r_e and its depth is ε, then the potential can be written in the form

$$\phi_{\mathrm{LJ}}(R) = \frac{\varepsilon n m}{n-m}\left[\frac{1}{n}\left(\frac{r_e}{R}\right)^n - \frac{1}{m}\left(\frac{r_e}{R}\right)^m\right] \tag{2.35}$$

with $n > m > 3$. These kind of potentials have been used extensively to describe the cohesive energy of rare-gas solids[220,221,223] with quantitatively not very precise results. However, their use in Monte Carlo and Molecular Dynamics simulations have given valuable insights and shown reasonable agreement with experimental data, and have been used even for systems other than the noble gases.[224]

One of the alternatives that incorporate a more realistic repulsive term is the 4-parameter Buckingham potential,[180,225]

$$\phi_{\mathrm{Bu}}(R) = Ae^{-\alpha R} - \frac{B}{R^6} - \frac{C}{R^8} \tag{2.36}$$

that also includes attractive dipole-dipole and dipole-quadrupole terms for the dispersion interaction. However, the exponential term makes the calculations more difficult in infinite lattice summations. This is why it can be more convenient to work with inverse powers of the internuclear distance in a way that both the long-range tails and the repulsive part are fairly well represented. This motivates the use of an extended Lennard-Jones class of potentials[226]

$$\phi_{\mathrm{ELJ}}(R) = \sum_n \frac{c_n}{R^n} \tag{2.37}$$

where $n > 3$ to ensure the convergence of the cohesive energy for a three-dimensional bulk system,[221,227] and the c_n's are parameters for fitting. The determination of the parameters can be done through experimental data as well as highly accurate ab initio calculations for the dimers involved, leading to predictions of thermodynamical data in agreement with experiment.[228–230] The lattice summations can be done to computer accuracy with the use of special techniques in treating the Epstein zeta function as described further below.

2.4 Lattice Thermodynamics

After having settled what kind of interactions are required between the atoms in the description of a solid (either through fitted interatomic potentials or ab initio potential energy surfaces), the next step is to associate its microscopic properties to thermodynamic properties with the tools of statistical mechanics. The general thermodynamic requirement for a solid to be stable is that its internal energy, U, is a minimum at equilibrium (in the case of finite temperatures, $T > 0$K

the free energy has to be minimized). This can be associated to relations between constant pressure heat capacities/bulk moduli and their constant volume counterparts.

From a microscopic approach, the stability can be related to the elastic properties of the crystal lattice, for example, by using Born's stability criteria.[231,232] However, it is important to notice that a real crystal is not static, even at 0 K. The zero-point energy and the excitation of the normal modes at high temperatures greatly influences thermodynamic properties such as heat capacity, thermal expansion, elastic moduli, sound propagation, melting, interaction with electromagnetic radiation, and phase transformations.[25,233] Even a static property as the cohesive energy can be altered by considering the zero-point energy. This is why a good description of the properties of a solid needs to include lattice dynamical aspects.

Let $\mathbf{L}(\boldsymbol{\ell})$ be a lattice vector of $\mathscr{L}$ written in the basis $\{\mathbf{a}_i | i = 1,2,3\}$ with r atoms in the unit cell. The position of the α-th atom in the $\boldsymbol{\ell}$-th unit cell is given by

$$\mathbf{x}_\alpha(\boldsymbol{\ell}) = \mathbf{L}(\boldsymbol{\ell}) + \mathbf{s}_\alpha(\boldsymbol{\ell}) \tag{2.38}$$

where $\mathbf{s}_\alpha(\boldsymbol{\ell})$ is the position of atom α in the unit cell $\boldsymbol{\ell}$ with respect to the lattice points. If there is just one atom in the unit cell, then $\mathbf{x}_\alpha(\boldsymbol{\ell}) = \mathbf{L}(\boldsymbol{\ell})$. The total kinetic energy of the crystal is

$$T_{\mathscr{L}} = \sum_{\boldsymbol{\ell},\alpha} \frac{\mathbf{p}_\alpha(\boldsymbol{\ell})^2}{2m_\alpha} = \frac{1}{2} \sum_{\boldsymbol{\ell},\alpha\mu} \frac{p_{\alpha\mu}(\boldsymbol{\ell})^2}{m_\alpha} \tag{2.39}$$

where m_α is the mass of the α-th atom, $\mathbf{p}_\alpha$ its momentum, and $\mu \in \{x, y, z\}$.

On the other hand, the potential energy is a function of the atomic positions that, in the general case, can include many-body interactions. Here, for simplicity and without loss of generality, only two-body forces will be considered, however the theory remains in the same form while the potential depends on the atomic positions only. Let $\phi(\mathbf{r})$ be the interaction potential between a pair of atoms separated by $\mathbf{r}$. Then, the total potential energy of the crystal is

$$\begin{aligned} V_{\mathscr{L}} &= \frac{1}{2} \sum_{\boldsymbol{\ell}\alpha} \sum_{(\boldsymbol{\ell}',\beta)\neq(\boldsymbol{\ell},\alpha)} \phi\left(\mathbf{x}_\alpha(\boldsymbol{\ell}) - \mathbf{x}_\beta(\boldsymbol{\ell}')\right) \\ &= \frac{1}{2} \sum_{\boldsymbol{\ell}\alpha} \sum_{(\boldsymbol{\ell}',\beta)\neq(\boldsymbol{\ell},\alpha)} \phi\left(\mathbf{x}_\alpha^{(eq)}(\boldsymbol{\ell}) - \mathbf{x}_\beta^{(eq)}(\boldsymbol{\ell}') + \mathbf{u}_\alpha(\boldsymbol{\ell}) - \mathbf{u}_\beta(\boldsymbol{\ell}')\right) \\ &\equiv \frac{1}{2} \sum_{\boldsymbol{\ell}\alpha} {\sum_{\boldsymbol{\ell}'\beta}}' \phi_{\alpha\beta}(\boldsymbol{\ell},\boldsymbol{\ell}') \end{aligned} \tag{2.40}$$

where $\mathbf{u}_\alpha(\boldsymbol{\ell}) = \mathbf{x}_\alpha(\boldsymbol{\ell}) - \mathbf{x}_\alpha^{(eq)}(\boldsymbol{\ell})$ is the atomic displacement of atom α from the equilibrium position in the lattice.

Although the Hamiltonian, $H_{\mathscr{L}} = T_{\mathscr{L}} + V_{\mathscr{L}}$, is specified by Equations (2.39) and (2.40), the solution of the equations of motion for a many-body problem like this is unfeasible either at the

classical or quantum level. Therefore, it is common to assume that the atomic displacements from equilibrium positions are small compared to the lattice constants. This allows a Taylor expansion of the potential around $\left\{\mathbf{x}_\alpha^{(eq)}(\boldsymbol{\ell})\right\}$ such that

$$V_{\mathscr{L}} = V_{\text{eq}} + \frac{1}{2}\sum_{\boldsymbol{\ell}\alpha}\sum_{\boldsymbol{\ell}'\beta}\underbrace{\left(\frac{\partial^2\phi_{\alpha\beta}(\boldsymbol{\ell},\boldsymbol{\ell}')}{\partial\mathbf{u}_\alpha(\boldsymbol{\ell})\partial\mathbf{u}_\beta(\boldsymbol{\ell}')}\right)_{\mathbf{u}=\mathbf{0}}}_{\Phi_{\alpha\beta}(\boldsymbol{\ell},\boldsymbol{\ell}')}\mathbf{u}_\alpha(\boldsymbol{\ell})\mathbf{u}_\beta(\boldsymbol{\ell}') + \dots \tag{2.41}$$

where the first derivatives vanish at equilibrium and the second derivatives $\Phi_{\alpha\beta}(\boldsymbol{\ell},\boldsymbol{\ell}')$ are called force constants, that can be related to experimental data as parameters. A further approximation is to truncate the expansion up to second order, in what is called the harmonic approximation.[231]

Three remarks need to be made here. First, the potential energy when the atoms are at the equilibrium positions is important when discussing static properties of the lattice, such as the cohesive energy, its equilibrium size or equilibrium compressibility, but irrelevant for lattice vibrations. Second, we usually want to study the ground-state of the crystals, meaning that the atomic vibrations are with respect to minimum energy configurations and thus all frequencies derived from the force constants should be positive. Otherwise, the lattice might be, for instance, in a transition state. Third, in most cases of importance, the equations of motion for a crystal in the harmonic approximation are exactly solvable.[25] Therefore, if an analytical expression for ϕ is given, then all force constants are determined by the parameters in the potential. For example, the general (n,m)-LJ potential has four parameters (n, m, ε and r_e) that can be fitted to experimental data to get the force constant matrix and hence all thermodynamic properties of the crystal within that model.

When there is no analytical form of the potential and its derivatives, a numerical error can be introduced in the elements of the force constant matrix. This might seem as a small error that can be neglected at first, but the sum over many terms may lead to unphysical consequences. Therefore, it is important that some exact constraints are fulfilled. Firstly, the system has to obey Newton's third law, which implies[234,235]

$$\Phi_{\alpha\mu,\beta\nu}(\boldsymbol{\ell},\boldsymbol{\ell}') = \Phi_{\beta\nu,\alpha\mu}(\boldsymbol{\ell}',\boldsymbol{\ell}) \tag{2.42}$$

where $\mu,\nu \in \{x,y,z\}$. If the force constants are not symmetric under pair exchange, some spurious non-real valued phonon frequencies may appear,[236] as will be shown later when defining the dynamical matrix. To avoid this situation, numerical noise and cutoff truncation errors can be corrected by enforcing symmetry

$$\Phi_{\alpha\mu,\beta\nu}(\boldsymbol{\ell},\boldsymbol{\ell}') \leftarrow \frac{1}{2}\left(\Phi_{\alpha\mu,\beta\nu}(\boldsymbol{\ell},\boldsymbol{\ell}') + \Phi_{\beta\nu,\alpha\mu}(\boldsymbol{\ell}',\boldsymbol{\ell})\right) \tag{2.43}$$

For the second constraint, let $\mathbf{u}_\alpha = \mathbf{w}$ be a constant rigid displacement for all atoms α. The total potential energy is unchanged under this displacement, which means that there is no net restoring force on each atom of the crystal under this uniform shift. Hence, the force on atom α is

$$F_{\alpha\mu} = -\sum_{\beta,\nu} \Phi_{\alpha\mu,\beta\nu}(\boldsymbol{\ell},\boldsymbol{\ell}')u_{\beta\nu} = -w_\nu \sum_{\beta} \Phi_{\alpha\mu,\beta\nu}(\boldsymbol{\ell},\boldsymbol{\ell}') = 0 \tag{2.44}$$

In other words, the center of mass of the system does not undergo a displacement without the action of an external force, i.e., the total momentum of the system is conserved and the potential energy is translationally invariant due to Noether's theorem.[237] In the solid-state literature, this is also referred to as the acoustic sum rule (ASR):[231,235,238]

$$\sum_{\boldsymbol{\ell}'\beta} \Phi_{\alpha\mu,\beta\nu}(\boldsymbol{\ell},\boldsymbol{\ell}') = 0 \tag{2.45}$$

for all α, μ, ν. A further physical consequence of the ASR is that there are at least three phonon modes that are exactly zero at the Γ point.[128] In case the ASR is not fulfilled, one can calculate the off-site blocks of the force constant matrix $\Phi_{\alpha\mu,\beta\nu}$ with $\beta \neq \alpha$ and then set the on-site block to[234]

$$\Phi_{\alpha\mu,\alpha\nu}(\boldsymbol{\ell},\boldsymbol{\ell}) = -\sum_{(\boldsymbol{\ell}',\beta)\neq(\boldsymbol{\ell},\alpha)} \Phi_{\alpha\mu,\beta\nu}(\boldsymbol{\ell},\boldsymbol{\ell}') \tag{2.46}$$

which automatically enforces the acoustic sum rule, even though a cutoff radius for the interaction is set. A further constraint can be imposed, namely, rotational invariance[235,239], which leads to conservation of angular momentum. However, since a rigid rotation is not a normal mode under Born-von Karman boundary conditions, breaking this symmetry does not destabilize the system beyond introducing small numerical errors in the sound velocities calculated from the phonon spectrum.[240]

To obtain the dispersion relations, it is necessary to solve the equation of motion of the crystal in the harmonic approximation. This can be done either classically or in the Heisenberg-picture of quantum mechanics (after defining an appropriate displacement operator and setting up the commutation relations with the momentum operator), both forms leading to the same differential equation[25,128]

$$m_\alpha \ddot{u}_{\alpha\mu}(\boldsymbol{\ell}) = -\sum_{\boldsymbol{\ell}'\beta} \Phi_{\alpha\mu,\beta\nu}(\boldsymbol{\ell},\boldsymbol{\ell}')u_{\beta\nu}(\boldsymbol{\ell}') \tag{2.47}$$

The periodicity of the lattice allows us to assume plane wave solutions of the form

$$u_{\alpha\mu}(t) = A_{\alpha\mu}(\mathbf{k})e^{\mathrm{i}(\mathbf{k}\cdot\mathbf{L}+\omega t)} \tag{2.48}$$

where $\mathbf{k}$ is a vector in reciprocal space, since they are eigenfunctions of the translation operators.

Then, one can obtain the following generalized eigenvalue problem

$$\sum_{\boldsymbol{\ell}',\beta} \Phi_{\alpha\mu,\beta\nu}(\boldsymbol{\ell},\boldsymbol{\ell}') A_{\beta\nu}(\mathbf{k}) e^{\mathbf{i}\mathbf{k}\cdot(\mathbf{L}'-\mathbf{L})} = m_\alpha \omega^2 A_{\alpha\mu}(\mathbf{k}) \tag{2.49}$$

where ω is the frequency of the vibration branch. This can be simplified to a simple eigenvalue problem by defining the dynamic matrix

$$D_{\alpha\mu,\beta\nu}(\mathbf{k}) = \frac{1}{\sqrt{m_\alpha m_\beta}} \sum_{\boldsymbol{\ell}'} \Phi_{\alpha\mu,\beta\nu}(\boldsymbol{\ell},\boldsymbol{\ell}') e^{\mathbf{i}\mathbf{k}\cdot(\mathbf{L}'-\mathbf{L})} \tag{2.50}$$

at every $\mathbf{k}$-point. In other words, the dynamical matrix is the discrete Fourier transform of the force constant matrix. Since the equations of motion, Equation (2.47), couple the movement of all atoms in all unit cells and the lattice is periodic, the Fourier transform to reciprocal space block-diagonalizes the initial matrix problem and then decouples the different wavevectors $\mathbf{k}$.[128] As a consequence, the eigenvectors of $D(\mathbf{k})$ define the normal modes (also called polarization vectors) of vibration, that behave like independent phonons in the harmonic approximation. The eigenvalues of the jth-mode of vibration are the frequencies $\omega_j(\mathbf{k})^2$, where j runs from 1 to $3r$, with r the number of atoms in the unit cell. The modes are classified as acoustic modes, where $\omega_j \to 0$ as $|\mathbf{k}| \to 0$, and optical branches, with a finite ω_j at $\mathbf{k} = \mathbf{0}$.

The thermodynamic properties of the lattice in the harmonic approximation can be obtained from the partition function[241]

$$Z = \mathrm{Tr}\left(e^{-\hat{H}/k_B T}\right) = \prod_{\mathbf{k},j} \frac{e^{-\hbar\omega_j(\mathbf{k})/2k_B T}}{1 - e^{-\hbar\omega_j(\mathbf{k})/k_B T}} \tag{2.51}$$

From this, we can write the Helmholtz free energy of the oscillators as

$$F = -k_B T \ln Z = \sum_{\mathbf{k},j} \left[\frac{\hbar\omega_j(\mathbf{k})}{2} + k_B T \ln\left(1 - e^{-\hbar\omega_j(\mathbf{k})/k_B T}\right)\right] \tag{2.52}$$

and the vibrational entropy as

$$S_{\mathrm{vib}} = -\left(\frac{\partial F}{\partial T}\right) = -k_B \sum_{\mathbf{k},j} \left[\frac{\hbar\omega_j(\mathbf{k})/k_B T}{1 - e^{\hbar\omega_j(\mathbf{k})/k_B T}} + \ln\left(1 - e^{-\hbar\omega_j(\mathbf{k})/k_B T}\right)\right] \tag{2.53}$$

These two expressions allow the calculation of the free energy and entropy due to lattice vibrations after knowing the phonon dispersion curves $\omega_j(\mathbf{k})$ from the force constants.

2.5 Phase Transitions in the Solid State

Up to this point, the stability of a crystal is determined by the interatomic interactions and lattice dynamics, however, the question of what happens when the structure is not a minimum energy one remains open. The thermodynamic quantity of interest is the free energy (either Helmholtz or Gibbs), which is the driving force of any change to occur. Although an elemental solid can have two or more crystal structures that are local minima, the one with the lowest energy is thermodynamically preferred. All states can transform to the minimum energy structure, provided the energy to overcome the barrier in between, by means of thermal vibrations, deformation or electromagnetic radiation.

In the molecular domain, a transition between to local minimum structures are described through a minimum energy path (MEP) on a potential hypersurface $E(\xi_i)$. Here ξ_i are the $3N-6$ internal coordinates ($3N-5$ for a linear molecule) of a molecule composed of N atoms, usually representing bond lengths, bond angles and torsion angles. One specific point along the MEP is called the transition state, which can be thought as a "point of no-return" when going from the initial structure to the final state.[242] This picture can be adopted for the structural phase transitions in the solid state as well, where the parameter set ξ_i contains all independent lattice parameters (6 for the unit cell and $3r$ for the r atoms in the unit cell).

The first classification of phase transitions was introduced by Eherenfest in 1933 according to the behavior of the free energy along a transformation.[243] A nth-order phase transition exhibits a discontinuity in the n-th derivative of the free energy at the transition point, where it was initially thought of the existence of only first- and second-order phase transitions. The modern definition for first-order transitions involve latent heat and coexistence of phases,[244] whereas a second-order transition is a continuous symmetry-breaking distortion, often described by an order parameter in Landau theory,[245] as discussed below.

2.5.1 Martensitic Transformations

Unlike melting or vaporization, a diffusionless (martensitic) phase transition in the solid state preserves the atomic connectivity throughout the transformation between two crystal structures.[34] This means that the transition pathway can be represented by a continuous deformation of the initial lattice into the final structure, thus imposing geometric and mechanical constraints in the lattice parameters, angles, and internal atomic coordinates. As a consequence, the mechanism of transformation is tied to symmetry relations between the space groups of the two phases.

The transformation mechanism between two crystals of the same element is severely affected by the interactions between the atoms involved. This adds an extra layer of complexity to microscopically describe martensitic transformations, therefore relying on phenomenological

theories that describe either the crystallography or the energetics of the transformation, but usually not simultaneously.[246,247] Nonetheless, it is generally accepted that the atoms rearrange concertedly by means of the nucleation of a new phase inside the initial phase, even if the kinetics of the transformation differs due to changes in the initial conditions.[246]

A martensitic transformation is generally considered a first-order phase transition since it is accompanied by latent heat, however, it is very closely related to a soft-mode-driven structural transformation,[248–250] which can be of first or second order. In the latter case, as the system approaches the phase transition, the frequencies of the so-called "soft mode" decrease anomalously, triggering a lattice instability.[248,249] Even though the role of soft modes has been criticized,[251] both types of phase transformations can be phenomenologically described by the Landau theory of phase transitions.

2.5.2 Landau Theory of Phase Transitions

The structural changes in a phase transition may also be accompanied by sudden changes in the physical properties. A good example of this is iron, which at ambient conditions adopts the ferromagnetic α form (bcc), but at high temperature the paramagnetic γ form (fcc).[64] Further, when α-Fe is at a temperature above 771° C (its Curie temperature), it becomes paramagnetic, meaning that a significant structural change is not mandatory to get different physical properties.

From a thermodynamic point of view, a phase transition can be characterized according to, at least, the internal energy and the entropy together with the temperature, volume and pressure. Let us assume that a phase A, with a highly symmetry structure, is more stable at high temperature than B, a low symmetry phase. When cooling the system and below a critical temperature, the transition $A \rightarrow B$ implies a symmetry breaking process. In other words, a sudden change in some property of the system.[128] Since thermodynamic variables, such as temperature, pressure or volume, vary continuously across the transition, it is better to introduce additional degrees of freedom by means of a set of order parameters χ which change drastically across the transition. For instance, the magnetization can be an order parameter in the ferromagnetic-paramagnetic phase transition of iron.

A phenomenological approach to describe phase transitions is the Landau theory,[245] which considers the free energy as an analytic function of a certain order parameter χ such that it can be expressed as

$$G(T,\chi) - G_0 = g_2(T)\chi^2 + \frac{g_4(T)\chi^4}{2} + \dots \tag{2.54}$$

The order parameters are assumed to be small around the transition point and only even powers of χ contribute since the free energy should be symmetric in going from $A \rightarrow B$ or $B \rightarrow A$. If we consider just two terms as shown in Eq. (2.54), then $g_4 > 0$ to have a stable phase

and a change in the sign of g_2 will be associated to the transition point between the two phases.

Landau theory has provided a good understanding of phase transitions in general, for example, the behavior of magnetic materials near the phase transitions or crystals close to the melting point,[252–255] however the parameters involved are generally unknown. Some approaches have been given to find explicit expressions of the parameters from a microscopic theory, but they can only be considered as a starting point. This is because the energy difference between two or more phases can be very small and, hence, a general quantitative microscopic explanation of phase transitions is still needed.

2.5.3 Transformation Between Cubic Lattices and hcp

As mentioned before, the geometric constraints on the transformation are characteristic of the structural transformations between two crystals. The exact pathway depends on the chemical nature of the system being investigated, however, there are some general transformation mechanisms that serve as good examples of diffusionless transformations (martensitic or non-martensitic).

The first mechanism was proposed by Bain in 1924 to describe the transformation from a bcc to a fcc structure (or vice versa) of iron and steels through a homogeneous deformation.[256] It can be seen as a tetragonal distortion of the fcc lattice, characterized by a compression along one axis and a expansion in the orthogonal directions. That is, the underlying symmetry of the mechanism follows a body-centered tetragonal (bct) lattice.[257,258] Although this mechanism predicts specific orientations between parents and product phases that are not seen in steels, the bct deformation is correctly describing the process. The bcc-to-fcc transformation has been studied under many approaches,[97,259–261] but, not long ago, a microscopic framework has been proposed to explain the lattice deformation for atoms interacting through Lennard-Jones potentials[126] and lithium from DFT calculations[127].

Another mechanism was proposed for the bcc to hcp transformation by Burgers in 1934, when studying the phase transition of zirconium.[262] This transformation is more complicated because the hcp structure is not a Bravais lattice. Hence, the Burgers mechanism is composed of two steps: first, a stretch along the $[110]_{\text{bcc}}$ direction while compressing the $[001]_{\text{bcc}}$ direction, and then an atomic shuffle that produces the ABAB stacking sequence of hcp. The transformation has also been studied with different approaches for many systems[263–266], however exact mechanism is still under debate since some studies hint the possibility of a direct path to fcc instead.[267–269]

Chapter 3

Computational Methods

In this chapter, all methods used to calculate the different properties of a system will be described in general terms. The detailed explanation of the application of these methods to each problem formulated for this work will be subject of the next chapters together with the corresponding results, however the discussion of the fundamentals will also provide an implicit justification for the choice of such methods.

3.1 Ab Initio Methods

One of the most widely used and powerful tools to study the behavior of many-body systems in the solid state from first principles is the KS-DFT framework.[270,271] This section briefly discusses the approximations used in density functional theory and their limitations in explaining solid state properties.

3.1.1 Density Functional Approximations

As discussed previously, the main problem of KS-DFT is to find the exact form of the exchange-correlation potential, which is equivalent to solve exactly the many-body Schrödinger equation. This is still an active research field and some approximations to v_{xc} have been found since the early days of KS-DFT.[272,273] The simplest functional is found under the local-density approximation (LDA), where the electron density is considered uniform within a small volume. The total exchange-correlation energy can then be approximated as[274–276]

$$E_{xc}^{\mathrm{LDA}}[\rho] = \int \rho(\mathbf{r})\varepsilon_{xc}[\rho]\ \mathrm{d}\mathbf{r} \tag{3.1}$$

where ε_{xc} is the exchange-correlation energy density. From this, the exchange-correlation potential is obtained from

$$v_{xc}^{\mathrm{LDA}}(\mathbf{r}) = \frac{\delta E_{xc}^{\mathrm{LDA}}[\rho]}{\delta\rho(\mathbf{r})} = \varepsilon_{xc}[\rho] + \rho(\mathbf{r}) \left(\frac{\partial \varepsilon_{xc}}{\partial \rho}\right)_{\rho=\rho(\mathbf{r})} \tag{3.2}$$

with the derivative being calculated using explicit expressions for ε_{xc}, which has been extensively developed with the aid of Monte Carlo simulations.[277] In principle, this simple approximation should be only applicable to systems where the density varies slowly, however it has proven to be mildly reliable for atoms and molecules and relatively good for metallic systems, but in general not enough to obtain highly accurate quantitative results.[275]

One way to improve LDA is to include the gradient of the electron density in the exchange-correlation energy functional. This approach, called generalized gradient approximation (GGA), will add a non-local content to v_{xc} and overcome some drawbacks found in LDA, such as overbinding due to the so-called delocalization error[278,279] or the electron self-interaction problem. It is worth noting that GGA functionals, specially the one developed by Perdew-Burke-Ernzernhof (PBE),[280] have been so successful in solid-state physics that they have become the standard approach in computational materials science.[281]

Yet, further improvements over GGA have been developed towards the goal of more accurate descriptions of electron systems. They are usually categorized in hierarchy as a ladder[282], with the next rung including the kinetic energy density to the exchange-correlation functional. This is the meta-GGA class of density functionals and yield highly accurate ground-state energies for molecules and solids. Recently, the SCAN meta-GGA functional[283] and its variations have shown to be very reliable for solids in general.[284] A different approach, more popular in the chemistry community and often associated to a higher rung in the ladder, is the use of hybrid functionals that mix the exact Hartree-Fock exchange with the one obtained from GGAs.[285,286]

3.1.2 Dispersion-Corrected DFT

When it comes to include weak interactions between atoms or molecules, such as van der Waals forces, most density functional approximations are not able to describe the long-range correctly.[287,288] This is, indeed, the case for the rare gas dimers and rare gas solids, where it has been pointed out that in general LDA functionals overestimate dissociation energies, while the application of GGA functionals produce repulsive potential energy curves.[289,290] The nature of dispersion interactions is intrinsically non-local, which explains why local and semi-local density functionals fail at providing a proper description of them.

Among the existing methods overcoming this difficulty, one of the most used is Grimme's DFT-D approach[291], which is basically an additive energy correction to the KS-DFT

self-consistent calculation and allows an efficient treatment of dispersion for large systems. The main idea is the inclusion of two-body interaction terms that depend on the inverse sixth and eight powers of the distance between a pair of atoms A and B, respectively. In one of the most successful methods, known as DFT-D3(BJ),[292] the general form of the dispersion energy is given by

$$E_{\text{disp}} = -\frac{1}{2}\sum_{A\neq B}\sum_{n=6,8}\frac{s_n C_n^{AB}}{r_{AB}^n + f^n(R_{AB}^0)} \tag{3.3}$$

with $R_{AB}^0 = \sqrt{C_8^{AB}/C_6^{AB}}$, and a_1 and a_2 being free-fit parameters controlling the dispersion correction in the regime from short- to medium-range and they are adjusted for each density functional approximation.

An overall improvement of the optimized geometries and thermochemistry can be obtained when combining the D3(BJ) corrections with different types of density functionals, from the GGA level to the upper rungs in Jacob's ladder.[293] Furthermore, this method can be easily extended to periodic systems by relying on the translational symmetry of crystal structures. For a given lattice with lattice vectors $\mathbf{L}$, the dispersion energy is written as

$$E_{\text{disp}} = -\frac{1}{2}\sum_{A\neq B}\sum_{n=6,8}\frac{s_n C_n^{AB}}{|\mathbf{r}_{AB}+\mathbf{L}|^n + f^n(R_{AB}^0)} \tag{3.4}$$

where $\mathbf{r}_{AB}$ is the distance vector between atoms in the same unit cell.

3.2 Lattice Sums for Close-Packed Structures

The evaluation of the physical properties of a system of atoms in a lattice interacting through model potentials can be done after having some knowledge of the geometrical properties of the lattice. A well-known example of this is the calculation of the lattice energy of an ionic crystal with Coulomb interactions between the ions forming it, where the electrostatic potential is defined in terms of the lattice parameters and the Madelung constant.[115] A similar procedure will apply in the case of LJ systems.

Since in many cases the interaction potentials depend on the distance between the particles, it is helpful to represent the lattice characteristics in terms of its quadratic forms. As described by Conway and Sloane,[28] the arithmetical properties of a lattice can be conveniently studied through quadratic forms, which represent an alternative language of lattices. Following this purpose, let $\mathbf{x}$ be a lattice vector of a three-dimensional lattice with basis vectors $\{\mathbf{a}_i\}$, generator matrix $\boldsymbol{B}$ and Gram matrix $\boldsymbol{G}$. Then, $\mathbf{x}$ can be written as

$$\mathbf{x} = \sum_n^3 i_n \mathbf{a}_n = \boldsymbol{B}^\top \mathbf{i} \tag{3.5}$$

where $\mathbf{i}$ is an arbitrary vector with integer components. The norm of this vector is the quadratic form associated with the lattice,[28]

$$q(\mathbf{i}) = \mathbf{i}^\top \boldsymbol{B}\boldsymbol{B}^\top \mathbf{i} = \mathbf{i}^\top \boldsymbol{G}\mathbf{i} = \sum_{\mu,\nu} i_\nu i_\mu \mathbf{a}_\mu \cdot \mathbf{a}_\nu \tag{3.6}$$

For two-body interactions depending just on interparticle distances, the total potential energy can easily be taken as the sum over all lattice points of the system, and here is where the quadratic forms become useful. Let us consider a two-body potential $\phi_2(r_{ij})$ as an inverse power law of the distance, r_{ij}^{-s}, between two lattice point i and j with some fixed exponent $s \in \mathbb{R}_+$. The calculation of the total potential energy of a crystal can be reduced, by means of the symmetries of a given crystal structure, to a geometrical constant (the lattice sum) times the distance of a lattice point from the origin. This is exactly the case to obtain the lattice energy of an ionic crystal in terms of the Madelung constant and the lattice parameters.[115,129] Nonetheless, special care has to be taken with the type of potential, since it can lead to an arbitrary constant which is defined by a conditionally convergent series according to Riemann's rearrangement theorem.[294] As we have

$$\sum_k r_k^{-s} = \left(\sum_{\mathbf{i}\in\mathbb{Z}^3} q^{-s}(\mathbf{i}) \right) r_0^{-s} \equiv L(s) r_0^{-s} \tag{3.7}$$

where the lattice points are located at distances r_k from a selected atom, on the right-hand side the sum is reduced to a lattice sum $L(s)$ multiplied by the nearest neighbor distance from the origin, r_0.

Explicit analytical formulas have been reported for different types of crystals, with special emphasis on sc, bcc, fcc and hcp structures. The relevant lattice sums for this work are listed below.[295]

$$\begin{aligned}
L_{\mathrm{fcc}}(s) &= {\sum_{\mathbf{i}\in\mathbb{Z}^3}}' \left(i_1^2 + i_2^2 + i_3^2 + i_1 i_2 + i_1 i_3 + i_2 i_3 \right)^{-s} \\
L_{\mathrm{bcc}}(s) &= {\sum_{\mathbf{i}\in\mathbb{Z}^3}}' \left(i_1^2 + i_2^2 + i_3^2 - \frac{2}{3}(i_1 i_2 + i_1 i_3 + i_2 i_3) \right)^{-s} \\
L_{\mathrm{hcp}}(s) &= {\sum_{\mathbf{i}\in\mathbb{Z}^3}}' \left(i_1^2 + i_2^2 + i_1 i_2 + \gamma^2 i_3^2 \right)^{-s} \\
&\quad + {\sum_{\mathbf{i}\in\mathbb{Z}^3}}' \left[\left(i_1 + \frac{1}{3} \right)^2 + \left(i_2 + \frac{1}{3} \right)^2 + \left(i_1 + \frac{1}{3} \right)\left(i_2 + \frac{1}{3} \right) + \gamma^2 \left(i_3 + \frac{1}{2} \right)^2 \right]^{-s}
\end{aligned} \tag{3.8}$$

where $\gamma = c/a$ in the hcp structure, which has the ideal value of $\sqrt{\frac{8}{3}}$.

It is noteworthy to point out that the use of efficient lattice sums is not restricted to two-body

inverse power potentials, but can also be extended to certain types of many-body interactions. One example, that will be shown in later chapters, is the Axilrod-Teller-Muto triple dipole interaction obtained from third-order perturbation theory.[187,188] The dependence on inverse powers of the internuclear distance makes plausible the use of such lattice sums, however the convergence and efficient calculation methods need to be developed.

3.3 Fast Converging Expansions

At first sight, the evaluation of the lattice sums for inverse power potentials seems to be straightforward, but actually it can be fairly troublesome to converge the series for small exponents s. Much work has been done on this topic since the seminal work of Lennard-Jones and Ingham,[112,220,221,296] who used Epstein zeta functions to get an accuracy in the summation of $L(s)$ up to 10^{-4}. Further improvement has made by Zucker[297] by means of the Mellin integral transformation reaching a convergence threshold of 10^{-8} and, more recently, Burrows et al[295] reported the evaluation of lattice sums up to computer precision (10^{-14}) within less of a second of computer time using an expansion in terms of Bessel functions.

Specifically, the expansion methods express the lattice sums as series of modified Bessel functions of the second kind of real order ν, which is defined as[298]

$$K_\nu(x) = \frac{1}{2}\int_0^\infty u^{\nu-1} e^{-x(u+u^{-1})/2}\,\mathrm{d}u \qquad \text{for } |\arg x| < \frac{\pi}{2} \tag{3.9}$$

This function has a symmetry property with respect to its order, $K_\nu(x) = K_{-\nu}(x)$, and, since the higher order Bessel functions can be reduced to lower orders by

$$K_\nu(x) = \frac{2(\nu-1)}{x} K_{\nu-1}(x) + K_{\nu-2}(x), \tag{3.10}$$

all of them can be cast in terms of K_0, K_1 and $K_{1/2}$. The fast convergence of the series containing Bessel functions is due to their asymptotic exponential decay,

$$K_\nu(x) \propto \sqrt{\frac{\pi}{2x}} e^{-x}\left(1 + \mathcal{O}\left(\frac{1}{x}\right)\right) \tag{3.11}$$

for $|x| \to \infty$.

3.3.1 Expansion Methods

It has been pointed out[112] that the lattice sums in Eq. (3.8) are special cases of the Epstein zeta functions:[111,113]

$$Z(s, \mathbf{g}, \mathbf{h}) = \sum_{\mathbf{l}}{}' \frac{e^{-2\pi i \mathbf{h}\cdot\mathbf{l}}}{q^{s/2}(\mathbf{l}+\mathbf{g})} \tag{3.12}$$

where the prime indicates that the term $\mathbf{l} = -\mathbf{g}$ is omitted if $\mathbf{g}$ is a lattice vector and $q(\mathbf{l})$ is a quadratic form. An alternative definition, in terms of $\boldsymbol{M}$ (a $n \times n$ positive definite real matrix) and ξ (a complex variable with $\Re(\xi) > n/2$) is[299]

$$Z(\boldsymbol{S}_n, \xi) = \frac{1}{2}{\sum_{a\in\mathbb{Z}}}' \left(\mathbf{a}^\top \boldsymbol{S}_n \mathbf{a}\right)^{-\xi} \tag{3.13}$$

This latter form makes more explicit the relation between the Epstein zeta and the lattice sums in Eq. (3.8). For example, if $\boldsymbol{S}$ is the Gram matrix of the fcc lattice, $\boldsymbol{G}$, then $Z(\boldsymbol{G}, s)$ is just twice its lattice sum. Indeed, this is the basis of the first expansion method developed by Terras, in which the Epstein zeta function for a symmetric positive definite 3×3 matrix $\boldsymbol{S}_3$ is decomposed as[299]

$$\begin{aligned} Z(\boldsymbol{S}_3, s) = {} & \frac{\pi\Gamma(s-1)t^{1-s}}{\Gamma(s)\sqrt{\det S_2}}\zeta(2s-2) + \frac{p^{\frac{1}{2}-s}\Gamma(s-\frac{1}{2})}{\Gamma(s)}\sqrt{\frac{\pi}{\sigma_{22}}}\zeta(2s-1) + \frac{\zeta(2s)}{\sigma_{22}^s} \\ & + \frac{4\pi^s}{\Gamma(s)}\left(\frac{p^{1-2s}}{\sigma_{22}^{1+2s}}\right)^{1/4} \sum_{u,v\in\mathbb{N}} \left(\frac{v}{u}\right)^{s-\frac{1}{2}} \cos\left(\frac{2\pi\sigma_{12}uv}{\sigma_{22}}\right) K_{s-\frac{1}{2}}\left(2\pi uv\sqrt{\frac{p(\alpha)}{\sigma_{22}}}\right) \\ & + \frac{2\pi^s}{\Gamma(s)}\sqrt{\frac{t^{1-s}}{\det S_2}} \sum_{\substack{u\in\mathbb{N} \\ \mathbf{w}\in\vec{\mathbb{Z}}^2\setminus\{\vec{0}_2\}}} \cos\left(2\pi u\mathbf{w}^\top\mathbf{y}\right) u^{1-s}\left(\mathbf{w}^\top \boldsymbol{S}_2^{-1}\mathbf{w}\right)^{\frac{s-1}{2}} K_{s-1}\left(2\pi u\sqrt{t\mathbf{w}^\top S_2^{-1}\mathbf{w}}\right) \end{aligned} \tag{3.14}$$

Here $\boldsymbol{S}_3$ has been block-diagonalized to obtain the (2×2) symmetric sub-matrix $\boldsymbol{S}_2 = (\sigma_{ij})$,

$$\boldsymbol{S}_3 = \begin{pmatrix} m & \mathbf{z}^\top \\ \mathbf{z} & S_2 \end{pmatrix} = \begin{pmatrix} 1 & \mathbf{y}^\top \\ \mathbf{0}_2 & \boldsymbol{I}_2 \end{pmatrix} \begin{pmatrix} t & \mathbf{0}_2^\top \\ \mathbf{0}_2 & \boldsymbol{S}_2 \end{pmatrix} \begin{pmatrix} 1 & \mathbf{0}_2^\top \\ \mathbf{y} & \boldsymbol{I}_2 \end{pmatrix} \tag{3.15}$$

and $\mathbf{y}$, $\mathbf{z}$ are simple 2-vectors. This gives the relations,

$$\mathbf{z} = \boldsymbol{S}_2\mathbf{y} \quad \Longrightarrow \quad \mathbf{y} = \boldsymbol{S}_2^{-1}\mathbf{z} \tag{3.16}$$

and

$$m = t + \mathbf{y}^\top \boldsymbol{S}_2\mathbf{y} \quad \Longrightarrow \quad t = m - \mathbf{z}^\top \boldsymbol{S}_2^{-1}\mathbf{z} \tag{3.17}$$

with $t \neq 0$ and

$$\boldsymbol{S}_2^{-1} = \det(\boldsymbol{S}_2)^{-1} \begin{pmatrix} \sigma_{22} & -\sigma_{12} \\ -\sigma_{12} & \sigma_{11} \end{pmatrix} \tag{3.18}$$

The other parameters and functions are defined as follows,

$$p = \left\{\sigma_{11} - \frac{\sigma_{12}^2}{\sigma_{22}}\right\} \tag{3.19}$$

Another expansion technique was developed by van der Hoff and Benson to write a series in terms of another series involving Bessel $K_\nu(x)$ functions,[300] making them as efficient as the Terras' expansion.

$$\sum_{i\in\mathbb{Z}}\left[x^2+(i+\zeta)^2\right]^{-s}=\frac{\sqrt{\pi}\Gamma(s-\frac{1}{2})}{\Gamma(s)\,|x|^{2s-1}}+\frac{4\pi^s}{\Gamma(s)}\sum_{n\in\mathbb{N}}\left(\frac{n}{|x|}\right)^{s-\frac{1}{2}}\cos(2\pi n\zeta)K_{s-\frac{1}{2}}(2\pi n|x|) \tag{3.20}$$

3.3.2 Theta Function Transformation

Yet another method of transforming the inverse s-th power terms in the lattice sums to series of Bessel K_ν functions is by using the gamma function, $\Gamma(s)$ with $s>0$, in the form[294]

$$q^{-s}=\frac{1}{\Gamma(s)}\int_0^\infty x^{s-1}e^{-qx}\,\mathrm{d}x \tag{3.21}$$

The form of q will be determined for each lattice sum studied here, but it should be pointed out that, in general, it is possible to find terms of the form i^2+ij+j^2 within q. This is specially useful because the exponential within the integral of Eq. (3.21) will contain terms that can be related to the theta functions and, more importantly, to the transformation formula

$$\sum_{i,j\in\mathbb{Z}}e^{-2\pi\left(i^2+ij+j^2\right)x}=\frac{1}{x\sqrt{3}}\sum_{i,j\in\mathbb{Z}}e^{-2\pi\left(i^2+ij+j^2\right)/3x} \tag{3.22}$$

and its variants. After some algebraic manipulation of the full quadratic forms, the integral in Eq. (3.21) will have exponential terms of the form $e^{-ax-b/x}$, which can be evaluated in terms of Bessel K_ν functions according to the relation

$$\int_0^\infty x^{s-1}e^{-ax-b/x}\,\mathrm{d}x=2\left(\frac{b}{a}\right)^{s/2}K_s\left(2\sqrt{ab}\right) \tag{3.23}$$

The details of the transformation process have been applied in previous studies for the hcp structure[294] and will be omitted here for brevity.

3.4 Optimization Methods for Crystal Structures

The evaluation of the energy through either density functional theory or lattice sums is just the first step towards a quantitative analysis of elemental solids. The next step is to know what lattice parameters minimize the energy of the system. For example, the bcc lattice has a defined geometry, but the volume of the cell can be changed by varying the sides of the cube. Likewise, an ideal hcp cell has two parameters that can change its volume: the length of hexagonal sides, a, and the height of the unit cell c.

The interactions of the atoms in the lattice can change the lattice parameters and, in some cases, the ideal structures are not even local minima, but approximations to it.[103,107] The optimization of the unit cell then becomes an important task prior to make quantitative predictions. In this setting, the energy of the system becomes a real function of all variable lattice parameters $\{\xi_i\}$, thus knowledge and understanding of the mathematical properties of the energy landscape is essential when choosing an optimization method.

In many cases, the energy function around an equilibrium configuration of a crystal exhibits a locally convex structure.[231] In other words, the existence of a minimum in that region is guaranteed and a solution via a gradient-based optimization can be computationally efficient. In general, smoothness conditions, such as Lipschitz continuity, provide insights on the variation of the parameters of the energy function and, hence, the convergence rate of the algorithm chosen.[301]

Two types of optimization algorithms were used here: gradient-based methods[302] and Bayesian optimization[303]. In general, one starts the process by defining either an initial guess, x_0, of the crystal structure or by providing bounds to the parameters of the unit cell and then the algorithm chooses a starting point. Thereafter, a sequence of steps are generated such that it terminates when the optimized point has been reached to within certain accuracy, or no further progress can be made. The next point, x_k, in the sequence is calculated by knowledge of the function at the previous step, x_{k-1}.

3.4.1 Gradient-Based Optimization

One of the approaches to create the sequence of solutions $\{x_i\}$ is to choose a direction p_k to find the next value x_k while satisfying $f(x_{k-1}) > f(x_k)$. That is, each iteration is given by[302]

$$x_{k+1} = x_k + \alpha_k p_k \tag{3.24}$$

where α_k is a positive constant that regulates how big is the step in the direction p_k. For a minimization, the direction has to be a descent direction that satisfies $p_k^\top \nabla f_k < 0$. The form of the search direction depends on the specific algorithm, but in general it is given by[302]

$$p_k = -\boldsymbol{B}_k^{-1} \nabla f_k \tag{3.25}$$

where $\boldsymbol{B}_k$ is a symmetric non-singular matrix which is positive definite in a descent direction. Three optimization methods use this form, namely, Steepest Descent (SD, with $\boldsymbol{B}_k = \boldsymbol{I}$), Newton-Raphson (NR, with $\boldsymbol{B}_k = \boldsymbol{H}(f_k)$, that is, the exact Hessian of the function at point x_k), and Broyden-Fletcher-Goldfarb-Shanno[304–308] (BFGS, $\boldsymbol{B}$ is an approximation to the Hessian that gets updated at each step).

In any case, the step length, when optimal, can lead to a substantial reduction of the

optimization iterations by finding the appropriate x_{k+1} that brings the function as close to the extremum (e.g. minimum) as possible at that step. Finding the optimal step length for each iteration may be too expensive to perform, hence it is common practice to rely on inexact line searches for the step length. A common criterion for sufficient decrease in the objective function f is the Armijo condition[309]

$$f(x_k + \alpha p_k) \leq f(x_k) + c_1 \alpha \nabla f_k^\top p_k \tag{3.26}$$

where $c_1 \in (0, 1)$ is the Armijo constant, often chosen to be small ($c_1 \approx 10^{-4}$). To actually choose the step length, a backtracking approach is taken which relies on the Armijo condition to terminate the search. In the backtracking procedure, the initial step length is multiplied by a constant $\rho \in (0, 1)$ for a finite number of trials until it becomes small enough such that Equation (3.26) is satisfied. This strategy has proven to be well suited with Newton and quasi-Newton methods, such as BFGS.[302]

3.4.2 Bayesian Optimization

When analytical gradients are not available, gradient-based optimization methods can become time consuming due to several function evaluations to obtain numerical gradients. This could be specially troublesome when performing DFT calculations at very high accuracy and the parameter space for optimization is large. Another issue here is the presence of noise due to limited accuracy, which could possibly decrease the quality of numerical gradients and even the function evaluation. Note that the energy differences in solid-solid phase transitions are tiny compared to the cohesive energy of each phase and very close to the computational accuracy of density functional approximations. A further difficulty could be the existence of kinks or discontinuities in the energy landscape, also associated to phase transitions.

To avoid all these computational complexities, we could start by assuming that the electronic energy with respect to the parameters is a black-box function, i.e., there is no analytical expression and no knowledge of its derivatives, defined on a bounded and compact domain $\mathcal{X}$, such that $f : \mathcal{X} \to \mathbb{R}$. Let $\phi = f(x)$ for $x \in \mathcal{X}$. Due to the noisy energy evaluations, we can assume that the value obtained, y, after sampling f at a point x is distributed according to an observation model $p(y|x, \phi)$ that has to be carefully designed. For example, one can use a Gaussian observation model[310] in which sampling at a point x gives the value $y = \phi + \varepsilon$, where ε is the error associated to the function evaluation, and the error follows a Gaussian distribution with mean zero. Hence, the observation model is

$$p(y|x, \phi, \sigma_n) = \frac{1}{\sqrt{2\pi\sigma_n^2}} e^{-(x-\phi)^2/2\sigma_n^2} \equiv \mathcal{N}(y; \phi, \sigma_n^2) \tag{3.27}$$

where σ_n is the observation noise scale (or standard deviation of the distribution). On the other hand, if function evaluations are exact, then $y = \phi$, and the observation model becomes a Dirac delta distribution.

The uncertainty in the sampling of the energy can be handled using Bayesian inference.[311] For this, a prior process containing all assumptions about f is established, then, an evaluation of the objective function at the point $\vec{x}$ in parameter space is performed to refine the prior and derive, through Bayes' theorem[312,313], a posterior process. This is the first stage of Bayesian optimization.[303]

The actual optimization machinery starts after defining an acquisition function that tells us how good is a potential observation location. This becomes useful when reducing the uncertainty about the critical points of the objective function, since the next step is doing the observation at $\vec{x}'$. This optimization method relies on the optimization of the acquisition functions, which are cheaper to evaluate compared to the original objective function. Therefore, a single complex problem is reduced to multiple simple problems and, in this case, the computationally more demanding step is just the energy evaluation with DFT.

3.5 Dynamical Matrix

The calculation of the dynamical matrix at each **k**-point within the irreducible Brillouin zone can be computationally demanding. When it comes to lattice vibrations, one of the simplest approximations is called the Einstein model, which assumes that all atoms vibrate independently at the same frequency ω_E.[314] That is, the dispersion relation is a constant in reciprocal space. Although it reproduces the Dulong-Petit law[315] at high temperature, it is not qualitatively correct at low temperatures and at describing acoustic modes of vibration. The Einstein model may be unrealistic for elemental solids,[231] but more suitable in molecular crystals where the internal molecular vibrations have higher frequencies (stronger restoring forces) than lattice vibrations. This makes the optical branches relatively flat and independent of the wave-vector **k**. Nevertheless, since around $\mathbf{k} = \mathbf{0}$ (the Γ point of the lattice) the optical branches are somewhat flat, the Einstein model works reasonably well to describe them.

As has been pointed out early in the theory of lattice dynamics, the atoms in a solid oscillate collectively as propagating waves.[231,316] Therefore, knowledge of the full phonon dispersion in the Brillouin zone gives a much better picture of the lattice vibrations, which allows an accurate calculation of the zero-point energy and the stability of lattices at finite temperatures.

3.5.1 Sampling the Dynamical Matrix in the Irreducible Brillouin Zone

The determination of the force constants from first principles relies upon the solution of the equations of motion of the lattice (see Equation (2.47)). When turning these equations into a

matrix problem, the force constant matrix becomes a $3N \times 3N$ matrix, with N the number of atoms in the whole crystal.[128] For example, consider the central potential $\phi(r)$. The elements of the force constant matrix are given by

$$\Phi_{\alpha\mu,\beta\nu}(\boldsymbol{\ell},\boldsymbol{\ell}') = \left(\frac{\partial^2\phi(r)}{\partial x_{\alpha\mu}\partial x_{\beta\nu}}\right) = \frac{x_{\alpha\mu}(\boldsymbol{\ell})x_{\beta\nu}(\boldsymbol{\ell}')}{r^2}\left(\frac{\partial^2\phi(r)}{\partial r^2} - \frac{1}{r}\frac{\partial\phi(r)}{\partial r}\right) + \frac{\delta_{\mu\nu}}{r}\frac{\partial\phi(r)}{\partial r} \tag{3.28}$$

where $\delta_{\mu\nu}$ is the Kronecker delta. Clearly, for a macroscopic sample with $N \approx 10^{23}$, the calculation of all $\Phi_{\alpha\mu,\beta\nu}$'s must be a very computationally demanding task. One approach to this is to truncate the crystal to a finite number of unit cells, forming a supercell.[128] The size of the supercell will determine how many coupled equations to solve, and this should be carefully determined by studying the convergence of the properties and by ensuring that the constraints mentioned in Section 2.4 (Newton's third law and ASR) are fulfilled. Further disadvantages of the real-space method above is the numerical noise accumulation, which may propagate across all points in the Brillouin Zone.

An alternative approach is by diagonalizing the dynamical matrix at each **k**-point. Since each **k**-point poses an independent eigenvalue problem, there is no error propagation across the Brillouin zone and a system with long-range interactions may converge more smoothly.

3.5.2 Dynamical Matrix at the Γ Point

When working with inverse-power-law potentials, it is possible to simplify lattice dynamics to an Einstein-like model with few vibration frequencies, depending on the symmetry of the lattice. For example, in a cubic lattice, this procedure reduces to the Einstein model with only one frequency for all atoms. The idea is to calculate the frequencies only at the center of the Brillouin zone, therefore obtaining only optical frequencies, in order to exploit efficient evaluation methods of lattice sums.

At the Γ point of the lattice, that is $\mathbf{k} = \mathbf{0}$, the dynamical matrix is

$$D_{\alpha\mu,\beta\nu}(\mathbf{0}) = \frac{1}{\sqrt{m_\alpha m_\beta}}\sum_{\mathbf{R}}\Phi_{\alpha\mu,\beta\nu}(\mathbf{R}) \tag{3.29}$$

The absence of the phase factor physically means that all unit cells are moving in phase. If the unit cell contains two atoms or more, they can either move in a symmetric way (uniform translation of the lattice associated to an acoustic mode) or in an asymmetric way, which leads to optical modes. In other words, for two atoms α and β, acoustic modes are symmetric under the exchange $\alpha \leftrightarrow \beta$, whereas optical modes are antisymmetric under this operation.

The dynamical matrix for two atoms in a unit cell is a 6×6 matrix that can be separated into

on-site and off-site blocks, such that

$$\boldsymbol{D} = \begin{pmatrix} \boldsymbol{D}_{\alpha\alpha} & \boldsymbol{D}_{\alpha\beta} \\ \boldsymbol{D}_{\beta\alpha} & \boldsymbol{D}_{\beta\beta} \end{pmatrix} \tag{3.30}$$

where each block is a 3×3 matrix. At the Γ point, the polarization vectors become $e_{\alpha\mu} = \sqrt{m_\alpha} u_{\alpha\mu}$. We can find a basis in which the dynamical matrix is block-diagonal by defining the following displacement vectors

$$\mathbf{u}^{(+)} = \frac{\mathbf{u}_\alpha + \mathbf{u}_\beta}{\sqrt{2}} \qquad \text{and} \qquad \mathbf{u}^{(-)} = \frac{\mathbf{u}_\alpha - \mathbf{u}_\beta}{\sqrt{2}} \tag{3.31}$$

where $\mathbf{u}_\alpha$ is the displacement vector of atom α around its equilibrium position and we assume that $m_\alpha = m_\beta$. Hence, the transformation between the two vectors is

$$\begin{pmatrix} \mathbf{u}_\alpha \\ \mathbf{u}_\beta \end{pmatrix} = \boldsymbol{F} \begin{pmatrix} \mathbf{u}^{(+)} \\ \mathbf{u}^{(-)} \end{pmatrix} \tag{3.32}$$

with

$$\boldsymbol{F} = \frac{1}{\sqrt{2}} \begin{pmatrix} 1_3 & 1_3 \\ 1_3 & -1_3 \end{pmatrix} = \boldsymbol{F}^\top \tag{3.33}$$

The similarity transformation of the dynamical matrix then leads to

$$\boldsymbol{D}' = \boldsymbol{F}^\top \boldsymbol{D} \boldsymbol{F} = \begin{pmatrix} \boldsymbol{D}_{\alpha\alpha} + \boldsymbol{D}_{\alpha\beta} & 0 \\ 0 & \boldsymbol{D}_{\alpha\alpha} - \boldsymbol{D}_{\alpha\beta} \end{pmatrix} = \begin{pmatrix} \boldsymbol{D}^{(+)} & 0 \\ 0 & \boldsymbol{D}^{(-)} \end{pmatrix} \tag{3.34}$$

When working with hcp, we can use the hexagonal symmetry of the unit cell to further simplify the dynamical matrix which allows splitting the frequencies into in-plane and out-of-plane modes. Since the main rotation axis is along the z axis, we have, due to hexagonal symmetry,

$$\begin{pmatrix} u_x \\ u_y \\ u_z \end{pmatrix} = \boldsymbol{R}_\theta \begin{pmatrix} u_x \\ u_y \\ u_z \end{pmatrix} = \begin{pmatrix} \cos\theta & -\sin\theta & 0 \\ \sin\theta & \cos\theta & 0 \\ 0 & 0 & 1 \end{pmatrix} \begin{pmatrix} u_x \\ u_y \\ u_z \end{pmatrix} \tag{3.35}$$

Since a 60° rotation about the z axis cannot change the potential energy in the crystal, we have $\boldsymbol{D}' = \boldsymbol{R}_\theta^\top \boldsymbol{D} \boldsymbol{R}_\theta$, thus the similarity-transformed dynamical matrix has to be a diagonal matrix of

the form

$$\boldsymbol{D}' = \begin{pmatrix} \xi^{(+)} & 0 & 0 & 0 & 0 & 0 \\ 0 & \xi^{(+)} & 0 & 0 & 0 & 0 \\ 0 & 0 & \chi^{(+)} & 0 & 0 & 0 \\ 0 & 0 & 0 & \xi^{(-)} & 0 & 0 \\ 0 & 0 & 0 & 0 & \xi^{(-)} & 0 \\ 0 & 0 & 0 & 0 & 0 & \chi^{(-)} \end{pmatrix} \tag{3.36}$$

where $\xi^{(\pm)} = D_{\alpha x,\alpha x} \pm D_{\alpha x,\beta x}$ and $\chi^{(\pm)} = D_{\alpha z,\alpha z} \pm D_{\alpha z,\beta z}$.

For a central force $\phi_n(r) = \frac{c_n}{r^n}$, we have

$$\begin{aligned} \Phi_{\alpha\mu,\beta\nu}(\mathbf{R}) &= -\left[\left(\phi_n''(r) - \frac{\phi_n'(r)}{r}\right)\frac{R_\mu R_\nu}{r^2} + \frac{\phi_n'(r)}{r}\delta_{\mu\nu}\right] \\ &= -nc_n\left[\left(\frac{n+2}{r^{n+2}}\right)\hat{R}_\mu\hat{R}_\nu - \frac{\delta_{\mu\nu}}{r^{n+2}}\right] = -nc_n\left[f_n(r)\hat{R}_\mu\hat{R}_\nu + g_n(r)\delta_{\mu\nu}\right] \end{aligned} \tag{3.37}$$

where $\hat{\mathbf{R}} = \mathbf{R}/r = \mathbf{R}/|\mathbf{R}|$ is the unit vector pointing from atom α to atom β. All terms containing $\hat{R}_\mu\hat{R}_\nu$ do not depend on the magnitude of $\mathbf{R}$, but in its direction.

Hence, to calculate the frequencies we encounter terms of the form

$$D_{\alpha x,\alpha x} = \frac{-nc_n}{m_\alpha}\sum_{\mathbf{R}\neq 0} f_n(r)\hat{R}_x^2 + g_n(r) \qquad \text{and} \qquad D_{\alpha x,\beta x} = \frac{-nc_n}{\sqrt{m_\alpha m_\beta}}\sum_{\mathbf{R}} f_n(r)\hat{R}_x^2 + g_n(r) \tag{3.38}$$

$$D_{\alpha z,\alpha z} = \frac{-nc_n}{m_\alpha}\sum_{\mathbf{R}\neq 0} f_n(r)\hat{R}_z^2 + g_n(r) \qquad \text{and} \qquad D_{\alpha z,\beta z} = \frac{-nc_n}{\sqrt{m_\alpha m_\beta}}\sum_{\mathbf{R}} f_n(r)\hat{R}_z^2 + g_n(r) \tag{3.39}$$

We can perform the summation over shells of symmetry-equivalent neighbors. Since $\hat{R}_x^2 = \sin^2\theta\cos^2\varphi$ and $\hat{R}_z^2 = \cos^2\theta$, in the hexagonal plane we have $\left\langle \hat{R}_x^2 \right\rangle_\varphi = (1-\cos^2\theta)/2$. The terms containing the angular dependence can be written in terms of Legendre polynomials such that

$$\left\langle \hat{R}_x^2 \right\rangle_\varphi = \frac{1 - P_2(\cos\theta)}{3} \qquad \text{and} \qquad \hat{R}_z^2 = \frac{1 + 2P_2(\cos\theta)}{3} \tag{3.40}$$

If we define the lattice constants

$$L_s^{(0,\alpha\alpha)} = \sum_{\mathbf{R}\neq 0} r_{\alpha\alpha}(\mathbf{R})^{-s} \tag{3.41}$$

$$L_s^{(0,\alpha\beta)} = \sum_{\mathbf{R}} r_{\alpha\beta}(\mathbf{R})^{-s} \tag{3.42}$$

$$L_s^{(2,\alpha\alpha)} = \sum_{\mathbf{R}\neq 0} P_2(\cos\theta) r_{\alpha\alpha}(\mathbf{R})^{-s} \tag{3.43}$$

$$L_s^{(2,\alpha\beta)} = \sum_{\mathbf{R}} P_2(\cos\theta) r_{\alpha\beta}(\mathbf{R})^{-s} \tag{3.44}$$

where $r_{\alpha\beta}(\mathbf{R}) = \left|\mathbf{R} + \boldsymbol{\tau}_\beta - \boldsymbol{\tau}_\alpha\right|$, we can write the lattice sums appearing in the dynamical matrix as

$$\sum_{\mathbf{R}} \frac{\hat{R}_x^2}{r^s} = \frac{L_s^{(0)} - L_s^{(2)}}{3} \qquad \text{and} \qquad \sum_{\mathbf{R}} \frac{\hat{R}_z^2}{r^s} = \frac{L_s^{(0)} + 2L_s^{(2)}}{3} \tag{3.45}$$

Therefore, we have

$$\begin{aligned} D_{\alpha x,\alpha x} &= \frac{-nc_n}{m_\alpha}\left[(n+2)\left(\frac{L_{n+2}^{(0,\alpha\alpha)} - L_{n+2}^{(2,\alpha\alpha)}}{3}\right) - L_{n+2}^{(0,\alpha\alpha)}\right] \\ &= \frac{-nc_n}{m_\alpha}\left[\left(\frac{n-1}{3}\right)L_{n+2}^{(0,\alpha\alpha)} - \left(\frac{n+2}{3}\right)L_{n+2}^{(2,\alpha\alpha)}\right] \end{aligned} \tag{3.46}$$

$$D_{\alpha x,\beta x} = \frac{-nc_n}{\sqrt{m_\alpha m_\beta}}\left[\left(\frac{n-1}{3}\right)L_{n+2}^{(0,\alpha\beta)} - \left(\frac{n+2}{3}\right)L_{n+2}^{(2,\alpha\beta)}\right] \tag{3.47}$$

$$\begin{aligned} D_{\alpha z,\alpha z} &= \frac{-nc_n}{m_\alpha}\left[(n+2)\left(\frac{L_{n+2}^{(0,\alpha\alpha)} + 2L_{n+2}^{(2,\alpha\alpha)}}{3}\right) - L_{n+2}^{(0,\alpha\alpha)}\right] \\ &= \frac{-nc_n}{m_\alpha}\left[\left(\frac{n-1}{3}\right)L_{n+2}^{(0,\alpha\alpha)} + \left(\frac{2(n+2)}{3}\right)L_{n+2}^{(2,\alpha\alpha)}\right] \end{aligned} \tag{3.48}$$

$$D_{\alpha z,\beta z} = \frac{-nc_n}{\sqrt{m_\alpha m_\beta}}\left[\left(\frac{n-1}{3}\right)L_{n+2}^{(0,\alpha\beta)} + \left(\frac{2(n+2)}{3}\right)L_{n+2}^{(2,\alpha\beta)}\right] \tag{3.49}$$

The $(+)$ sector of the dynamical matrix give raise to the acoustic modes that are zero at the Γ point, hence we only consider the optical modes $(-)$ to calculate the frequencies for hcp.

$$\omega_\parallel^2 = \xi^{(-)} = D_{\alpha x,\alpha x} - D_{\alpha x,\beta x} \tag{3.50}$$

$$\omega_\perp^2 = \chi^{(-)} = D_{\alpha z,\alpha z} - D_{\alpha z,\beta z} \tag{3.51}$$

This model can be easily expanded to lower-symmetry lattices or n-lattices, but the number of frequencies will increase according to the degrees of freedom in each case.

3.5.3 Density Functional Perturbation Theory

When the potential does not have an explicit analytical form but is obtained from ab initio methods, the evaluation of the force constant matrix can be made by two different methods: the direct method[317–319] and density functional perturbation theory (DFPT).[320,321] In the first method, a supercell is employed to calculate the energy change after displacing the atoms from the equilibrium positions and the dynamical matrix is calculated numerically. On the other hand, one can avoid the use of supercells with DFPT and calculate the response of the system to physical perturbations (such as phonons, applied electric fields, among others) from energy

derivatives to, in principle, any order within DFT. This latter method will be employed here.

Within the DFPT framework, the entries of the force constant matrix are given by[128]

$$\frac{\partial^2 E}{\partial u_i \partial u_j} = \frac{\partial^2 v_{nn}}{\partial u_i \partial u_j} + \int \left(\frac{\partial^2 v(\mathbf{r})}{\partial u_i \partial u_j} \right) \rho(\mathbf{r}) \, \mathrm{d}\mathbf{r} + \int \left(\frac{\partial \rho(\mathbf{r})}{\partial u_i} \right) \left(\frac{\partial v(\mathbf{r})}{\partial u_j} \right) \, \mathrm{d}\mathbf{r} \tag{3.52}$$

where v_{nn} is the nucleus-nucleus interaction potential. The first two terms can be calculated easily since they only require the atomic positions and the electron density at equilibrium. However, the third term involving the derivative of the density with respect to the atomic displacements can be challenging. Nonetheless, within KS-DFT this derivative can be obtained from the properties of the system at equilibrium and the primitive unit cell, such that

$$\frac{\partial \rho(\mathbf{r})}{\partial u_i} = \sum_a^{occ} \sum_r^{virt} \frac{2}{\varepsilon_r - \varepsilon_a} \left[\left\langle \varphi_a \left| \frac{\partial v_{KS}(\mathbf{r})}{\partial u_i} \right| \varphi_r \right\rangle \varphi_r^*(\mathbf{r}) \varphi_a^*(\mathbf{r}) + c.c. \right] \tag{3.53}$$

Since the KS potential is related to the density, this calculation has to be done self-consistently. The advantage of this method is that obtaining the derivative of the density is at the same computational cost as the energy calculation itself, including the use of symmetry in the unit cell.

MASSEY UNIVERSITY
TE KUNENGA KI PŪREHUROA
UNIVERSITY OF NEW ZEALAND

GRADUATE RESEARCH SCHOOL

STATEMENT OF CONTRIBUTION
DOCTORATE WITH PUBLICATIONS/MANUSCRIPTS

We, the student and the student's main supervisor, certify that all co-authors have consented to their work being included in the thesis and they have accepted the student's contribution as indicated below in the Statement of Originality.			
Student name:	Andres Eduardo Robles Navarro		
Name and title of main supervisor:	Peter Schwerdtfeger		
In which chapter is the manuscript/published work?	Chapter 4		
Describe the contribution that the student and members of the supervisory team have made to the manuscript/published work:[1] All the computations were performed by me with the guidance of Paul Jerabek. The theoretical development is equally divided between me and Peter Schwerdtfeger.			
Please select one of the following three options:			
◉	**The manuscript/published work is published or in press** Please provide the full reference of the research output: Angewandte Chemie International Edition, 2024, 63(1): e202313679		
○	**The manuscript is currently under review for publication** Please provide the name of the journal:		
○	**It is intended that the manuscript will be published, but it has not yet been submitted to a journal**		
Student's signature:	ARoblesNavarro	Main supervisor's signature:	PeterSchwerdtfeger Digitally signed by PeterSchwerdtfeger Date: 2025.12.08 14:24:46 +13'00'
This form should be placed at the beginning of each relevant thesis chapter.			

[1] Refer to the Massey University Publishing and Authorship guidelines (OneMassey for staff, Stream for students) and/ or Contributor Roles Taxonomy (CRediT) guidelines for guidance.

Chapter 4

Tipping the Balance Between the bcc and fcc Phase Within the Alkali and Coinage Metal Groups

Chemical intuition using basic bonding models, such as the ball-and-stick model, the VSEPR (valence-shell electron repulsion) model, hybridization concepts, covalent and ionic models, ligand-field theory or force field methods, to name but a few, is extremely successful in predicting molecular structures and chemical reaction paths.[322,323] We cannot imagine chemistry anymore without the use of such qualitative bonding models. However, such simple bonding models do not necessarily transfer so easily into the solid state where one requires a more elaborate quantum theoretical treatment and sophisticated algorithms[324] to correctly predict crystal structures at certain temperatures and pressures. This conundrum between the gas phase and the solid state was nicely summarized by John Maddox in 1988: *One of the continuing scandals in the physical sciences is that it remains in general impossible to predict the structure of even the simplest crystalline solids from a knowledge of their chemical composition*.[325]

A statistical evaluation of low-temperature crystal structures for 102 elements in the Periodic Table shows that the majority crystallize either in the face-centered cubic (fcc) or hexagonal close-packed (hcp) phase (48%), as one expects from a maximal packing density of $\rho_{\mathrm{fcc}} = \rho_{\mathrm{hcp}} = \pi/\sqrt{18}$ (74.05%) and a high coordination number of $N_{\mathrm{CN}} = 12$. Far fewer elements crystallize in the body-centered cubic (bcc) structure (21%) having a much lower packing density of $\rho_{\mathrm{bcc}} = \pi\sqrt{3}/8$ (68.02%) and $N_{\mathrm{CN}} = 8$. As prime examples, the known Group 1 solids all adopt the bcc lattice, while in contrast the Group 11 elements adopt the fcc lattice at standard conditions.

We recently argued that the bcc phase for the lightest Group 1 element, lithium, is stabilized over the fcc structure by zero-point vibrational effects.[127] This vibrational stabilization of the bcc phase is further enhanced by temperature effects through the Boltzmann distribution and the vibrational entropy term, which gives an atomistic explanation of the Landau theory

favouring the bcc phase close to the melting point.[252] However, lithium is quite different to the other group 1 elements. Furthermore, zero-point vibrational effects are much smaller for the heavier group 1 elements and one therefore seeks a different explanation for the dominance of the bcc phase within the (heavier) Group 1 metals. We therefore decided to carry out relativistic density functional calculations along the path of smooth cuboidal (body-centered tetragonal structures) transformations from bcc to fcc, see Figure 4.1. The important role of dispersion effects will be highlighted by using Grimme's add-on dispersion-energy correction, as well as relativistic effects for both silver and gold. We use the formalism as outlined by Jerabek et al.[127] which involves only a single cuboidal distortion parameter A with $A = 1$ set for fcc and $A = 1/2$ for bcc (see computational details).

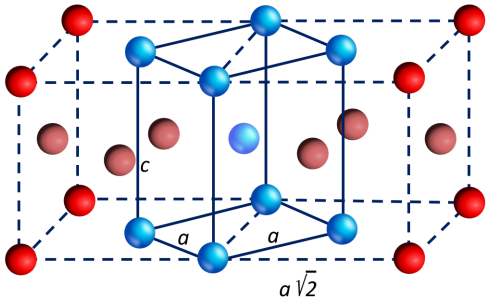

Figure 4.1: Body-centered tetragonal lattice shown in blue with lattice constants a and c. For $a = c$ we obtain the bcc lattice. The usual fcc unit cell with additional red atoms is shown as well with lattice constants $a' = a\sqrt{2} = c$.

Alkali metals are well-known for crystallizing into the bcc phase at standard conditions, however, some density functionals predict other phases like fcc or hcp to be more stable at 0 K as the energy differences between the different structures can be very small.[264,326] To analyse this in more detail, the cohesive energy with respect to the fcc phase along the cuboidal (Bain) distortion path[256] is obtained from density functional calculations (see computational details) for the alkali metals from Li to Fr as depicted in Figure 4.2. Care had been taken to converge the PBE calculations to the required accuracy of 10^{-3} kJ/mol. As can be seen, the differences in the cohesive energy between the bcc and fcc phases for each alkali metal are of the order of 0.1 kJ/mol (see Table 4.1), which provides a challenge to such calculations.[327] Nevertheless, when adding dispersion corrections by means of Grimme's DFT-D3(BJ) method,[328] the bcc phase of the Group 1 metals with the exception of lithium becomes stabilized with respect to fcc, but obviously not enough for francium to make bcc the most stable phase. This may however change with different density functional approximations, which is currently under investigation by our group. Thermal contributions to the free energy will further stabilize the bcc phase as already pointed out.[127]

Regarding the dispersion interaction we plot the ratio $q_{\mathrm{disp}}(A) = E_{\mathrm{disp}}(A)/E_{\mathrm{disp}}(1)$ in

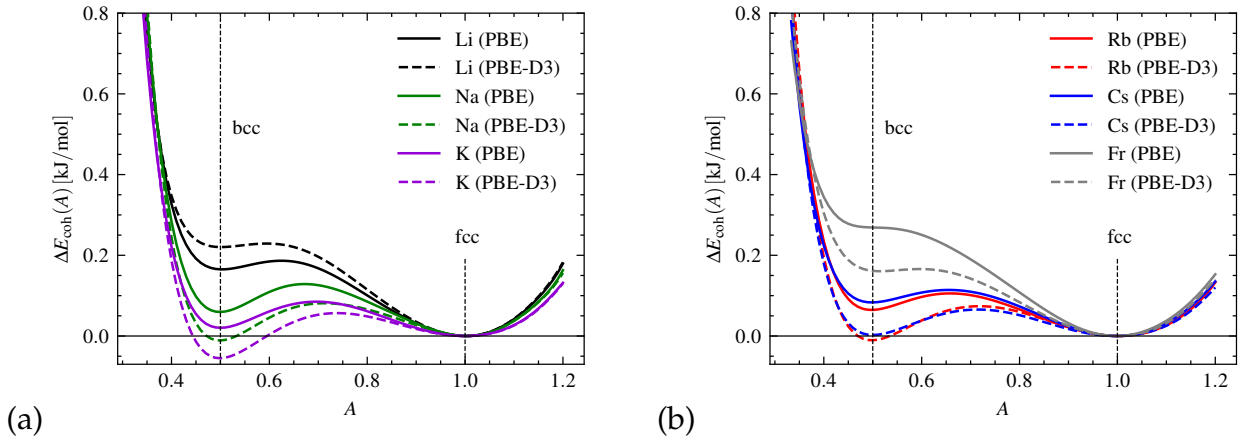

Figure 4.2: Cohesive energy of (a) lithium, sodium and potassium and (b) rubidium, cesium and francium relative to the fcc phase along the Bain path with the PBE functional and including dispersion interactions.

Figure 4.3 to point towards a very similar functional behavior for all the elements considered here. This ratio varies smoothly along the Bain path, having a maximum at the bcc phase. Further, the magnitude of the dispersion energy among the alkali metals is the highest in lithium. This is perhaps surprising as the dipole polarizabilities for the alkali atoms increase down the group (except for francium and element 119 where relativistic effects become important[329]) and the coordination number is 12 in fcc compared to only 8 in bcc. However, as defined in the DFT-D3(BJ) method,[328] the magnitude of the dispersion energy will critically depend on the nearest neighbor distance for all systems as the dominant London dispersion term is $\sim R^{-6}$. Further, the nearest neighbor distance decreases from fcc to bcc along the Bain path, see Table 4.1. Nonetheless, in Figure 4.4 we see an overall destabilization of the bcc phase for lithium compared to its fcc phase. Although dispersion interactions are always stabilizing, we notice that the electronic energy in the dispersion-corrected crystal is higher due to a smaller nearest neighbor distance when dispersion is included. Thus, the destabilizing effect from the electronic structure is added to the stabilization due to dispersion, generating an overall destabilization of the bcc phase for lithium with respect to fcc, contrary to all the other alkali metals. As shown in Figure 4.4, the group 11 metals behave in the same way as lithium in this aspect. Because of the small energy differences involved leading to quasi-degenerate phases at 0 K, the dispersion correction plays a decisive role when determining the correct ground state structure of the bulk.

We notice that the PBE-D3 functional often overestimates the cohesive energy compared to the experimental values (Table 4.1), but this error should be mostly compensated by taking the energy difference for the cuboidal structures with respect to fcc along the Bain path. In this respect, Grimme's D4 dispersion correction[328] has been tested recently for the solid state with in general only slight improvements for lattice energies compared to the most widely used D3

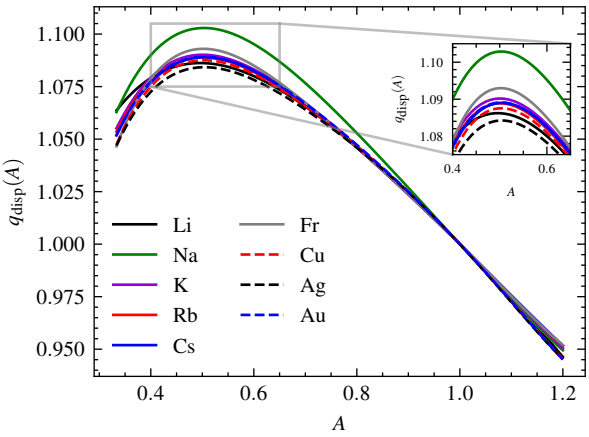

Figure 4.3: Ratio of dispersion energies along the cuboidal distortion path at the optimized PBE-D3 geometry for the Group 1 and 11 metals. The inset shows more details of the curves around the maximum.

approximation[330].

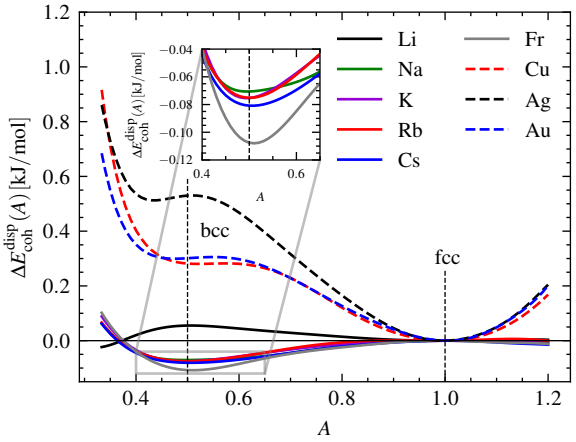

Figure 4.4: Change in the cohesive energy due to dispersion corrected-geometries along the Bain path with respect to the fcc structure for the Group 1 and 11 metals. The inset shows more details of the curves around the minimum for the heavier Group 1 metals

.

For the Group 11 elemental solids we see a completely different picture, that is the bcc phase is not a local minimum anymore (see Figure 4.5), but rather a transition state towards a meta-stable minimum lying close to the so-called axial centered cuboidal lattice $A = 1/3$ with a coordination number of $N_{\mathrm{CN}} = 10$.[331] The location of the transition state is practically unaltered by adding dispersion. In contrast, the location of the transition state (characterized by the distortion parameter $A^{\ddagger}$) along the Bain path for the alkali metals is close to the so-called self-dual mean-centered cubic lattice ($A = 1/\sqrt{2}$), which, in some sense, is an average between the bcc and fcc lattices as described in detail by Conway and Sloane.[331] This is even more apparent when dispersion is added, except for the lightest and heaviest Group 1 elements

Table 4.1: Optimized nearest neighbor distance R in Å, cohesive energies E_{coh} and zero-point energies E_0 in kJ/mol, location of the transition state $A^{\ddagger}$ in the Bain path and corresponding nearest neighbor distance $R^{\ddagger}$ and barrier height $\Delta E^{\ddagger}$ relative to the fcc structure in kJ/mol for the Group 1 and 11 metals. $\Delta E = E_{\mathrm{coh}}^{\mathrm{fcc}} - E_{\mathrm{coh}}^{\mathrm{bcc}}$ and $\Delta E^{\ddagger} = E_{\mathrm{coh}}^{\mathrm{fcc}} - E_{\mathrm{coh}}(A^{\ddagger})$ in kJ/mol. Experimental values are taken from Kittel.[129] Zero-point energy values in square brackets from Equation 4.1, and exp. values are estimated from the Debye temperatures.[129]

Metal		R^{fcc}	R^{bcc}	$R^{\ddagger}$	$A^{\ddagger}$	$E_{\mathrm{coh}}^{\mathrm{fcc}}$	$E_{\mathrm{coh}}^{\mathrm{bcc}}$	ΔE	$\Delta E^{\ddagger}$	E_0^{fcc}	E_0^{bcc}	$\Delta E + \Delta E_0$
	PBE	3.065	2.978	2.986	0.625	155.152	154.987	0.165	0.187	3.971	3.842	0.036
Li	PBE-D3	2.959	2.880	2.885	0.595	172.251	172.030	0.220	0.229			0.091
	Exp.		3.023				158.0				[3.22]	
	PBE	3.742	3.635	3.655	0.672	109.141	109.081	0.060	0.129	[1.617]	[1.565]	0.008
Na	PBE-D3	3.635	3.532	3.559	0.712	125.016	125.027	−0.011	0.081			−0.063
	Exp.		3.659				107.0				[1.48]	
	PBE	4.711	4.576	4.607	0.696	83.673	83.653	0.020	0.085	[0.878]	[0.850]	−0.008
K	PBE-D3	4.603	4.469	4.511	0.739	95.214	95.269	−0.055	0.057			−0.083
	Exp.		4.525				90.1				[0.85]	
	PBE	5.056	4.908	4.932	0.658	74.482	74.417	0.065	0.106	[0.534]	[0.517]	0.048
Rb	PBE-D3	4.947	4.804	4.844	0.718	84.531	84.542	−0.011	0.074			−0.028
	Exp.		4.837				82.2				[0.52]	
	PBE	5.502	5.336	5.360	0.655	68.642	68.559	0.083	0.114	[0.377]	[0.366]	0.072
Cs	PBE-D3	5.386	5.233	5.271	0.715	76.987	76.984	0.002	0.066			−0.009
	Exp.		5.235				77.6				[0.36]	
	PBE	5.499	5.326	—	—	61.079	60.810	0.269	—	[0.292]	[0.283]	0.260
Fr	PBE-D3	5.367	5.202	5.218	0.596	70.611	70.449	0.161	0.166			0.152
	Exp.											
	PBE	2.570	2.502	2.502	0.502	336.257	332.865	3.392	3.392	2.877	2.781	3.296
Cu	PBE-D3	2.523	2.456	2.456	0.499	393.195	389.521	3.674	3.674			3.578
	Exp.	2.56				336.0				[3.21]		
	PBE	2.932	2.859	2.858	0.499	243.013	240.034	2.979	2.979	[1.812]	[1.747]	2.914
	NR-PBE	3.009	2.933	2.933	0.500	218.742	216.273	2.469	2.469			2.404
Ag	PBE-D3	2.879	2.806	2.805	0.500	298.848	295.340	3.509	3.509			3.444
	Exp.	2.89				284.0				[2.11]		
	PBE	2.939	2.860	2.860	0.499	292.883	290.911	1.972	1.972	[1.336]	[1.292]	1.928
	NR-PBE	3.128	3.049	3.049	0.500	219.553	216.807	2.745	2.745			2.701
Au	PBE-D3	2.900	2.822	2.822	0.501	355.012	352.738	2.273	2.273			2.229
	Exp.	2.88				368.0				[1.53]		

lithium and francium. The energy barrier to go from fcc to bcc ($\Delta E^{\ddagger}$) is however very small for the Group 1 elements and around 0.1 kJ/mol, with a decreasing tendency going down the group for the PBE functional, but less pronounced when dispersion interactions are included because of the change in the nearest neighbor distance and the corresponding electronic energy. The energy barriers for the coinage metals are considerably larger compared to the alkali metals. This implies that the bonding within the Group 11 atoms in the bulk is far stronger for the fcc phase with the highest coordination number compared to all the other cuboidal phases along the Bain distortion path as is evident from the cohesive energies listed in Table 4.1.

It was shown by Jerabek et al.[127] that the vibrational contributions to the free energy are of huge importance in stabilizing the bcc phase for lithium. As phonon calculations require a computationally expensive supercell treatment for sampling the **k**-space, and are often difficult

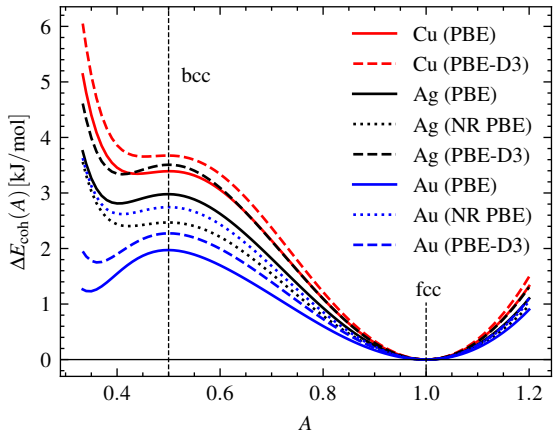

Figure 4.5: Cohesive energy of coinage metals relative to the fcc phase along the cuboidal transition path with the PBE functional including non-relativistic results for silver and gold.

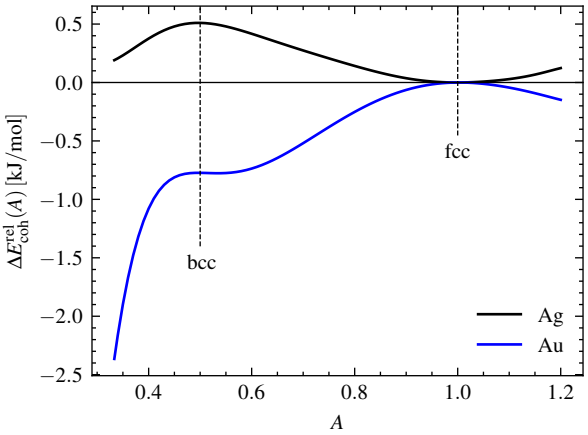

Figure 4.6: Change in the cohesive energy due to scalar relativistic corrections to the geometies along the Bain path with respect to the fcc structure for silver and gold.

to converge to the required accuracy, we used a simple model to calculate the zero-point vibrational energy (ZPE, E_0) within the harmonic approximation applying Badger's rule[332] for the heavier elements, and using lithium and copper as a reference system for the remaining Group 1 and 11 elements, respectively. Within this model, the ratio between the ZPE of the reference element RE = Li or Cu to a heavier atom X is given by

$$\frac{E_0^{\mathrm{X}}(A)}{E_0^{\mathrm{RE}}(A)} \approx \sqrt{\frac{R_{\mathrm{RE}}^3(A) M_{\mathrm{RE}}}{R_{\mathrm{X}}^3(A) M_{\mathrm{X}}}}, \tag{4.1}$$

where E_0^{X}, R_{X}, and M_{X} are the zero-point energy, optimized nearest-neighbor distance and atomic mass of element X. $E_0^{\mathrm{RE}}(A)$ is determined from elaborate phonon calculations (see computational details). Preliminary phonon dispersion calculations for Na show that this is an excellent approximation, and the trends with increasing mass are in line with Borelius.[333]

Further, one can estimate the zero-point vibrational energy contributions from the Debye temperatures θ_D, i.e. $E_0 = \frac{9}{8}k_B\theta_D$, which are also listed in Table 4.1. These show that our simple model gives very accurate results for the zero-point vibrational contribution. We note that Li cannot be used as a reference for the Group 11 metals as the phonon dispersion curves between the Group 1 and 11 elements are very different, and one cannot simply neglect the distance-dependent term in Equation 4.1 as it leads to large errors otherwise. Adding the difference between the bcc and fcc ZPEs, ΔE_0, to the electronic contribution, we see from Table 4.1 that Li, Fr and all Group 11 elements prefer the fcc structure at 0 K, whilst the elements from Na to Cs prefer bcc. This is consistent with experiment[129] except for francium where no solid state data are available.

Concerning relativistic effects, which are enhanced for the Group 11 and 12 elements,[164,334] for both silver and gold the nearest neighbor distances are shortened and the cohesive energies are increased substantially in agreement with previous work,[335] cf. Table 4.1. This produces an interesting behavior along the Bain path with the bcc phase being slightly stabilized in gold but destabilized in silver due to relativistic effects, see Figure 4.6. The relativistic stabilization in gold is however not enough to stabilize the bcc over the fcc phase. Furthermore, the meta-stable minimum located between acc and bcc is roughly at the same position as for the non-relativistic Bain path. In both cases, the relativistic effects in the differences in nearest neighbor distances and cohesive energies between fcc and bcc are very similar, see Table 4.1. Spin-orbit coupling, not considered here, might further influence these small energy differences.

In conclusion, the small energy differences between bcc and fcc for Group 1 metals makes dispersion and phonon contributions important for the question of which is the most stable phase at 0 K. For the Group 11 metals, fcc seems to be far more stabilized compared to bcc and both dispersion and phonon contributions do not change this trend. The activation barriers along the Bain bath from bcc to fcc are very small and comparable to a Lennard-Jones system[103], and rearrangements can easily happen at more elevated temperatures. It was already pointed out that simple two-body interactions such as Lennard-Jones favour the fcc phase[103,227], and stabilizing the bcc phase at low temperatures requires higher than 2-body interactions. A simple harmonic oscillator model can be used to estimate the zero-point vibrational energy for the heavier elements using the lightest element in the same group as a reference system. Further investigations are underway to simulate the bcc to fcc phase transition for the group 1 and 11 metals at higher temperatures and pressures.

Computational Details: The bcc and fcc lattices are closely related as they are dual to each other. Following the ideas of Conway and Sloane,[331] it is therefore possible to build a connection between the two lattices through a smooth diffusionless (martensitic) transformation by defining a set of basis vectors **b** depending only on two lattice parameters, A and R, the first being responsible for the phase transition and the latter the nearest neighbor

distance,

$$\mathbf{b}_1 = \frac{R}{\sqrt{A+1}}\begin{pmatrix}0\\1\\1\end{pmatrix}; \quad \mathbf{b}_2 = \frac{R}{\sqrt{A+1}}\begin{pmatrix}\sqrt{A}\\0\\1\end{pmatrix}; \quad \mathbf{b}_3 = \frac{R}{\sqrt{A+1}}\begin{pmatrix}\sqrt{A}\\1\\0\end{pmatrix} \tag{4.2}$$

with $R = \frac{a}{2}\sqrt{2+\left(\frac{c}{a}\right)^2}$ and $A = \frac{1}{2}\left(\frac{c}{a}\right)^2$. Here a and c are the lattice parameter of the basic bct (body-centered tetragonal) lattice as shown in Figure 4.1. The phase transition parameter A is characteristic of the Bain diffusionless martensitic transformation, which includes four important lattices along the path: the axial centered cuboidal lattice (acc, $A = 1/3$), the bcc lattice ($A = 1/2$, the mean centered cuboidal lattice (mcc, $A = 1/\sqrt{2}$), and the fcc lattice ($A = 1$). The volume of the lattice is related to the R and A parameters by

$$V(R,A) = \frac{ac^2}{2} = 2R^3\sqrt{\frac{A}{(A+1)^3}} \tag{4.3}$$

The bcc lattice has the largest volume within the Bain transformation path and hence the least dense packing density,

$$\rho(A) = \frac{\pi}{12}\sqrt{\frac{(A+1)^3}{A}} \tag{4.4}$$

Note that A classifies the crystal type, whereas the nearest-neighbor distance just expands or contracts the volume.

For each value of A within the chosen interval of $\left[\frac{1}{3}, 1.2\right]$ in steps of 0.01, an optimization of the nearest-neighbor distance was performed for all systems using the Perdew-Burke-Ernzerhof (PBE) exchange-correlation functional[280] including dispersion corrections with the DFT-D3 approach and the Becke-Johnson damping.[291,292] The importance of dispersion forces for metallic systems is now well documented[336]. Additionally, non-relativistic calculations were carried out for both silver and gold.[337] All electronic structure calculations were performed with the VASP 6.4.0 version[338–341] with the atomic cores as described by Blöchl's Projector Augmented Wave (PAW) method[342,343] and the recommended pseudopotentials. The electronic optimization was done using the tetrahedron smearing method with Blöchl corrections[344] with an energy width of 0.1 eV. Convergence tests regarding **k**-spacing and energy cut-off were performed guaranteeing a variation of less than 1 meV in the total energy with respect to more demanding accuracy settings. The energy cut-off was set to 500 eV for Li, Na, Fr, Ag, and Au, 600 eV for Cu, 700 eV for Cs and 800 eV for K and Rb, respectively. The **k**-point grid was set using KSPACING = 0.07 and centered at the Γ point. To calculate the cohesive energy for each metal, the isolated atoms were placed in a slightly

orthorhombic unit cell of size $14 \times 14.001 \times 14.002$ Å^3 and their total energy was computed at the Γ point in reciprocal space. After minimization of the total electronic energy with respect to the nearest-neighbor distance, the variation of A for a given element creates a continuous reaction path $E_{\mathrm{coh}}(A)$ along the specified lattices (Bain path).[256]

Phonon calculations on lithium and copper were performed using density functional perturbation theory with the aid of VASP 6.4.0 and Phonopy 2.14.0.[345] For this purpose, a $6 \times 6 \times 6$ supercell was built with the optimized nearest-neighbor distance and the force constants were calculated with a Γ-centered $3 \times 3 \times 3$ k-point grid for lithium and $4 \times 4 \times 4$ $\mathbf{k}$-point grid for copper.

MASSEY UNIVERSITY
TE KUNENGA KI PŪREHUROA
UNIVERSITY OF NEW ZEALAND

GRADUATE RESEARCH SCHOOL

STATEMENT OF CONTRIBUTION
DOCTORATE WITH PUBLICATIONS/MANUSCRIPTS

We, the student and the student's main supervisor, certify that all co-authors have consented to their work being included in the thesis and they have accepted the student's contribution as indicated below in the Statement of Originality.

Student name:	Andres Eduardo Robles Navarro
Name and title of main supervisor:	Peter Schwerdtfeger
In which chapter is the manuscript/published work?	Chapter 5

Describe the contribution that the student and members of the supervisory team have made to the manuscript/published work:[1]

All the computations were performed by me, except for the ones including the highly efficient method for three-body forces developed by Buchheit and Busse. The theoretical development of the publication is equally divided between me, Shaun Cooper, and Peter Schwerdtfeger. Further discussions also included Odile Smits and Antony Burrows.

Please select one of the following three options:

- (●) **The manuscript/published work is published or in press**

  Please provide the full reference of the research output:

  The Journal of Chemical Physics 2025, 163(9): 094104

- ( ) **The manuscript is currently under review for publication**

  Please provide the name of the journal:

- ( ) **It is intended that the manuscript will be published, but it has not yet been submitted to a journal**

Student's signature:	ARoblesNavarro	Main supervisor's signature:	PeterSchwerdtfeger Digitally signed by PeterSchwerdtfeger Date: 2025.12.08 14:24:30 +13'00'

This form should be placed at the beginning of each relevant thesis chapter.

[1] Refer to the Massey University Publishing and Authorship guidelines (OneMassey for staff, Stream for students) and/ or Contributor Roles Taxonomy (CRediT) guidelines for guidance.

Chapter 5

Exact Lattice Summations for Lennard-Jones Potentials Coupled to a Three-Body Axilrod-Teller-Muto Term Applied to Cuboidal Phase Transitions

5.1 Introduction

Crystalline solid-to-solid phase transitions are induced by temperature or pressure change and often involve symmetry breaking away from the original space group of the starting phase along the minimum energy transition path towards the final crystal phase.[346] The special class of martensitic phase transformations is described by diffusionless transitions induced by lattice strain and a collective movement of the atoms in the lattice.[81,253,347–349] Such martensitic transitions are found in many important materials such as steel or oxide ceramics,[350] but also for some elements in the Periodic Table such as lithium.[79,351] The body-centered cubic (bcc) to face-centered cubic (fcc) phase transition belongs to the class of martensitic transformations.[352] Both the bcc lattice ($c/a = 1$) and the face-centered cubic (fcc) lattice ($c/a = \sqrt{2}$) have the body-centered tetragonal (bct) lattice (crystallographic group #139 or $I4/mmm$) in common defined by the lattice constants $a_1 = a_2 = a$ and $a_3 = c$ and right angles $\alpha_1 = \alpha_2 = \alpha_3 = 90^o$) as shown in Figure 5.1.

Concerning the interactions between the atoms or molecules in a lattice, the associated infinite lattice sums describing such interactions have a long history in solid-state physics and discrete mathematics.[111] They connect lattices to observables such as the equation of state for a bulk system with inverse power potentials $V(r) = r^{-k}$ acting between lattice points.[219,227,353,354] Most notable cases for such interaction potentials are the Lennard-Jones potential[112] (see Reference 222 for a historical account), which in its most general case is

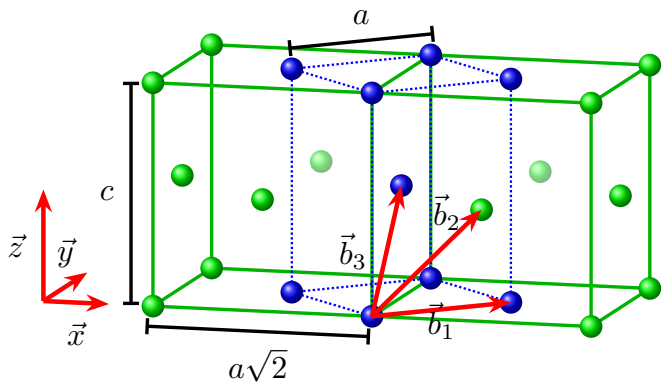

Figure 5.1: Body-centered tetragonal lattice shown in blue with lattice constants a and c. For $a = c$ we have the bcc lattice. The usual fcc unit cell with additional green atoms is shown as well with lattice constants $a' = a\sqrt{2} = c$.

given by

$$E_{\mathrm{LJ}}(r) = \epsilon \frac{nm}{n-m} \left[\frac{1}{n} \left(\frac{r_e}{r} \right)^n - \frac{1}{m} \left(\frac{r_e}{r} \right)^m \right], \tag{5.1}$$

and the Coulomb potential leading to the famous Madelung constant derived as early as 1918 by Madelung.[115] In Eq. (5.1), r_e is the equilibrium distance for a diatomic molecule, ϵ the corresponding dissociation energy, and we have the condition $n > m > d$ with d the dimension of the lattice. The application of the Lennard-Jones and other empirical potentials has been invaluable to gain deeper insight into bulk phases and their phase transitions[222,355–361].

In the following, we consider d-dimensional Bravais lattices $\Lambda = B^\top \mathbb{Z}^d = \{B^\top \vec{i} \mid \vec{i} \in \mathbb{Z}^d\}$, with $d = 1, 2, 3$, where the generator matrix $B^\top = (\vec{b}_1, \cdots, \vec{b}_d)$ contains the lattice basis vectors.[295] When evaluating energies or forces in such long-range interacting lattices, we encounter lattice sums of the form

$$L = \sum_{\vec{x} \in \Lambda} f(\vec{x}) = \sum_{\vec{i} \in \mathbb{Z}^d} f\left(B^\top \vec{i} \right), \tag{5.2}$$

where f is a scalar or vector-valued function that decreases sufficiently fast such that the sum is absolutely convergent. An important special case is given by an inverse power-law potential $f(\vec{x}) = |\vec{x}|^{-\nu}$, where the resulting lattice sum is a special case of the Epstein zeta function, a generalization of the Riemann zeta function to multidimensional lattice sums[113] with many applications in physics[112,362–364]. These lattice sums are often slowly convergent, and their efficient and precise computation poses significant challenges. Moreover, meaning can be given to conditionally convergent or even divergent series through techniques such as meromorphic continuation.[365] The theory of converting lattice sums, including their meromorphic continuations, into fast converging series has become a research field on its

own.[111]

The dominant long-range three-body interaction contribution comes from the triple-dipole interaction and is described approximately by the Axilrod-Teller-Muto (ATM) potential.[187,188] For a trimer of atoms at positions $\vec{r}_1, \vec{r}_2, \vec{r}_3$, the ATM potential reads[366]

$$E^{(3)}_{\mathrm{ATM}} = \lambda \frac{r_{12}^2 r_{13}^2 r_{23}^2 + 3(\vec{r}_{12} \cdot \vec{r}_{13})(\vec{r}_{21} \cdot \vec{r}_{23})(\vec{r}_{31} \cdot \vec{r}_{32})}{(r_{12} r_{13} r_{23})^5}. \tag{5.3}$$

Here, $\lambda > 0$ represents the ATM coupling constant, while $\vec{r}_{ij} = \vec{r}_i - \vec{r}_j$ denotes the relative position vector between distinct atoms i and j with norm $r_{ij} = |\vec{r}_{ij}|$. The coupling strength λ depends on the polarizabilities of the interacting atoms, where three-body interactions can become highly relevant, among others, for the heavier and more polarizable noble gases. Notably, for solid argon at 0 K, three-body forces have been shown to contribute approximately 8.9% of the total cohesive energy.[104] We should mention, however, that the expansion of the total interaction energy in terms of many-body interaction contributions in a cluster or bulk system can become problematic when atoms start to interact strongly .[183]

The precise simulation of solid-solid phase transitions can be highly challenging due to the movement of many atoms within the simulation cell.[350,367] Martensitic transformations are less complex in nature but are nevertheless difficult to predict theoretically and to measure experimentally.[265,266,349] For a general (n, m) LJ two-body potential, we recently showed by exact lattice summations that the bcc phase is at an extremum along the cuboidal distortion path and becomes either energetically unstable or metastable. In addition, one requires rather soft Lennard-Jones potentials to stabilize the bcc phase against rhombohedral distortion[355,356,368]. This bcc instability persists into the high-pressure regime for a LJ solid.[126] This result can most likely be generalized to all physically relevant two-body interactions. Thus, the existence of the bcc phase, known for a number of elements in the periodic table, likely results from vibrational and temperature effects, and/or from dominant higher than two-body forces. We note that Landau theory predicts that the bcc phase becomes dominant near the melting line for metals[252] and for other solids[110,369].

In this work, we analyze a smooth connection between the cuboidal body-centered tetragonal (bct) lattices through a martensitic Bain transformation including both general two-body LJ interactions and a three-body ATM potential.[256,370,371] We first write the lattice Λ along the transition path as a function of a single parameter A,[103,127] and collect the basic properties of the resulting lattice. We then present efficient methods to evaluate both the arising two-body and three-body lattice sums to full precision. For the two-body potential, we re-express the algebraically decaying sum in terms of a series of super-exponentially decaying sums, which can be efficiently evaluated. We then present a novel efficient method for computing general three-body lattice sums, based on integrals involving zeta functions on

multidimensional lattices. Using these advanced numerical techniques, we offer a rigorous study of the stability of the bcc phase relative to the fcc phase as a function of the ATM coupling constant λ. Here we neglect possible rhombohedral distortions[355,356,372] along the Bain path, which has not been investigated in detail yet beside the work by Ono and Ito[368], as it requires a different treatment of our lattice sums.

5.2 Theory

5.2.1 General lattice properties

We begin our treatment by defining lattices and important associated quantities. We call a point set $\Lambda \subseteq \mathbb{R}^d$ a (Bravais) lattice, if $\Lambda = B^\top \mathbb{Z}^d = \{\vec{i}^\top B = B^\top \vec{i} \mid \vec{i} \in \mathbb{Z}^d\}$ for some nonsingular matrix $B \in \mathbb{R}^{d\times d}$. The matrix $B = (\vec{b}_1, \cdots, \vec{b}_d)^\top$, called the generator matrix or the cell tensor contains the set of linearly independent lattice basis vectors $\vec{b}_i^\top$ as its rows. Lattices exhibit discrete translational invariance, meaning that $\Lambda + \vec{x} = \Lambda$ for any $\vec{x} \in \Lambda$. The Gram matrix G is defined in terms of the generator matrix as $G = BB^\top$ and appears in the computation of lattice vector norms. We further define the elementary lattice cell $B^\top(-\frac{1}{2}, \frac{1}{2})^d$. The lattice volume is defined by $V_\Lambda = |\det B| = \sqrt{\det G}$. An important lattice quantity is the minimum or nearest neighbor distance R_Λ with

$$R_\Lambda = \min\{|\vec{x} - \vec{y}| \mid \vec{x}, \vec{y} \in \Lambda,\ \vec{x} \neq \vec{y}\} = \min_{\vec{x}\in\Lambda\setminus\{0\}} |\vec{x}|, \tag{5.4}$$

due to translational invariance of the lattice, where $|\vec{x}|$ denotes the Euclidean distance. In terms of the Gram matrix this is equivalent to

$$R_\Lambda = \min_{\vec{i}\in\mathbb{Z}^d\setminus\{0\}} \sqrt{\vec{i}^\top G \vec{i}}. \tag{5.5}$$

The packing density Δ_Λ describes the ratio between the volume of particles with radius ρ and the volume of the elementary lattice cell,

$$\Delta_\Lambda = \frac{\pi^{d/2}}{\Gamma(d/2+1)} \frac{\rho^d}{V_\Lambda}, \tag{5.6}$$

with the gamma function Γ. For dense hard sphere packings we have $\rho = R_\Lambda/2$. Finally, the kissing number for dense hard sphere packings is defined as the number of nearest neighbors of an arbitrary lattice point,

$$\mathrm{kiss}(\Lambda) = \#\{\vec{v} \in \Lambda \mid |\vec{v}| = R_\Lambda\}. \tag{5.7}$$

5.2.2 Properties of cuboidal lattices

In case of the three-dimensional cuboidal lattices, we start from the work of Conway and Sloane[331] and consider the lattice generated by the vectors $(\pm u, \pm v, 0)^\top$ and $(0, \pm v, \pm v)^\top$, where u and v are non-zero real numbers. We now use the lattice basis vectors $\vec{b}_1^\top = (u, v, 0)$, $\vec{b}_2^\top = (u, 0, v)$, $\vec{b}_3^\top = (0, v, v)$, where u and v are non-zero real numbers. Let $A = u^2/v^2$. The generator matrix $B^\top$ and the Gram matrix G are

$$B^\top = \begin{pmatrix} \vec{b}_1 & \vec{b}_2 & \vec{b}_3 \end{pmatrix} = v \begin{pmatrix} \sqrt{A} & \sqrt{A} & 0 \\ 1 & 0 & 1 \\ 0 & 1 & 1 \end{pmatrix}, \qquad G = B\,B^\top = v^2 \begin{pmatrix} A+1 & A & 1 \\ A & A+1 & 1 \\ 1 & 1 & 2 \end{pmatrix}. \tag{5.8}$$

The determinant of the generator matrix reads $\det B = -2v^3\sqrt{A}$ and thus $V_\Lambda = 2|v^3|\sqrt{A}$.

Different lattice phases are obtained depending on the choice of the argument A. These are, in decreasing numerical order,

1. $A = 1$: the face-centered cubic (fcc) lattice,
2. $A = 1/\sqrt{2}$: the mean centred-cuboidal (mcc) lattice,
3. $A = 1/2$: the body-centred cubic (bcc) lattice,
4. $A = 1/3$: the axial centred-cuboidal (acc) lattice.

The resulting Gram matrices for the fcc and bcc lattices are identical to the ones shown in our previous work on lattice sums,[295] whereas the mcc and acc lattices occur in Refs. 331 and 373. A more detailed description of these cubic lattices and their transformations can be found in Refs. 103 and 127. The mcc lattice is the densest isodual lattice in three-dimensional space, but beside being of theoretical interest, has not been observed in nature so far. However, this lattice is expected to play a role in the dynamics of the cuboidal fcc to bcc transition, as we investigate in detail in this work.

Inserting either the generator matrix or the Gram matrix in Eq. (5.5) yields the nearest neighbor distance as a function of A,

$$R_\Lambda = \begin{cases} 2v\sqrt{A}, & 0 < A < 1/3, \\ v\sqrt{A+1}, & 1/3 \le A \le 1, \\ v\sqrt{2}, & A > 1. \end{cases} \tag{5.9}$$

From Eq. (5.6) then follows the packing density Δ_Λ for dense sphere packings,

$$\Delta_\Lambda = \begin{cases} (2\pi/3)A, & 0 < A < 1/3, \\ (\pi/12)\sqrt{(A+1)^3/A}, & 1/3 \le A \le 1, \\ (\pi/6)\sqrt{2/A}, & A > 1 \end{cases} \tag{5.10}$$

which is displayed in Fig. 5.2. On the interval $1/3 \le A \le 1$, which includes the acc, bcc, mcc, and fcc phases, the packing density has a maximum of $\pi\sqrt{2}/6 \approx 0.74$ at $A = 1$ corresponding to fcc, and a minimum of $\pi\sqrt{3}/8 \approx 0.68$ at $A = 1/2$ corresponding to bcc. The acc lattice has a rather large packing density of $\Delta_{\text{acc}} = \frac{2\pi}{9} \approx 0.698$, but is the least dense packing with kissing number 10[374,375]. However, it is most likely strictly jammed according to the definition by Torquato and Stillinger.[376] It consists of linear chains of touching spheres surrounded by four neighboring linear chain arranged within a bct cell. It is the starting point of separated linear chain formation within region I ($A \le \frac{1}{3}$).

Finally Eq. (5.7) yields the kissing number for dense sphere packings,

$$\text{kiss}(\Lambda) = \#\{\vec{v} \in \Lambda \mid |\vec{v}| = R_\Lambda\} = \begin{cases} 2, & A < 1/3, \\ 10, & A = 1/3 \text{ (acc)}, \\ 8, & 1/3 < A < 1 \\ 12 & A = 1 \text{ (fcc)}, \\ 4, & A > 1. \end{cases} \tag{5.11}$$

The limiting case $A \to \infty$ corresponds to infinitely separated two-dimensional square lattice layers with kissing number 4, while in the other extreme case, the limit $A \to 0$, we obtain infinitely dense 1D chains with kissing number 2 repeated on a two-dimensional grid, e.g. see Ref. 377.

Figure 5.2 shows a graph of the packing density as a function of the parameter A. Further information is recorded in Table 5.1.

The cuboidal lattices belong to the body-centered tetragonal lattices (bct) usually defined by the two lattice constants a and c, see Figure 5.1. We can easily transform our two parameter space (u, v) used by Conway in terms of (R_Λ, A) used here and (a, c) used for bct lattices in the interval $1/3 \le A \le 1$ by

$$(u, v) = \left(R_\Lambda \sqrt{\frac{A}{A+1}}, \frac{R_\Lambda}{\sqrt{A+1}} \right) \quad \text{and} \quad (R_\Lambda, A) = \left(\frac{a}{2}\sqrt{2+\gamma^2}\,,\ \frac{1}{2}\gamma^2 \right) \tag{5.12}$$

for the range $1/3 \le A \le 1$ (region II) and $\gamma = c/a$. For example, if we use for the bct lattice in Figure 5.1 the lattice constants a and $\gamma = \sqrt{2}$, we get $A = 1$ (fcc) and $R_\Lambda = a$, which is the

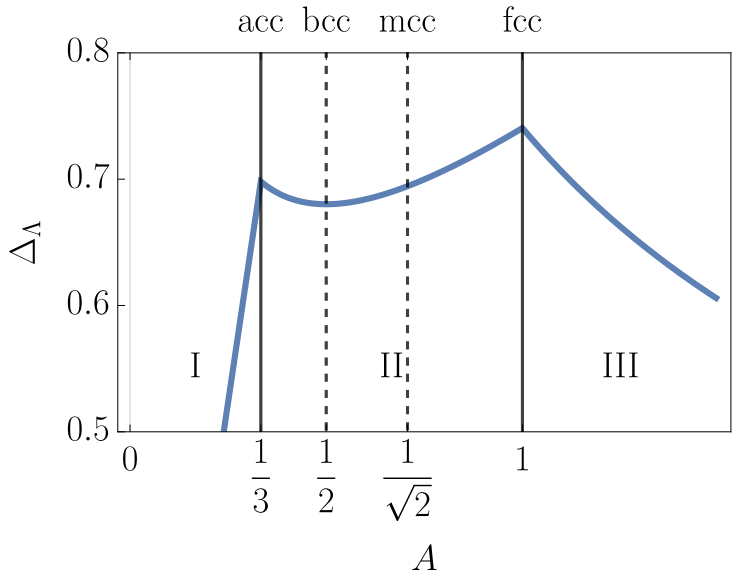

Figure 5.2: Graph of the packing density Δ_Λ versus A. The regions I, II and III, divided by the solid black lines, correspond to the different kissing numbers. Explicit formulas are given in Table 5.1. The location of the fcc, mcc, bcc and acc lattices are indicated the solid and dashed black lines.

distance from the origin of the lattice to the nearest face-centered point, whilst for $\gamma = 1$ we get $A = \frac{1}{2}$ (bcc) and $R_\Lambda = a\frac{\sqrt{3}}{2}$, which is the distance from the origin to the nearest body-centered (bc) point, i.e. $R_\Lambda = R_{\text{bc}}$. From Eq. (5.12) we see that for $A < \frac{1}{2}$ we have $\gamma < 1$ which implies $c < a$. For $A \geq 1$ (region III) we have $R_\Lambda = a$, the distance between nearest neighbors in the base layer. For $A < \frac{1}{3}$ we enter region I for which we get $\gamma < \sqrt{\frac{2}{3}}$ and therefore $c < R_{\text{bc}}$. Using the two lattice parameters (R_Λ, A) has the advantage that $R_\Lambda \in a[\frac{\sqrt{3}}{2}, 1]$ in region II varies only slowly, and the Bain transformation introduced in the next subsection is mostly described by one single dimensionless lattice parameter A.

5.2.3 The Bain transformation

The Bain transformation is a diffusionless smooth transformation from bcc to fcc and vice versa. If we start conveniently from the fcc generator matrix we find a smooth transformation in terms of a diagonal matrix

$$\tilde{B}^\top(A) = c(A)T_{\text{Bain}}(A)\tilde{B}_{\text{fcc}}^\top = c(A)\frac{1}{\sqrt{2}}\begin{pmatrix}\sqrt{A} & \sqrt{A} & 0\\ 1 & 0 & 1\\ 0 & 1 & 1\end{pmatrix}, \tag{5.13}$$

Table 5.1: Kissing number $\mathrm{kiss}(\Lambda)$ and packing density Δ_Λ for the lattice defined in Eq. (5.8). The values in the table depend only on A and are independent of v.

Region	A	$\mathrm{kiss}(\Lambda)$	Δ_Λ
I	$(0, \frac{1}{3})$	2	$\frac{2\pi A}{3}$
acc	$\frac{1}{3}$	10	$\frac{2\pi}{9}$
II	$(\frac{1}{3}, 1)$	8	$\frac{\pi}{12}\sqrt{\frac{(A+1)^3}{A}}$
fcc	1	12	$\frac{\pi\sqrt{2}}{6}$
III	$(1, \infty)$	4	$\frac{\pi}{6}\sqrt{\frac{2}{A}}$

with $\tilde{B}(A) = B(A)/R(A)$ and $\tilde{B}_{\mathrm{fcc}} = \tilde{B}(1)$. The diagonal Bain matrix reads

$$T_{\mathrm{Bain}}(A) = \begin{pmatrix} \sqrt{A} & 0 & 0 \\ 0 & 1 & 0 \\ 0 & 0 & 1 \end{pmatrix} \tag{5.14}$$

and the prefactor $c(A)$ is given by

$$c(A) = \begin{cases} 1/\sqrt{2A}, & 0 < A < 1/3, \\ \sqrt{2/(A+1)}, & 1/3 \leq A \leq 1, \\ 1, & A > 1. \end{cases} \tag{5.15}$$

In the particularly relevant range $1/3 \leq A \leq 1$, the rescaled generator matrix takes the form

$$\tilde{B}^\top(A) = \frac{1}{\sqrt{A+1}} \begin{pmatrix} \sqrt{A} & \sqrt{A} & 0 \\ 1 & 0 & 1 \\ 0 & 1 & 1 \end{pmatrix}. \tag{5.16}$$

In later sections, we will extend the above definition of $\tilde{B}^\top(A)$ in Eq. (5.16) to the whole range $0 < A \leq 1$, where the nearest neighbor distance for $A \geq 1/3$ is given by the lattice constant a (see Figure 5.1) and to the distance between the origin and the body-centered atom for $0 < A < \frac{1}{3}$. As always, the Bain transformation matrix depends on the particular choice of lattice basis vectors.

5.2.4 Cohesive energies from a Lennard-Jones potential coupled to a three-body Axilrod-Teller-Muto term

Using translational invariance of the lattice, the static cohesive energy for a lattice can be expressed in terms of a many-body perturbative expansion of the interaction energy from a chosen atom at the origin,

$$E_{\text{coh}} = \sum_{k=2}^{\infty} E_{\text{coh}}^{(k)} = \frac{1}{2} \sum_{i \in \mathbb{N}} E^{(2)}(\vec{r}_{0i}) + \frac{1}{3} \sum_{\substack{i,j \in \mathbb{N} \\ j>i}} E^{(3)}(\vec{r}_{0i}, \vec{r}_{0j}, \vec{r}_{ij}) + \text{h.o.t}, \tag{5.17}$$

with $\vec{r}_{ij} = \vec{r}_i - \vec{r}_j$, $r_{ij} = |\vec{r}_{ij}|$, $\mathbb{N} = \{1, 2, 3, \cdots\}$ the set of natural numbers, and $i = 0$ denotes the index of the atom at the chosen origin in the solid. The perturbative expansion is formally exact for finite clusters, but is often slowly convergent, or perhaps even divergent as suggested by Heine[378], especially for metallic systems.[183] In this work we focus our studies on the two- and three-body interactions, neglecting vibrational and temperature effects, as well as higher order terms (h.o.t.) such as four-body interactions. In the following, we adopt dimensionless units, writing length scales in units of the equilibrium distance r_e of the LJ potential and energies in units of the LJ dissociation energy ϵ.

The dimensionless two-body potential in (5.17) then takes the form,

$$E_{\text{LJ}}^{(2)}(\vec{r}) = \frac{nm}{n-m} \left(\frac{1}{n} |\vec{r}|^{-n} - \frac{1}{m} |\vec{r}|^{-m} \right). \tag{5.18}$$

with $n > m > 3$. The resulting cohesive energy can be written in terms of the Epstein zeta function, a generalization of the Riemann zeta function to higher-dimensional lattices. For a lattice Λ, an interaction exponent $\nu > d$, and a wavevector $\vec{k}$, it reads[113]

$$Z_{\Lambda,\nu}(\vec{k}) = \sum_{\vec{x} \in \Lambda}{}' \frac{e^{-2\pi i \vec{x} \cdot \vec{k}}}{|\vec{x}|^{\nu}}, \tag{5.19}$$

where the lattice sum can be meromorphically continued to $\nu \in \mathbb{C}$. For the LJ lattice sum, the Epstein zeta function is evaluated at $\vec{k} = 0$ only, where we omit the argument $Z_{\Lambda,\nu} = Z_{\Lambda,\nu}(0)$ to simplify the notation. General wavevectors will, however, become crucial in the evaluation of three-body lattice sums. The two-body term in the cohesive energy for a LJ potential can then be rewritten as

$$E_{\text{coh}}^{(2)} = \frac{nm}{2(n-m)} \sum_{\vec{x} \in \tilde{\Lambda}}{}' \left(\frac{|\vec{x}|^{-n}}{nR^n} - \frac{|\vec{x}|^{-m}}{mR^m} \right) = \frac{nm}{2(n-m)} \left(\frac{Z_{\tilde{\Lambda},n}}{nR^n} - \frac{Z_{\tilde{\Lambda},m}}{mR^m} \right) \tag{5.20}$$

where we use the normalized lattice $\tilde{\Lambda} = \Lambda / R$. This normalization is useful, as the distance R

(e.g. the nearest neighbor distance) will become a tuning parameter depending along the Bain path on the exponents n and m and on the parameter A as specified in the next sections. It also shows more clearly the link to the LJ potential (5.18) for a diatomic.

Different computationally efficient methods for evaluating the Epstein zeta function exist. In Appendix B, we evaluate the arising sums for particular lattices $\tilde{\Lambda}(A) = \tilde{B}^\top(A)\mathbb{Z}^3$ using Bessel function expansions in Equation (B.38) or Equation (B.39), with the more common notation

$$L(A, n/2) = Z_{\tilde{\Lambda}(A),n}. \tag{5.21}$$

As an alternative, for general d-dimensional lattice sums including oscillatory factors and lattice shifts, the recently created high-performance library EpsteinLib (`github.com/epsteinlib`) can be used.[379] Both approaches allow to compute the two-body term to machine precision.

In a similar way we express the three-body Axilrod-Teller-Muto (ATM) potential in Eq. (5.3) in dimensionless units. As the ATM potential only depends on relative distance vectors, we can set $\vec{x} = \vec{r}_{0i}$, $\vec{y} = \vec{r}_{0j}$ and $\vec{z} = \vec{r}_{ij} = \vec{y} - \vec{x}$, yielding the potential as a function of two vectors only,

$$E^{(3)}_{\mathrm{ATM}}(\vec{x}, \vec{y}) = \lambda \left(\frac{1}{|\vec{x}|^3|\vec{y}|^3|\vec{z}|^3} - 3\frac{(\vec{x}\cdot\vec{y})(\vec{y}\cdot\vec{z})(\vec{z}\cdot\vec{x})}{|\vec{x}|^5|\vec{y}|^5|\vec{z}|^5} \right)\Bigg|_{\vec{z}=\vec{y}-\vec{x}}, \tag{5.22}$$

where the minus sign on the right-hand side arises due to $\vec{r}_{ji} = -\vec{r}_{ij}$. The cohesive energy contribution due to the three-body interactions is given by the lattice sum

$$E^{(3)}_{\mathrm{coh}} = \frac{1}{6} \sum_{\vec{x},\vec{y}\in\Lambda}{}' E^{(3)}_{\mathrm{ATM}}(\vec{x}, \vec{y}), \tag{5.23}$$

where the prefactor $1/6$ avoids double counting and where the primed sum excludes the undefined cases $\vec{x} = 0$, $\vec{y} = 0$, and $\vec{x} = \vec{y}$. We now normalize the lattice, setting $\tilde{\Lambda} = \Lambda/R$ and subsequently split the three-body lattice sum into a radially isotropic and an anisotropic part,

$$E^{(3)}_{\mathrm{coh}} = \lambda f^{(3)}_{\mathrm{coh}} R^{-9} = \lambda (f^{(3)}_r + f^{(3)}_a) R^{-9} \tag{5.24}$$

with the normalized lattice sums

$$f^{(3)}_{\mathrm{coh}} = f^{(3)}_r + f^{(3)}_a, \quad f^{(3)}_r = \frac{1}{6} \sum_{\vec{x},\vec{y}\in\tilde{\Lambda}}{}' \frac{1}{|\vec{x}|^3|\vec{y}|^3|\vec{z}|^3}, \quad f^{(3)}_a = -\frac{1}{2} \sum_{\vec{x},\vec{y}\in\tilde{\Lambda}}{}' \frac{(\vec{x}\cdot\vec{y})(\vec{y}\cdot\vec{z})(\vec{z}\cdot\vec{x})}{|\vec{x}|^5|\vec{y}|^5|\vec{z}|^5} \tag{5.25}$$

where we adopt the convention $\vec{z} = \vec{y} - \vec{x}$ from now on. For simplicity, we leave away the tilde in the following, assuming that the lattices have been appropriately normalized. The above form for the three-body lattice form makes it immediately clear that the ATM potential becomes attractive in one dimension, as then $f_a = -3f_r$ and hence $E^{(3)}_{\mathrm{coh}} = -2\lambda f_r R^{-9} < 0$.

5.2.5 Efficient computation of the ATM cohesive energy

The efficient computation of three-body lattice sums has been an important open problem, which we solve in this work. In the past, elaborate direct summation methods have been used,[104,229,230,380–382] where, however, a single evaluation in three dimensions can demand up to 4 weeks of single core CPU time. In this section, we briefly show how general three-body interactions, including the ATM potential, can be computed from singular integrals that involve products of Epstein zeta functions. A deeper discussion, including a rigorous proof as well as numerical benchmarks, is provided in Ref. 364. For a lattice $\Lambda = B^\top \mathbb{Z}^d$ with $B \in \mathbb{R}^{d\times d}$ nonsingular, we consider general lattice sums of the form

$$\zeta_\Lambda^{(3)}(\vec{\nu}) = \sum_{\vec{x},\vec{y}\in\Lambda}{}' |\vec{x}|^{-\nu_1}|\vec{y}|^{-\nu_2}|\vec{y}-\vec{x}|^{-\nu_3}, \tag{5.26}$$

with $\vec{\nu} = (\nu_1,\nu_2,\nu_3)^T$, and its meromorphic continuations to $\nu_i \in \mathbb{C}$ (see Appendix E for details), which we call three-body zeta functions. One can show that the above double sum converges absolutely and independently of the summation order if and only if the conditions $\nu_i + \nu_j > d$ for $i \neq j$, and $\nu_1+\nu_2+\nu_3 > 2d$ hold. We note in passing that this lattice sum can be extended to the more general n-body zeta function, which will be addressed in our future work.

We first show that the normalized ATM cohesive energy in Eq. (5.25) can be written as a finite recombination of the above zeta functions. The radially symmetric term $f_r^{(3)}$ is already in the desired form with

$$f_r^{(3)} = \frac{1}{6}\zeta_\Lambda^{(3)}(3,3,3). \tag{5.27}$$

For the anisotropic part $f_a^{(3)}$, we note that the vector products can be rewritten as

$$2\vec{x}\cdot\vec{y} = |\vec{x}|^2+|\vec{y}|^2-|\vec{z}|^2, \quad 2\vec{y}\cdot\vec{z} = |\vec{y}|^2+|\vec{z}|^2-|\vec{x}|^2, \quad 2\vec{z}\cdot\vec{x} = -(|\vec{z}|^2+|\vec{x}|^2-|\vec{y}|^2). \tag{5.28}$$

As the above lattice sums remain unchanged under permutation of $\vec{x}$, $\vec{y}$, and $\vec{z}$, we find,

$$f_a^{(3)} = -\frac{1}{2}\sum_{\vec{x},\vec{y}\in\Lambda}{}' \frac{(\vec{x}\cdot\vec{y})(\vec{y}\cdot\vec{z})(\vec{z}\cdot\vec{x})}{|\vec{x}|^5|\vec{y}|^5|\vec{z}|^5} = -\frac{1}{16}\sum_{\vec{x},\vec{y}\in\Lambda}{}' \Big(3\frac{|\vec{x}|}{|\vec{y}|^5|\vec{z}|^5} - 6\frac{1}{|\vec{x}||\vec{y}|^3|\vec{z}|^5} + 2\frac{1}{|\vec{x}|^3|\vec{y}|^3|\vec{z}|^3}\Big).$$

Rewriting the above right-hand side in terms of three-body zeta functions yields

$$f_a^{(3)} = -\frac{1}{16}\Big(3\zeta_\Lambda^{(3)}(-1,5,5) - 6\zeta_\Lambda^{(3)}(1,3,5) + 2\zeta_\Lambda^{(3)}(3,3,3)\Big), \tag{5.29}$$

Recombining $f_r^{(3)}$ and $f_a^{(3)}$ finally yields the ATM cohesive energy in terms of three-body zeta

functions,

$$f_{\text{coh}}^{(3)} = \frac{1}{24}\zeta_\Lambda^{(3)}(3,3,3) - \frac{3}{16}\zeta_\Lambda^{(3)}(-1,5,5) + \frac{3}{8}\zeta_\Lambda^{(3)}(1,3,5). \tag{5.30}$$

The three-body zeta function can now be recast as an integral over products of Epstein zeta functions. Recall that for a wavevector $\vec{k} \in \mathbb{R}^d$, the Epstein zeta function reads

$$Z_{\Lambda,\nu}(\vec{k}) = \sum_{\vec{x}\in\Lambda}{}' \frac{e^{-2\pi i\vec{k}\cdot\vec{x}}}{|\vec{x}|^\nu}, \quad \nu > d,$$

which can be meromorphically continued to $\nu \in \mathbb{C}$. For an extensive discussion of the analytical properties of the Epstein zeta function, see Ref. 379. Using the properties of the Epstein zeta function, one can now show that for any $\nu_i > 0,\ i = 1,\ldots,3$,

$$\zeta_\Lambda^{(3)}(\vec{v}) = V_\Lambda \int_{E^*} Z_{\Lambda,\nu_1}(\vec{k}) Z_{\Lambda,\nu_2}(\vec{k}) Z_{\Lambda,\nu_3}(\vec{k})\,\mathrm{d}\vec{k}, \tag{5.31}$$

where V_Λ denotes the volume of the elementary lattice cell and where $E^* = B^{-1}(-1/2,1/2)^d$ defines the unit cell of the reciprocal lattice $\Lambda^* = B^{-1}\mathbb{Z}^d$ centered around the Γ-point. The proof of this formula is based on exchanging summation and integration for sufficiently large ν_i and then applying the relation

$$V_\Lambda \int_{E^*} e^{-2\pi i\vec{k}\cdot\vec{x}}\,\mathrm{d}\vec{k} = \delta_{\vec{x},\vec{0}}$$

with δ the Kronecker delta. A mathematically rigorous proof as well as details on the numerical computation of the integral will be provided elsewhere.

Special care needs to be taken in evaluating the resulting integral, as the Epstein zeta function exhibits a singularity at $\vec{k} = 0$. We can separate the Epstein zeta function into an analytic function and a singularity as follows

$$Z_{\Lambda,\nu}(\vec{k}) = Z_{\Lambda,\nu}^{\text{reg}}(\vec{k}) + \frac{1}{V_\Lambda}\hat{s}_\nu(\vec{k}), \tag{5.32}$$

where the regularized Epstein zeta function $Z_{\Lambda,\nu}^{\text{reg}}(\vec{k})$ is analytic in the reciprocal unit cell. The function $\hat{s}_\nu(\vec{k})$ can be understood as the Fourier transform of $|\vec{z}|^{-\nu}$ (in the distributional sense). It is defined as

$$\hat{s}_\nu(\vec{k}) = \frac{\pi^{\nu-d/2}}{\Gamma(\nu/2)}\Gamma\big((d-\nu)/2\big)|\vec{k}|^{\nu-d}, \quad \nu \notin (d+2\mathbb{N}).$$

In case that $\nu = d + 2n,\ n \in \mathbb{N}$, the Fourier transform is only uniquely defined up to a

polynomial of degree $2n$. We adopt the choice

$$\hat{s}_{d+2n}(\vec{k}) = \frac{\pi^{n+d/2}}{\Gamma(n+d/2)} \frac{(-1)^{n+1}}{n!} (\pi\vec{k}^2)^n \log(\pi\vec{k}^2).$$

Hence, the Epstein zeta function equals the sum of an analytic function and a power-law or logarithmic singularity. Therefore, the integral can be efficiently computed using either a specialized Gauss-Legendre quadrature or a Duffy transformation.[383] Our results are benchmarked against a direct summation approach, presented in Appendix D, where we reach full precision in one and two dimensions, where the direct sum can still be evaluated to machine precision.

5.2.6 Minimizing the cohesive energy

In order to analyze the impact of a long-range three-body ATM potential on the stability of lattices with two-body LJ interactions, we need to determine the optimal nearest neighbor distance $R > 0$ that minimizes the cohesive energy

$$E_{\text{coh}} = c_{n,m}\Big(\frac{Z_{\Lambda,n}}{nR^n} - \frac{Z_{\Lambda,m}}{mR^m}\Big) + \lambda f_{\text{coh}}^{(3)} R^{-9}, \tag{5.33}$$

with $n > m$ and

$$c_{n,m} = \frac{nm}{2(n-m)},$$

for a given lattice Λ with distance R. The resulting global minimization problem can be easily solved numerically using standard tools. It is, however, instructive to discuss particular special cases some of which allow for an analytic solution. Here we distinguish the cases where the repulsive part of the LJ potential dominates the three-body potential for small nearest neighbor distances or not.

1. $n > 9$. After setting $\partial E_{\text{coh}}/\partial R = 0$, this case reduces to solving the following root finding problem,

   $$c_{n,m}(Z_{\Lambda,n} - Z_{\Lambda,m}R^{n-m}) + 9\lambda f_{\text{coh}}^{(3)} R^{n-9} = 0. \tag{5.34}$$

   For the special case $n = 9 + k$ and $m = 9 - k$ the energy minimum can be determined analytically as

   $$R_{\min}(n,m,\lambda) = \left(\frac{9\lambda f_{\text{coh}}^{(3)}}{2c_{n,m}Z_{\Lambda,m}} + \sqrt{\left(\frac{9\lambda f_{\text{coh}}^{(3)}}{2c_{n,m}Z_{\Lambda,m}}\right)^2 + \frac{Z_{\Lambda,n}}{Z_{\Lambda,m}}}\right)^{1/(n-9)}. \tag{5.35}$$

   The often used $(12,6)$ LJ potential with $k = 3$ belongs to this class.

2. $n = 9$: In this special case, we find from Eq. (5.34) that

$$R_{\min}(n, m, \lambda) = \left(\frac{Z_{\Lambda,n}}{Z_{\Lambda,m}} + \frac{9\lambda f_{\text{coh}}^{(3)}}{c_{n,m} Z_{\Lambda,m}} \right)^{1/(9-m)}. \tag{5.36}$$

In case of attractive three-body interactions ($f_{\text{coh}}^{(3)} < 0$), the minimum only exists for sufficiently small ATM coupling strength λ with

$$\lambda \leq \frac{c_{n,m} Z_{\Lambda,n}}{9|f_{\text{coh}}^{(3)}|}. \tag{5.37}$$

3. $n < 9$: This case requires special care. The ATM potential dominates the LJ term for small R. For attractive three-body interactions, this means that the global minimum of the energy is obtained for $R \to 0$, leading to a collapse of the lattice into the origin. Local energy minima can however exist for $R > 0$. For the special case $n = 9 - k$, $m = 9 - 2k$, we find extrema at

$$R = \left(\frac{Z_{\Lambda,n}}{2Z_{\Lambda,m}} \pm \sqrt{\left(\frac{Z_{\Lambda,n}}{2Z_{\Lambda,m}} \right)^2 + \frac{9\lambda f_{\text{coh}}^{(3)}}{c_{n,m} Z_{\Lambda,m}}} \right)^{1/(9-n)}. \tag{5.38}$$

For attractive three-body interactions, a local minimum exists under the condition

$$\lambda \leq c_{n,m} \frac{Z_{\Lambda,n}^2}{36 Z_{\Lambda,m} |f_{\text{coh}}^{(3)}|}. \tag{5.39}$$

In the following we introduce instructive toy models in one- and two dimensions where R is chosen to be the nearest neighbor distance. We then analyze the influence of three-body interactions on the stability of cuboidal phases along a Bain path in three dimensions, where we choose R as the distance from the atom at the origin to the body-centered atom, which is the nearest neighbor distance in region I ($\frac{1}{3} \leq A \leq 1$, see Figure 5.2).

5.3 Results and Discussion

5.3.1 LJ+ATM Potential for a equidistant infinite linear chain

We begin our investigation with the effect of a three-body ATM potential coupled to a two-body LJ-potential in one dimension for an equidistant linear chain. The cohesive energy for the chain

with nearest neighbor distance R and normalized lattice $\Lambda = \mathbb{Z}$ becomes

$$E_{\text{coh}}(R,n,m) = E_{\text{coh}}^{(2)}(R,n,m) + E_{\text{coh}}^{(3)}(R,n,m) = c_{n,m}\Big(\frac{2\zeta(n)}{nR^n} - \frac{2\zeta(m)}{mR^m}\Big) + \lambda f_{\text{coh}}^{(3)} R^{-9}, \tag{5.40}$$

where we have used that the Epstein zeta function in 1D reduces to twice the Riemann zeta function, $Z_{\mathbb{Z},n} = 2\zeta(n)$. In this 1D case the simple pole is situated at $n = 1$ and $Z_{\mathbb{Z},n} \to 2$ for $n \to \infty$ as each atom has two nearest neighbors. The three-body ATM potential in 1D is purely attractive, which follows directly from Eq. (5.25),

$$f_{\text{coh}}^{(3)} = f_r^{(3)} + f_a^{(3)} = \frac{1}{6}\sum_{x,y\in\mathbb{Z}}{}' \frac{1}{|x|^3|y|^3|z|^3} - \frac{1}{2}\sum_{x,y\in\mathbb{Z}}{}' \frac{(xy)(yz)(zx)}{|x|^5|y|^5|z|^5} = -\frac{1}{3}f_r^{(3)} < 0. \tag{5.41}$$

The attractive behavior of the ATM potential for three atoms in a line has been discussed already by Axilrod and Teller[187] and will have important consequences in the following.

In one dimension, the three-body cohesive energy can still be evaluated to machine precision using exact summation. We obtain $f_{\text{coh}}^{(3)} = -0.2723018495076886$, which is in excellent agreement with the result from the Epstein zeta function treatment ($f_{\text{coh}}^{(3)} = -0.27230184950768865$) as outlined in section 5.2.5. This serves as a benchmark for higher dimensional lattices, where exact summation becomes exceedingly numerically expensive.

We now discuss the optimal nearest neighbor distance $R_{\min}(n,m,\lambda)$ as obtained in the previous Section 5.2.6 for different repulsive LJ exponents n.

1. $n > 9$: In this regime, the repulsive part of the LJ potential dominates the attractive ATM term. The solution to the root finding problem in Eq. (5.34) can be obtained numerically, with analytical solutions available for special cases such as the $(12,6)$-LJ potential in Eq. (5.35). We obtain $R_{\min}(12,6,0.0) = 0.997179263885806$, $R_{\min}(12,6,1.0) = 0.964148870884975$, $R_{\min}(12,6,3.0) = 0.902526982458744$ and $R_{\min}(12,6,5.0) = 0.847847116323818$. As expected, the nearest neighbor distance decreases with increasing coupling strength λ due to the increasing ATM attraction.

2. $n = 9$: Here, the repulsive part of the LJ potential and the attractive ATM potential share the same scaling and their prefactors determine the dominant term. The value of R that minimizes the energy is given by Eq. (5.36) as long as λ obeys the bound

$$\lambda \leq \frac{m\zeta(9)}{|(m-9)f_{\text{coh}}^{(3)}|}. \tag{5.42}$$

   If this critical value of λ is exceeded, then the energy diverges to $-\infty$ for $R \to 0$ and the chain collapses into the origin.

   For example, for the $(9,6)$-LJ potential we get $\lambda \leq 7.359541586938727$. At larger coupling

strengths, the minimum vanishes and the interaction becomes purely attractive and collapse occurs, i.e. $R \to 0$. This has consequences for 2D or 3D lattices as under this model, the crystal may distort into a set of linear chains, as we shall see later on.

3. $n < 9$. Here, the attractive ATM potential dominates at small distances R and the global minimum is obtained for $R \to 0$. Local minima can, however, exist for $R > 0$, as described in the previous section, with analytic solutions available for $n = 9 - k$ and $m = 9 - 2k$. A minimum then exists for sufficiently small λ as described by Eq. (5.39). For example, for $m = 4$ ($k = \frac{5}{2}$) and $n = \frac{13}{2}$, we obtain $\lambda < 1.003897458750910$ which is a rather small value. We find that by lowering the exponent for the repulsive force in the LJ potential, the existence of a minimum for the cohesive energy is achieved at lower critical values of the coupling strength λ.

Figure 5.3 summarizes our results for cases 1 and 3 for two different LJ potentials. When the two-body potential is of $(12, 6)$-LJ type, the repulsive LJ term dominates at short distances over the ATM term in the cohesive energy. On the other hand, for a softer two-body potential with exponent $n < 9$, as for the $(6, 4)$-LJ potential, the ATM potential completely dominates over the repulsive part of the LJ term for $\lambda > 0.9$ making the total cohesive energy behave like $-R^{-9}$ with a singularity at $R = 0$. When $\lambda \leq 0.689$, there is a competition between the attractive and repulsive parts of the cohesive energy, leading to a maximum in the short-range region that makes the cohesive energy slightly positive, followed by a divergence towards $-\infty$ due to the dominance of the attractive 3-body term. It is well known that the simple ATM term is valid only in the long-range,[384] and one has to correct the unphysical behavior of the 3-body term in the short range in order to avoid the collapse of all atoms towards the origin. On the other hand one should make sure that the repulsive wall in the two-body potential is described realistically.

5.3.2 LJ+ATM Potential for a square and hexagonal lattice

After analyzing the one-dimensional chain, we extend our focus to two-dimensional lattices. Among the five possible Bravais lattices, we restrict ourselves to the case of a square (SL) and hexagonal lattice (HL) with a nearest-neighbor distance R, as shown in Figure 5.4, and to the rectangular lattices as a mode to distort the square lattice into a set of linear chains. The hexagonal lattice is the densest packing of circles in a two-dimensional plane.

The two- and three-body terms of the cohesive energy for a square lattice $\Lambda = \mathbb{Z}^2$ are given by Eq. (5.33). Note that the Epstein zeta function for the square lattice appearing in the LJ term can be rewritten in terms of elementary functions,[124]

$$Z_{\mathbb{Z}^2,n} = 4\zeta(\tfrac{n}{2})\beta(\tfrac{n}{2}), \tag{5.43}$$

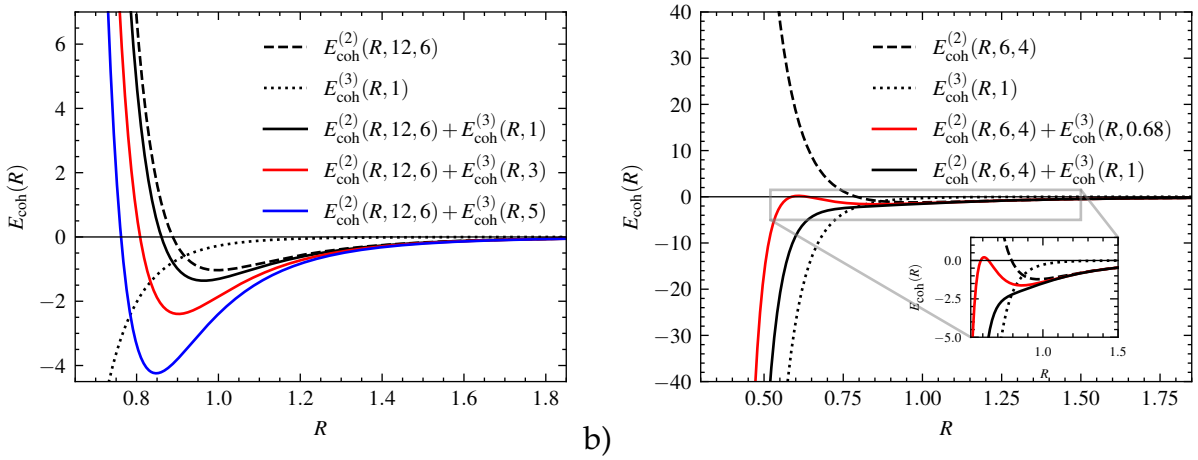

Figure 5.3: Cohesive energy of a linear chain with atoms interacting through: a) $(12,6)$-LJ coupled to an ATM potential, and b) $(6,4)$-LJ coupled to an ATM potential. Separate two- and three-body contributions are also shown in dashed and dotted lines, respectively.

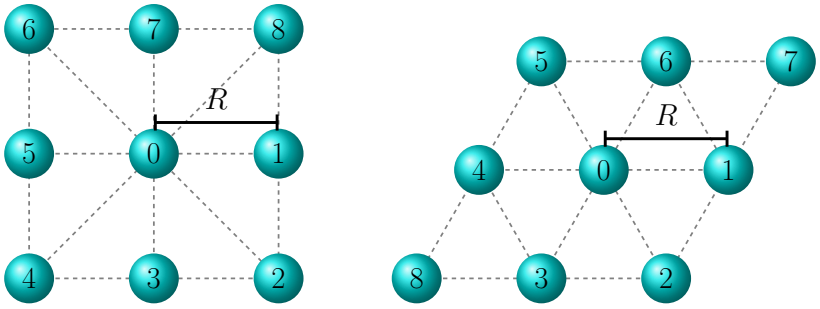

Figure 5.4: Square and hexagonal lattices of atoms interacting through LJ+ATM potentials with nearest neighbor distance R.

where β denotes the Dirichlet beta function.

The three-body term of the cohesive energy is given by Eq. (5.25). After an evaluation of the lattice sums through direct summation restricting the sums over integers to $N_{\rm max} = 1600$, the ATM term in the cohesive energy of the square lattice can be written as

$$E^{(3)}_{\rm coh} = \lambda f^{(3)}_{\rm coh} R^{-9} \tag{5.44}$$

with $f^{(3)}_{\rm coh} = f^{(3)}_r + f^{(3)}_a = 0.77009365051710454$ where $f^{(3)}_r = 2.2754822858923625$ and $f^{(3)}_a = -1.5053886353752584$, see Eq. (5.25). This compares well with the more accurate result from the Epstein zeta treatment as outlined in section 5.2.5, i.e. we get $f^{(3)}_{\rm coh} = 0.7700936505167162$ with $f^{(3)}_r = 2.27548228589309$ and $f^{(3)}_a = -1.5053886353763737$. The three-body contribution from an ATM potential to the cohesive energy is now repulsive for any R in the square lattice in contrast to the 1D case.

One can now perform a similar analysis compared to the 1D case. We only mention two examples here. For the (12,6)-LJ potential, the optimal

nearest neighbor distance is given by Eq. (5.35), where the ATM potential is now positive. This results in $R_{\min}(12,6,0.0) = 0.977489041852768$, $R_{\min}(12,6,1.0) = 1.021577293064089$, $R_{\min}(12,6,3.0) = 1.112586607942759$ and $R_{\min}(12,6,5.0) = 1.202957096531386$. We see that the distance is increasing rapidly with increasing coupling strength λ.

The other case we consider here is when the potential becomes completely repulsive over the whole range of R values. This can happen if the attractive R^{-m} term is always dominated by the repulsive ATM term, which can only occur for $m \geq 9$. Consider the case $m = 9$ which leads to the minimum distance,

$$R_{\min}(n,9,\lambda) = \left(\frac{Z_{\Lambda,n}}{Z_{\Lambda,9} - 9\lambda f^{(3)}_{\text{coh}}/c_{n,9}} \right)^{1/(n-9)} \tag{5.45}$$

and to the condition that

$$\lambda < \frac{c_{n,9} Z_{\Lambda,9}}{9 f^{(3)}_{\text{coh}}}. \tag{5.46}$$

For example, for $n = 12$ we get $\lambda < 10.88508744343488$. With increasing exponent n the critical λ value decreases as one would expect.

The cohesive energy for the square lattice as a function of R for two different (n,m)-LJ potentials coupled to the ATM potential is shown in Figure 5.5. We depict the two-body term $E^{(2)}_{\text{coh}}(R,n,m)$, the three-body contribution $E^{(2)}_{\text{coh}}(R,\lambda)$, and the full cohesive energy. An example of the long-range region becoming dominated by the repulsive ATM term is for the hard $(30,12)$-LJ potential as shown in Figure 5.5. For $\lambda = 1$, there is a region in which the square crystal is bounded around the equilibrium distance, however for $\lambda > 3.1834$ the cohesive energy becomes positive at any distance, meaning that we have a purely repulsive potential energy.

There is one small caveat here to consider as the square lattice might distort to a set of weakly interacting linear chains which may collapse to the origin for $n \leq 9$ as discussed in the previous section. In order to show this we consider the following generator matrix $B^\top$ and Gram matrix G,

$$B^\top = \begin{pmatrix} 1 & 0 \\ 0 & \gamma \end{pmatrix}, \quad G = \begin{pmatrix} 1 & 0 \\ 0 & \gamma^2 \end{pmatrix}, \tag{5.47}$$

which allow the square lattice to distort into a rectangular lattice where γ is the distortion parameter. Here, analytical solutions for the corresponding LJ lattice sums exist only for special cases of γ values.[295,385,386] We therefore use either the Van der Hoff Benson expansion[300] (see Appendix C) or EpsteinLib for the two-body term, and direct summation for the three-body term, where the latter approximation is sufficiently accurate to demonstrate the effect of such an unphysical distortion.

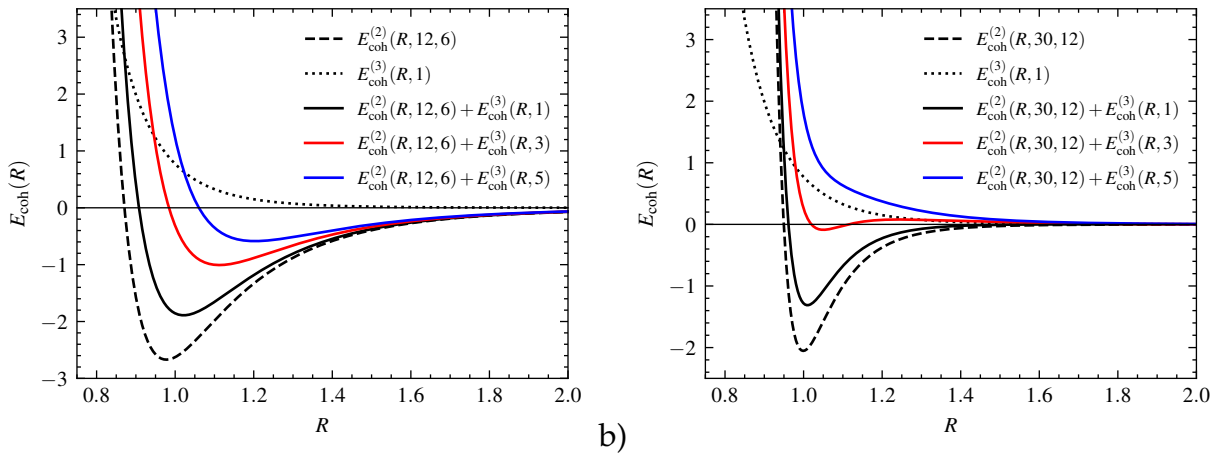

Figure 5.5: Cohesive energy of the square lattice with atoms interacting through: a) $(12,6)$-LJ potential coupled to an ATM potential, and b) $(30,12)$-LJ coupled to an ATM potential. Separate two- and three-body contributions are also shown in dashed and dotted lines, respectively.

As it turns out, there exists a critical value of $\gamma_c \approx 1.388$ that makes the three-body term of the cohesive energy neither repulsive nor attractive, i.e. $E^{(3)}_{\rm coh}(R,\gamma,\lambda) = 0, \lambda > 0$. This critical value remains basically constant along different λ values with a (shallow) saddle point appearing at $(\gamma_c,\lambda_c) = (1.388, 1.526)$. γ_c can be seen as the limit between the three-body attractive interaction in the linear chain and the three-body repulsion characteristic of the square lattice as shown before. The (γ,λ)-cohesive energy hypersurface for the difference in cohesive energy with respect to the square lattice with $(\gamma,\lambda) = (1,0)$, i.e.

$$\Delta E_{\rm coh}(R,\gamma,\lambda) = E_{\rm coh}(R,\gamma,\lambda) - E_{\rm coh}(R,1,0), \tag{5.48}$$

is shown in Figure 5.6. The square lattice without three-body interactions is located at a local minimum of the hypersurface at $(\gamma,\lambda) = (1,0)$, whereas the global minimum in the selected range is found at the upper right corner of the plot.

The point $(\gamma,\lambda) = (2,5)$ corresponds to a rectangular lattice with one of the sides of its unit cell being twice as large as the other. The reason for the high stability of this structure with respect to the square lattice is due to the fact that it is located at the region where the three-body potential becomes attractive, similar to the case of the linear chain. In fact, the square lattice structure is highly destabilized by the repulsive three-body forces, as shown in the lower right corner of Figure 5.6, whereas the rectangular lattice in the upper left corner is destabilized by due to two-body forces.

In a similar way, the generator matrix and the Gram matrix for the hexagonal lattice $\Lambda_{\rm hex} = B^\top \mathbb{Z}^2$, depicted in Figure 5.4, are given by

$$B^\top_{\rm hex} = \begin{pmatrix} 1 & \frac{1}{2} \\ 0 & \frac{\sqrt{3}}{2} \end{pmatrix}, \quad G_{\rm hex} = \begin{pmatrix} 1 & \frac{1}{2} \\ \frac{1}{2} & 1 \end{pmatrix}. \tag{5.49}$$

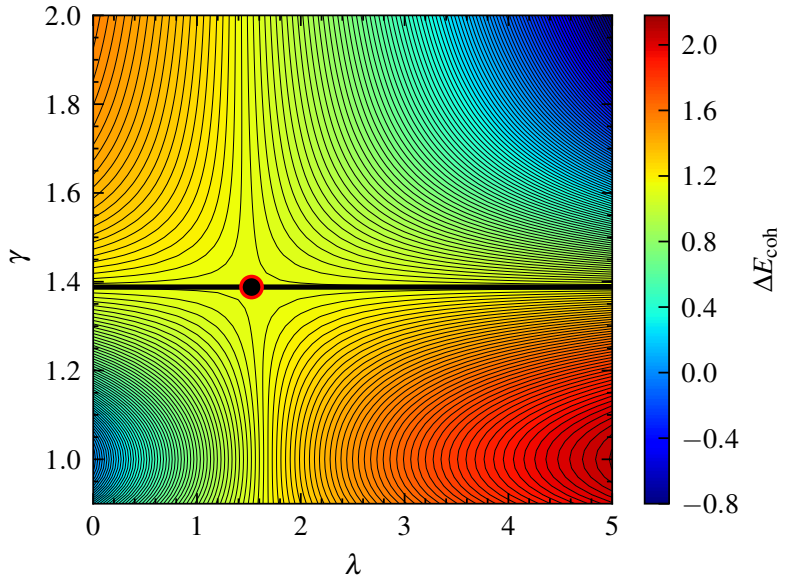

Figure 5.6: (γ, λ)-hypersurface for the difference in the cohesive energy of a rectangular lattice at optimized R with respect to the ideal square lattice at $(\gamma, \lambda) = (1, 0)$. The horizontal black line indicates the critical value of γ in which the ATM potential is neither repulsive nor attractive and the black point sits at the saddle point, located at $(\gamma_c, \lambda_c) = (1.388, 1.526)$.

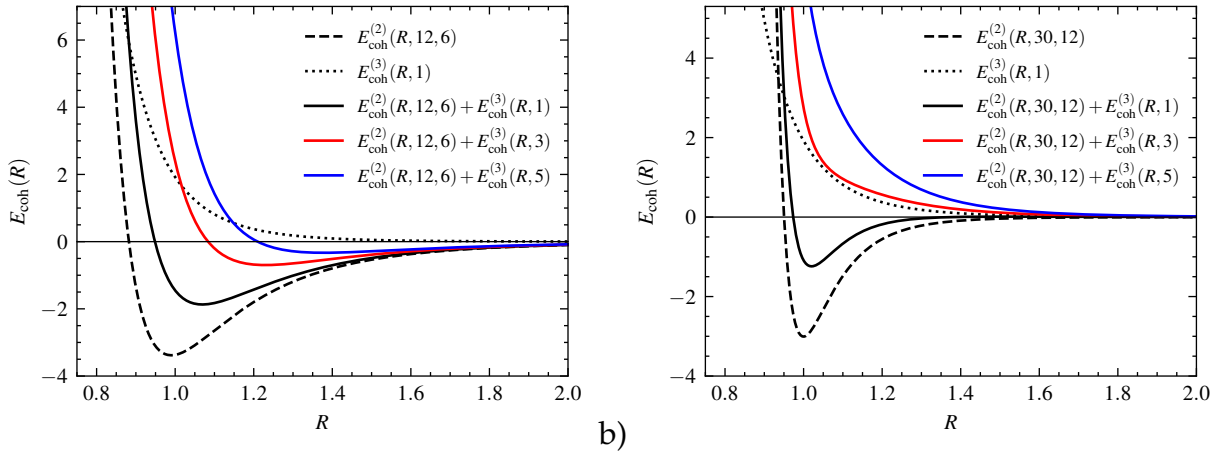

Figure 5.7: Cohesive energy of the hexagonal lattice with atoms interacting through: a) $(12,6)$-LJ potential coupled to an ATM potential, and b) $(30,12)$-LJ coupled to an ATM potential. Separate two- and three-body contributions are also shown in dashed and dotted lines, respectively.

The lattice sum of the hexagonal lattice also has an analytical formula given by Zucker and Robertson,[124]

$$Z_{\Lambda_{\rm hex},n} = 6\zeta(\tfrac{n}{2})\left[3^{-n/2}\left(\zeta(\tfrac{n}{2},\tfrac{1}{3}) - \zeta(\tfrac{n}{2},\tfrac{2}{3})\right)\right] \tag{5.50}$$

where $\zeta(n,x)$ is the Hurwitz zeta function, see Appendix A. The full cohesive energy is then given by Eq. (5.33).

For the three-body term in Eq. (5.25) we evaluate the 2D lattice sums through direct

summation with $N_{\max} = 1600$ to get

$$E_{\text{coh}}^{(3)}(R, \lambda) = \lambda f_{\text{coh}}^{(3)} R^{-9} \tag{5.51}$$

with $f_{\text{coh}}^{(3)} = 1.9183333648489187$ ($f_r^{(3)} = 4.263827935989311, f_a^{(3)} = -2.3454945711403923$) From Epstein zeta treatment, we get $f_{\text{coh}}^{(3)} = 1.9183333648478795$ ($f_r^{(3)} = 4.263827935991082$ and $f_a^{(3)} = -2.3454945711432025$). As in the square lattice, the three-body term also results in a repulsive contribution to the total cohesive energy, as shown in Figure 5.7. Furthermore, the lattice becomes unstable after a critical value of λ is reached, where the total cohesive energy is positive for any value of R. For example, this limit is obtained for the $(30, 12)$-LJ potential coupled with the ATM when $\lambda > 1.8854$. These results show that the hexagonal lattice is more strongly destabilized by adding three-body interactions compared to the square lattice because $f_{\text{coh,hex}}^{(3)} > f_{\text{coh,sq}}^{(3)}$. This is due to the hexagonal lattice being a close-packed structure in 2D with the highest packing density and kissing number.

Again we can do the same analysis as for the square lattice case, but mention only here the minimum distances for the (12,6)-LJ potential for which we get $R_{\min}(12, 6, 0.0) = 0.990193636287356$, $R_{\min}(12, 6, 1.0) = 1.06923072624940$, $R_{\min}(12, 6, 3.0) = 1.22992964510945$ and $R_{\min}(12, 6, 5.0) = 1.37801743468056$. Similar to the square lattice, a distortion into a set of linear chains can occur if $n \leq 9$ for large ATM coupling strengths λ.

5.3.3 LJ+ATM Potential for the cuboidal lattices

We are interested in the Bain minimum energy path $E_{\text{coh}}(R_{\min}, A)$ along the A-dependent cuboidal lattices at an optimized distance $R = R_{\min}$. The corresponding cohesive energy is obtained from Eq. (5.33) as

$$E_{\text{coh}}(n, m, A, \lambda, R_{\text{bc}}) = \frac{nm}{2(n-m)} \left(\frac{Z_{\Lambda(A),n}}{nR_{\text{bc}}^n} - \frac{Z_{\Lambda(A),m}}{mR_{\text{bc}}^m} \right) + \lambda f_{\text{coh}}^{(3)}(A) R_{\text{bc}}^{-9}, \tag{5.52}$$

for the lattice $\Lambda(A)$ along the Bain transformation path

$$\Lambda(A) = B^\top(A)\mathbb{Z}^3, \quad B^\top(A) = \frac{1}{\sqrt{A+1}} \begin{pmatrix} \sqrt{A} & \sqrt{A} & 0 \\ 1 & 0 & 1 \\ 0 & 1 & 1 \end{pmatrix}, \quad 0 < A \leq 1.$$

It is important to notice that the above lattice only exhibits unit nearest neighbor distance for $1/3 \leq A \leq 1$. We here define our measure of distance R_{bc} for all values of A as the distance from the atom in the origin to the body centered atom, otherwise one has to change the lattice sum in region I. In region I in Fig. 5.2, the resulting nearest neighbor distance can easily be obtained from R_{bc}. This choice is made to assure a smooth behavior of the resulting minimized distance

$R_{\min}$ across the whole range of A values and facilitates the exploration of region I, where we investigate the distortion of the cubic lattice to a set of weakly interacting linear chains along the c-axis. For ease of notation, we set $R = R_{\text{bc}}$ in the following.

The two-body contribution to the cohesive energy depends on the Epstein zeta function $Z_{\Lambda(A),n} = L(\frac{n}{2}, A)$, which is either obtained from the Bessel expansion in in Appendix B or using EpsteinLib. In the following we analyse the Bain phase transition for a range of (n,m)-LJ potentials, i.e. $(6,4)$-LJ, $(8,6)$-LJ, $(12,6)$-LJ and $(30,12)$-LJ. Note that the Epstein zeta function $Z_{\Lambda(A),n}$ becomes minimal for the bcc structure ($A = \frac{1}{2}$), as discussed in detail in Appendix F.

The three-body lattice sum $f^{(3)}_{\text{coh}}(A)$ is depicted in Figure 5.8 as a function of the parameter A. For region II the highest repulsive three-body energy occurs for the densely packed fcc lattice, while the energy minimum is reached for the bcc lattice within the studied parameter range, similar to the lattice sums for the Lennard-Jones (LJ) potential. This suggests that the fcc lattice may become unstable relative to the bcc lattice if the coupling parameter λ becomes sufficiently large. Moreover, at small A-values in region I we see that the three-body has a maximum and starts to go steeply down in energy becoming eventually attractive as discussed for the one- and two-dimensional cases.

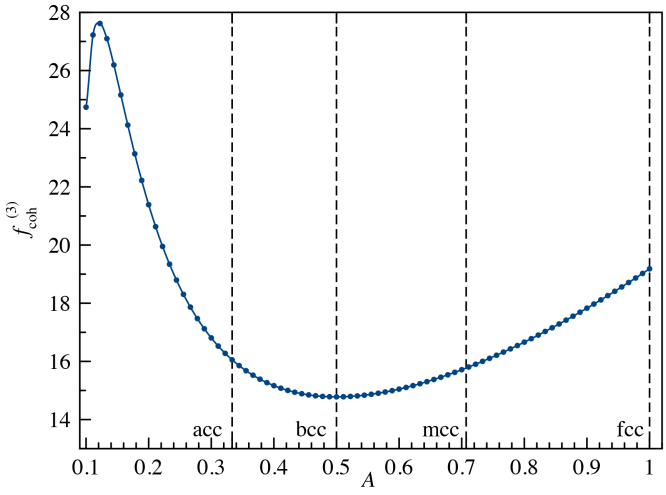

Figure 5.8: The normalized ATM cohesive energy $f^{(3)}_{\text{coh}}(A) = f^{(3)}_{r}(A) + f^{(3)}_{a}(A)$ is displayed along the Bain path as a function of the lattice parameter A.

In order to assess the stability of the bcc with respect to the fcc phase we need to minimize the cohesive energy (5.52) with respect to the distance R. The resulting optimization problem is discussed in detail in Sec. 5.2.6 and can be easily solved numerically with standard tools. However, as already explained in the previous sections, for the (12,6)-LJ potential coupled to an ATM potential we can derive analytical solutions for the minimum of Eq.(5.52), which we like to analyse in more detail.

The optimal distance $R_{\min}$ to the body-centered atom is obtain from Eq. (5.35) as

$$R_{\min}(12,6,\lambda,A) = \left(\sqrt{\left(\frac{3\lambda f^{(3)}(A)}{4Z_{\Lambda(A),6}} \right)^2 + \frac{Z_{\Lambda(A),12}}{Z_{\Lambda(A),6}}} + \frac{3\lambda f^{(3)}(A)}{4Z_{\Lambda(A),6}} \right)^{\frac{1}{3}} . \tag{5.53}$$

For $\lambda = 0$ we obtain the well known result,[226]

$$R_{\min}(12,6,\lambda=0,A) = \left(\frac{Z_{\Lambda(A),12}}{Z_{\Lambda(A),6}} \right)^{\frac{1}{6}} \tag{5.54}$$

and for $\lambda \to \infty$ we see that $R_{\min}(A) \to \infty$ for a repulsive three-body term. A few examples illustrate the behavior of the minimum distance $R_{\min}(\lambda)$ with increasing coupling strength: for $A = 1.0$ (fcc) we have $R_{\min}(0.0) = 0.9712336909596462$, $R_{\min}(1.0) = 1.3291651590715157$, $R_{\min}(3.0) = 1.8281263889243278$, $R_{\min}(5.0) = 2.1571214550726303$, and for $A = 0.5$ (bcc) we have $R_{\min}(0.0) = 0.9518648186624387$, $R_{\min}(1.0) = 1.2915727206984038$, $R_{\min}(3.0) = 1.7717531211610782$, $R_{\min}(5.0) = 2.0899090593393477$.

Because of $f^{(3)}_{\text{coh}}$(fcc)> $f^{(3)}_{\text{coh}}$(bcc) the minimum distance is more rapidly increasing for fcc than for bcc with increasing coupling strength λ. This is shown for different (n,m)-LJ potentials in Figure 5.9. The minimum properties are also shown in Table 5.2. We note that for the (30,6)-LJ potential we have $R_{\min} = 0.9828$ (bcc) and 0.9923 (fcc) at $\lambda = 0$, which is close to the unit distance for hard spheres. This is expected for a hard-wall potential that approaches the sticky hard-sphere limit.[209] Further, soft potentials (low n and m values) lead to larger contractions in $R_{\min}$ when moving along the cuboidal distortion path from fcc to bcc.

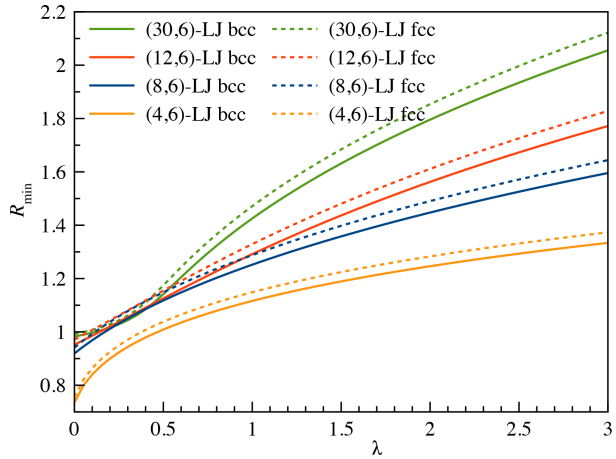

Figure 5.9: Minimum distances $R_{\min}(A,\lambda)$ for the bcc ($A = \frac{1}{2}$) and fcc ($A = 1$) structures for different (n,m)-LJ potentials as a function of the ATM coupling parameter λ.

To estimate the range of typical coupling strengths λ, we consider the formula derived

Table 5.2: Minimum distances and cohesive energies at $\lambda = 0$ derived analytically from the lattice sums (see also Ref. 103). For the bcc structure we have the general condition that $\partial E^{(2)}_{\mathrm{coh}}(A = \frac{1}{2})/\partial A = 0$. For the (8,6), (12,6) and (30,6) LJ potentials the bcc structure is a maximum along the Bain path.

	(6,4)	(8,6)	(12,6)	(30,6)
$R_{\mathrm{min}}(A=\frac{1}{2})$	0.7357107511	0.9192764815	0.9518648187	0.9827992166
$R_{\mathrm{min}}(A=1)$	0.7552731838	0.9411200107	0.9712336910	0.9922781478
$E^{(2)}_{\mathrm{coh}}(A=\frac{1}{2})$	-38.636118884	-10.152177739	-8.237291910	-6.799035350
$E^{(2)}_{\mathrm{coh}}(A=1)$	-38.934203192	-10.401252415	-8.610200157	-7.571032638
$\partial^2 E^{(2)}_{\mathrm{coh}}(A=\frac{1}{2})/\partial R^2$	3426.26165602	1153.28899200	1309.17106453	2534.07927284
$\partial^2 E^{(2)}_{\mathrm{coh}}(A=1)/\partial R^2$	3276.15467791	1127.37098543	1314.40215104	2768.15729574
$\partial^2 E^{(2)}_{\mathrm{coh}}(A=\frac{1}{2})/\partial A^2$	1.3106119526	-4.0072840086	-8.6586541684	-19.701773034
$\partial^2 E^{(2)}_{\mathrm{coh}}(A=1)/\partial A^2$	7.2332403470	4.8703884251	6.8704958970	17.713990956

from the Drude model describing the triple dipole interactions between three identical atoms at equilibrium distance r_e,[387,388]

$$\lambda = \frac{9}{16}\frac{I}{\epsilon}\frac{\alpha^3}{r_e^9} \tag{5.55}$$

where I is the first ionization potential of the atom and α the static dipole polarizability. For example, taking known experimental or theoretical values[389–391] we get for argon $\lambda_{\mathrm{Ar}} = 0.025$, for xenon $\lambda_{\mathrm{Xe}} = 0.034$, for the heaviest noble gas atom $\lambda_{\mathrm{Og}} = 0.101$, and for lithium (due to its large polarizability and small equilibrium distance) $\lambda_{\mathrm{Li}} = 6.0$. However, for bulk lithium the many-body expansion is not converging smoothly, as this is generally the case for metallic solids.[103,183] This implies that the ATM term is applicable only for small coupling parameters λ, as larger values suggest that higher-order terms in the expansion (5.17) become important as well. Based on these λ values we chose the following grid in our computations: $A \in [\frac{1}{10}, 1]$ with step size $\Delta A = \frac{1}{60}$, and $\lambda \in [0, 6.0]$ with step size $\Delta\lambda = 0.05$.

As the differences between the bcc and fcc minimum distances are relatively small compared to R_{min} at constant λ, we consider the difference in the minimum distances between the cuboidal and the fcc structures, i.e. $\Delta R_{\mathrm{min}}(A, \lambda) = R_{\mathrm{min}}(A, \lambda) - R_{\mathrm{min}}(A = 1, \lambda)$. Figure 5.10 shows $\Delta R_{\mathrm{min}}(A, \lambda)$ values for the four different LJ potentials. They all show a qualitatively similar behavior in the region $\frac{1}{3} \leq A \leq 1$. The smallest distance is always found at the bcc structure ($A = \frac{1}{2}$). However, we see some significant changes to lower ΔR_{min} values with minima occurring in the region $A < \frac{1}{3}$ for larger coupling strengths λ and larger repulsive walls (exponents $n = 12$ and 30), which is due to linear chain formation as will be discussed in the following.

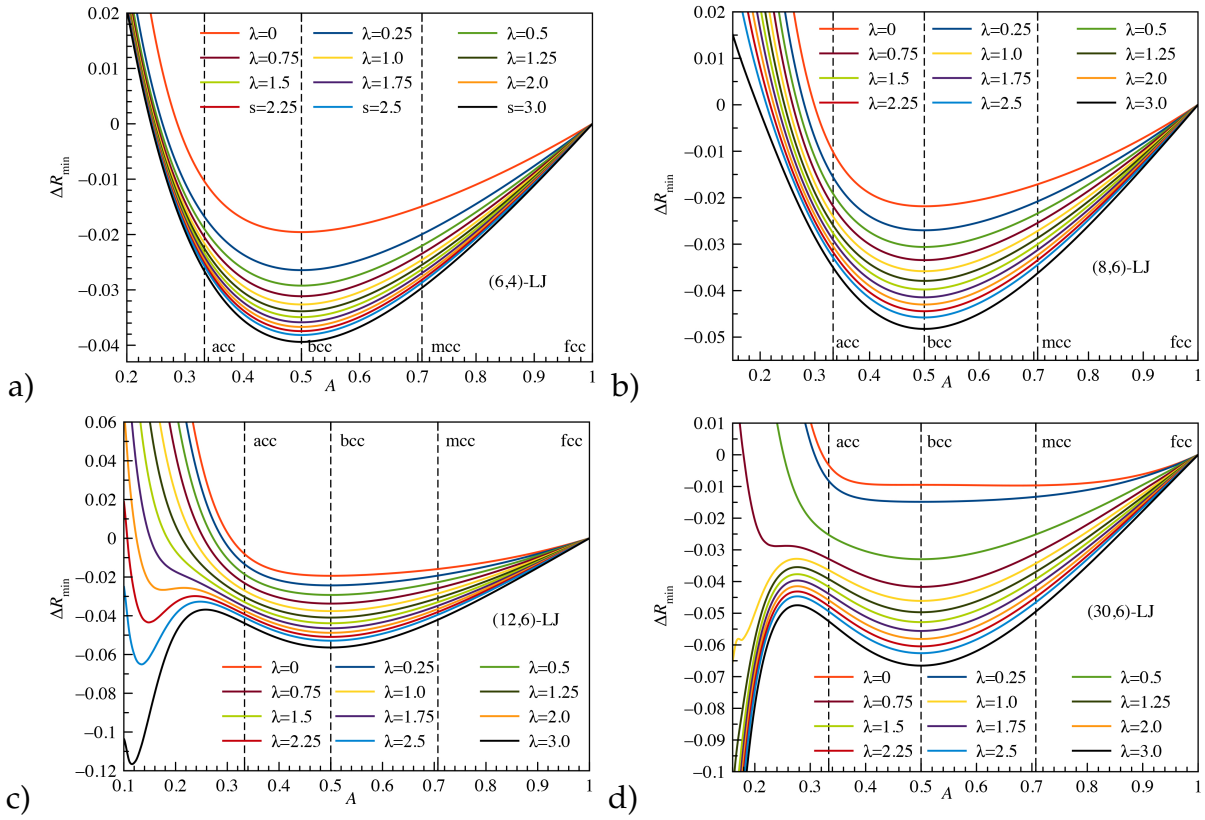

Figure 5.10: Difference $\Delta R_{\min}(A,\lambda) = R_{\min}(A,\lambda) - R_{\min}(A=1,\lambda)$ for the $(6,4)$ (a), $(8,6)$ (b), $(12,6)$ (c) and (30,6) (d) LJ potentials for different coupling parameters λ. The four distinct lattices acc ($A = \frac{1}{3}$ on the left, bcc ($A = 1$) and mcc ($A = \frac{1}{\sqrt{2}}$) at dashed lines, and fcc ($A = 1$) on the right are indicated.

Figure 5.11 shows the cohesive energies for a few selected λ values for the (12,6)-LJ potential. The energy curves are shifted towards higher energies with increasing λ value as we expect, and become very flat at high energies. At the optimized distance $R_{\min}(A,\lambda)$ it consistently holds that $\Delta E_{\text{coh}}(A,\lambda) < 0$, which is below the atomization limit as expected. With increasing λ, $R_{\min}$ becomes larger to the point that at long range the dispersive R^{-m} term ($m = 4, 6$) in the LJ potential dominates over the repulsive ATM force.

Details of the Bain transformation path become more transparent when we plot the difference in cohesive energies with respect to the fcc structure as shown in Figure 5.12. It was pointed out before that for a certain range of (n,m) values with $m < 5.25673, n > m$ and $\lambda = 0$ the bcc phase becomes metastable, otherwise it will distort towards lower A values, i.e. the acc structure.[103] However, the bcc structure strictly remains an extremum.[103] The instability of the bcc phase for certain LJ exponents was already discussed in 1940 by Born and Misra[355,356], and later by Wallace and Patrick.[372] Similar results are obtained for the generalized Morse potential[392] indicating that many-body forces have substantial influence on the bcc phase. However, a distortion from the ideal bcc phase was also found by Craievich et al for several

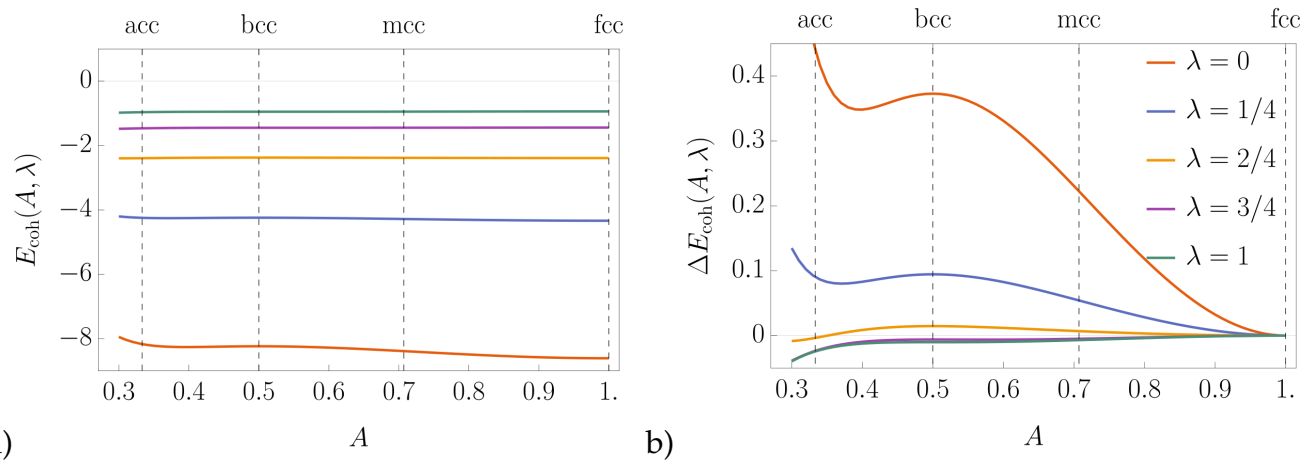

Figure 5.11: Cohesive energies, $E_{\rm coh}(A,\lambda)$ (a) at the corresponding $R_{\rm min}(A,\lambda)$ values dependent on the parameters A and λ for the $(12,6)$-LJ potential. The four distinct lattices acc ($A = \frac{1}{3}$ on the left, bcc ($A = 1$) and mcc ($A = \frac{1}{\sqrt{2}}$) at dashed lines, and fcc ($A = 1$) on the right are indicated. The difference $\Delta E_{\rm coh}(A,\lambda) = E_{\rm coh}(A,\lambda) - E_{\rm coh}(A = 1,\lambda)$ is shown in (b).

elemental metals.[393] Adding the ATM potential we see that at a critical coupling strength λ_c ($\lambda_c = 0.635$ for the (12,6)-LJ potential for example) the bcc phase starts to lie energetically below the fcc phase. The critical λ_c values obtained from a polynomial fit are listed in Table 5.3 for the four (n,m)-LJ potentials considered.

Figure 5.14 shows curves of the critical coupling parameters λ_c for fixed m and variable n for (n,m)-LJ potentials including the ATM potential. The λ_c values given in Table 5.3 are indicated as well. For very small values of both exponents (n,m) we see that λ_c is zero. At the other end, in the kissing hard-sphere (KHS) limit ($n,m \to \infty, n > m$) for a LJ potential the cohesive energy is given by $E^{(2)}_{\rm coh} = N_{\rm kiss}/2$, where $N_{\rm kiss}$ is the kissing number. Adding the three body term we get the condition for the critical coupling strength considering that $R = 1$,

$$-6 + \lambda_c E^{(3)}_{\rm coh}(A = 1) = -4 + \lambda_c E^{(3)}_{\rm coh}(A = \tfrac{1}{2}) \tag{5.56}$$

which gives $\lambda_c = 0.45430739956758$. This explains the asymptotic behaviour of the curves shown in Figure 5.14 for large m-values. However, this coupling parameter results in a purely repulsive force for the KHS limit for all cuboidal structures. The main message of this analysis here is that soft two-body interactions and strong repulsive many-body forces favor the bcc over the fcc phase. A prime example for this is lithium where the two phases are almost energetically degenerate.[79] This is also seen in Fig. 5.13, where for a soft $(8,4)$-LJ potential, bcc becomes energetically favorable compared to fcc for $\lambda > \lambda_c = 0.68740381212384$, with bcc forming a local minimum of the cohesive energy along the Bain path.

The first derivatives are $\partial E_{\rm coh}(A = \frac{1}{2},\lambda)/\partial A = 0$ at any λ value and a proof that $\partial f^{(3)}_{\rm coh}(A)/\partial A = 0$ at $A = \frac{1}{2}$ is given in Appendix E. This implies that the bcc structure remains

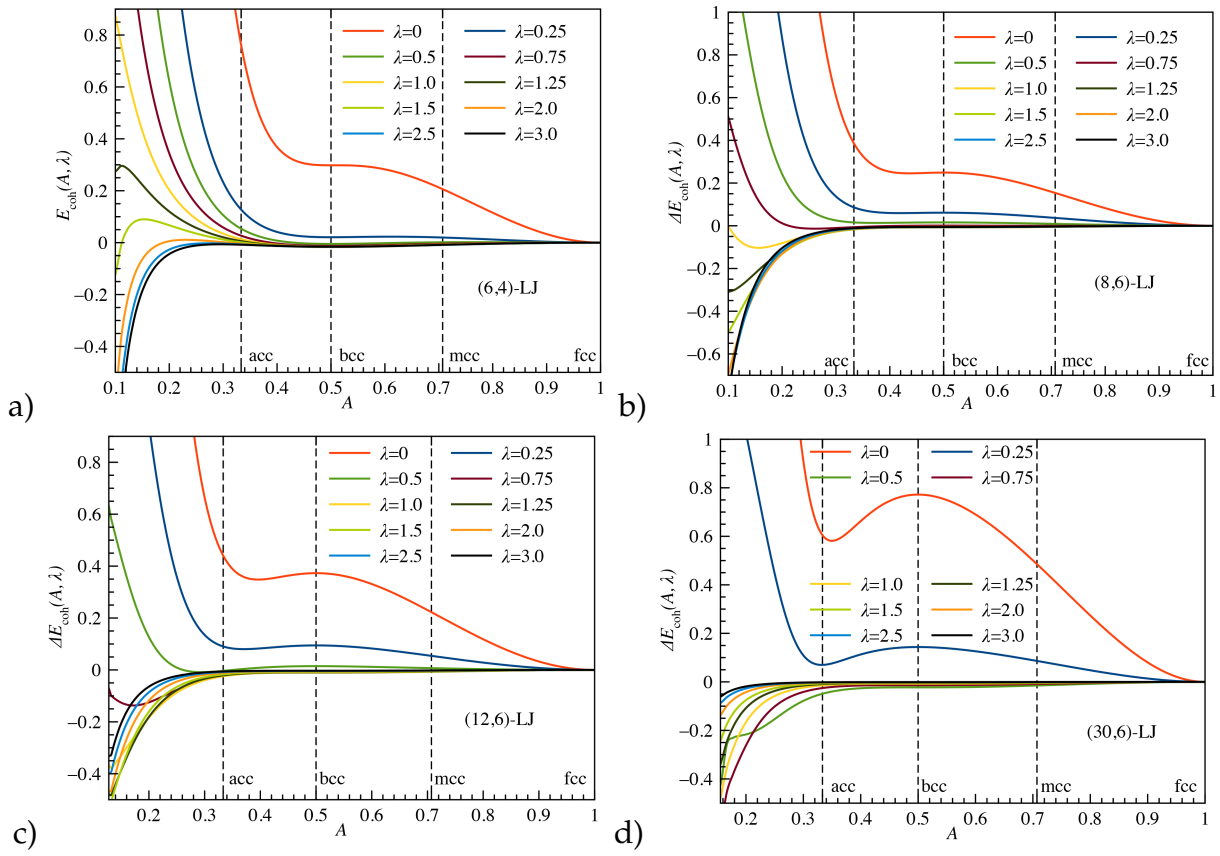

Figure 5.12: Cohesive energy differences, $\Delta E_{\mathrm{coh}}(A,\lambda) = E_{\mathrm{coh}}(A,\lambda) - E_{\mathrm{coh}}(A=1,\lambda)$ at the corresponding $R_{\mathrm{min}}(A,\lambda)$ values dependent on the parameters A and λ for the $(6,4)$ (a), $(8,6)$ (b), $(12,6)$ (c) and (30,6) (d) LJ potentials. The four distinct lattices acc ($A = \frac{1}{3}$ on the left, bcc ($A = 1$) and mcc ($A = \frac{1}{\sqrt{2}}$) at dashed lines, and fcc ($A = 1$) on the right are indicated.

an extremum if the ATM term is added. The rather small second derivatives compared to the corresponding values at $\lambda = 0$ show the flatness of the cohesive energy curves $E_{\mathrm{coh}}(A=\frac{1}{2},\lambda_{\mathrm{c}})$ clearly seen in Figure 5.12. However, the bcc structure at λ_c still remains a minimum for the $(6,4)$-LJ potential, and a maximum for the other three potentials considered. At even higher values, $\lambda \gg \lambda_{\mathrm{c}}$) the lattice distorts to much lower A values. While for the $(6,4)$-LJ potential we can still locate a very shallow minimum at λ values up to the maximum value considered, for the other potentials we change to a monotonically decreasing function to smaller A-values, that is the three-body force destabilizes both fcc and bcc.

Kwaadgras et al. discussed in detail the formation of linear chains for finite systems within the induced dipole interaction model,[394] and commented on the importance of the ATM potential. Figure 5.15 depicts the behavior at small A-values if the coupling strength λ becomes large. We see a formation of linear chains along the c-axis. The kissing number is reduced to 2 as listed in Table 5.1. This is easily explained through Eq. (5.12): For $A \to 0$ we have $\gamma \to 0$ and $R \to \frac{a}{\sqrt{2}} \to \infty$, which implies that for increasing coupling strength λ keeping c finite we

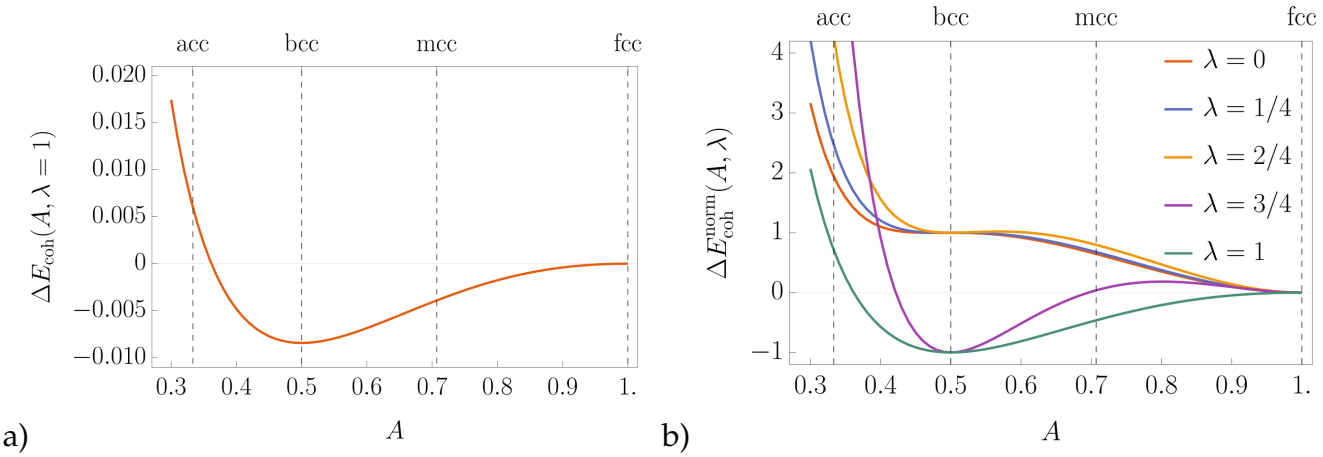

Figure 5.13: (a) Cohesive energy differences, $\Delta E_{\rm coh}(A,\lambda) = E_{\rm coh}(A,\lambda) - E_{\rm coh}(A=1,\lambda)$ at the corresponding $R_{\rm min}(A,\lambda)$ values for $\lambda = 1$ as a function of A for the $(8,4)$-LJ potential. (b) The normalized cohesive energy differences $\Delta E^{\rm norm}_{\rm coh}(A,\lambda) = \Delta E_{\rm coh}(A,\lambda)/|\Delta E_{\rm coh}(A=1/2,\lambda)|$ for different values of $0 \leq \lambda \leq 1$. Numerically, we observe that bcc becomes energetically favorable compared to fcc for $\lambda > \lambda_c = 0.68740381212384$.

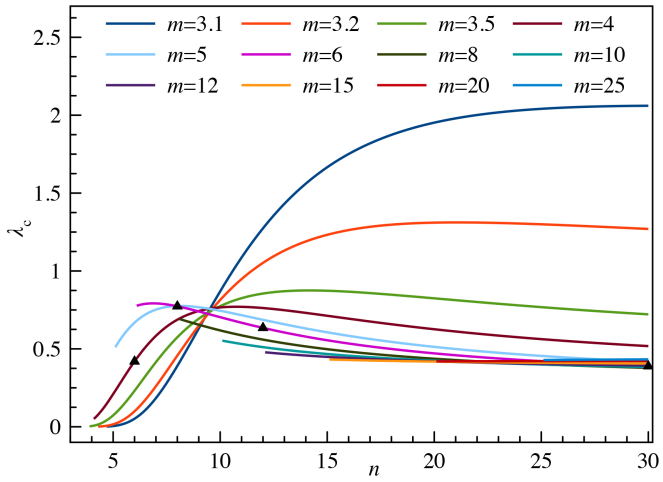

Figure 5.14: Critical coupling strength λ_c for different (n,m)-LJ combinations $n > m$. The values for the specific LJ potentials given in Table 5.3 are shown as black triangles.

see the formation of largely separated linear chains where the ATM force becomes attractive as explained in section 5.3.1. Hence we see exactly the same (unphysical) situation as for the 2D lattice where we allowed for distortion in one direction.

We add some final comments here. First, very large λ values are not realistic as shown above. Second, and more importantly, the ATM potential is only valid in the long range. In the very short range, the three-body force becomes even attractive for the rare gas elements.[395–397] Third, the many-body expansion of the total energy of a lattice described by quantum theory does not converge fast at short distances. This is especially the case for metallic systems as already mentioned.[183] Fourth, if we maintain the use of such a model system we need to

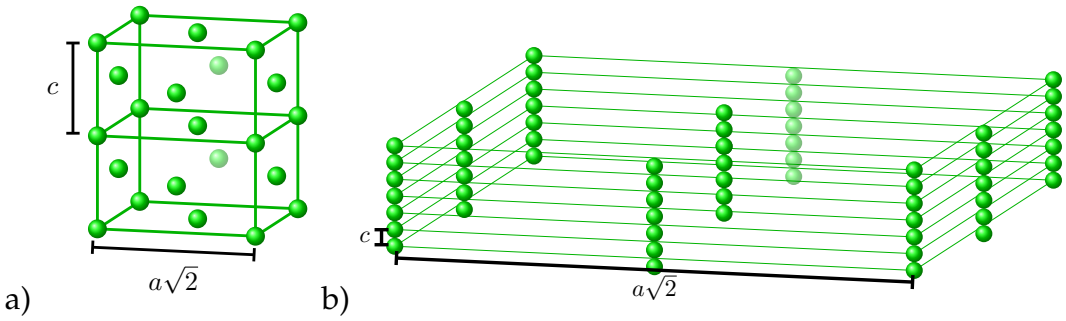

Figure 5.15: a) Conventional cell of the acc structure at $A = 1/3$ showing the linear chain formation parallel to the c-axis, and b) weakly interacting linear chains obtained from a cuboidal structure with $A = 0.005$.

Table 5.3: Minimum distances and LJ and ATM contributions to the cohesive energy at critical λ_c where $E_{coh}(A = \frac{1}{2}, \lambda_c) = E_{coh}(A = 1, \lambda_c)$.

	(6,4)	(8,6)	(12,6)	(30,6)
λ_c	0.4193457686	0.7733575166	0.6347968492	0.3886346322
$R_{min}(A=\frac{1}{2})$	0.9852364722	1.1958708129	1.1721405159	1.0793981795
$R_{min}(A=1)$	1.0137042601	1.2295453143	1.2038745402	1.1033397959
$E^{(2)}_{coh}(A=\frac{1}{2})$	-22.6422225486	-4.6655349480	-4.0473152968	-4.7402824565
$\lambda_c E^{(3)}_R(A=\frac{1}{2})$	11.6852182056	3.7683462411	3.7046445690	4.7625029058
$\lambda_c E^{(3)}_A(A=\frac{1}{2})$	-4.5992266773	-1.4831968267	-1.4581242585	-1.8744904913
$E_{coh}(A=\frac{1}{2})$	-15.5562310202	-2.3803855336	-1.8007949863	-1.8522700420
$E^{(2)}_{coh}(A=1)$	-22.6730462463	-4.6902916517	-4.0933436461	-4.9288827060
$\lambda_c E^{(3)}_R(A=1)$	11.6816642186	3.7915200539	3.7630292199	5.0500055052
$\lambda_c E^{(3)}_A(A=1)$	-4.5648491451	-1.4816139852	-1.4704806092	-1.9733929072
$E_{coh}(A=1)$	-15.5562310202	-2.3803855336	-1.8007949863	-1.8522700420
$\partial E_{coh}(A=\frac{1}{2})/\partial A\ [10^{-5}]$	-3.128265	-1.008829	-0.991775	-1.275000
$\partial^2 E_{coh}(A=\frac{1}{2})/\partial A^2$	1.319068	-0.194625	-0.423196	-0.811519

make sure that the exponent of the repulsive force in the LJ potential exceeds the one in the ATM potential, otherwise we observe a collapse of the linear chain for $n < 9$ as outlined in section 5.3.1.

5.4 Conclusion

In this work, we have explored the influence of three-body interactions on the stability of cuboidal lattices. To this end, we have studied the cohesive energy along a Bain phase transformation path connecting the fcc lattice structure to the mcc, bcc, and finally the acc

lattice, where we have included both a two-body (n,m)-LJ potential and a three-body ATM potential of increasing coupling strength. The two-body lattice sums were computed to full precision using either rapidly converging Bessel function expansions[111,295] or, alternatively, efficient evaluations based on the Epstein zeta function.[379] The challenging computation of the high-dimensional, slowly converging three-body lattice sums has been successfully achieved using a new representation based on singular integrals involving products of Epstein zeta functions. This approach enables, for the first time, the precise evaluation of three-body lattice sums within minutes on a standard laptop, and can (most likely) be extended to more general many-body terms and multiple zeta functions which is part of our future work.[398]

Using our advanced numerical framework, we have been able to precisely evaluate the small energy differences between the cuboidal structures along the Bain path. Our results demonstrate that the three-body potential can destabilize the fcc structure for large ATM coupling strengths. We analytically show and numerically confirm that the ATM potential exhibits a minimum along the Bain path at the bcc structure, resulting in the bcc structure becoming a metastable minimum for soft LJ potentials. For hard-wall LJ potentials, the structure distorts towards, and even beyond, the acc phase. Linear chain formation is observed at high ATM coupling strength, which is due to the short-range behavior of the ATM force.

Our results indicate that, beside the softness of the two-body potential, the stability of the bcc lattice may heavily rely on higher than two-body effects. While this study serves as an initial exploration of the martensitic bcc-to-fcc phase transition mechanism, more realistic systems, such as metals, need to be investigated in future work and possible symmetry breaking effects (such as rhombohedral distortions) need to be included[349]. This requires a more precise computation of many-body potentials based on density functional theory, as well as the incorporation of temperature and pressure effects.

MASSEY UNIVERSITY
TE KUNENGA KI PŪREHUROA
UNIVERSITY OF NEW ZEALAND

GRADUATE RESEARCH SCHOOL

STATEMENT OF CONTRIBUTION
DOCTORATE WITH PUBLICATIONS/MANUSCRIPTS

We, the student and the student's main supervisor, certify that all co-authors have consented to their work being included in the thesis and they have accepted the student's contribution as indicated below in the Statement of Originality.

Student name:	Andres Eduardo Robles Navarro
Name and title of main supervisor:	Peter Schwerdtfeger
In which chapter is the manuscript/published work?	Chapter 6

Describe the contribution that the student and members of the supervisory team have made to the manuscript/published work:[1]

All the computations were perfomed by me, except for the ones using the Nudged Elastic Band method for Argon which were done by Fabian Zehetmair. The theoretical development of the publication is equally divided between me, Shaun Cooper, and Peter Schwerdtfeger. Further discussions also included Odile Smits and Andreas Hauser.

Please select one of the following three options:

- (●) **The manuscript/published work is published or in press**

  Please provide the full reference of the research output:

  Physical Review B, 2026, 113: 024116

- ( ) **The manuscript is currently under review for publication**

  Please provide the name of the journal:

- ( ) **It is intended that the manuscript will be published, but it has not yet been submitted to a journal**

Student's signature:	ARoblesNavarro	Main supervisor's signature:	PeterSchwerdtfeger Digitally signed by PeterSchwerdtfeger Date: 2025.12.08 14:24:15 +13'00'

This form should be placed at the beginning of each relevant thesis chapter.

[1] Refer to the Massey University Publishing and Authorship guidelines (OneMassey for staff, Stream for students) and/ or Contributor Roles Taxonomy (CRediT) guidelines for guidance.

Chapter 6

Lattice Instabilities Along the Transformation from Hexagonal to Cuboidal Structures in Hard- and Soft-Sphere Models

6.1 Introduction

The relative stability between the face-centered cubic (fcc) and hexagonal close-packed (hcp) structures, and their formation from the gas or the liquid phase known as the nucleation problem, has been a matter of intense discussion and debate over the past 50 years[268,349,399]. Both phases have the same hard-sphere packing density of $\rho = \pi/3\sqrt{2} = 0.74048048969\ldots$, as have all possible associated Barlow structures (mixtures between $(AB)_\infty$ and $(ABC)_\infty$ stackings)[18,400–402] for which there are infinitely many. It was only in recent times that Kepler's original conjecture, stating that the fcc packing density cannot be surpassed for hard (unit) sphere packings and therefore is optimal, was proven by Hales[10,403].

Optimal sphere packings predict only a very small difference in the free energy up to the melting point[399,404,405]. For real atomic or molecular crystals the two close-packed structures are also found to be very close in energy[406]. A prominent example is solid argon, where at low temperatures and pressures, vibrational effects need to be included to stabilize the experimentally observed fcc over the hcp phase[104,109]. However, the cohesive energy difference between the two phases is predicted to be a mere 8.1 ± 0.7 J/mol[104,407] from relativistic coupled cluster calculations. Such small energy differences between the fcc and hcp phase for solids are also detected in nucleation processes[226,408–410]. On the other hand, for the heavier noble gas elements the hcp phase becomes the dominant phase at high pressures,[267,411,412] which is most likely due to the fact that with increasing pressure

vibrational effects become less important compared to the competing many-body electronic contributions.

Why one phase dominates over the other at certain temperatures and pressures delicately depends on the different static and dynamic contributions to the free energy. It is however notoriously difficult to get a detailed mechanistic insight into solid-state phase transitions by both experimental and theoretical methods,[352] and therefore such transitions are in general not so well understood[354,413]. One could naively slide some of the hexagonal layers to turn hcp into fcc, i.e. for the hexagonal layer sequences we have the transformation $(ABA{\downarrow}B{\downarrow}A{\uparrow}B{\uparrow})_\infty \rightarrow (ABCABC)_\infty$,[413] which involves a supercell treatment. However, it is not known if this is the lowest minimum energy path, for example, in such sliding of the hexagonal layers one may well access local minima such as dense Barlow packings, e.g. $(ABABA{\downarrow}B)_\infty \rightarrow (ABABCB)_\infty$.

In 1934 Burgers suggested a very simple diffusionless hcp↔bcc (body centred cubic) phase transition path[262], while Bain earlier in 1924 proposed a simple cuboidal fcc↔bcc transition path[256]. Since then, there has been some controversy whether or not the fcc phase is actually required in a minimum energy path for the hcp→bcc phase transition and if these transitions follow at all the diffusionless mechanism as suggested by Bain and Burgers[269,414–416]. Moreover, it is not clear if the Burgers transformation belonging to the class of martensitic transitions is a first-order phase transition or not[417]. More recently, Feng and Widom showed from DFT calculations of several transition metals that the hcp→bcc transition exhibits an alternating slide instability corresponding to a tetragonal symmetry breaking[418]. While this instability manifests in a distinct phonon instability, a detailed explanation is still missing.

Modeling solid-state phase transitions at the microscopic level poses significant challenges[266,350,352,419–421]. This is mainly due to the fact that often stacking faults or defects are involved in such phase changes, which requires a computationally expensive super-cell treatment in a molecular dynamics simulation[367,422,423]. Diffusionless martensitic transformations do not have these problems, but mapping out the correct minimum energy path for such a transition can still be a formidable task[260,367,371,414,415]. Moreover, various theoretical approximations (such as the density functional approximation) may not result in the correct energy sequence between the different (often quasi-degenerate) polymorphs involved[424]. Moreover, when empirical model potentials are used, the stability of the bcc phase heavily depends on its analytical form and parameters chosen[259].

Caspersen and Carter[352] generalized the climbing image-nudged elastic band algorithm[425,426] to find transition paths in solid-state phase transitions, and subsequently applied this to the diffusionless martensitic transformation[256,262] from hcp to the bcc structure and further to fcc for metallic lithium. They gave detailed information for the transformation matrices acting on the corresponding lattice vectors. In a different approach, Raju Natarajan

and Van der Ven used a set of two parameters derived from the Hencky logarithmic strain to map out the volume preserving potential energy surfaces for the Burgers-Bain transformation for metallic lithium, sodium and magnesium[427]. Cayron introduced transformation matrices (which he termed angular distortion matrices) for continuous atomic displacements between the three different phases[416]. Bingxi Li et al. performed molecular dynamics simulations using a (12,6)-Lennard-Jones potential for argon calibrated at $T = 40$ K and $P = 1$ bar[367]. They discussed different paths for the hcp↔fcc phase transition. However, the topology of the cohesive energy surface as a function of the lattice parameters to map minimum energy paths in such phase transitions may critically depend on the chosen model applied describing the interactions between the atoms in the lattice. Moreover, molecular dynamics (MD) or Monte-Carlo simulations for the phase transitions in the solid state are computer time consuming and depend on the size of the supercell chosen. From the dynamics at elevated temperatures it is often not easy to map out different minimum energy paths[428]. Hence, it would be advantageous to develop a simpler model capable of estimating the activation energy (or at least an upper bound) involved in such solid-state phase transitions.

In this paper we analyze in detail the Burgers-Bain hexagonal-to-cuboidal transformation path from hcp→fcc/bcc for the case of a general (n, m) Lennard-Jones (LJ) potential ($n > m, m > 3$),[112,222,296]

$$\phi_{\mathrm{LJ}}(r) = \frac{\epsilon n m}{n-m}\left[\frac{1}{n}\left(\frac{r_e}{r}\right)^n - \frac{1}{m}\left(\frac{r_e}{r}\right)^m\right] \tag{6.1}$$

describing the interactions between the atoms in a solid using exact lattice summations to obtain the cohesive energy[111,227,295,429]. Here, ϵ and r_e are the binding energy and the equilibrium distance of the diatomic molecule, respectively. Both of these parameters can be arbitrarily set to 1 in order to express them in dimensionless units. For very large exponents (n, m), the LJ potential approaches the kissing hard-sphere (KHS) model with

$$\phi_{\mathrm{KHS}}(r) = \begin{cases} \infty & \text{for} \quad r < r_e, \\ -\epsilon & \text{for} \quad r = r_e, \\ 0 & \text{for} \quad r > r_e. \end{cases} \tag{6.2}$$

as originally introduced by Baxter[209,430]. A preliminary account for the (12,6)-LJ potential is given in Ref. 431. Here we focus more on the theoretical details of the combined Burgers-Bain path and derivations of lattice sums. Many insights gained through this simple LJ model become invaluable in future applications for real systems using, for example, density functional theory. We note that the LJ potential has in principle uncountable infinitely many solid state structures representing minima (proof by number of Barlow packings[402,429]), and many for unit cells which are not too large in size. For example, not too long ago a new metastable LJ phase has been discovered by Parrinello and co-workers[432].

We have recently shown[127,433,434] that the Bain transformation can be effectively described within a two-parameter space (A, r_{NN}), where r_{NN} is the nearest neighbor distance in the solid and A is responsible for describing the martensitic transformation path from the axial centred-cuboidal (acc) lattice ($A = 1/3$), to the bcc lattice ($A = 1/2$), the mean centred-cuboidal (mcc) lattice ($A = 1/\sqrt{2}$), and finally the face-centred cubic (fcc) lattice ($A = 1$) in a general body-centered tetragonal (bct) arrangement. The advantage of this choice of parameters instead of the usual bct lattice parameters (a, c) is that the nearest neighbor distance changes only slightly along the Bain transformation path and a two-dimensional picture can therefore be avoided. We will show that a similar choice of parameters for a bi-lattice shown in Figure 6.1 can be used to describe the Burgers transformation from hcp to fcc, and demonstrate that symmetry breaking effects need to be considered in the Burgers-Bain transformation, with the possible appearance of a bcc phase representing a local minimum along the Burgers path. Furthermore, the observed symmetry breaking results in a connection between the Burgers and the Bain path. The formalism can be used for future density functional studies and the activation energy obtained can be seen as an upper bound to the true (and possibly more complex) minimum energy path requiring supercell treatments and consideration of Barlow packings.

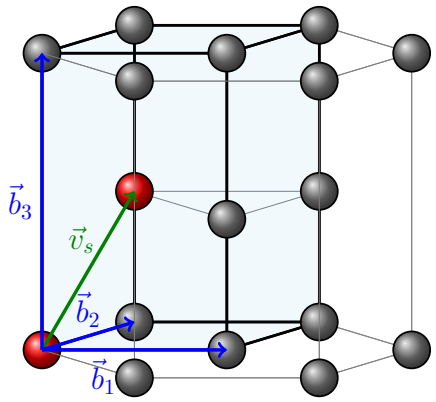

Figure 6.1: The (distorted) cuboidal (blue lines shown on the left) and the hcp structure both with a ABABAB... sequence shown in a hexagonal unit cell with corresponding basis vectors with cell parameters $|\vec{b}_1| = a$, $|\vec{b}_2| = b$, and $|\vec{b}_3| = c$. The ratio $\gamma_2 = c/a = \sqrt{8/3}$ together with $\angle(\vec{b}_1, \vec{b}_2) = 60^\circ$ and $|\vec{b}_1| = |\vec{b}_2| = a$ leads to the optimal hcp lattice with 12 kissing spheres around a central atom. For $c = a$ and $\angle(\vec{b}_1, \vec{b}_2) = 90^\circ$ we obtain the bcc lattice with 8 kissing spheres. Alternatively, we have $|\vec{b}_1| = |\vec{b}_2| = a$, $c/a = \sqrt{2}$ and $\angle(\vec{b}_1, \vec{b}_2) = 90^\circ$ for the fcc lattice with 12 kissing spheres.

In the coming section we detail the theory of the Burgers-Bain hcp↔fcc↔bcc transformation and develop the corresponding lattice sums for inverse power potentials in terms of fast converging Bessel sums to capture important long-range effects. We then apply these lattice sums to various (n, m) Lennard-Jones potentials and discuss the results for the transition paths. We will show that for such potentials, starting from the hcp phase, the minimum energy transition path leads to fcc rather than directly to the bcc phase within the parameter space

chosen, except when we allow for symmetry breaking within an extended parameter space for the lattice constants for soft LJ potentials, that is in the case where bcc becomes a metastable minimum. As a special case we discuss solid argon where we also apply density functional calculations together with the variable cell nudge elastic band algorithm to map out the MEP. A conclusion and future perspectives on this topic is given in the final section.

6.2 Theory

To correctly describe the Burgers-Bain martensitic hcp↔fcc/bcc phase transition,[256,262] we define the cuboidal and hexagonal lattices within the smallest common unit cell, that is, a monoclinic cell with two specified layers A and B as shown in Figure 6.1. We then introduce a common set of basis vectors containing parameters that transform the lattices smoothly into each other.

6.2.1 Lattice vectors and properties

The hexagonal close packed structure

The hcp phase is a bi-lattice[435] that requires two hexagonal Bravais lattices to describe the close-packed structure, or alternatively one hexagonal unit cell with one atom positioned inside specified by its fractional coordinates $(0,0,0)$ and $(\frac{1}{3},\frac{1}{3},\frac{1}{2})$. It belongs together with all the other Barlow lattices to the more general class of multi-lattices[435].

To define the hcp lattice, we start by considering the underlying hexagonal Bravais lattice (h) with the accompanying basis vectors,

$$\vec{b}_1^{\top} = a\,(1,0,0)\,, \quad \vec{b}_2^{\top} = b\left(\frac{1}{2},\frac{\sqrt{3}}{2},0\right), \quad \vec{b}_3^{\top} = c\,(0,0,1) \tag{6.3}$$

with the lattice parameters $|\vec{b}_1| = a$, $|\vec{b}_2| = b$, $|\vec{b}_3| = c$, $\angle(\vec{b}_1,\vec{b}_2) = 60^\circ$ and $\angle(\vec{b}_1,\vec{b}_3) = \angle(\vec{b}_2,\vec{b}_3) = 90^\circ$. These basis vectors build the A layers in Fig. 6.1. The parameters a, b and c, allow for flexibility in the cell dimensions, and the hexagonal unit cell is recovered when $a = b$. We define the generator matrix B (also called the cell tensor) with consisting of these three vectors as

$$B_h = \begin{pmatrix} \vec{b}_1^{\top} \\ \vec{b}_2^{\top} \\ \vec{b}_3^{\top} \end{pmatrix} = a \begin{pmatrix} 1 & 0 & 0 \\ \frac{\gamma_1}{2} & \frac{\sqrt{3}\gamma_1}{2} & 0 \\ 0 & 0 & \gamma_2 \end{pmatrix} \tag{6.4}$$

where we use the notation $\gamma_1 = \frac{b}{a}$ and $\gamma_2 = \frac{c}{a}$. This leads to the following positive definite

symmetric Gram matrix

$$\left(G_{ij}\right)_h = \left(\vec{b}_i^{\top}\vec{b}_j\right) = a^2 \begin{pmatrix} 1 & \frac{\gamma_1}{2} & 0 \\ \frac{\gamma_1}{2} & \gamma_1^2 & 0 \\ 0 & 0 & \gamma_2^2 \end{pmatrix} \tag{6.5}$$

or $G = BB^{\top}$, with $\det G = \frac{3}{4}a^6\gamma_1^2\gamma_2^2 = \frac{3}{4}a^2b^2c^2 > 0$. From an arbitrarily chosen atom at the origin, all points in the hexagonal lattice (A layers only) are described by

$$\vec{r}_1^{\,h}(\vec{i}) = B_h^{\top}\vec{i} = i_1\vec{b}_1 + i_2\vec{b}_2 + i_3\vec{b}_3 \tag{6.6}$$

with $\vec{i} \in \mathbb{Z}^3$. Their distances to the origin are given by the quadratic form

$$|\vec{r}_1^{\,h}(\vec{i})| = \sqrt{\vec{i}^{\top}G_h\vec{i}} = a\sqrt{i_1^2 + \gamma_1 i_1 i_2 + \gamma_1^2 i_2^2 + \gamma_2^2 i_3^2}\,. \tag{6.7}$$

The volume of the unit cell is determined through the Gram of B matrix

$$V(a,\gamma_1,\gamma_2) = \det B_h = \sqrt{\det G_h} = \frac{\sqrt{3}}{2}a^3\gamma_1\gamma_2 \tag{6.8}$$

which is just the product of the diagonal elements of the B-matrix as this matrix has been set is in triangular form eliminating unwanted rotations of the unit cell. The nearest neighbor distance is given by

$$r_{\mathrm{NN}}^h(a,b,c) = \min\{r_1^h(\vec{i})\} = \min\{a,b,c\}\ . \tag{6.9}$$

and the kissing number for a lattice $\mathcal{L}$ is defined as

$$\kappa(\mathcal{L}) = \#\{\vec{r}(\vec{i}) \in \mathcal{L} \mid |\vec{r}(\vec{i})| = r_{\mathrm{NN}}(\mathcal{L})\} \tag{6.10}$$

where # stands for the count (the number of distances). For the hcp structure with ideal value of $\gamma_{\mathrm{hcp}} = \sqrt{\frac{8}{3}}$ the kissing number is $\kappa = 12$. Similarly, we have $\kappa = 12$ for fcc and $\kappa = 8$ for bcc.

We now introduce the second layer, i.e. the B-layer as shown in Figure 6.1, to complete the hcp structure. If we assume, for example, that the sphere of the second layer lies above the centroid of the triangle defined by the vectors $\vec{b}_1$ and $\vec{b}_2$, then the B-layer is shifted by a vector of $\vec{v}_h^{\top} = \frac{a}{2}\left(\frac{2+\gamma_1}{3}, \frac{\gamma_1}{\sqrt{3}}, \gamma_2\right)$ with respect to the lattice vectors given in (6.3), such that the position of any atom in the B layers is given by

$$\vec{r}_2^{\,h}(\vec{i}) = B_h^{\top}\vec{i} + \vec{v}_h\ , \tag{6.11}$$

Note that the generator matrix $B^{\top}$ transforms the fractional into the Cartesian coordinates for atoms located inside the unit cell, and vice versa through the inverse $(B^{\top})^{-1}$. As a side note we could also have taken the center of the inscribing circle of the triangle defined by the vectors $\vec{b}_1$

and $\vec{b}_2$, but this is not important in our analysis as we shall see.

We call the set $\{\vec{b}_i, \vec{v}_h\}$ generalized lattice vectors describing the positions of additional atoms inside a unit cell. The resulting set of distance vectors $\{\vec{r}_1^{\,h}(\vec{i}), \vec{r}_2^{\,h}(\vec{i})\}$ then produce all points in 3D space for the hcp bi-lattice. For the minimum distance r^h_{NN} in an hcp bi-lattice we now have,

$$r^h_{\mathrm{NN}}(a,b,c,|\vec{v}_h|) = \min\{a,b,c,|\vec{v}_h|\} = a\min\left\{1,\gamma_1,\gamma_2,\frac{|\vec{v}_h|}{a}\right\}. \tag{6.12}$$

The cubic structures

From Figure 6.1 we see how the hcp and cubic structures are related and can be smoothly transformed into each other, which is what Burgers had in mind in his original 1934 paper[262]. We therefore make the transformation from cubic to the hexagonal lattices through an underlying monoclinic unit cell, as defined above for the hexagonal lattice. The description of the simple cubic (c) lattice in terms of a primitive monoclinic (mP) can be achieved by introducing the following basis vectors

$$\vec{b'}_1^{\,\top} = a\,(1,0,0)\,, \quad \vec{b'}_2^{\,\top} = a\,(0,\gamma_1,0)\,, \quad \vec{b'}_3^{\,\top} = a\,(0,0,\gamma_2)\,. \tag{6.13}$$

For the cubic structure we have $\angle(\vec{b}_1,\vec{b}_2) = \angle(\vec{b}_1,\vec{b}_3) = \angle(\vec{b}_2,\vec{b}_3) = 90^\circ$ and the simple cubic unit cell is obtained when $\gamma_1 = \gamma_2 = 1$. We conveniently keep γ_1 and γ_2 in the definition of the generator matrix for the cubic lattice as it becomes important later-on for the definition of the bcc and fcc lattices,

$$B_c = a\begin{pmatrix} 1 & 0 & 0 \\ 0 & \gamma_1 & 0 \\ 0 & 0 & \gamma_2 \end{pmatrix} \tag{6.14}$$

We can already see the familiarity between the two matrices B_h and B_c. This gives the following Gram matrix for B_c,

$$G_c = a^2\begin{pmatrix} 1 & 0 & 0 \\ 0 & \gamma_1^2 & 0 \\ 0 & 0 & \gamma_2^2 \end{pmatrix} \tag{6.15}$$

with $\det(G) = a^6\gamma_1^2\gamma_2^2 > 0$. The volume is therefore $V(a,\gamma_1,\gamma_2) = a^3\gamma_1\gamma_2 = abc$, or for the ideal bcc lattice $V = a^3$. The distances to all atoms within the A layers are given by $\vec{r}_1^{\,c}(\vec{i}) = B_c^\top\vec{i}$, and we have the expression in terms of the quadratic form $(\vec{i}^{\,\top}G_c\vec{i})$,

$$|\vec{r}_1^{\,c}(\vec{i})| = \left(\vec{i}^{\,\top}G_c\vec{i}\right)^{\frac{1}{2}} = a\sqrt{i_1^2+\gamma_1^2i_2^2+\gamma_2^2i_3^2}\,. \tag{6.16}$$

We now address again the B-layer in Figure 6.1 for the bcc lattice by using the shift vector $\vec{v}_c^{\,\top} = \frac{a}{2}(1,\gamma_1,\gamma_2)$ with length $|\vec{v}_c| = \frac{a}{2}\sqrt{1+\gamma_1^2+\gamma_2^2}$. The distances are given by $\vec{r}_2^{\,c}(\vec{i}) = B_c^\top\vec{i}+\vec{v}_c$.

Again, the set of both vectors $\{\vec{r}_1^c(\vec{i}), \vec{r}_2^c(\vec{i})\}$ produce all points in 3D space for the bcc lattice. So far we have a three-parameter space for the distances $\vec{r}_k(a, \gamma_1, \gamma_2)$ for the two lattices hcp and bcc. They will become variable parameters when we discuss the Lennard-Jones potential further below.

There is one important fact to note. In the anticipated hcp↔bcc transformation we start with an hcp multi-lattice using the hexagonal primitive cell as the underlying unit cell which transforms along a certain path into a cubic multi-lattice. This cubic unit cell is not the primitive bcc cell. In fact, the smallest distance in the bcc cell is given along the [111] direction to the center lattice point with a distance of $a_c = |\vec{v}_c| = a\sqrt{3}/2$ for $\gamma_1 = \gamma_2 = 1$. Lennard-Jones and Ingham therefore introduced an additional multiplicative factor to the lattice for the bcc cell[112], which we discuss further below for the more general Burgers transformation between the hcp and the cuboidal lattices.

The Burgers-Bain transformation

The connection between the hexagonal and the cubic generator matrices is given by

$$B_h = U_B B_c = \begin{pmatrix} 1 & 0 & 0 \\ \frac{\gamma_1}{2} & \frac{\sqrt{3}}{2} & 0 \\ 0 & 0 & 1 \end{pmatrix} B_c \tag{6.17}$$

This means that the distances will transform like $\vec{r}_k^h = U_B \vec{r}_k^c$ $(k = 1, 2)$. The second set of distances, $\vec{r}_2$, also concerns the transformation of the shift vector

$$\vec{v}' = U_B \vec{v}_c = \frac{a}{2}\left(1, \gamma_1\left(\tfrac{1+\sqrt{3}}{2}\right), \gamma_2\right)^\top \tag{6.18}$$

However, the vector $\vec{v}'$ differs markedly from $\vec{v}_h$ in its first and second component. It is therefore more suitable to introduce the shift vector directly with freely varying parameters β_1, β_2, and β_3 such that

$$\vec{v}_s^\top = \frac{a}{2}(\beta_1, \beta_2, \beta_3) \tag{6.19}$$

with $\beta_1^c = \beta_2^c = 1$ for the ideal cubical lattices and $\beta_1^h = 1$ and $\beta_2^h = \frac{1}{\sqrt{3}}$ for the ideal hexagonal lattices. The length of the shift vector becomes $|\vec{v}_s| = \frac{a}{2}\sqrt{\beta_1^2 + \beta_2^2 + \beta_3^2}$. This factor becomes important when we rescale our lattice sums.

The Gram matrices transform as

$$G_h = B_h B_h^\top = U_B B_c B_c^\top U_B^\top = U_B G_c U_B^\top = (U_B U_B^\top) G_c = \begin{pmatrix} 1 & \frac{\gamma_1}{2} & 0 \\ \frac{\gamma_1}{2} & \frac{\gamma_1^2+3}{4} & 0 \\ 0 & 0 & 1 \end{pmatrix} G_c = S G_c. \tag{6.20}$$

We can now formulate the smooth transition from the cuboidal lattice to hcp as

$$B(a,\alpha,\gamma_1,\gamma_2) = \alpha B_c(a,\gamma_1,\gamma_2) + (1-\alpha)B_h(a,\gamma_1,\gamma_2) = \{\alpha + (1-\alpha)U_B\}\, B_c(a,\gamma)$$
$$= a\begin{pmatrix} 1 & 0 & 0 \\ \frac{\gamma_1(1-\alpha)}{2} & \gamma_1\left[\alpha\left(1-\frac{\sqrt{3}}{2}\right)+\frac{\sqrt{3}}{2}\right] & 0 \\ 0 & 0 & \gamma_2 \end{pmatrix} = a\begin{pmatrix} 1 & 0 & 0 \\ \omega_1(\alpha,\gamma_1) & \omega_3(\alpha,\gamma_1) & 0 \\ 0 & 0 & \gamma_2 \end{pmatrix} \tag{6.21}$$

where α is the structure parameter defining the type of lattice being $\alpha = 0$ for the hexagonal and $\alpha = 1$ for the cubical lattice, by definition, $\omega_1(\alpha,\gamma_1) = \frac{\gamma_1}{2}(1-\alpha)$, and $\omega_3(\alpha,\gamma_1) = \gamma_1\left[\alpha\left(1-\frac{\sqrt{3}}{2}\right)+\frac{\sqrt{3}}{2}\right]$. Note that in this form, the length of the vector $\vec{b}_2$ changes during the transition at fixed b (in fact, b is a parameter to be optimized), and its variation with respect to α is given by

$$|\vec{b}_2| = b\sqrt{1-\alpha(\alpha-1)(\sqrt{3}-2)} = bf_s(\alpha) = a\gamma_1 f_s(\alpha) \tag{6.22}$$

where $f_s(\alpha)$ is a scaling factor that has its minimum value $f_s = 0.965926$ at $\alpha = 0.5$. Consequently, the transformation matrix B is describing the rotation and scaling of the vector $\vec{b}_2$. As shown in Figure 6.2, the angle $\angle(\vec{b}_1,\vec{b}_2) \equiv \theta_{12}$ approaches 0° at low α but never reaches 180°. In the interval of interest, $\alpha = [0,1]$, it varies almost linearly with α and is thus a good measure of the angle of the base of the unit cell. In fact we have

$$\cos\theta_{12} = \frac{\omega_1}{\sqrt{\omega_1^2+\omega_3^2}}. \tag{6.23}$$

The linear behavior in the plot could be approximated as $\theta_{12} \approx \frac{(\alpha+2)\pi}{6}$ in the $[0,1]$ region.

The two sets of distance vectors are given by

$$\vec{r}_1(\vec{i}) = B(a,\alpha,\gamma_1,\gamma_2)^\top \vec{i} \quad \text{and} \quad \vec{r}_2(\vec{i}) = B(a,\alpha,\gamma_1,\gamma_2)^\top \vec{i} + \vec{v}_s(a,\beta_1,\beta_2,\beta_3) \tag{6.24}$$

We now have a seven-parameter space $\{p_i\} = (a,\alpha,\beta_1,\beta_2,\beta_3,\gamma_1,\gamma_2)$ as a minimum set of parameters to describe the Burgers-Bain transformation with an underlying primitive monoclinic cell. If the middle layer sits exactly in between the two neighboring layers we expect that $\beta_3 = \gamma_2$.

The symmetric Gram matrix for $B(a,\alpha,\gamma_1,\gamma_2)$ becomes,

$$G(a,\alpha,\gamma_1,\gamma_2) = B(a,\alpha,\gamma_1,\gamma_2)B(a,\alpha,\gamma_1,\gamma_2)^\top = a^2\begin{pmatrix} 1 & \omega_1(\alpha,\gamma_1) & 0 \\ \omega_1(\alpha,\gamma_1) & \omega_2(\alpha,\gamma_1) & 0 \\ 0 & 0 & \gamma_2^2 \end{pmatrix} \tag{6.25}$$
$$= a^2 S_3(\alpha,\gamma_1,\gamma_2)$$

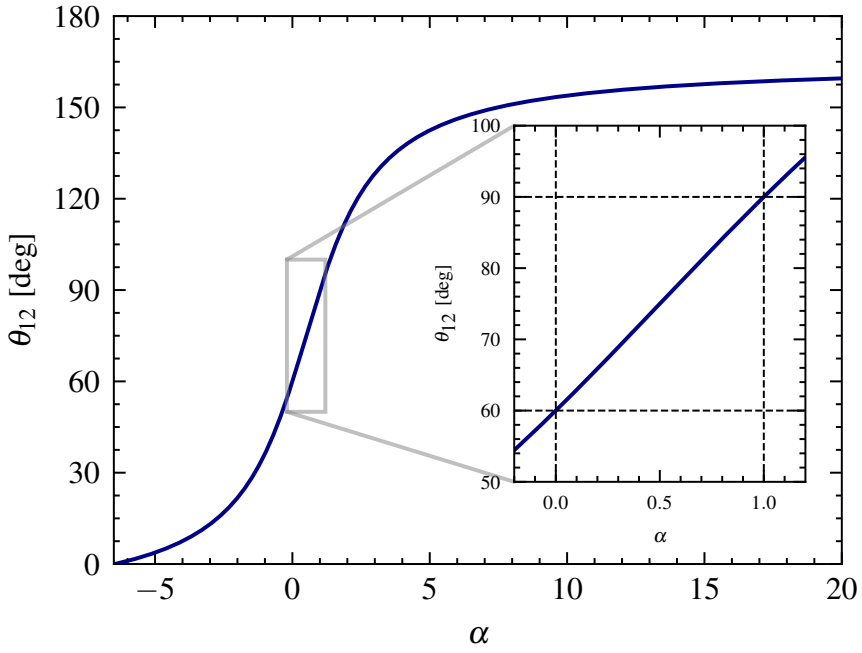

Figure 6.2: Relationship between the parameter α and the angle between the two base vectors $\vec{b}_1$ and $\vec{b}_2$.

where

$$\omega_2(\alpha, \gamma_1) = \omega_1(\alpha, \gamma_1)^2 + \omega_3(\alpha, \gamma_1)^2 \tag{6.26}$$

For $G(a, \alpha, \gamma_1, \gamma_2)$ to be positive definite we have the condition that $\omega_3(\alpha) > 0$, i.e. $\alpha > -(3 + \sqrt{3}) \approx -4.732$.

It is now clear that the martensitic transition is described by a shearing of the A-layer, related mainly to the parameter α, with a change in angle between the two basis vectors $\vec{b}_1$ and $\vec{b}_2$ together with a sliding of the B-layer in direction orthogonal to the $\vec{b}_1$ and $\vec{b}_3$ vectors and additional changes in the lattice parameters, which are summarized in Table 6.1 for the three lattices hcp, fcc and bcc. The Burgers transformation is shown schematically in Figure 6.3. We note that the Burgers path maintains the symmetry of a primitive monoclinic unit cell (space group mP).

The specific choice for the α-dependence of the basis vector $\vec{b}_2$ in (6.22) originates directly from the linear combination between the two B-matrices given in eq.(6.21). In the following we will call this model for the Burgers transformation *Model 1*. As it turns out, the minimum energy path for the Burgers transformation within Model 1 fulfills the condition $\gamma_1 f_S = 1$, that is for the whole path with $\alpha \in [0, 1]$ we have the condition that $|\vec{b}_1| = |\vec{b}_2|$ for the two basis vectors of the hexagonal sheet. This saves one parameter (γ_1) in our optimization procedure.

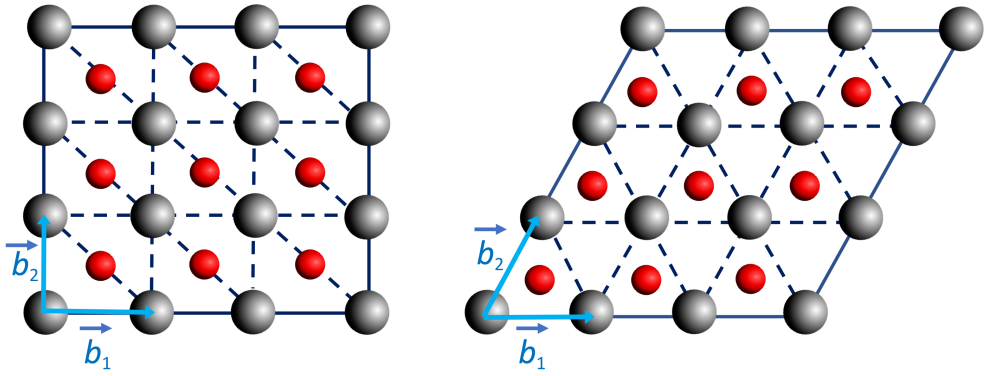

Figure 6.3: The shearing in the A-layer (gray spheres, change of angle between $\vec{b}_1$ and $\vec{b}_2$) of the base hexagonal plane and sliding of the B-layer (red spheres, sitting at $c/2$ above the A-layer) in the Burgers transformation. Left: bcc lattice with $\angle(\vec{b}_1, \vec{b}_2) = 90°$, $\gamma_2 = 1$ and fractional coordinates $\vec{u}^\top = (\frac{1}{2}, \frac{1}{2}, \frac{1}{2})$, or fcc lattice with $\gamma_2 = \sqrt{2}$ and $\vec{u}^\top = (\frac{1}{2}, \frac{1}{2}, \frac{1}{2})$. Right: hcp structure with $\angle(\vec{b}_1, \vec{b}_2) = 60°$, $\gamma_2 = \sqrt{\frac{8}{3}}$ and $\vec{u}^\top = (\frac{1}{3}, \frac{1}{3}, \frac{1}{2})$.

Table 6.1: Ideal lattice parameters using for the three lattices hcp, fcc and bcc with lattice constant a, b and c as shown in Figure 6.1. The values for ω_1, ω_2, ω_3 and the hard-sphere volumes V for hcp and fcc and for bcc (setting $a = 1$) and corresponding packing densities are also shown. The values for the bcc structure occurring in the vicinity of the Burgers path are also shown using Model 2.

Parameter	hcp	fcc	bcc(Bain)	bcc(Burgers)
α	0	1	1	$\frac{1}{3}$
γ_1	1	1	1	1
γ_2	$\sqrt{\frac{8}{3}}$	$\sqrt{2}$	1	$\sqrt{\frac{8}{3}}$
β_1	1	1	1	$\frac{4}{3}$
β_2	$\frac{1}{\sqrt{3}}$	1	1	$\frac{2\sqrt{2}}{3}$
β_3	$\sqrt{\frac{8}{3}}$	$\sqrt{2}$	1	$\sqrt{\frac{8}{3}}$
$\angle(\vec{b}_1, \vec{b}_2)$	60°	90°	90°	$\arccos\left(\frac{1}{3}\right)$
$\omega_1(\alpha, \gamma_1)$	$\frac{1}{2}$	0	0	$\frac{1}{3}$
$\omega_2(\alpha, \gamma_1)$	1	1	1	1
$\omega_3(\alpha, \gamma_1)$	$\frac{\sqrt{3}}{2}$	1	1	$\frac{2\sqrt{2}}{3}$
V	$\sqrt{2}$	$\sqrt{2}$	$\frac{8}{3\sqrt{3}}$	$\frac{8}{3\sqrt{3}}$
ρ	$\frac{\pi}{3\sqrt{2}}$	$\frac{\pi}{3\sqrt{2}}$	$\frac{\pi\sqrt{3}}{8}$	$\frac{\pi\sqrt{3}}{8}$

Alternatively, we could adopt from the beginning on the condition that $|\vec{b}_1| = |\vec{b}_2|$ for $\gamma_1 = 1$. This implies that

$$\omega_3 = \sqrt{1-\omega_1^2} = \frac{1}{2}\sqrt{4-(1-\alpha)^2} \tag{6.27}$$

and $\omega_2 = 1$, keeping the original definition for ω_1. This changes the B-matrix to a more natural choice for the lattice vectors,

$$B(a,\alpha,\gamma_2) = a(\vec{b}_1,\vec{b}_2,\vec{b}_3)^\top = a\begin{pmatrix} 1 & 0 & 0 \\ \frac{1}{2}(1-\alpha) & \frac{1}{2}\sqrt{(1+\alpha)(3-\alpha)} & 0 \\ 0 & 0 & \gamma_2 \end{pmatrix} = \begin{pmatrix} 1 & 0 & 0 \\ \cos\theta_{12} & \sin\theta_{12} & 0 \\ 0 & 0 & \gamma_2 \end{pmatrix} \tag{6.28}$$

We call this choice *Model 2*. In this model the angle $\angle(\vec{b}_1,\vec{b}_2) = \theta_{12} \in (0,\pi)$ used in (6.28) is easily obtained from the parameter α,

$$\cos\theta_{12} = \frac{\omega_1}{\sqrt{\omega_2}} = \omega_1 = \frac{1}{2}(1-\alpha). \tag{6.29}$$

and we have a nice linear relationship as shown in Figure 6.2. We also give the inverse B-matrix for model 2 required to obtain the fractional coordinates through $\vec{u} = (B^\top)^{-1}\vec{v}_s$,[436]

$$B^{-1}(a,\alpha,\gamma_2) = a^{-1}\begin{pmatrix} 1 & \frac{(\alpha-1)}{\sqrt{(1+\alpha)(3-\alpha)}} & 0 \\ 0 & \frac{2}{\sqrt{(1+\alpha)(3-\alpha)}} & 0 \\ 0 & 0 & \gamma_2^{-1} \end{pmatrix} \tag{6.30}$$

As we must get the same cohesive energies at a specific angle θ_{12}, we can use eq.(6.29) to derive the relationship between the α-values in the two different models, i.e.

$$\alpha_{\mathrm{M2}} = 1 - \frac{1-\alpha_{\mathrm{M1}}}{\sqrt{1-2C\alpha_{\mathrm{M1}}(1-\alpha_{\mathrm{M1}})}} \tag{6.31}$$

with $C = (1-\frac{\sqrt{3}}{2})$. The back-transformation requires the solution of a quadratic equation for which we get the following expression (taking the negative sign for the square-root expression in the quadratic equation),

$$\alpha_{\mathrm{M1}} = \frac{1-C(1-\alpha_{\mathrm{M2}})^2 - \sqrt{(1-\alpha_{\mathrm{M2}})^2(1+C(1-\alpha_{\mathrm{M2}})^2(C-2))}}{1-2C(1-\alpha_{\mathrm{M2}})^2} \tag{6.32}$$

Substituting α_{M1} by α_{M2} in (6.21) changes the Burgers transformation into a non-linear transformation of the B-matrices. However, for the reduction of the parameter space the B matrix (6.28) is quite useful as $\gamma_1 = 1$ if $|\vec{b}_1| = |\vec{b}_2|$ and any symmetry breaking through

$|\vec{b}_1| \neq |\vec{b}_2|$ will be described directly by $\gamma_1 \neq 1$. It is clear that $\alpha_{M1} = \alpha_{M2}$ for $\alpha_{M1} = 0$ and $\alpha_{M1} = 1$. The maximum deviation between the two α values is $\alpha_{M1} - \alpha_{M2} = 0.02078464$ with $\alpha_{M1} = 0.33846180$ and $\alpha_{M2} = 0.31767716$ in the interval $\alpha_{M1} \in [0,1]$. Note that the bcc structure found at $\alpha_{M2} = 1/3$ (see Table 6.1) corresponds to $\alpha_{M1} = 0.35411421\ldots$, highlighting the advantage of Model 2 locating the bcc structure at a rational value of the parameter α.

The volume of the α-dependent unit cell then is,

$$V(a,\alpha,\gamma_1,\gamma_2) = \sqrt{\det G(a,\alpha,\gamma_1,\gamma_2)} = a^3\gamma_2\omega_3(\alpha,\gamma_1) \tag{6.33}$$

This results in a packing density compared to spheres of radius r,

$$\rho = \frac{V_{\text{sphere}}}{V_{\text{hex}}} = \frac{4\pi r^3}{3a^3\gamma_2\omega_3(\alpha,\gamma_1)} \tag{6.34}$$

where we considered that we have two spheres in the unit cell. With the values listed in Table 6.1 this gives $\rho_{\text{bcc},\alpha=1} = \frac{\sqrt{3}}{8}\pi$ (with $r = \frac{|\vec{v}_c|}{2} = \frac{\sqrt{3}}{4}a$), $\rho_{\text{fcc}} = \frac{\sqrt{2}}{6}\pi$ ($r = \frac{1}{2}a$), and $\rho_{\text{hcp}} = \frac{\sqrt{2}}{6}\pi$ ($r = \frac{1}{2}a$).

Table 6.1 shows that at specific lattice parameters at $\alpha = \frac{1}{3}$ (Model 2) an additional bcc structure appears along the Burgers path situated in-between the hcp ($\alpha = 0$) and fcc ($\alpha = 1$) structures. The corresponding lattice vectors are $\vec{b}_1^\top = a(1,0,0)$, $\vec{b}_2^\top = a(\frac{1}{3},\frac{2\sqrt{2}}{3},0)$, and $\vec{b}_3^\top = a(0,0,\sqrt{\frac{8}{3}})$. Notice that the angle $\angle(\vec{b}_1,\vec{b}_2) = \arccos\left(\frac{1}{3}\right) = 180^\text{o} - \theta_T$, where $\theta_T = 109.4712206\ldots$ is the tetrahedral angle. The corresponding shift vector is $\vec{v}_s^\top = a(\frac{2}{3},\frac{\sqrt{2}}{3},\sqrt{\frac{2}{3}})$, or expressed in terms of fractional coordinates u, i.e. $\vec{u} = (B^\top)^{-1}\vec{v}_s = (\frac{1}{2},\frac{1}{2},\frac{1}{2})^\top$. Hence, the atom located inside the unit cell is exactly body-centered with a distance from the origin of $\frac{2a}{\sqrt{3}}$. This is just another unit cell definition for the bcc structure as shown (in blue color) in Figure 6.4. The primitive rhombohedral cell for bcc (in green color) with lattice parameters $a_1 = b_1 = c_1 = a, \alpha_1 = \beta_1 = \gamma_1 = \theta_T$, and the conventional unit cell (in red color) with lattice parameters $a_2 = b_2 = c_2 = \frac{2a}{\sqrt{3}}, \alpha_2 = \beta_2 = \gamma_2 = 90^\text{o}$ are also shown in Figure 6.4. In the interval $\alpha \in [0,1]$ we only have two occurrences of a bcc structure, i.e. at $\alpha = \frac{1}{3}$ and $\alpha = 1$, where the first one is convenient to discuss distortions along the Burgers path to either hcp or fcc, and the second one for cuboidal distortions to fcc along the Bain path.

We briefly summarize. For the Burgers transformation we reduced the, in principle, nine-parameter space (6 lattice constants for the Bravais lattice plus 3 parameters for the position of the middle layer) for a bi-lattice to a seven-parameter space $\{p_i\} = (a,\alpha,\gamma_1,\gamma_2,\beta_1,\beta_2,\beta_3)$, where $\alpha \in (-1,3)$ is the important structure parameter (our reaction coordinate) describing the Burgers-Bain phase transition. All other parameters $a,\gamma_1,\gamma_2,\beta_1,\beta_2,\beta_3$ have in principle to be optimized along the transformation path. We expect approximately the following parameter range for $\alpha \in [0,1]$: $a \in [a_{\text{hcp}}, a_{\text{bcc}}]$, $\gamma_1 \approx 1.0$,

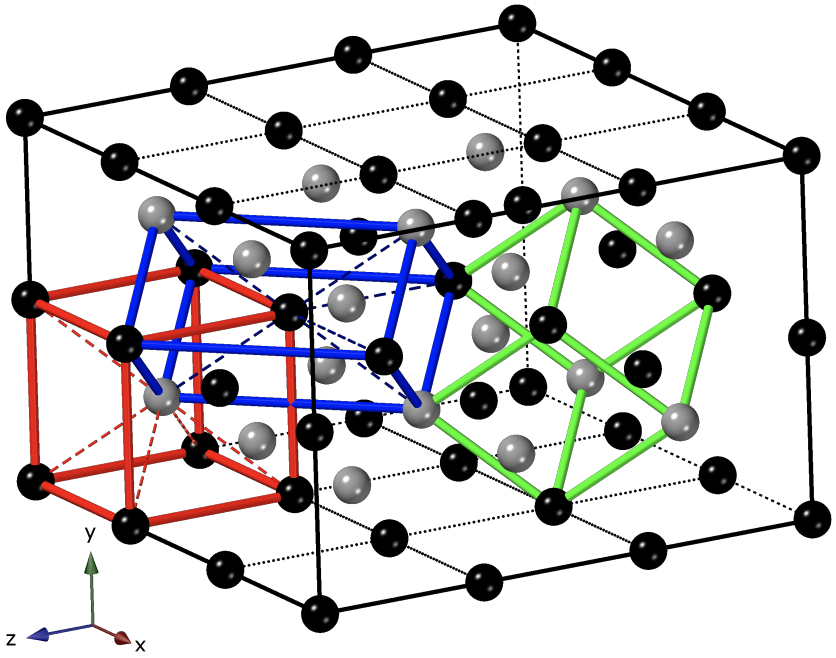

Figure 6.4: bcc phase shown in a $(3 \times 2 \times 3)$ super-cell. Left: the conventional bcc bi-lattice shown in red color (left) with the body-centered atom in grey; middle: the bi-lattice shown in blue with unit cell identical to the one defined in Fig.6.1 with $(\angle(\vec{b}_1, \vec{b}_2) = 70.5287794^o = 180^o - \theta_T)$, where θ_T is the tetrahedral angle; right: the rhombohedral primitive bcc cell of equal lengths shown in green (containing no central atom), with a ratio for the length of the lattice vectors compared to the conventional unit cell of $\frac{\sqrt{3}}{2}$. The angles between the lattice vectors are $180^o - \theta_T$. Note that the primitive bcc cell has half the volume of the conventional one.

$\gamma_2 \in \left[1, \sqrt{\frac{8}{3}}\right]$, $\beta_1 \approx 1.0$, $\beta_2 \in \left[\frac{1}{\sqrt{3}}, 1\right]$, $\beta_3 \approx \gamma_2$. For the Bain transformation the originally introduced distortion parameter A in Ref. 434 is simply related to the parameter γ_2 by $A = \gamma_2^2/2$, and similarly the nearest neighbor distance in the cuboidal lattice is given by $r_{NN} = \frac{a}{2}\sqrt{2+\gamma_2^2}$.[127,433] This implies that at $\alpha = 1$ the transformation from fcc to bcc is described mainly through the parameter γ_2. An additional bcc structure appears along the Burgers path at $\alpha = \frac{1}{3}$, which will be discussed in detail for the case of a LJ potential.

6.2.2 Quadratic forms and functions for the lattice sums

Lattice sums have a long history and are usually based on quadratic functions. For inverse power potentials $V(r) = r^{-2s}$ such as the Lennard-Jones potential or the Madelung constant for Coulomb potentials, these are related to the so-called Epstein zeta function[111,112,115]. For the cuboidal Bain transformation the associated lattice sums were already described in our previous papers[103,434]. For the more general Burgers-Bain transformation we need to introduce two lattice sums for all the distances in a bi-lattice.

We first introduce the quadratic form Q_A involving only atoms in the base A-layer,

$$\begin{aligned} Q_A(\vec{i},\alpha,\gamma_1,\gamma_2) &= \vec{i}^{\top} S_3(\alpha,\gamma_1,\gamma_2)\vec{i} = a^{-2}\vec{i}^{\top} G(a,\alpha,\gamma_1,\gamma_2)\vec{i} \\ &= i_1^2 + 2\omega_1(\alpha,\gamma_1)i_1 i_2 + \omega_2(\alpha,\gamma_1)i_2^2 + \gamma_2^2 i_3^2 \end{aligned} \tag{6.35}$$

with the associated lattice sum

$$H_A^h(s,\alpha,\gamma_1,\gamma_2) = {\sum_{\vec{i}\in\mathbb{Z}^3}}' \frac{1}{(\vec{i}^{\top} S_3(\alpha,\gamma_1,\gamma_2)\vec{i})^s} \tag{6.36}$$

The prime notation at the sum indicates that we avoid the term $i_1 = i_2 = i_3$ in the summation. This lattice sum can be re-expressed in terms of a fast converging Bessel functions[295,299] described in detail in Appendix H.

For the second lattice sum we need the quadratic function for the distances between the A- and B-layer lattice points derived from eq.(6.24),

$$Q_B(\vec{i},\{p_i\}) = a^{-2}\left(\vec{i}^{\top} B(a,\alpha,\gamma_1,\gamma_2) + \vec{v}_s^{\top}(\beta_1,\beta_2,\gamma_2)\right)\left(B(a,\alpha,\gamma_1,\gamma_2)^{\top}\vec{i} + \vec{v}_s(\beta_1,\beta_2,\gamma_2)\right) \tag{6.37}$$

$$\begin{aligned} &= a^{-2}\left[\vec{i}^{\top} G(a,\alpha,\gamma_1,\gamma_2)\vec{i} + 2\vec{i}^{\top} B(a,\alpha,\gamma_1,\gamma_2)\vec{v}_s(\beta_1,\beta_2,\gamma_2) + |\vec{v}_s(\beta_1,\beta_2,\gamma_2)|^2\right] \\ &= \left(i_1 + \omega_1(\alpha,\gamma_1)i_2 + \frac{\beta_1}{2}\right)^2 + \left(\omega_3(\alpha,\gamma_1)i_2 + \frac{\beta_2}{2}\right)^2 + \left(\gamma_2 i_3 + \frac{\beta_3}{2}\right)^2 \end{aligned} \tag{6.38}$$

where $\omega_1(\alpha,\gamma_1)$ and $\omega_3(\alpha,\gamma_1)$ have already been defined. The corresponding lattice sum becomes

$$H_B^h(s,\{p_i\}) = \sum_{\vec{i}\in\mathbb{Z}^3} \frac{1}{Q_B(\vec{i},\alpha,\gamma_1,\gamma_2,\beta_1,\beta_2,\beta_3)^s} \tag{6.39}$$

Both lattice sums are absolute convergent for finite $s > \frac{3}{2}$ with a simple pole at $s = \frac{3}{2}$, but can be analytically continued for $s < \frac{3}{2}$. However, for $s \to \infty$ the lattice sum $H_B^h \to \infty$ for the bcc lattice. This can be understood from the fact that some terms in $Q_B(\vec{i}$ for $(i_1,i_2,i_3) \in [-1,1]$ can become smaller than 1 in our definition of the lattice sum. This divergence of the lattice sum for $s \to \infty$ will be compensated by the optimized lattice constant a obtained from a Lennard-Jones potential as discussed further below, but this results in a $(0\times\infty)$ case for $s \to \infty$. It is therefore far more convenient to avoid such divergences by re-scaling the lattice constant such that $r_{\rm bc} = af(\beta_1,\beta_2,\beta_3)$, and $r_{\rm bc} = |\vec{v}_s|$ is the length from the atom at the base layer A to the nearest body-centered atom in layer B. $f(\beta_1,\beta_2,\beta_3)$ becomes part of the lattice sum assuring convergence to a finite value for $s \to \infty$. We now redefine the two lattice sums such that they

behave well in the limit $s \to \infty$,

$$L_A^h(s,\{p_i\}) = f(\beta_1,\beta_2,\beta_3)^{2s} H_A^h(s,\alpha,\gamma_1,\gamma_2) = f(\beta_1,\beta_2,\beta_3)^{2s} {\sum_{\vec{i}\in\mathbb{Z}^3}}' \frac{1}{(\vec{i}^{\top} S_3(\alpha,\gamma_1,\gamma_2)\vec{i})^s} \tag{6.40}$$

and

$$L_B^h(s,\{p_i\}) = f(\beta_1,\beta_2,\beta_3)^{2s} H_B^h(s,\{p_i\}) = f(\beta_1,\beta_2,\beta_3)^{2s} \sum_{\vec{i}\in\mathbb{Z}^3} \frac{1}{Q_B(\vec{i},\{p_i\})^s} \tag{6.41}$$

with

$$f(\beta_1,\beta_2,\beta_3) = \frac{r_{\mathrm{bc}}}{a} = \frac{1}{2}\sqrt{\beta_1^2+\beta_2^2+\beta_3^2} \tag{6.42}$$

This ensures that the bcc lattice sum is identical to the one defined originally by Lennard-Jones and Ingham[112]. The total lattice sum is then given by

$$L^h(s,\{p_i\}) = L_A^h(s,\{p_i\}) + L_B^h(s,\{p_i\}) \tag{6.43}$$

$$H^h(s,\{p_i\}) = H_A^h(s,\{p_i\}) + H_B^h(s,\{p_i\}) \tag{6.44}$$

Both lattice sums can be expressed in terms of fast converging series involving Bessel functions as derived in Appendix H. We note that it is sufficient to take just the sum of the two layer contributions, e.g. $L_A^h + L_B^h$, as in our definition of the bi-lattice each atom is equivalent to all the others, i.e. they have the same surrounding. This can also be seen from a more general formula for Barlow packings[402].

6.2.3 Lattice sums for the special cases of hcp, fcc and bcc

Using the parameters in Table 6.1 for the hcp structure we get $f(\beta_1,\beta_2,\beta_3) = 1$, and for the lattice sums

$$L_A^{\mathrm{hcp}} = {\sum_{\vec{i}\in\mathbb{Z}^3}}' \left(i_1^2 + i_1 i_2 + i_2^2 + \tfrac{8}{3} i_3^2\right)^{-s} \tag{6.45}$$

$$\begin{aligned} L_B^{\mathrm{hcp}} &= \sum_{\vec{i}\in\mathbb{Z}^3} \left((i_1+\tfrac{1}{2}i_2+\tfrac{1}{2})^2 + (\tfrac{\sqrt{3}}{2}i_2 + \tfrac{1}{2\sqrt{3}})^2 + \tfrac{8}{3}(i_3+\tfrac{1}{2})^2\right)^{-s} \\ &= \sum_{\vec{i}\in\mathbb{Z}^3} \left((i_1+\tfrac{1}{3})^2 + (i_2+\tfrac{1}{3})^2 + (i_1+\tfrac{1}{3})(i_2+\tfrac{1}{3}) + \tfrac{8}{3}(i_3+\tfrac{1}{2})^2\right)^{-s} \end{aligned}$$

These are exactly the lattice sums as shown in Refs. 294,295,437. For bcc we get $f(\beta_1, \beta_2, \beta_3) = \sqrt{3}/2$ and

$$L_A^{\rm bcc} = \left(\frac{\sqrt{3}}{2}\right)^{2s} {\sum_{\vec{i}\in\mathbb{Z}^3}}' \left(i_1^2 + i_2^2 + i_3^2\right)^{-s} \tag{6.46}$$
$$L_B^{\rm bcc} = 3^s \sum_{\vec{i}\in\mathbb{Z}^3} \left((2i_1+1)^2 + (2i_2+1)^2 + (2i_3+1)^2\right)^{-s}$$

These are identical to the ones given by Lennard-Jones and Ingham[112] and used in Ref. 295 for various Bessel function expansions.

For fcc we get $f(\beta_1, \beta_2, \beta_3) = 1$ and

$$L_A^{\rm fcc} = {\sum_{\vec{i}\in\mathbb{Z}^3}}' \left(i_1^2 + i_2^2 + 2i_3^2\right)^{-s} \tag{6.47}$$
$$L_B^{\rm fcc} = \sum_{\vec{i}\in\mathbb{Z}^3} \left((i_1+\tfrac{1}{2})^2 + (i_2+\tfrac{1}{2})^2 + 2(i_3+\tfrac{1}{2})^2\right)^{-s}$$

This can be brought into a more familiar form discussed in Ref. 295 (see Appendix I),

$$L_A^{\rm fcc} + L_B^{\rm fcc} = 2^{s-1} {\sum_{\vec{i}\in\mathbb{Z}^3}}' \left[1 + (-1)^{i_1+i_2+i_3}\right] \left(i_1^2 + i_2^2 + i_3^2\right)^{-s} \tag{6.48}$$

6.2.4 The Lennard-Jones cohesive energies for the lattices along the fcc to hcp transition path

The cohesive energy for the hexagonal-cuboidal structures for a general (n, m) LJ potential can be expressed in terms of lattice sums and is given by the expression[112,226,227]

$$E_{\rm LJ}^{\rm coh}(n, m, \{p_i\}) = \frac{\epsilon n m}{2(n-m)} \left[\frac{H^h(\frac{n}{2}, \{p_i\})}{n} \left(\frac{r_e}{a}\right)^n - \frac{H^h(\frac{m}{2}, \{p_i\})}{m} \left(\frac{r_e}{a}\right)^m\right] \tag{6.49}$$
$$= \frac{\epsilon n m}{2(n-m)} \left[\frac{L^h(\frac{n}{2}, \{p_i\})}{n} \left(\frac{r_e}{r_{\rm bc}}\right)^n - \frac{L^h(\frac{m}{2}, \{p_i\})}{m} \left(\frac{r_e}{r_{\rm bc}}\right)^m\right]$$

where the distance from the base to the body-centered atom is related to the lattice constant $r_{\rm bc} = a f(\beta_1, \beta_2, \beta_3)$ as already mentioned. Note that the factor $f(\beta_1, \beta_2, \beta_3)$ in eq.(6.42) cancels out when we with the lattice sums $H \to L$ and the distances $r_{\rm bc} \to a$ at the same time. The expression for the lattice sum $L^h(s, \{p_i\})$ is taken from Eq. (6.43) and the corresponding Bessel function expansions we used in our work are given in Appendix H. As these Bessel sum expansions are fast converging series, they can easily be obtained to arbitrary computer precision, i.e. to double precision accuracy within a few seconds of computer time.

In order to discuss the behavior for the LJ potential with varying parameters p_i we treat the lattice constant a independently from all the other parameters to be optimized. For this, we follow the procedure in Ref.[103] and get from $\partial E_{\mathrm{LJ}}^{\mathrm{coh}}/\partial a = 0$ the minimum lattice parameter,

$$a^*_{\mathrm{min}} = \frac{a_{\mathrm{min}}(\alpha,\beta_1,\beta_2,\beta_3,\gamma_1,\gamma_2)}{r_e} = \frac{1}{f(\beta_1,\beta_2,\beta_3)}\left(\frac{L^h(\frac{n}{2},\alpha,\beta_1,\beta_2,\beta_3,\gamma_1,\gamma_2)}{L^h(\frac{m}{2},\alpha,\beta_1,\beta_2,\beta_3,\gamma_1,\gamma_2)}\right)^{\frac{1}{n-m}}, \quad (6.50)$$

and the * indicates that reduced (or dimensionless) units are used. We can then evaluate the cohesive energy at a^*_{min} and get

$$E^*_{nm} = E_{\mathrm{LJ}}^{\mathrm{coh}}(n,m,a^*_{\mathrm{min}},\alpha,\beta_1,\beta_2,\beta_3,\gamma_1,\gamma_2)/\epsilon = -\frac{1}{2}\left[\frac{L^h(\frac{m}{2},\alpha,\beta_1,\beta_2,\beta_3,\gamma_1,\gamma_2)^n}{L^h(\frac{n}{2},\alpha,\beta_1,\beta_2,\beta_3,\gamma_1,\gamma_2)^m}\right]^{\frac{1}{n-m}} \quad (6.51)$$

We therefore have to deal only with the six-parameter space $\alpha,\beta_1,\beta_2,\beta_3,\gamma_1,\gamma_2$ for fixed exponents (n,m). As α is fixed to map out the Burgers path, we only have to optimize E^*_{nm} with respect to both sets $\{\beta_1,\beta_2,\beta_3\}$ and $\{\gamma_1,\gamma_2\}$ using a 5D Newton-Raphson procedure as outlined in the supporting information. We chose the interval $\alpha \in [-0.2, 1.2]$ in steps of $\Delta\alpha = 0.05$ for the Burgers path. For the following we omit the * notation, i.e. all quantities are in reduced (dimensionless) units unless otherwise stated.

The validity of using (6.51) instead of (6.49) has been checked by computations which show that we obtain exactly the same results for the extreme points (maxima and minima) and the minimum energy Burgers path. This is perhaps not surprising as we have $\partial E_{nm}/\partial a = 0$ and $\partial E_{nm}/\partial\gamma_1 = \partial E_{nm}/\partial\gamma_2 = 0$ for the minimum energy path. Thus, by performing the derivative $\partial E_{nm}/\partial a = 0$ and considering $\partial L^h(\frac{n}{2},\alpha,\beta_1,\beta_2,\beta_3,\gamma_1,\gamma_2)/\partial a = 0$ in (6.49) we can easily prove by substituting $\partial a = -a\gamma_i^{-1}\partial\gamma_i$ that (6.51) is valid. For the area around the Burgers path where this condition does not exactly hold, but we obtain rather small deviations from the exact solution (6.49). Here, the situation is similar to the hcp case as discussed before[294].

6.2.5 The Burgers-Bain transformation within the kissing hard-sphere model

For large exponents, the (n,m)-LJ potential approaches the kissing hard-sphere limit (KHS) as defined in eq.(6.2). Within the KHS limit we optimize the number of contacts between the spheres (atoms). It is therefore illustrative to discuss the Burgers/Bain type phase transition within the KHS limit first.

For the Burgers transformation the KHS cohesive energy, E_{KHS}, and kissing numbers κ are

given as

$$E_{\mathrm{KHS}} = \begin{cases} -4 & \text{for} \quad \alpha < 0 \quad \text{and} \quad \alpha > 1, \quad \kappa = 8 \\ -6 & \text{for} \quad \alpha = 0 \quad \text{and} \quad \alpha = 1, \quad \kappa = 12 \\ -5 & \text{for} \quad 0 < \alpha < 1, \quad \kappa = 10. \end{cases} \tag{6.52}$$

with $\alpha = \alpha_{\mathrm{M1}}$ or $\alpha = \alpha_{\mathrm{M2}}$. E_{KHS} is now a step function, i.e. we do not have a single point maximum for the energy anymore. In this Burgers transformation, the central atom in the middle layer is located at the bisecting line of the two lattice vectors $\vec{b}_1$ and $\vec{b}_2$ of length $a = 1$ (half unit sphere of radius $R = \frac{1}{2}$), i.e. the atom moves up- or downwards at half-distance ($\frac{1}{2}|\vec{b}_1| = \frac{a}{2}$) along the Burgers path. This is illustrated in Figure 6.5. The parameters change accordingly along the path and we have the boundary conditions $\beta_1 = 1$, $\gamma_1 f_S = 1$, $\beta_3 = \gamma_2$ and $r_{\mathrm{bc}} = 1$.

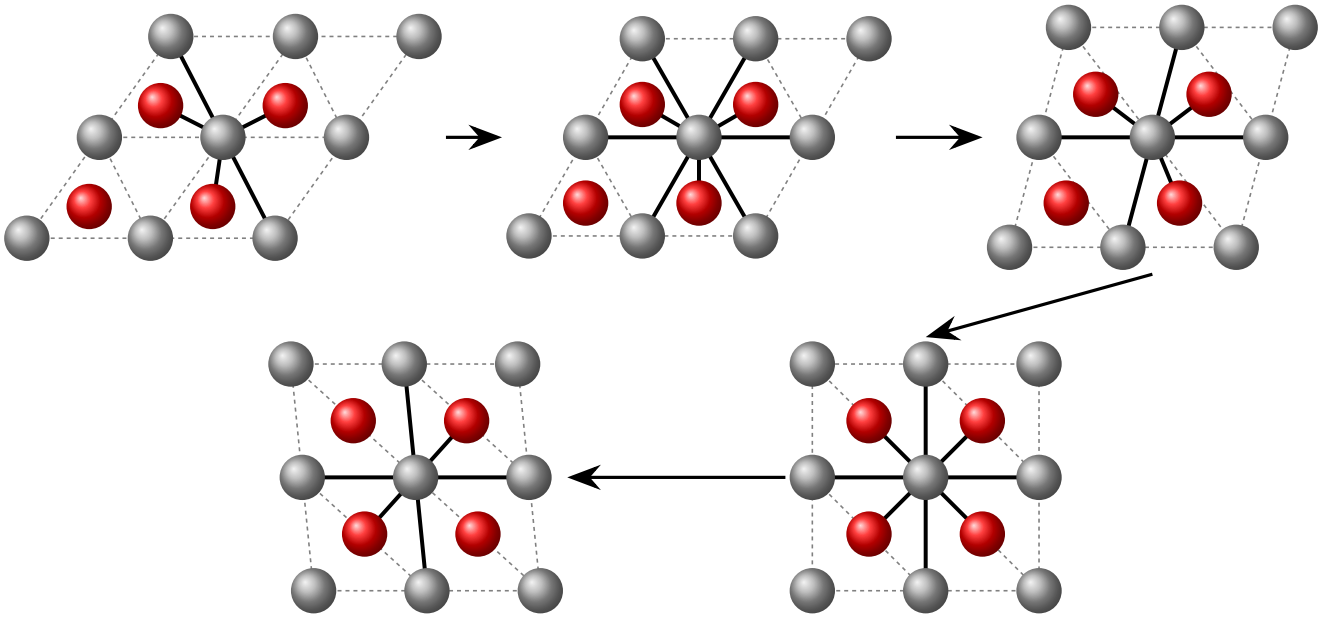

Figure 6.5: Burgers transformation using a kissing hard-sphere model potential along different values of α from $-0.2 \rightarrow 0.0 \rightarrow 0.5 \rightarrow 1.0 \rightarrow 1.2$. The continuous black lines show the bonds from the atom at the origin to its nearest neighbors (kissing spheres). The red atoms lie in the Wyckoff positions of the unit cell and form layers above and below (B layer) the layer of gray atoms (A layer). Including the bonds for the lower B layer we count the number of solid lines and get the kissing numbers as shown in (6.52).

We may naively assume a linear behavior for $\gamma_2(\alpha_{\mathrm{M1}})$ and $\beta_2(\alpha_{\mathrm{M1}})$, but this does not correctly describe the movement of the hard sphere in the second layer while the angle between $\vec{b}_1$ and $\vec{b}_2$ changes. We therefore need to derive analytical formulae for both $\gamma_2(\alpha_{\mathrm{M1}})$ and $\beta_2(\alpha_{\mathrm{M1}})$. For this we conveniently choose Model 2 as α_{M2} has a simple relationship with the angle between the two vectors $\vec{b}_1$ and $\vec{b}_2$ (cf. eq.(6.29)).

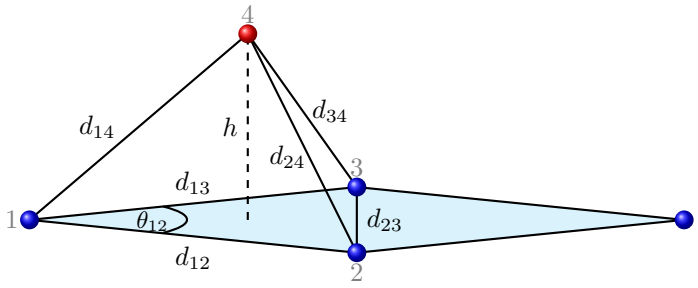

Figure 6.6: The movement of the second layer atom (red color) with respect to the base layer in the Burgers transformation with the parameters for the KHS limit $d_{12} = d_{13} = d_{14} = d_{24} = d_{34} = 1$, $d_{23} = 2\sin\frac{\theta_{12}}{2}$ with $\theta_{12} \in [60, 90]$ degrees, height $h = \frac{\gamma_2}{2}$ and $s = \frac{\beta_2}{2}$ described by an irregular tetrahedron. Note, the kissing number of each sphere is 10.

In order to derive the exact movement of a hard sphere of radius $a/2$ within the second (middle) layer relative to the layers above and below with changing base angle θ_{12} from 60 to 90 degrees, we use a well known relation for the volume V_T of an irregular tetrahedron,

$$V_T = \frac{1}{3} A_T h = \frac{1}{12\sqrt{2}} \sqrt{D_{\mathrm{CM}}} \tag{6.53}$$

where $A_T = \frac{1}{2}\sin\theta_{12}$ is the area of the base triangle between points 1, 2 and 3 as shown in Figure 6.6 and D_{CM} is the Cayley-Menger determinant for an irregular polyhedron[438]. The lengths of the edges for the hard-sphere model are fixed at $d_{12} = d_{13} = a = 1$, $d_{14} = r_{\mathrm{bc}} = 1$, $d_{24} = d_{34} = 1$, and we have $d_{23} = 2\sin\frac{\theta_{12}}{2}$. As $h = \gamma_2/2$ we obtain

$$\gamma_2 = \frac{1}{2\sqrt{2}} \frac{\sqrt{D_{\mathrm{CM}}}}{A} \tag{6.54}$$

The (5×5) Cayley-Menger determinant can easily be evaluated from the distance conditions above, and we have $D_{\mathrm{CM}} = 2d_{23}^2(3 - d_{23}^2)$. After applying some basic trigonometry, this leads to

$$\gamma_2 = \frac{d_{23}\sqrt{3 - d_{23}^2}}{2A} = \frac{2\sin\frac{\theta_{12}}{2}\sqrt{3 - 4\sin\frac{\theta_{12}^2}{2}}}{\sin\theta_{12}} = \sqrt{\frac{2 + 2\cos\theta_{12}(1 - 2\cos\theta_{12})}{1 - \cos^2\theta_{12}}} \tag{6.55}$$

From eq.(6.23) we finally get

$$\gamma_2(\alpha_{\mathrm{M2}}) = \sqrt{\frac{8 + 4\alpha_{\mathrm{M2}}(1 - \alpha_{\mathrm{M2}})}{4 - (1 - \alpha_{\mathrm{M2}})^2}} = 2\sqrt{\frac{2 - \alpha_{\mathrm{M2}}}{3 - \alpha_{\mathrm{M2}}}} \tag{6.56}$$

γ_2 is a monotonically decreasing function in the interval $\alpha_{\mathrm{M2}} \in [0, 1]$. Moreover, γ_2 changes from $\gamma_2 = \sqrt{\frac{8}{3}}$ at $\alpha_{\mathrm{M2}} = 0$ to $\gamma_2 = \sqrt{2}$ at $\alpha_{\mathrm{M2}} = 1$. In other words, the KHS model directly

connects the hcp with the fcc structure (in our specific unit cell treatment), unlike the original proposed transformation by Burgers which is between hcp and bcc[262].

Now that we have an expression for γ_2, we can give an analytical formula for our unit cell volume along the Burgers path (6.8) for the KHS limit,

$$V(\alpha_{\mathrm{M2}}) = \gamma_2\omega_3 = \sqrt{2 + \alpha_{\mathrm{M2}}(1 - \alpha_{\mathrm{M2}})} \tag{6.57}$$

which is an astonishingly simple function in α_{M2}. This function has a maximum at $\alpha_{\mathrm{M2}} = \frac{1}{2}$ with a volume of exactly $V_{\max} = \frac{3}{2}$. From Table 6.1 we see that $V_{\mathrm{bcc}} > V_{\max}$. The corresponding packing density becomes

$$\rho(\alpha_{\mathrm{M2}}) = \frac{\pi}{3\sqrt{2 + \alpha_{\mathrm{M2}}(1 - \alpha_{\mathrm{M2}})}} \tag{6.58}$$

which at maximum volume becomes $\rho(V = \frac{3}{2}) = 2\pi/9$. The ratio to the hard-sphere packing at fcc minimum is therefore $\rho(V = \frac{3}{2})/\rho(V = \sqrt{2}) = \frac{2\sqrt{2}}{3} = 0.942809....$ This value is significantly above the ratio near melting ($\rho = 0.739$) given by Mau and Huse[439].

From our expression of γ_2, we can easily derive an analytical expression for β_2 for the hard-sphere model using simple geometry,

$$\beta_2(\alpha_{\mathrm{M2}}) = \sqrt{\frac{4 - (1 - \alpha_{\mathrm{M2}})(\alpha_{\mathrm{M2}} + 3)}{4 - (1 - \alpha_{\mathrm{M2}})^2}} = \sqrt{\frac{1 + \alpha_{\mathrm{M2}}}{3 - \alpha_{\mathrm{M2}}}} \tag{6.59}$$

β_2 is a monotonically increasing smooth function in $\alpha_{\mathrm{M2}} \in [0, 1]$. We will see later on that this implies no symmetry breaking effects within this model.

We need to mention the bcc structure which can appear on the Burgers path at $\alpha = \frac{1}{3}$ at the right conditions for the lattice parameters. Within the KHS model at $\alpha = \frac{1}{3}$ we get $\gamma_2 = \sqrt{\frac{5}{2}} = 1.5811388\ldots$, $\beta_1 = 1$ and $\beta_2 = \frac{1}{\sqrt{2}} = 0.70710678\ldots$. The γ_2 value is perhaps closest to the one associated with the bcc structure ($\gamma_2 = 1.632993$ in our unit cell definition, but both the KHS values for β_1 and β_2 deviate substantially from the ones defined by the bcc structure, see Table 6.1). This clearly shows that the KHS model bypasses the bcc structure along the Burgers path, a general feature we also expect for harder LJ potentials close to the KHS limit. This is comes at no surprise as the kissing number is constant at $\kappa = 10$ for the Burgers path in the interval $\alpha \in (0, 1)$ compared to the bcc structure, where κ is reduced to 8.

As we will discuss also the fcc→bcc transformation in section 6.3.3 further down, we mention the Bain phase transition as a special case of our Burgers-Bain transformation by setting $\alpha = 1$ and varying $\gamma_2 \in [1, \sqrt{2}]$. In this transformation the 8 atoms at the edges of the cuboidal cell move slightly out as the unit cell gets compressed from fcc to bcc and we have $a > 1$. The kissing number changes from 12 to 8, i.e. the cuboidal structure for $\gamma_2 < \sqrt{2}$ lies energetically always above fcc or hcp and even above the hard-sphere Burgers transition path.

As we have $a > r_{\mathrm{bc}} = 1$ for $\gamma_2 < \sqrt{2}$ and $\alpha = 1$ within the KHS model, we can easily derive that for the lattice constant a we have

$$a(\gamma_2) = \frac{2}{\sqrt{2+\gamma_2^2}} \tag{6.60}$$

As $\omega_3(\alpha = 1) = 1$ we get for the volume of the Bain path of a cuboidal lattice

$$V_{\mathrm{cub}}(\gamma_2) = \frac{8\gamma_2}{(2+\gamma_2^2)^{\frac{3}{2}}} \tag{6.61}$$

that is the volume is monotonically increasing from fcc to bcc within the KHS model. We can easily verify that for the appropriate γ_2 values we get the results as shown in Table 6.1. We can now compare the KHS model with the results obtained from (n,m)-LJ potentials.

6.2.6 Density functional Calculations using the Variable Cell Nudge Elastic Band Method for Solid Argon

Solid argon is reasonably well described by two-body interactions[104] such as the (12,6)-LJ potential[226,227,440]. Hence, in order to verify our lattice sum calculations for the hcp→fcc phase transition path, we decided to carry out additional density functional theory (DFT) calculations[441] using the Perdew–Burke–Ernzerhof (PBE) exchange-correlation functional[280] together with an ultrasoft pseudopotential for argon[442] to replace the argon core, and the PBE functional including dispersion interactions through the DFT-D3(BJ) method[291–293], mapping out the Burgers path by applying the Variable Cell Nudge Elastic Band method (VC-NEB) for solid argon[426,443–445] using 25 grid points on the transition path between hcp and fcc. For this we used the same unit cell as shown in Figure 6.1 and optimized all variable parameters for the B-matrix and the shift vector to obtain the stress tensor for the path optimization. While the PBE functional may not reproduce solid state properties of argon accurately,[446] the PBE-D3 functional performs far better, and for the transition path we assume that the errors inherent in the DFT[327] or pseudopotential approximation[447] should cancel out for energy differences to some extent. We also included the local density approximation (LDA)[448] as a limiting case, as it is well known that this functional substantially overestimates the binding energy of Ar_2,[449] and therefore of solid argon as well.

6.3 Results and Discussions

6.3.1 The hcp↔fcc Burgers transformation in a restricted four-parameter space

For the following we adopt Model 2 for convenience, i.e. $\alpha \equiv \alpha_{\mathrm{M2}}$ and $\gamma_1 = 1$. We first consider the smaller four-parameter space $(a, \alpha, \beta_2, \gamma_2)$ by setting $\beta_1 = 1$ and $\beta_3 = \gamma_2$ in agreement with the hard-sphere model. Only a few combinations for the exponents (n, m) of the LJ potential are selected here, sufficient to discuss the most important features of a generalized LJ potential. Furthermore, we keep the discussion in this section rather short. More details can be found in the supplementary information, and preliminary results for the (12,6)-LJ potential were already published by our group[431]. Furthermore, extension of this small parameter space results in symmetry breaking effects with a bifurcation point occurring including the appearance of an additional minimum for the bcc structure, which will be discussed in detail in sections 6.3.2 and 6.3.3.

The optimized lattice parameters and corresponding energies are summarized in Table 6.2. As can be seen, the energy difference between fcc and hcp is very small for all LJ potentials applied, e.g. $\Delta E_{nm} = E_{nm}^{\mathrm{hcp}} - E_{nm}^{\mathrm{fcc}} = 8.703 \times 10^{-4}$ for the (12,6)-LJ potential and -1.6705×10^{-3} for the (6,4)-LJ potential. This is already well documented in the literature[104,192,227,372,406,450–452]. Figure 6.7 shows the hcp-fcc phase transition line between the two phases for a (n, m)-LJ potential where we have $\Delta E_{nm} = 0$. Only for very soft long-range potentials becomes the fcc phase more stable compared to hcp. The critical exponents n_c, m_c for the phase transition line can be approximated by the following functional form,

$$m_c = 3 + k_1 e^{-k_2 n_c} + \frac{c_1}{n_c} + \frac{c_2}{n_c^2} + \frac{c_3}{n_c^3} \quad \text{with} \quad n_c > 5.705 \tag{6.62}$$

where $k_1 = 3.322473067 \times 10^8$, $k_2 = 5.95017115$, $c_1 = -9.23169654$, $c_2 = 1.73880812 \times 10^2$ and $c_3 = -1.89668849 \times 10^2$ with a coefficient of determination of $R^2 = 0.9998$. For example, for $n_c = 12$ we get $m_c = 3.291725434064$, which implies that for the $(12, 6)$-LJ potential the hcp phase lies energetically below the fcc phase. It was recently shown[104] that, for a rare-gas solid like argon, phonon dispersion is required for the stabilization of the fcc over the hcp phase at 0K.

To obtain the minimum energy path, for which we have the condition $\partial E_{\mathrm{coh}}(\alpha)/\partial x_i = 0$ for $x_i \in \{a, \beta_2, \gamma_2\}$, we changed the parameter α in forward direction from -0.2 to $+1.2$ in steps of 0.025 optimizing all other lattice parameters. The results show that we automatically end up with the fcc structure at $\alpha = 1$ and $\gamma_2 = \sqrt{2}$ on that path for all LJ potentials considered here, in perfect agreement with the KHS model (cf. Figure 6.8). The reverse path starting from the bcc structure at $\alpha = 1$ and $\gamma_2 = 1$ goes steeply uphill.

Table 6.2: Optimized parameters for minima and transition states (TS) for various (n,m)-LJ potentials (Model 2) setting $\beta_1 = 1$, $\beta_3 = \gamma_2$ and $\gamma_1 = 1$. TS properties for the Burgers ($\partial E_{nm}/\partial\alpha = 0$) and Bain paths ($\partial E_{nm}/\partial\gamma_2 = 0$) are indicated by a # symbol. For the minimum structures we get exactly $\alpha = 0$ and $\beta_2 = 1/\sqrt{3}$ for hcp and $\alpha = 1$, $\beta_2 = 1$ and $\gamma_2 = \sqrt{2}$ for fcc. For hcp ($\alpha = 0$) we obtain a slight deviation from the ideal γ_2 value with $\delta_{nm} = \gamma_2(n,m) - \sqrt{8/3}$. cub2 indicates the second cuboidal structure after fcc, e.g. bcc if we have the ideal values of $\alpha = 1$, $\beta_2 = 1$ and $\gamma_2 = 1$. For fcc ($\alpha = 1$) we have $a^{\rm fcc}_{\rm min} = r^{\rm fcc}_{\rm bc,min}$. $\Delta E_{nm}(\alpha^{\#})$ for the Burgers path is taken relative to the hcp structure. The volume increase $\Delta V[\%]$ at the TS of the Burgers path relative to the fcc structure is defined as $100\{V(\alpha^{\#}) - V^{\rm fcc}\}/V^{\rm fcc}$. α_k defines the point on the Burger's path where the kissing number changes spontaneously from κ=4 ($\alpha < \alpha_k$) to 2 ($\alpha < \alpha_k$). For the Bain path TS we have $\alpha = 1$ and $\beta_2 = 1$, which is located at $\gamma_2 = 1$ except for the (6,4)-LJ potential for which we get $\gamma_2^{\#}$ =1.01301670. $\Delta E_{nm}(\alpha^{\#})$ values for the Bain path are relative to the fcc structure.

Parameter	$(6,4)$	$(8,6)$	$(12,4)$	$(12,6)$	$(30,6)$	$(30,12)$
minima						
$a^{\rm hcp}(\alpha=0)$	0.75523963	0.94115696	0.91206706	0.97127386	0.99229244	0.99939864
$r^{\rm hcp}_{\rm bc}(\alpha=0)$	0.75533453	0.94108456	0.91203445	0.97118272	0.99225828	0.99938521
$E^{\rm hcp}_{nm}(\alpha=0)$	-38.9325327	-10.4019067	-18.30985366	-8.61107046	-7.57167198	-6.11058661
$\delta^{\rm hcp}_{nm}(\alpha=0)$	0.00030779	-0.00018844	-0.00008759	-0.00022986	-0.00008431	-0.00003291
$a^{\rm fcc}(\alpha=1)$	0.75527318	0.94112001	0.91205036	0.97123369	0.99227815	0.99939381
$\Delta E^{\rm fcc}_{nm}(\alpha=1)$	-0.00167052	0.00065426	0.00053138	0.00087030	0.00063934	0.00034707
$a^{\rm cub2}(\alpha=1)$	0.84952560	1.08593491	1.06151441	1.14235260	1.20025739	1.21772324
$r^{\rm cub2}_{\rm bc}(\alpha=1)$	0.73571075	0.92022759	0.89393191	0.95447928	0.98606235	0.99654594
$\gamma^{\rm cub2}_2(\alpha=1)$	1	0.93401642	0.91472620	0.89022278	0.83649731	0.82395744
$\Delta E^{\rm cub2}_{nm}(\alpha=1)$	0.29641379	0.24620888	0.45584326	0.34906107	0.58211318	0.76315575
TS Burgers						
$\alpha^{\#}$	0.50124827	0.50070620	0.50055491	0.50036605	0.50007315	0.49998534
θ_{12}	75.55941782	75.54338146	75.53890556	75.53331802	75.52465212	75.52205406
$a^{\#}$	0.73561911	0.92214149	0.89552993	0.95622314	0.98638714	0.99664997
$r^{\#}_{\rm bc}$	0.76148854	0.94610839	0.91637703	0.97463898	0.99337015	0.99965780
$\beta^{\#}_2$	0.84563200	0.82802883	0.82241205	0.81445956	0.78931350	0.78087408
$\gamma^{\#}_2$	1.60349255	1.58902301	1.58494120	1.57867371	1.56007043	1.55383900
$\Delta E_{nm}(\alpha^{\#})$	0.63868037	0.34878984	0.59775652	0.41488952	0.59694720	0.76650812
$\Delta V[\%]$	1.45105875	2.35271163	2.73068082	3.15510867	4.92065604	5.51004680
α_k	0.52877	0.51028	0.50911	0.50408	0.49990	0.49905
TS Bain						
$a^{\#}$	0.84587206	1.06148905	1.03057025	1.09911882	1.13483878	1.14700157
$r^{\#}_{\rm bc}$	0.73573887	0.91927648	0.89250002	0.95186482	0.95186482	0.99333250
$\Delta E_{nm}(\alpha^{\#})$	0.29644955	0.24972893	0.47009499	0.37377855	0.77263663	1.17257580

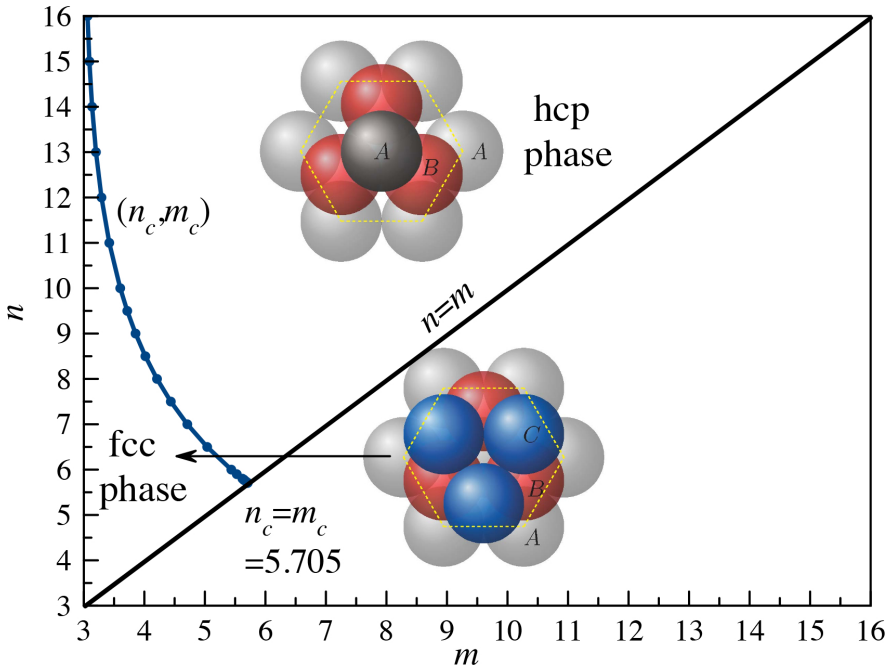

Figure 6.7: hcp/fcc phase transition line (n_c, m_c) for (n, m)-LJ potentials fulfilling the condition $\Delta E_{nm} = E_{nm}^{\text{hcp}} - E_{nm}^{\text{fcc}} = 0$.

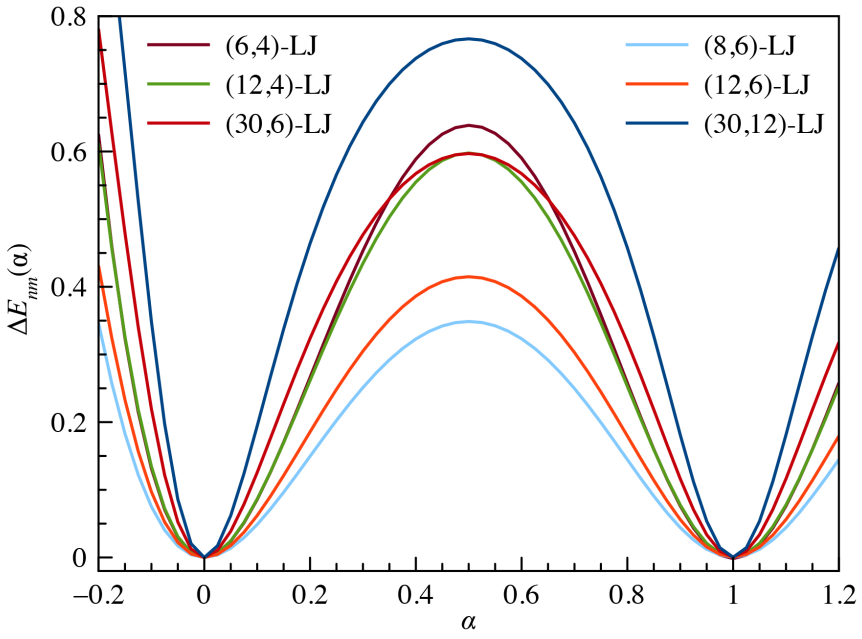

Figure 6.8: The cohesive energy difference $\Delta E_{nm}(\alpha) = E_{nm}(\alpha) - E_{nm}^{\text{hcp}}(\alpha = 0)$ for the Burgers path as a function of the distortion parameter α for various selected (n, m)-LJ potentials using Model 2 and $\beta_1 = 1$.

An analysis of the minimum distances reveals a kissing number of $\kappa = 12$ for the two points $\alpha = 0, \gamma_2 = \sqrt{\frac{8}{3}}$ and $\alpha = 1, \gamma_2 = \sqrt{2}$ as one expects. However, around the transition state we find $\kappa = 4$ for the interval $\alpha \in (0, \alpha_k)$ with shortest distances in the hexagonal layer, at critical

value α_k we find $\kappa = 6$ picking up two short distances to the central atom, and we have $\kappa = 2$ for the interval $\alpha \in (\alpha_k, 1)$ with shortest distances to the central atom as listed in Table 6.2 for various LJ potentials. We note that α_k is close to $\frac{1}{2}$. The optimized lattice parameters $\beta_2(\alpha)$ and $\gamma_2\alpha)$ follow qualitatively the KHS model, see supporting information.

The cohesive energies along the Burgers path for different (n, m)-LJ potentials are shown in Figure 6.8. The transition state is close to the midpoint of $\alpha = 1/2$ for all LJ potentials considered here as one would expect. For example, for the (12,6)-LJ potential we find the transition state at $\alpha^{\#} = 0.50037$ with an energy difference of $\Delta E_{12,6}(\alpha^{\#}) = E_{12,6}(\alpha^{\#}) - E_{12,6}^{\text{hcp}} = 0.41490$, see Table 6.2. An important finding here is that within this parameter space the energy and its first and second derivatives with respect to the lattice parameters show a smooth functional behavior. In the following section we will show that this is an artifact of limiting our parameter space according to the KHS limit.

The Bain transformation from fcc to bcc is well understood because of its simplicity in the crystal transformation[103,126,261,431]. For recent applications to group 1 and 11 metals we refer to refs. 127,433. In our limited parameter space model, the activation energies for the Bain phase transition are usually below the ones for the Burgers path (cf. Table 6.2), except for very repulsive walls. For example, the highest barrier for the Bain path is obtained by the most repulsive $(30, 12)$-LJ potential as expected from the KHS model, which puts bcc energetically above the Burgers path. In addition, the MD simulations by Bingxi Li et al[367] for solid argon show no transition from hcp or fcc to the bcc phase. We note that the hcp to fcc transition has been modeled before for LJ potentials by Jackson et al[413] using a fixed cutoff using the lattice-switch Monte Carlo method.

6.3.2 The Burgers phase transition along a symmetry broken minimum energy path

So far we adopted a fixed value of $\beta_1 = 1$ as derived from the KHS model resulting in a smooth Burgers-Bain transformation. This initial choice to save computer time leads to bypassing the bcc structure at $\alpha = \frac{1}{3}$ and $\beta_1 = \frac{4}{3}$ along the Burgers path. For example, for the (12,6)-LJ potential we obtain an optimized value of $\beta_2 = 0.73409675$ at $\alpha = \frac{1}{3}$ substantially different to $\beta_2 = 2\sqrt{2}/3 = 0.94280904$ expected for the bcc structure. The question therefore arises how valid the choice of parameters from the KHS approximation for LJ potentials really is to correctly describe the hcp transition to the cuboidal phase. We therefore decided to add the β_1 lattice constant to our variable parameter space. We therefore restricted our lattice sum treatment for the Burgers path from in principle nine (six for the B-matrix and three for the shift vector) to seven varying lattice parameters, with the two remaining fixed ones being the two angles $\angle(\vec{b_1}, \vec{b_3})$ and $\angle(\vec{b_2}, \vec{b_3})$ kept at 90°. This not only saves computer time, but has the advantage that we are able to derive efficient expansions of the required lattice sums in

terms of Bessel functions, see Appendix H. Otherwise one has to use different techniques for the efficient treatment of the Epstein zeta function, see for example Buchheit and Busse[364]. However, from preliminary optimization runs it turns out that we can impose two further restrictions, i.e. (i) $|\vec{b}_1| = |\vec{b}_2|$ resulting in $\gamma_1 f_S = 1$ for Model 1 and $\gamma_1 = 1$ for Model 2, and (ii) $\beta_3/\gamma_2 = 1$ as we observe no symmetry breaking in direction of the $c-$axis within the range of γ_2 values applied (if γ_2 becomes large one will eventually observe a Peierls distortion). Hence, for the Burgers path, our in general nine-dimensional optimization problem reduces to five, that is $x_i \in \{a, \alpha, \gamma_2, \beta_1, \beta_2\}$. This space of freely varying parameters is larger than used in previous work, cf. Ref. 427, and therefore allows for a more accurate treatment of the Burgers path within the LJ model. As we will see in the next section, there is an exact relation between the two parameters $\beta_1(\alpha)$ and $\beta_2(\alpha)$ in the interval $\alpha \in [0, 1]$, which would reduce our variable parameter space even further to four. As we shall see, the parameter β_1 is responsible for the appearance of a bifurcation point and symmetry breaking effect in the middle layer movement, leading to a significant lowering in energy especially for the soft LJ potentials. The optimized parameters x_i for the transition state along the Burgers path are shown in Table 6.3.

Parameter	$(6,4)$ LM	$(6,4)$	$(8,6)$	$(12,4)$	$(12,6)$	$(30,6)$	$(30,12)$
$\alpha^{\#}$	0.33333333	0.35642304	0.39334946	0.41043348	0.43318316	0.48184258	0.49317558
θ_{12}	70.52877937	71.22888103	72.34256361	72.85545878	73.53626429	74.98459698	75.32047856
$a^{\#}$	0.73571075	0.73573887	0.92025077	0.89394548	0.95452850	0.98609243	0.99655952
$r_{\mathrm{bc}}^{\#}$	0.84952560	0.84587207	1.01384023	0.97080269	1.01649542	1.00388530	1.00331254
$\beta_1^{\#}$	1.33333333	1.14969060	1.21375677	1.17935344	1.13411523	1.03648224	1.01364020
$\beta_2^{\#}$	0.94280904	0.73573887	0.88740177	0.87037568	0.84744319	0.79509947	0.78230716
$\gamma_2^{\#}$	1.63299316	1.62590804	1.61067804	1.60279158	1.59117300	1.56178561	1.55400238
$\Delta E_{nm}(\alpha^{\#})$	0.29641379	0.29644955	0.24610211	0.45568950	0.34858732	0.58118291	0.76251538
$\Delta V[\%]$	0.62414868	0.61309906	1.46557560	1.97613085	2.42740664	3.70201581	5.39593019

Table 6.3: Optimized parameters for the Burgers path transition state (TS) for various (n, m)-LJ potentials. See Table 6.2 for a detailed description of the parameters. $\Delta E_{nm}(\alpha^{\#})$ is taken relative to the hcp structure. The volume increase $\Delta V[\%]$ at the transition point of the Burgers path relative to the fcc structure is defined as $100\{V(\alpha^{\#}) - V^{\mathrm{fcc}}\}/V^{\mathrm{fcc}}$. For the (6,4) potential we report both the local minimum (LM) and the second transition state closer to the fcc structure (see text for details).

The minimum cohesive energy path $E_{\mathrm{coh}}(\alpha)$ for the Burgers transformation within our extended five parameter space is shown in Figure 6.9. We see that the transition state is now significantly lowered especially for the softer LJ potentials compared to our previous results where we imposed the hard-sphere limit restriction of $\beta_1 = 1$. For example, for the (12,6)-LJ potential the transition state is slightly shifted towards the hcp structure ($\Delta\alpha^{\#} = -0.06718$) while the energy is lowered by $\Delta E_{\mathrm{coh}} = -0.06630$ compared to the case where $\beta_1 = 1$. This is even more so for the soft (6,4)-LJ potential, i.e. $\Delta\alpha^{\#} = -0.18023$ and $\Delta E_{\mathrm{coh}} = -0.34222$ (here

we took the second transition state on the hcp→fcc path, see discussion below). The increase in volume from the minimum structure to the transition state is also reduced significantly. The KHS limit is an upper bound for the change in cohesive energy, and calculations show that the (100,90)-LJ potential is already very close to this limit with larger deviations only observed in the vicinity of the two limiting points of hcp ($\alpha = 0$) and fcc ($\alpha = 1$).

In order to analyse the influence of the β_1 parameter even further, we note that the kissing number changes from $\kappa(\alpha < 0) = 2 \rightarrow \kappa(\alpha = 0) = 12$ (ideal hcp) $\rightarrow \kappa(0 < \alpha < \alpha_k) = 4 \rightarrow \kappa(\alpha_k) = 8 \rightarrow \kappa(\alpha_k < \alpha < 1) = 4 \rightarrow \kappa(\alpha = 1) = 12 \rightarrow \kappa(\alpha > 1) = 4$ where α_k is close to the transition state. This implies a larger kissing number after the transition state towards fcc compared to the previous symmetric model where we fixed $\beta_1 = 1$, which rationalizes the significant energy lowering of the transition state. Moreover, we see a change in the shortest distances along the Burgers path, i.e. from hcp to the transition state the shortest distances are those within the hexagonal layers, while after the transition state towards the fcc structure the shortest connections are from the hexagonal to the middle layer atoms.

The lattice parameters shown in Figure 6.10 clearly demonstrate that we break symmetry along the Burgers path as compared to the symmetric path obtained for fixed $\beta_1 = 1$. This distinct symmetry breaking effect leads to a critical point α_c along the path where the parameters β_1 and β_2 change abruptly while the cohesive energy $E_{\text{coh}}(\alpha)$ still behaves like a smooth function. The distance to the middle layer r_{bc} also changes abruptly at the critical point due to its dependence on β_1 and β_2, see eq.(6.19). At the critical point α_c we have the following

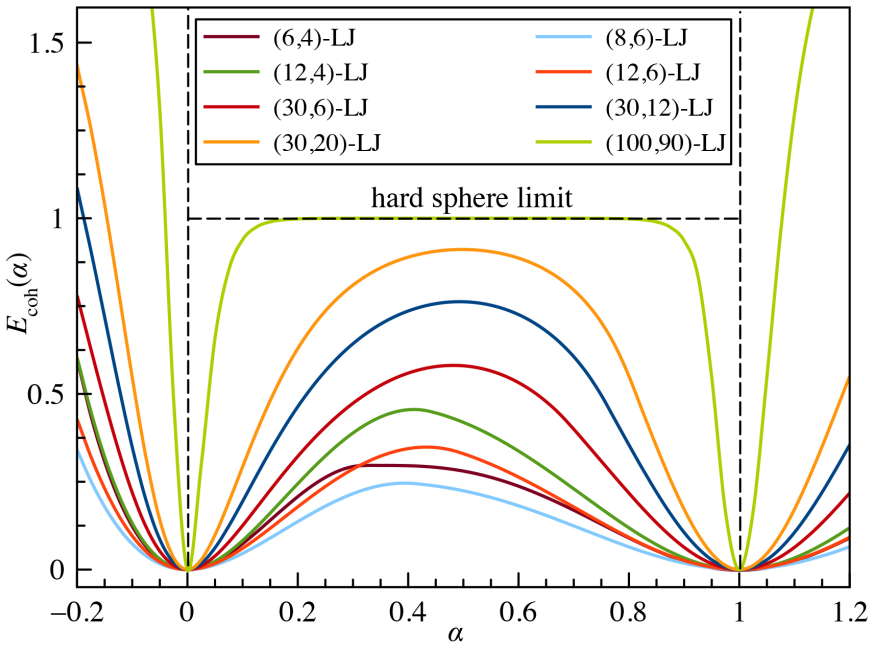

Figure 6.9: The cohesive energy difference $\Delta E_{nm}(\alpha) = E_{nm}(\alpha) - E_{nm}^{\text{hcp}}(\alpha = 0)$ for the symmetry-broken Burgers path as a function of the distortion parameter α for various selected (n, m)-LJ potentials using Model 2.

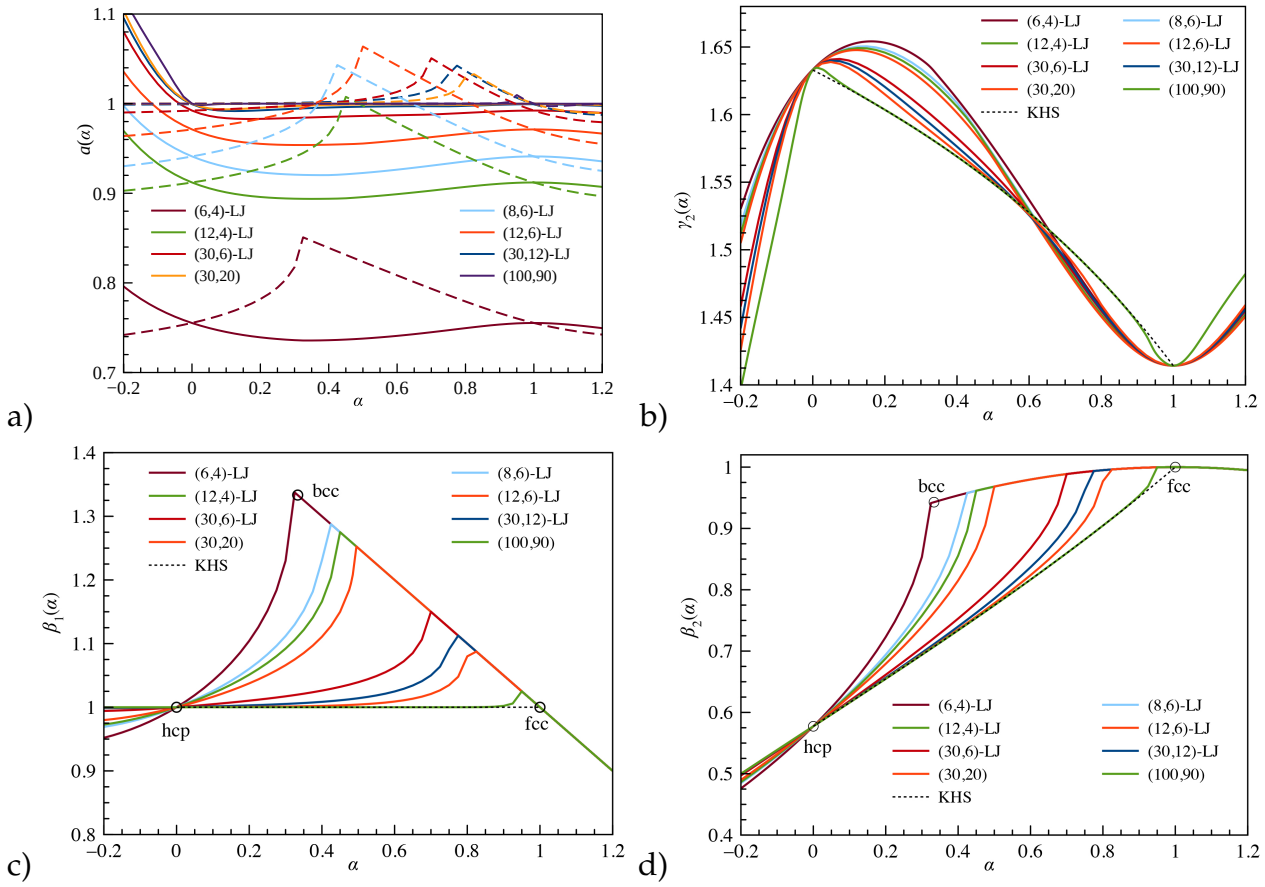

Figure 6.10: Dependence of the optimized parameters $a, \gamma_2, \beta_1, \beta_2$ on α along the symmetry-broken Burgers path for various selected (n,m)-LJ potentials using Model 2. For the lattice constant a, the solid lines show the distances between nearest neighbors in the base layer ($a = |\vec{b}_1|$), while the dashed lines show the optimized distances from the base to the body-centered atom ($r_{\text{bc}} = |\vec{v}_s|$), see Figure 6.1. The KHS limits are also shown as described in detail in section 6.2.5. In c) and d) the three different structures, hcp, fcc and bcc, are indicated by black circles.

conditions for the optimized parameters describing the movement of the middle layer (in the following we discuss the optimized parameters along the minimum energy path $E_{\text{coh}}(\alpha)$, i.e. we have the condition $\partial E_{\text{coh}}(\alpha)/\partial\beta_1 = 0$ and $\partial E_{\text{coh}}(\alpha)/\partial\beta_2 = 0$),

$$\lim_{\alpha\to\alpha_c} \beta_1(\alpha) = \lim_{\alpha_c\leftarrow\alpha} \beta_1(\alpha) \quad \text{and} \quad \lim_{\alpha\to\alpha_c} \beta_2(\alpha) = \lim_{\alpha_c\leftarrow\alpha} \beta_2(\alpha) \tag{6.63}$$

but

$$\lim_{\alpha\to\alpha_c} \partial\beta_1(\alpha)/\partial\alpha \neq \lim_{\alpha_c\leftarrow\alpha} \partial\beta_1(\alpha)/\partial\alpha \quad \text{and} \quad \lim_{\alpha\to\alpha_c} \partial\beta_2(\alpha)/\partial\alpha \neq \lim_{\alpha_c\leftarrow\alpha} \partial\beta_2(\alpha)/\partial\alpha \tag{6.64}$$

where the right arrow indicates that we move in forward direction, from hcp to fcc, and the left arrow for the reverse path from fcc to hcp. In fact, in forward direction the functions $\beta_1(\alpha)$

and $\beta_2(\alpha)$, $\alpha < \alpha_c$, terminate by joining another curve coming from the reverse direction which continues beyond α_c with increasing cohesive energy, in fact towards the bcc structure at $\alpha = \frac{1}{3}$ as discussed in more detail below. This implies that we have a bifurcation point along our minimum energy path for both $\beta_1(\alpha)$ and $\beta_2(\alpha)$ as shown in Figure 6.10. We refer to the two directions for the minimum energy path as left (forward) and right (backward) directions in the following. The second derivative of $\beta_1(\alpha)$ and $\beta_2(\alpha)$ with respect to α therefore shows a jump discontinuity. However, the ratio $\beta_1(\alpha)/\beta_2(\alpha)$ behaves smoothly as discussed in the next section.

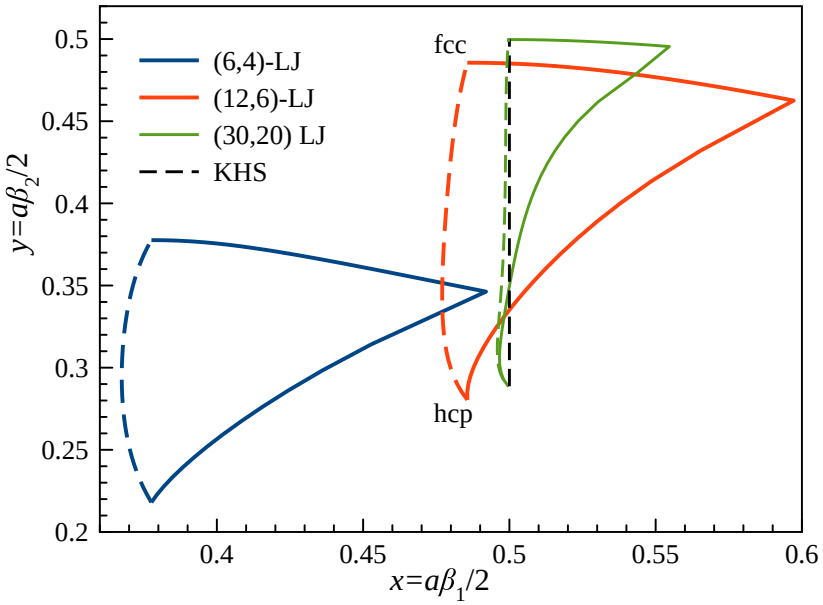

Figure 6.11: Movement of central atom within the (x, y)-plane, spanned by the vectors $\vec{b}_1$ and $\vec{b}_2$, for three selected LJ potential. For the hard-sphere limit we have $\beta_1 = 1$ and $\beta_2 = 1/\sqrt{3}$ for hcp and $\beta_2 = 1$ for fcc. The dashed lines are from calculations setting $\beta_1 = 1$.

The movement of the atom in the middle layer in the $(x, y) = (\vec{b}_1, \vec{b}_2)$ plane is shown in Figure 6.11. In this symmetry broken Burgers path, the central atom in the middle layer is moving away from the origin to the right up to the critical point where it starts to move back again. We also show the line for the KHS model and the one for the smooth transition with fixed $\beta_1 = 1$, the latter not being the correct minimum energy path in our extended parameter space. With increasing LJ exponents we converge towards the KHS limit.

It is computationally challenging to accurately obtain the bifurcation (critical) point α_c as we do not have smooth functions of $\beta_1(\alpha)$, $\beta_2(\alpha)$ or $r_{\text{bc}}(\alpha) = |\vec{v}_s(\alpha)|$ anymore. Moreover, it is difficult to converge into the left (forward) solution near the critical point, while the right (backward) solution causes no particular challenge. Nevertheless, as it turns out, the second derivatives $\partial^2 E_{\text{coh}}(\alpha)/\partial\beta_1^2$ and $\partial^2 E_{\text{coh}}(\alpha)/\partial\beta_2^2$ have an almost linear behavior for both the left and right solutions and can therefore be used to determine the critical point where the

two solutions have identical values. The lattice parameters and energies at the critical point obtained by this method are listed in Table 6.4 for a few selected LJ potentials. We note that α_c increases with increasing hardness of the potential, that is the bifurcation point moves towards the fcc minimum by increasing the exponents of the LJ potential, and for the KHS model we have $\alpha_c = 1$ where the bifurcation point becomes identical to the fcc minimum.

Table 6.4: Optimized parameters for the Burgers path critical point (CP) for various (n, m)-LJ potentials using Model 2. See Table 6.2 for details. The parameter α_c defines the location of the critical point.

Parameter	$(6,4)$	$(8,6)$	$(12,4)$	$(12,6)$	$(30,6)$	$(30,12)$
α_c	0.321022	0.409953	0.441264	0.491655	0.700331	0.756979
θ_{12}	70.154256	72.841043	73.777520	75.275443	81.382657	83.020728
a_c	0.735736	0.920300	0.894201	0.955241	0.965239	0.997027
$r_{\mathrm{bc},c}$	0.851483	1.046068	1.009332	1.065546	1.050608	1.046645
$\beta_{1,c}$	1.339486	1.295023	1.279364	1.254168	1.149835	1.121482
$\beta_{2,c}$	0.940608	0.955490	0.960181	0.967155	0.988711	0.992565
$\gamma_{2,c}$	1.636646	1.605597	1.592986	1.571241	1.561786	1.471437
$\Delta E_{nm}(\alpha_c)$	0.296457	0.245010	0.449619	0.334208	0.399023	0.477019

Figure 6.12 shows the change in volume along the Burgers-Bain path relative to the hcp phase. The symmetry breaking at the bifurcation point becomes visible, especially for the softer LJ potentials. Further, the change in volume becomes larger for the harder LJ potentials. We also see the the KHS limit given by eq.(6.57) enveloping all the LJ curves in the region $\alpha \in [0, 1]$.

Concerning cohesive energy derivatives with respect to the lattice parameters, we have for the two critical parameters the condition

$$\lim_{\alpha \to \alpha^c} \partial^2 E_{\mathrm{coh}}(\alpha)/\partial \beta_1^2 = \lim_{\alpha_c \leftarrow \alpha} \partial^2 E_{\mathrm{coh}}(\alpha)/\partial \beta_1^2 \tag{6.65}$$

and

$$\lim_{\alpha \to \alpha^c} \partial^2 E_{\mathrm{coh}}(\alpha)/\partial \beta_2^2 = \lim_{\alpha_c \leftarrow \alpha} \partial^2 E_{\mathrm{coh}}(\alpha)/\partial \beta_2^2 \tag{6.66}$$

with an abrupt change (kink) at α_c along the minimum energy path. Both the left and right second derivative curves with respect to the transition parameter α are very close to linearity (at least to numerical accuracy) and it is therefore difficult to predict accurately the higher order derivatives which will be very small for these two parameters. Ehrenfest's definition of a nth-order phase transition is that the free energy exhibits a discontinuity (jump discontinuity, singularities etc.) in the nth-order derivative with respect any thermodynamic variables like the pressure or temperature at a certain critical point[243,453]. Any discontinuity in the lattice

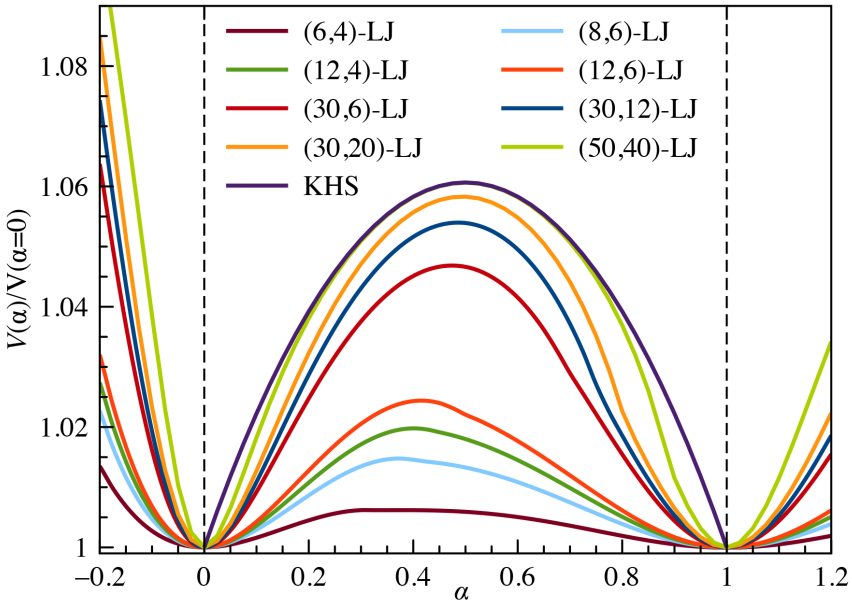

Figure 6.12: Volume change along the Burger-Bain path relative to the hcp volume at $\alpha = 0$. The kissing hard-sphere model is shown by a solid black line enveloping all the other LJ curves.

parameters for the middle layer may lead to a discontinuity in the Taylor expansion of the total energy in Cartesian space and therefore to a discontinuity in the phonon spectrum. Indeed, using DFT for several transition metals, Feng and Widom[418] observed a Λ-point phonon instability along the Burgers path from bcc to hcp related to the slide deformation of layer B (see Figure 6.1). They chose a three-parameter space for their definition of a bi-lattice directly connecting the bcc with the hcp phase as compared to our choice which includes hcp and all all cuboidal structures. At the point of instability the lattice reduces symmetry from a cubic to an orthorhombic phase moving towards the hcp structure. This symmetry breaking is clearly related to what we are observing here using LJ potentials. Similarly, Caspersen and Carter used a three-parameter space but different definition for the Burgers transformation for their DFT calculations of metallic lithium[352]. The calculations were carried out under finite pressure, but they did not observe any symmetry breaking effects most likely due to the fact that the cohesive energy is rather insensitive to such effects. We finally mention that the discontinuity in the second derivatives will lead to an abrupt change in the entropy however small this effect might be. One can therefore only speculate that the Burgers transition is a first-order phase transition. However, it would be very difficult if not impossible to detect this discontinuity either by experiment or by molecular dynamics simulations.

6.3.3 The bcc structure as an intermediate between the fcc and hcp phase

The question arises if there is a direct minimum energy path from hcp to bcc as suggested for example by Carter and co-workers for iron or lithium[266,352] and by several other

authors[416,418,427,454–456], or if the fcc phase is required as an intermediate[269,431]. In other words, we might have missed another transition path. Moreover, it was already shown in 1940 that the elastic stiffness tensor for cubic crystals fulfills Born's second stability criterium, $C_{11} - C_{12} > 0$, only for very soft LJ potentials for the bcc structure, e.g. for exponents such as $(n, m) = (6, 4)$ of $(5, 4)$, otherwise one observes a distortion of the rhombohedral bcc primitive cell[355,356] as shown in Figure 6.4, (loosely termed rhombohedral distortion in the literature). In contrast, the fcc phase for a (n, m)-LJ potential is always stable (local minimum). Surprisingly, the exact minimum energy path and mechanism of the rhombohedral distortion towards presumably either the fcc or the hcp phase has never been investigated in great detail apart from the conventional cuboidal distortion towards the fcc phase along a simple Bain path[103,127,431,433].

Figure 6.13 shows an interesting feature along the Burgers path in that we obtain an additional (metastable) minimum for the soft (6,4)-LJ potential. This is not the case for any of the other harder potentials studied here such as the usual (12,6)-LJ potential. The highest energy point for the (6,4)-LJ potential is now located at the critical point α_c where a bifurcation takes place, with a second transition state following at $\alpha^{\#}$ (compare the values in Tables 6.3 and 6.4). Between both maxima we have a minimum located exactly at the lattice parameters satisfying the condition for a bcc phase (cf. Table 6.1), e.g. $\alpha = \frac{1}{3}$, albeit the energy differences between the extremal points around the bcc phase are very small and the bcc phase is therefore easily overlooked in the Burgers phase transition. At this metastable bcc minimum we observe an increase in the kissing number from four to eight, which obviously implies increased stability for softer potentials (in the KHS limit we have $\kappa = 10$ for the whole of the Burgers path). Hence, if the bcc structure becomes a minimum along the Burgers path, we have a direct path from hcp to bcc and further to fcc. An unstable bcc structure will distort to either the hcp or the fcc structure, and the Burgers path will bypass bcc. In fact, bcc remains an extremum (zero gradient for all lattice parameters) for all LJ potentials considered, but eventually turns into a second-order saddle point if the exponents (n, m) of the LJ potential are increased[103]. A more detailed analysis reveals that in this case the negative eigenvalues of the Hessian with respect to our parameter space shows a distortion within the two-parameter space (α, β_1).

The question arises of how to describe the mechanism of the structural distortion of the bcc phase. Figure 6.10 shows that bcc lies on the straight $\beta_1(\alpha_c)$ line towards the fcc structure containing all the bifurcation points for the (n, m)-LJ potentials, i.e. we have

$$\beta_1(\alpha) = \frac{1}{2}(3 - \alpha) \tag{6.67}$$

with small deviations possibly due to numerical noise in our data (with a standard deviation of 1.6×10^{-5}). The Hessian for the cohesive energy shows that the modes along the lattice parameters α and β are strongly coupled with large off-diagonal elements $\partial^2 E_{\text{coh}}/\partial\alpha\partial\beta_1$ and

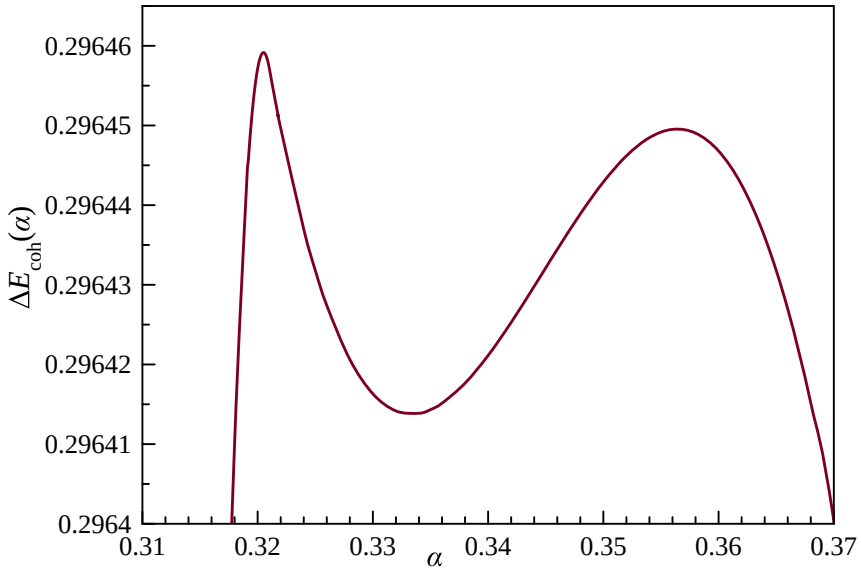

Figure 6.13: A closer look into the minimum energy path with the two transition states and the bcc minimum for the (6,4)-LJ potential with a minimum occurring at the bcc structure with $\alpha = \frac{1}{3}$.

$\partial^2 E_{\mathrm{coh}}/\partial\alpha^2 \approx \partial^2 E_{\mathrm{coh}}/\partial\beta_1^2$ along the bifurcation line. Solving the eigenvalue problem for the Hessian containing only the second derivatives with respect to α and β_1 one can easily show that the existence of a minimum for bcc solely depends on the sign of $\partial^2 E_{\mathrm{coh}}/\partial\alpha^2$ (or $\partial^2 E_{\mathrm{coh}}/\partial\beta_1^2$), which is positive for the (6,4)-LJ potential as seen in Figure 6.13.

For the second lattice parameter $\beta_2(\alpha)$ we get a simple analytical expression derived in appendix J,

$$\beta_2(\alpha) = \sqrt{1 - \tfrac{1}{4}(1-\alpha)^2} \tag{6.68}$$

This formula is substantially different to one derived for the KHS limit, eq.(6.59), except at the end point at $\alpha = 1$. This implies that for a specific value of the bifurcation point α_c for a (n,m)-LJ potential we can determine exactly the corresponding β_1 and β_2 values. Unfortunately, α_c for a specific (n,m)-LJ potential has to be determined numerically from the lattice sums. Furthermore, the ratio $\beta_1(\alpha)/\beta_2(\alpha)$ obtained from the two eqs. (6.67) and (6.68) is valid for the whole range of $\alpha \in [0,1]$ according to our calculations. Hence, this implies that the variable parameter space can be further reduced by using this simple relation. Furthermore, it implies that any symmetry breaking in β_1 leads to a symmetry breaking in β_2.

While rhombohedral primitive cells can be found for both fcc and bcc, for the whole cuboidal transformation we can define the basis vectors in the following way (see appendix

J),

$$\begin{aligned}\vec{p}_1 &= \frac{a_{\text{cub}}}{2}(1,-1,-\gamma_{\text{cub}})^\top \\ \vec{p}_2 &= \frac{a_{\text{cub}}}{2}(1,1,-\gamma_{\text{cub}})^\top \\ \vec{p}_3 &= \frac{a_{\text{cub}}}{2}(1,1,\gamma_{\text{cub}})^\top\end{aligned} \tag{6.69}$$

This implies that for the bcc→fcc transformation, $\gamma_{\text{cub}} = 1 \rightarrow \sqrt{2}$, we have equidistant basis vectors which transform as $|\vec{p}_i| = \frac{a_{\text{cub}}}{2}\sqrt{2+\gamma_{\text{cub}}^2}$, i.e. they are increasing from bcc to fcc as pointed out before[434]. The rhombohedral distortion of the bcc structure is then driven by the change in angles between these vectors, i.e. we have $\angle(\vec{p}_1,\vec{p}_2) = 180^{\text{o}} - \theta_T \rightarrow 60^{\text{o}}$, $\angle(\vec{p}_1,\vec{p}_3) = \theta_T \rightarrow 120^{\text{o}}$, and $\angle(\vec{p}_2,\vec{p}_3) = 180^{\text{o}} - \theta_T \rightarrow 90^{\text{o}}$, where $\theta_T = 109.47122063^{\text{o}}$ is the tetrahedral angle. We can see that this leads to a primitive fcc cell different to the normal primitive rhombohedral cell used in the literature where the corresponding angles are set to 60^{o}. The important result here is that the rhombohedral distortion of the bcc phase is along a Bain path and therefore identical to a cuboidal distortion along the Bain path(!). In addition, at the bifurcation point α_c along the Burgers distortion path towards hcp at $\alpha < \alpha_c$ the lattice becomes a true bi-lattice which cannot be described anymore by a single Bravais lattice without adding another atom inside the unit cell. Such topological changes are typical for bifurcation points. Hence, if we follow along this $bcc \rightarrow hcp$ path, the bcc distortion should perhaps not be described anymore as a simple rhombohedral distortion. In appendix J we demonstrate the Burgers path on the linear $\beta_1(\alpha)$ line containing all the bifurcation points for the different (n,m)-LJ potentials is identical to the original Bain path as discussed in ref. 434. This agrees with the analysis of Feng and Widom using density functional theory for several transition metals[418]. Moreover, the bifurcation point of symmetry breaking becomes exactly the point where we move from a simple lattice into a bi-lattice. We expect that this point of symmetry breaking becomes identical with the bcc structure when the bcc minimum vanishes, i.e. $\partial^2 E_{\text{coh}}/\partial\gamma_c^2 = 0$ at $\gamma_c = 1$, which needs to be further investigated. We should mention that by fixing two of the lattice parameters to $\alpha = \frac{1}{3}$ and $\beta_2 = \frac{2\sqrt{2}}{3}$ we automatically converge into the bcc structure by optimizing all other parameters.

It is perhaps useful to summarize our important findings in this section:

1) In our extended parameter space we observe a distinct symmetry breaking effect with a bifurcation point appearing at $\alpha = \alpha_c$, where the remaining hcp→fcc transition joins the traditional Bain path for $\alpha > \alpha_c$, and with the possibility of going through a metastable bcc minimum for very soft LJ-potentials. This explains the phonon instability observed by Feng and Widom[418].

2) For the remaining Bain path we obtain analytical relationships between the lattice parameters of a cuboidal transformation and our Burgers transformation for $\alpha > \alpha_c$, see appendix K.

3) The rhombohedral distortion of the bcc phase in our LJ model is along the path to fcc until one reaches the bifurcation point where distortion into hcp can happen and the lattice changes into a bi-lattice. If bcc is a metastable minimum in our chosen parameter space we see both distortion paths.

6.3.4 The case of solid argon

To give our results a physical meaning for real solids, we consider solid argon by multiplying the activation energy for the (12,6)-LJ potential with the most accurate available dissociation energy of $\epsilon = 99.351 \pm 0.32$ cm^{-1} for Ar_2 (1.189 ± 0.038 kJ/mol) obtained from relativistic coupled-cluster calculations by Patkowski and Szalewicz[457]. This results in an activation energy for the Burgers transition state of 34.6 cm^{-1} (0.41 kJ/mol) relative to the hcp structure. Calculations performed with the VC-NEB method using DFT with both the PBE and the PBE-D3 functional automatically results in a Burgers path for the hcp→fcc transformation in solid argon within our usual definition of the unit cell. However, the barrier is lower compared to the (12,6)-LJ result, i.e. 22.4 cm^{-1} (0.267 kJ/mol) for PBE-D3, 6.0 cm^{-1} (0.072 kJ/mol) for PBE, and 51.6 cm^{-1} (0.618 kJ/mol) for LDA. This compares to the experimentally known cohesive energy of fcc argon of 7722(11) J/mol,[458], i.e. the barrier height for PBE-D3 is only about 3.5% of the fcc cohesive energy. For a more precise notion, the cohesive energy of both fcc and hcp structures with the LDA functional is 13.45 kJ/mol, while for PBE is 2.23 kJ/mol. The effect of dispersion can be seen through the PBE-D3 cohesive energy of fcc and hcp being 8.33 and 8.32 kJ/mol, respectively, which is in good agreement with the value obtained in Ref. 104. This means that the actual barrier heights with the different density functionals are less than 5% of the total cohesive energy of each phase. Furthermore, the activation energy is smaller than the zero-point vibrational contribution for fcc argon which is 67.4 cm^{-1} (0.806 kJ/mol)[104]. Comparing PBE with PBE-D3 as shown in Figure 6.14, we see that the barrier height in the Burgers transformation is strongly influenced by the addition of Grimme's dispersion term. It is clear that by increasing the cohesive energy and decreasing the nearest neighbor distances the barrier height increases. It comes therefore at no surprise that LDA overestimates the phase transition barrier substantially. The sensitivity of reaction barriers to the density functional approximation applied in molecular systems is well documented[459]. Concerning the location of the transition state, it is very close to the midpoint of the path in agreement with the (12,6)-LJ potential, i.e. $\alpha = 0.456$ for PBE-D3, $\alpha = 0.478$ for PBE and $\alpha = 0.467$ for LDA. As argon is relatively well described by the (12,6)-LJ potential, we bypass the bcc structure along the Burgers path. For example, at the PBE-D3 level of theory we get at $\alpha = \frac{1}{3}$ the deviations from the ideal bcc lattice parameters (see Table 6.1) $\Delta\beta_1 = \beta_1 - \beta_1^{\text{bcc}} = 1.590074 - \frac{4}{3} = 0.256741$, $\Delta\beta_2 = 1.105303 - \frac{2\sqrt{2}}{3} = 0.162494$, $\Delta\beta_3 = 1.597552 - \sqrt{\frac{8}{3}} = -0.035441$, and $\Delta\gamma_2 = -0.035441$, and we have $\beta_3 \approx \gamma_2$.

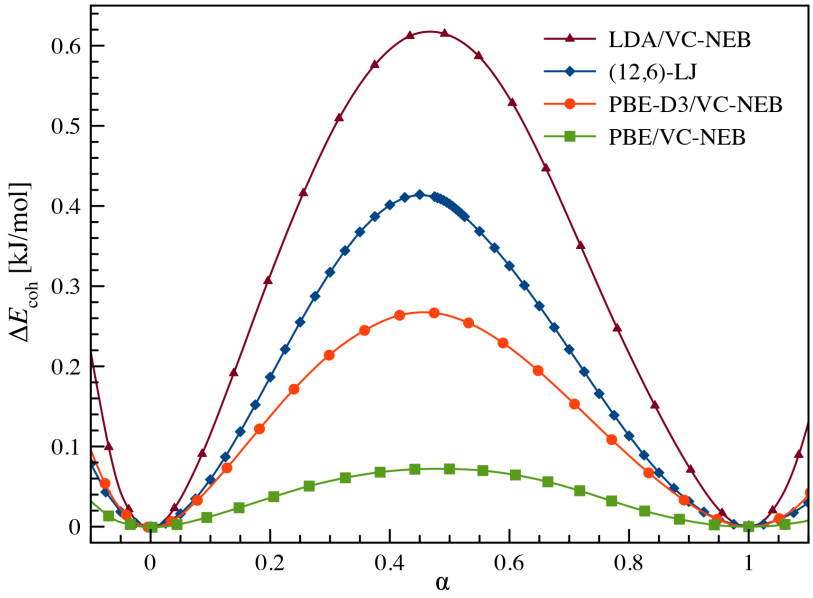

Figure 6.14: Comparison between the (12,6)-LJ (including symmetry breaking effects) and DFT calculations (LDA, PBE and PBE-D3) using the VC-NEB method for the Burgers path from hcp to fcc.

We can also compare with recent molecular dynamics (MD) simulation by Bingxi Li et al[367] using a (12,6)-LJ potential and 18,000 Ar atoms in a box adjusted to a temperature of T=40 K and pressure of P= 1 bar. They calculated a barrier height for the enthalpy of $\Delta H^{\#} = 16.0 \pm 1.0$ cm^{-1} (per atom) which lies in-between our PBE and PBE-D3 result. Even if we adjust for the more accurate dissociation energy of Patkowski and Szalewicz[457] then given in their paper, we get $\Delta H^{\#} = 19.2 \pm 1.1$ cm^{-1}. However, at 40 K the kinetic energy per atom $E_{\text{kin}} = \frac{3}{2} k_{\text{B}} T$ translates into 41.7 cm^{-1} per atom, which should be seen as an upper limit, and our values are smaller. Moreover, zero-point vibrational effects will also lower the activation energy. It is therefore difficult to compare the two very different (static vs. dynamic) methods. Furthermore, their MD simulations show an accumulation of defects, stacking disorders and growth of a less ordered structures towards the transition state. They also suggested three different phase transition paths. It is, however, difficult to provide a simple picture of the phase transition from such MD simulations, even more so if the simulation cell does not reflect the change in the lattice constants and surface effects can become important without proper periodic boundary conditions. On the contrary, the Burgers path provides a good upper bound for the activation energy in the hcp↔fcc transformation, as other hypothetical minimum energy paths lying below our ideal Burgers path on a high-dimensional energy hypersurface require a large super-cell treatment. Interestingly, the volume expansion at the transition state obtained by Bingxi Li et al[367] of about 2.6% and very close to our value of 2.4% with the (12,6)-LJ potential.

6.4 Conclusions

We investigated in detail the Burgers-Bain minimum energy path for the hcp↔fcc↔bcc phase transition for a number of representative (n,m)-LJ potentials using exact lattice summations. For this we expressed the lattice sums for a bi-lattice, connecting hcp with the cuboidal lattices such as fcc and bcc through a single lattice parameter $\alpha \in [0,1]$, in terms of a fast converging Bessel sum expansions yielding computer precision to cohesive energies. Our first chosen simple phase transition model based on the KHS model contained only four parameters describing the change in the base lattice parameters a and $c = a\gamma_2$, the shear force acting on the hexagonal base plane through the parameter α, and the sliding force of the middle layer through one variable parameter β_2. This limited choice of parameters made it possible to gain a first detailed insight into the Burgers-Bain phase transition[431]. However, upon extending this small parameter space, we observed a distinct symmetry breaking effect due to a single lattice parameter β_1, causing a non-smooth phase transition at a bifurcation point at critical value α_c where the Burgers path joins the Bain path. The bifurcation point shifts to larger α_c values for increasingly harder LJ potentials. For our softest (6,4)-LJ potential we observe a metastable minimum belonging to the bcc structure. This demonstrates that one has to be very careful in choosing a suitable definition for a bi-lattice. For the LJ potentials we were able to derive useful analytical formulas for the lattice parameters including the KHS model where the bifurcation point shifts into the fcc minimum. From this, we obtained a more complete picture of the rhombohedral bcc distortion towards either the fcc (Bain path) or hcp structure (Burgers path).

We chose the smallest unit cell combining both fcc and hcp, which restricts the phase transition to the Burgers-Bain path, that is, we detected no additional minimum energy path within our unit cell definition. The true (hypothetical) minimum energy path might well lie energetically below the ideal Burgers-Bain path involving a different mechanism for the sliding of the hexagonal planes[413]. However, this would require a super-cell treatment and a much larger set of variable lattice parameters. For example, we can transform from hcp to fcc through Barlow packing[18,402,429] arrangements, for example by changing the packing sequence for six hexagonal layers (number of hexagonal sheets 2 for the (AB) arrangement and 3 for (ABC) are divisors of 6 for the supercell) in the following way: hcp$(ABABAB)\rightarrow$ $(ABCBAB) \rightarrow (ABCBAC) \rightarrow$fcc$(ABCABC)$. This specific example involves one double shift of hexagonal layers in a Barlow packing of size $N = 6$. This path may well be lower than the Burgers transformation and some hexagonal layers such as BAB remain more or less intact with kissing number 12. The minimum energy path for such a mechanism still needs to be explored; however, we expect an increase in the angle from the original value of 60^o between the two basis vectors $\angle(\vec{b}_1, \vec{b}_2)$ defining the hexagonal plane, as this is the case in the simple Burgers transformation. Moreover, shifting hexagonal layers leads from hcp to fcc through different

Barlow structures, and not directly to bcc. Concerning the Bain path, the equivalence between the Bain and Zener transformation was already shown by Rifkin[371]. Other possible phase transitions[258,260] still need to be explored through exact lattice summations for inverse power potentials with a suitable set of lattice vectors. We are currently developing a more general theory on solid-state phase transitions using exact lattice summations for many-body inverse power potentials such as the LJ potential or the Axilrod-Teller-Muto three-body term[187,188]. Such many-body effects play a crucial role in stabilizing the bcc over the fcc phase[434].

We believe that our results obtained from using LJ potentials as simple model systems will guide future applications using more elaborate quantum theoretical methods such as DFT. For more realistic materials where strong many-body interactions[226] are encountered as for metallic systems,[460–463] the bcc phase might well be the global minimum and directly connected to the hcp phase, as it is for example indicated by calculations using density functional theory employing the nudged elastic band algorithm for mapping out the minimum energy path for bulk lithium, iron or silver nanowires[352,464,465]. We point out that a more advanced MD simulation[466,467] to obtain free energy values at finite temperatures and pressures requires again a super-cell treatment with a large set of independent parameters, which limits the accuracy in calculating the free energy. In such a case exact lattice sum treatments can be developed for LJ potentials. Our simple picture of the lattice transformation offers a useful estimate for the upper limit of the phase transition activation barrier in real systems. Finally, for argon we showed that the Burgers phase transition path is very sensitive to the density functional approximation applied and the inclusion of the dispersion force is important for such weakly interacting systems. A more detailed study for solid argon under pressure including three-body effects and different minimum energy paths is currently underway.

MASSEY UNIVERSITY
TE KUNENGA KI PŪREHUROA
UNIVERSITY OF NEW ZEALAND

GRADUATE RESEARCH SCHOOL

STATEMENT OF CONTRIBUTION
DOCTORATE WITH PUBLICATIONS/MANUSCRIPTS

We, the student and the student's main supervisor, certify that all co-authors have consented to their work being included in the thesis and they have accepted the student's contribution as indicated below in the Statement of Originality.	
Student name:	Andres Eduardo Robles Navarro
Name and title of main supervisor:	Peter Schwerdtfeger
In which chapter is the manuscript/published work?	Chapter 7

Describe the contribution that the student and members of the supervisory team have made to the manuscript/published work:[1]

All the computations were performed by me. The theoretical development of the publication is equally divided between me, Shaun Cooper and Peter Schwerdtfeger. Further discussions also included Odile Smits.

Please select one of the following three options:

- (●) **The manuscript/published work is published or in press**

  Please provide the full reference of the research output:

  The Journal of Physical Chemistry C, 2025, 129(17): 8389-8394

- ( ) **The manuscript is currently under review for publication**

  Please provide the name of the journal:

- ( ) **It is intended that the manuscript will be published, but it has not yet been submitted to a journal**

Student's signature:	ARoblesNavarro	Main supervisor's signature:	PeterSchwerdtfeger Digitally signed by PeterSchwerdtfeger Date: 2025.12.08 14:23:58 +13'00'

This form should be placed at the beginning of each relevant thesis chapter.

[1] Refer to the Massey University Publishing and Authorship guidelines (OneMassey for staff, Stream for students) and/ or Contributor Roles Taxonomy (CRediT) guidelines for guidance.

Chapter 7

Exploring the Mechanism of Phase Transitions Between the Hexagonal Close-Packed and the Cuboidal Structures

7.1 Introduction

Solid-state phase transitions are notoriously difficult to model[47]. While experimental methods can give quite detailed $(P, T, V, \mu, ...)$ phase diagrams, the specific mechanism (dynamics) of a phase transition around the boundary line of different phases often eludes such experiments even for the simplest solids such as the rare gases. On the computational side, phase transition simulations are computationally very demanding and often plagued by the accuracy of the underlying model chosen for describing the intermolecular forces[468,469]. Unlike in simple chemical reactions where the minimum energy path (MEP) from the reactants to the product can be obtained by certain algorithms[470] and sophisticated electronic structure methods such as coupled-cluster theory[471], for the solid state it is often difficult to map out phase transition MEPs[472]. Here one relies mostly on model potentials[110] or on computationally demanding density functional theory and sophisticated algorithms like machine learning to explore the potential energy hypersurface[473–475].

Martensitic transformations are a subclass of phase transitions described by diffusionless displacive transformations caused by lattice deformations where atoms move in a coordinated, homogeneous, and crystallographically oriented manner relative to their neighbors along some MEP[258,349,476]. It controls for example the mechanical properties of many materials such as steel at elevated temperatures[477]. Bain described such a transition from fcc to bcc (the so-called Bain path) as early as in 1924 on purely crystallographic grounds[256], and Burgers later in 1934 in a similar fashion for the hcp to bcc transformation (Burgers path)[262]. While the former only involves changes in the basic lattice parameters a and $\gamma_2 = c/a$ within a cuboidal lattice, the

latter is more complicated and involves a transition from a hexagonal based bi-lattice to some cuboidal (cub) lattices such as bcc[349,415]. It remains, however, an open question whether there is a direct path from hcp to bcc or if the fcc lattice is an intermediate step in the Burgers hcp→bcc transformation[263,269,478,479]. For a recent discussion on lattice instabilities see Grimvall et al[349].

In order to map out the MEP between hcp and the cuboidal lattices, we developed a simple and intuitive lattice model which we apply to three different models: the hard-sphere model[209], the (12,6)-Lennard-Jones potential[222], and to metallic lithium using density functional theory (DFT)[480]. Our treatment involves a much larger parameter space than previously applied[264,427,454] and will therefore give a detailed insight into the combined Burgers-Bain type of phase transition.

7.2 Methods

The generator matrix $B = \{\vec{b}_1, \vec{b}_2, \vec{b}_3\}$ containing the lattice vectors $\vec{b}_i$ and the shift vector $\vec{v}_s$ is defined as follows

$$B = a \begin{pmatrix} 1 & 0 & 0 \\ \frac{1}{2}\gamma_1(1-\alpha) & \frac{1}{2}\gamma_1\sqrt{(1+\alpha)(3-\alpha)} & 0 \\ 0 & 0 & \gamma_2 \end{pmatrix} \tag{7.1}$$

$$\vec{v}_s^{\top} = \frac{a}{2}(\beta_1, \beta_2, \beta_3)$$

The B-matrix has been obtained from the conditions that (a) we have a linear transformation between the hexagonal and the cuboidal (cub) B-matrices defining the unit cell and characterized by the transformation parameter α, (b) we have a bi-lattice introducing a middle layer with the atom in the unit cell situated at the Wyckoff position $\vec{v}_s$ as defined in eq.(7.1) and shown in Figure 7.1, (c) any distortion from the base lattice parameter $|\vec{b}_1| = |\vec{b}_2| = a$ is described by the lattice parameter γ_1 ($|\vec{b}_2| = \gamma_1 a$), and (d) we define $\gamma_2 = c/a$ as the ratio between the two lattice parameters in a Bravais lattice. We keep the angles between the vectors $\angle(\vec{b}_3, \vec{b}_1)$ and $\angle(\vec{b}_3, \vec{b}_2)$ at 90° reducing the problem from a complete 9 to a subset of 7 parameters for the set of lattices constants $\{p_i\}$, i.e. $\{p_i\} = \{\alpha, a, \gamma_1, \gamma_2, \beta_1, \beta_2, \beta_3\}$.

The transformation from bcc/fcc to hcp is visualized in Figure 7.1. The parameters for the three lattices are summarized in Table 7.1. From the table it is clear that the lattice parameter α is responsible for the hcp→cub (cub = fcc or bcc) transformation through the angle θ_{12} between the vectors $\vec{b}_1$ and $\vec{b}_2$, i.e. $\cos\theta_{12} = \frac{1}{2}(1-\alpha)$, and the parameter γ_2 for the fcc→bcc transformation.[461] This implies that we can describe the phase transition as a hypersurface of the cohesive energy, $E_{\text{coh}}(\alpha, \gamma_2)$ with the remaining lattice parameters being optimized.

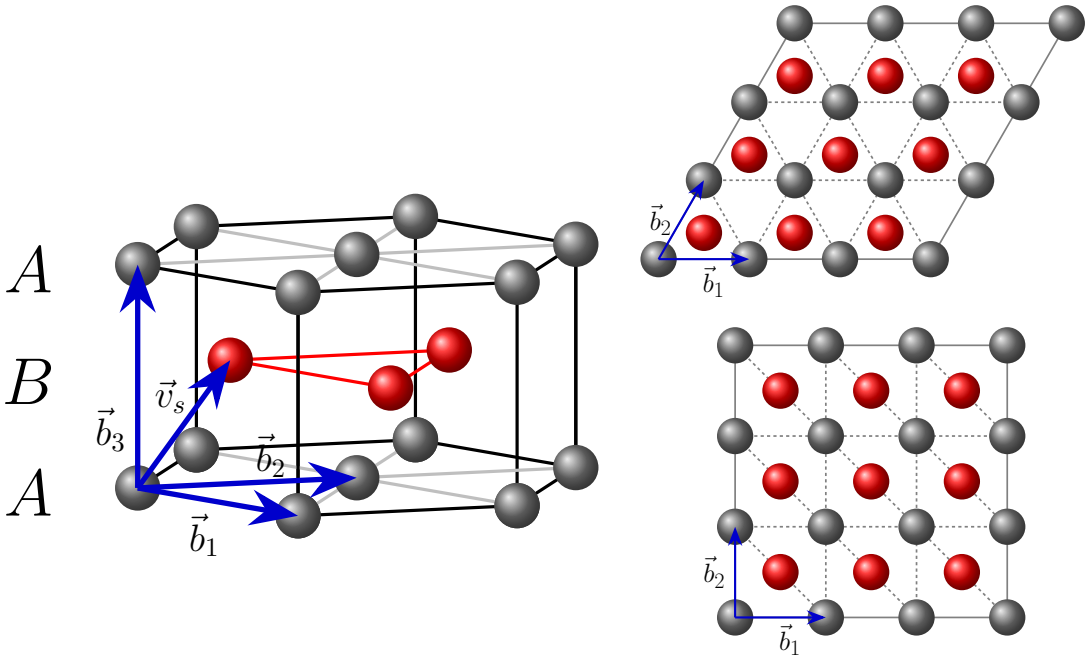

Figure 7.1: Left: The (distorted) cuboidal (blue lines shown on the left) and the hcp structure both with a ABABAB... sequence (layers A in red and B in blue) in a hexagonal unit cell with corresponding basis vectors. Right: The transformation between the cuboidal lattices fcc or bcc (top) and the hexagonal closed packed bi-lattice (bottom). The red atoms indicate the middle layer in the unit cell.

Table 7.1: Lattice parameters for kissing hard spheres of diameter 1 for the three lattices hcp, fcc and bcc. The volumes V, corresponding packing densities and kissing numbers N_{kiss} are also given.

Parameter	hcp	fcc	bcc
α	0	1	1
a	1	1	$\frac{2}{\sqrt{3}}$
γ_1	1	1	1
γ_2	$\sqrt{\frac{8}{3}}$	$\sqrt{2}$	1
β_1	1	1	1
β_2	$\frac{1}{\sqrt{3}}$	1	1
β_3	$\sqrt{\frac{8}{3}}$	$\sqrt{2}$	1
$\angle(\vec{b}_1, \vec{b}_2)$	60°	90°	90°
V	$\sqrt{2}$	$\sqrt{2}$	$\frac{8}{3\sqrt{3}}$
ρ	$\frac{\pi}{3\sqrt{2}}$	$\frac{\pi}{3\sqrt{2}}$	$\frac{\pi\sqrt{3}}{8}$
N_{kiss}	12	12	8

The volume of the unit cell can be easily derived from the B-matrix (7.1)

$$V = \det(B) = \frac{a^3\gamma_1\gamma_2}{2}\sqrt{(1+\alpha)(3-\alpha)} \tag{7.2}$$

Since $V > 0$ we have the condition that $\alpha \in (-1, 3)$.

For the Sutherland potential[216], i.e. the kissing hard-sphere (KHS) model with an attractive inverse power potential, we set the interaction potential between the lattice points as $\phi(r) = \infty$ for $r < 1$ and $\phi(r) = -r^{-n}$ for $r \geq 1$ (in reduced units). This model maximizes the number of nearest neighbors with distance 1, i.e. the kissing (or coordination) number N_{kiss}. For the cohesive energy we obtain $E_{\text{coh}} = -\frac{1}{2}L_{\frac{n}{2}}(p_i)$, where $L_{\frac{n}{2}}(p_i)$ are 3D infinite lattice sums dependent on the exponent n and the lattice parameters p_i as defined in the generator matrix B. These are slowly converging sums which we treat efficiently to computer accuracy in terms of fast converging Bessel function expressions.[295] A more detailed analysis of lattice sums for the Burgers-Bain transformation will be published elsewhere.

For a general (n, m)-LJ potential ($n > m$) in reduced units and we have[222]

$$\phi_{\text{LJ}}(r) = \frac{nm}{n-m}\left[\frac{1}{nr^n} - \frac{1}{mr^m}\right] \tag{7.3}$$

In this case we obtain the cohesive energy as a function of the lattice constant a ($m > 3$ to avoid a divergent series)[226]

$$E_{\text{coh}}(p_i) = \frac{nm}{2(n-m)}\left[\frac{L_{\frac{n}{2}}(p_i)}{na^n} - \frac{L_{\frac{m}{2}}(p_i)}{ma^m}\right] \tag{7.4}$$

in terms of the lattice sums $L_{\frac{n}{2}}(p_i)$. As both lattice parameters connect the three phases hcp, fcc and bcc in a natural way, we map out the $E_{\text{coh}}(\alpha, \gamma_2)$ hypersurface to obtain a detailed insight into the phase transitions. To save computational time we restrict three of the lattice parameters to their ideal values as shown in Table 7.1, i.e. $\gamma_1 = 1$, $\beta_3 = \gamma_2$ and $\beta_1 = 1$. Test calculations with a few random points in the parameter space revealed that the former two restrictions can be imposed and the latter is justified as it does not change the overall topology of the hypersurface. All other lattice parameters were optimized by using a Newton-Raphson procedure.[481]

For the DFT calculations for metallic lithium the crystal structure optimization have been carried out employing a Newton-Raphson procedure with the gradient and Hessian matrix calculated numerically through finite differences and ensuring an energy threshold for convergence of 10^{-6} eV in the electronic energy. The DFT single-point calculations were performed using the Perdew-Burke-Ernzerhof (PBE) exchange-correlation functional[280] coupled to the dispersion corrections by means of the DFT-D3 approach including the

Becke-Johnson damping function[291,292], as implemented in the VASP 6.4.0 version[338–341,343]. The atomic cores are described by the Projector Augmented Wave (PAW) method[342], and the electronic minimization was done using the tetrahedron method[344] with Blöchl correction with an energy width of 0.1 eV. The k-point grid was set using the keyword KSPACING=0.07 centered at the Γ point and an energy cut-off of 500 eV. The cohesive energies are obtained by comparing the energy of the bulk and the isolated atom, the latter calculated from a large orthorhombic unit cell of $14 \times 14.001 \times 14.002$ Å. Scanning the hypersurface and optimizing the lattice parameters is computationally very demanding.

7.3 Results and Discussion

The kissing hard-sphere model

In the limit $n \to \infty$ we obtain $E_{\text{coh}} = -N_{\text{kiss}}/2$. The minimum energy conditions yields $a = 1, \gamma_1 = 1$ and $\beta_1 = 1$ for the hcp→cub transition, leading to the analytic expressions for the lattice parameters and the volume V derived from simple geometric arguments,

$$\gamma_2(\alpha) = \sqrt{\frac{8 + 4\alpha(1-\alpha)}{4 - (1-\alpha)^2}} \tag{7.5}$$

$$\beta_2(\alpha) = \sqrt{\frac{4 - (1-\alpha)(\alpha+3)}{4 - (1-\alpha)^2}} \tag{7.6}$$

$$V(\alpha) = \sqrt{2 + \alpha(1-\alpha)} \tag{7.7}$$

$\gamma_2(\alpha)$ is a monotonically decreasing function in the interval $\alpha \in [0,1]$ changing from $\gamma_2(0) = \sqrt{\frac{8}{3}}$ to $\gamma_2(1) = \sqrt{2}$. Consequently, the KHS model directly connects the hcp with the fcc phase. The volume is at maximum at $\alpha = \frac{1}{2}$ with $V = \frac{3}{2}$, which we interpret as the transition state. Along the hcp→fcc transition path, the kissing number reduces to $N_{\text{kiss}} = 10$ for the interval $\alpha \in (0,1)$.

Proceeding to the bcc phase, the parameter γ_2 becomes our reaction coordinate for the fcc→bcc Bain path. Here the 8 atoms at the edges of the cuboidal cell move slightly outwards as the unit cell gets compressed along the c-axis and we have $a > r_{\text{bc}} = 1$, where r_{bc} is the distance from the sphere at the origin of the unit cell to the one in the middle layer. The kissing number changes from 12 (fcc) to 8 along the path to bcc. We can easily derive that

$$a(\gamma_2) = \frac{2}{\sqrt{2+\gamma_2^2}} \quad \text{and} \quad V(\gamma_2) = \frac{8\gamma_2}{(2+\gamma_2^2)^{\frac{3}{2}}} \tag{7.8}$$

In this case the volume is monotonically increasing from fcc to bcc.

The Sutherland potential

By adding an r^{-6} attractive potential to the KHS model, we locate the transition state at $\alpha^{\#} = 0.5000623690$ with an activation energy (with respect to the hcp structure) of $\Delta E^{\#}_{\mathrm{coh}} = 0.7061966753$. The small deviation from the ideal $\alpha = \frac{1}{2}$ value comes from the fact that the hcp structure is slightly more stable compared to fcc by an energy difference of $\Delta E_{\mathrm{coh}} = -4.881170486 \times 10^{-4}$. For this attractive potential, the bcc structure becomes a maximum at $\gamma_2 = 1.0$, with a difference to the fcc structure of $\Delta E_{\mathrm{coh}} = 1.100126588$, which lies energetically even above the transition state for the hcp→fcc path. In this model, the bcc phase is thus not stable against distortion to the fcc structure[103].

The Lennard-Jones potential

The $\Delta E_{\mathrm{coh}}(\alpha, \gamma_2) = E_{\mathrm{coh}}(0, \sqrt{\frac{8}{3}}) - E_{\mathrm{coh}}(\alpha, \gamma_2)$ hypersurface for the (12-6)-LJ potential is shown in Figure 7.2. It is clear that there is no direct MEP from hcp to bcc; the MEP starting at hcp leads directly to the fcc structure as predicted from the simple KHS model. Moreover, preliminary calculations reveal that neither of the more general (n, m)-LJ potentials have a direct MEP from hcp to bcc. Starting from bcc towards the hcp structure, by changing the parameter α and optimizing all others, ends in steep ascend energetically. As discussed before[103], the bcc structure at $\alpha = 1$ and $\gamma_2 = 1$ is a maximum for the (12,6)-LJ potential. In fact, for the general (n, m)-LJ potential the bcc structure is always an extremum along the fcc→bcc transition[103,377,482]. Concerning the transition state for the hcp→fcc path, we locate it at $\alpha^{\#} = 0.50036605$ with an activation energy of $\Delta E^{\#}_{\mathrm{coh}} = 0.41488952$ relative to the hcp structure. The volume at the transition state is 1.32709616 and below the KHS limit as we expect for soft penetrating spheres.

Lithium

For a real quantum system, we considered metallic lithium analyzed at the density functional theory (DFT) level. A detailed account of the lithium phase diagram has been given by Guillaume et al.[483] and Ackland et al.[79] Each point on the (α, γ_2)-energy hypersurface, as shown in Figure 7.2, corresponds to an optimization of a and β_2 at fixed values of α and γ_2, together with $\gamma_1 = 1$, $\beta_1 = 1$ and $\beta_3 = \gamma_2$.

Figure 7.2 shows that the topology of the lithium cohesive energy surface is quite similar to the one obtained for the $(12, 6)$-LJ potential, with the deepest minima located at the hcp and the fcc structures, fcc being the ground state, see Table 7.2. This is in agreement with a

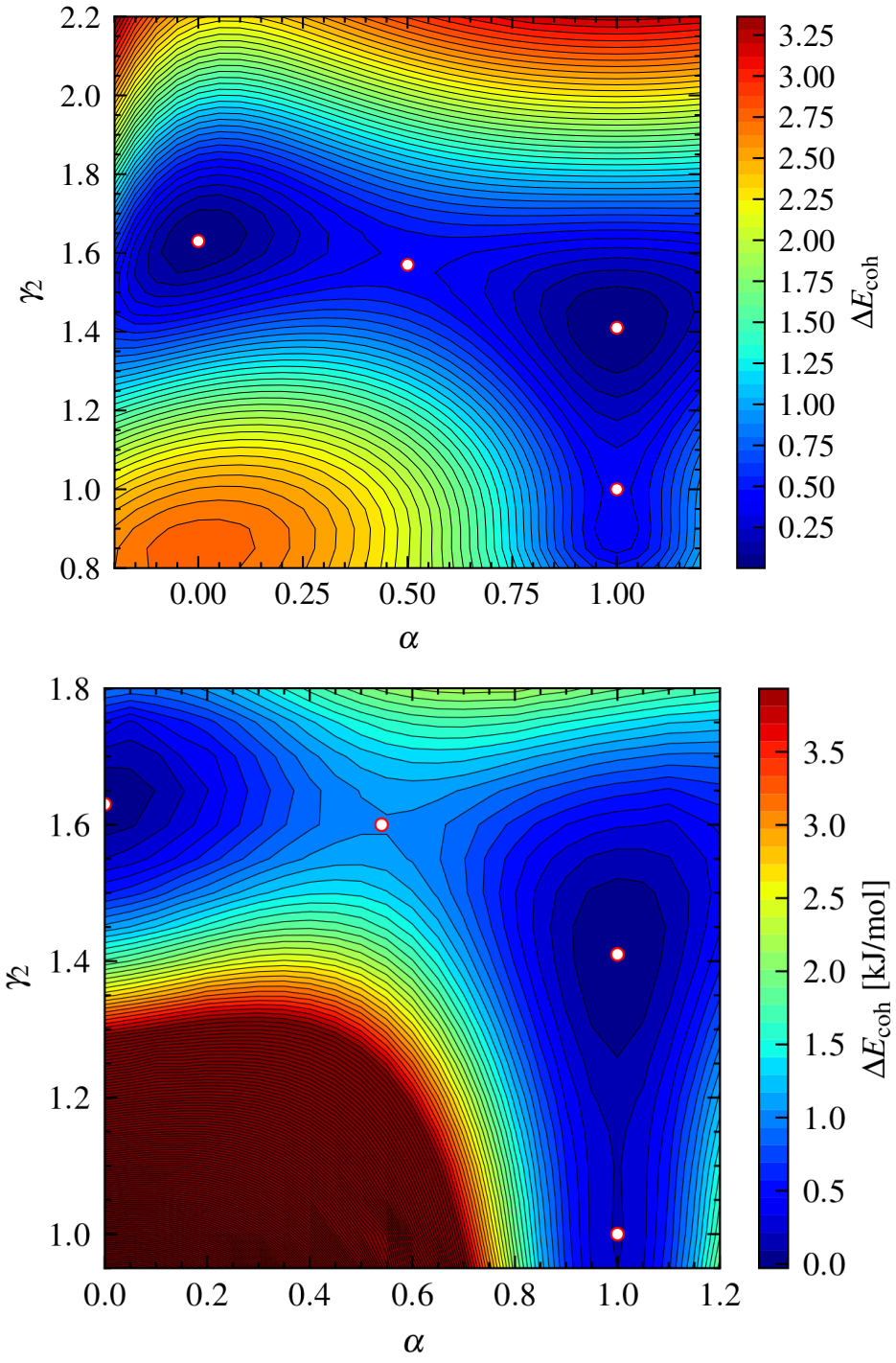

Figure 7.2: Cohesive energy hypersurface, $\Delta E_{\mathrm{coh}}(\alpha, \gamma_2)$, with all other lattice parameters optimized for (top) the $(12,6)$-LJ potential (in reduced units), and (bottom) the lithium metal (in kJ/mol) calculated using the PBE-D3 functional. The white circles represent the position of the hcp ($\alpha = 0, \gamma_2 = \sqrt{8/3}$), hcp→fcc transition state ($\alpha \approx 0.54$), fcc ($\alpha = 1, \gamma_2 = \sqrt{2}$) and bcc ($\alpha = 1, \gamma_2 = 1$) structures.

detailed phase diagram study of Ackland et al.[79] At standard conditions, the lithium metal is found in the bcc structure with a measured cohesive energy of 158 kJ/mol[129]. The difference

Prop.	hcp	fcc	bcc	TS_1	TS_2
E_{coh}	172.2216	172.2515	172.0344	171.1907	172.0212
α	0.000	1.000	1.000	0.541	1.000
a	2.962	2.963	3.325	2.9079	3.230
γ_2	1.632	1.411	1.000	1.599	1.095
β_2	0.577	1.000	1.000	0.820	1.000
V	36.731	36.708	36.757	38.268	36.900

Table 7.2: Lattice parameters and volume V for the hcp, fcc and bcc structures of lithium together with the transition states along the Burgers-Bain transformation path. The transition state of the hcp↔fcc transformation is denoted as TS_1, whereas for the fcc↔bcc is denoted by TS_2.

from the experimental cohesive energy comes from temperature effects, zero-point vibrational contributions (3.971 kJ/mol for the fcc structure using the PBE functional[433]) and the density functional approximation applied. We expect that this error is mostly compensated when taking energy differences along the transformation path[433]. The bcc structure of lithium is shown to be a very shallow minimum, in agreement with previous work[127,433]. The path connecting hcp to the cuboidal structures leads directly to the fcc structure and has a transition state at $\alpha^{\#} = 0.541$ with an energy difference from hcp of $\Delta E^{\#}_{coh} = 1.031$ kJ/mol. The transformation from fcc to bcc occurs through a second transition state at $\gamma_2 = 1.095$ with an energy difference of $\Delta E^{\#}_{coh} = 0.230$ kJ/mol from the fcc phase. Noticeably, the hcp→fcc transition state lies energetically above the fcc→bcc Bain path. The maximum volume increase for the hcp→fcc transition is 4.18% compared to the hcp structure (see Table 7.2), and is less compared to the hard-sphere limit of 6.07% $(3/2\sqrt{2})$ as we expect.

7.4 Conclusions

In summary, for the unit cell, lattice parameters and four different interaction models applied we do not observe a direct minimum energy path from hcp to bcc as originally suggested by Burgers[262] and others[264,427]. The transition states on the (α, γ_2)-hypersurface MEP for lithium comes at rather low energies of about 1 kJ/mol. Classical molecular dynamics simulations at higher temperatures will explore the whole region of the parameter space outside the MEP[367], and from such simulations it is therefore often difficult to get a detailed picture of the phase transition compared to directly mapping out the MEP as presented here. For solid-state systems such as barium,[461] or iron[462], where the bcc phase is significantly stabilized over the fcc or the hcp phase, the topology of the hypersurface might well change[349,484,485]. Furthermore, finite temperature and pressure effects will change the topology of the free energy hypersurface. For example, the bcc phase is well known to be stabilized near the melting point (Landau theory). These effects will be the subject of our future

investigations.

MASSEY UNIVERSITY
TE KUNENGA KI PŪREHUROA
UNIVERSITY OF NEW ZEALAND

GRADUATE RESEARCH SCHOOL

STATEMENT OF CONTRIBUTION
DOCTORATE WITH PUBLICATIONS/MANUSCRIPTS

We, the student and the student's main supervisor, certify that all co-authors have consented to their work being included in the thesis and they have accepted the student's contribution as indicated below in the Statement of Originality.			
Student name:	Andres Robles Navarro		
Name and title of main supervisor:	Peter Schwerdtfeger		
In which chapter is the manuscript/published work?	Chapter 8		
Describe the contribution that the student and members of the supervisory team have made to the manuscript/published work:[1] All computations were performed by me. The theoretical development and discussions involved me and Peter Schwerdtfeger on equal grounds.			
Please select one of the following three options:			
◉	**The manuscript/published work is published or in press** Please provide the full reference of the research output: Physical Chemistry Chemical Physics, 2026, Advance Article, DOI: 10.1039/D5CP04548G		
○	**The manuscript is currently under review for publication** Please provide the name of the journal:		
○	**It is intended that the manuscript will be published, but it has not yet been submitted to a journal**		
Student's signature:	ARoblesNavarro	Main supervisor's signature:	PeterSchwerdtfeger Digitally signed by PeterSchwerdtfeger Date: 2025.12.08 14:21:46 +13'00'
This form should be placed at the beginning of each relevant thesis chapter.			

[1] Refer to the Massey University Publishing and Authorship guidelines (OneMassey for staff, Stream for students) and/ or Contributor Roles Taxonomy (CRediT) guidelines for guidance.

Chapter 8

Accurate Relativistic Density Functional Calculations for the Solid-State of Metallic Francium

8.1 Introduction

Francium is a naturally occurring but highly radioactive alkali metal.[486] The most stable isotope is $^{223}_{87}$Fr, a dominant β-emitter (with a minuscule 0.02% α branching ratio) and a half-life of 21.8 m.[487] Unlike the lighter element radon,[229,488] where the most stable isotope, $^{222}_{86}$Rn, has a half-life of 3.8235 d, spectroscopic and chemical investigations into francium are very scarce[489–491] and bulk properties of this element have never been observed. Instead, one has to rely on predictions from periodic trends[492–495] or accurate computational simulations.[496–498] For a historical overview on francium and its chemistry see Adloff and Kauffman[490] or Orna[499]. Here we mention that francium has received recent attention for the study of parity-violation in electronic transitions and the search for a permanent electric dipole moment in order to test the standard model of physics.[500–503]

Only very few theoretical investigations into bulk properties of francium are available.[433,504] It is however well known that the Group 1 elements up to cesium adopt the less dense packed body-centered cubic (bcc) structure at normal conditions[505] with a phase transition into a closed-packed structure with possible stacking faults of the hexagonal sheets at low temperatures,[74,506,507] albeit there is some recent controversy on the low temperature structure of lithium.[79,431,433] For the alkaline metals up to cesium, computational studies, with few exceptions,[508,509] all involve density functional theory[510–512] with only a few correcting for long-range dispersive type of interactions or zero-point vibrational effects.[127,433] Upadhyaya et al. showed already in 1980 by using simple models that Van der Waals dispersive type of interactions cannot be neglected anymore for the cohesive energy

differences between the different phases of the heavier alkali metals, because of the increase in the Group 1 dipole polarizability with nuclear charge[498], and that these interactions slightly favor the bcc arrangement compared to the close packed structures.[513] This may seem perhaps counter-intuitive because of the very different coordination numbers, but changes in the nearest neighbor distances play a crucial role as well. Moreover, the transition path from bcc to the more densely packed face-centered cubic (fcc) arrangement is predicted to be rather shallow for the Group 1 metals,[127,433] and the stability of various phases depends critically on the pressure and temperature applied. In addition, for francium one should include spin-orbit effects as the higher lying 7p levels are spin-orbit split by 0.209 eV[514] and the core 6p levels by 5.26 eV[515]. This may influence the relative stability of the different phases considered here. It is now clear that predicting correctly the small energy differences between the different low-temperature and pressure phases for francium constitutes a major challenge to current computational solid-state theory. In this respect, the accuracy of the density functional approximation for the solid state has been discussed intensively in the literature.[33,327,516]

In this work we try to identify the most stable low-temperature bulk phase of francium by using relativistic density functional theory including spin-orbit effects and dispersive type of interactions through the Grimme energy correction,[291,292,517] as well as accounting for zero-point vibrational energies.[127,433] The bulk phases studied are the ones generally considered for the bulk Group 1 metals, i.e. bcc, fcc and hcp (hexagonal close packing).

8.2 Computational Details

To accurately obtain the small energy differences expected for the three low-energy phases, hcp, bcc and fcc, we need to treat the hexagonal and cubical unit cells on an equal basis to consistently sample the k-space in our electronic structure calculations. For this we use the basis vectors as defined in Ref.[222] describing the different phases through a common underlying bi-lattice, which will briefly be described here.

The connection between the cubical lattices including both bcc and fcc along a so-called Bain path of deformation[127,433,434] can be further generalized to include the hexagonal close-packed structure[222]. This can be achieved by introducing a bi-lattice with corresponding lattice vectors and parameters which smoothly connect the hexagonal with the cuboidal lattices, resulting in two atoms for the unit cell. This implies that in addition to the (a, c) (variable) lattice parameters as shown in Fig. 8.1 we have an angle between the two base vectors of the hexagonal prism, plus the position of the second atom inside the unit cell. For the entire transformation between the different phases we thus have an underlying monoclinic unit cell with two atoms.

Our lattice-parameter space for the bi-lattice is defined by $(\alpha, a, \gamma, \beta)$, where α indicates the type of structure (cuboidal for $\alpha = 1$, hexagonal for $\alpha = 0$, or monoclinic for other α values)

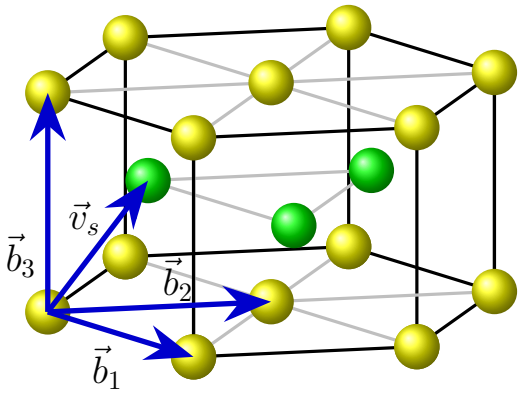

Figure 8.1: Monoclinic unit cell (shown as the hexagonal cell here) with a two-atom basis. Here we set $|\vec{b}_1| = |\vec{b}_2| = a$ and $|\vec{b}_3| = c$. See Ref. 431 for details.

used previously for describing the Burger deformation path, which correlates directly with the angle between the vectors at the base of the unit cell, both with magnitude a (see Fig. 8.1), $\gamma = c/a$ as the height of the unit cell with respect to a, and β as the second component of the position vector of the atom in the center of the unit cell, that is, $\vec{r}_2 = \frac{a}{2}(1, \beta, \gamma)$. Using these parameters, the monoclinic skeleton for the different lattices is defined by

$$\begin{aligned} &\vec{b}_1 = a(1,0,0)^\top, \quad \vec{b}_2 = a\left(\frac{1-\alpha}{2}, \frac{\sqrt{(1+\alpha)(3-\alpha)}}{2}, 0\right)^\top, \\ &\vec{b}_3 = a(0,0,\gamma)^\top \end{aligned} \tag{8.1}$$

and the positions of the atoms within the unit cell are

$$\vec{r}_1 = (0,0,0)^\top \qquad \text{and} \qquad \vec{r}_2 = \tfrac{a}{2}(1,\beta,\gamma)^\top \tag{8.2}$$

The volume of the unit cell can be used to restrict the range of values for α and it is written as

$$V = \frac{a^3\gamma}{2}\sqrt{(1+\alpha)(3-\alpha)} \tag{8.3}$$

The definition of a common unit cell for hcp, fcc and bcc results in volumes and densities that are very similar. Since $V > 0$, a physically meaningful α parameter lies in the interval $(-1, 3)$. For $\alpha = 0$, the structure is of hexagonal type with $\angle(\vec{b}_1, \vec{b}_2) = 60°$, whereas for $\alpha = 1$ the same angle becomes $90°$ with a unit cell being a rectangular prism. Hence, the ideal hcp structure is obtained when $(\alpha, \gamma, \beta)_{\text{hcp}} = \left(0, \sqrt{\frac{8}{3}}, \sqrt{\frac{1}{3}}\right)$. On the other hand, for the ideal fcc structure we have $(\alpha, \gamma, \beta)_{\text{fcc}} = (1, \sqrt{2}, 1)$ and the ideal bcc lattice is reached at $(\alpha, \gamma, \beta)_{\text{bcc}} = (1, 1, 1)$. It is worth pointing out that the Bain transformation path defined in previous works[127,433] by a

single parameter A is a special case of the transformation above for fixed $\alpha = 1$ and $\beta = 1$ and by setting $\gamma = \sqrt{2A}$.

Our definition of the bi-lattice is applied to the Group 1 elemental metals Li, Na, and Fr in order to determine their solid-state properties and possible ground state structures. For a fixed value of α, an optimization of the three lattice parameters (a, γ, β) using an hybrid method of Bayesian optimization[303,518] (BO) and the Broyden-Fletcher-Goldfarb-Shanno[302] (BFGS) algorithm is performed using density functional theory (DFT) at different levels of approximations, i.e. the local spin-density approximation (LSDA, with Slater exchange[519] and Volko-Wilk-Nusair correlation functional[520]) and the generalized gradient approximation (GGA, with the Perdew-Burke-Ernzerhof (PBE) exchange-correlation[280], along with PBEsol[521]). In addition, dispersion corrections were incorporated to the PBE functional through the DFT-D3 approach including the Becke-Johnson damping function[291,292]. Spin-orbit (SO) interactions are also considered when using the PBEsol functional. All electronic structure calculations were carried out with the VASP 6.4.0 version[338–341] with the atomic cores as described by Blöchl's Projector Augmented Wave (PAW) method[342,343] with the recommended scalar relativistic pseudopotentials. As the focus was on the total energy of the system, the electronic minimization was done using the tetrahedron smearing method[344] with Blöchl corrections with an energy width of 0.1 eV. Convergence tests regarding k-spacing and energy cut-off were performed guaranteeing a variation of less than 1 meV in the total energy with respect to more demanding accuracy settings. The energy cut-off was set to 500 eV for Li, Na, and Fr with a k-point grid set by using KSPACING=0.07 and centered at the Γ point. The calculation of the cohesive energy requires the energy of the isolated atom, which was obtained by building a lattice of one atom in a large and slightly orthorhombic unit cell of size $14 \times 14.001 \times 14.002$ Å.

The Bayesian optimization was performed through a custom algorithm where we used a Gaussian Process surrogate with a kernel of the form

$$k(x, x') = \sigma_f^2 k_{\text{Matern}}(x, x'; \nu) + \sigma_n^2 \delta(x, x') \tag{8.4}$$

where $k_{\text{Matern}}(x, x'; \nu)$ is the Matérn kernel[522] with a smoothness parameter $\nu = 5/2$, σ_f^2 is the prior signal variance (learned during training), and a fixed noise variance $\sigma_n^2 = 10^{-5}$ via the WhiteKernel class from the Python package scikit-learn[523]. The acquisition function employed was Expected Improvement[524–526] with a jitter value of 0.01 and its optimization was done using the limited-memory BFGS (L-BFGS) method with 10 random restarts. The search started with 10 initial random samples and 40 Bayesian steps, then a BFGS optimization of the electronic energy was performed starting with the best point after BO convergence.

The zero-point energy (ZPE) of both sodium and francium is obtained in an approximate way using Badger's rule[332] together with density functional perturbation theory (DFPT)

phonon calculations for the lithium metal as implemented in VASP 6.4.0 with the aid of Phonopy 2.14.0[345]. For this we used a $6 \times 6 \times 6$ supercell with a Γ-centered $3 \times 3 \times 3$ k-point grid. This approximation uses a reference element (RE), whose phonon calculations are less computationally demanding and with a similar phonon density of states to that of the heavier atom (X). Then, the ratio between the zero-point energies for a specific phase becomes

$$\frac{E_0^{\mathrm{X}}}{E_0^{\mathrm{RE}}} \approx \sqrt{\frac{R_{\mathrm{RE}}^3 M_{\mathrm{RE}}}{R_{\mathrm{X}}^3 M_{\mathrm{X}}}} \tag{8.5}$$

where R is the nearest neighbor distance of the solid. This simple model has proven to be in good agreement with the vibrational ZPE obtained from the Debye temperature for the alkali and coinage metals[433]. However, care must be taken in choosing the right reference element with a similar phonon dispersion, such as lithium for the Group 1 elements.

To calculate the bulk modulus at the minimum energy structure, we first fix the value of $\gamma = \gamma(a)$ to the optimized value (shown in Table 8.1 for each metal) and then proceed to vary the value of a around the minimum. The energy variation with respect to the volume, V, is then fitted into the fourth-order Birch-Murnaghan equation of state (BM-EOS),[527,528]

$$\begin{aligned} E(\eta) = E_0 + \frac{9B_0V_0}{16}\Big[&2(\eta-1)^2 + \left(B_0'-4\right)(\eta-1)^3 \\ &+\frac{3}{8}\left(B_0B_0'' + \left(B_0'-4\right)\left(B_0'-3\right) + \frac{35}{9}\right)(\eta-1)^4\Big] \end{aligned} \tag{8.6}$$

where $\eta = (V_0/V)^{2/3}$, E_0, and V_0 are the total energy and equilibrium volume, respectively, B_0 is the bulk modulus at zero pressure and B_0' and B_0'' its first and second pressure derivative, respectively. We notice that a fit to a third-order BM-EOS[529] is not sufficient in some cases leading to larger deviations from the fourth-order result. We also include the bulk moduli obtained from a fourth-order polynomial fit in $B(V)$ leading to results close to our BM-EOS values.

The Debye temperature used in this work is obtained from the equation[530]

$$\Theta_D = 131.6\sqrt{\frac{r_s B_0}{M}} \tag{8.7}$$

where r_s is the Wigner-Seitz radius in a.u., B_0 the bulk modulus in GPa, and M is the atomic mass in amu. This property can be then used to calculate the vibrational ZPE through

$$E_0 = \frac{9}{8}k_B\Theta_D \tag{8.8}$$

8.3 Results and Discussions

Table 8.1 shows the lattice parameters for lithium, sodium and francium where the values of γ are presented as the deviation from the ideal values for each lattice, that is, $\Delta\gamma^X = \gamma^X_{\text{opt}} - \gamma^X_{\text{ideal}}$, with $X = \{\text{bcc}, \text{fcc}, \text{hcp}\}$. As the largest deviation found for β is $\Delta\beta^X = \beta^X_{\text{opt}} - \beta^X_{\text{ideal}} = -0.0049$ due numerical noise, the difference with respect to the ideal values is omitted for this lattice parameter in our discussion.

Table 8.1: Properties of optimized structures for Li, Na, and Fr. Lattice parameter a for the common bi-lattice is given in Å, and cohesive and zero-point energies are in kJ/mol. The deviation in γ is with respect to the ideal hard-sphere value with $\gamma^{\text{bcc}}_{\text{ideal}} = 1$, $\gamma^{\text{fcc}}_{\text{ideal}} = \sqrt{2}$, $\gamma^{\text{hcp}}_{\text{ideal}} = \sqrt{8/3}$.

	Metal	a^{hcp}	a^{fcc}	a^{bcc}	$\Delta\gamma^{\text{hcp}}$	$\Delta\gamma^{\text{fcc}}$	$\Delta\gamma^{\text{bcc}}$	$E^{\text{hcp}}_{\text{coh}}$	$E^{\text{fcc}}_{\text{coh}}$	$E^{\text{bcc}}_{\text{coh}}$	E^{hcp}_0	E^{fcc}_0	E^{bcc}_0
	LDA	2.9943	2.9873	3.3653	0.0027	0.0026	0.0000	173.7099	173.7508	173.5187	—	—	—
	PBE	3.0632	3.0621	3.4443	−0.0012	−0.0005	−0.0020	155.1413	155.1418	154.9859	3.658	3.971	3.842
Li	PBE-D3	2.9549	2.9599	3.3197	0.0024	−0.0002	0.0012	172.2305	172.2587	172.0417	—	—	—
	PBEsol	3.0627	3.0615	3.4433	−0.0012	−0.0003	−0.0018	162.0904	162.0913	161.9339	—	—	—
	PBEsol+SO	3.0618	3.0619	3.4355	−0.0031	−0.0003	0.0034	162.0775	162.0786	161.9217	—	—	—
	LDA	3.6118	3.6112	4.0886	0.0014	0.0013	−0.0151	123.2987	123.3046	123.2073	—	—	—
	PBE	3.7419	3.7436	4.1966	0.0006	−0.0023	0.0004	109.1666	109.1563	109.0883	[1.488]	[1.617]	[1.565]
Na	PBE-D3	3.6368	3.6364	4.0891	0.0017	0.0010	−0.0027	124.5986	124.6103	124.6097	—	—	—
	PBEsol	3.7186	3.7201	4.1713	0.0007	0.0000	0.0001	111.2742	111.2743	111.2035	—	—	—
	PBEsol+SO	3.7187	3.7185	4.1709	0.0007	−0.0014	0.0002	111.2772	111.2770	111.2065	—	—	—
	LDA	5.0920	5.1199	5.7048	−0.0009	−0.0006	0.0009	78.5290	78.3809	78.2760	—	—	—
	PBE	5.4485	5.4855	6.1478	0.0150	0.0014	0.0003	61.0826	61.0616	60.8333	[0.268]	[0.292]	[0.283]
Fr	PBE-D3	5.3706	5.3660	6.0073	−0.0043	0.0007	−0.0001	70.6475	70.6072	70.4832	—	—	—
	PBEsol	5.3178	5.3124	5.9629	−0.0052	0.0027	0.0035	70.4832	68.9475	68.7412	—	—	—
	PBEsol+SO	5.2804	5.2707	5.9923	−0.0056	0.0005	−0.0227	70.0579	70.0329	69.8153	—	—	—

The quality of our DFT approximation applied can be evaluated from the available experimental data for both lithium and sodium. For bcc lithium we have an experimental nearest neighbor distance of $R_{\text{NN}} = 3.023$ Å,[74] a cohesive energy of $E_{\text{coh}} = 158$ kJ/mol,[129] and a bulk modulus of $B = 12.95$ GPa (for 7-Li) from Felice et al.[531] or 12.65 GPa from Anderson and Swenson[532] (extrapolated to 0 K). These are in very good agreement with our PBEsol+SO results of 2.972 Å, 158.1 kJ/mol (including ZPE) and 13.4 GPa respectively (see Tables 8.1 and 8.2), albeit the change of the bulk modulus due to spin-orbit coupling is most likely overestimated. Here we took the bcc phase for comparison, but note that the experimental phase for lithium has also been postulated to be a Barlow 9R structure with an (ABACABAC) sequence of hexagonal layers (often referred to as stacking faults) as deducted from neutron diffraction studies at low temperatures[507,533]. We can interpret this sequence as a mixture of $\frac{2}{3}$ of hcp with $\frac{1}{3}$ of fcc phase[377]. We have recently shown that different Barlow packings[18] lie close in energy and vary little in their basic properties with varying sequence of hexagonal layers, and the main properties can accurately be determined from the two limiting cases hcp and fcc alone together with their packing fraction[402]. Indeed, our data show the

fcc and hcp cohesive energies are very close. Furthermore, the low temperature phase of lithium is still being debated as the possible phases are quasi-degenerate in energy.[79] We also mention that the PBE+D3 results including long-range dispersion also give very good results, albeit the cohesive energy is overestimated by 6.5%. They do bring the bcc phase closer to the close-packed structures, albeit this effect is quite small. Dispersion effects are important as they contribute 9.9% to the cohesive energy of lithium.

Table 8.2: Bulk moduli B_0 in GPa and corresponding unit cell volumes V_0 in Å^3 at the optimized stable structures. BM: Derived from a fourth-order Birch-Murnaghan fit. P: From a fourth-order polynomial fit in $B(V)$.

	Metal	B_0^{hcp}(BM)	B_0^{fcc}(BM)	B_0^{bcc}(BM)	B_0^{hcp}(P)	B_0^{fcc}(P)	B_0^{bcc}(P)	V_0^{hcp}	V_0^{fcc}	V_0^{bcc}
	LDA	14.04	16.14	14.15	14.11	16.11	14.20	38.04	37.86	38.12
	PBE	13.99	12.84	13.38	14.01	12.80	13.51	40.65	40.58	40.77
Li	PBE-D3	16.17	12.64	15.84	16.11	13.07	15.81	36.61	36.66	36.74
	PBEsol	13.75	12.49	12.79	13.77	12.45	12.84	40.63	40.55	40.77
	PBEsol+SO	15.21	15.40	13.29	15.21	15.48	13.41	40.64	40.50	40.79
	LDA	8.70	10.63	9.82	8.68	10.63	9.87	66.68	66.83	66.86
	PBE	7.65	7.61	7.88	7.66	7.60	7.65	74.13	74.02	73.96
Na	PBE-D3	8.40	9.81	11.74	8.37	9.73	10.70	68.19	68.03	68.38
	PBEsol	7.65	8.08	8.46	7.66	8.06	8.40	72.71	72.66	72.57
	PBEsol+SO	7.64	8.22	7.91	7.65	8.24	7.91	72.71	72.65	72.57
	LDA	2.42	2.64	2.95	2.43	2.64	2.92	186.64	189.75	185.65
	PBE	2.62	1.95	1.89	2.58	1.95	1.89	231.30	233.73	232.45
Fr	PBE-D3	1.84	2.46	2.91	1.77	2.44	3.01	218.79	218.64	218.10
	PBEsol	1.68	1.75	2.03	1.86	1.78	2.08	211.97	211.18	213.31
	PBEsol+SO	2.08	2.57	2.67	2.08	2.58	2.71	207.50	207.36	209.36

Concerning sodium we have the experimental values for the nearest neighbor distance of $R_{\mathrm{NN}} = 3.766$ Å (at 20K),[534] cohesive energy of $E_{\mathrm{coh}} = 107$ kJ/mol,[129] and bulk moduli of $B = 7.7$ GPa (extrapolated to 0K)[535], so we can compare to our bcc results which are 3.612 Å, 109.6 kJ/mol (corrected for ZPE) and 7.9 GPa respectively for the PBEsol+SO functional. This is again in very good agreement with experiment. However, as for lithium, the low-temperature phase could be a Barlow 9R structure rather than bcc. Again, PBE-D3 overestimates slightly the cohesive energy by 2.6%. Except for the bulk moduli, SO effects are rather small for both lithium and sodium as one expects. LDA overestimates cohesive energies and are included only for comparison. We note that the performance of various DFT approximations for metals including the Group 1 elements has been discussed before, and the good overall performance of PBEsol for the alkali metals up to Cs has also been noted[281,536]. This is clearly seen in the Figures 8.2, 8.3, and 8.4.

Turning now to the relative stability of the three different phases we notice that for PBEsol+SO including ZPE corrections we have the sequences in cohesive energies (in kJ/mol, ZPE included) 158.420 (hcp) $>$ 158.108 (fcc) $>$ 158.080 (bcc) for lithium, and 109.790 (hcp) $>$ 109.660 (fcc) $>$ 109.642 (bcc) for sodium. Thus these three phases (and the infinitely many close-packed Barlow structures) can be seen as being quasi-degenerate with a slight preference

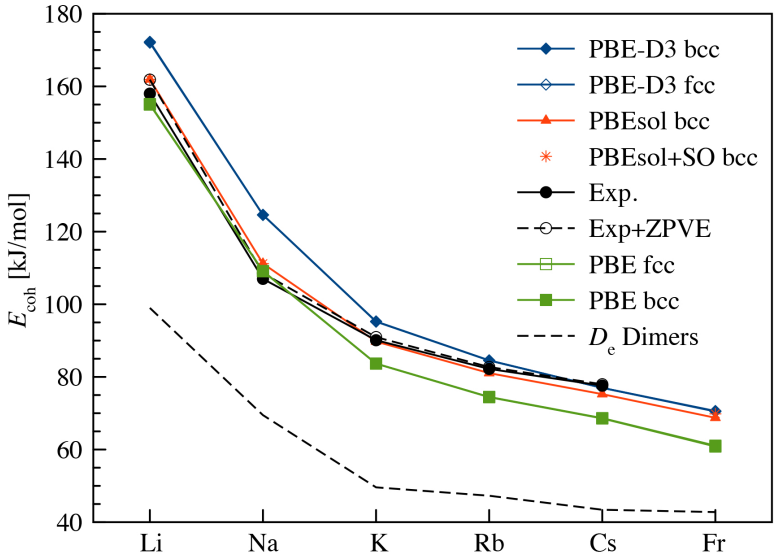

Figure 8.2: Trend in cohesive energies (in kJ/mol) for the Group 1 metals for the fcc and bcc structures using various density functionals. Data for K, Rb and Cs are taken from Refs.[433,536]. Experimental data are taken from Ref.[536]. Exp.+ZPVE is the cohesive energy with added ZPVE for better comparison with the density functional results which are not corrected for ZPVE. The dissociation energies for the Group 1 dimers are also shown for comparison (experimental data for Li_2 to Cs_2 from Refs.[390,537], calculated data for Fr_2 from Ref.[498]).

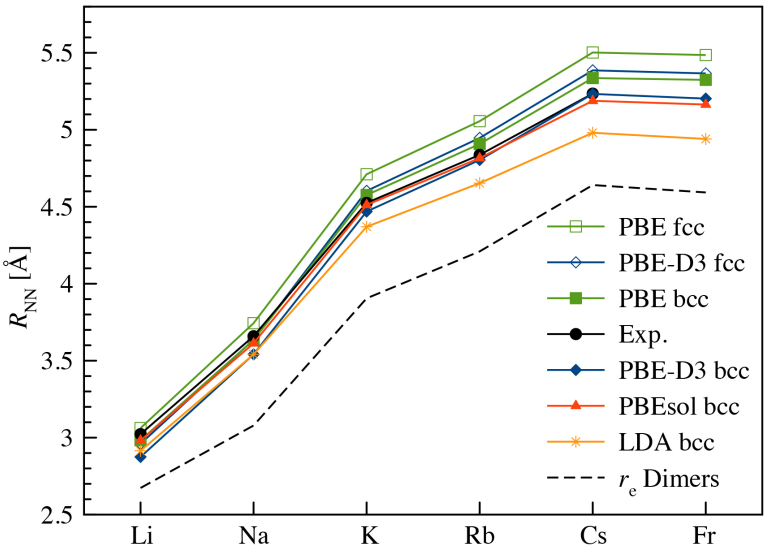

Figure 8.3: Trend in nearest neighbor distances (in Å) for the Group 1 metals for the fcc and bcc structures using various density functionals. Data for K, Rb and Cs are from Refs.[281,433]. Experimental data are taken from from Ref.[281]. The equilibrium distances for the Group 1 dimers are also shown for comparison (experimental data for Li_2 to Rb_2 from Ref.[390], calculated data for Cs_2 and Fr_2 from Ref.[498]).

for the hcp structure at this level of theory. In our previous paper[402] we iterated the fact that quasi-degeneracy between fcc and hcp is most likely a condition for the (rather rare)

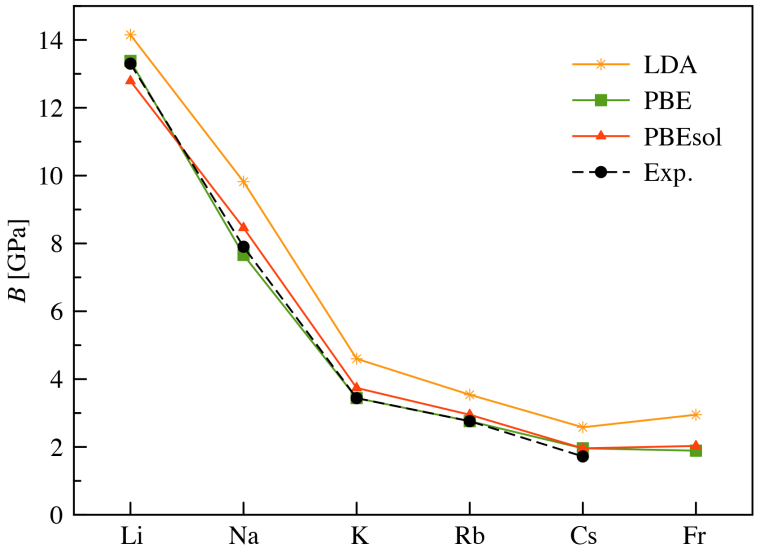

Figure 8.4: Trend in bulk moduli (in GPa) for the Group 1 metals (for the bcc structure only) using various density functionals. Data for K, Rb and Cs are from Refs.[281]. Experimental data from Ref.[281].

Barlow sequences to be observed experimentally. This quasi-degeneracy is maintained at the PBE-D3 level of theory. It is well known that at higher temperatures the bcc phase becomes dominant in accordance with Landau theory[252], which can be traced back to vibrational entropy contributions to the free energy. This gives a consistent picture of what is observed experimentally for the Group 1 elements[74,506,534]. PBE-D3 overestimates the cohesive energies of the Group 1 metals, which could well be due to an overestimation of electron correlation effects in the combination of the PBE functional[280] with Grimme's dispersion correction[517]. Nevertheless, we see that dispersion corrections lead to a substantial stabilization of the Group 1 elements, i.e. by approx. 16% for the cohesive energy of the three phases of francium.

For francium, we see again a quasi-degeneracy of the two closed packed structures with the same sequence compared to lithium and sodium, i.e. (in kJ/mol) 69.790 (hcp) $>$ 69.741 (fcc) $>$ 69.532 (bcc) at the PBEsol+SO level of theory including vibrational corrections. Hence we predict that in a hypothetical experiment for bulk francium we would observe a low temperature Barlow structure (fcc, hcp or 9R for example) followed by a phase transition to bcc at higher temperatures. In this case francium is not special compared to all the other Group 1 elements (beside its nuclear instability), albeit SO effects become a bit more sizable stabilizing both fcc and bcc in contrast to hcp.

Concerning periodic trends we see that francium sits below the cohesive energy of cesium with 77.6 kJ/mol, thus continuing the trend of decreasing stability of the solid state down the (currently known) Group 1 elements similar to the trend in dissociation energies for the diatomic compounds, see Figure 8.2. In this respect, cesium has a nearest neighbor distance of R_{NN}=5.235 Å[129] close to the one we calculate for hcp francium of 5.280 Å , mainly due to

scalar relativistic effects (note that $R_{NN} < a$ because $\gamma < \sqrt{\frac{8}{3}}$), see Figure 8.3. Thus we observe a trend of increasing bond distances down the Group 1 elements up to Cs, with Fr being the exception. This is in line with the increasing bond distances and dissociation energies of the Group 1 diatomics[390]. For the bulk moduli shown in Fig.8.4 we see a smooth decreasing trend from Li to Fr, with LDA deviating substantially from the experimental values. Here we note that the (not yet discovered) superheavy element 119 is the first element breaking this trend due to strong scalar relativistic effects[538–542]. We should also mention a previous study on the Group 1 metals by Koufos and Papaconstantopoulos[504]. They used a linearized augmented plane wave (LAPW) method together with LDA as well as GGA to discuss trends within the Group 1 element properties obtaining results similar to ours. However, they report energy differences between the different phases rather than directly the cohesive energies and did not include SO effects in their optimizations or ZPE corrections required for the discussion of the small energy differences between the different lattices.

From the volume per atom of the hcp unit cell of 207.50/2=103.75 Å^3 and the molar mass of 223 g/mol, we can estimate a density at $\rho = 3.57$ g/cm^3 at 0K much larger than the estimated value[543] of 2.458 g/cm^3 (at room temperature). However, a simple estimate from the density and molar mass of cesium ($\rho = 1.886$ g/cm^3, $M = 132.91$ g/mol) we can estimate an upper bound for cesium at room temperature if the volumes of the two metals are close to each other, i.e. $\rho_{\mathrm{Fr}} \approx \rho_{\mathrm{Cs}} V_{\mathrm{Fr}}/V_{\mathrm{Cs}}$ =3.16 g/cm^3, closer to our value. Finally, Table 8.3 contains additional useful data such as Wigner-Seitz radii, Debye temperatures and ZPEs obtained from eq.(8.8). These estimated ZPEs are in reasonable agreement to what we believe the more accurate data listed in Table 8.1.

8.4 Conclusions

We obtained of what we believe the most accurate data yet for the solid-state properties of francium at 0K by using DFT including SO corrections. We calibrated our results on calculations for lithium and sodium where experimental data are available. We found that the PBEsol functional including SO coupling gives excellent results in comparison with experimental data for both lithium and sodium, adding confidence to our results for francium. We predict that bulk francium is very similar to the rest of the Group 1 metals adopting a low temperature closed packed structure (fcc, hcp or Barlow structures) with bcc occurring at higher temperatures in agreement with Landau theory[252]. We recommend the following solid-state values for francium: a nearest neighbor distance of 5.28 Å, cohesive energy of 70 kJ/mol, a bulk modulus between 2.1 and 2.6 GPa, and a density at 3.57 g/cm^3 (at 0K).

Table 8.3: Wigner-Seitz radii in atomic units, Debye temperatures, calculated from Eq.(8.7) in K, and zero point energies, calculated from Eq.(8.8) in kJ/mol, are obtained from the bulk modulus in the Birch-Murnagham equation of state.

	Metal	r_s^{hcp}	r_s^{fcc}	r_s^{bcc}	Θ^{hcp}	Θ^{fcc}	Θ^{bcc}	E_0^{hcp}	E_0^{fcc}	E_0^{bcc}
	LDA	3.129	3.124	3.131	329.38	352.97	330.82	3.081	3.302	3.094
	PBE	3.199	3.198	3.203	332.54	318.44	325.43	3.111	2.979	3.044
Li	PBE-D3	3.089	3.094	3.093	351.27	310.83	347.91	3.286	2.907	3.254
	PBEsol	3.199	3.197	3.202	329.67	314.13	318.06	3.084	2.938	2.975
	PBEsol+SO	3.199	3.195	3.203	346.77	348.68	324.27	3.244	3.261	3.033
	LDA	3.773	3.775	3.775	157.24	173.90	167.10	1.471	1.627	1.563
	PBE	3.909	3.907	3.906	150.06	149.67	150.17	1.404	1.400	1.405
Na	PBE-D3	3.801	3.799	3.804	155.09	167.56	183.39	1.451	1.567	1.715
	PBEsol	3.883	3.882	3.880	149.59	153.69	157.29	1.399	1.438	1.471
	PBEsol+SO	3.883	3.883	3.881	149.47	155.09	152.09	1.398	1.451	1.423
	LDA	5.317	5.347	5.310	31.63	33.13	34.85	0.296	0.310	0.326
	PBE	5.713	5.732	5.721	34.08	29.45	28.99	0.319	0.276	0.271
Fr	PBE-D3	5.609	5.607	5.606	28.31	32.70	35.59	0.265	0.306	0.333
	PBEsol	5.512	5.545	5.560	26.84	27.45	29.61	0.251	0.257	0.277
	PBEsol+SO	5.508	5.507	5.523	29.81	33.17	33.84	0.279	0.310	0.317

MASSEY UNIVERSITY
TE KUNENGA KI PŪREHUROA
UNIVERSITY OF NEW ZEALAND

GRADUATE RESEARCH SCHOOL

STATEMENT OF CONTRIBUTION
DOCTORATE WITH PUBLICATIONS/MANUSCRIPTS

We, the student and the student's main supervisor, certify that all co-authors have consented to their work being included in the thesis and they have accepted the student's contribution as indicated below in the Statement of Originality.

Student name:	Andres Eduardo Robles Navarro
Name and title of main supervisor:	Peter Schwerdtfeger
In which chapter is the manuscript/published work?	Chapter 9

Describe the contribution that the student and members of the supervisory team have made to the manuscript/published work:[1]

All the computations were performed by me. The theoretical development of the publication is equally divided between me, Shaun Cooper, and Peter Schwerdtfeger. Further discussions also included Odile Smits.

Please select one of the following three options:

- (●) **The manuscript/published work is published or in press**

  Please provide the full reference of the research output:

  The Journal of Physical Chemistry Letters, 2024, 15(32): 8387-8392.

- ( ) **The manuscript is currently under review for publication**

  Please provide the name of the journal:

- ( ) **It is intended that the manuscript will be published, but it has not yet been submitted to a journal**

Student's signature:	ARoblesNavarro	Main supervisor's signature:	PeterSchwerdtfeger Digitally signed by PeterSchwerdtfeger Date: 2025.12.08 14:19:14 +13'00'

This form should be placed at the beginning of each relevant thesis chapter.

[1] Refer to the Massey University Publishing and Authorship guidelines (OneMassey for staff, Stream for students) and/ or Contributor Roles Taxonomy (CRediT) guidelines for guidance.

Chapter 9

From Hard to Soft Dense Sphere Packings: The Cohesive Energy of Barlow Structures Using Exact Lattice Summations for a General Lennard-Jones Potential

Dense packings of solids such as spheres in three dimensions (3D) intrigued both chemists and mathematicians for a very long time.[544] In 1902, Hilbert presented 23 difficult mathematical problems that were to be solved[545]. His 18th problem concerned the build-up of space with spheres or congruent polyhedra, and the Kepler conjecture formed part of this problem[28]. The conjecture states that there is no arrangement of equally sized, non-overlapping unit spheres in 3D space with a higher density than the face-centered cubic (fcc) or hexagonal close packed (hcp) structures. The packing density of these arrangements is exactly $\rho = \pi/\sqrt{18}$ (= 74.0480...%). In 1831 Gauss proved that Kepler's conjecture is true if the spheres are arranged in a regular lattice. Hales proved in 1998[10,403] that Kepler's conjecture holds for any unit sphere packing in 3D space, whether regular or irregular. Reviews on understanding condensed phases through packing models have been provided by Stillinger and Torquato[139,546]. For an introduction to sphere packing in higher dimensions see Sloane[547].

There are uncountable infinitely many distinguishable densest sphere packings in 3D space with a packing density of exactly $\rho_{\max} = \pi/\sqrt{18}$[401,548]. These were originally introduced by Barlow in 1883[18] and the different polymorphs are called Barlow packings[549]. In general, Barlow packings are strictly jammed[138] multi-lattices that consist of densely packed hexagonal layers with lattice point positions for the unit spheres at $\vec{b}_{ijk} = i(1,0,0) + j(1/2,\sqrt{3}/2,0) + k(0,0,\gamma_0) + \vec{v}(k)$ where for each k the shift vectors $\vec{v}(k) \in \{\vec{v}_A, \vec{v}_B, \vec{v}_C\}$ are defined as $\vec{v}_A = (0,0,0), \vec{v}_B = (1/2, 1/\sqrt{12}, 0), \vec{v}_C = (1/2, -1/\sqrt{12}, 0)$ with $\gamma_0 = \sqrt{2/3}$, such that we have no repeat neighboring layer sequence such as AA, BB or CC, that is $\vec{v}(k) \neq \vec{v}(k+1)$. Both hcp and

fcc, with layer sequences $(AB)_\infty$ and $(ABC)_\infty$ respectively, belong to the class of periodic Barlow packings. Fig. 9.1 illustrates such Barlow packings including the 9R lattice, a rare lattice that is found in very few martensitic materials[79,435,550,551].

For the sticky hard-sphere model with an interaction potential between the spheres of $V(r) = \epsilon$ with $\epsilon = 0$ for $r > 1$, $\epsilon = -1$ for $r = 1$, and $\epsilon = \infty$ for $r < 1$, r being the distance between two spheres, all Barlow packings have the same cohesive energy of $E_{\text{coh}} = -\frac{1}{2}K(3) = -6$ (in reduced units), where the kissing number (number of nearest neighbors) in 3D is $K(3) = 12$. Within the hard-sphere model at specific packing densities, Mau and Huse found that fcc has the highest entropy, albeit the entropy difference between fcc and hcp is very small ($\Delta S \approx 10^{-3} k_B$, k_B being the Boltzmann constant)[439]. However, this simple potential model does not explain why Barlow packings other than fcc and hcp are extremely rare in nature[74,79,435,550]. There is currently no consensus on the explanation why hcp and fcc are the dominant structures out of the infinitely many Barlow packings.[552] More realistic interaction potentials are therefore required to resolve this long-standing problem.

In order to analyze the cohesive energies of Barlow packings we require a few important definitions. Suppose $\boldsymbol{X} = \{X_i\}$ is a Barlow sequence of hexagonal close packed layers of period N, that is, for each integer i we have $X_i \in \{\text{A,B,C}\}$, $X_i \neq X_{i+1}$ and $X_i = X_{i+N}$. Write $\boldsymbol{X} = (X_1 X_2 ... X_N)_\infty$. The stacking sequence $\{p_i\}_{i=1}^N$ for $\boldsymbol{X}$ is defined by $p_i = 0$ if $X_i = X_{i+2}$ and $p_i = 1$ otherwise, and we call the numbers p_i the stacking numbers, similar to the *hc* notion by Thompson and Downs.[553] Further, the *fcc packing fraction* is defined as $\alpha = \frac{1}{N}\sum_{i=1}^N p_i$. For example, the stacking sequence for the 9R Barlow sequence $(ABCBCACAB)_\infty$ shown in Figure 9.1 is (100100100), and the fcc packing fraction is $\alpha = 1/3$. For the extremal cases we have $\alpha = 0$ for hcp, $(AB)_\infty$, and $\alpha = 1$ for fcc, $(ABC)_\infty$. For all other periodic Barlow packings we have $0 < \alpha < 1$. The fcc packing fraction is a measure of how often the fcc sequence with $(X_i \neq X_{i+2})$ appears in the Barlow sequence and originates from local cluster statistics introduced by Wilson and Bradley[554] and used by Middlemas et al. for Barlow packings[435]. From the stacking number sequence it is clear that the number of distinct Barlow packings $(X_1 X_2 ... X_N)_\infty$ of period N is bounded above by $2^{N-2} (N \geq 2)$ (note that the first two letters are fixed as AB), see Fig. 9.2. In fact, the number of distinct Barlow packings is directly related to the more general mathematical problem of the n-coloring of beads in a bracelet[555] (see Figure 9.1). In our case we have three different colors ($n = 3$) and the precise number of distinct Barlow packings can be found in the A011768 sequence of Sloane's Encyclopedia of Integer Sequences[556]. Thompson and Downs[553] listed all possible Barlow packings up to $N = 12$.

To explore the energetic stability of Barlow packings we apply a general (n, m) Lennard-Jones (LJ) potential between the interacting spheres (or atoms)

$$V_{nm}(r) = \frac{m}{n-m} r^{-n} - \frac{n}{n-m} r^{-m}, \tag{9.1}$$

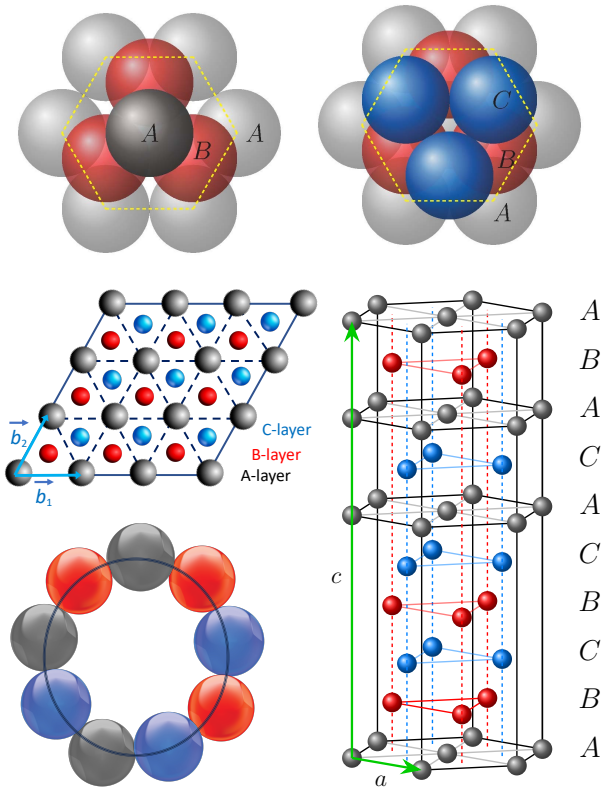

Figure 9.1: (top) Packing sequence for hcp $(AB)_\infty$ and fcc $(ABC)_\infty$. (bottom) The three possible layers A, B and C in Barlow packings (left) and the 9R structure with a sequence of $(ABCBCACAB)_\infty$ (right) and the definition of the lattice constant a and c. The last layer at the top of the 9R structure belongs to the next unit cell with the same layer sequence. Also shown is the 3-colored bracelet with 9 beads equivalent to the Barlow 9R packing at the bottom left.

which allows the spheres to overlap ($r < 1$). This potential has a minimum at $r_e = 1$ with minimum value given by $V(r_e) = -1$ (reduced units). Since $V_{nm}(r) = V_{mn}(r)$, we may assume $n > m$. This potential was originally introduced by Grüneisen in 1912[219] and later in 1925 applied by Lennard-Jones and Ingham[112] to cubic crystals using lattice sum techniques. For increasing exponents n and m ($n > m$), the (n,m)-LJ potential approaches the sticky hard-sphere limit as shown in Figure 9.3. The $(12,6)$-LJ potential has been extensively used in the past for phase transitions or cluster simulations[559,560]. For a historical review on LJ potentials see ref. 222.

Applying the (n,m)-LJ potential to periodic Barlow packings $\boldsymbol{X}$ with lattice parameters a and c (see Figure 9.1 for the 9R lattice), we obtain for the cohesive energy in a similar fashion as derived previously for the hcp structure[294],

$$E_{\text{coh}}^{\boldsymbol{X}}(n,m,a,\gamma) = \frac{mL_n^{\boldsymbol{X}}(N,\gamma)}{2(n-m)}a^{-n} - \frac{nL_m^{\boldsymbol{X}}(N,\gamma)}{2(n-m)}a^{-m} \tag{9.2}$$

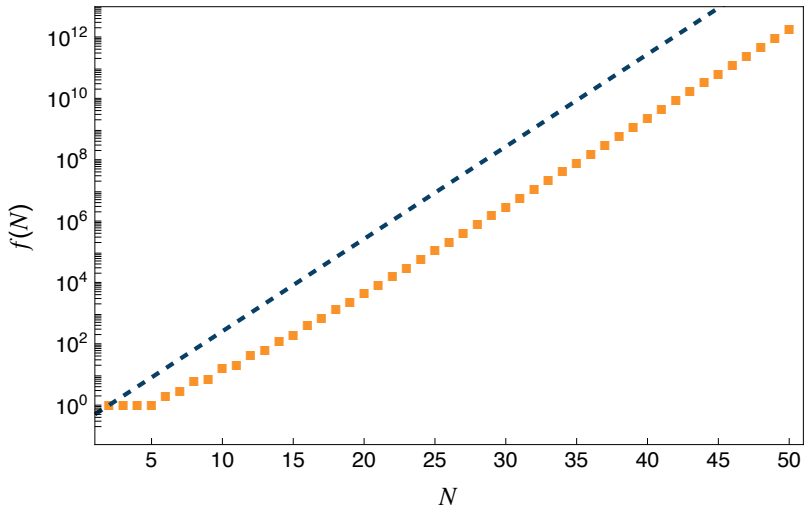

Figure 9.2: Number of nonidentical sequences $f(N)$ for Barlow packings $(X_1X_2...X_N)_\infty$ for a specific N value discarding repeats from lower N values. A logarithmic scale is used for $f(N)$. Data are taken from Refs. 557,558. The dashed line shows the upper bound of $f(N) \leq 2^{N-2}$.

with $\gamma = c/a = N\gamma_0$ ($\gamma_0 = \sqrt{2/3}$ for a dense packing of hard spheres), and $L_n^{\boldsymbol{X}}(N,\gamma)$ are the lattice sums for a specific Barlow packing of period N (see computational details). For the definition of the lattice constants a and c see Figure 9.1. We restrict our attention to $m > 3$ as there is a pole at $m = 3$ and the series diverges for $m < 3$. The lattice parameter a is defined as the smallest distance between two lattice points in the 2D hexagonal layer of the Barlow packing and c is the height of the large hexagonal unit cell, see Figure 9.1. The mathematical treatment of lattice sums L has been reviewed extensively by Borwein et al.[111], and our research group has recently applied this to cubic crystals as well as to the hcp structure[103,294].

The cohesive energy for a Barlow structure can be obtained by minimizing (9.2) with respect to the lattice parameter a at fixed γ, and is given by

$$\min_a E_{\text{coh}}^{\boldsymbol{X}}(n,m,a) = -\frac{1}{2}\left[\frac{L_m^{\boldsymbol{X}}(N,\gamma)^n}{L_n^{\boldsymbol{X}}(N,\gamma)^m}\right]^{\frac{1}{n-m}} \tag{9.3}$$

with the minimum occurring at

$$a = a_{\min} = \left[\frac{L_n^{\boldsymbol{X}}(N,\gamma)}{L_m^{\boldsymbol{X}}(N,\gamma)}\right]^{\frac{1}{n-m}} . \tag{9.4}$$

That is, the cohesive energy of a Barlow packing $\boldsymbol{X}$ of period N for a (n,m)-LJ interaction potential is completely determined by the corresponding lattice sums dependent on the LJ exponents n and m in (9.2). Because $L_n > L_m$ for $n > m$, we have $a_{\min} < 1$. For example, for the (12,6)-LJ potential one obtains for the hcp structure $a_{\min} = 0.97123$, while for the (30,20)-LJ potential one gets $a_{\min} = 0.99995$, which is very close to the sticky hard-sphere limit of 1.0.

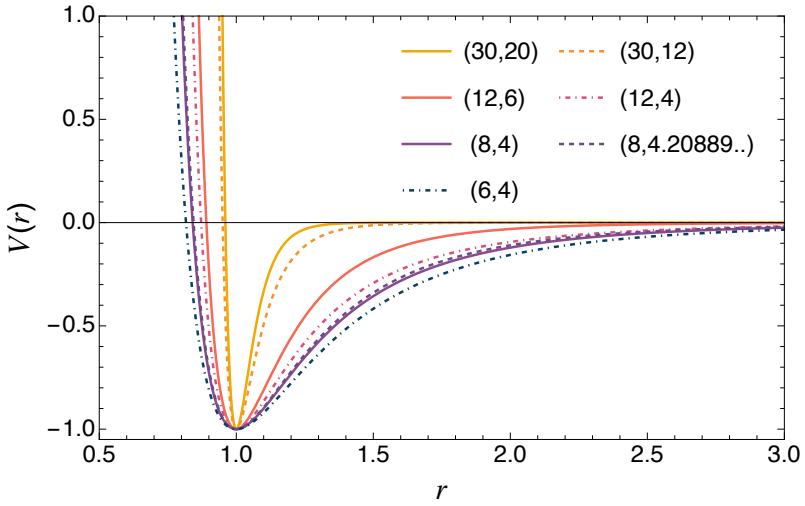

Figure 9.3: Lennard-Jones potentials for a selection of exponents (n, m). The value of $m_c = 4.20889094798800$ sits on the critical line depicted in Figure 9.4.

The hcp structure is generally preferred over fcc, except for small values of the LJ exponent m (i.e. for very soft LJ potentials)[227]. In the solid-state community, this fact was the reason for decades-long debates of why the rare gas crystals crystallize in the fcc and not in the hcp phase, which has been resolved only very recently for the case of argon[104]. Figure 9.4 shows the hcp to fcc phase transition line defined by $E_{\text{coh}}^{\text{hcp}} = E_{\text{coh}}^{\text{fcc}}$ with the critical values for the LJ exponents (n_c, m_c) ($m_c < 5.7094$) fulfilling this condition. As can be seen, m_c decreases with increasing n_c with a pole at $m_c = 3$.

Concerning the Barlow packings, we investigated all periodic structures $(X_1 X_2 ... X_N)_\infty$ up to $N = 15$, resulting in a total of 497 different Barlow packings including fcc and hcp, and the 9R structure with a packing sequence of $(\text{ABCBCACAB})_\infty$ ($N = 9$). The calculated cohesive energy differences $\Delta E_{\text{coh}}^{\boldsymbol{X}}(\alpha) = E_{\text{coh}}^{\boldsymbol{X}}(\alpha) - E_{\text{coh}}^{\text{hcp}}(\alpha = 0)$ obtained from (9.3) for different (n, m) combinations are shown in Figure 9.5 as a function of the fcc packing fraction α. As can be seen, the Barlow structures lie energetically in between hcp and fcc, although the energy differences are very small and in the range of 10^{-3} to 10^{-4} (in reduced units). Surprising is the linear correlation of the cohesive energies with respect to the fcc packing fraction α, i.e. the linear relation approximately is

$$\Delta E_{\text{coh}}^{\boldsymbol{X}}(\alpha) = \alpha (E_{\text{coh}}^{\text{fcc}} - E_{\text{coh}}^{\text{hcp}}) \tag{9.5}$$

For example, a linear fit for the (12,6)-LJ potential yields $\Delta E_{\text{coh}}^{\boldsymbol{X}}(\alpha) = 8.695754 \times 10^{-4} \alpha$ with a very small standard deviation of 1.2×10^{-7}. This implies that the cohesive energy of a Barlow packing can be obtained to high accuracy from the energy difference between hcp and fcc, and the fcc packing fraction of the corresponding Barlow structure. Moreover, the Barlow structures energetically lie slightly above the line determined by (9.5). Variations become more apparent for LJ potentials close to the (n_c, m_c) critical line where $E_{\text{coh}}^{\text{hcp}} \approx E_{\text{coh}}^{\text{fcc}}$. For example, for $n_c = 8$

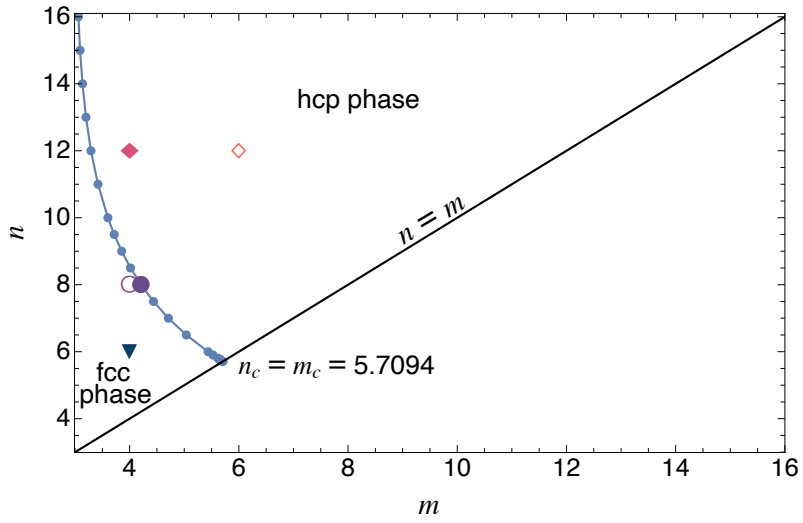

Figure 9.4: hcp/fcc phase transition line (n_c, m_c) for LJ potentials in blue. Selection of exponents (n, m) marked as used in Figs. 9.3 and 9.5

and $m_c = 4.20889094798800$ we find the Barlow structures energetically above the zero line (see Figure 9.6), but still very close to both the fcc or hcp structures. The energy distribution has an interesting shape of a triangle with a maximum deviation from the zero line at $\alpha = 0.5$ originating from the $(ABAC)_\infty$ Barlow packing.

Within the kissing hard-sphere model the hexagonal layers are ideally located half-distance between the neighboring layers. However, for Barlow packings of periodicity $N > 3$ interacting through a (n, m)-LJ potential, symmetry will break especially for softer potentials (small (n, m) exponents). To include such effects one has to optimize all the distances $\gamma_i = c_i/a$ between the hexagonal layers (see computational details). It turns out that such dislocations are rather small and can be neglected, i.e. they do not affect in any significant way the results presented here. Figure 9.6 shows the rather negligible variations between the different choices of γ values for the deviations of the cohesive energy from the linear regression line with fcc and hcp at the two extreme points. For example, for the 9R structure and a (12,6)-LJ potential we get (the corresponding (6,4)-LJ values are given in parentheses) $\Delta\gamma = \max\{\gamma_i\} - \min\{\gamma_i\} = 3.039 \times 10^{-5} (3.406 \times 10^{-5})$. For this structure the total energy lowers by $3.2245 \times 10^{-7} (9.4337 \times 10^{-7})$ if only the total γ-value is optimized, and by $3.4627 \times 10^{-7} (1.0092 \times 10^{-6})$ if all γ_i-values are optimized.

In conclusion, using a more realistic interaction potential compared to the sticky hard-sphere model we were able to show that the Barlow packings lie energetically in between the hcp and fcc lattices. Their cohesive energies can be estimated to high accuracy from the energy difference between fcc and hcp and the associated fcc packing fraction, the latter can easily be obtained from the stacking sequence of a Barlow structure. How this translates to the real world of atomic or molecular crystals remains to be seen.[552] For example, Mau and Huse investigated the entropy of hard-sphere crystals using Monte-Carlo simulations with periodic boundary

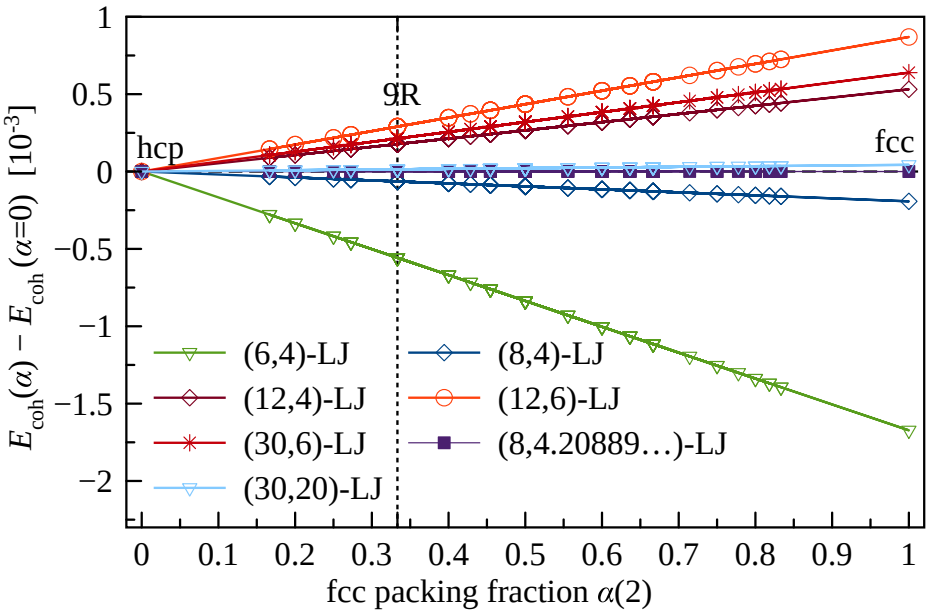

Figure 9.5: Cohesive energy difference with respect to the hcp structure ($\alpha = 0$) for various (n, m)-LJ potentials plotted against the complementary fcc packing fraction α. The 9R structure ($\alpha = \frac{1}{3}$) is also indicated. The dashed horizontal zero line indicates the hard-sphere limit and LJ interactions with critical values of (n_c, m_c). The vertical dotted line indicates where the 9R structure is located. See Figure 9.3 for the distribution of exponents used.

conditions[439]. They included a few Barlow packings in their simulations and concluded that hcp has the lowest and fcc the highest entropy. This implies that higher temperatures may favor the fcc structure. This alone does not explain why Barlow packings other than fcc or hcp are extremely rare in nature. We hypothesize that fcc and hcp are the extreme points for the free energies, and only when both structures are quasi-degenerate one may observe other Barlow packings at certain temperatures and pressures. It will however be a future challenge to accurately simulate Barlow lattices for elemental systems using accurate quantum theoretical methods such as density functional theory as the energy differences between the different packings are very small demonstrated in this work. A more detailed study including temperature and pressure effects is currently underway.

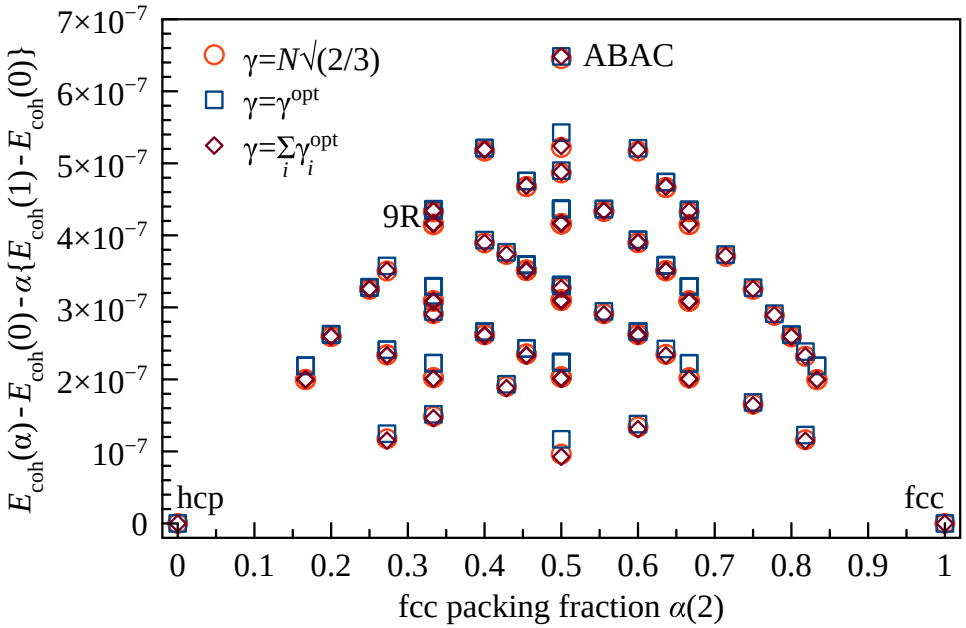

Figure 9.6: Deviation of the cohesive energy from the linear behavior for $n_c = 8$ and $m_c = 4.2088909480185$ at the fcc/hcp phase transition line. The deviation for the 9R structure at $\alpha = \frac{1}{3}$ is 4.334×10^{-7} at $\gamma = 9\sqrt{2/3}$ and 4.346×10^{-7} if all γ_i are optimized.

Computational Details

The expression for the lattice sum of a Barlow packing is given by

$$L_n^X(N,\gamma) = L_n^Q(N,\gamma) + \frac{2}{N}\sum_{1\le k_1<k_2\le N} L_n^{X_{k_1}X_{k_2}}(N,\gamma) \tag{9.6}$$

for a LJ exponent of n and N stacking hexagonal layers. The corresponding infinite sums are given by

$$L_n^{X_{k_1}X_{k_2}}(N,\gamma) = \sum_{\vec{i}\in\mathbf{Z}^3}\left[i_1^2 + i_2^2 + i_1 i_2 + \gamma^2\left(i_3 + \frac{k_2-k_1}{N}\right)^2\right]^{-\frac{n}{2}} \tag{9.7}$$

if $X_{k_1} = X_{k_2}$, and

$$L_n^{X_{k_1}X_{k_2}}(N,\gamma) = \sum_{\vec{i}\in\mathbf{Z}^3}\left[(i_1+\tfrac{1}{3})^2 + (i_2+\tfrac{1}{3})^2 + (i_1+\tfrac{1}{3})(i_2+\tfrac{1}{3}) + \gamma^2\left(i_3 + \frac{k_2-k_1}{N}\right)^2\right]^{-\frac{n}{2}} \tag{9.8}$$

if $X_{k_1} \neq X_{k_2}$ and $\gamma = N\gamma_0$. The lattice sum L_n^Q is a special case of $L_n^{X_{k_1}X_{X_2}}$ in (9.7) for $k_1 = k_2 = 0$, and where the term corresponding to $\vec{i} = \vec{0}$ is omitted from the summation. These lattice sums are slowly converging infinite series for small exponents and various techniques have to be used to bring them into fast converging series. The derivation of fast converging series and corresponding derivatives in terms of Bessel function expansions similar to the procedures discussed in Refs. 294,295 is rather lengthy and will be presented elsewhere. Once the lattice sums are obtained, the cohesive energy of any Barlow packing can be calculated to the desired computer precision within a few seconds of CPU time for $N \leq 15$ using a Newton-Raphson minimization procedure for the parameter $\gamma = c/a$ at optimized cell parameter a. This procedure has the advantage that the tiny energy differences between the different Barlow structures can be calculated accurately (which remains a challenge for density functional approximations).[327] Thus we avoid the use of a cut-off function for the Lennard-Jones potential which can influence the energy differences between the Barlow structures significantly[552,561].

Symmetry breaking effects were also investigated as the hexagonal layers can slightly dislocate from the ideal half-distance location between the two neighboring hexagonal layers along the c-axis. This implies optimizing the N distances $\gamma_i = c_i/a$ between two neighboring layers i and $i+1$ with $\gamma_i \approx \gamma_0 = \sqrt{2/3}$ and $\gamma = \sum_i \gamma_i$. This substantially increases the parameter space required for the Newton-Raphson geometry optimization. Because of this and the tiny changes compared to the ideal value of $\gamma_i = \gamma_0$, analytical derivatives for $\partial E_{\text{coh}}/\partial\gamma_i$ and $\partial^2 E_{\text{coh}}/\partial\gamma_i\partial\gamma_j$ were used in the optimization procedure and the Hessian was checked for positive eigenvalues. A FORTRAN program to determine these lattice sums can be found on our website[562].

MASSEY UNIVERSITY
TE KUNENGA KI PŪREHUROA
UNIVERSITY OF NEW ZEALAND

GRADUATE RESEARCH SCHOOL

STATEMENT OF CONTRIBUTION
DOCTORATE WITH PUBLICATIONS/MANUSCRIPTS

We, the student and the student's main supervisor, certify that all co-authors have consented to their work being included in the thesis and they have accepted the student's contribution as indicated below in the Statement of Originality.

Student name:	Andres Eduardo Robles Navarro
Name and title of main supervisor:	Peter Schwerdtfeger
In which chapter is the manuscript/published work?	Chapter10

Describe the contribution that the student and members of the supervisory team have made to the manuscript/published work:[1]

All the computations were performed by me. Code development and theoretical framework is equally divided between me, Shaun Cooper, and Peter Schwerdtfeger.

Please select one of the following three options:

- (●) **The manuscript/published work is published or in press**

  Please provide the full reference of the research output:

  The Journal of Chemical Physics, 2025, 162(1): 014105.

- ( ) **The manuscript is currently under review for publication**

  Please provide the name of the journal:

- ( ) **It is intended that the manuscript will be published, but it has not yet been submitted to a journal**

Student's signature:	ARoblesNavarro	Main supervisor's signature:	PeterSchwerdtfeger Digitally signed by PeterSchwerdtfeger Date: 2025.12.08 14:22:21 +13'00'

This form should be placed at the beginning of each relevant thesis chapter.

[1] Refer to the Massey University Publishing and Authorship guidelines (OneMassey for staff, Stream for students) and/ or Contributor Roles Taxonomy (CRediT) guidelines for guidance.

Chapter 10

The Theory of Barlow Packings: Basic Properties and Cohesive Energies from Exact Lattice Summations within the Sticky Hard-Sphere Model

10.1 Introduction

Barlow packings (also known as close-packed rhombohedral structures) were introduced as early as in 1883[18] and consist of an infinite stacking of the form $(X_1X_2X_3...)$ of two-dimensional hexagonal close packed layers. Here, X_i represents one of the three possible densely packed hexagonal layers by location, A, B or C, such that we do not have identical neighboring layers, that is $X_iX_{i+1} \neq AA$ or BB or CC $(i \in \mathbb{N})$, see Figure 10.1. The two prime examples for Barlow packings are the hexagonal close-packing (hcp) with a periodic stacking sequence of $(AB)_\infty$ and the face-centered close-packing (fcc) with $(ABC)_\infty$. There are uncountably infinitely many (strictly jammed) Barlow packings all having the same maximal sphere packing density of $\rho = \pi/3\sqrt{2} = 0.74048048969\ldots$ [18,138,139,401,563]. Kepler's original conjecture states that the fcc $(ABC)_\infty$ packing density cannot be surpassed which has been proven only very recently by Hales[10,403].

It is currently difficult to predict crystal structures from basic chemical concepts. For example, it is not known why Barlow structures appear only in very few compounds[550] compared to the more common hcp and fcc structures. Well known elemental examples are La, Pr, Nd, Am, Ce with a $(ABAC)_\infty$ stacking, and Sm, the only element to adopt a $(ABABCBCAC)_\infty$ stacking order (9R structure) at standard conditions.[435,550] The 9R structure is also experimentally predicted to be involved in the martensitic transformation of metallic lithium from the body-centered cubic structure (bcc) to fcc or 9R.[74,79] It is clear that the

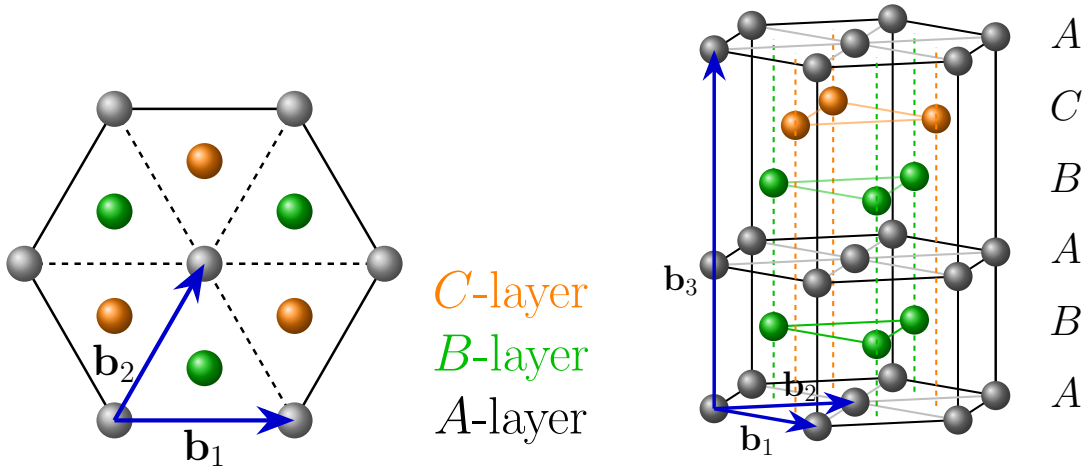

Figure 10.1: Left: The three possible hexagonal layers A, B and C in a Barlow packing. Right: A Barlow packing with the sequence $(ABABC)_\infty$. The last layer at the top belongs to the next unit cell with the same layer sequence.

description of Barlow packings requires a detailed understanding of concepts from basic lattice theory.[401,435,553]

The study of lattice sums in three (and more generally in N) dimensions is an old but important problem in lattice theory.[28,111,147] It dates back to the work of Appell in 1886[564], and later to Born and Landé[565], Madelung[115] and Lennard-Jones and Ingham[112,296] to name but a few. An excellent account on lattice sums is given by Borwein et al.[111] For the case of inverse power potentials, $V(r) \sim r^{-n}$, used in this work, the problem of computing lattice sums is related to the efficient treatment of the so-called Epstein zeta function,[113,299,566,567] an extension of the Riemann or Hurwitz zeta function. Lattice sums for inverse power potentials have been formulated and treated for the simple cubic, body-centered cubic and face-centered cubic lattices already by Lennard-Jones and Ingham in 1925,[112] and for the hexagonal close-packed lattice by Kane and Goeppert-Mayer[568], Bell and Zucker[437], and more recently by our research group.[294,295]

The stability of Barlow close-packed structures has not been treated systematically in the past and there are only few studies available.[435,439] Here we try to close this gap by evaluating cohesive energies of Barlow packings within the sticky hard-sphere model (SHS)[209,430] containing an attractive long-range r^{-n} potential,

$$\phi(n,\epsilon,r) = \begin{cases} \infty & \text{for } r < r_e, \\ -\epsilon r^{-n} & \text{for } r \geq r_e \end{cases} \tag{10.1}$$

where r is the distance between two lattice points (or atoms), r_e is the equilibrium distance set conveniently to the unit length (i.e. $r_e = 1$ in reduced units), and $\epsilon > 0$ is a prefactor which

determines the binding energy between two interacting atoms at equilibrium distance r_e ($\epsilon = 1$ in reduced units). For the kissing hard-sphere model (KHS) where the potential is zero except when two spheres touch (kiss) we have the limit $\lim_{n\to\infty} r^{-n} = \delta(r-1), r \geq 1$, where $\delta(x)$ is the Dirac delta function. The SHS model prevents any overlap between two hard spheres of radius $r_e/2$ (spheres of unit diameter in our KHS model). The cohesive energy at unit distance is then given by the simple expression,

$$E_{\text{coh}}(n, \epsilon = 1, r_e = 1) = \frac{1}{2} L\left(\tfrac{n}{2}\right) \tag{10.2}$$

where $L(\frac{n}{2})$ is the specific lattice sum of a Barlow packing described in detail in the theory section, and the cohesive energy is defined here to be positive, $E_{\text{coh}}(n) > 0$. Thus, within this simple model we equate directly the cohesive energy of a Barlow packing with its corresponding lattice sum which becomes convenient for our discussion on stability of Barlow packings.[294,295]

In the following we outline the theory of Barlow packings, introduce our lattice sum treatment through fast convergent series using Bessel function expansions, and analyze the obtained lattice sum properties for different Barlow packings in detail through the SHS model. This analysis will be important for future work on lattice properties using classical interaction potentials such as the Lennard-Jones potential.[112,219,222,296,402,435]

10.2 Theory

10.2.1 Barlow packings, packing sequence numbers and packing fractions

Before we address the interaction between lattice points in a Barlow packing, we introduce the basic definition of a Barlow packing in terms of its letter sequence. A bilateral sequence $(\dots, X_{-2}, X_{-1}, X_0, X_1, X_2, X_3, \dots)$ is said to represent a Barlow packing if

$$X_i \in \{A, B, C\} \quad \text{and} \quad X_i \neq X_{i+1} \quad \text{for all} \quad i \in \mathbb{Z}. \tag{10.3}$$

The packing is said to be periodic with period N if

$$X_{i+N} = X_i \quad \text{for all } i \in \mathbb{Z}. \tag{10.4}$$

We assume that the period N is minimal, that is, N is the smallest positive integer for which (10.4) holds. Clearly, $N \geq 2$ because the definition (10.3) requires $X_{i+1} \neq X_i$ and hence $N \neq 1$. When a Barlow packing is periodic with period N, we will omit the commas and write $(X_1 X_2 \dots X_N)_\infty$. For example:

- $(AB)_\infty$ corresponds to the hexagonal close packing structure of period 2;
- $(ABC)_\infty$ corresponds the face centred cubic packing lattice of period 3;
- $(ABABCBCAC)_\infty$ is a packing with period 9, called the 9R structure.

In the following, we further omit the infinity sign and we understand that a sequence of letters set in parentheses defines a Barlow packing, e.g. $(X_1X_2\dots X_N)_\infty \equiv (X_1X_2\dots X_N)$. Suppose $(X_1X_2\dots X_N)$ represents a Barlow packing of period N. The packing sequence numbers $p(i,\ell)$ are defined for $1 \le i,\ell \le N$ by

$$p(i,\ell) = \begin{cases} 1 & \text{if} \quad X_i = X_{i+\ell}, \\ 0 & \text{if} \quad X_i \neq X_{i+\ell} \end{cases} \tag{10.5}$$

and the ℓth packing fraction $\delta(\ell)$ is defined by

$$\delta(\ell) = \frac{1}{N}\sum_{i=1}^{N} p(i,\ell), \tag{10.6}$$

so that $0 \le \delta(\ell) \le 1$. We will be mostly interested in the second packing fraction $\delta(2)$. For example, for the 9R Barlow packing $(ABCBCACAB)$ we get the packing sequence numbers as shown in Table 10.1. As $\delta(2) = 1$ for hcp and $\delta(2) = 0$ for fcc, $\delta(2)$ measures the fraction of hcp type (AB) occurrences in a Barlow packing. Alternatively, we can define the complementary packing fraction by

$$\alpha(\ell) = 1 - \delta(\ell) = \frac{1}{N}\sum_{i=1}^{N}[1 - p(i,\ell)] \equiv \frac{1}{N}\sum_{i=1}^{N}\bar{p}(i,\ell), \tag{10.7}$$

Table 10.1: Packing sequence numbers $p(i,\ell)$ and fractions $\delta(\ell)$ and $\alpha(\ell)$ for the 9R lattice $(ABCBCACAB)$.

ℓ	$p(i,\ell)$, $1 \le i \le 9$	$\delta(\ell)$	$\alpha(\ell)$
1	0,0,0,0,0,0,0,0,0	0	1
2	0,1,1,0,1,1,0,1,1	2/3	1/3
3	0,0,0,0,0,0,0,0,0	0	1
4	0,0,1,0,0,1,0,0,1	1/3	2/3
5	1,0,0,1,0,0,1,0,0	1/3	2/3
6	0,0,0,0,0,0,0,0,0	0	1
7	1,1,0,1,1,0,1,1,0	2/3	1/3
8	0,0,0,0,0,0,0,0,0	0	1
9	1,1,1,1,1,1,1,1,1	1	0

and note that $\alpha(2)$ measures the fcc packing fraction, as stated by Middlemas et al[435]. We use both definitions in the following. We note that the smallest non-zero fcc packing fractions $\alpha(2)$ are obtained (non-uniquely) from the combinations $((AB)_{(N-1)/2}C)$ if $N > 2$ is odd with $\alpha(2) = 3/N$ and $((AB)_{(N-2)/2}AC)$ if $N > 2$ is even with $\alpha(2) = 2/N$. For $\alpha(2) = 0$ we have the hcp structure.

The representation $R = (X_1X_2 \dots X_N)$ of a periodic Barlow lattice is not unique. All the possible letter sequences that can be generated and fulfill the conditions of a Barlow packing contain equivalent sequences under certain symmetry operations. These need to be sorted into equivalence classes where one representative sequence can be chosen from each class. For example, the cyclic permutation $\sigma(R)$ defined by

$$\sigma(R) = \sigma(X_1X_2 \dots X_N) = (X_2X_3 \dots X_NX_1)$$

returns the same Barlow lattice as R, as does the negative permutation $\eta(R)$ defined by

$$\eta(R) = \eta(X_1X_2 \dots X_N) = (X_NX_{N-1} \dots X_2X_1).$$

The transposed permutation $\sigma_{AB}(R)$ defined by switching all occurrences of A and B also defines the same Barlow lattice, as do the transposed permutations $\sigma_{AC}(R)$ and $\sigma_{BC}(R)$ defined similarly by switching A with C, or B with C, respectively. These permutations form a group G with order 6 isomorphic to the symmetric group S_3 : $G = \{I, \sigma_{AB}, \sigma_{AC}, \sigma_{BC}, \sigma_{ABC}, \sigma_{ACB}\}$, where I is the identity operator and, for example, $\sigma_{ACB}(ABAC) = (CACB)$. Furthermore, it is convenient to also define the shift operators $\mathcal{S}_l^+ = \sigma^{l-1}$ and $\mathcal{S}_l^- = \eta\sigma^l$, such that $\mathcal{S}_2^-(ABABC) = (BACBA)$ and $\mathcal{S}_3^+(ABAC) = (ACAB)$. Note that the identity operation is obtained as $I(R) = \mathcal{S}_1^+(R) = \sigma^0(R) = R$.

In order to standardise the representation of a Barlow lattice, we define the weight of a representation $R = (X_1X_2 \dots X_N)$ by

$$w(R) = \sum_{i=1}^{N} 2^{N-i}\overline{p}(i, 2).$$

The representation that has minimum weight and satisfies $X_1 = A$ and $X_2 = B$ will be called the standard representation of the lattice and denoted by R^*. For example, one of the sequences given by Thompson and Downs is $R = (ABABABCAC)$. The standard representation of this sequence $R^* = (ABABABCBC)$. To see this, first note that

$$\begin{aligned}\sigma^3(\eta(\sigma_{AB}(ABABABCAC))) &= \sigma^3(\eta(BABABACBC)) \\ &= \sigma^3(CBCABABAB) = (ABABABCBC).\end{aligned}$$

Therefore $R^* = \sigma^3(\eta(\sigma_{AB}(R)))$ and so R and R^* represent the same Barlow lattice. Second, the complementary stacking sequence $\{\overline{p}(i,2)\}$ for R^* is 000010011 and the weight $w(R^*) = 2^4 + 2^1 + 2^0$ is minimal. Third, we have $R_1^* = A$ and $R_2^* = B$, i.e., the first two symbols of R^* are AB. If follows that R^* is the standard representation for R.

The distinct periodic Barlow packings up to $N = 10$ are listed according to their standard representations in Table 10.2. Observe from the table that the following two conditions appear to hold:

1. If $N \geq 3$ then $\overline{p}(N,2) = 1$. Equivalently, the last symbol in the standard representation is $R_N^* = C$.

2. The integers N and $\sum_i \overline{p}(i,2)$ have the same parity. That is,

$$N + \sum_{i=1}^{N} \overline{p}(i,2) \quad \text{is even.} \tag{10.8}$$

The first condition is easy to prove by contradiction. If $\overline{p}(N,2) = 0$ then the complementary packing sequence $\overline{p}(N,2)\,\overline{p}(1,2)\,\overline{p}(2,2)\ldots\overline{p}(N-1,2)$ represents the same Barlow packing and has smaller weight. This contradicts the minimum weight property of R^*. The condition $\overline{p}(N,2) = 1$ implies $X_N \neq X_{N+2}$ and since $X_{N+2} = X_2 = B$ it follows that $X_N \neq B$. We also have $X_N \neq X_{N+1}$ and so $X_N \neq A$. It follows that $X_N = C$. The second condition, which we shall call the parity condition, is proved in Appendix L. The two conditions are useful in the algorithm that we will use to generate unique Barlow sequences.

10.2.2 Number of non-identical periodic Barlow sequences

Counting the number of non-identical periodic Barlow sequences and enumerating them has been addressed by several authors[557,558,569–571]. The problem is identical to the more general one of counting colorful bracelets with N beads and c colors[555]. The solutions are known for $c = 3$ which we briefly present here.

Let $\phi(N)$ be Euler's totient function, i.e., $\phi(N)$ counts the number of integers less than or equal to N that are relatively prime to N. Let $\mu(N)$ be the Möbius function, i.e., $\mu(N)$ equals 1 if N is a square-free positive integer with an even number of prime factors; equals -1 if N is a square-free positive integer with an odd number of prime factors; and equals 0 if N is divisible by the square of a prime number. Let $\chi(N)$ be defined to be 1 if $N \equiv 2 \pmod 6$ or if $N \equiv 4 \pmod 6$, and 0 otherwise. Another way of writing it is

$$\chi(N) = \tfrac{4}{3}\sin^2(\tfrac{\pi N}{3})\cos^2(\tfrac{\pi N}{2}). \tag{10.9}$$

Let $f(N)$ be the number of non-identical Barlow packings of period N. The very last formula

Table 10.2: Unique Barlow sequences $\{X_i\}$ (up to period $N = 10$) in standard form and their natural stacking sequence numbers $\{\bar{p}(i,2)\}$), fcc packing fractions $\alpha(2)$, entropy difference ΔS with respect to the hcp structure (in units of $10^{-5}k_B$), number of nonidentical lattice sums n_{NILS}, and letter counts, i.e. number of A's, B's and C's in ascending order $(n_1 n_2 n_3)$ discussed for Algorithm 1. The Barlow packings are ordered according to the period N followed by further ordering according to $\alpha(2)$ followed by their $\bar{p}(i,2)$ sequence. The two selected examples for $N = 11$ and 12 have the lowest non-zero fcc packing fractions for the specific N value. An asterix in the table means that the standard form differs from the representation used by Thompson and Downs[553].

No.	Standard representation	N	$\{\bar{p}(i,2)\}$	$\alpha(2)$	ΔS	n_{NILS}	$(n_1 n_2 n_3)$
1	(AB) (hcp)	2	00	0/2	0	2	11
2	(ABC) (fcc)	3	111	3/3	116.0	2	111
3	$(ABAC)$	4	0101	1/2	45.8	4	112
4	$(ABABC)$	5	00111	3/5	65.2	4	122
5	$(ABABAC)$	6	000101	1/3	33.0	5	123
6	$(ABACBC)$	6	011011	2/3	65.1	6	222
7	$(ABABABC)$	7	0000111	3/7	46.6	6	133
8	$(ABABCBC)$	7	0010011	3/7	45.2	6	223
9	$(ABACABC)$	7	0101111	5/7	74.1	6	223
10	$(ABABABAC)$	8	00000101	1/4	24.8	7	134
11	$(ABABACAC)$	8	00010001	1/4	26.6	7	224
12	$(ABABACBC)$	8	00011011	1/2	50.7	8	233
13	$(ABABCBAC)$	8	00101101	1/2	49.2	8	233
14	$(ABABCABC)$	8	00111111	3/4	84.3	7	233
15	$(ABACBABC)$	8	01110111	3/4	77.8	8	233
16	$(ABABABABC)$	9	000000111	1/3	36.2	8	144
17	$(ABABABCBC)$*	9	000010011	1/3	35.2	8	234
18	$(ABABCBCAC)$ (9R)	9	001001001	1/3	35.5	7	333
19	$(ABABACABC)$	9	000101111	5/9	59.3	8	234
20	$(ABABCBABC)$*	9	001010111	5/9	56.6	8	234
21	$(ABABCACBC)$	9	001101011	5/9	55.2	8	333
22	$(ABACBCABC)$*	9	011011111	7/9	82.0	8	333
23	$(ABABABABAC)$	10	0000000101	1/5	19.8	8	145
24	$(ABABABACAC)$	10	0000010001	1/5	21.3	8	235
25	$(ABABABACBC)$	10	0000011011	2/5	40.5	10	244
26	$(ABABABCBAC)$	10	0000101101	2/5	39.3	9	244
27	$(ABABACACBC)$	10	0001001011	2/5	40.8	10	334
28	$(ABABACABAC)$	10	0001010101	2/5	38.1	8	235
29	$(ABABACBCBC)$	10	0001100011	2/5	42.0	10	334
30	$(ABABCBABAC)$	10	0010100101	2/5	39.6	9	244
31	$(ABABABCABC)$	10	0000111111	3/5	67.4	10	244
32	$(ABABACBABC)$	10	0001110111	3/5	63.7	10	244
33	$(ABABCBCABC)$*	10	0010011111	3/5	66.4	10	334
34	$(ABABCBACBC)$*	10	0010111011	3/5	61.3	10	334
35	$(ABABCACABC)$*	10	0011001111	3/5	65.2	9	334
36	$(ABACABACBC)$	10	0101011011	3/5	57.4	9	334
37	$(ABACABCABC)$	10	0101111111	4/5	86.7	10	334
38	$(ABACBACABC)$	10	0111101111	4/5	85.4	10	334
39	$(ABABABABABC)$	11	00000000111	3/11	29.6	10	155
40	$(ABABABABABAC)$	12	000000000101	1/6	16.5	10	156

Table 10.3: Number of non-identical Barlow packings of period N.

N	1	2	3	4	5
$f(N)$	0	1	1	1	1
N	6	7	8	9	10
$f(N)$	2	3	6	7	16
N	11	12	13	14	15
$f(N)$	21	43	63	129	203
N	16	17	18	19	20
$f(N)$	404	685	1343	2385	4625

in Ref. 555 gives:

$$f(N) = \sum_{d|N} \mu\left(\tfrac{N}{d}\right) S(d) \tag{10.10}$$

where

$$S(N) = \frac{1}{2}\left(K(N) + L(N)\right), \tag{10.11}$$

$$L(N) = \begin{cases} 2^{N/2-1} & \text{if } N \text{ is even,} \\ \frac{1}{3}\left(2^{(N-1)/2} - (-1)^{(N-1)/2}\right) & \text{if } N \text{ is odd,} \end{cases} \tag{10.12}$$

and

$$K(N) = \left\lfloor \frac{1}{6N} \sum_{d|N} (1 + \chi(d)) \gcd(d, 6) \phi(d) 2^{N/d} \right\rfloor. \tag{10.13}$$

where $\gcd(N, m)$ is the greatest common divisor of both N and m.

Some values calculated by formula (10.10) are shown in Table 10.3. This is in agreement with values of the sequence A011768 in Sloane's encyclopedia[556]. From Eq.(10.10) we deduce that the number of nonidentical Barlow packings increases exponentially as $O(2^{N/2})$. In fact we have an upper bound of $f(N) \leq 2^{N-3}$ for $N > 2$ since there are at most two choices for each of $X_3, X_4, ..., X_{N-1}$ (remember, we have $X_1 = A, X_2 = B, X_N = C$). This implies that there are countably infinitely many unique periodic Barlow packings. On the other hand, there are uncountably infinitely many non-periodic Barlow packings.

A histogram for the number of Barlow packings with value $\alpha(2)$ for period $N = 32$ is shown in Figure 10.2a. It shows that if $4|N$ the frequencies are well described by a normal distribution. The frequency distribution for all Barlow packings up to $N = 32$ are shown in Figure 10.2b. It clearly demonstrates that most packings are found in the vicinity of $\alpha(2) = \frac{1}{2}$ as one expects. We observe dips in the frequency distributions around $\frac{p}{N} = \alpha(2) = \frac{1}{2}$ for periods where $4 \nmid N$. This can be understood from the simple fact that as $2p = N$ and p even for N even, we have the condition that $\alpha(2) = \frac{1}{2}$ only if $4|N$. The first Barlow packing where this occurs is at $N = 4$, $(ABAC)$.

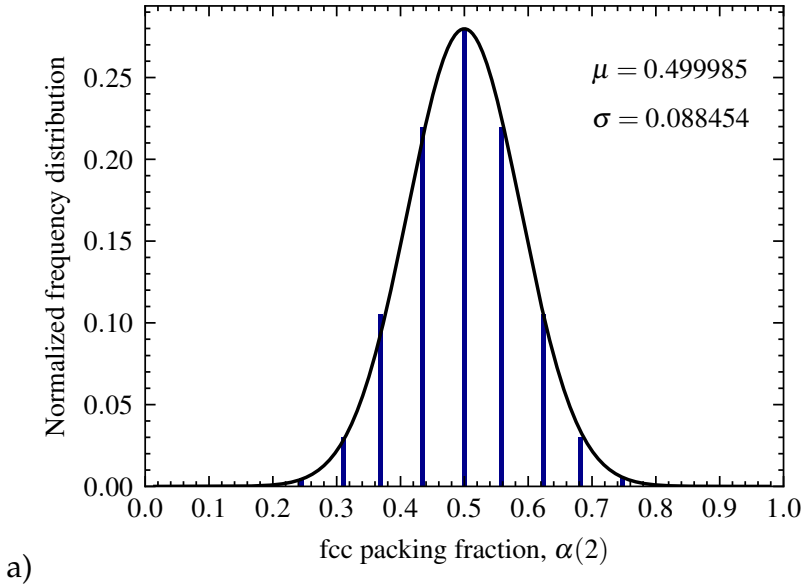

a)

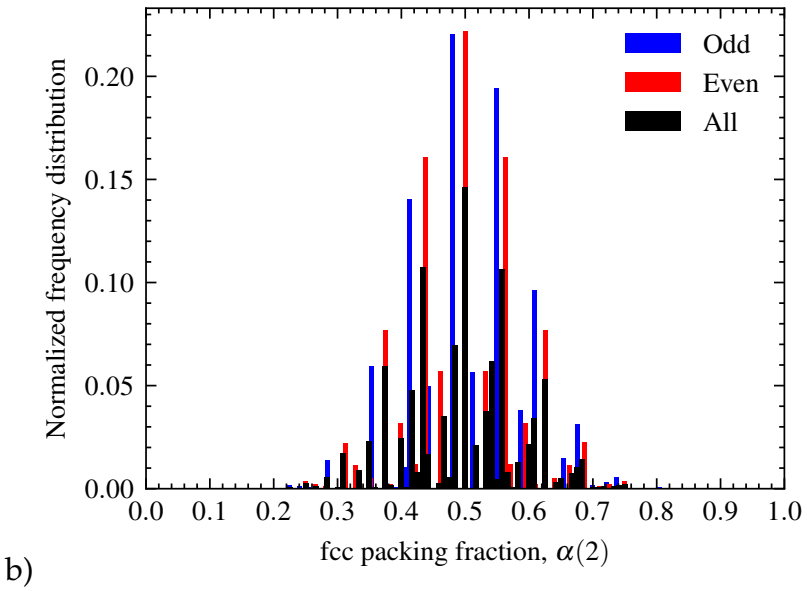

b)

Figure 10.2: Normalized frequency distribution for values of $\alpha(2)$. The number of bins is set to 120. (a) For period $N = 32$ showing that if $4|N$ it follows a normal distribution with a mean of the distribution μ and standard deviation σ shown in the figure. (b) For all 23,189,443 Barlow packings up to period $N = 2^5 = 32$. The normalized frequency distributions for N restricted to even and odd numbers are also shown.

10.2.3 Algorithms for producing a complete set of non-identical Barlow sequences

An algorithm for producing all non-identical Barlow sequences up to period N has been introduced already by Thompson and Downs relying on orbits in a tree graph.[553] They listed all possible Barlow packings up to period $N = 12$, but included non-minimal sequences of lower period N_R where N_R divides N. These can, however, be easily eliminated. For the sake of completeness, we introduce their algorithm first, with some slight modifications to speed up the selection and elimination process. After that we introduce our more efficient algorithm which we use in this work.

Algorithm 1 (modified Thompson and Downs[553])

- *Production step*: We produce a set $\{\Omega_k(N)\}, k = 1, ..., 2^{N-2}, N > 1$ containing different in general non-identical letter sequences (orbits) of Barlow packings $\Omega_k(N) = (ABX_3X_4...X_N)$, $X_3, X_4, ...X_N = A, B, C$, and $X_N \neq A$ in a simple binary tree graph up to period N to obtain all sequences $\Omega_k(N)$ as illustrated in Figure 10.3.

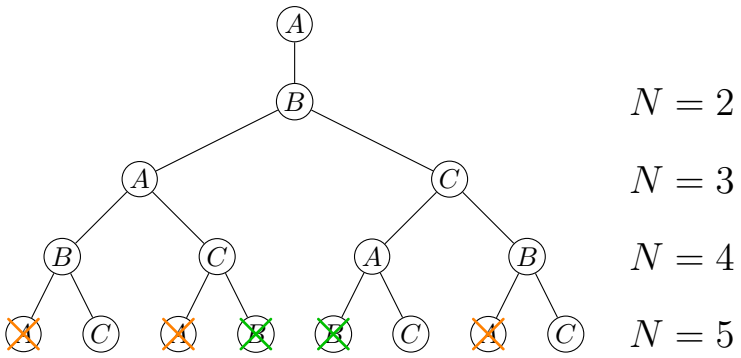

Figure 10.3: An ordered binary tree graph of all the possible Barlow sequences $\Omega_i(N)(ABX_3X_4...X_N)$ read from the top to the endpoint for a specific period N (orbits). If we terminate the tree at period N ($N = 5$ in this figure), the sequences ending with either $X_N = A$ or $X_N = B$ can be deleted immediately in the set of Barlow sequences.

- *1st elimination step*: For all orbits of length N we delete any sequence with $X_N = A$ or B from the set $\{\Omega_k(N)\}$. In total, this deletes approximately 2/3 of the Barlow sequences for a specific period N and leaves a reduced set of sequences $\{\Omega_i'(N)\}$. For example, only one sequence $\Omega_2(4) = (ABAC)$ (orbit 2 counting from the left) survives after this elimination step, i.e. in this case it deletes the repeat sequence $\Omega_1(4) = (ABAB) \equiv (AB)$ (hcp) and the identical ones from letter permutations.

- *2nd elimination step*: We start with the first sequence in the reduced set $\{\Omega_i'(N)\}$ and act with permutation and shift operators (as introduced in section 10.2.1) to compare with all others in the set. We delete the identical ones and move to the second sequence where we apply the same procedure until all sequences have been checked. In these shift/permutation operations we can immediately delete those which do not fulfill the Barlow condition $X_1 = A, X_2 = B, X_N = C$.

- *3rd elimination step*: If N is non-prime we search for reducible sequences of length $N_R|N$ (see algorithm 2).

- Bring the sequence in its natural letter sequence if required. This concludes the algorithm.

- *Example*: For $N = 5$ three sequences are left after the first elimination step which reduce just to one, $(ABABC)$. For example, we have $\sigma_{BC}\mathcal{S}_1^-(ABCAC) = \sigma_{BC}(ACACB) = (ABABC)$.

As the number of Barlow sequences in the tree grows exponentially, it is clear that the comparison with other sequences in the 2nd elimination step becomes rather computer time consuming. Care has to be taken to write the code in a most efficient way achieving a smaller prefactor in the exponential scaling. For this algorithm it is therefore advisable to put the sequences into different equivalence classes. For example, for each letter sequence $\Omega_i(N)$ we can count the total number of letters for each A, B and C and arrange the three numbers in ascending order $n_1 \leq n_2 \leq n_3, \sum_i n_i = N$. Further, as defined in Eq. (10.7), obtain $\lambda = N\alpha(2)$. We can put all sequences with the same number combinations (n_1, n_2, n_3, λ) into distinct subsets $\mathcal{M}_k = \mathcal{M}_{n_{1_k} n_{2_k} n_{3_k} \lambda_k}(N) \subset \Omega_i(N)$ (k is the cardinal number), with the subset $\mathcal{M}_k$ containing l_k such sequences. For example, for $N = 4$ we get only one subset from our tree structure, $\mathcal{M}_1(4) = \{(ABAC), (ABCB)\}$ with $l_1 = 2, (n_{1_1} n_{2_1} n_{3_1}) = (112), \lambda_1 = 2$, as the reducible sequence $(ABAB)$ has already been deleted. As Table 10.2 shows, for $N = 10$ we get 7 subsets. This sorting procedure reduces the number of step in the elimination procedure.

We now introduce a second far more efficient algorithm relying on stacking sequence numbers $p(i, 2)$ as introduced in Section 10.2.1 instead of letter sequences.

Algorithm 2

Here we describe a second way to generate the unique Barlow lattices of period $N \geq 4$. We assume that N is the minimal period as described in Section 10.2.1. Each Barlow lattice R of period N has a weight $w = w(R)$ which satisfies $1 \leq w \leq 2^N - 2$. The case $w = 0$ corresponds to hcp and occurs only for $N = 2$, while the case $w = 2^N - 1$ only occurs for $N = 3$ and corresponds to fcc.

- For a given period $N \geq 4$, let the weight range over the values $1 \leq w \leq 2^N - 2$. For each w, let $\overline{p}_w(i,2) \in \{0,1\}$ be defined for $i = 1, 2, \ldots, N$ by

$$w = \sum_{i=1}^{N} 2^{N-i} \overline{p}_w(i,2).$$

  Essentially, $\overline{p}_w(i,2)$ are the digits in the binary representation of w.

- *1st elimination step*: eliminate w from further consideration if the parity condition (10.8) does not hold. That is, continue to the next step if and only if

$$N + \sum_{i=1}^{N} \overline{p}_w(i,2) \quad \text{is even.}$$

- *2nd elimination step*: eliminate any w which do not correspond to a Barlow sequence of period N. That means, we calculate X_3, $X_4, \ldots, X_{N+2}$ in the letter sequence $(ABX_3X_4 \cdots X_N)X_{N+1}X_{N+2}$ successively by the rule

$$X_{j+2} = \begin{cases} X_j & \text{if } \overline{p}(j,2) = 0, \\ \{A,B,C\} \setminus \{X_j, X_{j+1}\} & \text{if } \overline{p}(j,2) = 1, \end{cases}$$

  for $1 \leq j \leq N$, and continue to the next step if and only if $X_{N+1} = A$ and $X_{N+2} = B$.

- *3rd elimination step*: eliminate w unless it is the minimal weight for the corresponding periodic Barlow lattice. Thus, let

$$\sigma(w) = 2^{N-1} \overline{p}_w(N,2) + \sum_{i=1}^{N-1} 2^{N-1-i}\, \overline{p}_w(i,2)$$

  and

$$\eta(w) = \sum_{i=1}^{N} 2^{i-1}\, \overline{p}_w(i,2)$$

  be the shifted and reflected weights, respectively. We keep w and continue to the next step if and only if

$$\min \left\{ w, \sigma(w), \sigma^2(w), \ldots, \sigma^{N-1}(w), \eta(w), \sigma(\eta(w)), \ldots, \sigma^{N-1}(\eta(w)) \right\} = w.$$

- *4th elimination step*: eliminate w if N is not the minimal period. If N is not prime, then for each divisor $d|N$ with $1 < d < N$, test if the letter sequence $(ABX_3X_4 \cdots X_N)$ has period d. Reject w if a smaller period is found.

- Any w that survives all four tests is a minimum weight for a periodic Barlow sequence of (minimal) period N. The letter sequence was already computed in the second elimination step and can be outputted from the computer program. As a final test, we check that the number of Barlow sequences of period N obtained agrees with the theoretical value in (10.10).

Here are some examples.

1. For $N = 4$ and $w = 7$ we have

$$7 = 0 \times 2^3 + 1 \times 2^2 + 1 \times 2^1 + 1 \times 2^0 \quad \text{so} \quad \overline{p}(1,2)\overline{p}(2,2)\overline{p}(3,2)\overline{p}(4,2) = 0111$$

   and therefore

$$N + \sum_{i=1}^{N} \overline{p}(i,2) = 4 + 0 + 1 + 1 + 1 \quad \text{is odd.}$$

   This violates the parity condition (10.8), so $w = 7$ is removed at the first elimination step.

2. For $N = 4$ and $w = 9$ we have

$$9 = 1 \times 2^3 + 0 \times 2^2 + 0 \times 2^1 + 1 \times 2^0 \quad \text{so} \quad \overline{p}(1,2)\overline{p}(2,2)\overline{p}(3,2)\overline{p}(4,2) = 1001.$$

   This passes the parity condition. For the second elimination step we start with $X_1 = A$, $X_2 = B$ and calculate $X_3, \ldots, X_6$, to obtain

$$X_1X_2X_3X_4X_5X_6 = ABCBCA.$$

   The test $X_5 = X_1$ and $X_6 = X_2$ fails, so the period of the Barlow lattice is not $N = 4$. The second elimination step fails.

3. For $N = 9$ the value $w = 25$ passes the first two steps, but fails the third, because

$$\overline{p}(1,2)\overline{p}(2,2)\ldots\overline{p}(9,2) = 000011001$$

   is not mimimal. The minimal representation is given by

$$\sigma^4(\eta(000011001)) = \sigma^4(100110000) = 000010011$$

   with corresponding weight $w = 2^4 + 2^1 + 2^0 = 19$. Thus, the corresponding 9-periodic Barlow lattice would have been detected earlier by the algorithm with the value $w = 19$. The value $w = 25$ fails the third elimination test and is rejected.

4. For $N = 8$, the value $w = 85$ passes the first three conditions but fails the fourth, because

$$\overline{p}(1,2)\overline{p}(2,2)\ldots\overline{p}(8,2) = 01010101,$$

corresponding to the Barlow sequence $(ABACABAC)$ which has period 4; i.e., $N = 8$ is not the minimal period.

The Barlow letter sequences and binary number sequences up to $N = 20$ and a Fortran90 program for producing these periodic Barlow packings using Algorithm 2 are given in the supplementary material. Concerning the actual calculation, for the largest period we selected, $N = 32$, the program produces 11,201,472 unique Barlow sequences out of $2^{32} - 2 = 4{,}294{,}967{,}294$ binary sequences with a frequency distribution as shown in Figure 10.2, taking 28.6 minutes of CPU time on a 2.3 GHz Intel i7 processor. The size of the output file produced is 975 MByte (71 MByte zipped).

10.2.4 Lattice vectors and properties

As we can only analyze a few examples of the infinitely many Barlow packings, we need to consider instead a finite sequence of layers $\boldsymbol{X} \equiv (X_1X_2...X_N)$ in a hexagonal unit cell (h) of finite volume with period N of a Barlow packing. We start with the underlying hexagonal Bravais lattice defined by the following basis vectors,

$$\vec{b}_1^h = a\,(1,0,0)^\top, \quad \vec{b}_2^h = a\left(\frac{1}{2},\frac{\sqrt{3}}{2},0\right)^\top, \quad \vec{b}_3^h = c\,(0,0,1)^\top. \tag{10.14}$$

with the lattice parameters $|\vec{b}_1^h| = |\vec{b}_2^h| = a$ and $|\vec{b}_3^h| = c$, and $\angle(\vec{b}_1^h, \vec{b}_2^h) = 60^o$ and $\angle(\vec{b}_1^h, \vec{b}_3^h) = \angle(\vec{b}_2^h, \vec{b}_3^h) = 90^o$. The associated generator matrix is defined as

$$B^{\mathrm{h}} = \begin{pmatrix} \vec{b}_1^{h\top} \\ \vec{b}_2^{h\top} \\ \vec{b}_3^{h\top} \end{pmatrix} = a \begin{pmatrix} 1 & 0 & 0 \\ \frac{1}{2} & \frac{\sqrt{3}}{2} & 0 \\ 0 & 0 & \gamma \end{pmatrix} \tag{10.15}$$

where $\gamma = \frac{c}{a}$. This leads to the following positive definite symmetric Gram matrix,

$$G^h = B^h {B^h}^\top = a^2 \begin{pmatrix} 1 & \frac{1}{2} & 0 \\ \frac{1}{2} & 1 & 0 \\ 0 & 0 & \gamma^2 \end{pmatrix} \tag{10.16}$$

with $\det(G^h) = \frac{3}{4}a^4c^2 > 0$. From an arbitrarily chosen atom at the origin, all points in the hexagonal Bravais lattice are described by

$$\vec{r}^h(\vec{i}) = B^{h^\top}\vec{i} = i_1\vec{b}_1^h + i_2\vec{b}_2^h + i_3\vec{b}_3^h \tag{10.17}$$

with $\vec{i} \in \mathbb{Z}^3$. Their distances to the origin are given by the quadratic form

$$|\vec{r}^h(\vec{i})| = \left(\vec{i}^\top G^h\vec{i}\right)^{\frac{1}{2}} = a\left(i_1^2 + i_1i_2 + i_2^2 + \gamma^2 i_3^2\right)^{\frac{1}{2}} . \tag{10.18}$$

The volume of the hexagonal unit cell is given by

$$V^h(a,\gamma) = \sqrt{\det G^h} = \frac{\sqrt{3}}{2}a^3\gamma \tag{10.19}$$

The nearest neighbor distance in the lattice is

$$r_{\mathrm{NN}}^h(a,c) = \min\{r^h(\vec{i})\} = \min\{a,c\} . \tag{10.20}$$

We now introduce all the other layers within the hexagonal unit cells, i.e. the A, B and C layers as shown in Figure 10.1, to complete the Barlow structure. As the Barlow packing is a multi-lattice, we have to introduce a shift vector for each hexagonal layer such that

$$\vec{r}^{X_k}(\vec{i}) = B_h^\top\vec{i} + \vec{v}^{X_k} , \tag{10.21}$$

to obtain the Wyckoff positions for all the layers $X_1, X_2, ..., X_N$ in the unit cell. We use the following form ($1 \le k \le N$):

$$\vec{v}^{X_k^\top} = \begin{cases} \left(0, 0, \frac{k-1}{N}c\right) & \text{if } X_k = A, \\ \left(\frac{a}{2}, a\frac{1}{2\sqrt{3}}, \frac{k-1}{N}c\right) & \text{if } X_k = B, \\ \left(\frac{a}{2}, -a\frac{1}{2\sqrt{3}}, \frac{k-1}{N}c\right) & \text{if } X_k = C. \end{cases} \tag{10.22}$$

For $k = 1$ we have $\vec{v}^{X_1^\top} = (0,0,0)$. These shift vectors can be derived from the fact that an atom in the subsequent layer sits above the centroid of a triangle of neighboring lattice points in the A layer, see Figure 10.1. The set of all vectors $\{\vec{r}^{X_k}(\vec{i})\}$ produce all the points in 3D space for a Barlow multi-lattice.

For a Barlow structure within the KHS model we have the ideal value of $\gamma = c/a = N\gamma_0$ with $\gamma_0 = \sqrt{\frac{2}{3}}$ (for the close packed hcp structure with $N = 2$ we have $\gamma = 2\sqrt{\frac{2}{3}} = \sqrt{\frac{8}{3}}$), and the kissing number defined by the number of minimum distances around a hard sphere is $\kappa = 12$. For the minimum distance r_{NN} in a general Barlow packing with varying γ value we

get from the lattice vectors,

$$\begin{aligned} r_{\mathrm{NN}}(a,\gamma) &= \min\left\{a, \frac{c}{N}\min_{XX}(k_2-k_1), \sqrt{\frac{a^2}{3}+\frac{c^2}{N^2}}\right\} \\ &= a\min\left\{1, \frac{\gamma}{N}\min_{XX}(k_2-k_1), \sqrt{\frac{1}{3}+\frac{\gamma^2}{N^2}}\right\} \\ &= a\min\left\{1, \gamma_0\min_{XX}(k_2-k_1), \sqrt{\frac{1}{3}+\gamma_0^2}\right\} \end{aligned} \tag{10.23}$$

where $\min_{XX}(k_2-k_1)$ is the minimum layer distance between two repeat layers $XX = AA$, BB, or CC, which is 2 except for the fcc packing where it is 3. If $N = 2$ the only possible Barlow packing is $(AB)_\infty$, which is hcp. For this case we have $\min_{XX}(k_2-k_1) = 3-1 = 2$. For $N = 3$ the only possibility is (ABC) which is fcc. Multiple stacking possibilities start in principle at $N = 4$ for which we have two choices, $(ABAB)$ and $(ABAC) \equiv (ABCB)$. However, as mentioned before the $(ABAB)$ sequence is identical to hcp (AB) and is therefore omitted in this list. For a list of unique Barlow packings up to $N = 20$ see supplementary material.

The volume per lattice point (atom) of a general Barlow packing is derived from Eq.(10.19)

$$V^{\mathrm{Barlow}}(a,\gamma) = \frac{1}{N}\frac{\sqrt{3}}{2}a^3\gamma = \frac{\sqrt{3}}{2}a^3\gamma_0 \tag{10.24}$$

from which one derives that the packing density of all Barlow packings are identical to the one of hcp or fcc,

$$\rho = \frac{V_{\mathrm{sphere}}(a)}{V^{\mathrm{Barlow}}(a,\gamma_0=\sqrt{\frac{2}{3}})} = \frac{\frac{4\pi}{3}\left(\frac{a}{2}\right)^3}{\frac{\sqrt{3}}{2}a^3\sqrt{\frac{2}{3}}} = \frac{\pi}{3\sqrt{2}} \tag{10.25}$$

and in the KHS limit all Barlow packings are energetically degenerate.

Concerning the symmetry of Barlow packings we see from Fig. 10.1 that inversion i or rotation by the angle β around the 3-fold axis parallel to $\vec{b}_3$, i.e. $R_\beta = R_{\frac{\pi}{3}(2n-1)}$ with $n \in \mathbb{N}$, transforms the layers according to $A \to A$, $B \to C$, and $C \to B$, while a rotation of $R_{\frac{2\pi}{3}(2n-1)}$ or a roto-inversion $R_{\frac{\pi}{3}(2n-1)}i = iR_{\frac{\pi}{3}(2n-1)}$ leaves the Barlow packing unchanged.

10.2.5 Quadratic forms/functions and corresponding lattice sums

Consider an inverse power potential (Riesz potential) of the form

$$\phi(r) = -\epsilon r^{-n}. \tag{10.26}$$

with $n > 3, n \in \mathbb{R}$[226]. If all lattice points (atoms) in a Bravais lattice interact through such a potential the cohesive energy becomes

$$E_{\text{coh}} = \epsilon \lim_{M\to\infty} \frac{1}{M} \sum_{i<j}^{M} \Delta r_{ij}^{-n} = \frac{\epsilon}{2} \lim_{M\to\infty} \frac{1}{M} \sum_{i\neq j}^{M} \Delta r_{ij}^{-n} = \frac{\epsilon}{2} \sum_{i\in\mathbb{N}} r_{0i}^{-n} \tag{10.27}$$

where Δr_{ij} is the distance between atom i and j. For the last sum we used translational symmetry for a Bravais lattice with an arbitrarily chosen origin at the position of one of the atoms in the lattice. We need to extend this formalism to the more general case of a multi-lattice for our Barlow packings.

Using the definitions in Eq. (10.21), we get for the distances between the different lattice points in the layers X_{k_1} and X_{k_2}

$$r(N,a,c,\vec{i},\vec{j},X_{k_1},X_{k_2}) = \left|\vec{r}^{X_{k_1}}(\vec{i}) - \vec{r}^{X_{k_2}}(\vec{j})\right| = \left|B_h^{\top}\left(\vec{i}-\vec{j}\right) + \left(\vec{v}^{X_{k_1}} - \vec{v}^{X_{k_2}}\right)\right| \tag{10.28}$$

$k_1, k_2 = 1, ..., N$ are the cardinal numbers for the individual layers. We have to consider 6 different cases for these distances, i.e. the cases $(X_{k_1}X_{k_2}) = (AA), (BB), (CC), (AB), (AC)$ and (BC),

$$r(x_i)= \begin{cases} \left|B^{h^{\top}}\left(\vec{i}-\vec{j}\right) + \left(0,0,\{k_1-k_2\}\frac{c}{N}\right)^{\top}\right| & \text{if } (X_{k_1}X_{k_2})=(AA),(BB) \text{ or } (CC) \\ \left|B^{h^{\top}}\left(\vec{i}-\vec{j}\right) + \left(\frac{a}{2},\frac{a}{2\sqrt{3}},\{k_1-k_2\}\frac{c}{N}\right)^{\top}\right| & \text{if } (X_{k_1}X_{k_2})=(AB) \\ \left|B^{h^{\top}}\left(\vec{i}-\vec{j}\right) + \left(\frac{a}{2},-\frac{a}{2\sqrt{3}},\{k_1-k_2\}\frac{c}{N}\right)^{\top}\right| & \text{if } (X_{k_1}X_{k_2})=(AC) \\ \left|B^{h^{\top}}\left(\vec{i}-\vec{j}\right) + \left(0,\frac{a}{\sqrt{3}},\{k_1-k_2\}\frac{c}{N}\right)^{\top}\right| & \text{if } (X_{k_1}X_{k_2})=(BC) \end{cases} \tag{10.29}$$

with $r(x_i) = r(N,a,c,\vec{i},\vec{j},X_{k_1},X_{k_2})$ and $k_2 > k_1$. We can now write for the cohesive energy

$$\begin{aligned} E_{\text{coh}} &= \frac{\epsilon}{2} \sum_{k_1,k_2=1}^{N} \lim_{M\to\infty} \frac{1}{M} \sum_{\vec{i},\vec{j}\in[-M,M]^3,\vec{i}\neq\vec{j}} r(N,a,c,\vec{i},\vec{j},X_{k_1},X_{k_2})^{-n} \\ &= \frac{\epsilon}{2} \sum_{k_1,k_2=1}^{N} \sum_{\vec{i}\in\mathbb{Z}^3} q(N,a,c,\vec{i},X_{k_1},X_{k_2})^{-n/2} \end{aligned} \tag{10.30}$$

where we used translational symmetry to obtain the last sum and used the abbreviation $q(N,a,c,\vec{i},X_{k_1},X_{k_2}) = r(N,a,c,\vec{i},\vec{0},X_{k_1},X_{k_2})^2$. This implies that we have to consider only the layers within the hexagonal unit cell as all interactions with the other layers are included in the lattice summation. It is convenient to separate out the diagonal terms in the k_1, k_2 summation,

$$E_{\text{coh}} = \frac{\epsilon}{2}\left(N \sum_{\vec{i}\in\mathbb{Z}^3}{}' Q(a,c,\vec{i})^{-s} + 2\sum_{k_1<k_2}^{N} \sum_{\vec{i}\in\mathbb{Z}^3} q(N,a,c,\vec{i},X_{k_1},X_{k_2})^{-s}\right) \tag{10.31}$$

and for convenience we introduced the notation $s = n/2$. We can now derive the quadratic form Q and quadratic function q for the different cases ($\gamma = c/a$),

$$Q(a,\gamma,\vec{i}) = \vec{i}^{\top} B^{h^{\top}} B^h \vec{i} = \vec{i}^{\top} G^h \vec{i} = a^2 \left(i_1^2 + i_1 i_2 + i_2^2 + \gamma^2 i_3^2 \right) \tag{10.32}$$

and

$$\begin{aligned} q(N,a,\gamma,\vec{i},X_{k_1},X_{k_2}) &= \left(\vec{i}^{\top} B^h + \left(\vec{w}^{X_{k_1}X_{k_2}} \right)^{\top} \right) \left(B^{h^{\top}} \vec{i} + \vec{w}^{X_{k_1}X_{k_2}} \right) \\ &= \left[\vec{i}^{\top} G^h \vec{i} + 2\vec{i}^{\top} B^h \vec{w}^{X_{k_1}X_{k_2}} + |\vec{w}^{X_{k_1}X_{k_2}}|^2 \right] \\ &= a^2 \left[\left(i_1 + \frac{1}{2} i_2 + \beta_1 \right)^2 + \left(\frac{\sqrt{3}}{2} i_2 + \beta_2 \right)^2 + \gamma^2 \left(i_3 + \frac{k_1 - k_2}{N} \right)^2 \right] \end{aligned} \tag{10.33}$$

where $\vec{w}^{X_{k_1}X_{k_2}} = \vec{v}^{X_{k_1}} - \vec{v}^{X_{k_2}}$, and according to Eq. (10.29) we have $\beta_1 = 0$ for the AA or BC sequence, $\beta_1 = \frac{1}{2}$ for AB or AC, $\beta_2 = 0$ for AA, $\beta_2 = \frac{1}{2\sqrt{3}}$ for AB, $\beta_2 = -\frac{1}{2\sqrt{3}}$ for AC, and $\beta_2 = \frac{1}{\sqrt{3}}$ for BC. The quadratic form with zero shift vector leads to the following definition of the lattice sum

$$L^A(s,\gamma) = a^{-2s} {\sum_{\vec{i}\in\mathbb{Z}^3}}' Q(a,\gamma,\vec{i})^{-s} = {\sum_{\vec{i}\in\mathbb{Z}^3}}' \left(i_1^2 + i_1 i_2 + i_2^2 + \gamma^2 i_3^2 \right)^{-s} \tag{10.34}$$

for which a rapidly converging series in terms of Bessel functions have already been provided for the hcp structure in one of our previous papers[294]. The prime notation for the sum indicates that we avoid the case $\vec{i} = \vec{0}$ in our summation. The two different fast converging expansions we are using are given in Appendix O.

For the more complicated lattice sums including the quadratic function we have

$$\begin{aligned} L^{X_{k_1}X_{k_2}}(s,r,\gamma) &= a^{-2s} \sum_{\vec{i}\in\mathbb{Z}^3} q(n,a,\gamma,\vec{i},X_{k_1},X_{k_2})^{-s} \\ &= \sum_{\vec{i}\in\mathbb{Z}^3} \left[\left(i_1 + \frac{1}{2} i_2 + \beta_1 \right)^2 + \left(\frac{\sqrt{3}}{2} i_2 + \beta_2 \right)^2 + \gamma^2 (i_3 + r)^2 \right]^{-s} \end{aligned} \tag{10.35}$$

with $\beta_1 = \beta_2 = 0$, AB or AC with $\beta_1 = \frac{1}{2}$ and $\beta_2 = \frac{1}{2\sqrt{3}}$, and BC with $\beta_1 = 0$ and $\beta_2 = \frac{1}{\sqrt{3}}$, and we have chosen $r = (k_2 - k_1)/N \in \mathbb{Q}, 0 < r < 1$ (not to be confused with the distance used above). One can show that because of symmetry the cases AA, BB and CC become identical for a fixed r value, so are the case AB, AC and BC. For example, as the summation index i_2 ranges over the integers, the sign of β_2 does not matter and the cases AB and AC become identical. A similar argument applies for β_1. That is we only have two cases to consider for the non-diagonal

($r > 0$) terms, AA and AB,

$$L^{AA}(s,r,\gamma) = \sum_{\vec{i}\in\mathbb{Z}^3} \left[i_1^2 + i_1 i_2 + i_2^2 + \gamma^2 \left(i_3 + r\right)^2 \right]^{-s} \tag{10.36}$$

and

$$L^{AB}(s,r,\gamma) = \sum_{\vec{i}\in\mathbb{Z}^3} \left[\left(i_1 + \frac{1}{3}\right)^2 + \left(i_1 + \frac{1}{3}\right)\left(i_2 + \frac{1}{3}\right) + \left(i_2 + \frac{1}{3}\right)^2 + \gamma^2 \left(i_3 + r\right)^2 \right]^{-s}. \tag{10.37}$$

The first lattice sum reduces to the quadratic form expression for $r = 0$ if we take care to remove the divergent term in the summation, which is discussed in more detail in the Appendix O. Further, we do not need to calculate all terms of the Barlow lattice sum as we have the symmetry conditions

$$\begin{aligned} L^{AA}(s,r,\gamma) &= L^{AA}(s,1-r,\gamma) \\ L^{AB}(s,r,\gamma) &= L^{AB}(s,1-r,\gamma) \end{aligned} \tag{10.38}$$

because the summation in (10.36) and (10.37) is over $i_3 \in \mathbb{Z}$.

For the total lattice sum of a Barlow packing we have

$$E_{\text{coh}} = \frac{\epsilon}{2a^{2s}} \left(N L^{A}(s,\gamma) + 2 \sum_{1\le k_1 < k_2 \le N} L^{X_{k_1} X_{k_2}}(s,r,\gamma) \right) \tag{10.39}$$

We redefine the cohesive energy in terms of per atom (layer) in the unit cell,

$$E_{\text{coh}} = \frac{1}{N} E_{\text{coh}} = \frac{\epsilon}{2a^{2s}} L^{\boldsymbol{X}}(N,s,\gamma) = \frac{\alpha}{2a^{2s}} \left\{ L^{A}(s,\gamma) + \frac{2}{N} \sum_{1\le k_1 < k_2 \le N} L_q^{X_{k_1} X_{k_2}}(s,r,\gamma) \right\} \tag{10.40}$$

where we call $L^{\boldsymbol{X}}(N,s,\gamma)$ the Barlow lattice sum. The limits $\lim_{s\to\infty} L^{AA}(s,r,\gamma)$ and $\lim_{s\to\infty} L^{AB}(s,r,\gamma)$ are discussed in detail in Appendix M.

10.2.6 hcp and fcc as special cases

For hcp (AB) we have $N = 2$ and the second term becomes,

$$L^{AB}(s,\gamma) = \sum_{\vec{i}\in\mathbb{Z}^3} \left[\left(i_1 + \tfrac{1}{3}\right)^2 + \left(i_1 + \tfrac{1}{3}\right)\left(i_2 + \tfrac{1}{3}\right) + \left(i_2 + \tfrac{1}{3}\right)^2 + \gamma^2 \left(i_3 + \tfrac{1}{2}\right)^2 \right]^{-s}. \tag{10.41}$$

We therefore have

$$L^{\mathrm{hcp}}(s,\gamma) = {\sum_{\vec{i}\in\mathbb{Z}^3}}' \left(i_1^2 + i_1 i_2 + i_2^2 + \gamma^2 i_3^2\right)^{-s} + \sum_{\vec{i}\in\mathbb{Z}^3} \left[\left(i_1+\tfrac{1}{3}\right)^2 + \left(i_1+\tfrac{1}{3}\right)\left(i_2+\tfrac{1}{3}\right) + \left(i_2+\tfrac{1}{3}\right)^2 + \gamma^2\left(i_3+\tfrac{1}{2}\right)^2 \right]^{-s} \tag{10.42}$$

For the densest sphere packing we have $\gamma = 2\times\sqrt{\frac{2}{3}} = \sqrt{\frac{8}{3}}$. The formula is identical to the one given in Refs.[294,437].

For fcc, (ABC), we have $N = 3$ and the lattice sum in the second term in (10.40) becomes,

$$L^{AB}(s,\gamma) = \sum_{\vec{i}\in\mathbb{Z}^3} \left[\left(i_1+\tfrac{1}{3}\right)^2 + \left(i_1+\tfrac{1}{3}\right)\left(i_2+\tfrac{1}{3}\right) + \left(i_2+\tfrac{1}{3}\right)^2 + \gamma^2\left(i_3+\tfrac{1}{3}\right)^2 \right]^{-s} \tag{10.43}$$

and we have

$$L^{\mathrm{fcc}}(s,\gamma) = {\sum_{\vec{i}\in\mathbb{Z}^3}}' \left(i_1^2 + i_1 i_2 + i_2^2 + \gamma^2 i_3^2\right)^{-s} + \frac{2}{3}\sum_{\vec{i}\in\mathbb{Z}^3} \left[\left(i_1+\tfrac{1}{3}\right)^2 + \left(i_1+\tfrac{1}{3}\right)\left(i_2+\tfrac{1}{3}\right) + \left(i_2+\tfrac{1}{3}\right)^2 + \gamma^2\left(i_3+\tfrac{1}{3}\right)^2 \right]^{-s} \tag{10.44}$$

and we have used Eq. (10.38), i.e. $L^{AB}(s,\frac{1}{3},\gamma) = L^{AB}(s,\frac{2}{3},\gamma)$. The similarity between the two lattice sums hcp and fcc is obvious. For the densest sphere packing we have $\gamma = 3\times\sqrt{\frac{2}{3}} = \sqrt{6}$ The fcc lattice sum is different compared to the ones derived in Ref. 295, for example in[297] one has

$$L^{\mathrm{fcc}}(s,\gamma) = 2^{\frac{s}{2}-1} {\sum_{\vec{i}\in\mathbb{Z}^3}}' \left[1 + (-1)^{i+j+k}\right] \left(i_1^2 + i_2^2 + i_3^2\right)^{-s} \tag{10.45}$$

which is computationally more efficient, but leads to the identical result of course.

10.3 Results and Discussions

The basic properties for the different Barlow sequences are listed in Table 10.2 for periods up to $N = 10$ and two selected examples for $N = 11$ and $N = 12$. The corresponding lattice sums as a difference to the reference hcp structure at a fixed hard-sphere value of $\gamma = \sqrt{\frac{2}{3}}N$ are shown in Figure 10.4 (up to $N = 12$) for selected integer exponents s, and are collected in Table 10.4 for up to $N = 10$. More information can be found in an excel sheet of the supporting information.

The cohesive energies for the SHS model (10.1) are directly related to the lattice sums as

Table 10.4: Unique Barlow sequences (AB...) ordered according to their natural stacking sequence numbers (p_i) (see Table 10.2) and lattice sums $(L^X(s,\gamma) - 12)$ (for fixed $\gamma = \sqrt{\frac{2}{3}N}$). Last digit is rounded.

No.	Stacking	$s = 2$	$s = 3$	$s = 4$	$s = 6$	$s = 10$	$s = 15$
1	(AB)	1.3339082338055e1	2.4548972778416e0	8.0282185280990e-1	1.3229376909892e-1	6.3091581146587e-3	1.8522285178827e-4
2	(ABC)	1.3338304305130e1	2.4539210437445e0	8.0193723137813e-1	1.3188019654458e-1	6.2800413263427e-3	1.8479005982120e-4
3	(ABAC)	1.3338692760904e1	2.4544087098975e0	8.0237928685684e-1	1.3208693956631e-1	6.2945994125031e-3	1.8500645562560e-4
4	(ABABC)	1.3338615292863e1	2.4543113563384e0	8.0229097757393e-1	1.3204560823994e-1	6.2916879184319e-3	1.8496317653637e-4
5	(ABABAC)	1.3338822619307e1	2.4545715654964e0	8.0252680868420e-1	1.3215588273038e-1	6.2994523132004e-3	1.8507858767982e-4
6	(ABACBC)	1.3338563274999e1	2.4542461541307e0	8.0223193487361e-1	1.3201802521227e-1	6.2897467170951e-3	1.8493432369080e-4
7	(ABABABC)	1.3338748734346e1	2.4544787624819e0	8.0244265621270e-1	1.3211651134250e-1	6.2966794030681e-3	1.8503736946549e-4
8	(ABABCBC)	1.3338748573595e1	2.4544786333268e0	8.0244258315322e-1	1.3211649897226e-1	6.2966793150506e-3	1.8503736941430e-4
9	(ABACABC)	1.3338526279582e1	2.4541997099542e0	8.0218983444170e-1	1.3199833540838e-1	6.2883602327110e-3	1.8491371456657e-4
10	(ABABABAC)	1.3338887548994e1	2.4546529935827e0	8.0260056971562e-1	1.3219035432252e-1	6.3018787635650e-3	1.8511465370694e-4
11	(ABABACAC)	1.3338887548509e1	2.4546529932958e0	8.0260056959787e-1	1.3219035431242e-1	6.3018787635491e-3	1.8511465370693e-4
12	(ABABACBC)	1.3338693040279e1	2.4544089347720e0	8.0237941424007e-1	1.3208696117384e-1	6.2945995664701e-3	1.8500645571517e-4
13	(ABABCBAC)	1.3338692900349e1	2.4544088221913e0	8.0237935048958e-1	1.3208695036503e-1	6.2945994894786e-3	1.8500645567038e-4
14	(ABABCABC)	1.3338498672463e1	2.4541649891157e0	8.0215832275051e-1	1.3198357885418e-1	6.2873204463984e-3	1.8489825776818e-4
15	(ABACBABC)	1.3338498532534e1	2.4541648765350e0	8.0215825900002e-1	1.3198356804536e-1	6.2873203694070e-3	1.8489825772340e-4
16	(ABABABABC)	1.3338822868504e1	2.4545717658952e0	8.0252692212319e-1	1.3215590195504e-1	6.2994524500882e-3	1.8507858775944e-4
17	(ABABABCBC)	1.3338822743474e1	2.4545716654410e0	8.0252686529909e-1	1.3215589233374e-1	6.2994523816302e-3	1.8507858771963e-4
18	(ABABCBCAC)	1.3338822618661e1	2.4545715651145e0	8.0252680852738e-1	1.3215588271693e-1	6.2994523131792e-3	1.8507858767982e-4
19	(ABABACABC)	1.3338649847700e1	2.4543547247855e0	8.0233028286336e-1	1.3206398733064e-1	6.2929819842408e-3	1.8498241172695e-4
20	(ABABCBABC)	1.3338649723103e1	2.4543546245867e0	8.0233022614405e-1	1.3206397771832e-1	6.2929819157969e-3	1.8498241168714e-4
21	(ABABCACBC)	1.3338649722887e1	2.4543546244590e0	8.0233022609166e-1	1.3206397771383e-1	6.2929819157898e-3	1.8498241168714e-4
22	(ABACBCABC)	1.3338476951710e1	2.4541377840023e0	8.0213370037524e-1	1.3197208232305e-1	6.2865115868443e-3	1.8488623573426e-4
23	(ABABABABAC)	1.3338926506806e1	2.4547018504345e0	8.0264482633448e-1	1.3221103727780e-1	6.3033346337837e-3	1.8513629332320e-4
24	(ABABABACAC)	1.3338926506418e1	2.4547018502050e0	8.0264482624028e-1	1.3221103726972e-1	6.3033346337710e-3	1.8513629332320e-4
25	(ABABABACBC)	1.3338770899834e1	2.4545066033859e0	8.0246790195404e-1	1.3212832275886e-1	6.2975112761078e-3	1.8504973492979e-4
26	(ABABABCBAC)	1.3338770787890e1	2.4545065133212e0	8.0246785095359e-1	1.3212831411180e-1	6.2975112145146e-3	1.8504973489396e-4
27	(ABABACACBC)	1.3338770787502e1	2.4545065130921e0	8.0246785085950e-1	1.3212831410373e-1	6.2975112145019e-3	1.8504973489396e-4
28	(ABABACABAC)	1.3338770675946e1	2.4545064232568e0	8.0246779995325e-1	1.3212830546475e-1	6.2975111529215e-3	1.8504973485813e-4
29	(ABABACBCBC)	1.3338770899446e1	2.4545066031568e0	8.0246790185995e-1	1.3212832275079e-1	6.2975112760951e-3	1.8504973492979e-4
30	(ABABCBABAC)	1.3338770675559e1	2.4545064230277e0	8.0246779985917e-1	1.3212830545668e-1	6.2975111529088e-3	1.8504973485813e-4
31	(ABABABCABC)	1.3338615405581e1	2.4543114468607e0	8.0229102876233e-1	1.3204561690312e-1	6.2916879800505e-3	1.8496317657220e-4
32	(ABABACBABC)	1.3338615293250e1	2.4543113565672e0	8.0229097766791e-1	1.3204560824800e-1	6.2916879184446e-3	1.8496317653637e-4
33	(ABABCBCABC)	1.3338615293056e1	2.4543113564524e0	8,0229097762081e-1	1.3204560824396e-1	6.2916879184382e-3	1.8496317653637e-4
34	(ABABCBACBC)	1.3338615181116e1	2.4543112663877e0	8.0229092662036e-1	1.3204559959691e-1	6.2916878568451e-3	1.8496317650054e-4
35	(ABABCACABC)	1.3338615292863e1	2.4543113563380e0	8.0229097757382e-1	1.3204560823993e-1	6.2916879184319e-3	1.8496317653637e-4
36	(ABACABACBC)	1.3338615069361e1	2.4543111764374e0	8.0229087566690e-1	1.3204559095389e-1	6.2916877952583e-3	1.8496317646472e-4
37	(ABACABCABC)	1.3338459687246e1	2.4541161100913e0	8.0211405352263e-1	1.3196289374924e-1	6.2858645608005e-3	1.8487661814296e-4
38	(ABACBACABC)	1.3338459687053e1	2.4541161099769e0	8.0211405347564e-1	1.3196289374521e-1	6.2858645607941e-3	1.8487661814296e-4
39	(ABABABABABC)	1.3338870044786e1	2.4546309498854e0	8.0258054588441e-1	1.3218096870847e-1	6.3012171163738e-3	1.8510481758286e-4
40	(ABABABABABAC)	1.3338952478681e1	2.4547344216690e0	8.0267433074705e-1	1.3222482591465e-1	6.3043052139296e-3	1.8515071973404e-4

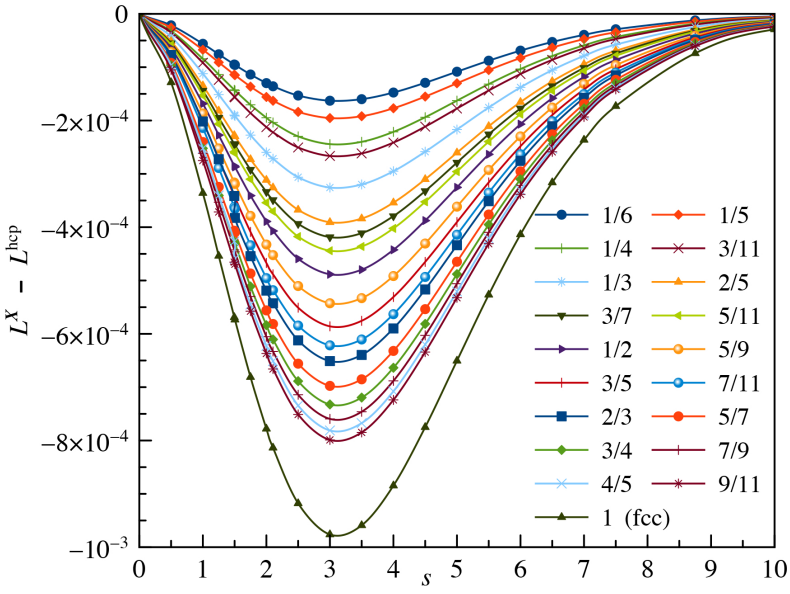

Figure 10.4: Difference of Lattice sums $L^{\boldsymbol{X}}(s,\gamma) - L^{\mathrm{hcp}}(s,\gamma)$ between a Barlow packing of a specific fcc packing fraction $\alpha(2) = p/q$ and the hcp structure ($\alpha(2) = 0$) as a function of the exponent s (analytically continued to $s = 0$). $\gamma_0 = \sqrt{2/3}$ is fixed at the hard-sphere limit. Different Barlow packings with the same $\alpha(2)$ value are indistinguishable on this graph, see discussion in main text.

shown in eq.(10.2). We can therefore restrict our discussion to the lattice sums for the moment. These all show a very similar behavior with a minimum around $s = 3$ ($n = 6$), and deviate from the hcp lattice sum at most by 10^{-3}. This already indicates that the difference in cohesive energies (10.30) between the different Barlow structures will be quite small. In fact, we see a linear behavior for the lattice sums for a chosen exponent s with respect to the fcc packing fraction $\alpha(2)$, cf. Figure 10.5(a), with hcp and fcc being the two limiting cases. This linear behavior can be well understood from the interactions between the next nearest hexagonal closed-packed layers, which is analyzed in detail in Appendix N. The analytical continuation beyond the pole at $s = 1.5$ has already been discussed in detail for the hcp structure[294]. We only mention here that $\lim_{s\to 1.5^-} L^{\boldsymbol{X}}(s) = -\infty$ and $\lim_{s\to 1.5^+} L^{\boldsymbol{X}}(s) = +\infty$ and $L^{\boldsymbol{X}}(s = 0) = -1$ for all Barlow packings ($\gamma_0 = \sqrt{2/3}$). However, the difference $L^{\boldsymbol{X}}(s,\gamma) - L^{\mathrm{hcp}}(s,\gamma)$ has a removable singularity at $s = \frac{3}{2}$ and therefore is analytic (and hence smooth) for all positive real values of s as illustrated in Figure 10.5. Because of the change of sign at the pole the region $s \leq 3$ is not physically relevant[294] in contrast to the interaction of opposite charges through a Coulomb r^{-1} potential for which the Madelung potential has a physical interpretation[572].

Interestingly, the lattice sums with the same packing fraction $\alpha^{\boldsymbol{X}}(2)$ and period N differ only minutely from each other, see Figure 10.5(b). In fact, all Barlow lattice sums lie very close to a straight line, and to high accuracy (root mean square error RMS = 2.36×10^{-7} for $s = 3$ for

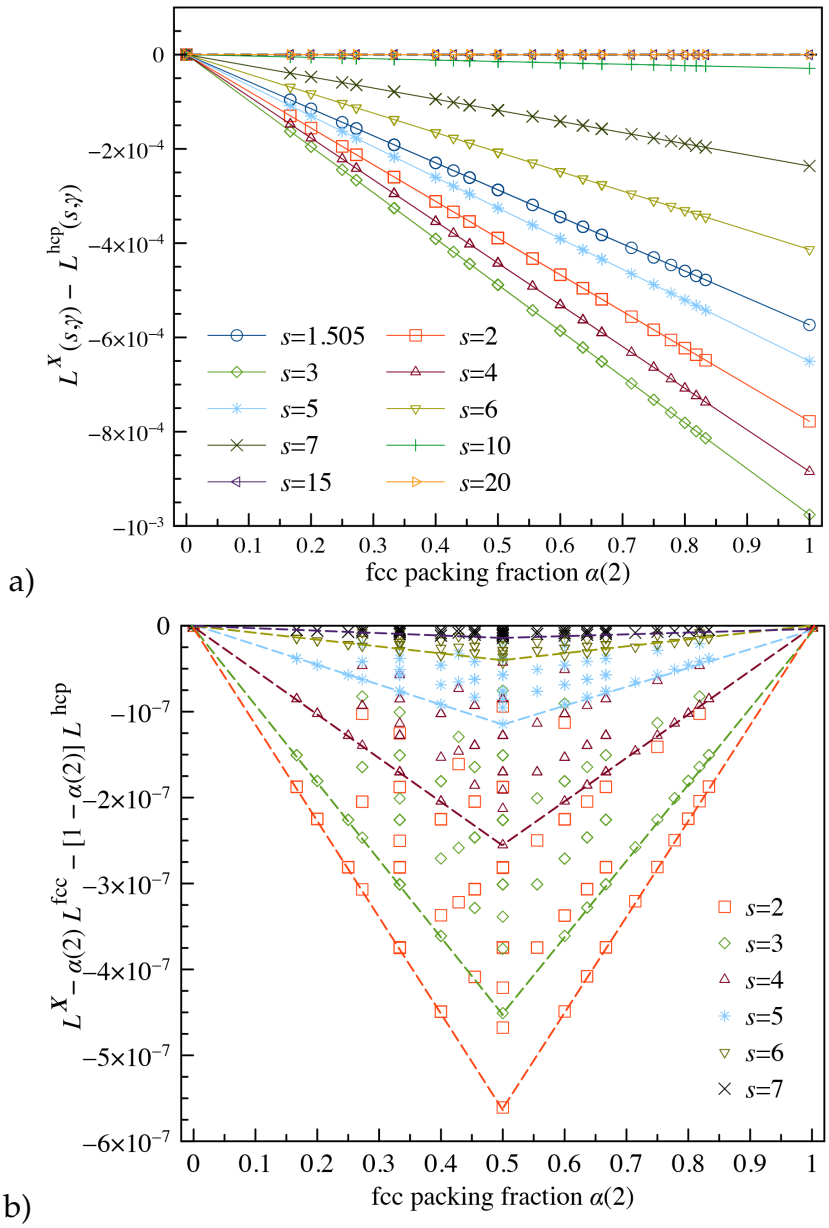

Figure 10.5: (a) Difference between lattice sums of Barlow packings with respect to the hcp structure ($\alpha(2) = 0$) as a function of the fcc packing fraction $\alpha(2)$ for various s values. γ_0 is set to $\sqrt{2/3}$. (b) Deviation of lattice sum differences $\Delta_\alpha L^X(s,\gamma)$ from the ideal line for Barlow packings for various exponents s as defined in Eq.(10.47).

example) can be represented by

$$L^X(s,\gamma) = L^{hcp}(s,\gamma) + \alpha^X(2)\left[L^{fcc}(s,\gamma) - L^{hcp}(s,\gamma)\right] \tag{10.46}$$

with $\gamma = \sqrt{\frac{2}{3}}N$. If we define the difference from the linear behavior as

$$\Delta_\alpha L^X(s,\gamma) = L^X(s,\gamma) - L^{hcp}(s,\gamma) - \alpha^X(2)\left[L^{fcc}(s,\gamma) - L^{hcp}(s,\gamma)\right] \tag{10.47}$$

we see an interesting pattern arising with respect to the fcc packing fraction, i.e. these differences $\Delta_\alpha L^X(s,\gamma)$ lie approximately within a triangle as shown in Figure 10.5(b). A detailed analysis of this feature can be found in Appendix N. Figure 10.6 shows that the maximum deviation from the ideal linear behavior is obtained for the $ABAC$ Barlow sequence. Further, for $s = 2.04327799$ we see the largest deviation ($-5.60992314 \times 10^{-7}$) for this sequence.

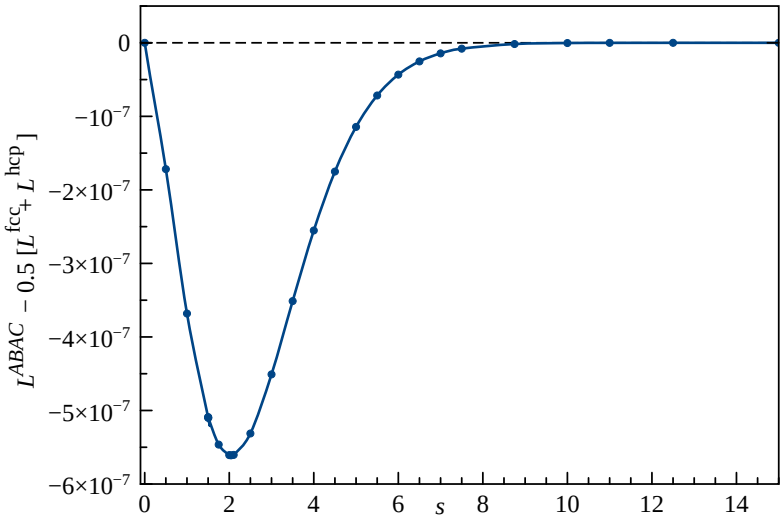

Figure 10.6: Deviation of lattice sum differences $\Delta_\alpha L^X(s,\gamma)$ from the ideal line for the Barlow sequence $ABAC$ as a function of the exponent s.

Translating this into the cohesive energies as defined in eq.(10.2) we see that $E_{\rm coh}^{\rm hcp}(s) > E_{\rm coh}^{\mathbf{X}}(s,\alpha)$ for all $\alpha > 0$, that is within the SHS model with an attractive inverse power potential the hcp structure is preferred with fcc being the least stable one. All Barlow packings lie energetically in between the hcp and fcc structures, and according to eq.(10.46) have approximately a linear behaviour with respect to the packing fraction α. From Figure 10.5(b) we see that $L^X(s,\gamma) \leq L^{\rm hcp}(s,\gamma) + \alpha^X(2)\left[L^{\rm fcc}(s,\gamma) - L^{\rm hcp}(s,\gamma)\right]$, with the equal sign being valid only within the KHS limit for which we have $E_{\rm coh} = 6$ for all Barlow packings, i.e. there are no differences in cohesive energies in this limit, see Figure 10.6. However, for finite exponents s the Barlow packings are destabilized by a tiny energy amount (a few 10^{-7} in reduced units) compared to the linear behavior expressed in eq.(10.46).

For the free energy difference between Barlow packings one has to include entropy and pressure effects. However, in our SHS model the PV term cancels out for free energy differences at low temperatures as the volume remains constant at the ideal dense packing value (10.24) at pressures $P > 0$. Mau and Huse investigated the entropy of hard-sphere crystals using Monte-Carlo simulations with periodic boundary conditions and different packing densities.[439] Their results were fitted to an Ising-type layer-coupling model for the entropy

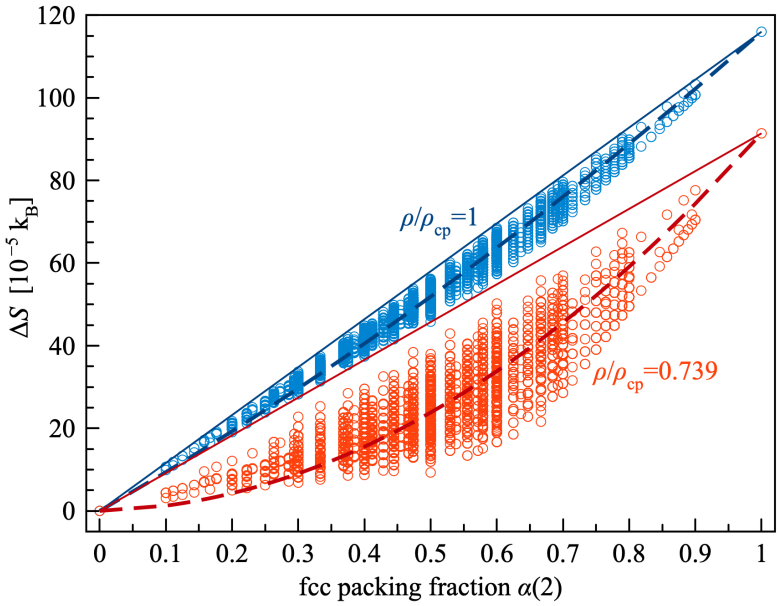

Figure 10.7: Stacking entropy differences of Barlow packings up to $N = 20$ with respect to the hcp structure, $\Delta S(\alpha) = S(\alpha) - S(0)$, as a function of the fcc packing fraction $\alpha(2)$. In blue the entropies in the close packing limit ($\rho/\rho_{cp} = 1$), and in red entropies at a density near melting ($\rho/\rho_{cp} = 0.739$). The linear line connecting the fcc and hcp structure is given as a solid line, the parabolic fit as a dashed line.

(per atom),

$$S = S_0 + \frac{h}{N}\sum_{i=1}^{N}\sigma_i + \frac{J}{N}\sum_{i=1}^{N}\sigma_i\sigma_{i+1} + \frac{J'}{N}\sum_{i=1}^{N}\sigma_i\sigma_{i+2} + \frac{h'}{N}\sum_{i=1}^{N}\sigma_i\sigma_{i+1}\sigma_{i+2} \tag{10.48}$$

with $\sigma_i = 1$ if for the layer sequence $\bar{p}(i,2) = 0$ and $\sigma_i = -1$ if for the layer sequence $\bar{p}(i,2) = 1$. We can therefore identify the "spin" parameter with our fcc packing sequence by setting $\sigma_i = (-1)^{\bar{p}(i,2)+1}$. S_0 is a constant independent of the layer sequence and cancels out in entropy differences between Barlow packings.

Using their fitting parameters for the close packing limit ($\rho/\rho_{cp} = 1$ with ρ_{cp} being the close packing density), i.e. $h = 54.6$, $J = 6.1$, $J' = -0.3$ and $h' = 3.4$ (in units of $10^{-5}\,k_B$), we calculated the entropy for a set of in total 9,939 Barlow packings (up to period $N = 20$) and plotted the results against the fcc packing fraction $\alpha(2)$ as shown in Figure 10.7. The entropy differences with respect to the hcp structure for a selection of Barlow sequences are listed in Table 10.2. Within this hard-sphere model and the density used, the hcp structure has the lowest and fcc the highest entropy with a entropy difference of about $\Delta S_{\max} = 115(4) \times 10^{-5}\,k_B$ as pointed out by Mau and Huse.[439] Hence, at higher temperatures fcc becomes the dominant phase within the set of Barlow structures.

In the close packing limit we have $h \gg J$, resulting in an almost linear correlation, with the Barlow entropies falling in between the extreme values of fcc and hcp. In this case the

shortest-range entropic interactions are the strongest, meaning that the interactions with the directly neighboring layers contribute the most. The deviation from linearity can be included by a parabolic fit leading to the simple $\alpha(2)$-dependence

$$\Delta S(\alpha(2)) = c\alpha(2)^2 + (\Delta S_{\max} - c)\alpha(2) \tag{10.49}$$

with $c = 24.55(8) \times 10^{-5}$ k_B, see Figure 10.7. However, at reduced densities the entropic contributions are not as linearly correlated anymore as in the hard-sphere limit, that is, non-next neighbor corrections become much larger. In fact, at a density close to the melting limit of $\rho/\rho_{cp} = 0.739$, the fitting parameters change to $h = 36.9$, $J = 18.2$, $J' = 2.5$ and $h' = 8.8$ (in units of $10^{-5}k_B$) and we get $\Delta S_{\max} = 91.4(4.3) \times 10^{-5}$ k_B. In this case, the relative magnitude of the entropic interactions with distance decrease much more slowly,[439] resulting in a lesser linear correlation and a larger spread in the entropies at specific $\alpha(2)$ values as shown in Figure 10.7, which somehow reflects the histogram as shown in Figure 10.2. Here the parabolic fit gives $c = 87.58(21) \times 10^{-5}$ k_B with an almost negligible linear term. At lower densities (higher temperatures) the entropy difference $\Delta S(\alpha(2))$ of the Barlow packings are substantially decreased. As a result, in the region of temperature where the entropic contribution to the free energy dominates, the Barlow packings are less likely to be stabilized within the hard-sphere model (remember, within the KHS model all the Barlow packings have the same internal energy). However, a more realistic interaction model requires the proper treatment of vibrational effects from phonon dispersion, which is the major contribution for the entropy at low temperatures. Moreover, for a (12,6)-Lennard-Jones potential the bcc phase becomes dominant near the solid-liquid phase line[110] in agreement with Landau theory.[252]

In conclusion, we studied the properties and derived important lattice sums for inverse power potentials for periodic Barlow packings used within a SHS model. Both the internal energy and the entropy differences of periodic Barlow packings with respect to hcp lie in between the two extreme points of hcp and fcc,[429] which is perhaps a more general feature in solid-state properties of Barlow packings. Internal energy favors hcp while entropy favors fcc. While this paper focused more on the theory part, in forthcoming more detailed studies we focus on various solid-state properties of periodic Barlow packings at finite pressures and temperatures using Lennard-Jones interaction potentials and density functional theory. Some preliminary results for Lennard-Jones systems have already been published.[227,429]

MASSEY UNIVERSITY
TE KUNENGA KI PŪREHUROA
UNIVERSITY OF NEW ZEALAND

GRADUATE RESEARCH SCHOOL

STATEMENT OF CONTRIBUTION
DOCTORATE WITH PUBLICATIONS/MANUSCRIPTS

We, the student and the student's main supervisor, certify that all co-authors have consented to their work being included in the thesis and they have accepted the student's contribution as indicated below in the Statement of Originality.			
Student name:	Andres Eduardo Robles Navarro		
Name and title of main supervisor:	Peter Schwerdtfeger		
In which chapter is the manuscript/published work?	Chapter 11		
Describe the contribution that the student and members of the supervisory team have made to the manuscript/published work:[1] All the computations were performed by me. The theoretical development of the publication is equally divided between me, Shaun Cooper, and Peter Schwerdtfeger. Alex Travesset has contributed with discussions and code on the entropy section of LJ systems.			
Please select one of the following three options:			
○	The manuscript/published work is published or in press Please provide the full reference of the research output:		
○	The manuscript is currently under review for publication Please provide the name of the journal:		
◉	It is intended that the manuscript will be published, but it has not yet been submitted to a journal		
Student's signature:	ARoblesNavarro	Main supervisor's signature:	PeterSchwerdtfeger Digitally signed by PeterSchwerdtfeger Date: 2025.12.08 14:22:46 +13'00'
This form should be placed at the beginning of each relevant thesis chapter.			

[1] Refer to the Massey University Publishing and Authorship guidelines (OneMassey for staff, Stream for students) and/ or Contributor Roles Taxonomy (CRediT) guidelines for guidance.

Chapter 11

The Theory of Barlow Packings II: Application to Lennard-Jones Solids and Metallic Lithium

11.1 Introduction

A Barlow packing[18,146] is an infinite stacking of two-dimensional hexagonal close packed layers X_i with stacking sequence $(X_1X_2X_3...)$, where $X_i = A, B, C$ being one of the three possible densely packed hexagonal layers distinguished by location such that we do not have identical neighboring layers, i.e. $(X_iX_{i+1}) \neq AA$ or BB or CC $(i \in \mathbb{N})$, see Figure 11.1. There are infinitely many Barlow packings and all have the same maximum packing density of $\rho = \pi/3\sqrt{2}$=0.74048...[18,401,563], which for hard (non-overlapping) spheres cannot be surpassed[10,403]. Some general concepts of lattice theory for Barlow packings can be found in Refs. 139,377,401,553,573.

Apart from the two most common densest packings, i.e. the hexagonal close packing (hcp), $(AB)_\infty$, and the face-centered close packing (fcc), $(ABC)_\infty$, Barlow structures are extremely rare[74,75,79,435,550,574,575] and are sometimes referred to as dense packings with stacking faults[576]. For example, the low temperature phase of lithium was proposed to be of close-packed rhombohedral (9R)[74,75] with a $(ABABCBCAC)_\infty$ stacking sequence of hexagonal layers (in the natural notation[377]), see Figure 11.1, but this was challenged recently by Ackland to be fcc instead[79] and supported by recent density functional calculations for the Burgers phase transition[431]. The prime example of a non-typical densest packing is the paramagnetic α-Sm 9R room-temperature phase[574,575], which transforms into hcp at 731^{o}C[577]. In this case the double hexagonal cole packing (dhcp) with sequence $ABAC$ has also been observed[577], which shows the transient character of Sm. There are few other materials adopting unusual Barlow structures[550]. The 9R structure appears also as a transitional phase in metals and

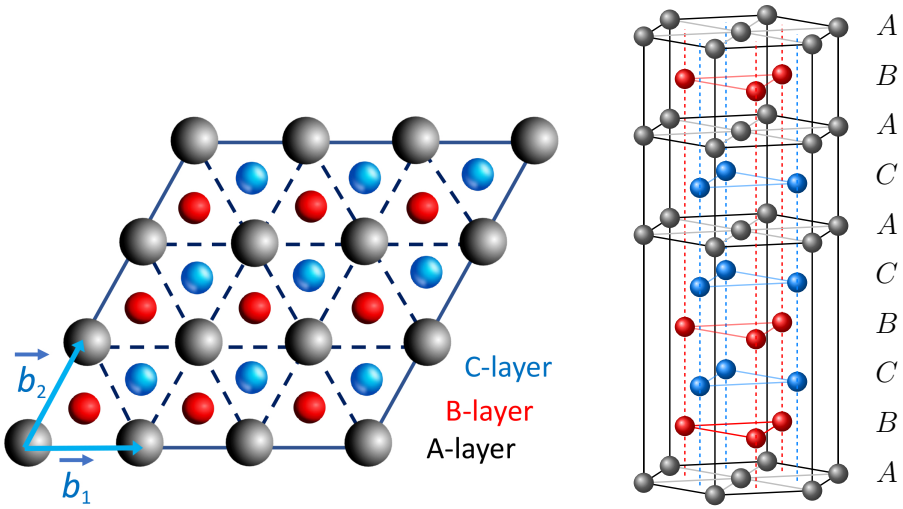

Figure 11.1: Left: The three possible layers A, B and C in Barlow packings. Right: The 9R structure with a sequence of $(ABCBCACAB)_\infty$ observed for example for samarium at room temperature[574,575] and metallic lithium at 75K[75]. The last layer at the top of the R9 structure belongs to the next unit cell with the same layer sequence.

high-entropy alloys[420,578]. It is, however, generally not known why fcc and hcp are so dominant out of the infinite many Barlow packing possibilities. Preliminary work in our group suggests that both fcc and hcp are extremal cases in the stability sequence of all Barlow packings.[429]

The theory behind Barlow packings has been studied by several groups in the past[377,435,553,563,573,579]. In a recent paper we presented a rigorous mathematical analysis for periodically repeating Barlow sequences of the form $(X_1X_2...X_N)_\infty$, and introduced an efficient algorithm and Fortran program[377] to create such stacking sequences up to a computationally feasible periodicity N. In this paper we further develop the theory of Barlow packings considering symmetry breaking effects, and analyze in detail the energetics and thermodynamics of such packings for the case of a general (n,m) Lennard-Jones (LJ) potential,[112,222,296]

$$V_{\rm LJ}(r) = \frac{\epsilon n m}{n-m}\left[\frac{1}{n}\left(\frac{r_e}{r}\right)^n - \frac{1}{m}\left(\frac{r_e}{r}\right)^m\right], \tag{11.1}$$

with $n > m$. Here, ϵ and r_e are the binding energy and the equilibrium distance of the diatomic respectively, which both can be set arbitrarily to 1 using dimensionless units. As the energy differences between the different Barlow packings are expected to very small ($\sim 10^{-5}$ eV)[104,377], we derive fast converging lattice sums in terms of Bessel function expansions for the accurate determination of the long-range part in the interactions to obtain the cohesive energy to computer precision[111,227,295].

11.2 Theory

11.2.1 Barlow packings

A detailed account on the theory of Barlow packings can be found in our previous work[377]. We only repeat the most important features required for this paper.

A Barlow packing is defined as a bi-infinite sequence $(\ldots, X_{-2}, X_{-1}, X_0, X_1, X_2, X_3, \ldots)$ with the condition that

$$X_i \in \{A, B, C\} \quad \text{and} \quad X_i \neq X_{i+1} \quad \text{for all} \quad i \in \mathbb{Z}. \tag{11.2}$$

The infinite Barlow sequence is said periodic with period $N \geq 2$ if

$$X_{i+N} = X_i \quad \text{for all } i \in \mathbb{Z}. \tag{11.3}$$

Without loss of generality, we can set $X_1 = A$, $X_2 = B$, and $X_N = C$[377]. Further, we assume that the period N is minimal, i.e. N is the smallest positive integer for which (11.3) holds. The most commonly observed Barlow packings are the hexagonal close packed structure of period 2, (AB), and the face centred cubic packing lattice of period 3, (ABC), and we understand that the letters in parentheses are periodically continued at the left and right to infinity, i.e. $(ABC) \equiv (ABC)_\infty$.

We define the packing fraction $\alpha(\ell)$ by

$$\alpha(\ell) = \frac{1}{N} \sum_{i=1}^{N} \left[1 - p(i, \ell)\right]. \tag{11.4}$$

with $1 \leq i, \ell \leq N$, which measures the fcc packing fraction identical to the one used by Middlemas et al[435]. Here, $p(i, \ell)$ are the packing sequence numbers defined by

$$p(i, \ell) = \begin{cases} 1 & \text{if} \quad X_i = X_{i+\ell}, \\ 0 & \text{if} \quad X_i \neq X_{i+\ell} \end{cases} \tag{11.5}$$

Next we define the natural sequence by

$$\{p_i^{'}\} = \{p_i\} \text{ with } \quad \max\{N_c = \sum_{i=0}^{N} 2^i p(i, 2) \quad \forall \text{ left or right cycle } \{p(i, 2)\}\} \tag{11.6}$$

For example, for the 9R structure[74] ($N = 9$) we get the sequence $(ABABCBCAC)$ with packing fraction $\alpha(2) = \frac{1}{3}$. An efficient algorithm to produce all non-isomorphic Barlow structures for the exponentially growing numbers of sequences can be found in Ref. 377.

11.2.2 Lattice constants and sums

The generator matrix for the underlying hexagonal Bravais lattice of a Barlow packing of period N may be defined as[377],

$$B = \begin{pmatrix} \vec{b}_1^{\top} \\ \vec{b}_2^{\top} \\ \vec{b}_3^{\top} \end{pmatrix} = a \begin{pmatrix} 1 & 0 & 0 \\ \frac{1}{2} & \frac{\sqrt{3}}{2} & 0 \\ 0 & 0 & \gamma_T \end{pmatrix} \tag{11.7}$$

where $\gamma_T = \frac{c}{a}$. Here the lattice basis vectors and parameters are defined by $|\vec{b}_1| = |\vec{b}_2| = a$ and $|\vec{b}_3| = c$, and $\angle(\vec{b}_1, \vec{b}_2) = 60^o$ and $\angle(\vec{b}_1, \vec{b}_3) = \angle(\vec{b}_2, \vec{b}_3) = 90^o$. The corresponding positive definite and symmetric Gram matrix then becomes,

$$G = BB^{\top} = a^2 \begin{pmatrix} 1 & \frac{1}{2} & 0 \\ \frac{1}{2} & 1 & 0 \\ 0 & 0 & \gamma_T^2 \end{pmatrix} \tag{11.8}$$

with $\det(G) = \frac{3}{4}a^4c^2 = \frac{3}{4}a^6\gamma_T^2 > 0$. From an arbitrarily chosen lattice point as the origin we obtain all other lattice points in the hexagonal lattice from,

$$\vec{r}(\vec{i}) = B^{\top}\vec{i} = i_1\vec{b}_1 + i_2\vec{b}_2 + i_3\vec{b}_3 \tag{11.9}$$

with $\vec{i} \in \mathbb{Z}^3$ with their distances from the origin given by the quadratic form

$$|\vec{r}(\vec{i})| = \left(\vec{i}^{\top} G \vec{i}\right)^{\frac{1}{2}} = a\left(i_1^2 + i_1 i_2 + i_2^2 + \gamma_T^2 i_3^2\right)^{\frac{1}{2}} . \tag{11.10}$$

The volume is determined through the generator or Gram matrix

$$V(a, \gamma) = \det B = \sqrt{\det G} = \frac{\sqrt{3}}{2}a^2c = \frac{\sqrt{3}}{2}a^3\gamma_T \tag{11.11}$$

The Barlow packing is a multi-lattice, and the atoms at different Wyckoff positions in the hexagonal layers $X_1, X_2, ..., X_N$ within the unit cell are defined by the shift vectors,

$$\vec{r}^{X_k}(\vec{i}) = B^{\top}\vec{i} + \vec{v}^{X_k} . \tag{11.12}$$

The set of all vectors $\{\vec{r}^{X_k}(\vec{i})\}$ produce all points (atomic positions) in 3D space for a Barlow

multi-lattice. We use the following shift vectors ($1 \leq k \leq N$),

$$\left(\vec{v}^{X_k}\right)^\top = \begin{cases} a\,(0,0,z_k) & \text{if } X_k = \text{A}, \\ a\left(\frac{1}{2}, \frac{1}{2\sqrt{3}}, z_k\right) & \text{if } X_k = \text{B}, \\ a\left(\frac{1}{2}, -\frac{1}{2\sqrt{3}}, z_k\right) & \text{if } X_k = \text{C}. \end{cases} \tag{11.13}$$

with $\left(\vec{v}^{X_1}\right)^\top = (0,0,0)$. These shift vectors can be derived from the fact that an atom in the subsequent layer sits above the centroid of a triangle of neighboring lattice points in the A layer as seen in Figure 11.1. The kissing number, defined by the number of minimum distances around a hard sphere, for a Barlow packing is $\kappa = 12$, although for real crystals such as samarium there might be distortions reducing the kissing number[574,575].

For the vertical distance z_k between one of the hexagonal layers X_k and the base layer X_1, consider an ideal close-packed Barlow structure for which we have $\gamma_T = N\gamma_0$ with $\gamma_0 = \sqrt{\frac{2}{3}}$. For example, for $N = 2$ we have the hcp structure with the well known ratio of $c/a = \gamma_T = 2\gamma_0 = \sqrt{\frac{8}{3}}$. For equally distributed layers in the hexagonal unit cell we then have $z_k = \frac{k-1}{N}\gamma_T = (k-1)\gamma_0$. This neglects small distortions between the individual hexagonal layers along the c-axis. For example, already for the hcp structure using a (12,6)-LJ potential one gets[294] $\gamma_T = \sqrt{\frac{8}{3}} - \delta$ with $\delta = 2.298569 \times 10^{-4}$.

Let the distance (in units of a) between two neighboring hexagonal planes with the cardinal numbers for the individual layers k_1 and $k_2 > k_1$ ($k_1, k_2 = 1, ..., N$) be

$$d_{k_1 k_2} = z_{k_2} - z_{k_1} = \sum_{i=k_1}^{k_2-1} \gamma_i \quad \text{with} \quad \gamma_T \equiv d_{1N} = \sum_{i=1}^{N} \gamma_i \tag{11.14}$$

For the case that $\gamma_i = \gamma_0$ for all $i = 1, ..., N$ we simply have $d_{k_1 k_2} = (k_2 - k_1)\gamma_T/N$.

Using the definitions in (11.12), we get for the distances between the different lattice points in layers X_{k_1} and X_{k_2} in terms of the generator matrix B and shift vectors $\vec{v}^{X_k}$,

$$r(N, B, \vec{i}, \vec{j}, X_{k_1}, X_{k_2}) = \left|\vec{r}^{X_{k_2}}(\vec{i}) - \vec{r}^{X_{k_1}}(\vec{j})\right| = \left|B^\top\left(\vec{i} - \vec{j}\right) + \left(\vec{v}^{X_{k_2}} - \vec{v}^{X_{k_1}}\right)\right| \tag{11.15}$$

We need to consider 6 different cases for these distances, i.e. the cases $(X_{k_1} X_{k_2}) =$

$(AA), (BB), (CC), (AB), (AC)$ and (BC)[],

$$r(N, B, \vec{i}, \vec{j}, X_{k_1}, X_{k_2}) = \tag{11.16}$$
$$\begin{cases} \left| B^\top \left(\vec{i} - \vec{j}\right) + a\left(0, 0, d_{k_1,k_2}\right) \right| & \text{if} \quad (X_{k_1} X_{k_2}) = \text{(AA), (BB) or (CC)} \\ \left| B^\top \left(\vec{i} - \vec{j}\right) + a\left(\frac{1}{2}, \frac{1}{2\sqrt{3}}, d_{k_1,k_2}\right) \right| & \text{if} \quad (X_{k_1} X_{k_2}) = \text{(AB)} \\ \left| B^\top \left(\vec{i} - \vec{j}\right) + a\left(\frac{1}{2}, -\frac{1}{2\sqrt{3}}, d_{k_1,k_2}\right) \right| & \text{if} \quad (X_{k_1} X_{k_2}) = \text{(AC)} \\ \left| B^\top \left(\vec{i} - \vec{j}\right) + a\left(0, \frac{1}{\sqrt{3}}, d_{k_1,k_2}\right) \right| & \text{if} \quad (X_{k_1} X_{k_2}) = \text{(BC)} \end{cases}$$

To derive the lattice sums we consider an inverse power potential of the form

$$V(r) = \alpha r^{-n}. \tag{11.17}$$

with $n > 3, n \in \mathbb{R}$[226]. The cohesive energy per atom in the unit cell for such a potential becomes[377],

$$E_{\text{coh}} = \frac{\alpha}{2N} \left(N {\sum_{\vec{i} \in \mathbb{Z}^3}}' Q(B, \vec{i})^{-s} + 2 \sum_{k_1 < k_2}^{N} \sum_{\vec{i} \in \mathbb{Z}^3} q(N, B, \vec{i}, X_{k_1}, X_{k_2})^{-s} \right) \tag{11.18}$$

with exponent $s = n/2$. The prime notation for the sum indicates that we avoid the case $\vec{i} = \vec{0}$ in our summation. The quadratic form Q originates from the unit cell and is given by,

$$Q(B, \vec{i}) = \vec{i}^\top B B^\top \vec{i} = a^2 \left(i_1^2 + i_1 i_2 + i_2^2 + \gamma_T^2 i_3^2 \right) \tag{11.19}$$

while the quadratic function q for the interaction between the hexagonal layers becomes

$$\begin{aligned} q(N, B, \vec{i}, X_{k_1}, X_{k_2}) &= \left(\vec{i}^\top B + \left(\vec{w}^{X_{k_1} X_{k_2}} \right)^\top \right) \left(B^\top \vec{i} + \vec{w}^{X_{k_1} X_{k_2}} \right) \\ &= \left[\vec{i}^\top G \vec{i} + 2 \vec{i}^\top B \vec{w}^{X_{k_1} X_{k_2}} + |\vec{w}^{X_{k_1} X_{k_2}}|^2 \right] \\ &= a^2 \left[\left(i_1 + \frac{1}{2} i_2 + \beta_1 \right)^2 + \left(\frac{\sqrt{3}}{2} i_2 + \beta_2 \right)^2 + \left(\gamma_T i_3 + d_{k_1 k_2} \right)^2 \right] \end{aligned} \tag{11.20}$$

where $\vec{w}^{X_{k_1} X_{k_2}} = \vec{v}^{X_{k_2}} - \vec{v}^{X_{k_1}}$ and $\beta_1 = 0$ for the (AA), (BB), (CC) or (BC) sequence, $\beta_1 = \frac{1}{2}$ for (AB) or (AC), $\beta_2 = 0$ for (AA), (BB), (CC), $\beta_2 = \frac{1}{2\sqrt{3}}$ for (AB), $\beta_2 = -\frac{1}{2\sqrt{3}}$ for (AC), and $\beta_2 = \frac{1}{\sqrt{3}}$ for (BC). As shown in our first paper[377], the lattice sums for the cases (AA), (BB) and

(CC) are formally identical, and so are the cases (AB), (AC) and (BC).

We now rewrite the cohesive energy in the following form,

$$E_{\text{coh}} = \frac{\alpha}{2a^{2s}} L^{X}(N,s,\{\gamma_i\}) = \frac{\alpha}{2a^{2s}} \left\{ L^{A}(s,\gamma_T) + \frac{2}{N} \sum_{1\le k_1<k_2\le N} L_q^{X_{k_1}X_{k_2}}(s,\{\gamma_i\}) \right\} \tag{11.21}$$

with the Barlow lattice sums L for a specific period N defined as,

$$L^{A}(s,\gamma_T) = {\sum_{\vec{i}\in\mathbb{Z}^3}}' S^{A}(\vec{i},\gamma_T)^{-s} = {\sum_{\vec{i}\in\mathbb{Z}^3}}' \left[i_1^2 + i_1 i_2 + i_2^2 + \gamma_T^2 i_3^2 \right]^{-s} , \tag{11.22}$$

$$\begin{aligned} L^{AA}(s,\gamma_T,\{\gamma_{k_1},\ldots,\gamma_{k_2}\}) &= \sum_{\vec{i}\in\mathbb{Z}^3} S^{AA}(\vec{i},k_1,k_2,\{\gamma_i\})^{-s} \\ &= \sum_{\vec{i}\in\mathbb{Z}^3} \left[i_1^2 + i_1 i_2 + i_2^2 + \left(\gamma_T i_3 + d_{k_1k_2}\right)^2 \right]^{-s} \end{aligned} \tag{11.23}$$

and

$$\begin{aligned} L^{AB}(s,\gamma_T,\{\gamma_{k_1},\ldots,\gamma_{k_2}\}) &= \sum_{\vec{i}\in\mathbb{Z}^3} S^{AB}(\vec{i},k_1,k_2,\{\gamma_i\})^{-s} \\ &= \sum_{\vec{i}\in\mathbb{Z}^3} \left[\left(i_1+\tfrac{1}{3}\right)^2 + \left(i_1+\tfrac{1}{3}\right)\left(i_2+\tfrac{1}{3}\right) + \left(i_2+\tfrac{1}{3}\right)^2 + \left(\gamma_T i_3 + d_{k_1k_2}\right)^2 \right]^{-s} \end{aligned} \tag{11.24}$$

where $\{\gamma_i\}$ stands for the set of all N parameters γ_i which need to be optimized.

Rapidly converging series in terms of Bessel functions have already been provided for the special case of equally distributed hexagonal layers in the unit cell[377]. For the more general case including symmetry breaking along the c-axis we refer to Appendix P. However, we expect small deviations from the ideal value of $\gamma_0 = \sqrt{\frac{2}{3}}$ for each γ_i.[429] For some specific Barlow packings one has additional symmetry relations between the parameters γ_i, e.g. in the case of a Barlow sequence (ABCB) we have $\gamma_1 = \gamma_4$ and $\gamma_2 = \gamma_3$.

11.2.3 Properties for a general Lennard-Jones potential

The cohesive energy for periodic Barlow packings of length N, with the lattice points interacting through a general (n,m)-LJ potential, expressed in terms of lattice sums, is given by

$$E_{\text{coh}}^{X}(n,m,a,\{\gamma_i\}) = \frac{\epsilon n m}{2(n-m)} \left[\frac{L^{X}(\frac{n}{2},\{\gamma_i\})}{n} \left(\frac{r_e}{a}\right)^n - \frac{L^{X}(\frac{m}{2},\{\gamma_i\})}{m} \left(\frac{r_e}{a}\right)^m \right] \tag{11.25}$$

with $n > m > 3$ and the lattice sums $L^{\boldsymbol{X}}(\frac{n}{2}, \{\gamma_i\})$ as defined in (11.22), (11.23) and (11.24). Here we wrote the cohesive energy in terms of lattice sums in a special form by taking (arbitrarily) the lattice parameter a out of the lattice sum so we can more easily see the link to a Lennard-Jones potential for two interacting atoms. Alternatively, we could have taken the inverse power term a^{-n} into the lattice sum. This has the advantage that for the minimum cohesive energy at fixed values of γ_i we get the lattice parameter a directly from[377],

$$a^*_{\min}(n, m, \{\gamma_i\}) = \left(\frac{L^{\boldsymbol{X}}(\frac{n}{2}, \{\gamma_i\})}{L^{\boldsymbol{X}}(\frac{m}{2}, \{\gamma_i\})} \right)^{\frac{1}{n-m}} . \tag{11.26}$$

The * notation implies that reduced (or dimensionless) units are used ($E^* = E/\epsilon, a^* = a/r_e$). This results in the minimum cohesive energy[103],

$${E^{\boldsymbol{X}}_{\text{coh}}}^*(n, m, a^*_{\min}, \{\gamma_i\}) = -\frac{1}{2} \left[\frac{L^{\boldsymbol{X}}(\frac{m}{2}, \{\gamma_i\})^n}{L^{\boldsymbol{X}}(\frac{n}{2}, \{\gamma_i\})^m} \right]^{\frac{1}{n-m}} . \tag{11.27}$$

As the Barlow lattice sums $L^{\boldsymbol{X}}(s, \gamma_0)$ are monotonically decreasing functions with increasing s in the interval $s \in [1.5, \infty)$ we have the condition that $a^*_{\min}(n, m, \gamma_0) \leq 1$ for all Barlow packings. In the sticky hard-sphere limit we have $a^*_{\min}(\gamma) = 1$. Similarly we have ${E^{\boldsymbol{X}}_{\text{coh}}}^*(a^*_{\min}, n, m, \gamma_0) \leq 0$. The minimum value of the cohesive energy with respect to the optimized $\{\gamma_i\}$ is obtained through a Newton-Raphson procedure as detailed in Appendix T.

The bulk modulus B can be derived in a similar way. In reduced units we have

$$B^*(V) = V^* \frac{\partial^2 {E^{\boldsymbol{X}}_{\text{coh}}}^*(n, m, a^*, \gamma_T)}{\partial {V^*}^2} \tag{11.28}$$

with $V^* = \frac{\sqrt{3}}{2}\gamma_0 {a^*}^3 = \frac{\sqrt{3}}{2N}\gamma_T {a^*}^3$. Here and for the following properties introduced we keep the distances between the hexagonal layers at constant $\gamma_i = \gamma_0$. This is justified as the deviations from the ideal γ_0 value are very small as discussed in detail in section 11.3. Using zero pressure $P = dE/dV = 0$ we get the following expression for the bulk modulus in terms of lattice sums[227],

$$B^*(n, m, a^*, \gamma_T) = \frac{Nnm}{9\sqrt{3}\gamma(n-m)} \left[(n+3)(a^*)^{-(n+3)} L^{\boldsymbol{X}}(\tfrac{n}{2}, \gamma_T) - (m+3)(a^*)^{-(m+3)} L^{\boldsymbol{X}}(\tfrac{m}{2}, \gamma_T) \right] \tag{11.29}$$

Using (11.26) we get

$$B^*(n,m,a^*_{\min},\gamma_T) = \frac{Nnm}{9\sqrt{3}\gamma_T(n-m)}\left[(n+3)L^{\boldsymbol{X}}(\tfrac{n}{2},\gamma_T)\left(\frac{L^{\boldsymbol{X}}(\frac{m}{2},\gamma_T)}{L^{\boldsymbol{X}}(\frac{n}{2},\gamma_T)}\right)^{\frac{n+3}{n-m}}\right. \tag{11.30}$$

$$\left. -(m+3)L^{\boldsymbol{X}}(m,\gamma_T)\left(\frac{L^{\boldsymbol{X}}(\frac{m}{2},\gamma_T)}{L^{\boldsymbol{X}}(\frac{n}{2},\gamma_T)}\right)^{\frac{m+3}{n-m}}\right] \tag{11.31}$$

For the vibrational contribution to the entropy, discussed in the next section, we require the average Einstein frequency ω_E in the lattice sum model by taking the expression from Ref. 227,

$$\omega_E(n,m,a^*,\gamma_T) = \sqrt{\frac{\epsilon}{r_e^2 M}}\sqrt{\frac{nm}{3(n-m)}}\left\{(n-1)L^{\boldsymbol{X}}(\tfrac{n+2}{2},\gamma_T)(a^*)^{-n-2}\right. \tag{11.32}$$

$$\left. -(m-1)L^{\boldsymbol{X}}(\tfrac{m+2}{2},\gamma_T)(a^*)^{-m-2}\right\}^{1/2} \tag{11.33}$$

where M is the mass of the atom in the lattice for a homonuclear system. In order to obtain a frequency that is only dependent on lattice constants (in dimensionless units) and some prefactors, we rewrite this equation and use (11.26),

$$\omega_E^{'} = \sqrt{\frac{r_e^2 M}{\epsilon}}\omega_E = \sqrt{\frac{nm}{3(n-m)}}\left\{(n-1)L^{\boldsymbol{X}}(\tfrac{n+2}{2},\gamma_T)\left(\frac{L^{\boldsymbol{X}}(\frac{m}{2},\gamma_T)}{L^{\boldsymbol{X}}(\frac{n}{2},\gamma_T)}\right)^{\frac{n+2}{n-m}}\right. \tag{11.34}$$

$$\left. -(m-1)L^{\boldsymbol{X}}(\tfrac{m+2}{2},\gamma_T)\left(\frac{L^{\boldsymbol{X}}(\frac{m}{2},\gamma_T)}{L^{\boldsymbol{X}}(\frac{n}{2},\gamma_T)}\right)^{\frac{m+2}{n-m}}\right\}^{1/2} \tag{11.35}$$

which results in a zero-point vibrational energy of

$$E_0 = \frac{3}{2}\hbar\omega_E = \frac{3}{2}\sqrt{\frac{\epsilon}{r_e^2 M}}\,\hbar\omega_E^{'} \tag{11.36}$$

The Einstein frequency describes the vibration of an atom in the field of all other atoms. However, this simplified model, although analytical in terms of lattice sums, neglects the frequency splitting between the parallel and perpendicular components of an atom in the hexagonal layer, i.e. for Barlow packing one generally has $\omega_E^{\parallel} \neq \omega_E^{\perp}$. Only for the fcc phase are these three frequency components perfectly degenerate[227]. Moreover, one should in principle consider the change in geometry due to zero-point vibrations. In addition, phonon dispersion cannot be neglected anymore when small zero-point energy differences or differences in vibrational entropies between different structures are considered[104]. We therefore decided

to include phonon dispersion calculations for both fcc and hcp by diagonalizing the $(3N, 3N)$ hermitian dynamical matrix $D(\vec{k})$ ($N = 1$ for fcc and $N = 2$ for hcp) in k-space[580],

$$D(\vec{k})v(\vec{k}) = \omega^2(\vec{k})v(\vec{k}) \tag{11.37}$$

where the matrix $D(\vec{k})$ is related to the mass-weighted force-field matrix F in real space through a Fourier transformation, $v(\vec{k})$ the corresponding eigenvector and the $3N$ real solutions $\omega(\vec{k})$ at a specific $\vec{k}$-point are the phonon frequencies. In our case, $D(\vec{k})v(\vec{k})$ becomes a real and symmetric matrix because of roto-inversion symmetry for the Barlow packings. This implies that only the cosine term in the Fourier transformation $e^{i\vec{k}\cdot\vec{R}} = \cos(\vec{k}\cdot\vec{R}) + i\sin(\vec{k}\cdot\vec{R})$ needs to be considered in our calculations. Hence for Barlow packings we get the following $(3N, 3N)$ dynamical matrix,

$$D_{\alpha\kappa,\beta\kappa'}(\vec{k}) = \frac{1}{M}\sum_b F_{\alpha\kappa,\beta\kappa'}(0,b)\cos(\vec{k}\cdot\vec{R}_b) \tag{11.38}$$

where α and β label the coordinate axes x, y, z, κ and κ' characterize the two coupled atoms with mass M in the vibration, and F is the force-field matrix in real space between an atom in the reference unit cell 0 and an atom in unit cell b. The harmonic phonon frequencies can be normalized such that the mass and the ϵ parameter of the (n, m)-LJ potentials become just multiplying scalars. Then, we have in a similar way to (11.34)

$$\omega'(\vec{k}) = \sqrt{\frac{r_e^2 M}{\epsilon}}\omega(\vec{k}) \tag{11.39}$$

This has the advantage that due to the simple mass scaling we need to determine the phonon branches from one calculation for a specific (n, m)-LJ potential. Diagonalizing D gives $3N$ solutions (N being the period) from which the frequencies can be obtained. Hence, instead of diagonalizing a $3N_A$-dimensional (mass-weighted) force field matrix which computationally is $\mathcal{O}(N_A^3)$ (N_A being the number of vibrating atoms chosen in the solid), one has to diagonalize a far smaller $(3N, 3N)$ dynamical matrix at many different k-points. Nevertheless, both methods were used for cross checking. A detailed description of lattice dynamics theory can be found in the book by Born and Huang[231].

11.2.4 Entropy

The entropy for materials with a sizable electronic band gap comes mainly from the vibrational contribution, which within the Einstein approximation is given by the expression

$$S_{\text{vib}}(T) = 3k_B\left[-\ln\left(1 - e^{-\beta\omega_E}\right) - \frac{\beta\omega_E}{1 - e^{\beta\omega_E}}\right] \tag{11.40}$$

where $\beta = \hbar/k_B T$. For more details see Appendix S. This approximation neglects phonon dispersion and anharmonicity effects and therefore is only approximate for multi-lattices, but nevertheless useful as we shall see. Moreover, it has been shown that for the hcp lattice the error coming from such an approximate treatment is small for the Einstein frequency[227]. We re-express this in terms of our dimensionless Einstein frequency for better comparison,

$$S_{\mathrm{vib}}(T') = 3k_B \left[-\ln\left(1 - e^{-\beta' \omega_E'}\right) - \frac{\beta' \omega_E'}{1 - e^{\beta' \omega_E'}} \right] \tag{11.41}$$

where $\beta' = 1/T'$ with the temperature

$$T' = \frac{k_B r_e}{\hbar} \sqrt{\frac{M}{\epsilon}} T \tag{11.42}$$

and we keep the entropy in the usual SI units. T' is a dimensionless mass-, distance- and energy-weighted temperature which means that we have shifted the mass dependency conveniently out of the Einstein frequency and can study the temperature dependence of the function $S_{\mathrm{vib}}(T')$ (alternatively we can set the mass, energy in equilibrium distance to 1 as for reduced units and reintroduce them at a later stage). To give an example for using dimensionless units, the argon triple (melting) point is at 83.81 K. Using a mass of $M = 39.962$ g/mol for the 40-Ar isotope, a distance of $r_e = 3.7624$ Å and dissociation energy of $\epsilon = 1.1885$ kJ/mol for diatomic argon[457], we obtain $T' = 23.941$ for the triple point. Hence we can easily convert the dimensionless temperature T' into the real temperature for specific isotopes of solids such as the rare gas elements. We note that $S_{\mathrm{vib}} \to 0$ for $T' \to 0$ or $M \to 0$, $S_{\mathrm{vib}} \to \infty$ for $T' \to \infty, M \to \infty$. Further, $S_{\mathrm{vib}}(T')$ increases monotonically from zero with increasing T'.

Eq.(11.40) can be easily extended to include phonon dispersion,

$$S_{\mathrm{vib}}(T') = k_B \sum_{\mathbf{k},\mu} \left[-\ln\left(1 - e^{-\beta' \omega_\mu'(\mathbf{k})}\right) - \frac{\beta' \omega_\mu'(\mathbf{k})}{1 - e^{\beta' \omega_\mu'(\mathbf{k})}} \right] \tag{11.43}$$

where the index μ runs over the $3N$ solutions ($N = 1$ for fcc and $N = 2$ for a bi-lattice such as hcp) for (11.37) at a specific $\mathbf{k}$-point. As we discuss the high temperature (or low frequency) limit in this work, we can use a simple Taylor expansion (see appendix S) of the exponential and obtain

$$S_{\mathrm{vib}}(T' \gg 0) \approx k_B \left[1 - \sum_{\mathbf{k},\mu} \ln\left(\beta' \omega_\mu'(\mathbf{k})\right) \right] \tag{11.44}$$

As $\beta' \omega_\mu'(\mathbf{k} \ll 1$, the entropy remains positive but approaches infinity for $T' \to \infty$.

For the following we focus on entropy difference between a specific Barlow packing and the

hcp structure,

$$\Delta S^{\boldsymbol{X}}_{\mathrm{vib}}(T') = S^{\boldsymbol{X}}_{\mathrm{vib}}(T') - S^{\mathrm{hcp}}_{\mathrm{vib}}(T') \tag{11.45}$$

which, as we shall see, is very sensitive to phonon dispersion. The formalism can be extended if we take anharmonicity effects into account affecting the phonon frequencies, which we however neglect in this work as it comes at a significant computational cost. For the high-temperature limit we simply get from (11.44)

$$\Delta S^{\boldsymbol{X}}_{\mathrm{vib}}(T' \to \infty) = -k_B \left[\sum_{\mathbf{k},\mu} \ln\left(\omega'^{\,X}_{\mu}(\mathbf{k})\right) - \sum_{\mathbf{k},\mu} \ln\left(\omega'^{\,\mathrm{hcp}}_{\mu}(\mathbf{k})\right) \right] \tag{11.46}$$

that is we get a finite value for ΔS_{vib} as the term β' causing the infinity drops out. In fact, in this limit it does not matter what units are used for the phonon frequencies as the conversion factor f drops out for entropy differences because of the simple relation for the logarithm, $\ln(f(T)\omega) = \ln(f(T)) + \ln(\omega)$, where in the usual units we have $f(T) = \hbar/k_B T$.

11.2.5 Density Functional Calculations

In order to assess the stability for Barlow packings for more realistic systems, we carried out DFT calculations[338–341,343] for metallic lithium where we used the Perdew-Burke-Ernzerhof (PBE) exchange-correlation functional[280] with dispersion corrections by means of the DFT-D3 approach with the Becke-Johnson damping function[291,292,581]. The atomic cores are described by the Projector Augmented Wave (PAW) method[342], and the electronic minimization was done using the tetrahedron method[344] with Blöchl correction with an energy width of 0.1 eV. The k-point grid was set using the keyword KSPACING=0.07 centered at the Γ point and an energy cut-off of 500 eV. The crystal parameters a and γ_T where optimized using a Newton-Raphson procedure with the gradient and Hessian matrix calculated numerically applying a threshold for convergence of 10^{-5} kJ/mol for the electronic energy. For the isolated atom required for the cohesive energy we used a large orthorhombic unit cell of $14 \times 14.001 \times 14.002$ Å. The following Barlow packings were investigated: $(AB$ (hcp, $N = 2)$, (ABC) (fcc, $N = 3)$, $(ABAC)$ $(N = 4)$, and $(ABABAC)$ and $(ABACBC)$ $(N = 6)$, as the periodicity of hcp is a divisor of 4 and 6, and that of fcc a divisor of 6. We checked the accuracy of our results from supercell treatments of both hcp and fcc, e.g. for fcc we also included the redundant packing sequence $(ABCABC)$.

For comparison to our LJ entropy calculations including phonon dispersion, we decided to carry out additional DFT calculations to obtain the phonon frequencies and subsequently the entropy difference between the fcc and hcp phases of solid argon at the optimized lattice geometries. For this we used the DFT-D3 approach as described above. The phonon frequencies were obtained through a finite difference method with a $6 \times 6 \times 6$ supercell centered at the Γ

point. The temperature dependent entropy was obtained through eq.(11.43).

11.3 Results and discussions

The Barlow lattice sums $L^{\mathbf{X}}(N, s, \{\gamma_i\})$ with equal packing fraction $\alpha^{\mathbf{X}}(2)$ and period N differ only minutely from each other and lie approximately on a straight line with respect to $\alpha^{\mathbf{X}}(2)$, with a very small root mean square error of RMS = 2.361×10^{-7} for $s = \frac{n}{2} = 3$ as shown in our previous paper[377]. As we shall see, this translates into a linear behavior for many other properties as well. We therefore introduce the following definition for a property P of a specific Barlow packing with packing fraction $\alpha^{\mathbf{X}}(2)$,

$$\tilde{P}^{\mathbf{X}}(n, m, \{\gamma_i\}) = P^{\text{hcp}}(n, m, \{\gamma_i\}) + \alpha^{\mathbf{X}}(2) \left[P^{\text{fcc}}(n, m, \{\gamma_i\}) - P^{\text{hcp}}(n, m, \{\gamma_i\}) \right] \tag{11.47}$$

with $\bar{\gamma} = \frac{1}{N}\gamma_T = \frac{1}{N}\sum_{i=1,\dots N} \gamma_i \approx \gamma_0$, and the deviation from the ideal linear behavior by

$$\Delta P^{\mathbf{X}}(n, m, \{\gamma_i\}) = P^{\mathbf{X}}(n, m, \{\gamma_i\}) - \tilde{P}^{\mathbf{X}}(n, m, \{\gamma_i\}) \tag{11.48}$$

Furthermore, $\Delta L^{\mathbf{X}}(s, \gamma_i = \gamma_0)$ values with $\gamma_0 = \sqrt{\frac{2}{3}}$ lie approximately within a triangle along the packing fraction α.[377]

For the following discussion we neglect the * notation (e.g. $P \equiv P^*$) and work with reduced units if not otherwise stated. We further distinguish between three different cases for our optimization procedure for the different (n, m)-LJ potentials:

- Case 1: The Barlow packings are kept at ideal $\gamma_T = N\gamma_0 = N\sqrt{\frac{2}{3}}$;
- Case 2: γ_T is optimized with the restriction that $\gamma_i = \gamma_j$, for all $i \neq j$ and $i = 1, \dots, N$;
- Case 3: All γ_i are optimized.

For case 2 or 3 we refer to the optimized γ_i values as $\gamma_{\text{min}} = \frac{1}{N}\gamma_T = \frac{1}{N}\sum_{i=1,N} \gamma_i \approx \sqrt{\frac{2}{3}}$.

11.3.1 Lattice constants

The optimized minimum lattice constants with respect to hcp, $\Delta a^{\mathbf{X}}_{\text{min}}(\{\gamma_i\}) = a^{\mathbf{X}}_{\text{min}}(\{\gamma_i\}) - a^{\text{hcp}}_{\text{min}}(\{\gamma_i\})$, for case 1 are shown in Figure 11.2a. We observe a very strong linear behavior with respect to the fcc packing fraction ($\tilde{a}_{\text{min}} \cong a_{\text{min}}$) with a tiny RMS error for the 102 different Barlow structures considered (up to $N = 12$), e.g. 2.280×10^{-9} for the (12,6)-LJ potential. This can be rationalized by a simple Taylor expansion in terms of the ratio between the Barlow and reference hcp lattice sums (see appendix R), where the strong linear correlation with respect to the fcc packing fraction is directly related to the linear behavior seen for the lattice sums[377]. In

fact, the deviation from the ideal linear behavior, $\Delta a^{\mathbf{X}}_{\min}$, according to eq.(11.48) is four orders of magnitude smaller compared to the actual $\tilde{a}^{\mathbf{X}}_{\min}$ values, as shown in Figure 11.3a. Here we observe an interesting triangle pattern with both positive and negative deviations from the ideal line depending on the choice of the exponents (n, m) in the LJ potential. This originates from the similar pattern found for the lattice sums[377]. We note that the largest deviation from the ideal linear behavior is found for the (ABAC) ($N = 4$) Barlow packing with fcc packing fraction $\alpha(2) = 0.5$.

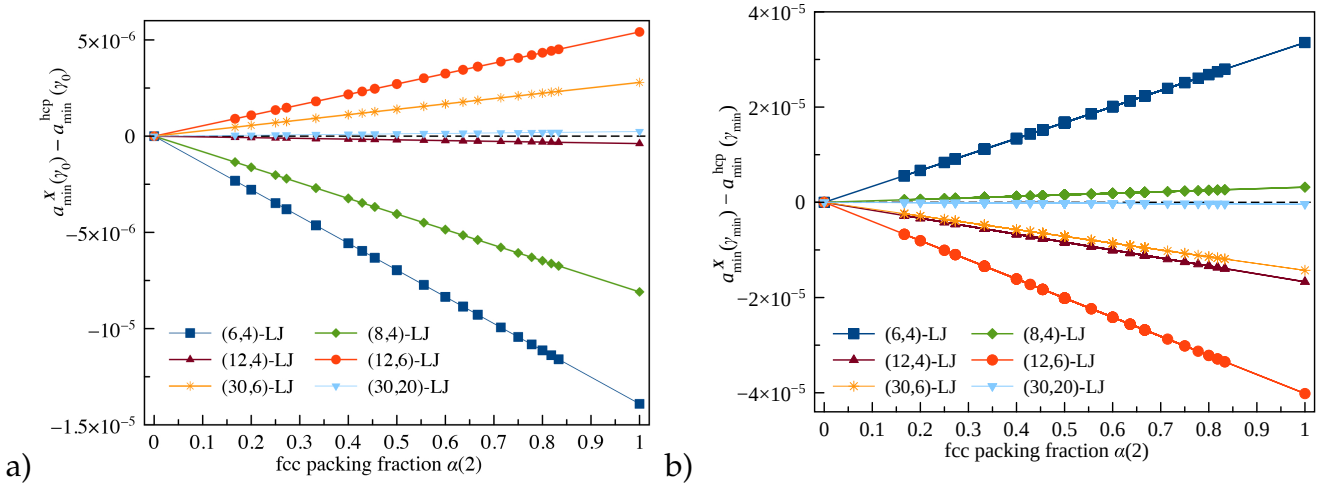

Figure 11.2: (a) Difference in the minimum lattice constants $a_{\min}$ at fixed $\gamma_T = N\gamma_0 = N\sqrt{\frac{2}{3}}$ (case 1) for Barlow packings compared to the reference hcp structure ($\alpha(2) = 0$) as a function of the fcc packing fraction $\alpha(2)$ for various (n, m)-LJ potentials. (b) Same as (a) but at the optimized γ_T or $\{\gamma_i\}$ lattice parameters, i.e. case 2 or 3 (the difference between the two cases is not visible on this scale, see discussion).

Cases 2 and 3 involve the optimization of the lattice parameters γ_i through a Newton-Raphson procedure as outlined in appendix T. Because of the small differences between the γ_i values for a specific Barlow packing, analytical first and second derivatives of the lattice sums with respect to γ_i were required as outlined in appendix P. One could assume that the small $\Delta\gamma$ values (see eq.(11.48) for the definition) translates into small changes in the other lattice constant such as $a^{\mathbf{X}}_{\min}$. While this is indeed the case, for the differences $\Delta a^{\mathbf{X}}_{\min} = a^{\mathbf{X}}_{\min} - a^{\text{hcp}}_{\min}$, which are already very small, it nevertheless becomes significant as a comparison between the two figures 11.2 (a) and (b) shows. Here $a^{\text{fcc}}_{\min}(n, m, \{\gamma_i\}) - a^{\text{hcp}}_{\min}(n, m, \{\gamma_i\})$ become very sensitive to the γ_i-values chosen which can change significantly the slope of the individual linear curves for the different (n, m)-LJ potentials leading even to a different sign in the slops. However, the strong linear behavior still persists with a small RMS error of 3.739×10^{-8} for case 2 and 3.368×10^{-8} for case 3 for the (12,6)-LJ potential. However, case 2 and 3 lead to a very similar linear behavior as shown in Figure 11.2b.

The deviations from the ideal $\gamma_0 = \sqrt{\frac{2}{3}}$ value, $\Delta\gamma_{\min} = \gamma_{\min} - \gamma_0$, are listed in Table U.2,

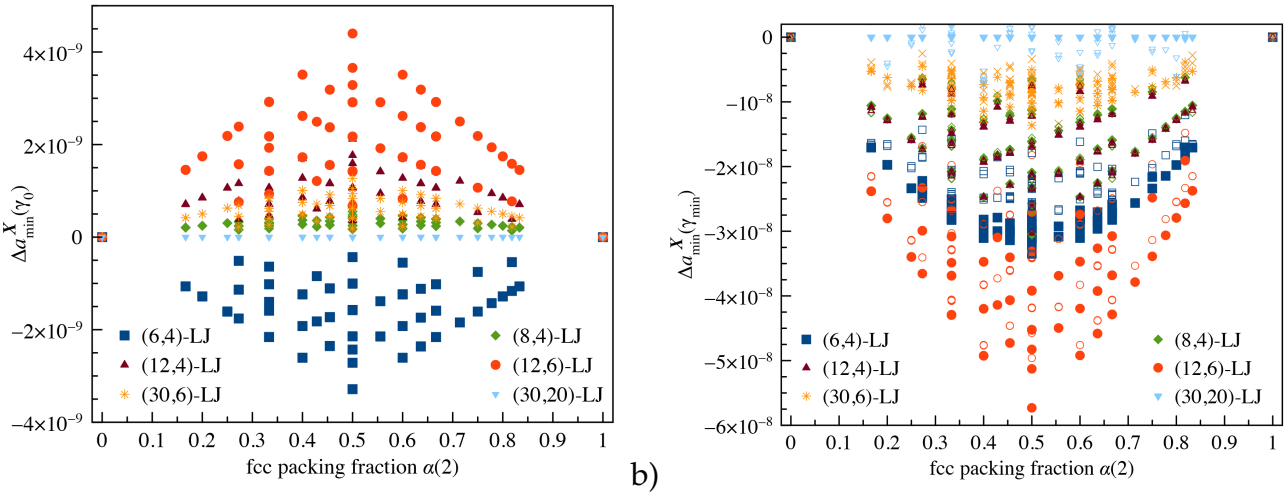

Figure 11.3: (a) Distribution of the difference in the minimum lattice constants $\Delta a^X_{\min}(n, m, \gamma_i = \gamma_0)$ (case 1) for Barlow packings at $\gamma_0 = \sqrt{2/3}$ compared to the hcp structure ($\alpha(2) = 0$) as a function of the fcc packing fraction $\alpha(2)$ for various (n, m)-LJ potentials according to eq.(11.48). (b) Same as (a) but at the optimized $\gamma_{\min}$ (filled symbols for case 2 and open symbols for case 3).

appendix U, and are shown in Figure 11.4a. Howard[582] already showed as early as in 1970 by direct lattice summations over 450 shells within the hcp lattice, using a $(12, 6)$LJ potential, that the $\gamma_0 = \sqrt{\frac{2}{3}}$ value is reduced by tiny amount of $\Delta\gamma_{\min} = -1.15 \times 10^{-4}$. Through exact lattice summations we get a more accurate value of $\Delta\gamma = -1.14928459 \times 10^{-4}$, see Table U.2 and Ref. 294. Not surprisingly, for the fcc lattice we have exactly $\Delta\gamma_{\min} = 0$ for all (n, m) combinations, while hcp shows the largest absolute deviation compared to all other Barlow structures for all the LJ potentials studied here. Even for the case where hcp and fcc are energetically degenerate, e.g. at $n = 8.0$ and $m = 4.208890947988$, we get the largest absolute value for $\Delta\gamma_{\min}$ for the hcp structure. As a result, we see again an almost perfect linear behavior for $\Delta\gamma_{\min}(\alpha(2))$ with deviations from the ideal straight line three orders of magnitude smaller than the actual $\Delta\gamma_{\min}$ value. In addition, we get this interesting triangle pattern for the deviations in the $\Delta\gamma_{\min}$ values (see Figure 11.5). The spread of the optimized γ_i values as shown in Figure 11.4b shows larger values for the soft potentials. For the hard potentials approaching the hard-sphere limit one obtains $\max(\gamma_i) - \min(\gamma_i) = 0$ as expected.

We briefly consider the volume using the linear relationships we found for the lattice constant. Using a Taylor expansion up to first order because of the smallness of the hcp/fcc

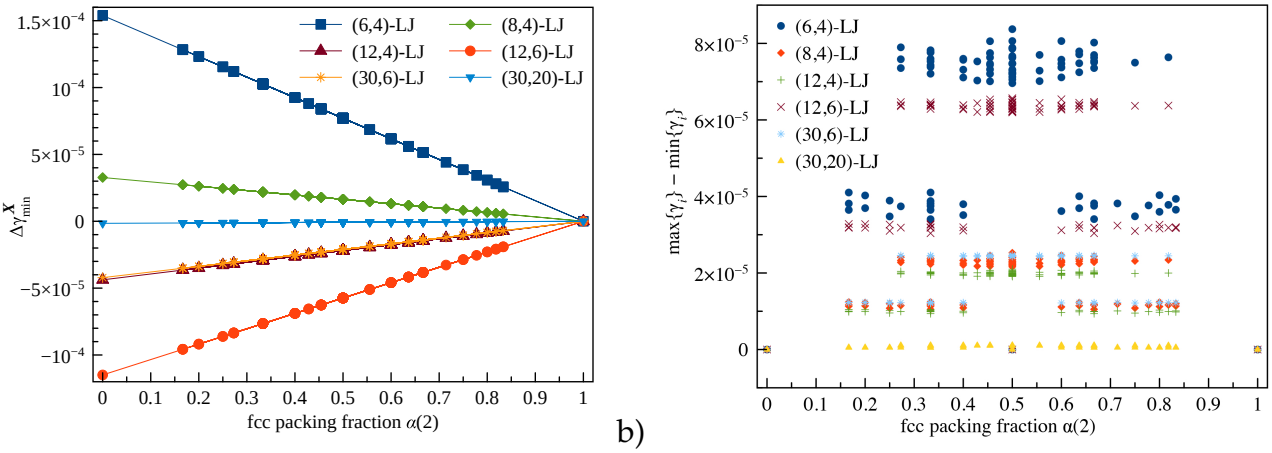

a) b)

Figure 11.4: (a) Difference $\Delta\gamma_{\min} = \gamma_{\min} - \gamma_0$ between the optimized $\gamma_{\min}$ value and the ideal one of $\gamma_0 = \sqrt{2/3}$ for Barlow packings as a function of the fcc packing fraction $\alpha(2)$ for various (n,m)-LJ potentials for cases 2 and 3 (the difference between case 2 and 3 cannot be seen by the naked eye). (b) Spread of γ_i values, $\max(\gamma_i) - \min(\gamma_i)$.

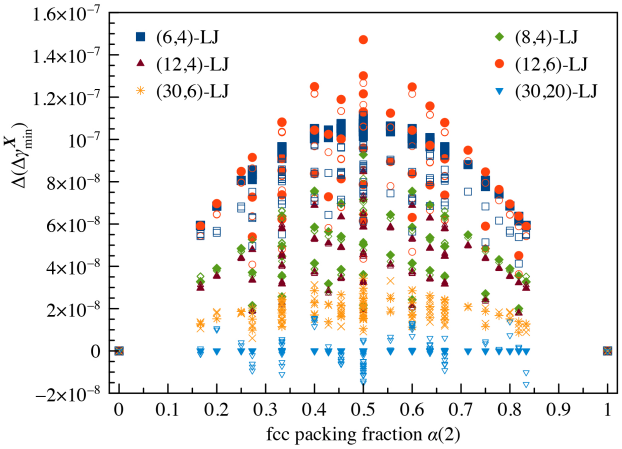

Figure 11.5: Deviation of the $\Delta\gamma_{\min}$ values from the ideal straight line connecting the fcc and hcp structures according to eq.(11.48) using case 2 (filled symbols) and case 3 (open symbols).

differences in the lattice constants we get

$$\tilde{V}^X = \frac{\sqrt{3}}{2}(a^X)^3\gamma_T^X = \frac{\sqrt{3}}{2}\left[a^{\rm hcp} + \alpha^X(2)\left(a^{\rm fcc} - a^{\rm hcp}\right)\right]^3\left[\gamma_T^{\rm hcp} + \alpha^X(2)\left(\gamma_T^{\rm fcc} - \gamma_T^{\rm hcp}\right)\right] \quad (11.49)$$

$$\approx V^{\rm hcp}\left[1 + 3\alpha^X(2)\frac{\left(a^{\rm fcc} - a^{\rm hcp}\right)}{a^{\rm hcp}}\right]\left[1 + \alpha^X(2)\frac{\left(\gamma_T^{\rm fcc} - \gamma_T^{\rm hcp}\right)}{\gamma_T^{\rm hcp}}\right]$$

$$\approx V^{\rm hcp} + \alpha^X(2)V^{\rm hcp}\left[3\frac{\left(a^{\rm fcc} - a^{\rm hcp}\right)}{a^{\rm hcp}} + \frac{\left(\gamma_T^{\rm fcc} - \gamma_T^{\rm hcp}\right)}{\gamma_T^{\rm hcp}}\right] \quad (11.50)$$

As for $\alpha(2) = 1$ we have $V = V^{\text{fcc}}$ we get the relationship

$$V^{\text{fcc}} - V^{\text{hcp}} \approx V^{\text{hcp}} \left[3\frac{\left(a^{\text{fcc}} - a^{\text{hcp}}\right)}{a^{\text{hcp}}} + \frac{\left(\gamma_T^{\text{fcc}} - \gamma_T^{\text{hcp}}\right)}{\gamma_T^{\text{hcp}}} \right] \tag{11.51}$$

We thus obtain to a very good approximation a linear relationship for the volume of the Barlow packings, which will become useful for the discussion of the free energy of the system at finite pressure, see section 11.3.6.

11.3.2 Cohesive energies

In order to compare the thermodynamic stabilities of the Barlow packings we need to analyze their cohesive energies first. Figure 11.6a shows the difference in cohesive energies of the Barlow packings as a function of the fcc packing fraction $\alpha(2)$ for various (n, m)-LJ potentials. We see again a nice linear behavior as a function of $\alpha(2)$ originating from the linear behavior in the lattice sums[377], as demonstrated by a Taylor expansion in Appendix R. As for the lattice constants, the deviation from linearity for the cohesive energies is rather small with an RMS error of 2.673×10^{-7} for case 1 using the (12,6)-LJ potential. Figure 11.7a shows a triangular distributions pattern for these deviations with the largest absolute value for the $ABAC$ Barlow packing ($\alpha(2) = 0.5$). This implies that the LJ cohesive energy for a Barlow packing can be estimated to relatively high accuracy from the fcc packing fraction and the cohesive energies for fcc and hcp. The cohesive energy for the sticky hard-sphere (SHS) limit is exactly -6 and $\Delta E^{X}_{\text{SHS}} = 0$, which is nearly satisfied by the (30,20)-LJ potential as shown in Table U.1 and Figure 11.6a. This linear relationship will be important for the discussion of the natural appearance of Barlow packings as we shall see when we discuss the free energy of the system. We note that for very soft potentials the fcc phase has a lower cohesive energy compared to hcp as already discussed by us before.[227,294,429]

Considering the effect of changing $\gamma_0 \rightarrow \gamma_{\text{min}}$ upon optimization, case 2 and 3 leads to almost identical linear curves compared to case 1 not distinguishable by the naked eye, Figure 11.6a. Figure 11.6b shows that the cohesive energy difference between the two γ values (difference between case 1 and 2) changes quadratically with the fcc packing fraction. This change is however about three orders of magnitude smaller compared to the fcc/hcp cohesive energy difference (compare Figures 11.6a and 11.6b) and therefore has only a minor effect on the linear behavior. Case 3 where all γ_i-values are optimized leads interestingly to a spread in the γ_i-values for a specific fcc packing fraction $\alpha(2)$, see Figure 11.6b. We also see a slight change in the distribution for the deviation from the linear behavior of the cohesive energy difference, i.e. compares Figures 11.7 a and b. Nevertheless, the important result here is that the cohesive energy difference for the Barlow structures with the respect to hcp behaves linearly with the fcc

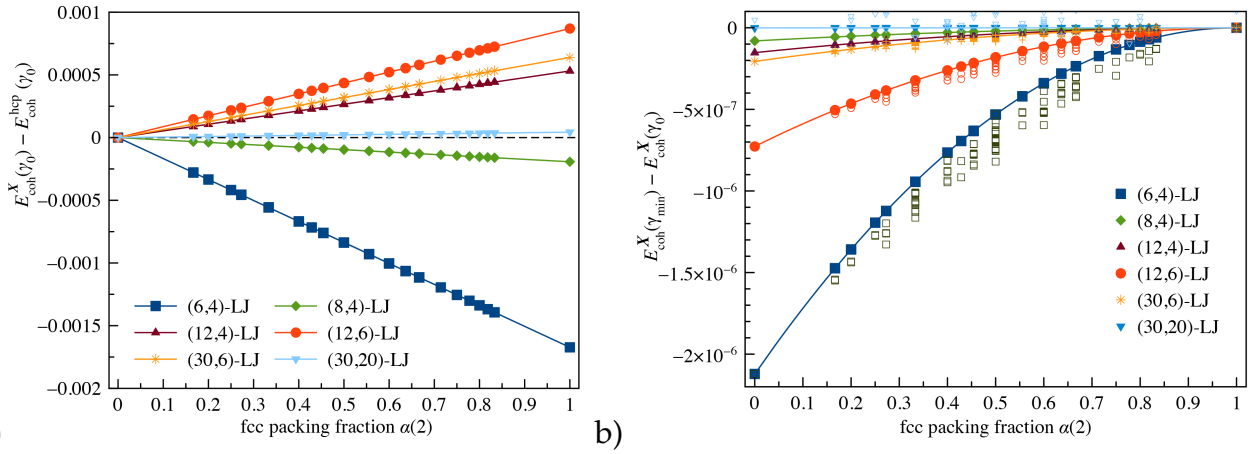

Figure 11.6: (a) Cohesive energy difference for Barlow packings with respect to the hcp structure as a function of the fcc packing fraction $\alpha(2)$ for various (n,m)-LJ potentials and $\gamma_0 = \sqrt{\frac{2}{3}}$ (case 1). Data are listed in Table U.1 and supporting information. (b) Difference in cohesive energies $\Delta E_{\rm coh}(\gamma_{\rm min}) = E_{\rm coh}(\gamma_{\rm min}) - E_{\rm coh}(\gamma_0)$. A quadratic polynomial was used for the fit procedure for case 2 (filled symbols). Case 3 results are shown by open symbols.

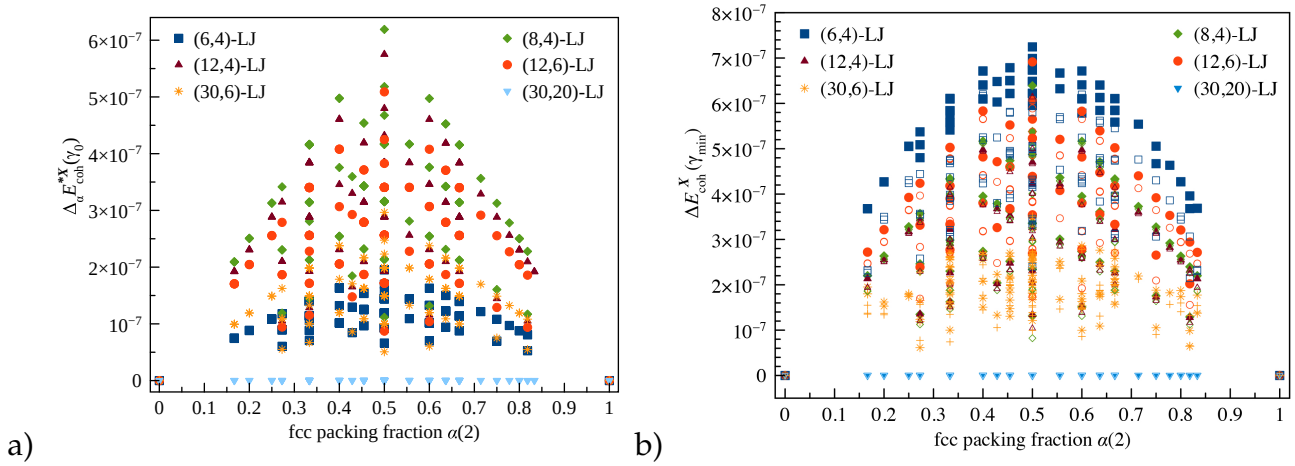

Figure 11.7: (a) Deviation of cohesive energies of Barlow packings from the line connecting the fcc and hcp cohesive energy values according to eq.(11.48) for various (n,m)-LJ potentials and for $\gamma_0 = \sqrt{\frac{2}{3}}$. (b) Deviation of the $\Delta E_{\rm coh}(\gamma_{\rm min})$ values from the line of Barlow packings connecting the fcc and hcp values for various (n,m)-LJ potentials. Filled symbols for case 2 and open symbols for case 3.

packing fraction and optimizing the lattice parameters γ_i-values does not significantly change this result. Moreover, these deviations are all positive for the LJ potentials considered, that is the Barlow differences in cohesive energies are all above the line.

From the results using LJ potentials we observe that very small differences in lattice constants and in cohesive energies required exact lattice summations to accurately obtain the linear behavior and the small deviations from it. The LJ potential is a good toy model and

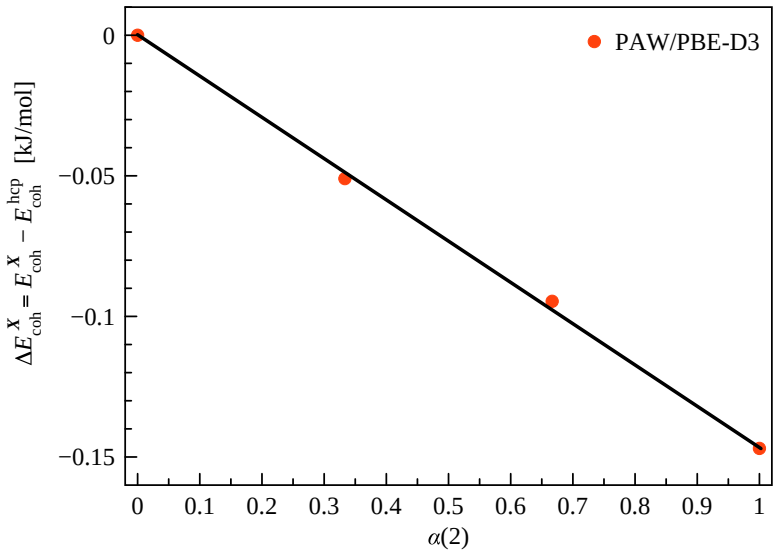

Figure 11.8: Cohesive energy difference for few Barlow packings with periodicity N =2,3,4,6 with respect to the hcp structure as a function of the fcc packing fraction $\alpha(2)$ for metallic lithium at the PBE-D3 level of theory.

most relevant for the rare gases at low pressures, but for more interesting systems such as metallic systems, many-body effects play a crucial role and one has to see whether a linear behavior between the packing fraction with the cohesive energy is maintained or not. This, however, constitutes a major challenge to density functional calculations as high numerical accuracy is required. Nevertheless, we decided to perform DFT calculations for metallic lithium converging out the cohesive energy to ¡ 10^{-3} kJ/mol. The cohesive energies with respect to the fcc packing fraction is shown in Figure 11.8. We see an almost perfect linear behaviour.

11.3.3 Bulk moduli

Figure 11.9a shows the bulk moduli for various (n, m)-LJ potentials as a function of the fcc packing fraction $\alpha(2)$, again showing this strong linear behavior. One cannot distinguish the differences in the bulk moduli for the different cases 1-3 from this graph. Figure 11.9b therefore shows the differences between the bulk moduli with optimized γ-values with respect to case 1 ($\gamma_i = \gamma_0 = \sqrt{\frac{2}{3}}$). These differences are 8 orders of magnitude smaller than the actual bulk modulus values. We therefore see already some numerical noise for the LJ potentials with large repulsive walls ($n = 30$). The RMS error for the deviation from the linear line in Figure 11.9a is again very small, i.e RMS = 4.09×10^{-6} for the (12,6)-LJ potential, and the distribution of the differences from the linear behavior as shown in Figure 11.10 exhibits the same features as discussed for the other properties. Note the different behavior in the deviations between the case 1 and 2, i.e. compare Figures 11.10 a and b.

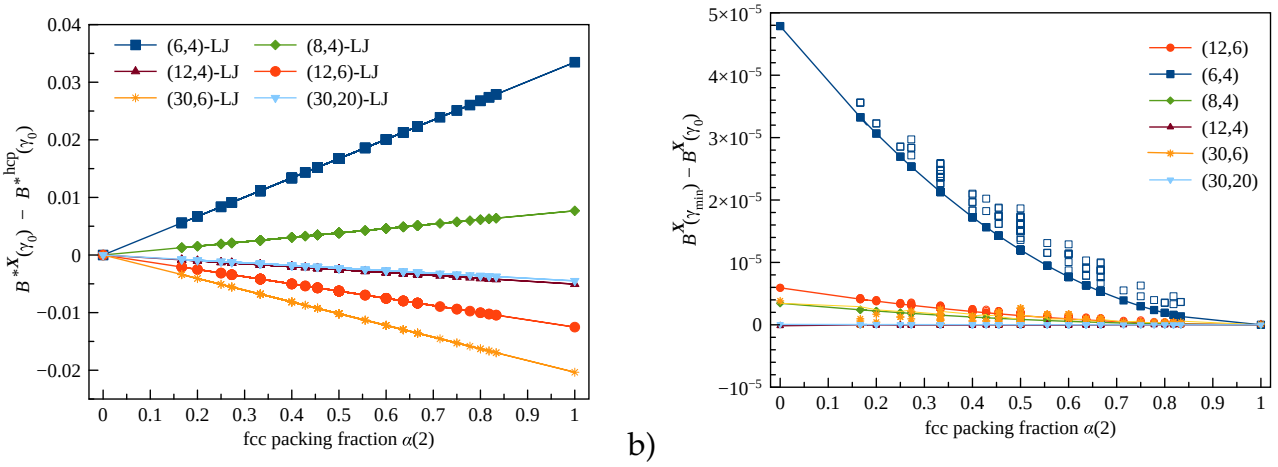

a) b)

Figure 11.9: (a) Differences in bulk moduli for Barlow packings compared to the hcp structure ($\alpha(2) = 0$) as a function of the fcc packing fraction $\alpha(2)$ for various (n,m)-LJ potentials. γ_0 is set to $\sqrt{\frac{2}{3}}$. Data are listed in the supplementary information. (b) Difference in cohesive energies $\Delta B(\gamma_{\min}) = EB(\gamma_{\min}) - B(\gamma_0)$. Case 2 results are shown by (filled symbols) and case 3 open symbols.

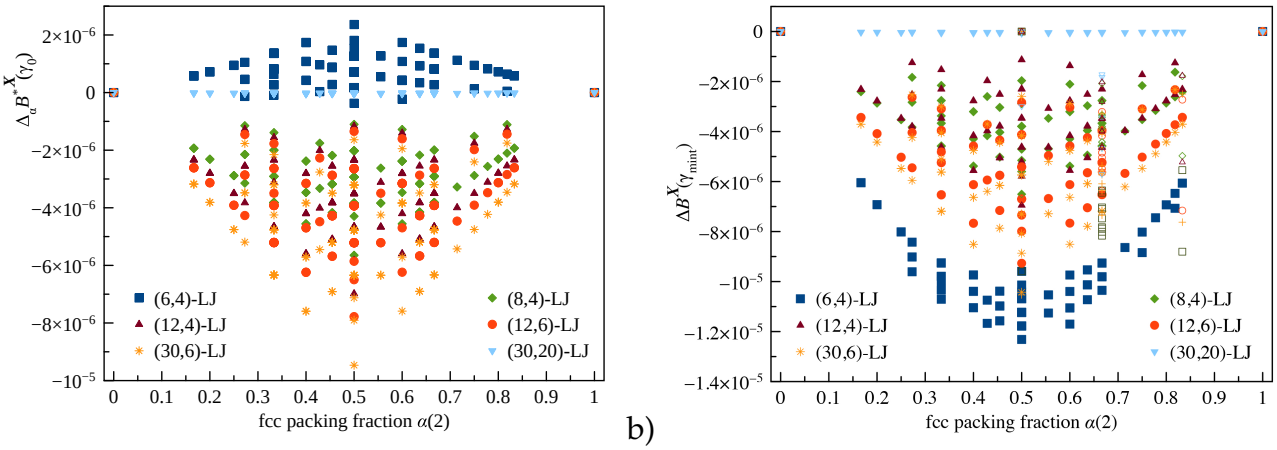

a) b)

Figure 11.10: (a) Deviation of bulk moduli of Barlow packings from the line connecting the fcc and hcp values for various (n,m)-LJ potentials (case 1). (b) Same as for (a) but for case 2 (closed symbols) and case 3 (open symbols).

As the (12,6)-LJ potential is rather close to the exact potential curve for solid argon in the long-range[227], we may compare the bulk modulus to more accurate calculations[104] and to experimental results[583,584]. For the fcc lattice we have $B^* = 106.327846$ (in reduced units) using the (12,6)-LJ potential, which translates into a value of $B = B^*\epsilon/r_e^3 = 3.947$ GPa using the equilibrium distance for Ar_2 of $r_e = 3.7624$ Å and the dissociation energy of $\epsilon = 1188.5$ J/mol from accurate relativistic coupled-cluster calculations of Jaeger et al.[585]. This compares well with the more accurate two-body potential result of 3.732 GPa.[104] The low temperature experimental values are 2.64 GPa[584] by Batchelder et al. and 2.38(1.7) GPa by Dorner et al.[583]

This significantly lower value is a manifestation of many-body and vibrational effects.[104] Note that the hcp bulk modulus for argon is only by 0.02 GPa smaller compared to the fcc value,[104] and therefore perhaps beyond current experimental limits to accurately determine the differences between possible Barlow structures.

11.3.4 Vibrational frequencies

The Einstein (or Debye) model for vibrational frequencies is usually a reasonably good approximation to estimate zero-point vibrational energies, specific heats or entropic contributions to the free energy[25]. They are listed in Table 11.1 for different LJ potentials. For example, for fcc argon we get from (11.36) using a (12,6)-LJ potential a harmonic zero-point vibrational energy of 79.6 cm^{-1} using $r_e = 3.7618$ Å, $\epsilon = 1.1900$ kJ/mol[585] and $M = 39.948$ g/mol. This is in reasonable agreement with a more accurate two-body result of 68.0 cm^{-1} from our previous work.[104] However, as we shall see, for zero-point vibrational energy or entropy differences between the two quasi-degenerate phases fcc and hcp, this simple approximation breaks down requiring a more accurate treatment of phonon dispersion. We therefore only discuss case 1 for the Einstein frequencies and introduce phonon dispersion only for the two extreme Barlow structures fcc and hcp.

The calculated Einstein frequencies are shown in Figure 11.11a. We see exactly the same linear behavior, with an RMS error of 4.04×10^{-7} for the (12,6) LJ potential, and distribution for the differences from the line shown in Figure 11.11b. Thus, the zero-point vibrational energy, $E_0 = \frac{3}{2}\omega_E^{'}$ (in dimensionless units), will also show an almost perfect linear behavior. We briefly mention that the changes in the Einstein frequencies caused by changing $\gamma_0 \rightarrow \gamma_{\text{min}}$ are too small to influence this (almost perfect) linear behavior, they only change the distribution.

Table 11.1: Harmonic frequencies $\omega^{'}$ for the Einstein model and for the phonon dispersion (averaged over all frequencies) for the fcc and hcp lattices and differences $\Delta\omega^{'} = \omega_{\text{fcc}}^{'} - \omega_{\text{hcp}}^{'}$ for various (n,m)-LJ potentials (in dimensionless units) and entropy differences $\Delta S = S_{\text{fcc}} - S_{\text{hcp}}$ in the high temperature limit $T^{'} \rightarrow \infty$ in units of k_B according to eq.(11.46).

LJ	Einstein				Phonon dispersion			
(n,m)	$\omega_{\text{hcp}}^{'}$	$\omega_{\text{fcc}}^{'}$	$\Delta\omega^{'}$	ΔS	$\omega_{\text{hcp}}^{'}$	$\omega_{\text{fcc}}^{'}$	$\Delta\omega^{'}$	ΔS
$(6,4)$	38.5165422	38.5184768	1.9346×10^{-3}	-1.5068×10^{-4}	7.0560514	6.9453406	-0.11071	0.118253
$(8,4)$	30.7329725	30.7339135	9.4102×10^{-4}	-9.1856×10^{-5}	8.4748053	8.3468950	-0.12391	0.112104
$(12,4)$	28.4954081	28.4953490	-5.9129×10^{-5}	6.2254×10^{-6}	11.0551343	10.9009752	-0.15416	0.102934
$(12,6)$	21.7963095	21.7953645	-9.4504×10^{-4}	1.3008×10^{-4}	13.9503325	13.7628320	-0.18750	0.099128
$(30,6)$	30.7370491	30.7356701	-1.3790×10^{-3}	1.3460×10^{-4}	26.9804930	26.6397369	-0.34076	0.092906
$(30,20)$	49.0421487	49.0419002	-2.4847×10^{-4}	1.5200×10^{-5}	55.5361793	54.8483352	-0.68784	0.091216

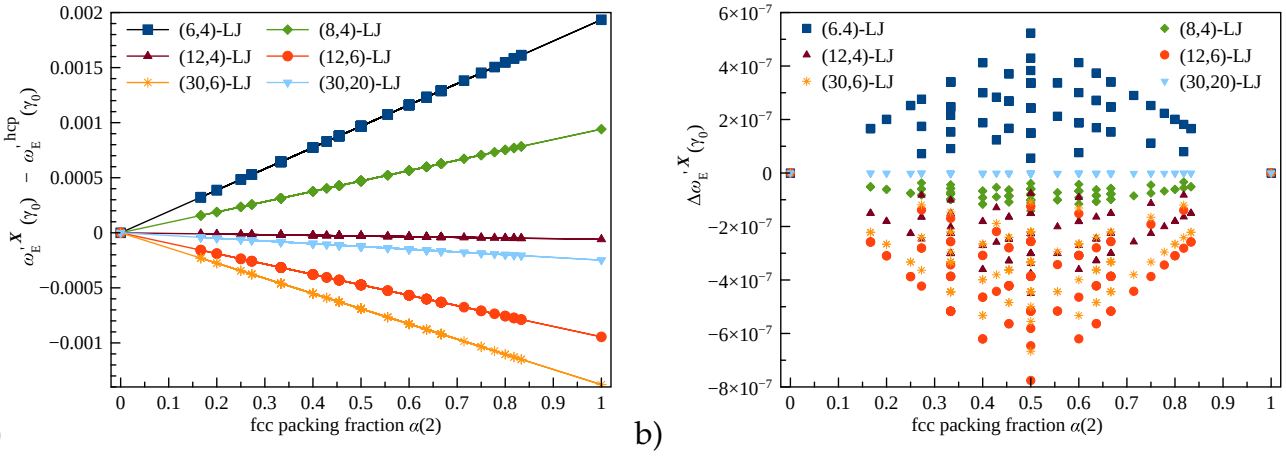

Figure 11.11: (a) Differences in Einstein frequencies (in dimensionless units) for Barlow packings compared to the hcp structure ($\alpha(2) = 0$) as a function of the fcc packing fraction $\alpha(2)$ for various (n,m)-LJ potentials. $\gamma_0 = \sqrt{\frac{2}{3}}$ is used (case 1). (b) Deviation of Einstein frequencies of Barlow packings from the line connecting the fcc and hcp values for various (n,m)-LJ potentials.

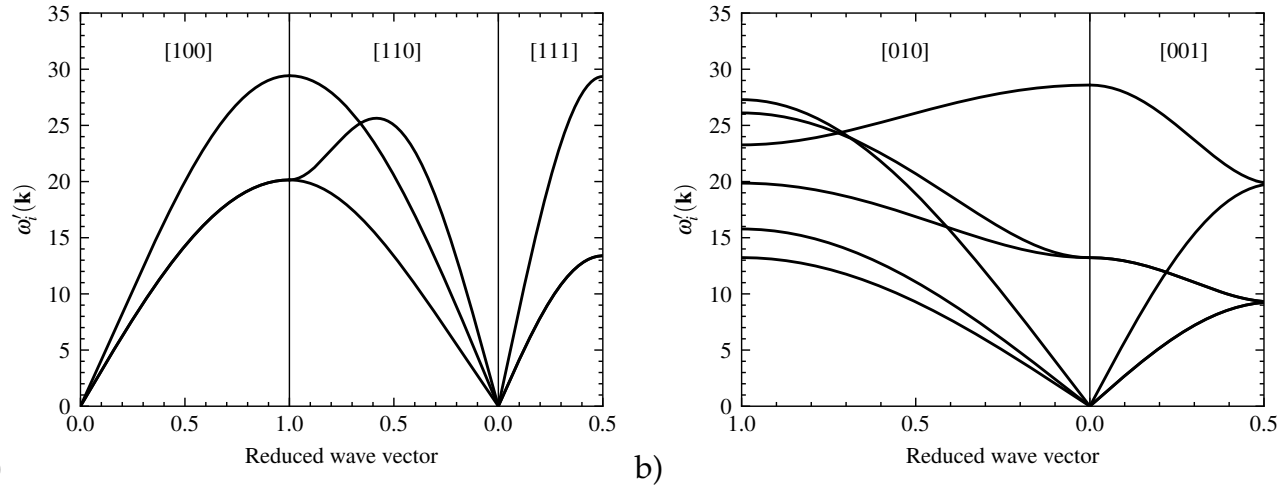

Figure 11.12: Phonon dispersion curves for (a) the fcc and (b) the hcp crystals using the (12,6)-LJ potential.

The (harmonic) phonon dispersion curves for fcc and hcp are shown in Figure 11.12 for the (12,6)-LJ potential. In general, the number of branches is at most $3N$ for the Barlow packages, which is 6 for hcp. A lower number of branches is due to symmetry, e.g. we have 3 phonon branches for fcc as in the more common unit cell definition we require only 1 atom per unit cell. The average phonon frequency for hcp and fcc are 13.9503325 and 13.7628320 respectively, compared to the Einstein frequencies of 21.796309541 and 21.795364501 respectively, obtained from exact lattice summations. The difference in the former case is 0.1875005 and more than two orders of magnitude larger than the difference we get from the Einstein frequencies (9.4504×10^{-4}) using exact lattice summations. Moreover, we see a sign

change in $\Delta\omega^{'} = \omega^{'}_{\rm fcc} - \omega^{'}_{\rm hcp}$ for the Einstein frequencies using softer LJ potential, which is not the case for the phonon dispersion results. This shows that one has to be careful if small differences in properties between different Barlow packing are involved. One may, however, expect that the linear behavior as seen in Figure 11.11a is preserved for the phonon frequencies including dispersion. A computer code for phonon dispersion for general Barlow packings is currently being developed in our group.

11.3.5 Entropy

From the Shannon information entropy[586] one may naively expect that quasi-degenerate Barlow packings with random packing sequences $\{X_1, X_2, \cdots\}$, $X_i = A, B$ or C with $X_i \neq X_{i+1}$, should be entropically preferred. However, letter sequences have little to do with the entropy of a real quantum system. The link between the Gibbs and Shannon entropy for a vibrating solid can be found for example by Huang and Widom[587]. Furthermore, from (11.41) we follow that $\Delta S^{\mathbf{X}}_{\rm vib}(T) \rightarrow 0$ for $T \rightarrow 0$ K. This agrees with the third law of thermodynamics, i.e. $S \rightarrow 0$ for all (nondegenerate) materials because quantum mechanics inhibits the excitation of vibrational modes with frequencies greater than $k_B T/\hbar$[587,588]. This implies that there is no residual vibrational entropy difference for ideal periodic Barlow packings at 0K. Moreover, for a perfect crystal (perfectly ordered without any defects or irregularities) the entropy is zero as well (Nernst's third law of thermodynamics). Differences in entropy between different (periodic and perfect) Barlow structures are nonzero only at finite temperatures ($T \neq 0$).

The entropy difference $\Delta S(T') = S^{\rm fcc}(T') - S^{\rm hcp}(T')$ as a function of the (dimensionless) temperature $T^{'}$ for various (n, m)-LJ potentials within the Einstein vibrational model is shown in Figure 11.13, while Figure 11.14 shows entropy differences at a fixed temperature of $T^{'} = 20$. This temperature is close to the melting (triple) point of $T^{'} = 23.941$ (see section 11.2.4), and also near the high temperature limit for the (12,6)-LJ potential. Again, we see a nice linear behavior for the Barlow packings. Furthermore, the entropy difference is at maximum at the high temperature limit, $T^{'} \rightarrow \infty$. Figure 11.14a shows the $\Delta S(T')$ curves for different atomic masses underpinning the usefulness of our definition of a mass weighted temperature. However, in the high temperature limit (eq.(11.46)) the Einstein model produces entropy differences at least one order of magnitude smaller compared to previous Monte-Carlo simulations,[110,439] which is discussed in more detail below. In addition, Figure 11.14 suggests that entropy favors the hcp structure for small values of the LJ exponent m. In order to relate this clear failure of the Einstein model for entropy differences to the missing phonon dispersion contributions, we analyze the high temperature limit in some more detail.

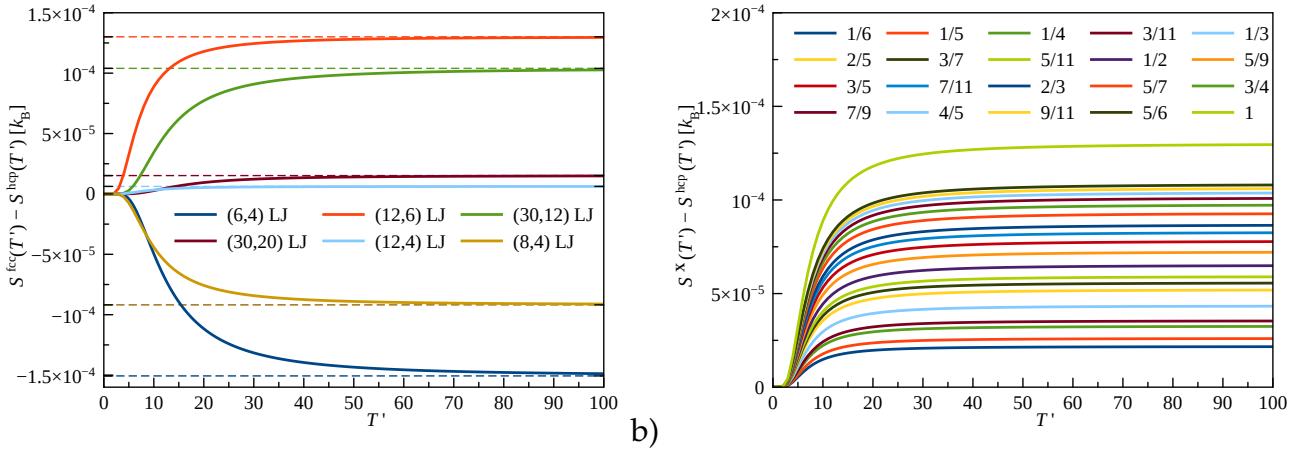

Figure 11.13: (a) Entropy difference $\Delta S(T') = S^{\text{fcc}}(T') - S^{\text{hcp}}(T')$ for different temperatures T' and (n,m)-LJ potentials. The dashed lines represent the high temperature limits $T' \to \infty$. (b) Entropy difference $\Delta S(T')$ for the $(12,6)$-LJ potential and various Barlow packings with different fcc packing fractions $\alpha(2)$.

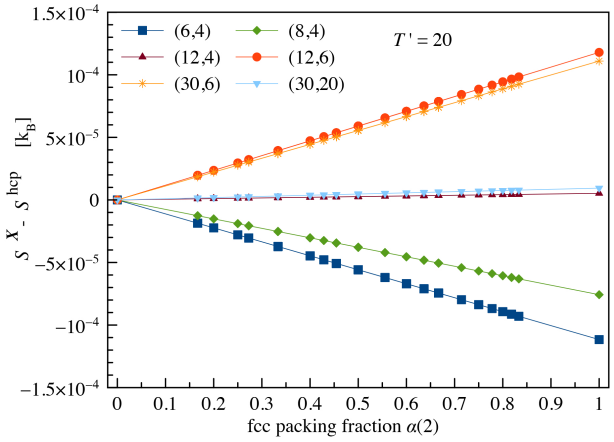

Figure 11.14: Vibrational entropy difference at $T' = 20$ with respect to the fcc packing fraction $\alpha(2)$ for various LJ potentials.

Within the Einstein model we have the high-temperature limit

$$\Delta S^{X}_{\text{vib}}(T' \to \infty) = 3\ln\left(\frac{\omega'^{\text{hcp}}_E}{\omega'^{X}_E}\right) = 3\ln\left(1 + \frac{\omega'^{X}_E - \omega'^{\text{hcp}}_E}{\omega'^{\text{hcp}}_E}\right)^{-1} \approx 3\frac{\omega'^{X}_E - \omega'^{\text{hcp}}_E}{\omega'^{\text{hcp}}_E} \tag{11.52}$$

where we used a Taylor expansion for the logarithmic expression. This implies that $\Delta S^{X}_{\text{vib}}(T' \to \infty) = 0$ only if $\omega'^{\text{hcp}}_E = \omega'^{X}_E$. Furthermore, the entropy difference between fcc and hcp becomes very sensitive to the corresponding difference in the Einstein frequencies. We already showed in the previous section that the difference in the Einstein frequencies energy is not well described by this simple model beside the fact that the frequency in itself approximates

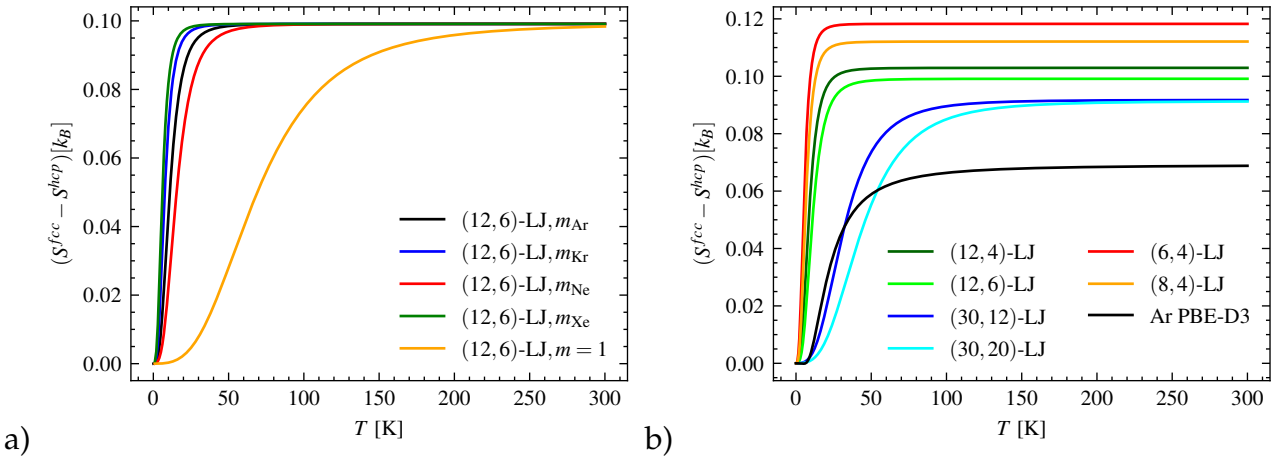

Figure 11.15: (a) Mass (M) and temperature T dependency of the entropy difference between fcc and hcp due to harmonic phonon contribution using the $(12,6)$-LJ potential. (b) Variation of the entropy difference between fcc and hcp due to harmonic phonon contribution with temperature T for different (n,m)-LJ potentials and PBE-D3 for solid argon.

the zero-point vibrational energy reasonably well. Furthermore, as a comparison between the fcc/hcp entropy differences between the Einstein and the phonon dispersion model in the high temperature limit shows (cf. Table 11.1) that the Einstein model consistently underestimates entropy differences by about three orders of magnitude. Moreover, the entropy differences between the different (n,m)-LJ potentials in the high temperature limit are very similar if phonon dispersion is included.

To further test the validity of our entropy calculations by using LJ potentials, we carried out more computer intensive DFT calculations for solid argon to obtain phonon frequencies and vibrational entropies for the two phases fcc and hcp. It is well known that the (12,6)-LJ potential is a reasonably good approximation for the solid state of argon under normal conditions[440]. For example, the phonon dispersion curves derived from DFT as shown in Figure 11.12 are very similar to the (12,6)-LJ potential. However, when it comes to entropy differences, we see some larger deviations from the simple LJ potentials as Figure 11.15 shows, e.g. the convergence to the high temperature limit is far slower at the PBE-D3 level of theory and we see an overall decrease in the fcc/hcp entropy difference compared to the (12,6)-LJ potential. For example, in the high-temperature limit the DFT-D3 is 30.6 % below the (12,6)-LJ result. This again demonstrates the sensitivity of entropy differences between quasi-degenerate phases to the model applied.

Concerning previous work on entropy differences, Mau and Huse showed from Monte-Carlo simulations of hard-spheres close to the maximum packing density that the entropy of the fcc lattice is greater than that of hcp, i.e. $\Delta S = S^{\mathrm{fcc}} - S^{\mathrm{hcp}} = 1.156 \times 10^{-3} k_B$ per sphere.[439,589] Using their parametrization one can in fact show that the entropy of a Barlow packing is correlated to the fcc packing fraction[377] and lying in-between that of fcc and

hcp[439]. Travesset[110] used classical dynamic lattice theory (CDLT) for a (12,6)-LJ potential and obtained very similar results compared to Mau and Huse, i.e. $S^{\text{fcc}} - S^{\text{hcp}} = 1.4754 \times 10^{-3} k_B$ in the phonon hard-sphere limit. He argued that the higher entropy of fcc is the reason why it is the equilibrium phase at sufficiently high temperatures, albeit bcc is often preferred close to the melting line usually explained by Landau theory[252]. For a solid, most of the entropy contribution comes from thermal fluctuations described by the vibrating atoms, see appendix S. This is especially the case for insulators at low temperatures where electronic entropy contributions can be neglected. We therefore focused our attention solely on the vibrational contribution to the entropy for Barlow packings described by Lennard-Jones interactions. We note, however, that our simplified (static) picture neglects dynamic effects which requires a larger supercell treatment. Most notably, for the (30,20)-LJ potential close to the hard-sphere limit we have $\Delta S^{\boldsymbol{X}}_{\text{vib}}(T' \to \infty) = 9.9128 \times 10^{-2} k_B$ from phonon dispersion calculations in the high temperature limit, in stark contrast to Mau and Huse.[439]

11.3.6 Free energy

We can now turn to the question why fcc and hcp are the preferred crystal packings over the infinitely many Barlow structures even so they have equal packing density and are energetically quasi-degenerate. For this we consider the free energy G,

$$G(T) = E_{\text{coh}} + E_0 + pV - TS \tag{11.53}$$

In our simplified static model we neglect dynamic effects, such as temperature effects on lattice constants which changes the internal energy, anharmonicity effects and other smaller contributions. Given that we may assume a linear behavior of the internal energy, volume and (to a certain approximation)[377,439] the entropy as well, such that we have

$$G^{\boldsymbol{X}}(s,\gamma,T) \approx G^{\text{hcp}}(s,\gamma,T) + \alpha^{\boldsymbol{X}}(2)\left[G^{\text{fcc}}(s,\gamma,T) - G^{\text{hcp}}(s,\gamma,T)\right] \tag{11.54}$$

Assuming (11.54) to be valid, we have the Barlow packings lying in-between the two limiting phases of either fcc or hcp at a given temperature T, i.e.

$$G^{\text{Ph1}}(s,\gamma,T) \leq G^{\boldsymbol{X}}(s,\gamma,T) \leq G^{\text{Ph2}}(s,\gamma,T) \tag{11.55}$$

where (Ph1,Ph2) either (fcc,hcp) or (hcp,fcc). Exceptions are for the near degeneracy case, i.e. when $G^{\text{Ph1}}(s,\gamma,T) = G^{\text{Ph2}}(s,\gamma,T)$ (co-existence line) or very close to, at certain temperatures and pressures. This implies that the free energy will prefer either the fcc or the hcp phase over any of the other Barlow packings in most cases. However, the difference in free energies between the Barlow packings is predicted to be very small, e.g. for solid argon the fcc phase

dominates over the hcp phase by only a few J/mol[104]. Here we mention that experiments by solid argon a phase transition from fcc to hcp starts at 4.2 GPa with both phases coexisting in a very wide pressure domain up to $>$ 100 GPa[412]. It is assumed that in this co-existence region of the two phases the bulk is dominated by stacking faults of the two-dimensional close-packed hexagonal layers, i.e. by different Barlow packings. In this respect kinetic effects at finite temperatures and pressures become important as well giving access to metastable Barlow structures apart from the extremal cases fcc and hcp.

11.4 Conclusions

We showed by exact lattice summations that an almost perfect linear relationship with respect to the fcc packing fraction $\alpha(2)$ holds for a number of important solid-state properties of Barlow packings. The treatment through Bessel function expansions of the required lattice sums made it possible to obtain accurate results for energy differences between the different bulk phases. We hypothesize that this results in a linear relationship for the free energy with respect to $\alpha(2)$ at low temperatures and pressures. This hypothesis needs to be tested for real solids and first results were provide for metallic lithium at the PBE-D3 level of theory. It remains, however, a difficult task to describe such small free energy differences accurately by DFT for any material. For a careful numerical comparison one must perhaps use the same unit cell size which allows Barlow packings of period N only for values if $N_i|\max(N)$. We also showed that it is aquite challenging to accurately obtain small entropy differences between the fcc and hcp structures. Nevertheless, we could confirm the result that fcc has a higher entropy than hcp. Our treatment neglects phonon dispersion for Barlow packings other than fcc or hcp, finite pressure and temperature effects, anharmonicities, and a correct many-body treatment. This is the subject of future investigations.

Appendix A

Formulas for Special Functions

A few special functions have been used in this work. For clarity and ease of use, they are stated here along with references.

The *gamma function* may be defined for $s > 0$ by

$$\Gamma(s) = \int_{[0,\infty)} t^{s-1}\, e^{-t}\, \mathrm{d}t. \tag{A.1}$$

By the change of variable $t = wx$ this can be rewritten in the form[590]

$$\frac{1}{w^s} = \frac{1}{\Gamma(s)} \int_{[0,\infty)} x^{s-1}\, e^{-wx}\, \mathrm{d}x. \tag{A.2}$$

The following integral may be evaluated in terms of the *modified Bessel function*:

$$\int_{[0,\infty)} x^{s-1} e^{-ax-b/x} \mathrm{d}x = 2 \left(\frac{b}{a}\right)^{s/2} K_s(2\sqrt{ab}). \tag{A.3}$$

By the change of variable $x = u^{-1}$ it can be shown that

$$K_s(z) = K_{-s}(z). \tag{A.4}$$

When $s = 1/2$ the modified Bessel function reduces to an elementary function

$$K_{1/2}(z) = \sqrt{\frac{\pi}{2z}}\, e^{-z}. \tag{A.5}$$

The asymptotic formula holds

$$K_s(z) \sim \sqrt{\frac{\pi}{2z}}\, e^{-z} \quad \text{as} \quad z \to \infty, \quad (\, |\arg z| < 3\pi/2). \tag{A.6}$$

For all of these properties, see [590] or [591].

The transformation formula for *theta functions* is:[590,592]

$$\sum_{n\in\mathbb{Z}} e^{-\pi n^2 t+2\pi i n a} = \frac{1}{\sqrt{t}} \sum_{n\in\mathbb{Z}} e^{-\pi(n+a)^2/t}, \quad \text{assuming } \mathrm{Re}(t) > 0. \tag{A.7}$$

We will need the special cases $a = 0$ and $a = 1/2$, which are

$$\sum_{n\in\mathbb{Z}} e^{-\pi n^2 t} = \frac{1}{\sqrt{t}} \sum_{n\in\mathbb{Z}} e^{-\pi n^2/t} \tag{A.8}$$

and

$$\sum_{n\in\mathbb{Z}} (-1)^n e^{-\pi n^2 t} = \frac{1}{\sqrt{t}} \sum_{n\in\mathbb{Z}} e^{-\pi(n+\frac{1}{2})^2/t}, \tag{A.9}$$

respectively. The sum of two squares formula is[593]

$$\left(\sum_{j\in\mathbb{Z}} q^{j^2}\right)^2 = \sum_{j,k\in\mathbb{Z}} q^{j^2+k^2} = \sum_{N\in\mathbb{N}_0} r_2(N) q^N \tag{A.10}$$

where

$$r_2(N) = \#\left\{j^2+k^2 = N\right\} = \begin{cases} 1 & \text{if } N = 0, \\ 4\sum_{d|N} \chi_{-4}(d) & \text{if } N \geq 1, \end{cases} \tag{A.11}$$

the sum being over the positive divisors d of N. For example,

$$\begin{aligned} r_2(18) &= 4\left(\chi_{-4}(1)+\chi_{-4}(2)+\chi_{-4}(3)+\chi_{-4}(6)+\chi_{-4}(9)+\chi_{-4}(18)\right) \\ &= 4\left(1+0-1+0+1+0\right) = 4. \end{aligned}$$

By [593] we also have

$$\left(\sum_{j\in\mathbb{Z}} q^{(j+\frac{1}{2})^2}\right)^2 = \sum_{N\in\mathbb{N}_0} r_2(4N+1) q^{(4N+1)/2}. \tag{A.12}$$

The *Riemann zeta function* $\zeta(s)$ and *Dirichlet L function* are defined by

$$\zeta(s) = \sum_{j\in\mathbb{N}} \frac{1}{j^s} \tag{A.13}$$

$$L_{-4}(s) = \sum_{j\in\mathbb{N}} \frac{\chi_{-4}(j)}{j^s} = 1 - \frac{1}{3^s} + \frac{1}{5^s} - \frac{1}{7^s} + \cdots. \tag{A.14}$$

For even integers the Riemann zeta function can be expressed as $\zeta(2n) = \pi^{2n} B_n / A_n$ where A_n and B_n are positive integers, e.g. we have $\zeta(2) = \pi^2/6$, $\zeta(4) = \pi^4/90$, $\zeta(6) = \pi^6/945$, $\zeta(8) = \pi^8/9450$, $\zeta(10) = \pi^{10}/93555$, $\zeta(12) = 691\pi^{12}/638512875$, $\zeta(14) = 2\pi^{14}/18243225$ and $\zeta(16) = 3617\pi^{16}/325641566250$. The coefficients A_n and B_n are listed in the On-Line Encyclopedia of Integer Sequences A002432 and A046988, respectively.[594]

For an integer n, the *Dirichlet character* $\chi_{-4}(n)$ is defined by

$$\chi_{-4}(n) = \sin(\pi n/2) = \begin{cases} 1 & \text{if } n \equiv 1 \pmod 4, \\ -1 & \text{if } n \equiv 3 \pmod 4, \\ 0 & \text{otherwise.} \end{cases} \tag{A.15}$$

The Riemann zeta function has a pole of order 1 at $s = 1$, and in fact

$$\lim_{s \to 1} (s-1)\zeta(s) = 1. \tag{A.16}$$

This is a consequence of [590]. See also [591].

We require the following functional equations

$$\pi^{-s/2}\Gamma(s/2)\zeta(s) = \pi^{-(1-s)/2}\Gamma((1-s)/2)\zeta(1-s) \tag{A.17}$$

and

$$\pi^{-s}\Gamma(s)\,\zeta(s)L_{-4}(s) = \pi^{-(1-s)}\Gamma(1-s)\,\zeta(1-s)L_{-4}(1-s) \tag{A.18}$$

and the special values

$$\zeta(2) = \frac{\pi^2}{6}, \quad \zeta(0) = -\frac{1}{2}, \quad \zeta(-1) = -\frac{1}{12}, \quad \zeta(-2) = \zeta(-4) = \zeta(-6) = \cdots = 0, \tag{A.19}$$

$$L_{-4}(1) = \frac{\pi}{4}, \quad L_{-4}(0) = \frac{1}{2}, \quad L_{-4}(-1) = L_{-4}(-3) = L_{-4}(-5) = \cdots = 0, \tag{A.20}$$

See [595] or [385]. Other equalities used are

$$\sum_{j \in \mathbb{N}_0} \frac{1}{(j+\frac{1}{2})^s} = (2^s - 1)\zeta(s) \tag{A.21}$$

$$\sum_{j \in \mathbb{N}} \frac{(-1)^j}{j^s} = -(1 - 2^{1-s})\zeta(s) \tag{A.22}$$

$$\sum_{j,k \in \mathbb{Z}}{}' \quad \frac{1}{(j^2+k^2)^s} = 4\zeta(s)L_{-4}(s) \tag{A.23}$$

$$\sum_{j,k\in\mathbb{Z}}{}' \quad \frac{(-1)^{j+k}}{(j^2+k^2)^s} = -4(1-2^{1-s})\zeta(s)L_{-4}(s). \tag{A.24}$$

The identities (A.21) and (A.22) follow from the definition of $\zeta(s)$ by series rearrangements. For (A.23) and (A.24) see (1.4.14) and (1.7.5) respectively, of [111].

Given a positive definite quadratic form $g(i,j,k)$, the corresponding *theta series* is defined for $|q|<1$ by

$$\theta_g(q) = \sum_{i,j,k\in\mathbb{Z}} q^{g(i,j,k)}. \tag{A.25}$$

For the quadratic form in (B.3) the theta series is

$$\theta(A;q) = \sum_{i,j,k\in\mathbb{Z}} q^{(A(i+j)^2+(j+k)^2+(i+k)^2)/(A+1)} \quad \text{where } 1/3 \le A \le 1. \tag{A.26}$$

The first few terms in the theta series for fcc, mcc, bcc and acc as far as q^9 are given respectively by

$$\begin{aligned}
\theta(1;q) &= 1+12q+6q^2+24q^3+12q^4+24q^5+8q^6+48q^7+6q^8+36q^9+\cdots,\\
\theta\left(\tfrac{1}{\sqrt{2}};q\right) &= 1+8q+4q^{4-2\sqrt{2}}+2q^{4\sqrt{2}-4}+4q^{8-4\sqrt{2}}+8q^{2\sqrt{2}}+16q^{-4\sqrt{2}+9}\\
&\quad +8q^4+8q^{8\sqrt{2}-7}+4q^{16-8\sqrt{2}}+8q^{-8\sqrt{2}+17}+8q^{20-10\sqrt{2}}+8q^{-4\sqrt{2}+12}\\
&\quad +2q^{16\sqrt{2}-16}+16q^{4\sqrt{2}+1}+16q^{-6\sqrt{2}+16}+8q^{14\sqrt{2}-12}+16q^{-12\sqrt{2}+25}\\
&\quad +8q^{-8+12\sqrt{2}}+8q^9+\cdots,\\
\theta\left(\tfrac{1}{2};q\right) &= 1+8q+6q^{4/3}+12q^{8/3}+8q^4+24q^{11/3}+6q^{16/3}+24q^{19/3}+24q^{20/3}\\
&\quad +24q^8+32q^9+\cdots,\\
\theta\left(\tfrac{1}{3};q\right) &= 1+10q+4q^{3/2}+8q^{5/2}+12q^3+26q^4+8q^{11/2}+20q^6+32q^7\\
&\quad +8q^{15/2}+16q^{17/2}+10q^9+\cdots.
\end{aligned}$$

Since the quadratic form $g(A;i,j,k)$ has been normalised to make the minimum distance 1, the kissing number occurs in each theta series as the coefficient of q. That is, we have kiss(fcc) $=12$, kiss(mcc) $=8$, kiss(bcc) $=8$ and kiss(acc) $=10$.

Finally, we mention the d-dimensional Epstein zeta function[113,596] in its most general form for a matrix A, vectors $\vec{c}$ and $\vec{v}$, and exponent $\rho\in\mathbb{C}$,

$$Z_d(A,\rho) = \sum_{\vec{k}\in\mathbb{Z}^d}{}' \frac{e^{2\pi i\vec{c}\cdot A\vec{k}}}{|A\vec{k}-\vec{v}|^\rho}. \tag{A.27}$$

The connection to the generator matrix B in lattices is by setting $A=B^\top$, and the Gram matrix

becomes $G = BB^\top = A^\top A$. The vector $\vec{v}$ is often called the shift vector in lattice theory.

Appendix B

Evaluation of the Lattice Sum $L(A;s)$

Consider the quadratic form

$$g(i,j,k) = (i,j,k)G(i,j,k)^\top, \tag{B.1}$$

with the Gram matrix in Eq. (5.8). To eliminate v, we divide the above equation by the squared nearest neighbor distance R^2, yielding

$$g(A;i,j,k) = \frac{g(i,j,k)}{R^2} = \begin{cases} \dfrac{1}{4A}\left(A(i+j)^2+(j+k)^2+(i+k)^2\right) & \text{if } 0 < A < 1/3, \\ \dfrac{1}{A+1}\left(A(i+j)^2+(j+k)^2+(i+k)^2\right) & \text{if } 1/3 \le A \le 1, \\ \dfrac{1}{2}\left(A(i+j)^2+(j+k)^2+(i+k)^2\right) & \text{if } A > 1. \end{cases} \tag{B.2}$$

The cases which we are mainly interested in are fcc, mcc, bcc, acc, all of which satisfy $1/3 \le A \le 1$, but we will go slightly beyond this limit mainly to discuss distortions towards the acc structure. In the important range $1/3 \le A \le 1$, we have

$$g(A;i,j,k) = \frac{1}{A+1}\left(A(i+j)^2+(j+k)^2+(i+k)^2\right), \tag{B.3}$$

corresponding to the rescaled Gram matrix

$$G(A) = \frac{1}{A+1}\begin{pmatrix} A+1 & A & 1 \\ A & A+1 & 1 \\ 1 & 1 & 2 \end{pmatrix} \tag{B.4}$$

which is used throughout this work.

The lattice sum for inverse power potentials in terms of the quadratic form $g(A;i,j,k)$

defined in (B.3) is then given by[111,295]

$$L(A;s) = {\sum_{i,j,k\in\mathbb{Z}}}' \left(\frac{1}{g(A;i,j,k)}\right)^s = {\sum_{i,j,k\in\mathbb{Z}}}' \left(\frac{A+1}{A(i+j)^2+(j+k)^2+(i+k)^2}\right)^s \tag{B.5}$$

where $1/3 \leq A \leq 1$. Here and throughout this work, a prime on the summation symbol will denote that the sum ranges over all integer values except for the term when all of the summation indices are simultaneously zero, i.e., the sums in (B.5) are over all integer values of i, j and k except for the term $(i,j,k) = (0,0,0)$, which is omitted. This lattice sum smoothly connects four different lattices along a cuboidal transition path (the Bain transformation), i.e., when $A = 1$, $1/\sqrt{2}$, $1/2$ or $1/3$ we obtain the expressions for the lattice sums of fcc, mcc, bcc and acc respectively (face-centered cubic, mean centred-cuboidal, body-centred cubic, and axial centred cuboidal). In these cases, we also write $L_3^{\text{fcc}}(s) = L(1;s), L_3^{\text{mcc}}(s) = L(1/\sqrt{2};s), L_3^{\text{bcc}}(s) = L(1/2;s)$, and $\quad L_3^{\text{acc}}(s) = L(1/3;s)$.

Our objective is to find formulas for $L(A;s)$ that are both simple and computationally efficient. The formulas we obtain can be used to show that $L(A;s)$ can be analytically continued to complex values of s, with a simple pole at $s = 3/2$ and no other singularities.

One method of evaluating the sum $L(A;s)$ is to use the Terras decomposition.[299] This was done in our previous work for the fcc and bcc lattices,[295] and can in principle also be applied for general $L(A;s)$ with symmetric Gram matrices related to the Epstein zeta function.[113] Here we use an easier method that works for the entire parameter range $1/3 \leq A \leq 1$ along the Bain transformation path and hence gives the lattice sum for all four lattices fcc, mcc, bcc and acc. The advantage is that we obtain two formulas, which not only can be used as checks, but also provide distinct information about their analytic continuation.

We begin by writing the lattice sum in the form

$$\begin{aligned} L(A;s) &= {\sum_{i,j,k\in\mathbb{Z}}}' \left(\frac{A+1}{A(i+j)^2+(j+k)^2+(i+k)^2}\right)^s = {\sum_{\substack{I,J,K\in\mathbb{Z} \\ I+J+K \text{ even}}}}' \left(\frac{A+1}{AI^2+J^2+K^2}\right)^s \\ &= \frac{(A+1)^s}{2} {\sum_{i,j,k\in\mathbb{Z}}}' \frac{1+(-1)^{i+j+k}}{(Ai^2+j^2+k^2)^s} = \frac{(A+1)^s}{2}\left(T_1(A;s)+T_2(A;s)\right). \end{aligned} \tag{B.6}$$

with the two sums

$$T_1(A;s) := {\sum_{i,j,k\in\mathbb{Z}}}' \frac{1}{(Ai^2+j^2+k^2)^s} \tag{B.7}$$

and

$$T_2(A;s) := {\sum_{i,j,k\in\mathbb{Z}}}' \frac{(-1)^{i+j+k}}{(Ai^2+j^2+k^2)^s} \tag{B.8}$$

which we evaluate separately. For $A = 1$, T_1 is identical to the lattice sum of a simple cubic

lattice and T_2 to the Madelung constant.

The lattice sum $T_1(A;s)$. We shall consider two ways for handling the sum in (B.7). The first is to separate the terms according to whether $i = 0$ or $i \neq 0$, which gives rise to

$$T_1(A;s) = f(s) + 2F(s) \tag{B.9}$$

where

$$f(s) = \sum_{j,k\in\mathbb{Z}}{}' \ \frac{1}{(j^2+k^2)^s} \quad \text{and} \quad F(s) = \sum_{i\in\mathbb{N}} \sum_{j,k\in\mathbb{Z}} \frac{1}{(Ai^2+j^2+k^2)^s} \tag{B.10}$$

and $\mathbb{N}$ is the set of positive integers. For simplicity we omit the parameter A from the notation and just write $f(s)$ and $F(s)$ in place of $f(A;s)$ and $F(A;s)$. This is the starting point of the approach taken by Selberg and Chowla.[597] Using theta series and Mellin transforms, Zucker showed that the double sum can be expressed in terms of standard functions,[124]

$$f(s) = \sum_{j,k\in\mathbb{Z}}{}' \ \frac{1}{(j^2+k^2)^s} = 4\zeta(s)L_{-4}(s) \tag{B.11}$$

where $\zeta(s)$ is the Riemann zeta function defined in (A.13), and $L_{-4}(s)$ is the Dirichlet beta series from (A.14) described in Appendix A. It remains to analyze $F(s)$. Using the integral formula for the gamma function (A.2) we get

$$\begin{aligned} \pi^{-s}\Gamma(s)F(s) &= \int_{[0,\infty)} x^{s-1} \sum_{i\in\mathbb{N}} e^{-\pi Axi^2} \sum_{j,k\in\mathbb{Z}} e^{-\pi x(j^2+k^2)} \, \mathrm{d}x \\ &= \int_{[0,\infty)} x^{s-1} \sum_{i\in\mathbb{N}} e^{-\pi Axi^2} \left(\sum_{j\in\mathbb{Z}} e^{-\pi xj^2} \right)^2 \, \mathrm{d}x. \end{aligned} \tag{B.12}$$

Now apply the modular transformation for theta functions (A.10) to obtain

$$\begin{aligned} \pi^{-s}\Gamma(s)F(s) &= \int_{[0,\infty)} x^{s-1} \sum_{i\in\mathbb{N}} e^{-\pi Axi^2} \left(\frac{1}{\sqrt{x}} \sum_{j\in\mathbb{Z}} e^{-\pi j^2/x} \right)^2 \, \mathrm{d}x \\ &= \int_{[0,\infty)} x^{s-2} \sum_{i\in\mathbb{N}} e^{-\pi Axi^2} \sum_{N\in\mathbb{N}_0} r_2(N) e^{-\pi N/x} \, \mathrm{d}x \end{aligned} \tag{B.13}$$

where $r_2(N)$ is the number of representations of N as a sum of two squares, e.g., see (3.23), and $\mathbb{N}_0 = \mathbb{N} \cup \{0\}$. Separating out the $N = 0$ term and evaluating the resulting integrals, we find

that

$$\begin{aligned}\pi^{-s}\Gamma(s)F(s) &= \sum_{i\in\mathbb{N}}\int_{[0,\infty)} x^{s-2}e^{-\pi Axi^2}\,\mathrm{d}x + \sum_{i,N\in\mathbb{N}} r_2(N)\int_{[0,\infty)} yx^{s-2}e^{-\pi Axi^2-\pi N/x}\,\mathrm{d}x \\ &= \frac{\Gamma(s-1)\zeta(2s-2)}{A^{s-1}\pi^{s-1}} + 2\sum_{i,N\in\mathbb{N}} r_2(N)\left(\frac{N}{Ai^2}\right)^{(s-1)/2} K_{s-1}\left(2\pi i\sqrt{AN}\right)\end{aligned}$$

where we have used the formula (A.3) for the K-Bessel function. On using all of the above back in (B.9) we obtain

$$\begin{aligned}\sum_{i,j,k\in\mathbb{Z}}{}' \frac{1}{(Ai^2+j^2+k^2)^s} &= 4\zeta(s)L_{-4}(s) + \frac{2\pi}{(s-1)}\frac{\zeta(2s-2)}{A^{s-1}} \\ &+ \frac{4\pi^s}{\Gamma(s)}A^{(1-s)/2}\sum_{i,N\in\mathbb{N}} r_2(N)\left(\frac{N}{i^2}\right)^{(s-1)/2} K_{s-1}\left(2\pi i\sqrt{AN}\right).\end{aligned} \tag{B.14}$$

This is essentially Selberg and Chowla's formula[597], although they write it in terms of a sum over the divisors of N to minimize the number of Bessel function evaluations. We will leave it as it is for simplicity.

Second formula for the sum $T_1(A;s)$. Another way is to separate the terms according to whether $(j,k)=(0,0)$ or $(j,k)\neq(0,0)$ and write

$$T_1(A;s) = 2g(s) + G(s) \tag{B.15}$$

where

$$g(s) = \sum_{i\in\mathbb{N}}\frac{1}{(Ai^2)^s} \quad\text{and}\quad G(s) = \sum_{j,k\in\mathbb{Z}}{}'\sum_{i\in\mathbb{Z}}\frac{1}{(Ai^2+j^2+k^2)^s}. \tag{B.16}$$

For simplicity we omit the parameter A from the notation and just write $g(s)$ and $G(s)$ in place of $g(A;s)$ and $G(A;s)$, respectively. Now apply the integral formula for the gamma function (A.2) and then the modular transformation for the theta function (A.7) to obtain

$$\begin{aligned}\pi^{-s}\Gamma(s)G(s) &= \int_{[0,\infty)} x^{s-1}\sum_{j,k\in\mathbb{Z}}{}' e^{-\pi(j^2+k^2)x}\sum_{i\in\mathbb{Z}} e^{-\pi i^2 Ax}\,\mathrm{d}x \\ &= \frac{1}{\sqrt{A}}\int_{[0,\infty)} x^{s-3/2}\sum_{j,k\in\mathbb{Z}}{}' e^{-\pi(j^2+k^2)x}\sum_{i\in\mathbb{Z}} e^{-\pi i^2/Ax}\,\mathrm{d}x.\end{aligned} \tag{B.17}$$

Separate the $i = 0$ term, to get

$$\pi^{-s}\Gamma(s)G(s) = \frac{1}{\sqrt{A}}\int_{[0,\infty)} x^{s-3/2}\sum_{j,k\in\mathbb{Z}}{}' e^{-\pi(j^2+k^2)x}\,\mathrm{d}x + \frac{2}{\sqrt{A}}\int_{[0,\infty)} x^{s-3/2}\sum_{j,k\in\mathbb{Z}}{}' e^{-\pi(j^2+k^2)x}\sum_{i\in\mathbb{N}} e^{-\pi i^2/Ax}\,\mathrm{d}x. \tag{B.18}$$

The first integral can be evaluated in terms of the gamma function by (A.2), while the second integral can be expressed in terms of the modified Bessel function by (A.3). The result is

$$\begin{aligned}\pi^{-s}\Gamma(s)G(s) &= \frac{\Gamma\left(s-\frac{1}{2}\right)}{\sqrt{A}\,\pi^{s-\frac{1}{2}}}\sum_{j,k\in\mathbb{Z}}{}'\frac{1}{(j^2+k^2)^{s-\frac{1}{2}}} \\ &\quad + \frac{4}{A^{\frac{s}{2}+\frac{1}{4}}}\sum_{j,k\in\mathbb{Z}}{}'\sum_{i\in\mathbb{N}}\left(\frac{i}{\sqrt{j^2+k^2}}\right)^{s-\frac{1}{2}} K_{s-\frac{1}{2}}\left(2\pi i\sqrt{\frac{j^2+k^2}{A}}\right) \\ &= \frac{4}{\sqrt{A}}\,\pi^{-(s-\frac{1}{2})}\,\Gamma\left(s-\frac{1}{2}\right)\,\zeta\left(s-\frac{1}{2}\right)\,L_{-4}\left(s-\frac{1}{2}\right) \\ &\quad + \frac{4}{A^{\frac{s}{2}+\frac{1}{4}}}\sum_{N,i\in\mathbb{N}} r_2(N)\left(\frac{i}{\sqrt{N}}\right)^{s-\frac{1}{2}} K_{s-\frac{1}{2}}\left(2\pi i\sqrt{\frac{N}{A}}\right).\end{aligned} \tag{B.19}$$

On using all of the above back in (B.15) we obtain

$$\begin{aligned}\sum_{i,j,k\in\mathbb{Z}}{}'\ \frac{1}{(Ai^2+j^2+k^2)^s} &= 2A^{-s}\zeta(2s) + 4\sqrt{\frac{\pi}{A}}\,\frac{\Gamma\left(s-\frac{1}{2}\right)}{\Gamma(s)}\,\zeta\left(s-\frac{1}{2}\right)\,L_{-4}\left(s-\frac{1}{2}\right) \\ &\quad + \frac{4}{A^{\frac{s}{2}+\frac{1}{4}}}\,\frac{\pi^s}{\Gamma(s)}\sum_{N,i\in\mathbb{N}} r_2(N)\left(\frac{i}{\sqrt{N}}\right)^{s-\frac{1}{2}} K_{s-\frac{1}{2}}\left(2\pi i\sqrt{\frac{N}{A}}\right).\end{aligned} \tag{B.20}$$

The terms in (B.14) involve K_{s-1} Bessel functions whereas $K_{s-\frac{1}{2}}$ Bessel functions occur in (B.20). That is because each application of the theta function transformation formula lowers the subscript in the resulting Bessel function by $1/2$, due to the creation of a $x^{-1/2}$ factor in the integral. The theta function transformation formula is used twice (i.e., the formula is squared) in the derivation of (B.14) and only once in the derivation of (B.20). Each of (B.14) and (B.20) turns out to have its own advantages when it comes to convergence for specific A and s values.

The alternating lattice sum $T_2(A;s)$. The analysis in the previous sections can be modified to handle the alternating series (B.8) which has the term $(-1)^{i+j+k}$ in the numerator, as follows. Separating the terms according to whether $i = 0$ or $i \neq 0$ gives

$$T_2(A;s) = h(s) + 2H(S) \tag{B.21}$$

where

$$h(s) = \sum_{j,k\in\mathbb{Z}}{}' \frac{(-1)^{j+k}}{(j^2+k^2)^s} \quad \text{and} \quad H(s) = \sum_{i\in\mathbb{N}} \sum_{j,k\in\mathbb{Z}} \frac{(-1)^{i+j+k}}{(Ai^2+j^2+k^2)^s}. \tag{B.22}$$

Using (A.14), we obtain $h(s) = -4(1-2^{1-s})\zeta(s)L_{-4}(s)$. Next, using the integral formula for the gamma function (A.2) we obtain

$$\pi^{-s}\Gamma(s)H(s) = \int_{[0,\infty)} x^{s-1} \sum_{i\in\mathbb{N}} (-1)^i e^{-\pi A x i^2} \sum_{j,k\in\mathbb{Z}} (-1)^{j+k} e^{-\pi x(j^2+k^2)} \, \mathrm{d}x \tag{B.23}$$

$$= \int_{[0,\infty)} x^{s-1} \sum_{i\in\mathbb{N}} (-1)^i e^{-\pi A x i^2} \left(\sum_{j\in\mathbb{Z}} (-1)^j e^{-\pi x j^2} \right)^2 \mathrm{d}x. \tag{B.24}$$

Applying the modular transformation for theta functions leads to

$$\pi^{-s}\Gamma(s)H(s) = \int_{[0,\infty)} x^{s-1} \sum_{i\in\mathbb{N}} (-1)^i e^{-\pi A x i^2} \left(\frac{1}{\sqrt{x}} \sum_{j\in\mathbb{Z}} e^{-\pi(j+\frac{1}{2})^2/x} \right)^2 \mathrm{d}x. \tag{B.25}$$

By formula (A.12) this can be expressed as

$$\pi^{-s}\Gamma(s)H(s) = \int_{[0,\infty)} x^{s-2} \sum_{i\in\mathbb{N}} (-1)^i e^{-\pi A x i^2} \sum_{N\in\mathbb{N}_0} r_2(4N+1) e^{-\pi(4N+1)/2x} \, \mathrm{d}x \tag{B.26}$$

$$= \sum_{i\in\mathbb{N}} \sum_{N\in\mathbb{N}_0} (-1)^i r_2(4N+1) \int_{[0,\infty)} x^{s-2} e^{-\pi A x i^2 - \pi(4N+1)/2x} \, \mathrm{d}x.$$

The integral can be expressed in terms of Bessel functions using (A.3)

$$\pi^{-s}\Gamma(s)H(s) = 2\sum_{i\in\mathbb{N}} \sum_{N\in\mathbb{N}_0} (-1)^i r_2(4N+1) \left(\frac{2N+\frac{1}{2}}{Ai^2} \right)^{(s-1)/2} K_{s-1}\left(2\pi i \sqrt{A(2N+\frac{1}{2})} \right). \tag{B.27}$$

Incorporating all of the above back in (B.21) results in

$$\sum_{i,j,k\in\mathbb{Z}}{}' \frac{(-1)^{i+j+k}}{(Ai^2+j^2+k^2)^s} = -4(1-2^{1-s})\zeta(s)L_{-4}(s) \tag{B.28}$$

$$+ \frac{4\pi^s}{\Gamma(s)} A^{(1-s)/2} \sum_{i\in\mathbb{N}} \sum_{N\in\mathbb{N}_0} (-1)^i r_2(4N+1) \left(\frac{2N+\frac{1}{2}}{i^2} \right)^{(s-1)/2} K_{s-1}\left(2\pi i \sqrt{A(2N+\frac{1}{2})} \right).$$

Second formula for $T_2(A;s)$. This time we separate the terms according to whether $(j,k) =$

$(0,0)$ or $(j,k) \neq (0,0)$ and write

$$T_2(A;s) = 2\sum_{i\in\mathbb{N}} \frac{(-1)^i}{(Ai^2)^s} + J(s) \tag{B.29}$$

where

$$J(s) = \sum_{j,k\in\mathbb{Z}}{}' \sum_{i\in\mathbb{Z}} \frac{(-1)^{i+j+k}}{(Ai^2+j^2+k^2)^s}. \tag{B.30}$$

Using (A.22) gives

$$2\sum_{i\in\mathbb{N}} \frac{(-1)^i}{(Ai^2)^s} = -2A^{-s}(1-2^{1-2s})\zeta(2s). \tag{B.31}$$

It remains to analyse the sum for $J(s)$. Using the integral formula for the gamma function (A.2) leads to

$$\pi^{-s}\Gamma(s)J(s) = \int_{[0,\infty)} x^{s-1} \sum_{j,k\in\mathbb{Z}}{}'(-1)^{j+j} e^{-\pi(j^2+k^2)x} \sum_{i\in\mathbb{Z}} (-1)^i e^{-\pi i^2 Ax}\,\mathrm{d}x. \tag{B.32}$$

Applying the modular transformation (A.9) gives

$$\pi^{-s}\Gamma(s)J(s) = \frac{1}{\sqrt{A}} \int_{[0,\infty)} x^{s-3/2} \sum_{j,k\in\mathbb{Z}}{}'(-1)^{j+k} e^{-\pi(j^2+k^2)x} \sum_{i\in\mathbb{Z}} e^{-\pi(i+\frac{1}{2})^2/Ax}\,\mathrm{d}x. \tag{B.33}$$

Setting $N = j^2+k^2$ and using

$$\sum_{i\in\mathbb{Z}} e^{-\pi(i+\frac{1}{2})^2/Ax} = 2\sum_{i\in\mathbb{N}_0}^{\infty} e^{-\pi(i+\frac{1}{2})^2/Ax} = 2\sum_{i\in\mathbb{N}} e^{-\pi(i-\frac{1}{2})^2/Ax} \tag{B.34}$$

gives

$$\pi^{-s}\Gamma(s)J(s) = \frac{2}{\sqrt{A}} \sum_{N,i\in\mathbb{N}} (-1)^N r_2(N) \int_{[0,\infty)} x^{s-3/2}\, e^{-\pi Nx - \pi(i-\frac{1}{2})^2/Ax}\,\mathrm{d}x. \tag{B.35}$$

The integral can be evaluated in terms of the modified Bessel function, (A.3),

$$\pi^{-s}\Gamma(s)J(s) = \frac{4}{A^{\frac{s}{2}+\frac{1}{4}}} \sum_{N,i\in\mathbb{N}} (-1)^N r_2(N) \left(\frac{i-\frac{1}{2}}{\sqrt{N}}\right)^{s-\frac{1}{2}} K_{s-\frac{1}{2}}\left(2\pi(i-\frac{1}{2})\sqrt{\frac{N}{A}}\right). \tag{B.36}$$

It follows that

$$\sum_{i,j,k\in\mathbb{Z}}{}' \frac{(-1)^{i+j+k}}{(Ai^2+j^2+k^2)^s} = -2A^{-s}(1-2^{1-2s})\zeta(2s) \tag{B.37}$$
$$+ \frac{4}{A^{\frac{s}{2}+\frac{1}{4}}}\frac{\pi^s}{\Gamma(s)}\sum_{N,i\in\mathbb{N}}(-1)^N r_2(N)\left(\frac{i-\frac{1}{2}}{\sqrt{N}}\right)^{s-\frac{1}{2}} K_{s-\frac{1}{2}}\left(2\pi(i-\frac{1}{2})\sqrt{\frac{N}{A}}\right).$$

Two formulas for $L(A;s)$. On substituting the results of (B.14) and (B.28) back into (B.6) we obtain a formula for $L(A;s)$ in terms of K_{s-1} Bessel functions:

$$L(A;s) = 4\left(\frac{A+1}{2}\right)^s\zeta(s)L_{-4}(s) + \frac{\pi A}{s-1}\left(1+\frac{1}{A}\right)^s\zeta(2s-2) \tag{B.38}$$
$$+ \frac{2\pi^s\sqrt{A}}{\Gamma(s)}\left(\sqrt{A}+\frac{1}{\sqrt{A}}\right)^s\sum_{N,i\in\mathbb{N}} r_2(N)\left(\frac{N}{i^2}\right)^{(s-1)/2}K_{s-1}\left(2\pi i\sqrt{AN}\right)$$
$$+ \frac{2\pi^s\sqrt{A}}{\Gamma(s)}\left(\sqrt{A}+\frac{1}{\sqrt{A}}\right)^s\sum_{i\in\mathbb{N}}\sum_{N\in\mathbb{N}_0}(-1)^i r_2(4N+1)\left(\frac{2N+\frac{1}{2}}{i^2}\right)^{(s-1)/2}K_{s-1}\left(2\pi i\sqrt{A(2N+\frac{1}{2})}\right).$$

On the other hand, if the results of (B.20) and (B.37) are used in (B.6), the resulting formula for $L(A;s)$ involves $K_{s-1/2}$ Bessel functions:

$$L(A;s) = 2\left(\frac{A+1}{4A}\right)^s\zeta(2s) + 2\sqrt{\frac{\pi}{A}}\,(A+1)^s\frac{\Gamma\left(s-\frac{1}{2}\right)}{\Gamma(s)}\zeta\left(s-\frac{1}{2}\right)L_{-4}\left(s-\frac{1}{2}\right)$$
$$+ \frac{2}{A^{1/4}}\left(\sqrt{A}+\frac{1}{\sqrt{A}}\right)^s\frac{\pi^s}{\Gamma(s)}\sum_{N,i\in\mathbb{N}}N^{(1-2s)/4}r_2(N) \tag{B.39}$$
$$\times\left\{i^{s-\frac{1}{2}}K_{s-\frac{1}{2}}\left(2\pi i\sqrt{\frac{N}{A}}\right) + (-1)^N\left(i-\frac{1}{2}\right)^{s-\frac{1}{2}}K_{s-\frac{1}{2}}\left(2\pi(i-\frac{1}{2})\sqrt{\frac{N}{A}}\right)\right\}.$$

The formulas (B.38) and (B.39) can be used as checks against one another. Moreover, the formulas offer different information about special values of the lattice sum, as will be seen in Section G.

Appendix C

Evaluation of the Two-Body Lattice Sum for a Rectangular 2D Lattice

For the lattice sum with Gram matrix (5.47) ,

$$\sum_{i\in\mathbb{Z}}{}' \left[i^2+(\gamma j)^2\right]^{-s} = 2\zeta(2s)\left\{1+\gamma^{-2s}+2\left(1+\gamma^2\right)^{-s}\right\} + 4\sum_{i,j\in\mathbb{N},i\neq j}{}' \left[i^2+(\gamma j)^2\right]^{-s}, \tag{C.1}$$

we use Van der Hoff and Benson's original expression derived from a Mellin transformation and the use of theta functions,[300]

$$\sum_{i\in\mathbb{Z}}{}' \left[x^2+(i+a)^2\right]^{-s} = \frac{\sqrt{\pi}\Gamma(s-\frac{1}{2})}{\Gamma(s)\,|x|^{2s-1}} + \frac{4\pi^s}{\Gamma(s)}\sum_{n\in\mathbb{N}}\left(\frac{n}{|x|}\right)^{s-\frac{1}{2}}\cos(2\pi na)K_{s-\frac{1}{2}}(2\pi n|x|) \tag{C.2}$$

with $a\in(0,1)$. Using $a=0$ and $x=\gamma j$ $(\gamma>0)$ we get a fast converging series in terms of Bessel functions,

$$\sum_{i,j\in\mathbb{Z}}{}' \left[i^2+(\gamma j)^2\right]^{-s} = 2\zeta(2s) + \sum_{j\in\mathbb{Z}}{}'\frac{\sqrt{\pi}\Gamma(s-\frac{1}{2})}{\Gamma(s)\,|\gamma j|^{2s-1}} + \frac{4\pi^s}{\Gamma(s)}\sum_{j\in\mathbb{Z}}{}'\sum_{n\in\mathbb{N}}\left(\frac{n}{|\gamma j|}\right)^{s-\frac{1}{2}}K_{s-\frac{1}{2}}(2\pi n\gamma|j|) \tag{C.3}$$

which simplifies to

$$\sum_{i,j\in\mathbb{Z}}{}' \left[i^2+(\gamma j)^2\right]^{-s} = 2\zeta(2s) + \frac{2\sqrt{\pi}\Gamma(s-\frac{1}{2})\zeta(2s-1)}{\Gamma(s)\gamma^{2s-1}} + \frac{8\pi^s}{\Gamma(s)}\sum_{n,j\in\mathbb{N}}\left(\frac{n}{\gamma j}\right)^{s-\frac{1}{2}}K_{s-\frac{1}{2}}(2\pi\gamma nj). \tag{C.4}$$

The additional Riemman zeta function comes from the case when $(j=0, i\neq 0)$. As the Bessel function $K_n(x)$ decays exponentially with the argument x, for $\gamma<1$ it is computationally

advantageous to rewrite the sum into

$$\sum_{i,j\in\mathbb{Z}}{}' \left[i^2+(\gamma j)^2\right]^{-s} = \gamma^{-2s}\sum_{i,j\in\mathbb{Z}}{}' \left[\gamma^{-2}i^2+j^2\right]^{-s} = \gamma^{-2s}\sum_{i,j\in\mathbb{Z}}{}' \left[i^2+(j/\gamma)^2\right]^{-s} \tag{C.5}$$

and we get in a similar fashion

$$\begin{aligned}\gamma^{-2s}\sum_{i,j\in\mathbb{Z}}{}' \left[i^2+(j/\gamma)^2\right]^{-s} &= 2\gamma^{-2s}\zeta(2s) + \frac{2\sqrt{\pi}\Gamma(s-\frac{1}{2})\zeta(2s-1)}{\Gamma(s)\gamma} \\ &\quad + \frac{8\pi^s}{\Gamma(s)\gamma^{s+\frac{1}{2}}}\sum_{n,j\in\mathbb{N}}\left(\frac{n}{j}\right)^{s-\frac{1}{2}} K_{s-\frac{1}{2}}(2\pi\gamma^{-1}nj)\end{aligned} \tag{C.6}$$

This formula is identical to the one given by Bateman and Grosswald.[598] For computational efficiency, we rewrite Eq.(C.4),

$$\begin{aligned}\sum_{i,j\in\mathbb{Z}}{}' \left[i^2+(\gamma j)^2\right]^{-s} &= \zeta(2s) + \frac{2\sqrt{\pi}\Gamma(s-\frac{1}{2})\zeta(2s-1)}{\Gamma(s)\gamma^{2s-1}} + \frac{8\pi^s}{\Gamma(s)\gamma^{s-\frac{1}{2}}}\sum_{n\in\mathbb{N}} K_{s-\frac{1}{2}}(2\pi\gamma n^2) \\ &\quad + \frac{8\pi^s}{\Gamma(s)\gamma^{s-\frac{1}{2}}}\sum_{n<j\in\mathbb{N}}\left\{\left(\frac{n}{j}\right)^{s-\frac{1}{2}} + \left(\frac{j}{n}\right)^{s-\frac{1}{2}}\right\} K_{s-\frac{1}{2}}(2\pi\gamma nj)\end{aligned} \tag{C.7}$$

and we can do the same for Eq.(C.6).

Appendix D

Direct Summation Approach to Three-body Lattice Sums

Unfortunately, the three-body sum is slowly convergent and cannot be analytically expressed in terms of lattice sums containing a single quadratic form as for the Epstein zeta function.[113] It has therefore been treated in the past by direct summation methods. Along the Bain path, we can express the ATM potential in terms of lattice sums dependent on the parameter A similar to the two-body potential such that

$$E_{\mathrm{coh}}^{(3)}(R, A, \lambda) = \lambda \left\{ E_R(R, A) + E_A(R, A) \right\} \tag{D.1}$$

with $E_R = f_r / R^9$ and $E_A = f_a / R^9$.

In our previous work[104,229,230,380–382], where more complicated forms of three-body forces were used, we produced the cartesian coordinates of the vectors $\vec{R}_{0i}$ for a specific lattice first and stored them for further use in (5.17). For this, one could use the fcc lattice basis vectors $(1,1,0)^\top$, $(1,0,0)^\top$, and $(0,1,1)^\top$, as a starting point and for the different cuboidal lattices scale the cartesian coordinates (x_n, y_n, z_n) such that we have $\frac{R}{\sqrt{A+1}}(x_n\sqrt{A}, y_n, z_n)$.[104,397,599] However, for the simple ATM potential this offers no advantage in terms of computer time and memory requirements. Moreover, as we shall see the simple form has some advantage for the determination of the minimum distance for a λ dependent energy (D.1) at a specific A value. We therefore decided to use (D.1) directly by utilizing the permutation symmetry $i_1 \leftrightarrow j_1$ for the vectors $\vec{i}$ and $\vec{j}$.

The convergence for the two individual 3-body terms as well as the sum of both in Eq. (D.1) is shown in Figure D.1 for the bcc lattice ($A = \frac{1}{2}$) setting $\lambda = 1$ and R_{min} to the minimum nearest-neighbor distance of a (12,6)-LJ potential. The rather slow convergence of both terms $E_R^{(3)}(R_{\mathrm{min}}, A)$ and $E_A^{(3)}(R_{\mathrm{min}}, A)$ with increasing N_{max} is obvious. Nevertheless, the sum of these terms exhibits significantly faster convergence, and $N_{\mathrm{max}} = 100$ proves in principle to be sufficiently accurate for our analysis. However, due to the computational time scaling of

$\mathcal{O}(N_{\max}^6)$, calculating the ATM term for a specific A value already demands 4 weeks of CPU time on a single processor. We therefore use a far more efficient evaluation of the three-body term through the Epstein zeta function as introduced originally by Crandall and put into a computer efficient form by Buchheit and co-workers.[379] This allows to evaluate general three-body lattice sums to machine precision within minutes on a standard laptop.

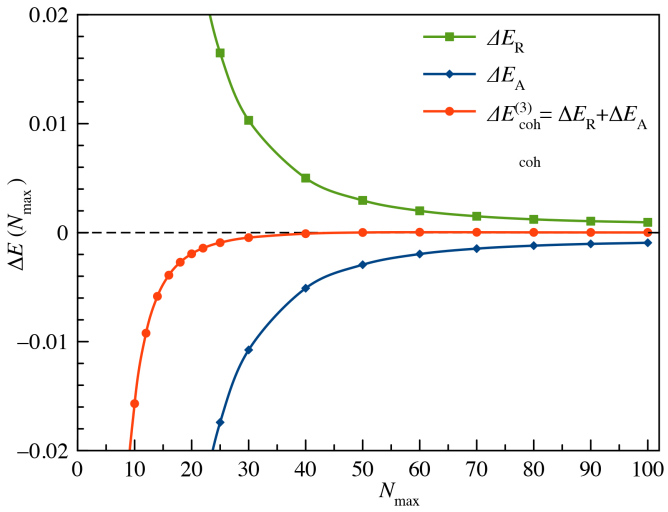

Figure D.1: Convergence of the ATM terms $E_R(N_{\max}, R_{\min}, A)$, $E_A(N_{\max}, R_{\min}, A)$ and $E^{(3)}_{\text{coh}}(N_{\max}, R_{\min}, A)$ (Eq.(D.1)) for the bcc lattice $A = \frac{1}{2}$ using a $(12,6)$-LJ potential. $R_{\min}$ is set to 0.951864818662439, the minimum distance for the bcc lattice of a $(12,6)$-LJ potential. The values show the difference in energies $\Delta E = E(N_{\max} \to \infty) - E(N_{\max})$ to the extrapolated value $N_{\max} \to \infty$. The limit for $N_{\max} \to \infty$ was obtained from a linear extrapolation over $N_{\max}^{-1}$ of the last two values at $N_{\max} = 90$ and 100. This gives $\Delta E_R(N_{\max} = 100) = -9.283159 \times 10^{-4}$, $\Delta E_A(N_{\max} = 100) = 9.461724 \times 10^{-4}$ and $\Delta E_R(N_{\max} = 100) + E_A(N_{\max} = 100) = 1.785654 \times 10^{-5}$.

For our detailed analysis, we tabulate the following properties along the Bain path: $E_{\text{coh}}(A, R_{\min})$, $\partial E_{\text{coh}}(A)/\partial R|_{R_{\min}}$, $\partial^2 E_{\text{coh}}(A)/\partial R^2|_{R_{\min}}$, $\partial E_{\text{coh}}(A)/\partial A|_{R_{\min}}$, $\partial^2 E_{\text{coh}}(A)/\partial A^2|_{R_{\min}}$. The latter two derivatives are obtained analytically for the two-body force (see Ref. 103 for details) and numerically for the three-body force. For the general LJ potential we used the (n,m) combinations $(6,4)$, $(8,6)$, $(12,6)$ and $(30,6)$. The latter represents a hard-wall potential accompanied by a attractive long-range dispersive r^{-6} term.

Appendix E

Three-body Lattice Sums

The three-body lattice sums for the ATM potential for different A-values according to Eq. (5.25) are listed in Table E.1. The data was obtained from the treatment of the Epstein zeta function as described in section 5.2.5.

Table E.1: Values for ATM three-body lattice sums.

A	$f_r^{(3)}(A)$	$f_a^{(3)}(A)$	$f_{\text{coh}}^{(3)} = f_r^{(3)}(A) + f_r^{(3)}(A)$
0.10000000000000000	94.323511425615860	-69.582608619579300	24.740902806036560
0.11111111111111111	78.996234807153090	-51.772409380650180	27.223825426502913
0.12222222222222222	68.141987707984340	-40.523230176857204	27.618757531127130
0.13333333333333333	60.127931145011650	-33.031920833977730	27.096010311033922
0.14444444444444444	54.014423818716900	-27.821816896120083	26.192606922596810
0.15555555555555555	49.227632547044850	-24.065452623566330	25.162179923478533
0.16666666666666666	45.399641069773320	-21.274409710807973	24.125231358965350
0.17777777777777777	42.284826583051180	-19.147330114086900	23.137496468964287
0.18888888888888888	39.713541043931286	-17.491030258502235	22.222510785429050
0.20000000000000000	37.565176004582040	-16.177483733401676	21.387692271180384
0.21111111111111111	35.751832524862300	-15.119334299395149	20.632498225467145
0.22222222222222222	34.208057391103196	-14.255421758422894	19.952635632680300
0.23333333333333333	32.884186353006996	-13.541936344866237	19.342250008140766
0.24444444444444444	31.741906110675053	-12.946849917296078	18.795056193378983
0.25555555555555555	30.751222581342716	-12.446315486424176	18.304907094918548
0.26666666666666666	29.888344501346580	-12.022282828652422	17.866061672694160
0.27777777777777777	29.134177122870604	-11.660884764889580	17.473292357981023
0.28888888888888888	28.473231311321676	-11.351323228504182	17.121908082817498
0.30000000000000000	27.892820967578835	-11.085086344259825	16.807734623319007
0.31111111111111111	27.382464087618917	-10.855388996987124	16.527075090631797
0.32222222222222222	26.933429942612158	-10.656766985644794	16.276662956967370
0.33333333333333333	26.538392635746654	-10.484778456088293	16.053614179658368
0.34444444444444444	26.191163135730186	-10.335781403352645	15.855381732377538
0.35555555555555555	25.886479914810245	-10.206765870266250	15.679714044544000
0.36666666666666666	25.619843846530660	-10.095225986419386	15.524617860111277
0.37777777777777777	25.387386879598203	-9.9990613779312730	15.388325501666927
0.38888888888888888	25.185766737800538	-9.9165004740401060	15.269266263760429
0.40000000000000000	25.012081855389425	-9.8460403104795870	15.166041544909831
0.41111111111111111	24.863802178265250	-9.7863988838762060	15.077403294389043
0.42222222222222222	24.738712502866125	-9.7364771433200620	15.002235594546063
0.43333333333333333	24.634865795888576	-9.6953284459936560	14.939537349894920
0.44444444444444444	24.550544514439906	-9.6621338408291200	14.888410673610792
0.45555555555555555	24.484228380961902	-9.6361819377060480	14.848046443255853
0.46666666666666666	24.434567397857776	-9.6168524107358490	14.817714987121931
0.47777777777777777	24.400359140141877	-9.6036024011992400	14.796756738942634
0.48888888888888888	24.380529560080320	-9.5959552491335140	14.784574310946809
0.50000000000000000	24.374116689926883	-9.5934911064150800	14.780625583511807
0.51111111111111111	24.380256747943890	-9.5958390788033300	14.784417669140566
0.52222222222222222	24.398172246700100	-9.6026706173911090	14.795501629308987
0.53333333333333333	24.427161776971960	-9.6136939362561870	14.813467840715774
0.54444444444444444	24.466591199811035	-9.6286492771770470	14.837941922633988
0.55555555555555555	24.515886026805056	-9.6473048769029430	14.868581149902113
0.56666666666666666	24.574524806789046	-9.6694535196819120	14.905071287107134
0.57777777777777777	24.642033368202980	-9.6949095794417950	14.947123788761190
0.58888888888888888	24.717979791452187	-9.7235064733021200	14.994473318150071
0.60000000000000000	24.801970006178507	-9.7550944620320370	15.046875544146474
0.61111111111111111	24.893643925210420	-9.7895387441317570	15.104105181078666
0.62222222222222222	24.992672040848475	-9.8267177994030350	15.165954241445434
0.63333333333333333	25.098752420626415	-9.8665219451811340	15.232230475445277
0.64444444444444444	25.211608049226257	-9.9088520744194820	15.302755974806772
0.65555555555555555	25.330984471164940	-9.9536185498382640	15.377365921326671
0.66666666666666666	25.456647695517326	-10.000740232325285	15.455907463192048
0.67777777777777777	25.588382329509372	-10.050143625200935	15.538238704308440
0.68888888888888888	25.725989912504650	-10.101762118796010	15.624227793708641
0.70000000000000000	25.869287425869180	-10.155535322025365	15.713752103843817
0.71111111111111111	26.018105957551953	-10.211408469676325	15.806697487875624
0.72222222222222222	26.172289503063816	-10.269331895722843	15.902957607340980
0.73333333333333333	26.331693886967138	-10.329260564360926	16.002433322606210
0.74444444444444444	26.496185791055442	-10.391153651638422	16.105032139417020
0.75555555555555555	26.665641877180228	-10.454974171488043	16.210667705692188
0.76666666666666666	26.839947994200763	-10.520688640873030	16.319259353327737
0.77777777777777777	27.018998459845170	-10.588266779406624	16.430731680438555
0.78888888888888888	27.202695409400450	-10.657681239450945	16.545014169949510
0.80000000000000000	27.390948204127140	-10.728907363179943	16.662040840947200
0.81111111111111111	27.583672893138015	-10.801922963620449	16.781749929517560
0.82222222222222222	27.780791723221473	-10.876708126908810	16.904083596312660
0.83333333333333333	27.982232691721270	-10.953245033538540	17.028987658182730
0.84444444444444444	28.187929138152157	-11.031517796468115	17.156411341684050
0.85555555555555555	28.397819370709860	-11.111512314338800	17.286307056371058
0.86666666666666666	28.611846324266285	-11.193216138171746	17.418630186094546
0.87777777777777777	28.829957246812050	-11.276618350194180	17.553338896617873
0.88888888888888888	29.052103411639130	-11.361709453496548	17.690393958142580
0.90000000000000000	29.278239852844173	-11.448481271471891	17.829758581372290
0.91111111111111111	29.508325121990370	-11.536926856036661	17.971398265953710
0.92222222222222222	29.742321063989510	-11.627040403757988	18.115280660231520
0.93333333333333333	29.980192610464800	-11.718817179160165	18.261375431304643
0.94444444444444444	30.221907589035680	-11.812253444459664	18.409654144576024
0.95555555555555555	30.467436547115813	-11.907346395178287	18.560090151937530
0.96666666666666666	30.716752588962620	-12.004094101029036	18.712658487933580
0.97777777777777777	30.969831224834856	-12.102495451618665	18.867335773216197
0.98888888888888888	31.226650231227172	-12.202550106530040	19.024100124697128
1.00000000000000000	31.487189521251523	-12.304258449363747	19.182931071887780

The total lattice sum shows a minimum at the bcc structure ($A = \frac{1}{2}$), see Figure 5.8. In order

to prove this, we show that for any $\nu_i \in \mathbb{C}$

$$\frac{\partial}{\partial A}\zeta^{(3)}_{\Lambda(A)}(\vec{\nu})\bigg|_{A=1/2} = 0 \tag{E.1}$$

holds. As the ATM potential is a finite sum of three-body zeta functions, its derivative therefore also vanishes. Let $\vec{x}(A) = B^\top(A)\vec{n}$ with $\vec{n} \in \mathbb{Z}^d$. Then

$$\frac{\partial}{\partial A}\frac{1}{|B^\top(A)\vec{n}|^\nu}\bigg|_{A=1/2} = -\nu\frac{\vec{x}(1/2)^T D\vec{x}(1/2)}{|\vec{x}(1/2)|^{\nu+1}},$$

with the diagonal traceless matrix

$$D = B^{\top\prime}(1/2)\big(B^\top(1/2)\big)^{-1} = \begin{pmatrix} -2/3 & 0 & 0 \\ 0 & 1/3 & 0 \\ 0 & 0 & 1/3 \end{pmatrix}.$$

which is convenient for our proof as we shall see. Thus

$$\frac{\partial}{\partial A}\zeta^{(3)}_{\Lambda(A)}(\vec{\nu})\bigg|_{A=1/2} = -\sum_{\vec{x},\vec{y}\in\Lambda(1/2)}{}' \left(\nu_1\frac{\vec{x}^T D\vec{x}}{|\vec{x}|^{\nu_1+1}}\frac{1}{|\vec{y}|^{\nu_2}}\frac{1}{|\vec{z}|^{\nu_3}} + \nu_2\frac{1}{|\vec{x}|^{\nu_1}}\frac{\vec{y}^T D\vec{y}}{|\vec{y}|^{\nu_2+1}}\frac{1}{|\vec{z}|^{\nu_3}} + \nu_3\frac{1}{|\vec{x}|^{\nu_1}}\frac{1}{|\vec{y}|^{\nu_2}}\frac{\vec{z}^T D\vec{z}}{|\vec{z}|^{\nu_3+1}}\right) \tag{E.2}$$

with the convention $\vec{z} = \vec{y} - \vec{x}$. As $\Lambda(1/2)$ is the bcc lattice, we can choose a rotated lattice Λ_0 such that $\Lambda_0 = c\Big(\mathbb{Z}^d \cup (\mathbb{Z}^d + 1/2)\Big)$ and the resulting lattice sums do of course not depend on this particular choice.

The bcc lattice Λ_0 in this representation now exhibits the property that for $\vec{z} \in \Lambda_0$ also its cyclic permutation

$$\sigma\vec{z} = (z_2, \ldots, z_d, z_1)^T,$$

is an element of Λ_0. Thus we have $\sigma^n\Lambda_0 = \Lambda_0$ for any $n \in \mathbb{N}$.

We now show that sum over the first term in Eq. (E.2) vanishes and thus, in complete analogy, the two remaining sums as well. Averaging over cyclic permutations and using that permutations of the elements of $\vec{z}$ do not change the norm, we find

$$-\nu_1\sum_{\vec{x},\vec{y}\in\Lambda_0}\frac{\vec{x}^T D\vec{x}}{|\vec{x}|^{\nu_1+1}}\frac{1}{|\vec{y}|^{\nu_2}}\frac{1}{|\vec{z}|^{\nu_3}} = -\nu_1\frac{1}{3}\sum_{\vec{x},\vec{y}\in\Lambda_0}{}'\sum_{n=0}^{2}\Big((\sigma^n\vec{x})^T D(\sigma^n\vec{x})\Big)\frac{1}{|\vec{x}|^{\nu_1+1}}\frac{1}{|\vec{y}|^{\nu_2}}\frac{1}{|\vec{z}|^{\nu_3}}.$$

But as D is diagonal, we have

$$\sum_{n=0}^{2}\Big((\sigma^n\vec{x})^T D(\sigma^n\vec{x})\Big) = |\vec{x}|^2\,\mathrm{Tr}(D) = 0,$$

as D is traceless. With the same argument for the remaining two sums, we have thus shown that all three terms in Eq. (E.2) vanish. Thus also

$$\frac{\partial}{\partial A}\zeta^{(3)}_{\Lambda(A)}(\vec{v})\bigg|_{A=1/2} = 0.$$

Finally, recall that the three-body cohesive energy is a recombination of three-body zeta functions

$$E^{(3)}_{\mathrm{coh}}/\lambda = \frac{1}{24}\zeta^{(3)}_{\Lambda(A)}(3,3,3) - \frac{3}{16}\zeta^{(3)}_{\Lambda(A)}(-1,5,5) + \frac{3}{8}\zeta^{(3)}_{\Lambda(A)}(1,3,5),$$

and therefore,

$$\frac{\partial}{\partial A}E^{(3)}_{\mathrm{coh}}\bigg|_{A=1/2} = 0.$$

□

The defining integral for $\zeta^{(3)}_{\Lambda}$ can be meromorphically continued to $\nu_i \in \mathbb{C}$ by means of the Hadamard integral. This, however, requires the computation of derivatives of the Epstein zeta function, which can be avoided for the special case of the ATM potential. Here, only the $\vec{v} = (-1,3,5)^T$ term leads to a hypersingular Hadamard integral, which can be reduced to a standard integral as follows. We readily find that

$$\int_{E^*} Z_{\Lambda,\nu}(\vec{k})\,\mathrm{d}\vec{k} = 0, \quad \nu > d,$$

and thus also the meromorphic continuation to $\nu \in \mathbb{C}$ equals zero. Hence, we have

$$\zeta^{(3)}_{\Lambda}(-1,1,3) = \frac{1}{V_\Lambda}\int_{E^*} Z_{\Lambda,-1}(\vec{k})\Big(Z_{\Lambda,1}(\vec{k})Z_{\Lambda,3}(\vec{k}) - Z_{\Lambda,1}(\vec{0})Z_{\Lambda,3}(\vec{0})\Big)\,\mathrm{d}\vec{k},$$

where the right-hand side is defined as a regular integral as the term in brackets scales as $\vec{k}^2$ around $\vec{k} = 0$, due to reflection symmetry as $\vec{k} \to -\vec{k}$. In conclusion, the ATM potential for any lattice and any dimension can be written in terms of three generalized zeta functions that can, in turn, be efficiently computed to machine precision from singular integrals that involve products of Epstein zeta functions.

We display the behavior of the one-dimensional three-body zeta function $Z^{(3)}_{\mathbb{Z}}$ and two-dimensional three-body zeta functions $Z^{(3)}_{\mathrm{SL}}$ for $\mathrm{SL} = \mathbb{Z}^2$ and $Z^{(3)}_{\mathrm{HL}}$ for

$$\mathrm{HL} = \begin{bmatrix} 1 & 1/2 \\ 0 & \sqrt{3}/2 \end{bmatrix}\mathbb{Z}^2$$

as a function of $\vec{v}$, including its meromorphic continuation, in Fig. E.1 and Fig. E.2. We observe simple poles at $\nu_1 + \nu_2 + \nu_3 = 2d$ and $\nu_i + \nu_j = d - 2n$, $n \in \mathbb{N}$, where $i \neq j$.

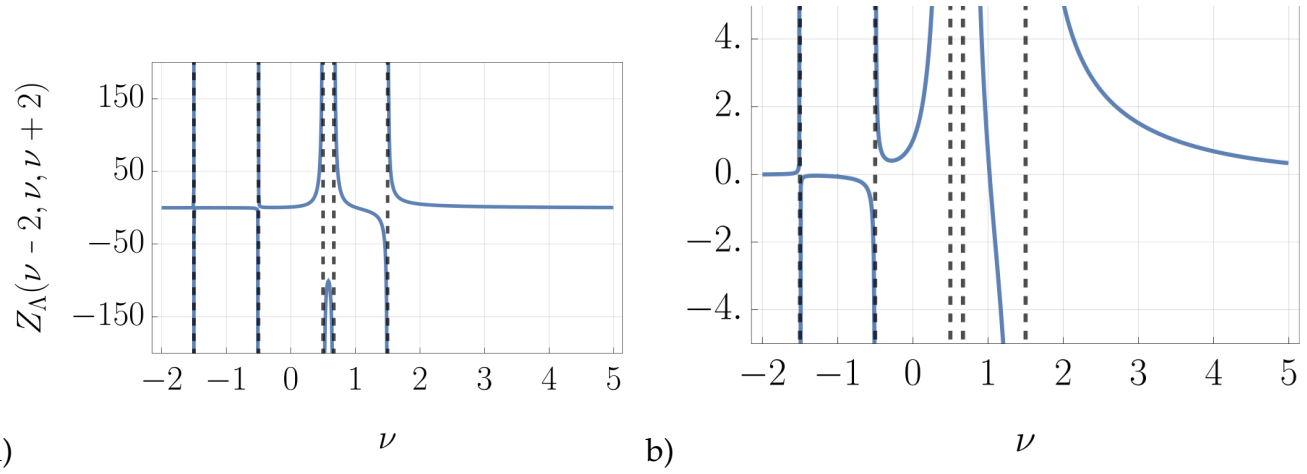

Figure E.1: Three-body zeta function for $\Lambda = \mathbb{Z}$ computed via the Epstein integral representation for $\vec{v} = (\nu-2, \nu, \nu+2)^T$ including its meromorphic continuation (a). The dashed gray lines indicate the simple poles at $\nu \in 3/2 - \mathbb{N}$, corresponding to the condition $\nu_i + \nu_j \in d + 2\mathbb{N}$ for $i \neq j$, and $\nu = 2/3$, corresponding to $\nu_1 + \nu_2 + \nu_3 = 2d$. Panel (b) offers a magnified view of the region close to the origin.

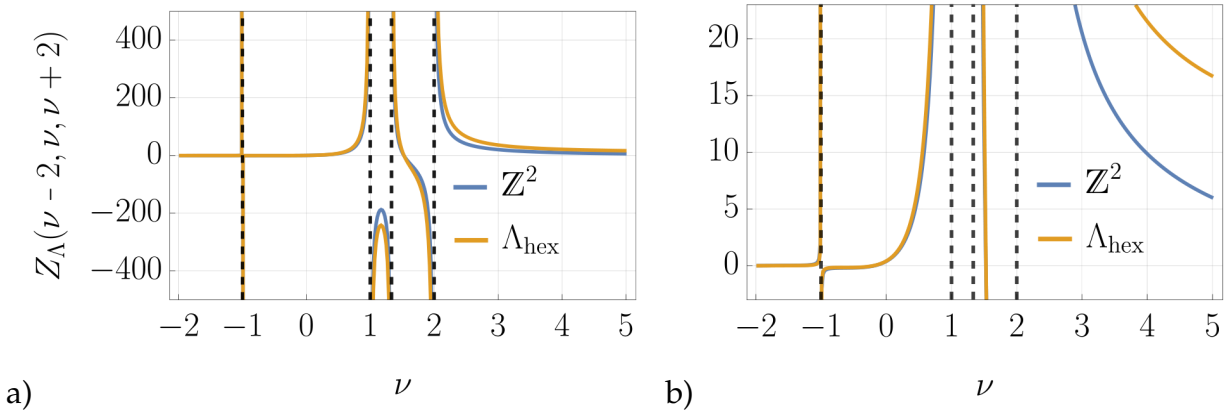

Figure E.2: Two dimensional three-body zeta function a) for the square lattice $\Lambda = \text{SL} = \mathbb{Z}^2$ (blue) and the hexagonal lattice $\Lambda = \text{HL}$ (orange) as shown in Figure 5.4 for $R = 1$ via the Epstein integral representation for $\vec{v} = (\nu-2, \nu, \nu+2)^T$ including its meromorphic continuation. For $\nu \leq 1$, the three-body zeta function for the square lattice and the three-body zeta function for the hexagonal lattice are visually indistinguishable. The dashed gray lines indicate the simple poles at $\nu \in 1 - 2\mathbb{N}$, corresponding to the condition $\nu_i + \nu_j \in d + 2\mathbb{N}$ for $i \neq j$, and $\nu = 4/3$, corresponding to $\nu_1 + \nu_2 + \nu_3 = 2d$. Panel (b) offers a magnified view of the region close to the origin.

Appendix F

A Minimum Property of the Lattice Sum $L(A;s)$

It was noted that on the interval $1/3 \leq A \leq 1$, the packing density function Δ_Λ has a minimum value when $A = 1/2$. Provided that $s > 3/2$, the corresponding lattice sum $L(A;s)$ also attains a minimum at the same value $A = 1/2$. The proof for this condition is provided in ref. 377.

Theorem F.0.1. *Let $L(A;s)$ be the lattice defined by* (B.5)*, that is,*

$$L(A;s) = \sum_{i,j,k\in\mathbb{Z}}{}' \left(\frac{1}{g(A;i,j,k)}\right)^s = \sum_{i,j,k\in\mathbb{Z}}{}' \left(\frac{A+1}{A(i+j)^2+(j+k)^2+(i+k)^2}\right)^s \tag{F.1}$$

where $s > 3/2$ and $1/3 \leq A \leq 1$. Then

$$\frac{\partial}{\partial A} L(A;s)\bigg|_{A=1/2} = 0 \quad \textit{and} \quad \frac{\partial^2}{\partial A^2} L(A;s)\bigg|_{A=1/2} > 0. \tag{F.2}$$

As consequence, for any fixed value $s > 3/2$, the lattice sum $L(A;s)$ attains a minimum when $A = 1/2$. Graphs of $L(A;s)$ to illustrate this minimum property are shown in Fig.F.1. In the limiting case $s \to \infty$ we have

$$L(A;\infty) = \lim_{s\to\infty} L(A;s) = \mathrm{kiss}(\Lambda) = \begin{cases} 10 & \text{if } A = 1/3, \\ 8 & \text{if } 1/3 < A < 1, \\ 12 & \text{if } A = 1. \end{cases} \tag{F.3}$$

We find an interesting relation between the lattice sum and its first derivative,

$$\frac{\partial}{\partial A} L(A;s)\bigg|_{A=1} = \frac{s}{6} L(A;s)\bigg|_{A=1} \tag{F.4}$$

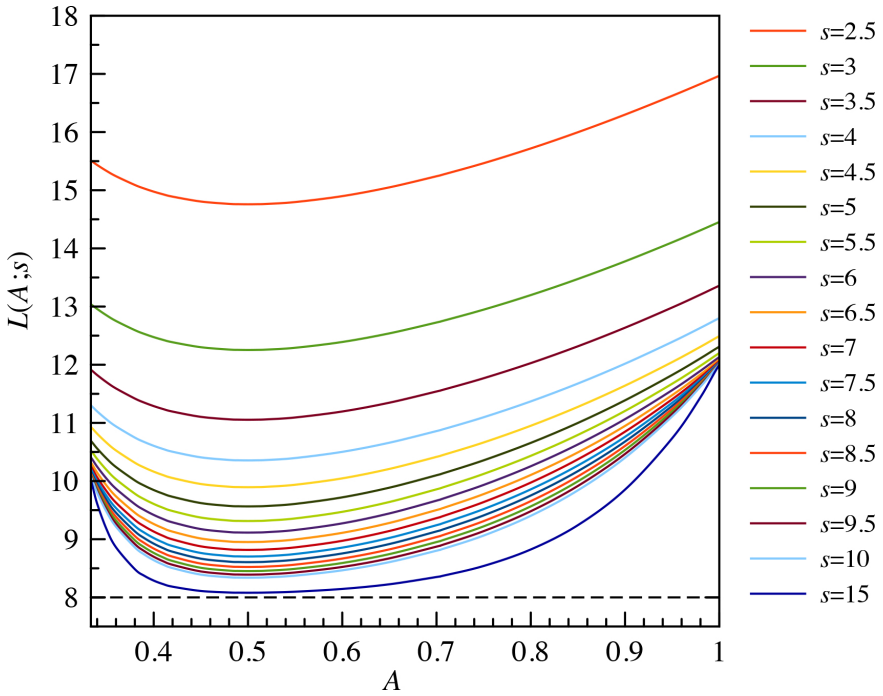

Figure F.1: Graph of $L(A;s)$ versus A for various values of s For $s \to \infty$ we have at both ends of the interval $L(A = \frac{1}{3};\infty) = 10$ and $L(A = 1;\infty) = 12$.

which can be proved as follows. On calculating the derivative using (F.1) we obtain

$$\frac{\partial}{\partial A} L(A;s) = \frac{2s}{(A+1)^2} {\sum_{i,j,k\in\mathbb{Z}}}' (k^2 + ik + jk - ij) \left(\frac{A+1}{A(i+j)^2 + (j+k)^2 + (i+k)^2} \right)^{s+1}$$

and on setting $A = 1$ it follows that

$$\frac{\partial}{\partial A} L(A;s)\Big|_{A=1} = \frac{s}{2} {\sum_{i,j,k\in\mathbb{Z}}}' \frac{k^2 + ik + jk - ij}{(i^2 + j^2 + k^2 + ij + jk + ki)^{s+1}}.$$

Now replace the summation indices (i,j,k) with the cyclic permutations (j,k,i) and (k,i,j) and add the three equations to obtain

$$\begin{aligned} 3\,\frac{\partial}{\partial A} L(A;s)\Big|_{A=1} &= \frac{s}{2} {\sum_{i,j,k\in\mathbb{Z}}}' \frac{i^2 + j^2 + k^2 + ij + jk + ki}{(i^2 + j^2 + k^2 + ij + jk + ki)^{s+1}} \\ &= \frac{s}{2} {\sum_{i,j,k\in\mathbb{Z}}}' \frac{1}{(i^2 + j^2 + k^2 + ij + jk + ki)^{s}} = \frac{s}{2} L(A;s)\Big|_{A=1}. \end{aligned}$$

This proves (F.4).

Appendix G

Analytic Continuations of the Lattice Sums $L(A;s)$

We will now show that the lattice sums $L(A;s)$ can be continued analytically to the whole s-plane, and that the resulting functions have a single simple pole at $s = 3/2$ and no other singularities. We do this in steps. First, we show that the lattice sums each have a simple pole at $s = 3/2$ and determine the residue. Then, we show that the analytic continuations obtained are valid for the whole s-plane and there are no other singularities. Finally, values of the analytic continuations at the points $s = 1/2$ and $s = 1,\ 0,\ -1,\ -2, \ldots$ are computed. In particular, the evaluation of $T_2(A;s)$ at $s = 1/2$ in the case $A = 1$ gives the Madelung constant, e.g., see [365], [111], [115].

We start by showing that $L(A;s)$ has a simple pole at $s = 3/2$ and determine the residue. In the formula (B.38), all of the terms are analytic at $s = 3/2$ except for the term involving $\zeta(2s-2)$. It follows that

$$\begin{aligned}\lim_{s\to 3/2}(s-3/2)L(A;s) &= \lim_{s\to 3/2}(s-3/2)\frac{\pi A}{s-1}\left(1+\frac{1}{A}\right)^s\zeta(2s-2) \qquad \text{(G.1)}\\ &= 2\pi A\left(1+\frac{1}{A}\right)^{3/2}\lim_{s\to 3/2}(s-3/2)\zeta(2s-2)\\ &= \frac{2\pi}{\sqrt{A}}\,(A+1)^{3/2}\times\frac{1}{2}\lim_{u\to 1}(u-1)\zeta(u) = \frac{\pi}{\sqrt{A}}\,(A+1)^{3/2}\end{aligned}$$

where (A.16) was used in the last step of the calculation. It follows further that $L(A;s)$ has a simple pole at $s = 3/2$ and the residue is given by

$$\mathrm{Res}(L(A;s),3/2) = \frac{\pi}{\sqrt{A}}\,(A+1)^{3/2}. \qquad \text{(G.2)}$$

This corresponds to 12 times the packing density, i.e.,

$$\mathrm{Res}(L(A;s),3/2) = 12\Delta_\Lambda. \tag{G.3}$$

For example, taking $A = 1$ gives

$$\mathrm{Res}(L_3^{\mathrm{FCC}}(s),3/2) = 2\sqrt{2}\,\pi \tag{G.4}$$

while taking $A = 1/2$ gives

$$\mathrm{Res}(L_3^{\mathrm{BCC}}(s),3/2) = 3\sqrt{3}\,\pi/2. \tag{G.5}$$

Laurent's theorem implies there is an expansion of the form

$$L(A;s) = \frac{c_{-1}}{s-3/2} + c_0 + \sum_{n=1}^{\infty} c_n (s-3/2)^n \tag{G.6}$$

where

$$c_{-1} = \mathrm{Res}(L(A;s),3/2) = \frac{\pi}{\sqrt{A}}\,(A+1)^{3/2} \tag{G.7}$$

and the coefficients c_0, c_1, c_2, ... depend on A but not on s. To calculate c_0, start with the fact that

$$\lim_{s\to 3/2}\left(\frac{\pi A}{s-1}\left(1+\frac{1}{A}\right)^s \zeta(2s-2) - \frac{c_{-1}}{s-3/2}\right) = \frac{\pi}{\sqrt{A}}\,(A+1)^{3/2}\left(2\gamma - 2 + \log\left(1+\frac{1}{A}\right)\right) \tag{G.8}$$

where $\gamma = 0.57721\,56649\,01532\,86060\cdots$ is the Euler–Mascheroni constant. Then use (B.38) and (A.5) to deduce

$$\begin{aligned} c_0 = \lim_{s\to 3/2}\left(L(A;s) - \frac{c_{-1}}{s-3/2}\right) &= \sqrt{2}\,(A+1)^{3/2}\,\zeta\left(\frac{3}{2}\right) L_{-4}\left(\frac{3}{2}\right) \\ &+ \frac{\pi}{\sqrt{A}}\,(A+1)^{3/2}\left(2\gamma - 2 + \log\left(1+\frac{1}{A}\right)\right) \\ &+ \frac{2\pi}{\sqrt{A}}\,(A+1)^{3/2} \sum_{k,N\in\mathbb{N}} \frac{1}{k}\, r_2(N) \exp\left(-2\pi k\sqrt{AN}\right) \\ &+ \frac{2\pi}{\sqrt{A}}\,(A+1)^{3/2} \sum_{k,N\in\mathbb{N}} \frac{(-1)^k}{k}\, r_2(4N+1)\, \exp\left(-2\pi k\sqrt{A\left(2N+\frac{1}{2}\right)}\right). \end{aligned} \tag{G.9}$$

Interchanging the order of summation and evaluating the sum over k gives

$$\begin{aligned} c_0 =& \sqrt{2}\,(A+1)^{3/2}\,\zeta\left(\frac{3}{2}\right) L_{-4}\left(\frac{3}{2}\right) \\ &+ \frac{\pi}{\sqrt{A}}\,(A+1)^{3/2}\left(2\gamma - 2 + \log\left(1+\frac{1}{A}\right)\right) \\ &- \frac{2\pi}{\sqrt{A}}\,(A+1)^{3/2} \sum_{N\in\mathbb{N}} r_2(N) \log\left(1-e^{-2\pi\sqrt{AN}}\right) \\ &- \frac{2\pi}{\sqrt{A}}\,(A+1)^{3/2} \sum_{N\in\mathbb{N}_0} r_2(4N+1)\, \log\left(1+e^{-\pi\sqrt{2A(4N+1)}}\right). \end{aligned} \tag{G.10}$$

Numerical evaluation in the case $A = 1$ gives

$$c_0|_{A=1} = 6.98405\,25503\,22247\,93406\ldots. \tag{G.11}$$

We now evaluate the analyticity of the lattice sums at other values of s. By (A.6), the double series of Bessel functions in (B.38) converges absolutely and uniformly on compact subsets of the s-plane and therefore represents an entire function of s. It follows that $L(A;s)$ has an analytic continuation to a meromorphic function which is analytic except possibly at the singularities of the terms

$$4\left(\frac{A+1}{2}\right)^s \zeta(s) L_{-4}(s) \tag{G.12}$$

and

$$\frac{\pi A}{s-1}\left(1+\frac{1}{A}\right)^s \zeta(2s-2). \tag{G.13}$$

The function in (G.12) is analytic except at $s = 1$ due to the pole of $\zeta(s)$. The function $L_{-4}(s)$ and the exponential function are both entire. The function in (G.13) is analytic except at $s = 1$ and $s = 3/2$.

The singularity at $s = 3/2$ was already studied before.[226,295] Using (A.16) and the values of $\zeta(0)$ and $L_{-4}(1)$ in (A.19) and (A.20) we find that

$$4\left(\frac{A+1}{2}\right)^s \zeta(s) L_{-4}(s) = \frac{(A+1)\pi}{2(s-1)} + O(1) \quad \text{as } s \to 1 \tag{G.14}$$

and

$$\frac{\pi A}{s-1}\left(1+\frac{1}{A}\right)^s \zeta(2s-2) = -\frac{(A+1)\pi}{2(s-1)} + O(1) \quad \text{as } s \to 1. \tag{G.15}$$

It follows that the sum of the functions in (G.12) and (G.13) has a removable singularity at $s = 1$ and thus $L(A;s)$ is also analytic at $s = 1$. The analyticity at $s = 1$ can also be seen directly from the alternative formula for $L(A;s)$ in (B.39). We thus showed that $L(A;s)$ has an analytic continuation to a meromorphic function of s which has a simple pole at $s = 3/2$ and no

other singularities. Because $L(A;s)$ has only one singularity, namely $s = 3/2$, the Laurent expansion (G.6) is valid in the annulus $0 < |s - 3/2| < \infty$, i.e., for all $s \neq 3/2$.

By the theory of complex variables, the analytic continuation, if one exists, is unique, e.g., see Ref. 600. Therefore analytic continuation formulas can be used to assign values to divergent series. For example, the Madelung constant is defined by

$$M = \sum_{i,j,k\in\mathbb{Z}}{}' \quad \frac{(-1)^{i+j+k}}{(i^2+j^2+k^2)^s}\bigg|_{s=1/2}. \tag{G.16}$$

This is interpreted as being the value of the analytic continuation of the series at $s = 1/2$, because the sum diverges if $s = 1/2$. From now on, we shall use the expression "the value of a series at a point s" to mean "the value of the analytic continuation of the series at the point s".

For the A-dependent case, on putting $s = 1/2$ in (B.28) we obtain an analytic expression for the value of

$$M(A) = \sum_{i,j,k\in\mathbb{Z}}{}' \quad \frac{(-1)^{i+j+k}}{(Ai^2+j^2+k^2)^s}\bigg|_{s=1/2} \tag{G.17}$$

which specialises to the Madelung constant in the case $A = 1$. We have

$$\begin{aligned} M(A) = &-4(1-2^{1-s})\zeta(s)L_{-4}(s)\Big|_{s=1/2} \\ &+ \frac{4\pi^s}{\Gamma(s)}\,A^{(1-s)/2}\sum_{i\in\mathbb{N}}\sum_{N\in\mathbb{N}_0}(-1)^i r_2(4N+1)\left(\frac{2N+\frac{1}{2}}{i^2}\right)^{(s-1)/2} K_{s-1}\left(2\pi i\sqrt{A(2N+\frac{1}{2})}\right)\Bigg|_{s=1/2}. \end{aligned} \tag{G.18}$$

Now use (A.4) and (A.5) to express the Bessel functions in terms of exponential functions. The result simplifies to

$$M(A) = 4(\sqrt{2}-1)\zeta\left(\frac{1}{2}\right)L_{-4}\left(\frac{1}{2}\right) + 2\sum_{i\in\mathbb{N}}\sum_{N\in\mathbb{N}_0}(-1)^i\,\frac{r_2(4N+1)}{\sqrt{2N+\frac{1}{2}}}\,e^{-2\pi i\sqrt{A(2N+1/2)}}. \tag{G.19}$$

On interchanging the order of summation and summing the geometric series, we obtain

$$M(A) = 4(\sqrt{2}-1)\zeta\left(\frac{1}{2}\right)L_{-4}\left(\frac{1}{2}\right) - 2\sqrt{2}\sum_{N\in\mathbb{N}_0}\frac{r_2(4N+1)}{\sqrt{4N+1}}\left(\frac{1}{e^{\pi\sqrt{2A(4N+1)}}+1}\right). \tag{G.20}$$

When $A = 1$ this gives the Madelung constant defined by (G.16). Numerical evaluation gives

$$M = M(1) = -1.74756\ 45946\ 33182\ 19063\ldots \tag{G.21}$$

which is in agreement with [111] (apart from the minus sign which we have corrected here) and matches the value of $d(1)$ in [111].

In a similar way, starting from (B.14) and using (A.5) and (A.19) we obtain

$$\begin{aligned}\sum_{i,j,k\in\mathbb{Z}}{}' \quad \frac{1}{(Ai^2+j^2+k^2)^s}\bigg|_{s=1/2} &= 4\zeta\left(\frac{1}{2}\right)L_{-4}\left(\frac{1}{2}\right)+\frac{\pi\sqrt{A}}{3}+2\sum_{i,N\in\mathbb{N}}\frac{r_2(N)}{\sqrt{N}}\,e^{-2\pi i\sqrt{AN}} \\ &= 4\zeta\left(\frac{1}{2}\right)L_{-4}\left(\frac{1}{2}\right)+\frac{\pi\sqrt{A}}{3}+2\sum_{N\in\mathbb{N}}\frac{r_2(N)}{\sqrt{N}}\left(\frac{1}{e^{2\pi\sqrt{AN}}-1}\right). \end{aligned} \tag{G.22}$$

Numerical evaluation in the case $A=1$ gives

$$\sum_{i,j,k\in\mathbb{Z}}{}' \quad \frac{1}{(i^2+j^2+k^2)^s}\bigg|_{s=1/2} = -2.83729\ 74794\ 80619\ 47666\ldots. \tag{G.23}$$

Now, from (B.6) we have for the fcc lattice

$$L\left(A=1;\tfrac{1}{2}\right)=\frac{1}{\sqrt{2}}\sum_{i,j,k\in\mathbb{Z}}{}'\frac{1}{(i^2+j^2+k^2)^s}\bigg|_{s=1/2}+\frac{1}{\sqrt{2}}\sum_{i,j,k\in\mathbb{Z}}{}'\frac{(-1)^{i+j+k}}{(i^2+j^2+k^2)^s}\bigg|_{s=1/2}. \tag{G.24}$$

Hence, using the values from (G.21) and (G.23) we obtain

$$L\left(A=1;\tfrac{1}{2}\right) = -3.24198\ 70634\ 10888\ 39428\ldots. \tag{G.25}$$

We now turn to the value of the lattice sum at $s=1$. It was noted above that (B.38), which involves K_{s-1} Bessel functions, contains terms with singularities at $s=1$ and therefore is not suitable for calculations at that value of s. Instead we can use (B.39), which involves $K_{s-1/2}$ Bessel functions. As in the previous section, two steps are involved. First, the the $K_{1/2}$ Bessel functions can be expressed in terms of the exponential function by (A.5). Then, the double sum can be reduced to a single sum by geometric series. We omit the details and just record the final results and corresponding numerical values. From (B.20) we have

$$\sum_{i,j,k\in\mathbb{Z}}{}' \quad \frac{1}{(Ai^2+j^2+k^2)^s}\bigg|_{s=1} = \frac{\pi^2}{3A}+\frac{4\pi}{\sqrt{A}}\zeta\left(\frac{1}{2}\right)L_{-4}\left(\frac{1}{2}\right)+\frac{2\pi}{\sqrt{A}}\sum_{N\in\mathbb{N}}\frac{r_2(N)}{\sqrt{N}}\left(\frac{1}{e^{2\pi\sqrt{N/A}}-1}\right) \tag{G.26}$$

while (B.37) gives

$$\sum_{i,j,k\in\mathbb{Z}}{}' \quad \frac{(-1)^{i+j+k}}{(Ai^2+j^2+k^2)^s}\bigg|_{s=1} = \frac{-\pi^2}{6A}+\frac{2\pi}{\sqrt{A}}\sum_{N\in\mathbb{N}}(-1)^N\frac{r_2(N)}{\sqrt{N}}\left(\frac{1}{e^{\pi\sqrt{N/A}}-e^{-\pi\sqrt{N/A}}}\right). \tag{G.27}$$

Then (B.6) can be used to write down the value of $L(A;s)$. For example, when $A=1$ the above

formulas give

$$\sum_{i,j,k\in\mathbb{Z}}{}' \quad \frac{1}{(i^2+j^2+k^2)^s}\bigg|_{s=1} = -8.91363\ 29175\ 85151\ 27268\ldots \tag{G.28}$$

and

$$\sum_{i,j,k\in\mathbb{Z}}{}' \quad \frac{(-1)^{i+j+k}}{(i^2+j^2+k^2)^s}\bigg|_{s=1} = -2.51935\ 61520\ 89445\ 31334\ldots. \tag{G.29}$$

Then taking $s=1$ in (B.6) gives for the fcc lattice

$$L(A=1,1) = \sum_{i,j,k}{}' \quad \frac{1}{(i^2+j^2+k^2)^s}\bigg|_{s=1} + \sum_{i,j,k}{}' \quad \frac{(-1)^{i+j+k}}{(i^2+j^2+k^2)^s}\bigg|_{s=1} \tag{G.30}$$

$$= -11.43298\ 90696\ 74596\ 58602\ldots. \tag{G.31}$$

We note a connection between two of the values in the above analysis. By setting $A=1$ in each of (G.22) and (G.26) we obtain the remarkable result

$$\sum_{i,j,k\in\mathbb{Z}}{}' \quad \frac{1}{(i^2+j^2+k^2)^s}\bigg|_{s=1} = \pi \sum_{i,j,k\in\mathbb{Z}}{}' \quad \frac{1}{(i^2+j^2+k^2)^s}\bigg|_{s=1/2}. \tag{G.32}$$

This is consistent with [111] and is the special case $s=1$ of the functional equation

$$\pi^{-s}\Gamma(s)T_1(1;s) = \pi^{-(\frac{3}{2}-s)}\Gamma\left(\frac{3}{2}-s\right)T_1\left(1;\frac{3}{2}-s\right). \tag{G.33}$$

This functional equation can be deduced from the two formulas for $T_1(A;s)$ in (B.14) and (B.20), as follows. Replace s with $\frac{3}{2}-s$ in (B.14), then multiply by $\pi^{s-\frac{3}{2}}\Gamma(\frac{3}{2}-s)$ and set $A=1$ to get

$$\begin{aligned}
&\pi^{s-\frac{3}{2}}\Gamma\left(\frac{3}{2}-s\right)T_1\left(1;\frac{3}{2}-s\right) \\
&= 4\pi^{s-\frac{3}{2}}\Gamma\left(\frac{3}{2}-s\right)\zeta\left(\frac{3}{2}-s\right)L_{-4}\left(\frac{3}{2}-s\right) + 2\pi^{s-\frac{1}{2}}\Gamma\left(\frac{1}{2}-s\right)\zeta(1-2s) \\
&\quad + 4\sum_{i,N\in\mathbb{N}} r_2(N)\left(\frac{N}{i^2}\right)^{(\frac{1}{2}-s)/2} K_{\frac{1}{2}-s}\left(2\pi i\sqrt{N}\right),
\end{aligned} \tag{G.34}$$

where we have used the functional equation for the gamma function in the form $\Gamma(3/2-s) = (1/2-s)\Gamma(1/2-s)$ to obtain the second term on the right hand side. Now apply the functional

equations (A.4), (A.17) and (A.18) to deduce

$$\begin{aligned}
&\pi^{-(\frac{3}{2}-s)}\Gamma\left(\frac{3}{2}-s\right)T_1\left(1;\frac{3}{2}-s\right) \qquad (G.35)\\
&= 4\pi^{\frac{1}{2}-s}\,\Gamma\left(s-\frac{1}{2}\right)\zeta\left(s-\frac{1}{2}\right)L_{-4}\left(s-\frac{1}{2}\right)+2\pi^{-s}\,\Gamma(s)\zeta(2s)\\
&\quad+4\sum_{i,N\in\mathbb{N}} r_2(N)\left(\frac{i}{\sqrt{N}}\right)^{s-\frac{1}{2}}K_{s-\frac{1}{2}}\left(2\pi i\sqrt{N}\right).
\end{aligned}$$

The functional equation (G.33) follows from this by using (B.20). In addition to providing another proof of the functional equation, the calculation above also demonstrates the interconnection between the formulas (B.14) and (B.20). Further functional equations of this type are considered in [111].

We now evaluate the values at $s = 0,\ -1,\ -2,\ -3, \ldots$ for the lattice sum. Recall from (B.38) that

$$\begin{aligned}
L(A;s) &= 4\left(\frac{A+1}{2}\right)^s\zeta(s)L_{-4}(s)+\frac{\pi A}{s-1}\left(1+\frac{1}{A}\right)^s\zeta(2s-2) \qquad (G.36)\\
&\quad+\frac{2\pi^s\sqrt{A}}{\Gamma(s)}\left(\sqrt{A}+\frac{1}{\sqrt{A}}\right)^s\sum_{i,N\in\mathbb{N}} r_2(N)\left(\frac{N}{i^2}\right)^{(s-1)/2}K_{s-1}\left(2\pi i\sqrt{AN}\right)\\
&\quad+\frac{2\pi^s\sqrt{A}}{\Gamma(s)}\left(\sqrt{A}+\frac{1}{\sqrt{A}}\right)^s\sum_{i\in\mathbb{N}}\sum_{N\in\mathbb{N}_0}(-1)^i r_2(4N+1)\left(\frac{2N+\frac{1}{2}}{i^2}\right)^{(s-1)/2}K_{s-1}\left(2\pi i\sqrt{A(2N+\frac{1}{2})}\right)
\end{aligned}$$

On using the values $\zeta(0) = -\frac{1}{2}$, $\zeta(-2) = 0$, $L_{-4}(0) = \frac{1}{2}$ and the limiting value $\lim_{s\to 0} 1/\Gamma(s) = 0$ we readily obtain the result $L(A;0) = -1$. Moreover, since

$$\zeta(-2) = \zeta(-4) = \zeta(-6) = \cdots = 0, \qquad (G.37)$$

$$L_{-4}(-1) = L_{-4}(-3) = \zeta(-5) = \cdots = 0, \qquad (G.38)$$

$$\text{and} \quad \lim_{s\to N}\frac{1}{\Gamma(s)} = 0 \quad \text{if } N = 0,\ -1,\ -2,\ \ldots \qquad (G.39)$$

it follows that

$$L(A;-1) = L(A;-2) = L(A;-3) = \cdots = 0. \qquad (G.40)$$

The graph of $L(A = 1, s)$ obtained from the formulas (B.38) and (B.39) on the intervals $-10 < s < 10$ and $-7 < s < 0$ is shown in Figure G.1, which illustrates the properties discussed in this section.

We briefly consider the behaviour of the lattices in the limiting cases $A \to 0^+$ and $A \to +\infty$. For example, from Eq.(5.13) we can easily see that one of the basis vectors become zero in the

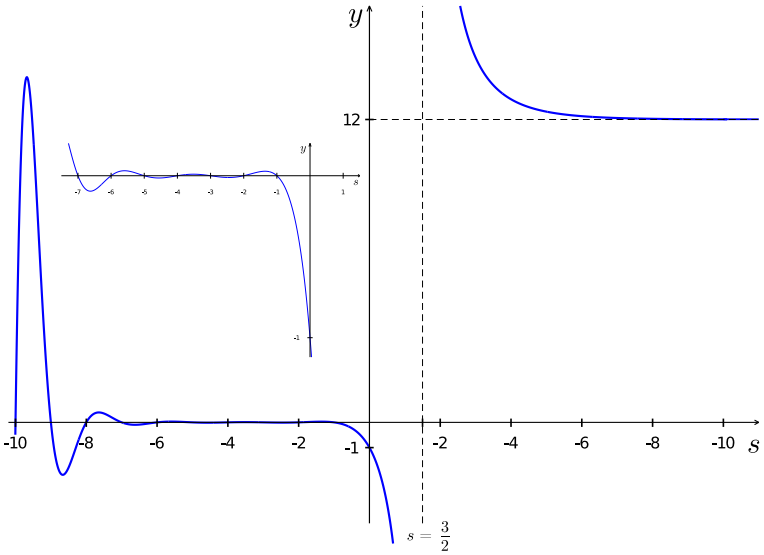

Figure G.1: Graph of $y = L(A = 1; s)$ for $-10 < s < 10$ for the fcc structure. Inlet shows $y = L(A = 1; s)$ for $-7 < s < 0$

limit $A \to 0^+$, leaving a sub-lattice of lower dimension. We therefore discuss each case $A \to 0^+$ and $A \to +\infty$ both in terms of theta functions and then in terms of the lattice basis vectors.

First, consider the limit $A \to 0^+$. In the interval $0 < A < 1/3$ the theta function is

$$\theta(A; q) = \sum_{i,j,k \in \mathbb{Z}} q^{g(A;i,j,k)} = \sum_{i,j,k \in \mathbb{Z}} q^{(A(i+j)^2 + (j+k)^2 + (i+k)^2)/4A}. \tag{G.41}$$

As $A \to 0^+$ we have $q^{(j+k)^2/4A} \to 0$ and $q^{(i+k)^2/4A} \to 0$ unless $j = -k$ and $i = -k$, respectively. Hence,

$$\begin{aligned} \lim_{A \to 0^+} \theta(A; q) &= \lim_{A \to 0^+} \sum_{k \in \mathbb{Z}} \left(\sum_{i=-k} \sum_{j=-k} q^{(A(i+j)^2 + (j+k)^2 + (i+k)^2)/4A} \right) \\ &= \lim_{A \to 0^+} \sum_{k \in \mathbb{Z}} q^{A(-k-k)^2/4A} = \sum_{k=-\infty}^{\infty} q^{k^2}. \end{aligned} \tag{G.42}$$

This corresponds to the one-dimensional lattice with minimal distance 1. The kissing number is 2, which is in agreement with the other lattices in the range $0 < A < 1/3$, as indicated in Table 1. In terms of the lattice basis vectors for the bct lattice we have

$$\vec{b}_1 = \left(\frac{1}{2}, \frac{1}{2\sqrt{A}}, 0 \right)^\top, \quad \vec{b}_2 = \left(\frac{1}{2}, 0, \frac{1}{2\sqrt{A}} \right)^\top, \quad \vec{b}_3 = \left(0, \frac{1}{2\sqrt{A}}, \frac{1}{2\sqrt{A}} \right)^\top. \tag{G.43}$$

The only linear combinations $\vec{v} = i\vec{b}_1 + j\vec{b}_2 + k\vec{b}_3$ (for $i, j, k \in \mathbb{Z}$) that remain finite in the limit $A \to 0^+$ occur when $i = -k$, $j = -k$ in which case we obtain $\vec{v} = -k\vec{b}_1 - k\vec{b}_2 + k\vec{b}_3 =$

$-k(1,0,0)^\top$. That is, the limiting lattice is just the one-dimensional lattice consisting of integer multiples of $(1,0,0)^\top$.

Now consider the limit $A \to +\infty$. For $A > 1$ the theta function is

$$\theta(A;q) = \sum_{i,j,k\in\mathbb{Z}} q^{g(A;i,j,k)} = \sum_{i,j,k\in\mathbb{Z}} q^{(A(i+j)^2+(j+k)^2+(i+k)^2)/2}. \tag{G.44}$$

Since $q^{A(i+j)^2/2} \to 0$ as $A \to +\infty$ unless $i = -j$, it follows that

$$\begin{aligned}\lim_{A\to+\infty} \theta(A;q) &= \sum_{j,k\in\mathbb{Z}} \left(\sum_{i=-j} q^{(A(i+j)^2+(j+k)^2+(i+k)^2)/2} \right) \\ &= \sum_{j,k\in\mathbb{Z}} q^{((j+k)^2+(-j+k)^2)/2} = \sum_{j,k\in\mathbb{Z}} q^{j^2+k^2}.\end{aligned} \tag{G.45}$$

This is the theta series for the two-dimensional square close packing lattice with minimal distance 1. The kissing number is 4, in agreement with other values in the range $A > 1$ given by Table 1. In terms of the lattice basis vectors we have

$$\vec{b}_1 = \frac{1}{\sqrt{2}}(\sqrt{A},1,0)^\top, \quad \vec{b}_2 = \frac{1}{\sqrt{2}}(\sqrt{A},0,1)^\top, \quad \vec{b}_3 = \frac{1}{\sqrt{2}}(0,1,1)^\top. \tag{G.46}$$

The only linear combinations $\vec{v} = i\vec{b}_1 + j\vec{b}_2 + k\vec{b}_3$ (for $i,j,k \in \mathbb{Z}$) that remain finite in the limit $A \to +\infty$ occur when $i = -j$, in which case we obtain

$$\vec{v} = -j\vec{b}_1 + j\vec{b}_2 + k\vec{b}_3 = \frac{1}{\sqrt{2}}\left[j(0,-1,1)^\top + k(0,1,1)^\top \right]. \tag{G.47}$$

This is isomorphic to the two-dimensional square close packing lattice with minimal distance 1, rotated from the coordinate axes by 45 degrees.

Appendix H

Bessel Function Expansions of the Lattice Sums for the Burgers Path

In the following we concentrate on the lattice sums H_A^h and H_B^h so we do not have to carry the factor $f(\beta_1, \beta_2, \beta_3)$ along.

H.1 The lattice sum H_A^h

In three dimensions the lattice sum defined through a quadratic form is related to the Epstein zeta function Z by $H_{S_3} = 2Z_{S_3}(s)$ as discussed by Terras[299], where S_3 is a three-dimensional symmetric and positive definite Gram matrix. The Terras decomposition of the Epstein zeta function[299] can be used for any Bravais lattice and an inverse power potential, and has been detailed in our previous paper for cubic lattices,[295]

$$\begin{aligned} Z_{S_3}(s) = {} & \frac{\pi\Gamma(s-1)t^{1-s}}{\Gamma(s)\sqrt{\det S_2}}\zeta(2s-2) + \frac{p^{\frac{1}{2}-s}\Gamma(s-\frac{1}{2})}{\Gamma(s)}\sqrt{\frac{\pi}{\sigma_{22}}}\zeta(2s-1) + \frac{\zeta(2s)}{\sigma_{22}^s} \\ & + \frac{4\pi^s}{\Gamma(s)}\left(\frac{p^{1-2s}}{\sigma_{22}^{1+2s}}\right)^{1/4} \sum_{u,v\in\mathbb{N}} \left(\frac{v}{u}\right)^{s-\frac{1}{2}} \cos\left(\frac{2\pi\sigma_{12}uv}{\sigma_{22}}\right) K_{s-\frac{1}{2}}\left(2\pi uv\sqrt{\frac{p(\alpha)}{\sigma_{22}}}\right) \\ & + \frac{2\pi^s}{\Gamma(s)}\sqrt{\frac{t^{1-s}}{\det S_2}} \sum_{\substack{u\in\mathbb{N} \\ \vec{w}\in\mathbb{Z}^2\setminus\{\vec{0}_2\}}} \cos\left(2\pi u\vec{w}^\top\vec{y}\right) u^{1-s}\left(\vec{w}^\top S_2^{-1}\vec{w}\right)^{\frac{s-1}{2}} K_{s-1}\left(2\pi u\sqrt{t\vec{w}^\top S_2^{-1}\vec{w}}\right) \end{aligned} \tag{H.1}$$

Here S_3 has been block-diagonalized to obtain the (2×2) symmetric sub-matrix $S_2 = (\sigma_{ij})$,

$$S_3 = \begin{pmatrix} m & \vec{z}^\top \\ \vec{z} & S_2 \end{pmatrix} = \begin{pmatrix} 1 & \vec{y}^\top \\ \vec{0}_2 & I_2 \end{pmatrix}\begin{pmatrix} t & \vec{0}_2^\top \\ \vec{0}_2 & S_2 \end{pmatrix}\begin{pmatrix} 1 & \vec{0}_2^\top \\ \vec{y} & I_2 \end{pmatrix} \tag{H.2}$$

and $\vec{y}, \vec{z}$ are simple 2-vectors. This gives the relations,

$$\vec{z} = S_2\vec{y} \quad \Longrightarrow \quad \vec{y} = S_2^{-1}\vec{z} \tag{H.3}$$

and

$$m = t + \vec{y}^{\top} S_2 \vec{y} \quad \Longrightarrow \quad t = m - \vec{z}^{\top} S_2^{-1} \vec{z} \tag{H.4}$$

with $t \neq 0$ and

$$S_2^{-1} = \det(S_2)^{-1} \begin{pmatrix} \sigma_{22} & -\sigma_{12} \\ -\sigma_{12} & \sigma_{11} \end{pmatrix} \tag{H.5}$$

The other parameters and functions are defined as follows,

$$p = \left\{ \sigma_{11} - \frac{\sigma_{12}^2}{\sigma_{22}} \right\} \tag{H.6}$$

The modified Bessel function is defined as

$$K_\nu(x) = \frac{1}{2} \int_0^\infty u^{\nu-1} \exp\left\{ -x \left(u + u^{-1} \right) / 2 \right\} du \quad \text{for} \quad |\arg(x)| < \tfrac{1}{2}\pi \tag{H.7}$$

with $K_\nu(x) = K_{-\nu}(x)$,[601] The higher-order Bessel functions can be successively reduced to lower order Bessel functions by

$$K_\nu(x) = \frac{2(\nu-1)}{x} K_{\nu-1}(x) + K_{\nu-2}(x) \tag{H.8}$$

and all what remains to be evaluated are the Bessel functions K_1, K_0 and $K_{\frac{1}{2}}$. Further, for half-integer orders of the Bessel function we can use the equation

$$K_{\frac{1}{2}}(x) = K_{-\frac{1}{2}}(x) = \sqrt{\frac{\pi}{2x}} e^{-x} \tag{H.9}$$

The relation for the Γ-functions is

$$\Gamma(x+1) = x\Gamma(x) \tag{H.10}$$

For the symmetric matrix S_3 we permute the rows and columns in (6.25) and take

$$S_3(\alpha, \boldsymbol{\gamma}) = \begin{pmatrix} \gamma_2^2 & 0 & 0 \\ 0 & 1 & \omega_1(\alpha, \gamma_1) \\ 0 & \omega_1(\alpha, \gamma_1) & \omega_2(\alpha, \gamma_1) \end{pmatrix} \quad \text{and} \quad S_2(\alpha, \gamma_1) = \begin{pmatrix} 1 & \omega_1(\alpha, \gamma_1) \\ \omega_1(\alpha, \gamma_1) & \omega_2(\alpha, \gamma_1) \end{pmatrix} \tag{H.11}$$

which for $\vec{z}^{\top} = (0,0)$ gives $\vec{y}^{\top} = (0,0)$, and for the other parameters $m = t = \gamma_2^2$. Taking $\sigma_{11} = 1, \sigma_{12}(\alpha, \gamma_1) = \omega_1(\alpha, \gamma_1)$, $\sigma_{22}(\alpha) = \omega_2(\alpha, \gamma_1)$, $p(\alpha) = 1 - \frac{\omega_1(\alpha,\gamma_1)^2}{\omega_2(\alpha,\gamma_1)} = \frac{\omega_3^2(\alpha,\gamma_1)}{\omega_2(\alpha,\gamma_1)} > 0$ and

$\det S_2(\alpha,\gamma_1) = \omega_2(\alpha,\gamma_1) - \omega_1(\alpha,\gamma_1)^2 = \omega_3(\alpha,\gamma_1)^2 = \omega_2(\alpha,\gamma_1)p(\alpha) > 0$ for $\alpha \in [0,1]$, and we get

$$
\begin{aligned}
H_A^h(s) = {} & \frac{2\pi\Gamma(s-1)}{\gamma_2^{2s-2}\Gamma(s)\omega_3(\alpha,\gamma_1)}\zeta(2s-2) + \frac{2p(\alpha)^{\frac{1}{2}-s}\Gamma(s-\frac{1}{2})}{\Gamma(s)}\sqrt{\frac{\pi}{\omega_2(\alpha,\gamma_1)}}\zeta(2s-1) + \frac{2\zeta(2s)}{\omega_2(\alpha,\gamma_1)^s} \\
& + \frac{8\pi^s\omega_3(\alpha,\gamma_1)^{\frac{1}{2}-s}}{\Gamma(s)\sqrt{\omega_2(\alpha,\gamma_1)}} \sum_{u,v\in\mathbb{N}} \left(\frac{v}{u}\right)^{s-\frac{1}{2}} \cos\left(\frac{2\pi uv\omega_1(\alpha,\gamma_1)}{\omega_2(\alpha,\gamma_1)}\right) K_{s-\frac{1}{2}}\left(\frac{2\pi uv\omega_3(\alpha,\gamma_1)}{\omega_2(\alpha,\gamma_1)}\right) \\
& + \frac{4\pi^s}{\gamma_2^{s-1}\Gamma(s)\omega_3(\alpha,\gamma_1)} \sum_{\substack{u\in\mathbb{N} \\ \vec{w}\in\mathbb{Z}^2\setminus\{\vec{0}_2\}}} u^{1-s}\left(\vec{w}^\top S_2^{-1}\vec{w}\right)^{\frac{s-1}{2}} K_{s-1}\left(2\pi\gamma_2 u\sqrt{\vec{w}^\top S_2^{-1}\vec{w}}\right)
\end{aligned}
\tag{H.12}
$$

and for the inverse S_2 matrix we have

$$
S_2^{-1} = \frac{1}{\omega_3^2(\alpha,\gamma_1)}\begin{pmatrix} \omega_2(\alpha,\gamma_1) & -\omega_1(\alpha,\gamma_1) \\ -\omega_1(\alpha,\gamma_1) & 1 \end{pmatrix} \tag{H.13}
$$

The parameter p does not depend on γ_1 and $p(\alpha) = \sin^2(\theta_{12})$ where θ_{12} is the angle between $\vec{b}_1$ and $\vec{b}_2$ that can be approximated as $\frac{\pi(2+\alpha)}{6}$ when $\alpha \in [0,1]$.)

H.2 The lattice sum H_B^h

This is the more complicated case, but we can use the expansion derived from Van der Hoff and Benson's original expression derived from a Mellin transformation and the use of theta functions,[300]

$$
\sum_{i\in\mathbb{Z}}\left[x^2 + (i+\zeta)^2\right]^{-s} = \frac{\sqrt{\pi}\Gamma(s-\frac{1}{2})}{\Gamma(s)\,|x|^{2s-1}} + \frac{4\pi^s}{\Gamma(s)}\sum_{n\in\mathbb{N}}\left(\frac{n}{|x|}\right)^{s-\frac{1}{2}}\cos(2\pi n\zeta)K_{s-\frac{1}{2}}(2\pi n|x|) \tag{H.14}
$$

with $\zeta \in [0,1)$. We rewrite the quadratic function (6.37) into

$$
\begin{aligned}
Q_B(i,j,k,\alpha,\beta_1,\beta_2,\beta_3,\gamma_1,\gamma_2) &= \gamma_2^2\left[\gamma_2^{-2}(i + j\omega_1(\alpha,\gamma_1) + \tfrac{\beta_1}{2})^2 + \gamma_2^{-2}(j\omega_3(\alpha,\gamma_1) + \tfrac{\beta_2}{2})^2 + (k + \tfrac{\beta_3}{2\gamma_2})^2\right] \\
&= \gamma_2^2\left[\gamma_2^{-2}x_{ij}^2(\alpha,\beta_1,\beta_2,\gamma_1) + (k + \tfrac{\beta_3}{2\gamma_2})^2\right]
\end{aligned}
\tag{H.15}
$$

and get

$$H_B^h(s,\alpha,\beta_1,\beta_2,\beta_3,\gamma_1,\gamma_2) = \sum_{\vec{i}\in\tilde{\mathbb{Z}}^3} Q_B(\vec{i},\alpha,\beta_1,\beta_2,\beta_3,\gamma_1,\gamma_2)^{-s} = \frac{\sqrt{\pi}\Gamma\left(s-\frac{1}{2}\right)}{\gamma_2\Gamma(s)} \sum_{i,j\in\mathbb{Z}} \left|x_{ij}(\alpha,\beta_1,\beta_2,\gamma_1)\right|^{1-2s}$$
$$+ \frac{4\pi^s}{\gamma_2^{s+\frac{1}{2}}\Gamma(s)} \sum_{i,j\in\mathbb{Z}} \sum_{n\in\mathbb{N}} \cos\left(\frac{\pi n\beta_3}{\gamma_2}\right) \left(\frac{n}{\left|x_{ij}(\alpha,\beta_1,\beta_2,\gamma_1)\right|}\right)^{s-\frac{1}{2}} K_{s-\frac{1}{2}}\left(\frac{2\pi n|x_{ij}(\alpha,\beta_1,\beta_2,\gamma_1)|}{\gamma_2}\right) \tag{H.16}$$

with

$$x_{ij}(\alpha,\beta_1,\beta_2,\gamma_1)^2 = (i+j\omega_1(\alpha,\gamma_1)+\tfrac{\beta_1}{2})^2 + (j\omega_3(\alpha,\gamma_1)+\tfrac{\beta_2}{2})^2 \tag{H.17}$$

One has to avoid $x_{ij}^2 = 0$ for this expansion. For the approximate range of (α,β_1,β_2) parameters (Table 6.1) with $\omega_1 \in [0,\frac{1}{2}]$, $\omega_3 \in [\frac{\sqrt{3}}{2},1]$, one can easily show that $x_{ij}^2 > 0$. This expansion reduces the problem into a fast converging triple sum involving Bessel functions, and into an additional double sum,

$$W(\alpha,\beta_1,\beta_2,\gamma_1) = \sum_{i,j\in\mathbb{Z}} \left\{(i+j\omega_1(\alpha,\gamma_1)+\tfrac{\beta_1}{2})^2 + (j\omega_3(\alpha,\gamma_1)+\tfrac{\beta_2}{2})^2\right\}^{\frac{1}{2}-s} \tag{H.18}$$

which however is slowly convergent for low s values. We therefore use again expansion (H.14) with $\zeta = j\omega_1(\alpha,\gamma_1)+\frac{\beta_1}{2}$ and $x = j\omega_3(\alpha,\gamma_1)+\frac{\beta_2}{2}$ and get

$$W(\alpha,\beta_1,\beta_2,\gamma_1) = \frac{\sqrt{\pi}\Gamma(s-1)}{\Gamma(s-\frac{1}{2})} \sum_{j\in\mathbb{Z}} \frac{1}{|j\omega_3(\alpha,\gamma_1)+\frac{\beta_2}{2}|^{2s-2}} \tag{H.19}$$
$$+ \frac{4\pi^{s-\frac{1}{2}}}{\Gamma(s-\frac{1}{2})} \sum_{j\in\mathbb{Z}} \sum_{n\in\mathbb{N}} \left(\frac{n}{|j\omega_3(\alpha,\gamma_1)+\frac{\beta_2}{2}|}\right)^{s-1} \cos\left(2\pi n\left[j\omega_1(\alpha,\gamma_1)+\frac{\beta_1}{2}\right]\right)$$
$$\times K_{s-1}\left(2\pi n\left|j\omega_3(\alpha,\gamma_1)+\frac{\beta_2}{2}\right|\right)$$

The first sum can be turned into a Hurwitz zeta function $h(s,x)$,

$$\sum_{j\in\mathbb{Z}} \frac{1}{|j+\frac{\beta_2}{2\omega_3(\alpha,\gamma_1)}|^{2s-2}} = h\left(2s-2,\tfrac{\beta_2}{2\omega_3(\alpha,\gamma_1)}\right) + h\left(2s-2,1-\tfrac{\beta_2}{2\omega_3(\alpha,\gamma_1)}\right) \tag{H.20}$$

with

$$h(s,x) = \sum_{n\in\mathbb{N}_0} \frac{1}{(n+x)^s} \tag{H.21}$$

In summary, the lattice sum H_B is

$$H_B^h(s,\alpha,\beta_1,\beta_2,\beta_3,\gamma_1,\gamma_2) = \frac{\pi\Gamma(s-1)}{\gamma_2\Gamma(s)\omega_3(\alpha,\gamma_1)^{2s-2}}\left[h\left(2s-2,\tfrac{\beta_2}{2\omega_3(\alpha,\gamma_1)}+h\left(2s-2,1-\tfrac{\beta_2}{2\omega_3(\alpha,\gamma_1)}\right)\right)\right]$$
$$+\frac{4\pi^s}{\gamma_2\Gamma(s)}\sum_{j\in\mathbb{Z}}\sum_{n\in\mathbb{N}}\left(\frac{n}{|j\omega_3(\alpha,\gamma_1)+\frac{\beta_2}{2}|}\right)^{s-1}\cos\left(2\pi n\left[j\omega_1(\alpha,\gamma_1)+\frac{\beta_1}{2}\right]\right)K_{s-1}\left(2\pi n\left|j\omega_3(\alpha,\gamma_1)+\frac{\beta_2}{2}\right|\right)$$
$$+\frac{4\pi^s}{\gamma_2^{s+\frac{1}{2}}\Gamma(s)}\sum_{i,j\in\mathbb{Z}}\sum_{n\in\mathbb{N}}\cos\left(\frac{\pi n\beta_3}{\gamma_2}\right)\left(\frac{n}{|x_{ij}(\alpha,\beta_1,\beta_2,\gamma_1)|}\right)^{s-\frac{1}{2}}K_{s-\frac{1}{2}}\left(\frac{2\pi n|x_{ij}(\alpha,\beta_1,\beta_2,\gamma_1)|}{\gamma_2}\right) \tag{H.22}$$

H.3 Adding both lattice sums

We can now add both lattice sums H_A^h and H_B^h

$$H^h(s,\alpha,\beta_1,\beta_2,\gamma_1,\gamma_2) = g_0(s,\alpha,\beta_1,\beta_2,\gamma_1,\gamma_2)+\sum_{n=1}^{4}g_n(s,\alpha,\beta_1,\beta_2,\beta_3,\gamma_1,\gamma_2) \tag{H.23}$$

with

$$g_0(s,\alpha,\beta_1,\beta_2,\gamma_1,\gamma_2) = \frac{2\pi\Gamma(s-1)}{\gamma_2^{2s-2}\Gamma(s)\omega_3(\alpha,\gamma_1)}\zeta(2s-2)+\frac{2p(\alpha)^{\frac{1}{2}-s}\Gamma(s-\frac{1}{2})}{\Gamma(s)}\sqrt{\frac{\pi}{\omega_2(\alpha,\gamma_1)}}\zeta(2s-1)$$
$$+\frac{2\zeta(2s)}{\omega_2(\alpha,\gamma_1)^s}+\frac{\pi\Gamma(s-1)}{\gamma_2\Gamma(s)\omega_3(\alpha,\gamma_1)^{2s-2}}\left\{h\left(2s-2,\tfrac{\beta_2}{2\omega_3(\alpha,\gamma_1)}\right)+h\left(2s-2,1-\tfrac{\beta_2}{2\omega_3(\alpha,\gamma_1)}\right)\right\} \tag{H.24}$$

where the first three terms originate from H_A and the last one from H_B, and each of the following g_n terms containing an infinite sum of Bessel functions such that

$$g_1(s,\alpha,\gamma_1) = \frac{8\pi^s\omega_3(\alpha,\gamma_1)^{\frac{1}{2}-s}}{\Gamma(s)\sqrt{\omega_2(\alpha,\gamma_1)}}\sum_{i,j\in\mathbb{N}}\left(\frac{i}{j}\right)^{s-\frac{1}{2}}\cos\left(\frac{2\pi\omega_1(\alpha,\gamma_1)ij}{\omega_2(\alpha,\gamma_1)}\right)K_{s-\frac{1}{2}}\left(2\pi ij\frac{\omega_3(\alpha,\gamma_1)}{\omega_2(\alpha,\gamma_1)}\right) \tag{H.25}$$

$$g_2(s,\alpha,\gamma_1,\gamma_2) = \frac{4\pi^s}{\gamma_2^{s-1}\Gamma(s)\omega_3(\alpha,\gamma_1)}\sum_{\substack{n\in\mathbb{N}\\ \vec{w}\in\tilde{\mathbb{Z}}^2\setminus\{\vec{0}_2\}}}\left(\frac{\vec{w}^\top S_2^{-1}\vec{w}}{n^2}\right)^{\frac{s-1}{2}}K_{s-1}\left(2\pi n\gamma_2\sqrt{\vec{w}^\top S_2^{-1}\vec{w}}\right) \tag{H.26}$$

$$g_3(s,\alpha,\beta_1,\beta_2,\gamma_1,\gamma_2) = \frac{4\pi^s}{\gamma_2\Gamma(s)} \sum_{j\in\mathbb{Z}} \sum_{n\in\mathbb{N}} \left(\frac{n}{|j\omega_3(\alpha,\gamma_1)+\frac{\beta_2}{2}|} \right)^{s-1} \cos\left(2\pi n \left[j\omega_1(\alpha)+\frac{\beta_1}{2} \right] \right) \times K_{s-1}\left(2\pi n \left| j\omega_3(\alpha,\gamma_1)+\frac{\beta_2}{2} \right| \right) \tag{H.27}$$

$$g_4(s,\alpha,\beta_1,\beta_2,\beta_3,\gamma_1,\gamma_2) = \frac{4\pi^s}{\gamma_2^{s+\frac{1}{2}}\Gamma(s)} \sum_{i,j\in\mathbb{Z}} \sum_{n\in\mathbb{N}} \cos\left(\frac{\pi n\beta_3}{\gamma_2}\right) \left(\frac{n}{|x_{ij}(\alpha,\beta_1,\beta_2,\gamma_1)|} \right)^{s-\frac{1}{2}} \times K_{s-\frac{1}{2}}\left(2\pi n\gamma_2^{-1}|x_{ij}(\alpha,\beta_1,\beta_2,\gamma_1)|\right) \tag{H.28}$$

with $p(\alpha,\gamma_1) = 1-\frac{\omega_1(\alpha,\gamma_1)^2}{\omega_2(\alpha,\gamma_1)} > 0$ as defined before. Here g_1 and g_2 originate from the lattice sum H_A, and g_3 and g_4 from the lattice sum H_B.

For computational purposes we need to treat the first three Bessel sums more efficiently. For the first Bessel sum g_1 appearing in H_A^h we use permutation symmetry between i and j and get,

$$g_1(s,\alpha,\gamma_1) = \frac{8\pi^s\omega_3(\alpha,\gamma_1)^{\frac{1}{2}-s}}{\Gamma(s)\sqrt{\omega_2(\alpha,\gamma_1)}} \sum_{i\geq j\in\mathbb{N}} \left(1-\tfrac{1}{2}\delta_{ij}\right) \left[\left(\frac{i}{j}\right)^{s-\frac{1}{2}} + \left(\frac{j}{i}\right)^{s-\frac{1}{2}} \right] \cos\left(\frac{2\pi\omega_1(\alpha,\gamma_1)ij}{\omega_2(\alpha,\gamma_1)}\right) \times K_{s-\frac{1}{2}}\left(2\pi ij\frac{\omega_3(\alpha,\gamma_1)}{\omega_2(\alpha,\gamma_1)}\right) \tag{H.29}$$

where δ_{ij} is the Kronecker symbol.

For the triple sum g_2 we simply use the fact that S_2^{-1} is a symmetric matrix and get,

$$g_2(s,\alpha,\gamma) = \frac{4\pi^s}{\gamma_2^{s-1}\Gamma(s)\omega_3(\alpha,\gamma_1)} \sum_{n\in\mathbb{N}} \sum_{\substack{\vec{w}\in\tilde{\mathbb{Z}}^2\setminus\{\vec{0}_2\} \\ w_1\leq w_2}} (2-\delta_{w_1w_2}) \left(\frac{\vec{w}^\top S_2^{-1}\vec{w}}{n^2}\right)^{\frac{s-1}{2}} \times K_{s-1}\left(2\pi n\gamma_2\sqrt{\vec{w}^\top S_2^{-1}\vec{w}}\right) \tag{H.30}$$

The last sum g_3 and g_4 for H_B^h cannot be further simplified, only for the special case $\beta_1 = 1$

we get for g_3

$$
\begin{aligned}
g_3(s,\alpha,\beta_1,\beta_2,\gamma_1,\gamma_2) &= \frac{4\pi^s}{\gamma_2\Gamma(s)} \sum_{i\in\mathbb{N}} (-1)^i \left(\frac{2i}{\beta_2}\right)^{s-1} K_{s-1}\left(\pi\beta_2 i\right) \\
&+ \frac{4\pi^s}{\gamma_2\Gamma(s)} \sum_{i,j\in\mathbb{N}} (-1)^i \cos\left(2\pi\omega_1(\alpha,\gamma_1)ij\right) \\
&\times \sum_{k\in\{-1,+1\}} \left(\frac{i}{\left(j\omega_3(\alpha,\gamma_1)+\frac{k\beta_2}{2}\right)}\right)^{s-1} K_{s-1}\left(2\pi i\left(j\omega_3(\alpha,\gamma_1)+\frac{k\beta_2}{2}\right)\right)
\end{aligned}
\tag{H.31}
$$

and we used $\cos(x+n\pi) = (-1)^n\cos(x)$ and remember that $\beta_2 > 0$ and $j\omega_3(\alpha) > \frac{1}{2}k\beta_2$. The first single sum is related to the infinite sum in (H.14) and is one of the most common Bessel function series in the literature[602]. In general, however, the two triple sums g_3 and g_4 are fast convergent. We note that for larger s values we obtain large compensating numbers for the individual terms in the lattice sums, which offsets double precision results. In this case, taking the direct summation for the lattice sum for values $s \geq 8$ is the preferred option as outlined in the next section. Alternatively, one can switch to quadruple precision arithmetic.

Appendix I

Relation between the lattice sums of the fcc lattice

Here we show how eq. (6.47) can be brought into the more common form (6.48). Starting with (6.47) we have

$$L_A^{\mathrm{fcc}} + L_B^{\mathrm{fcc}} = \sum_{\vec{i}\in\mathbb{Z}^3}{}' (i_1^2 + i_2^2 + 2i_3^2)^{-s} + \sum_{\vec{i}\in\mathbb{Z}^3} \left((i_1+\tfrac{1}{2})^2 + (i_2+\tfrac{1}{2})^2 + 2(i_3+\tfrac{1}{2})^2\right)^{-s} \tag{I.1}$$

$$= \sum_{i_1\equiv i_2\equiv i_3 (\mathrm{mod}\,2)}{}' \left(\left(\tfrac{i_1}{2}\right)^2 + \left(\tfrac{i_2}{2}\right)^2 + 2\left(\tfrac{i_3}{2}\right)^2\right)^{-s} = 2^{2s} \sum_{i_1\equiv i_2\equiv i_3 (\mathrm{mod}\,2)}{}' \left(i_1^2 + i_2^2 + 2i_3^2\right)^{-s}$$

using the standard notation for congruences. Since i_1 and i_2 have the same parity, both of $i_1 - i_2$ and $i_1 + i_2$ will be even. Hence, we make the change of variable $i_1 - i_2 = 2x$ and $i_1 + i_2 = 2y$, or equivalently $i_1 = x + y$ and $i_2 = x - y$. This gives

$$L_A^{\mathrm{fcc}} + L_B^{\mathrm{fcc}} = 2^{2s} \sum_{x+y\equiv i_3 (\mathrm{mod}\,2)}{}' \left(2x^2 + 2y^2 + 2i_3^2\right)^{-s} = 2^s \sum_{x+y\equiv i_3 (\mathrm{mod}\,2)}{}' \left(x^2 + y^2 + i_3^2\right)^{-s}. \tag{I.2}$$

Now $x + y$ and i_3 will have the same parity if and only if $x + y + i_3 \equiv 0 \pmod 2$. The indicator function for this condition is

$$\tfrac{1}{2}\left(1 + (-1)^{x+y+i_3}\right) = \begin{cases} 1 & \text{if } x+y+i_3 \equiv 0 \pmod 2, \\ 0 & \text{if } x+y+i_3 \not\equiv 0 \pmod 2. \end{cases}$$

On applying this to the sum above we deduce

$$L_A^{\mathrm{fcc}} + L_B^{\mathrm{fcc}} = 2^s \sum_{\vec{i}\in\mathbb{Z}^3}{}' \tfrac{1}{2}\left(1 + (-1)^{x+y+i_3}\right)\left(x^2 + y^2 + i_3^2\right)^{-s} \tag{I.3}$$

and this is (6.48).

Appendix J

The Bain path as part of the symmetry-broken Burgers transformation

In this appendix, we show that part of the Burgers path[262] after joining the bcc↔fcc transformation path for values $\alpha > \alpha_c$, where α_c is the bifurcation points dependent on the exponents (n, m) of the LJ potential, is identical to the classical Bain path[256,434] at $\alpha = 1$ with variable γ_2. From continuum mechanics we know that the position of each material point, $\vec{x}$, within a body at a reference configuration $\mathcal{S}_\alpha$ can be followed along a deformation to a target configuration $\mathcal{S}_{\alpha'}$ through the displacement field $\chi(\vec{x})$, such that the new position is given by $\vec{y} = \chi(\vec{x})$. The mapping from the initial to the end point is given by the deformation gradient tensor, $F = \nabla\chi(\vec{x})$, that maps every vector from the reference configuration to the target[603,604]. If $\mathrm{d}x$ is a line element in $\mathcal{S}_\alpha$, its length in $\mathcal{S}_{\alpha'}$ is therefore $|\mathrm{d}y| = \sqrt{|F\mathrm{d}x|^2} = \sqrt{\mathrm{d}x^\top C \mathrm{d}x}$, where $C = F^\top F$ is the symmetric positive definite Cauchy-Green tensor. Hence, C has positive eigenvalues, λ_i, corresponding to the transformation $|F\mathrm{d}x|^2$, and orthonormal eigenvectors.

For a lattice $\mathcal{L}(A) = \{A\vec{i} = \sum_n i_n \vec{a}_n | \vec{i} \in \mathbb{Z}^N\}$, the transformation to a lattice $\mathcal{L}(B)$ is given by an affine map $\chi(\vec{x}) = F\vec{x} + \vec{c}$, where $\vec{c}$ is a translation vector that can be set to zero. Thus, the transformation $\mathcal{L}(A) \to \mathcal{L}(B)$ is represented by $B\vec{i} = FA\vec{i}$, which leads to $F = BA^{-1}$. Applying this formalism to the current three-dimensional case of the Burgers transformation, we see that the relation between two conventional unit cells defined along the Burgers path with α and α' is given by the deformation gradient tensor,

$$F = B_{\alpha'} B_\alpha^{-1} = \frac{a'}{a} \begin{pmatrix} 1 & 0 & 0 \\ \omega_1' - \frac{\omega_1 \omega_3'}{\omega_3} & \frac{\omega_3'}{\omega_3} & 0 \\ 0 & 0 & \frac{\gamma_2'}{\gamma_2} \end{pmatrix} \tag{J.1}$$

where $\omega_1 = \frac{1-\alpha}{2}$, $\omega_3 = \frac{1}{2}\sqrt{(1+\alpha)(3-\alpha)}$ and for $\alpha = \alpha'$ we trivially have $F = B_\alpha B_\alpha^{-1} = I$. The

shift vector transforms under this deformation as

$$\vec{v}_s{}' = \frac{a'}{2}\begin{pmatrix}\beta_1'\\ \beta_2'\\ \beta_3'\end{pmatrix} = F\vec{v}_s = \frac{a'}{2}\begin{pmatrix}\beta_1\\ \left[\omega_1' - \frac{\omega_1\omega_3'}{\omega_3}\right]\beta_1 + \left[\frac{\omega_3'}{\omega_3}\right]\beta_2\\ \left[\frac{\gamma_2'}{\gamma_2}\right]\beta_3\end{pmatrix} \tag{J.2}$$

A polar decomposition can be performed on the deformation gradient tensor, such that $F = RU$, where R is a rotation (orthogonal) matrix and U is a symmetric positive definite matrix called stretch tensor[603,604]. Hence, the Cauchy-Green tensor is $C = U^\top U$, since $\det R = 1$. Therefore, the stretch tensor is calculated as $U = \sqrt{C}$ and its eigenvalues are $s_i = \sqrt{\lambda_i}$, corresponding to the stretches of the body along each direction in the lattice, thus capturing shape changes without considering rotations. The stretch tensor is then given by

$$U = \frac{a'}{a}\begin{pmatrix}\frac{1+\eta_1^2+|\eta_2|}{t} & \frac{\eta_1\eta_2}{t} & 0\\ \frac{\eta_1\eta_2}{t} & \frac{\eta_2^2+|\eta_2|}{t} & 0\\ 0 & 0 & |\eta_3|\end{pmatrix} \tag{J.3}$$

where $t = \sqrt{1+\eta_1^2+\eta_2^2+2|\eta_2|}$, $\eta_1 = \omega_1' - \frac{\omega_1\omega_3'}{\omega_3}$, $\eta_2 = \omega_3'/\omega_3$, and $\eta_3 = \gamma_2'/\gamma_2$. The eigenvalues of U show the scale factors along each direction are given by

$$s_{1,2} = \frac{a'}{a}\sqrt{\frac{1}{2}\left[1+\eta_1^2+\eta_2^2 \pm \sqrt{(1+\eta_1^2+\eta_2^2)^2 - 4\eta_2^2}\right]} \quad \text{and} \quad s_3 = \frac{a'\gamma_2'}{a\gamma_2} \tag{J.4}$$

Both transformations from the bcc structure at $\alpha = \frac{1}{3}$ (Burgers) and $\alpha = 1$ (Bain) to fcc have the eigenvalues $s_1 = 1.2573106383758839$ and $s_{2,3} = 0.8890528784535745$, which implies that both follow the Bain path but with different orientations in three-dimensional space. Note that $s_1 = \sqrt{2}s_{2,3}$ which is characteristic of the Bain transformation. This concludes our proof.

Appendix K

Some useful relations for the lattice parameters along the bcc-to-fcc phase transition

To discuss the rhombohedral distortion of the bcc phase to another phase as mentioned already by Max Born in 1940[355,605], we need to analyze the Bain part of the Burgers transformation in more detail. The transformation from our unit cell (shown in blue color in Figure 6.4), spanned by the vectors $\vec{b}_i$ (see eq.(6.28)) chosen for the Burgers path with an additional atom at position $\vec{v}_s$ (thus a bi-lattice by definition), to a primitive unit cell (shown green color in Figure 6.4) is only possible along the cuboidal transformation path from bcc ($\alpha = 1/3$) to fcc ($\alpha = 1$) (or vice versa) where the crystal is completely defined by a single unit cell. Since the unit cell, given by B_{cub}, defined here contains two atoms, the condition for the primitive unit cell, B_{p}, is that

$$V_{\mathrm{p}} = \det(B_{\mathrm{p}}) = \det(B_{\mathrm{cub}})/2 = V_{\mathrm{cub}}/2 \quad . \tag{K.1}$$

Choosing the lattice basis vectors for the primitive unit cell as $\vec{p}_1 = \vec{v}_s$, $\vec{p}_2 = \vec{b}_2$, and $\vec{p}_3 = \vec{b}_3$, the only way to ensure that the volume per atom is preserved is by the following condition

$$\beta_1 - \frac{\beta_2 \omega_1(\alpha)}{\omega_3(\alpha)} = 1 \tag{K.2}$$

where $\beta_3 = \gamma_2$ as detailed below. From eqs.(6.27) and (6.29) we get the condition for two of the β parameters in terms of α,

$$\beta_1 = \frac{\beta_2(1-\alpha)}{\sqrt{4-(1-\alpha)^2}} + 1 \tag{K.3}$$

A further condition can be applied that keeps the tetragonal body-centered symmetry followed during the Bain path, namely, that the central atom is located at the center of the parallelepiped

during the transformation,

$$\vec{v}_s = \frac{1}{2}\left(\vec{b}_1 + \vec{b}_2 + \vec{b}_3\right) \tag{K.4}$$

Further, it is convenient to write the shift vector $\vec{v}_s$ in terms of the $\vec{b}_i$-basis as

$$\vec{v}_s = \frac{1}{2}\left[\beta_1 - \frac{\beta_2\omega_1(\alpha)}{\omega_3(\alpha)}\right]\vec{b}_1 + \frac{1}{2}\left[\frac{\beta_2}{\omega_3(\alpha)}\right]\vec{b}_2 + \frac{1}{2}\left[\frac{\beta_3}{\gamma_2}\right]\vec{b}_3 \quad . \tag{K.5}$$

such that in addition to eq.(K.2) we get

$$\beta_2 = \omega_3(\alpha) \quad \text{and} \quad \beta_3 = \gamma_2 \tag{K.6}$$

for any $\alpha \in [\frac{1}{3}, 1]$. From this we derive

$$\beta_1 = 1 + \omega_1(\alpha) = \frac{3-\alpha}{2} \qquad . \tag{K.7}$$

Let ϕ_1 be the angle between $\vec{b}_1$ and the projection of $\vec{p}_1$ into the $(\vec{b}_1\vec{b}_2)$-plane. The constraint on the position of the second atom in the cell also implies $\phi_1 = \theta_{12}/2$, where θ_{12} is the angle between $\vec{b}_1$ and $\vec{b}_2$. Therefore, using the half-angle formulas for cosine and sine together with Eq. (6.29), we obtain

$$\frac{\beta_1}{\sqrt{\beta_1^2+\beta_2^2}} = \sqrt{\frac{3-\alpha}{4}} \qquad \text{and} \qquad \frac{\beta_2}{\sqrt{\beta_1^2+\beta_2^2}} = \sqrt{\frac{1+\alpha}{4}} \tag{K.8}$$

which then fixes the ratio to

$$\frac{\beta_1}{\beta_2} = \sqrt{\frac{3-\alpha}{1+\alpha}} \tag{K.9}$$

This relation is in agreement with the KHS model values where we fixed $\beta_1 = 1$, see Eq. (6.59). From Figure K.1a, it can be seen that the largest deviation from eq.(K.9) within $\alpha \in [0,1]$ is found for the $(30,20)$-LJ potential with a magnitude less than 2×10^{-9} due to numerical errors. Hence we get the interesting result that Eq.(K.9) is valid for the whole range of $\alpha \in [0,1]$ and for any choice of LJ potentials. Moreover, any symmetry breaking effect in β_1 will lead to a symmetry breaking in β_2. And last, the derivatives of β_1 with respect to α are also connected to the corresponding derivatives of β_2. Also note that from Eqs. (K.6) and (K.7) it follows that $\beta_1^2 + \beta_2^2 = 2\beta_1$ along the Bain path for $\alpha \in [\frac{1}{3}, 1]$.

We can also derive more approximate but useful relationships for the lattice parameters. The tangent of the angle between $\vec{b}_3$ and the projection of $\vec{p}_1$ in the $(\vec{b}_2\vec{b}_3)$-plane is

$$\tan\phi_3 = \frac{\beta_1\omega_1 + \beta_2\omega_3}{\beta_3\gamma_2} \tag{K.10}$$

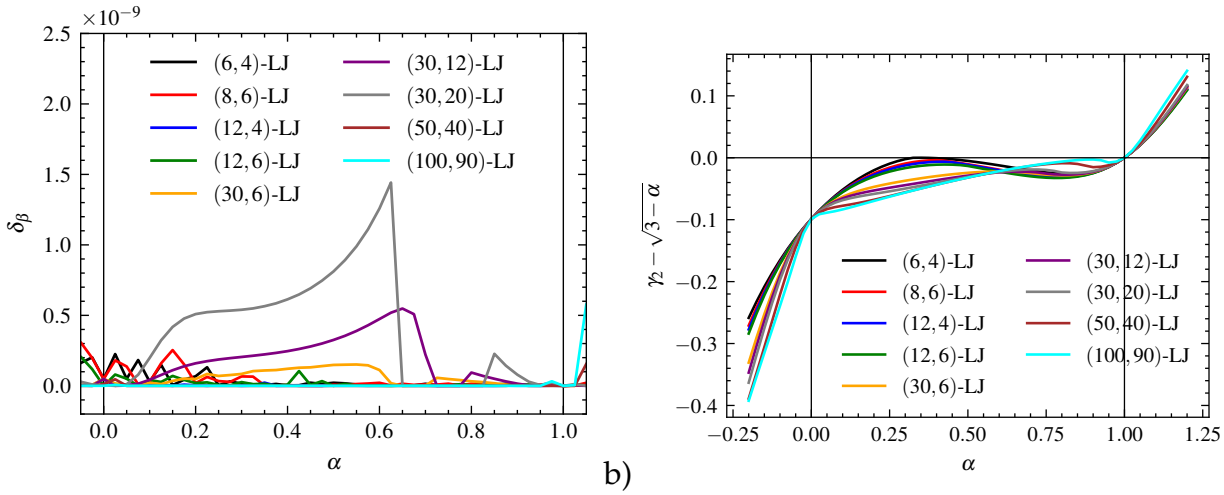

Figure K.1: a) Deviation from Eq. (K.9) for the Lennard-Jones potentials studied here, where $\delta_\beta = \left|\frac{\beta_1}{\beta_2} - \sqrt{\frac{3-\alpha}{1+\alpha}}\right|$. b) Deviation from Eq. (K.12) for the Lennard-Jones potentials.

The numerator in this formula is equal to 1 for fcc and bcc at $\alpha = 1$. For hcp, $\phi_3 = 20.56°$, whereas for both fcc and bcc ($\alpha = \frac{1}{3}$), we get $\phi_3 = 26.57°$. Using the centering conditions in Eq. (K.6), this relation simplifies to

$$\tan\phi_3 = \frac{1+\omega_1}{\gamma_2^2} \tag{K.11}$$

As can be seen in Figure K.2 for the different Lennard-Jones potentials, the variation of this angle is small during the cuboidal transformation between bcc ($\alpha = \frac{1}{3}$) and fcc. One could naively constrain this angle to be constant along the Bain transformation, such that $\tan\phi_3 = \frac{1}{2}$, i.e., $\phi_3 = 26.57°$. Therefore, the parameter γ_2 can be approximately related to α along this path by

$$\gamma_2(\alpha) \approx \sqrt{3-\alpha} \tag{K.12}$$

Keeping this angle constant means that as the base gets skewed along a variable α path, the height of the unit cell must compensate to keep the tilt of the body-centered atom position in the $(\vec{b}_2, \vec{b}_3)$ plane fixed, making all right triangles in this plane similar.

Instead of fixing the angle ϕ_3, another possible constraint is keeping the volume fixed along the transformation. That is, for $a = 1$, we have $V = \gamma_2\omega_3 = K$. From Figure S3 in the Supporting Information, we see that the volume changes slightly when using a very soft potential. Since both hcp and fcc have the same volume, we can arbitrarily set $K = \sqrt{2}$. Therefore, another approximate formula for γ_2 appears:

$$\gamma_2(\alpha) \approx \sqrt{\frac{8}{4-(1-\alpha)^2}} \tag{K.13}$$

Since this formula for γ_2 is highly dependent on the choice of K, its usefulness could be limited,

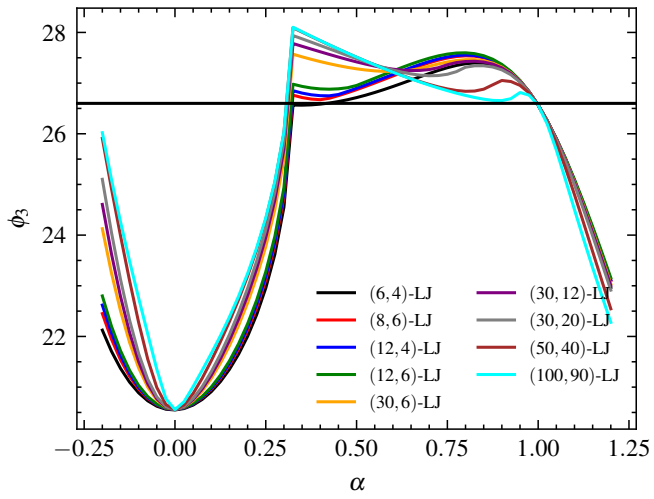

Figure K.2: Angle between $\vec{b}_3$ and the projection of $\vec{p}_1$ on the plane spanned by $\vec{b}_2$ and $\vec{b}_3$. The horizontal line is $\phi_3 = 26.57°$, which correspond to both fcc and bcc.

however the deviations are less than 0.15 from hcp to fcc when $K = \sqrt{2}$. Furthermore, Figure K.1b shows that the deviation of γ_2 from Eq. (K.12) is also less than 0.10 within the interval of the Burgers transformation. Hence, these two formulas can be used for initial guesses at optimizations with exact lattice sums or ab initio methods.

In the case of a cuboidal transformation at constant $\alpha = 1$, it is straightforward to show that $|\vec{p}_1| = \frac{a}{2}\sqrt{2+\gamma_2^2}$ leads to $\beta_1^2 + \beta_2^2 + \beta_3^2 = 2 + \gamma_2^2$, or, due to $\gamma_2^2 = \beta_3^2$,

$$\beta_1^2 + \beta_2^2 = 2 \tag{K.14}$$

while keeping the centering conditions. By means of Eq. (K.9), we see that this condition leads to $\beta_1(\alpha = 1) = \beta_2(\alpha = 1) = 1$.

Appendix L

Proof of the Parity Condition

We use mathematical induction to prove the parity condition that was mentioned at the end of Section 10.2.1.

Suppose N is a positive integer. For $\mathbf{x} = x_1x_2\cdots x_N \in \mathbb{Z}_2^N$ let $|\mathbf{x}| = \sum_{j=1}^N x_i$ and define $f_\mathbf{x} : \{1, 2, \ldots, N+1, N+2\} \to \{A, B, C\}$ by $f_\mathbf{x}(1) = A$, $f_\mathbf{x}(2) = B$, and for $j = 1, 2, \ldots, N$ by

$$f_\mathbf{x}(j+2) = \begin{cases} f_\mathbf{x}(j) & \text{if} \quad x_j = 0, \\ \{A, B, C\} \setminus \{f_\mathbf{x}(j), f_\mathbf{x}(j+1)\} & \text{if} \quad x_j = 1. \end{cases} \tag{L.1}$$

For example, if $\mathbf{x} = 00101 \in \mathbb{Z}_2^5$, then $|\mathbf{x}| = 2$ and

$$(f_\mathbf{x}(1), f_\mathbf{x}(2), f_\mathbf{x}(3), f_\mathbf{x}(4), f_\mathbf{x}(5), f_\mathbf{x}(6), f_\mathbf{x}(7)) = (A, B, A, B, C, B, A).$$

Theorem 1. Suppose N and $\mathbf{x}$ are as above.
If N and $|\mathbf{x}|$ have the same parity, i.e., $N + |\mathbf{x}|$ is even, then

$$(f_\mathbf{x}(N+1), f_\mathbf{x}(N+2)) = (A, B),\ (B, C) \quad \text{or} \quad (C, A). \tag{L.2}$$

If N and $|\mathbf{x}|$ have the opposite parity, i.e., $N + |\mathbf{x}|$ is odd, then

$$(f_\mathbf{x}(N+1), f_\mathbf{x}(N+2)) = (C, B),\ (B, A) \quad \text{or} \quad (A, C). \tag{L.3}$$

That is, $f_\mathbf{x}(N+1)$ and $f_\mathbf{x}(N+2)$ occur in the positive cyclic order $A \to B \to C \to A$ if N and $|\mathbf{x}|$ have the same parity, and in the negative cyclic order $C \to B \to A \to C$ if N and $|\mathbf{x}|$ have the opposite parity.

For the example, if $\mathbf{x} = 00101 \in \mathbb{Z}_2^5$ as mentioned above, then $n + |\mathbf{x}| = 5 + 2$ is odd, and $(f_\mathbf{x}(6), f_\mathbf{x}(7)) = (B, A)$. This is an instance of Case 2 of the theorem.

Proof. Use induction on N. If $N = 1$ then $(f_\mathbf{x}(2), f_\mathbf{x}(3)) = (B, A)$ or (B, C) according to

whether $\mathbf{x} = 0$ or 1. Hence, the result holds true for $N = 1$, and that is enough to start the induction. For clarity, we include the case $N = 2$, and note that

$$(f_{\mathbf{x}}(3), f_{\mathbf{x}}(4)) = (A, B),\ (A, C),\ (C, B) \quad \text{or} \quad (C, A)$$

according to whether $\mathbf{x} = 00,\ 01,\ 10$ or 11, respectively. Thus, the result holds for $N = 2$.

Now assume that the result holds for some value of N. Let $\mathbf{y} \in \mathbb{Z}_2^{N+1}$ and write $\mathbf{y} = x_1 x_2 \cdots x_N x_{N+1}$. Let $\mathbf{x} = x_1 x_2 \cdots x_N$. By the inductive hypothesis we have

$$(f_{\mathbf{x}}(N+1), f_{\mathbf{x}}(N+2)) = \begin{cases} (A, B),\ (B, C) \text{ or } (C, A) & \text{if } N + |\mathbf{x}| \text{ is even,} \\ (C, B),\ (B, A) \text{ or } (A, C) & \text{if } N + |\mathbf{x}| \text{ is odd.} \end{cases}$$

There are four cases to consider. When $N + |\mathbf{x}|$ is even, we have

$$\big(f_{\mathbf{y}}(N+1), f_{\mathbf{y}}(N+2), f_{\mathbf{y}}(N+3)\big) = (A, B, A),\ (B, C, B) \text{ or } (C, A, C) \text{ if } x_{N+1} = 0 \tag{L.4}$$

and

$$\big(f_{\mathbf{y}}(N+1), f_{\mathbf{y}}(N+2), f_{\mathbf{y}}(N+3)\big) = (A, B, C),\ (B, C, A) \text{ or } (C, A, B) \text{ if } x_{N+1} = 1. \tag{L.5}$$

When $N + |\mathbf{x}|$ is odd, we have

$$\big(f_{\mathbf{y}}(N+1), f_{\mathbf{y}}(N+2), f_{\mathbf{y}}(N+3)\big) = (C, B, C),\ (B, A, B) \text{ or } (A, C, A) \text{ if } x_{N+1} = 0 \tag{L.6}$$

and

$$\big(f_{\mathbf{y}}(N+1), f_{\mathbf{y}}(N+2), f_{\mathbf{y}}(N+3)\big) = (C, B, A),\ (B, A, C) \text{ or } (A, C, B) \text{ if } x_{N+1} = 1. \tag{L.7}$$

Observe that $(N+1) + |\mathbf{y}|$ is even in the cases (L.5) and (L.6), and for those cases we have

$$\big(f_{\mathbf{y}}(N+2), f_{\mathbf{y}}(N+3)\big) = (B, C),\ (C, A) \text{ or } (A, B).$$

Similarly, $(N+1) + |\mathbf{y}|$ is odd in the cases (L.4) and (L.7), and in those cases we have

$$\big(f_{\mathbf{y}}(N+2), f_{\mathbf{y}}(n+3)\big) = (B, A),\ (A, C) \text{ or } (C, B).$$

This completes the proof by induction.

Now let $\mathbf{x} = x_1 x_2 \cdots x_N \in \mathbb{Z}_2^N$ as before, and let $\mathbf{X} = X_1 X_2 \cdots$ be its periodic extension with period N by defining $X_m = x_r$ where m is any integer, and r is the unique integer satisfying

$N|(m-r)$ and $1 \leq r \leq N$. Define $f_{\mathbf{X}} : \mathbb{Z}^+ \to \{A, B, C\}$ by $f_{\mathbf{X}}(1) = A$, $f_{\mathbf{X}}(2) = B$ and for $j \in \mathbb{Z}^+$ by

$$f_{\mathbf{X}}(j+2) = \begin{cases} f(j) & \text{if} \quad X_j = 0, \\ \{A, B, C\} \setminus \{f_{\mathbf{X}}(j), f_{\mathbf{X}}(j+1)\} & \text{if} \quad X_j = 1. \end{cases}$$

For example, if $\mathbf{x} = 00101 \in \mathbb{Z}_2^5$, then its periodic extension is $001010010100101 \cdots$ and

$$(f_{\mathbf{X}}(1), f_{\mathbf{X}}(2), f_{\mathbf{X}}(3), \ldots) = (A, B, A, B, C, B, A, B, A, C, A, B, \ldots).$$

The next result gives a necessary (but not sufficient) condition for $f_{\mathbf{X}}$ to be periodic with period N.

Theorem 2. Suppose $\mathbf{x} \in \mathbb{Z}_2^N$ and let $\mathbf{X}$ be its periodic extension. If $f_{\mathbf{X}}$ is periodic with period n, then $N + |\mathbf{x}|$ is even.

Proof. We prove the contrapositive. If $N + |\mathbf{x}|$ is odd, then by the second part of Theorem 1, $f_{\mathbf{X}}$ is not periodic with period N. This completes our proof.

In summary: For periodic Barlow packings with period N we have the condition that $N + |\mathbf{x}|$ is even.

Appendix M

Properties of the Lattice Sums L^A, L^{AA} and L^{AB}

We discuss some important properties of the lattice sums for the Barlow packing. For simplicity we set $s' = s/2$ and neglect the prime for the following. We remember that $r = (k_2 - k_1)/N \in \mathbb{Q}, 0 < r < 1$. Suppose $\gamma = N\gamma_0$ is a positive real number and let

$$L^{AA}(s, r, \gamma) = \sum_{i,j,k \in \mathbb{Z}} \left(i^2 + ij + j^2 + \gamma^2 (k + r)^2 \right)^{-s} \tag{M.1}$$

and

$$L^{AB}(s, r, \gamma) = \sum_{i,j,k \in \mathbb{Z}} \left((i + \tfrac{1}{3})^2 + (i + \tfrac{1}{3})(j + \tfrac{1}{3}) + (j + \tfrac{1}{3})^2 + \gamma^2 (k + r)^2 \right)^{-s} \tag{M.2}$$

In fact, the series for $L^{AA}(s, r, \gamma)$ is defined for all real values of r except integers. The series for $L^{AB}(s, r, \gamma)$ is defined for all real values of r. Both series converge for $s > 3/2$ and diverge for $s \leq 3/2$. The rapidly converging series that we will obtain in Appendix O will provide analytic continuations to other values of s. For large exponents s one can use direct summation and by exploiting the permutation symmetry between i_1 and i_2 in the equations above.

On replacing the summation index k with $k + 1$ it follows that

$$L^{AA}(s, r + 1, \gamma) = L^{AA}(s, r, \gamma) \quad \text{and} \quad L^{AB}(s, r + 1, \gamma) = L^{AB}(s, r, \gamma) \tag{M.3}$$

and so both functions are periodic in r with period 1.

By replacing k with $-k - 1$ in the series, it follows further that

$$L^{AA}(s, r, \gamma) = L^{AA}(s, 1 - r, \gamma) \quad \text{and} \quad L^{AB}(s, r, \gamma) = L^{AB}(s, 1 - r, \gamma). \tag{M.4}$$

Therefore, it is sufficient to study and evaluate $L^{AA}(s, r, \gamma)$ for $0 < r \leq 1/2$ and $L^{AB}(s, r, \gamma)$ for

$0 \leq r \leq 1/2$. In fact, for the case that $r \in \mathbb{Q}$ we only need the lattice sums for $r = 1/N, ..., m$ with $m = 1/2$ or $m = (N-1)/2N$ if N is even or odd. This saves considerable computer time as the lattice sums to be evaluated scale now linearly with N. This only holds if symmetry breaking due to the shifting of hexagonal layers along the c-axis is neglected where the number of lattice sums still scale like N^2 (see Eq.(10.39)).

The series $L^{AB}(s, r, \gamma)$ is well defined for $r = 0$ as the denominator is never zero. The series $L^{AA}(s, r, \gamma)$ is not defined for $r = 0$ because the term corresponding to $i = j = k = 0$ is undefined. We therefore subtract that term and consider the limiting function $L^A(s, \gamma)$ defined by

$$L^A(s,\gamma) = \lim_{r\to 0}\left(L^{AA}(s,r,\gamma) - \frac{1}{\gamma^{2s}r^{2s}}\right) = {\sum_{i,j,k\in\mathbb{Z}}}' \frac{1}{(i^2+ij+j^2+\gamma^2k^2)^s} \tag{M.5}$$

where the prime indicates that the term corresponding to $i = j = k = 0$ is omitted from the sum.

The following result will be required later in our analysis:

Lemma 1. Suppose N is an integer, $N \geq 2$ and $\gamma_0 = \frac{\gamma}{N}$. Then

$$\sum_{\ell=1}^{N-1} L^{AA}\left(s, \frac{\ell}{N}, \gamma\right) = L^A(s, \gamma_0) - L^A(s, \gamma) \tag{M.6}$$

and

$$\sum_{\ell=1}^{N-1} L^{AB}\left(s, \frac{\ell}{N}, \gamma\right) = L^{AB}(s, 0, \gamma_0) - L^{AB}(s, 0, \gamma). \tag{M.7}$$

Proof. By straightforward calculation we have

$$\begin{aligned}
\sum_{\ell=1}^{N-1} L^{AA}\left(s, \frac{\ell}{N}, \gamma\right) &= \sum_{\ell=1}^{N-1} \sum_{i,j,k\in\mathbb{Z}} \left(i^2+ij+j^2+\gamma^2(k+\tfrac{\ell}{N})^2\right)^{-s} \\
&= \sum_{i,j,k\in\mathbb{Z}} \sum_{\ell=1}^{N-1} \left(i^2+ij+j^2+\tfrac{\gamma^2}{N^2}(kN+\ell)^2\right)^{-s} \\
&= {\sum_{i,j,k\in\mathbb{Z}}}' \sum_{\ell=0}^{N-1} \left(i^2+ij+j^2+\gamma_0^2(kN+\ell)^2\right)^{-s} - {\sum_{i,j,k\in\mathbb{Z}}}' \left(i^2+ij+j^2+\gamma^2k^2\right)^{-s}
\end{aligned}$$

where the primes indicate that the terms corresponding to $i = j = k = \ell = 0$ and $i = j = k = 0$ in the respective sums are omitted. Now set $K = kN + \ell$ and observe that K takes each integer

value exactly once as k and ℓ range over their respective domains. It follows that

$$\begin{aligned}\sum_{\ell=1}^{N-1} L^{AA}\left(s, \frac{\ell}{N}, \gamma\right) &= {\sum_{i,j,K\in\mathbb{Z}}}' \left(i^2+ij+j^2+\gamma_0^2K^2\right)^{-s} - {\sum_{i,j,k\in\mathbb{Z}}}' \left(i^2+ij+j^2+\gamma^2k^2\right)^{-s} \\ &= L^A\left(s,\gamma_0\right) - L^A(s,\gamma).\end{aligned}$$

This proves the first result.
The proof of the second result is similar and easier because there are no primes as the term corresponding to $i = j = k = 0$ is not omitted. This finishes our proof.

We now analyse the limiting behaviour for $s \to \infty$, which is related to the kissing number of the packing. Therefore, we calculate the limits of $L^{AA}(s,r,\gamma)$, $L^{AB}(s,r,\gamma)$ and $L^A(s,\gamma)$ as $s \to \infty$. We start with the latter.

Lemma 2. The following limit holds:

$$\lim_{s\to\infty} L^A(s,\gamma) = \begin{cases} 6 & \text{if } \gamma > 1, \\ 8 & \text{if } \gamma = 1, \\ +\infty & \text{if } 0 < \gamma < 1. \end{cases} \tag{M.8}$$

Furthermore,

$$\lim_{s\to\infty} \gamma^{2s} L^A(s,\gamma) = 2 \quad \text{if } 0 < \gamma < 1. \tag{M.9}$$

Proof. If $|\gamma| \geq 1$ then

$$\min_{\substack{i,j,k\in\mathbb{Z} \\ (i,j,k)\neq(0,0,0)}} \left(i^2+ij+j^2+\gamma^2k^2\right) = 1$$

with the minimum occurring for

$$(i,j,k) \in \{(\pm1,0,0),(0,\pm1,0),(1,-1,0),(-1,1,0)\} \quad \text{if } \gamma > 1$$

and for

$$(i,j,k) \in \{(\pm1,0,0),(0,\pm1,0),(1,-1,0),(-1,1,0),(0,0,\pm1)\} \quad \text{if } \gamma = 1.$$

By counting the number of points in each set, it follows that $\lim_{s\to\infty} L^A(s,\gamma) = 6$ if $\gamma > 1$ and $\lim_{s\to\infty} L^A(s,\gamma) = 8$ if $\gamma = 1$.

If $0 < |\gamma| < 1$ then

$$\min_{\substack{i,j,k\in\mathbb{Z}\\(i,j,k)\neq(0,0,0)}} \left(i^2 + ij + j^2 + \gamma^2 k^2\right) = \gamma^2 < 1$$

with the minimum occurring for $(i, j, k) = (0, 0, \pm 1)$. It follows that
$\lim_{s\to\infty} L^A(s,\gamma) = +\infty$ and $\lim_{s\to\infty} \gamma^{2s} L^A(s,\gamma) = 2$.
This proves our lemma. Next we look at the corresponding limits for $L^{AA}(s, r, \gamma)$ and $L^{AB}(s, r, \gamma)$.

Lemma 3 Suppose $\gamma > 0$. Then

$$\lim_{s\to\infty} \gamma^{2s} r^{2s} L^{AA}(s,r,\gamma) = \begin{cases} 1 & \text{if } 0 < r < 1/2, \\ 2 & \text{if } r = 1/2, \end{cases} \tag{M.10}$$

and

$$\lim_{s\to\infty} \left(\frac{1}{3} + \gamma^2 r^2\right)^s L^{AB}(s,r,\gamma) = \begin{cases} 3 & \text{if } 0 < r < 1/2, \\ 6 & \text{if } r = 1/2. \end{cases} \tag{M.11}$$

Hence,

$$\lim_{s\to\infty} L^{AA}(s,r,\gamma) = \begin{cases} 0 & \text{if } \gamma > \frac{1}{r}, \\ 1 & \text{if } \gamma = \frac{1}{r} \text{ and } 0 < r < 1/2, \\ 2 & \text{if } \gamma = \frac{1}{r} \text{ and } r = 1/2, \\ +\infty & \text{if } 0 < \gamma < \frac{1}{r}. \end{cases} \tag{M.12}$$

and

$$\lim_{s\to\infty} L^{AB}(s,r,\gamma) = \begin{cases} 0 & \text{if } \gamma > \frac{1}{r}\sqrt{\frac{2}{3}}, \\ 3 & \text{if } \gamma = \frac{1}{r}\sqrt{\frac{2}{3}} \text{ and } 0 < r < 1/2, \\ 6 & \text{if } \gamma = \frac{1}{r}\sqrt{\frac{2}{3}} \text{ and } r = 1/2, \\ +\infty & \text{if } 0 < \gamma < \frac{1}{r}\sqrt{\frac{2}{3}}. \end{cases} \tag{M.13}$$

Proof. Since $0 < r \leq 1/2$, it follows that

$$\min_{i,j,k\in\mathbb{Z}} \left(i^2 + ij + j^2 + \gamma^2 (k + r)^2\right) = \gamma^2 r^2$$

and this minimum occurs only for $(i, j, k) = (0, 0, 0)$ if $0 < r < 1/2$, and additionally at $(i, j, k) = (0, 0, -1)$ if $r = 1/2$. This accounts for the limits of 1 and 2 in the result for $L^{AA}(s, r, \gamma)$.

Next, we have

$$\min_{i,j,k\in\mathbb{Z}} \left((i+\tfrac{1}{3})^2 + (i+\tfrac{1}{3})(j+\tfrac{1}{3}) + (j+\tfrac{1}{3})^2 + \gamma^2(k+r)^2 \right) = \frac{1}{3} + \gamma^2 r^2$$

and this minimum occurs for

$$(i,j,k) = (0,0,0),\ (-1,0,0),\ (0,-1,0)$$

if $0 < r < 1/2$, and additionally at

$$(i,j,k) = (0,0,-1),\ (-1,0,-1),\ (0,-1,-1)$$

if $r = 1/2$. This accounts for the limits 3 and 6 for the function $L^{AB}(s,r,\gamma)$. This proves our lemma.

Appendix N

Properties of Barlow Lattice Sums

The lattice sum for the periodic Barlow packing $\mathbf{X} = (X_1 X_2 \dots X_N)_\infty$ is given by

$$L^{\mathbf{X}}(s) = L^{A}(s,\gamma) + \frac{1}{N}\sum_{i=1}^{N}\sum_{\ell=1}^{N-1} L^{X_i X_{i+\ell}}(s,\gamma) \tag{N.1}$$

where $\gamma = N\gamma_0$ and $\gamma_0 = \sqrt{2/3}$ for the densest packing, and

$$L^{X_i X_{i+\ell}}(s,\gamma) = \begin{cases} L^{AA}\left(s, \frac{\ell}{N}, \gamma\right) & \text{if } X_i = X_{i+\ell}, \\ L^{AB}\left(s, \frac{\ell}{N}, \gamma\right) & \text{if } X_i \neq X_{i+\ell}, \end{cases} \tag{N.2}$$

or equivalently

$$L^{X_i X_j}(s,\gamma) = \begin{cases} L^{AA}\left(s, \frac{j-i}{N}, \gamma\right) & \text{if } X_i = X_j, \\ L^{AB}\left(s, \frac{j-i}{N}, \gamma\right) & \text{if } X_i \neq X_j. \end{cases} \tag{N.3}$$

By separating the terms in (N.1) into the two cases $1 \le \ell \le N-i$ and $N+1-i \le \ell \le N$, we deduce

$$\sum_{i=1}^{N}\sum_{\ell=1}^{N-1} L^{X_i X_{i+\ell}}(s,\gamma) = \sum_{i=1}^{N}\sum_{\ell=1}^{N-i} L^{X_i X_{i+\ell}}(s,\gamma) + \sum_{i=1}^{N}\sum_{\ell=N+1-i}^{N-1} L^{X_i X_{i+\ell}}(s,\gamma). \tag{N.4}$$

Put $j = i+\ell$ in the first double sum on the right, and put $j = i+\ell-N$ in the second double sum, to deduce

$$\begin{aligned} \sum_{i=1}^{N}\sum_{\ell=1}^{N-1} L^{X_i X_{i+\ell}}(s,\gamma) &= \sum_{i=1}^{N-1}\sum_{j=i+1}^{N} L^{X_i X_j}(s,\gamma) + \sum_{i=2}^{N}\sum_{j=1}^{i-1} L^{X_i X_{j+N}}(s,\gamma) \\ &= \sum_{1\le i<j\le N} L^{X_i X_j}(s,\gamma) + \sum_{1\le j<i\le N} L^{X_i X_j}(s,\gamma) = 2\sum_{1\le i<j\le N} L^{X_i X_j}(s,\gamma), \end{aligned} \tag{N.5}$$

where the properties $L^{X_iX_{j+N}}(s,\gamma) = L^{X_iX_j}(s,\gamma)$ and $L^{X_iX_j}(s,\gamma) = L^{X_jX_i}(s,\gamma)$ have been used in the last two steps. Using (N.5) back in (N.1) gives

$$L^{\mathbf{X}}(s) = L^A(s,\gamma) + \frac{2}{N}\sum_{1\le i<j\le N} L^{X_iX_j}(s,\gamma) \tag{N.6}$$

and this is the form given earlier in (10.40). Interchanging the order of summation in (N.1) gives

$$\begin{aligned} L^{\mathbf{X}}(s) &= L^A(s,\gamma) + \frac{1}{N}\sum_{\ell=1}^{N-1}\sum_{i=1}^{N} L^{X_iX_{i+\ell}}(s,\gamma) \qquad (N.7)\\ &= L^A(s,\gamma) + \frac{1}{N}\sum_{\ell=1}^{N-1}\sum_{i=1}^{N} p(i,\ell)L^{AA}\left(s,\tfrac{\ell}{N},\gamma\right) + \frac{1}{N}\sum_{\ell=1}^{N-1}\sum_{i=1}^{N}(1-p(i,\ell))L^{AB}\left(s,\tfrac{\ell}{N},\gamma\right)\\ &= L^A(s,\gamma) + \sum_{\ell=1}^{N-1}\delta(\ell)L^{AA}\left(s,\tfrac{\ell}{N},\gamma\right) + \sum_{\ell=1}^{N-1}(1-\delta(\ell))L^{AB}\left(s,\tfrac{\ell}{N},\gamma\right). \end{aligned}$$

Now apply (M.7) to deduce

$$L^{\mathbf{X}}(s) = L^{AB}(s,0,\gamma_0) + \left\{L^A(s,\gamma) - L^{AB}(s,0,\gamma)\right\} + \sum_{\ell=1}^{N-1}\delta(\ell)\left\{L^{AA}\left(s,\tfrac{\ell}{N},\gamma\right) - L^{AB}\left(s,\tfrac{\ell}{N},\gamma\right)\right\}. \tag{N.8}$$

Since $\delta(1) = \delta(N-1) = 0$ and $\delta(\ell) = \delta(N-\ell)$ for $2 \le \ell \le N-2$, we can use the relations in (M.4) to finally write

$$L^{\mathbf{X}}(s) = L^{AB}(s,0,\gamma_0) + \left\{L^A(s,\gamma) - L^{AB}(s,0,\gamma)\right\} + \sum_{\ell=2}^{N-2}\delta(\ell)\left\{L^{AA}\left(s,\tfrac{\ell}{N},\gamma\right) - L^{AB}\left(s,\tfrac{\ell}{N},\gamma\right)\right\} \tag{N.9}$$

or

$$\begin{aligned} L^{\mathbf{X}}(s) &= L^{AB}(s,0,\gamma_0) + \left\{L^A(s,\gamma) - L^{AB}(s,0,\gamma)\right\}\\ &\quad + 2\sum_{2\le\ell\le(N-1)/2}\delta(\ell)\left\{L^{AA}\left(s,\tfrac{\ell}{N},\gamma\right) - L^{AB}\left(s,\tfrac{\ell}{N},\gamma\right)\right\}\\ &\quad + \delta(\tfrac{N}{2})\left\{L^{AA}\left(s,\tfrac{1}{2},\gamma\right) - L^{AB}\left(s,\tfrac{1}{2},\gamma\right)\right\} \end{aligned} \tag{N.10}$$

where $\delta(\frac{N}{2})$ is defined to be zero if N is odd.

Assume $N \ge 4$. The observed phenomena about the lattice sum for a Barlow structure lying between the hcp and fcc sums in proportion given by $\delta(2)$ would follow immediately from

(N.9) (or equivalently (N.10)) whenever the dominant term of the functions

$$L^{AA}\left(s, \tfrac{\ell}{N}, \gamma\right) - L^{AB}\left(s, \tfrac{\ell}{N}, \gamma\right), \quad 2 \leq \ell \leq \tfrac{N}{2}$$

is the term corresponding to $\ell = 2$. Numerical evidence appears to back this up, and this needs to be investigated further to determine the precise conditions when $\ell = 2$ gives the dominant term.

Example: Consider the hexagonal close packing, face-centred cubic, and 9R structures. For simplicity we use $\gamma_N = N\gamma_0$. Then (N.10) gives

$$L^{(AB)}(s) = L^{AB}(s, 0, \gamma_1) + \left\{L^{A}(s, \gamma_2) - L^{AB}(s, 0, \gamma_2)\right\}, \tag{N.11}$$

$$L^{(ABC)}(s) = L^{AB}(s, 0, \gamma_1) + \left\{L^{A}(s, \gamma_3) - L^{AB}(s, 0, \gamma_3)\right\}, \tag{N.12}$$

$$\begin{aligned} L^{(ABCBCACAB)}(s) = {} & L^{AB}(s, 0, \gamma_1) + \left\{L^{A}(s, \gamma_9) - L^{AB}(s, 0, \gamma_9)\right\} \\ & + \tfrac{4}{3}\left\{L^{AA}(s, \tfrac{2}{9}, \gamma_9) - L^{AB}(s, \tfrac{2}{9}, \gamma_9)\right\} + 0\left\{L^{AA}(s, \tfrac{1}{3}, \gamma_9) - L^{AB}(s, \tfrac{1}{3}, \gamma_9)\right\} \\ & + \tfrac{2}{3}\left\{L^{AA}(s, \tfrac{4}{9}, \gamma_9) - L^{AB}(s, \tfrac{4}{9}, \gamma_9)\right\}. \end{aligned} \tag{N.13}$$

In order to compare the sums, let N be the least common multiple of the periods 2 (hcp), 3 (fcc) and 9 (9R) so that

$$N = \operatorname{lcm}(2, 3, 9) = 18.$$

Extend each structure to the common period $N = 18$ and use (N.10) to deduce

$$\begin{aligned} L^{(AB)}(s) = {} & L^{AB}(s, 0, \gamma_1) + \left\{L^{A}(s, \gamma_{18}) - L^{AB}(s, 0, \gamma_{18})\right\} \\ & + 2\left\{L^{AA}(s, \tfrac{2}{18}, \gamma_{18}) - L^{AB}(s, \tfrac{2}{18}, \gamma_{18})\right\} + 2\left\{L^{AA}(s, \tfrac{4}{18}, \gamma_{18}) - L^{AB}(s, \tfrac{4}{18}, \gamma_{18})\right\} \\ & + 2\left\{L^{AA}(s, \tfrac{6}{18}, \gamma_{18}) - L^{AB}(s, \tfrac{6}{18}, \gamma_{18})\right\} + 2\left\{L^{AA}(s, \tfrac{8}{18}, \gamma_{18}) - L^{AB}(s, \tfrac{8}{18}, \gamma_{18})\right\}, \end{aligned} \tag{N.14}$$

$$\begin{aligned} L^{(ABC)}(s) = {} & L^{AB}(s, 0, \gamma_1) + \left\{L^{A}(s, \gamma_{18}) - L^{AB}(s, 0, \gamma_{18})\right\} \\ & + 2\left\{L^{AA}(s, \tfrac{3}{18}, \gamma_{18}) - L^{AB}(s, \tfrac{3}{18}, \gamma_{18})\right\} + 2\left\{L^{AA}(s, \tfrac{6}{18}, \gamma_{18}) - L^{AB}(s, \tfrac{6}{18}, \gamma_{18})\right\} \\ & + \quad \left\{L^{AA}(s, \tfrac{9}{18}, \gamma_{18}) - L^{AB}(s, \tfrac{9}{18}, \gamma_{18})\right\}, \end{aligned} \tag{N.15}$$

Table N.1: Values of $L^{AA}(s, \frac{\ell}{18}, \gamma_{18}) - L^{AB}(s, \frac{\ell}{18}, \gamma_{18})$ for various values of s, for the 9R packing $(ABCBCACAB)$.

ℓ	$s = 3$	$s = 6$
2	4.8858×10^{-4}	2.0683×10^{-4}
3	4.5147×10^{-7}	4.3276×10^{-8}
4	5.7369×10^{-10}	2.0192×10^{-11}
5	8.6516×10^{-13}	1.4325×10^{-14}
6	1.4521×10^{-15}	1.3144×10^{-17}
7	2.6228×10^{-18}	1.4350×10^{-20}
8	4.9967×10^{-21}	1.7758×10^{-23}
9	1.9828×10^{-23}	1.6104×10^{-26}

$$
\begin{aligned}
L^{(ABCBCACAB)}(s) = L^{AB}(s,0,\gamma_1) + \left\{L^{A}(s,\gamma_{18}) - L^{AB}(s,0,\gamma_{18})\right\} \\
+ \tfrac{4}{3}\left\{L^{AA}(s,\tfrac{2}{18},\gamma_{18}) - L^{AB}(s,\tfrac{2}{18},\gamma_{18})\right\} + \tfrac{2}{3}\left\{L^{AA}(s,\tfrac{4}{18},\gamma_{18}) - L^{AB}(s,\tfrac{4}{18},\gamma_{18})\right\} \\
+ \tfrac{2}{3}\left\{L^{AA}(s,\tfrac{5}{18},\gamma_{18}) - L^{AB}(s,\tfrac{5}{18},\gamma_{18})\right\} + \tfrac{4}{3}\left\{L^{AA}(s,\tfrac{7}{18},\gamma_{18}) - L^{AB}(s,\tfrac{7}{18},\gamma_{18})\right\} \\
+ \quad \left\{L^{AA}(s,\tfrac{9}{18},\gamma_{18}) - L^{AB}(s,\tfrac{9}{18},\gamma_{18})\right\}.
\end{aligned}
\tag{N.16}
$$

The values in (N.14), (N.15) and (N.16) are exactly equal to the values in (N.11), (N.12) and (N.13), respectively, by Lemma 1. If the dominant term of the functions $L^{AA}(s, \frac{\ell}{18}, \gamma_{18}) - L^{AB}(s, \frac{\ell}{18}, \gamma_{18})$, $2 \leq \ell \leq 9$, is the one corresponding to $\ell = 2$, then we deduce the approximations

$$
\begin{aligned}
L^{(AB)}(s) \approx L^{AB}(s,0,\gamma_1) + \left\{L^{A}(s,\gamma_{18}) - L^{AB}(s,0,\gamma_{18})\right\} \\
+ 2\left\{L^{AA}(s,\tfrac{2}{18},\gamma_{18}) - L^{AB}(s,\tfrac{2}{18},\gamma_{18})\right\},
\end{aligned}
$$

$$
L^{(ABC)}(s) \approx L^{AB}(s,0,\gamma_1) + \left\{L^{A}(s,\gamma_{18}) - L^{AB}(s,0,\gamma_{18})\right\},
$$

$$
\begin{aligned}
L^{(ABCBCACAB)}(s) \approx L^{AB}(s,0,\gamma_1) + \left\{L^{A}(s,\gamma_{18}) - L^{AB}(s,0,\gamma_{18})\right\} \\
+ \tfrac{4}{3}\left\{L^{AA}(s,\tfrac{2}{18},\gamma_{18}) - L^{AB}(s,\tfrac{2}{18},\gamma_{18})\right\}
\end{aligned}
$$

and hence we obtain

$$
L^{(ABCBCACAB)}(s) \approx \delta(2)L^{(AB)}(s) + (1-\delta(2))L^{(ABC)}(s)
$$

where $\delta(2) = 2/3$ is the second packing fraction for the structure $ABCBCACAB$ calculated in Table 10.1 and defined in Eq. (10.6). Some data to support the claim about the dominant term is in Table N.1.

Appendix O

Rapidly Converging Series of the Lattice Sums for Barlow Packings

The lattice sum L^A

The formulas presented in the following will provide analytic continuations to any complex value of the exponent s. We start with the lattice sum for the quadratic form (10.34) which has been derived before using a Mellin transformation and Jacobi theta functions[294],

$$L^A(\gamma,s) = 6\zeta(s)\,L_{-3}(s) + \frac{4\pi}{\sqrt{3}(s-1)}\gamma^{2-2s}\zeta(2s-2) + \frac{4}{\sqrt{3}}\frac{(2\pi)^s}{\Gamma(s)}\sum_{k,n\in\mathbb{N}} u_2(n)\left(\frac{n}{3\gamma^2k^2}\right)^{(s-1)/2} K_{s-1}\left(\frac{4\pi}{\sqrt{3}}\gamma k\sqrt{n}\right) \tag{O.1}$$

$u_2(n)$ is the number of representations of n by the form i^2+ij+j^2. $\zeta(s)$ is the Riemann zeta function, $\Gamma(s)$ is the gamma function and $K_s(x)$ the modified Bessel function of the second kind. They are defined in Appendix A including the Dirichlet $L_{-3}(s)$ function. This expansion is suitable for larger values of γ because of the asymptotic behavior of the Bessel function, $K_s(z) \sim z^{-1/2}e^{-z}$, and the pole at $z=0$. This is especially important as $\gamma = c/a$ grows with increasing period N. In fact, for very large cells (large γ values) the Bessel sum can be neglected.

A second form of this lattice sum is given by

$$L^A(\gamma,s) = 2\gamma^{-2s}\zeta(2s) + 6\sqrt{\pi}\gamma^{-1}\,\frac{\Gamma(s-\frac{1}{2})}{\Gamma(s)}\,\zeta(s-\tfrac{1}{2})L_{-3}(s-\tfrac{1}{2}) + \frac{4\pi^s}{\Gamma(s)}\,\gamma^{-(2s+1)/2}\sum_{k,n\in\mathbb{N}} u_2(n)\,\left(\frac{k^2}{n}\right)^{(2s-1)/4} K_{s-\frac{1}{2}}\left(\frac{2\pi k}{\gamma}\sqrt{n}\right). \tag{O.2}$$

Similarly, Eq. (O.2) is numerically more stable for smaller values of γ. We will find two rapidly

converging series for both $L^{AA}(s,r,\gamma)$ and $L^{AB}(s,r,\gamma)$. It is important to have two formulas so they can be checked against each other.

The first formula for L^{AA}

Applying the gamma function integral in the form

$$w^{-s} = \frac{1}{\Gamma(s)} \int_{[0,\infty)} x^{s-1} e^{-wx} \mathrm{d}x \tag{O.3}$$

gives

$$(2\pi)^{-s}\Gamma(s)L^{AA}(s,r,\gamma) = \int_{[0,\infty)} x^{s-1} \sum_{k\in\mathbb{Z}} e^{-2\pi\gamma^2(k+r)^2 x} \sum_{i,j\in\mathbb{Z}} e^{-2\pi(i^2+ij+j^2)x}\, \mathrm{d}x. \tag{O.4}$$

Now apply the transformation formula for the theta functions to the double sum to deduce

$$\begin{aligned}(2\pi)^{-s}\Gamma(s)L^{AA}(s,r,\gamma) &= \frac{1}{\sqrt{3}} \int_{[0,\infty)} x^{s-2} \sum_{k\in\mathbb{Z}} e^{-2\pi\gamma^2(k+r)^2 x} \sum_{i,j\in\mathbb{Z}} e^{-2\pi(i^2+ij+j^2)/3x}\, \mathrm{d}x \qquad \text{(O.5)}\\ &= \frac{1}{\sqrt{3}} \sum_{k\in\mathbb{Z}} \int_{[0,\infty)} x^{s-2} e^{-2\pi\gamma^2(k+r)^2 x}\, \mathrm{d}x + \frac{1}{\sqrt{3}} \sum_{k\in\mathbb{Z}} {\sum_{i,j\in\mathbb{Z}}}' \int_{[0,\infty)} x^{s-2} e^{-2\pi\gamma^2(k+r)^2 x - 2\pi(i^2+ij+j^2)/3x}\, \mathrm{d}x,\end{aligned}$$

where the prime means that the terms corresponding to $i = j = 0$ are omitted from the summation. The first integral may be evaluated in terms of the gamma function, while the second integral can be evaluated in terms of the K-Bessel function by means of the formula

$$\int_{[0,\infty)} x^{s-1} e^{-ax-b/x} \mathrm{d}x = 2\left(\frac{b}{a}\right)^{s/2} K_s(2\sqrt{ab}). \tag{O.6}$$

Hence we obtain

$$\begin{aligned}(2\pi)^{-s}\Gamma(s)L^{AA}(s,r,\gamma) &= \frac{\Gamma(s-1)}{\sqrt{3}(2\pi\gamma^2)^{s-1}} \sum_{k\in\mathbb{Z}} \frac{1}{|k+r|^{2s-2}} \qquad \text{(O.7)}\\ &+ \frac{2}{\sqrt{3}} \sum_{k\in\mathbb{Z}} {\sum_{i,j\in\mathbb{Z}}}' \left(\frac{i^2+ij+j^2}{3\gamma^2(k+r)^2}\right)^{(s-1)/2} K_{s-1}\left(\frac{4\pi}{\sqrt{3}}\gamma|k+r|\sqrt{i^2+ij+j^2}\right).\end{aligned}$$

This can be rewritten as

$$L^{AA}(s,r,\gamma) = \frac{2\pi\gamma^{2-2s}}{\sqrt{3}(s-1)} \sum_{k\in\mathbb{Z}} \frac{1}{|k+r|^{2s-2}} + \frac{2(2\pi)^s}{\sqrt{3}\Gamma(s)} \sum_{k\in\mathbb{Z}} \sum_{n\in\mathbb{N}} u_2(n) \left(\frac{n}{3\gamma^2(k+r)^2}\right)^{(s-1)/2} K_{s-1}\left(\frac{4\pi\gamma}{\sqrt{3}}|k+r|\sqrt{n}\right) \tag{O.8}$$

where $u_2(n)$ is the number of representations of N by the form i^2+ij+j^2. The sums over k can be separated into the non-negative and negative cases to give, for $0<r<1$,

$$\begin{aligned} L^{AA}(s,r,\gamma) &= \frac{2\pi\gamma^{2-2s}}{\sqrt{3}(s-1)} \left(\zeta(2s-2,r)+\zeta(2s-2,1-r)\right) \\ &+ \frac{2\gamma^{1-s}}{\Gamma(s)} \left(\frac{2\pi}{\sqrt{3}}\right)^s \sum_{n\in\mathbb{N}} n^{(s-1)/2} u_2(n) \sum_{k\in\mathbb{N}_0} (k+r)^{1-s} K_{s-1}\left(\frac{4\pi\gamma}{\sqrt{3}}(k+r)\sqrt{n}\right) \\ &+ \frac{2\gamma^{1-s}}{\Gamma(s)} \left(\frac{2\pi}{\sqrt{3}}\right)^s \sum_{n\in\mathbb{N}} n^{(s-1)/2} u_2(n) \sum_{k\in\mathbb{N}_0} (k+1-r)^{1-s} K_{s-1}\left(\frac{4\pi\gamma}{\sqrt{3}}(k+1-r)\sqrt{n}\right), \end{aligned} \tag{O.9}$$

where $\mathbb{N}_0$ are the positive integers including the zero, and $\zeta(s,r)$ is the Hurwitz zeta function and $\zeta(s)$ the Riemann zeta function defined in Appendix A. The formula shows the symmetry that $L^{AA}(s,r,\gamma) = L^{AA}(s,1-r,\gamma)$.

A second formula for L^{AA}

First separate out the terms corresponding to $i=j=0$ to write

$$\begin{aligned} L^{AA}(s,r,\gamma) &= \gamma^{-2s} \sum_{k\in\mathbb{Z}} \frac{1}{|k+r|^{2s}} + {\sum_{i,j\in\mathbb{Z}}}' \sum_{k\in\mathbb{Z}} \left(i^2+ij+j^2+\gamma^2(k+r)^2\right)^{-s} \\ &= \gamma^{-2s}\left(\zeta(2s,r)+\zeta(2s,1-r)\right) + {\sum_{i,j\in\mathbb{Z}}}' \sum_{k\in\mathbb{Z}} \left(i^2+ij+j^2+\gamma^2(k+r)^2\right)^{-s}. \end{aligned} \tag{O.10}$$

Once again we use the integral for the gamma function to write

$${\sum_{i,j\in\mathbb{Z}}}' \sum_{k=\in\mathbb{Z}} \left(i^2+ij+j^2+\gamma^2(k+r)^2\right)^{-s} = \frac{\pi^s}{\Gamma(s)} \int_{[0,\infty)} x^{s-1} {\sum_{i,j\in\mathbb{Z}}}' e^{-\pi(i^2+ij+j^2)x} \sum_{k\in\mathbb{Z}} e^{-\pi\gamma^2(k+r)^2 x}\,\mathrm{d}x. \tag{O.11}$$

Now apply the transformation formula for the theta functions to the sum over k to deduce

$$\begin{aligned}\sum_{i,j\in\mathbb{Z}}{}' \sum_{k\in\mathbb{Z}} \left(i^2+ij+j^2+\gamma^2(k+r)^2\right)^{-s} &= \frac{\pi^s}{\gamma\,\Gamma(s)} \int_{[0,\infty)} x^{s-\frac{3}{2}} \sum_{i,j\in\mathbb{Z}}{}' e^{-\pi(i^2+ij+j^2)x} \sum_{k\in\mathbb{Z}} e^{-\pi k^2/\gamma^2 x+2\pi ikr}\,\mathrm{d}x \\ &= \frac{\pi^s}{\gamma\,\Gamma(s)} \int_{[0,\infty)} x^{s-\frac{3}{2}} \sum_{i,j\in\mathbb{Z}}{}' e^{-\pi(i^2+ij+j^2)x} \left(1+2\sum_{k\in\mathbb{N}} e^{-\pi k^2/\gamma^2 x}\cos(2\pi kr)\right)\mathrm{d}x \\ &= \frac{\pi^s}{\gamma\,\Gamma(s)} \int_{[0,\infty)} x^{s-\frac{3}{2}} \sum_{i,j\in\mathbb{Z}}{}' e^{-\pi(i^2+ij+j^2)x}\,\mathrm{d}x \qquad\qquad (O.12) \\ &+ \frac{2\pi^s}{\gamma\,\Gamma(s)} \int_{[0,\infty)} x^{s-\frac{3}{2}} \sum_{n\in\mathbb{N}} u_2(n) e^{-\pi nx} \sum_{k\in\mathbb{N}} e^{-\pi k^2/\gamma^2 x}\cos(2\pi kr)\,\mathrm{d}x\end{aligned}$$

where $u_2(n)$ is as before. On evaluating the integrals, we obtain

$$\begin{aligned}\sum_{i,j\in\mathbb{Z}}{}' \sum_{k=\in\mathbb{Z}} \left(i^2+ij+j^2+\gamma^2(k+r)^2\right)^{-s} &= \frac{\sqrt{\pi}\,\Gamma(s-\frac{1}{2})}{\gamma\,\Gamma(s)} \sum_{i,j\in\mathbb{Z}}{}' \frac{1}{(i^2+ij+j^2)^{s-\frac{1}{2}}} \\ &+ \frac{4\pi^s}{\gamma\,\Gamma(s)} \sum_{k,n\in\mathbb{N}} u_2(n)\cos(2\pi kr) \left(\frac{k}{\gamma\sqrt{n}}\right)^{s-\frac{1}{2}} K_{s-\frac{1}{2}}\left(\frac{2\pi k\sqrt{n}}{\gamma}\right). \qquad (O.13)\end{aligned}$$

This simplifies further, using the result[385,606]

$$\sum_{i,j\in\mathbb{Z}}{}' \left(i^2+ij+j^2\right)^{-s} = 2\times 3^{1-s}\,\zeta(s)\left(\zeta(s,\tfrac{1}{3})-\zeta(s,\tfrac{2}{3})\right). \qquad (O.14)$$

Hence we finally obtain, for $0<r<1$,

$$\begin{aligned}L^{AA}(s,r,\gamma) &= \gamma^{-2s}\left(\zeta(2s,r)+\zeta(2s,1-r)\right) + \frac{2\sqrt{\pi}}{3^{s-\frac{3}{2}}\gamma}\frac{\Gamma(s-\frac{1}{2})}{\Gamma(s)}\,\zeta(s-\tfrac{1}{2})\,\left(\zeta(s-\tfrac{1}{2},\tfrac{1}{3})-\zeta(s-\tfrac{1}{2},\tfrac{2}{3})\right) \\ &+ \frac{4\pi^s}{\gamma^{s+\frac{1}{2}}\Gamma(s)} \sum_{k\in\mathbb{N}} k^{s-\frac{1}{2}}\cos(2\pi kr) \sum_{n\in\mathbb{N}} \frac{u_2(n)}{n^{(2s-1)/4}} K_{s-\frac{1}{2}}\left(\frac{2\pi k\sqrt{n}}{\gamma}\right). \qquad (O.15)\end{aligned}$$

The first formula for L^{AB}

We again apply the gamma function integral to write

$$L^{AB}(s,r,\gamma) = \frac{(2\pi)^s}{\Gamma(s)} \int_0^\infty x^{s-1} \sum_{k\in\mathbb{Z}} e^{-2\pi\gamma^2(k+r)^2 x} \sum_{i,j\in\mathbb{Z}} e^{-2\pi\{(i+\frac{1}{3})^2+(i+\frac{1}{3})(j+\frac{1}{3})+(j+\frac{1}{3})^2\}x}\,\mathrm{d}x\,. \quad (O.16)$$

Next, apply the transformation formula for theta functions to the double sum to deduce

$$L^{AB}(s,r,\gamma) = \frac{(2\pi)^s}{\sqrt{3}\,\Gamma(s)} \int_{[0,\infty)} x^{s-2} \sum_{k\in\mathbb{Z}} e^{-2\pi\gamma^2(k+r)^2 x} \sum_{i,j\in\mathbb{Z}} \omega^{i-j} e^{-2\pi(i^2+ij+j^2)/3x}\,\mathrm{d}x \tag{O.17}$$

where $\omega = \exp(2\pi i/3)$ is a primitive cube root of 1. Now separate the term $i = j = 0$ to deduce

$$\begin{aligned} L^{AB}(s,r,\gamma) &= \frac{(2\pi)^s}{\sqrt{3}\,\Gamma(s)} \int_{[0,\infty)} x^{s-2} \sum_{k\in\mathbb{Z}} e^{-2\pi\gamma^2(k+r)^2 x}\,\mathrm{d}x \\ &\quad + \frac{(2\pi)^s}{\sqrt{3}\,\Gamma(s)} \int_{[0,\infty)} x^{s-2} \sum_{k\in\mathbb{Z}} e^{-2\pi\gamma^2(k+r)^2 x} \sum_{n\in\mathbb{N}} \cos\left(\tfrac{2\pi n}{3}\right) u_2(n)\, e^{-2\pi n/3x}\,\mathrm{d}x \end{aligned} \tag{O.18}$$

where $u_2(n)$ is as before. Here we used Euler's formula, $e^{i\theta} = \cos\theta + i\sin\theta$ and retain only the real part as $L^{AB}(s,r,\gamma)$ is real when s is real. On evaluating the integrals we obtain

$$\begin{aligned} L^{AB}(s,r,\gamma) &= \frac{2\pi}{\sqrt{3}(s-1)}\gamma^{-2s+2} \sum_{k\in\mathbb{Z}} \frac{1}{(k+r)^{2s-2}} \\ &\quad + \frac{2}{\sqrt{3}} \frac{(2\pi)^s}{\Gamma(s)} \sum_{k\in\mathbb{Z}} \sum_{n\in\mathbb{N}} \cos\left(\tfrac{2\pi n}{3}\right) u_2(n) \left(\tfrac{n}{3\gamma^2(k+r)^2}\right)^{(s-1)/2} K_{s-1}\left(\tfrac{4\pi}{\sqrt{3}}\gamma|k+r|\sqrt{n}\right). \end{aligned} \tag{O.19}$$

On separating the sum over k into non-negative and negative cases, we deduce

$$\begin{aligned} L^{AB}(s,r,\gamma) &= \frac{2\pi\gamma^{-2s+2}}{\sqrt{3}(s-1)} \left(\zeta(2s-2,r) + \zeta(2s-2,1-r)\right) \\ &\quad + \frac{2\gamma^{1-s}}{\Gamma(s)} \left(\frac{2\pi}{\sqrt{3}}\right)^s \sum_{n\in\mathbb{N}} n^{(s-1)/2} u_2(n) \cos\left(\tfrac{2\pi n}{3}\right) \sum_{k\in\mathbb{N}_0} \frac{1}{(k+r)^{s-1}} K_{s-1}\left(\tfrac{4\pi}{\sqrt{3}}\gamma\,(k+r)\,\sqrt{n}\right) \\ &\quad + \frac{2\gamma^{1-s}}{\Gamma(s)} \left(\frac{2\pi}{\sqrt{3}}\right)^s \sum_{n\in\mathbb{N}} n^{(s-1)/2} u_2(n) \cos\left(\tfrac{2\pi n}{3}\right) \sum_{k\in\mathbb{N}_0} \frac{1}{(k+1-r)^{s-1}} K_{s-1}\left(\tfrac{4\pi}{\sqrt{3}}\gamma\,(k+1-r)\,\sqrt{n}\right). \end{aligned} \tag{O.20}$$

Note that (O.20) is identical to (O.10) apart from the cosine term. This formula does not hold when $r = 0$ due to the $\zeta(2s-2,0)$ Hurwitz zeta function and also the term $k = 0$ in the first sum involving Bessel functions. We could take a limit, but it is easier to use the second formula for $L^{AB}(s,r,\gamma)$, which we shall derive next. Again, the formula shows the symmetry that $L^{AB}(s,r,\gamma) = L^{AB}(s,1-r,\gamma)$.

A second formula for L^{AB}

We introduce the abbreviation

$$Y_{ij} = \left(i+\tfrac{1}{3}\right)^2 + \left(i+\tfrac{1}{3}\right)\left(j+\tfrac{1}{3}\right) + \left(j+\tfrac{1}{3}\right)^2 \tag{O.21}$$

to write (O.16) in the form

$$L^{AB}(s,r,\gamma)(s) = \frac{(2\pi)^s}{\Gamma(s)} \int_{[0,\infty)} x^{s-1} \sum_{i,j\in\mathbb{Z}} e^{-2\pi Y_{ij} x} \sum_{k\in\mathbb{Z}} e^{-2\pi\gamma^2(k+r)^2 x}\, \mathrm{d}x\ . \tag{O.22}$$

Apply the transformation formula for theta functions to the sum over k to obtain

$$L^{AB}(s,r,\gamma)(s) = \frac{(2\pi)^s}{\gamma\sqrt{2}\,\Gamma(s)} \int_{[0,\infty)} x^{s-3/2} \sum_{i,j\in\mathbb{Z}} e^{-2\pi Y_{ij} x} \sum_{k\in\mathbb{Z}} e^{-\pi k^2/(2\gamma^2 x)} \cos(2\pi k r)\, \mathrm{d}x\ . \tag{O.23}$$

This is the same as the equation (42) in our previous paper[294] except that we now have $\cos(2\pi kr)$ in place of $(-1)^k$. Proceeding as we did in that paper and with this modification, we obtain

$$\begin{aligned} L^{AB}(s,r,\gamma)(s) &= \frac{3\sqrt{\pi}\,\Gamma(s-\frac{1}{2})}{\gamma\,\Gamma(s)} \left(1-3^{-(s-1/2)}\right) \zeta\left(s-\tfrac{1}{2}\right) \left(\zeta(s-\tfrac{1}{2},\tfrac{1}{3}) - \zeta(s-\tfrac{1}{2},\tfrac{2}{3})\right) \\ &+ \frac{2\pi^s}{\gamma^{s+\frac{1}{2}}\Gamma(s)} \sum_{k\in\mathbb{N}} k^{s-\frac{1}{2}} \cos(2\pi kr) \sum_{n\in\mathbb{N}} \frac{u_2(3n-2)}{(n-\frac{2}{3})^{(2s-1)/4}} K_{s-\frac{1}{2}}\left(\frac{2\pi k}{\gamma}\sqrt{n-\tfrac{2}{3}}\right). \end{aligned} \tag{O.24}$$

This reduces to the formula (45) in Ref. 294 when $r = 1/2$. The formula (O.24) can also be used to calculate the series when $r = 0$. As already mentioned for the lattice sum L_A, because of the asymptotic behavior of the Bessel function, $K_s(z) \sim z^{-1/2}e^{-z}$, and a pole appearing at $z = 0$, eqs. (O.10) and (O.20) are better suited for large values of $\gamma = N\gamma_0$ and therefore ideal for Barlow packings with a large period N, while eqs. (O.15) and (O.24) are better suited for small values of γ.

Appendix P

Bessel Function Expansions of Lattice Sums and Their Derivatives

Formulae for the expansions of the Barlow lattice sums (11.22), (11.23) and (11.24) in terms of Bessel functions have already been provided in our previous paper[377]. For the corresponding lattice sum derivatives with respect to the lattice constants $\{\gamma_i\}$ required for the Newton-Raphson procedure we rewrite the Bessel function expansions in a more convenient short-hand notation and set $\gamma \equiv \gamma_T = \sum_{i=1,\ldots N} \gamma_i$,

$$L^A(s,r,\gamma) = A_1(s) + \gamma^{2-2s} A_2(s) + 2\gamma^{1-s} A_3(s) \sum_{k,n\in\mathbb{N}} t_{kn}(s) K_{s-1}(\gamma p_{kn}) \tag{P.1}$$

$$L^{AA}(s,r,\gamma) = \gamma^{2-2s} A_2(s,r) + \gamma^{1-s} A_3(s) \sum_{k\in\mathbb{Z}} \sum_{n\in\mathbb{N}} t_{kn}(s,r) K_{s-1}(\gamma p_{kn}(r)) \tag{P.2}$$

$$L^{AB}(s,r,\gamma)(s) = \gamma^{2-2s} A_2(s,r) + \gamma^{1-s} A_3(s) \sum_{k\in\mathbb{Z}} \sum_{n\in\mathbb{N}} u_{kn}(s,r) K_{s-1}(\gamma p_{kn}(r)) \,. \tag{P.3}$$

with the coefficients,

$$\begin{aligned} A_1(s) &= 6\zeta(s)\, L_{-3}(s) \quad , \quad A_2(s,r) = \frac{2\pi}{\sqrt{3}(s-1)} \left(\zeta(2s-2,r) + \zeta(2s-2,1-r)\right) \\ A_3(s) &= \frac{2}{\Gamma(s)} \left(\frac{2\pi}{\sqrt{3}}\right)^s \quad , \quad t_{kn}(s,r) = u_2(n) n^{(s-1)/2} \left|k+r\right|^{1-s} \\ u_{kn}(s,r) &= u_2(n) \left(\frac{n}{3(k+r)^2}\right)^{(s-1)/2} \cos\left(\frac{2\pi n}{3}\right) \quad , \quad p_{kn}(r) = \frac{4\pi}{3}\sqrt{n}\left|k+r\right| \end{aligned} \tag{P.4}$$

where $A_2(s) = A_2(s, r=0)$, $t_{kn}(s) = t_{kn}(s, r=0)$, $u_{kn}(s) = u_{kn}(s, r=0)$, $p_{kn} = p_{kn}(r=0)$ and $r = (k_2 - k_1)/N \in \mathbb{Q}, 0 < r < 1$, if we neglect symmetry breaking effects along the c-axis, and $r \equiv r_{k_1 k_2} = \gamma^{-1} d_{k_1,k_2}$ with $d_{k_1 k_2} = \sum_{i=k_1,\ldots,k_2-1} \gamma_i$ otherwise. Here, $u_2(n)$ is the number of representations of the positive integer n by the form $i^2 + ij + j^2$. The gamma $\Gamma(s)(s > 0)$ and

modified Bessel functions $K_s(x)$ may be defined by[298,590]

$$\Gamma(s) = \int_{[0,\infty)} t^{s-1}\, e^{-t}\, \mathrm{d}t \ . \tag{P.5}$$

and

$$\int_{[0,\infty)} x^{s-1} e^{-ax-b/x} \mathrm{d}x = 2\left(\frac{b}{a}\right)^{s/2} K_s(2\sqrt{ab}) \ . \tag{P.6}$$

with the properties

$$K_s(z) = K_{-s}(z) \ . \tag{P.7}$$

$$K_s(z) = K_{s+2}(z) - \frac{2s+2}{z} K_{s+1}(z) \ , \tag{P.8}$$

and the asymptotic formula,

$$K_s(z) \sim \sqrt{\frac{\pi}{2z}}\, e^{-z} \quad \text{as} \quad z \to \infty, \quad (\ |\arg z| < 3\pi/2) \ . \tag{P.9}$$

The L_{-3} function is defined by

$$L_{-3}(s) = 3^{-s}\left[\zeta(s, \tfrac{1}{3}) - \zeta(s, \tfrac{2}{3})\right] . \tag{P.10}$$

where $h(s,x)$ is the Hurwitz zeta function, which for $x = 1$ reduces to the Riemann zeta function, i.e. $\zeta(s,1) = \zeta(s)$.

We also introduced a second set of Bessel function expansions in our previous paper[377],

$$L^{AA}(s,r,\gamma) = \gamma^{-2s} B_1(s,r) + \gamma^{-1} B_2(s) + \gamma^{-(s+\frac{1}{2})} B_3(s) \sum_{k,n\in\mathbb{N}} v_{kn}(s,r) K_{s-\frac{1}{2}}\left(\gamma^{-1} f_{kn}\right) \tag{P.11}$$

$$L^{AB}(s,r,\gamma) = \gamma^{-1} B_4(s) + \gamma^{-(s+\frac{1}{2})} B_5(s) \sum_{k,n\in\mathbb{N}} w_{kn}(s,r) K_{s-\frac{1}{2}}\left(\gamma^{-1} g_{kn}\right) \tag{P.12}$$

with the coefficients

$$\begin{aligned}
B_1(s,r) &= (\zeta(2s,r) + \zeta(2s,1-r)) \quad , \quad B_3(s) = \frac{4\pi^s}{\Gamma(s)} = \frac{1}{2} B_5(s) \\
B_2(s,r) &= \frac{2\sqrt{\pi}}{3^{s-\frac{3}{2}}} \frac{\Gamma(s-\frac{1}{2})}{\Gamma(s)}\, \zeta(s-\tfrac{1}{2})\, \left(\zeta(s-\tfrac{1}{2},\tfrac{1}{3}) - \zeta(s-\tfrac{1}{2},\tfrac{2}{3})\right) \\
B_4(s) &= 3\sqrt{\pi}\,(1-3^{-(s-1/2)}) \frac{\Gamma(s-\frac{1}{2})}{\Gamma(s)}\, \zeta\left(s-\tfrac{1}{2}\right) \left(\zeta(s-\tfrac{1}{2},\tfrac{1}{3}) - \zeta(s-\tfrac{1}{2},\tfrac{2}{3})\right) \\
v_{kn}(s,r) &= \frac{k^{s-\frac{1}{2}}}{n^{(2s-1)/4}} u_2(n) \cos(2\pi k r) \quad , \quad w_{kn}(s,r) = k^{s-\frac{1}{2}} \cos(2\pi k r) \frac{u_2(3n-2)}{(n-\frac{2}{3})^{(2s-1)/4}} \\
f_{kn} &= 2\pi k \sqrt{n} \quad , \quad g_{kn} = 2\pi k \sqrt{n-\tfrac{2}{3}}
\end{aligned} \tag{P.13}$$

For the lattice sum derivatives we require the derivatives of the Bessel functions,

$$\partial_x K_s(x) = -K_{s+1}(x) + \frac{s}{x} K_s(x) \tag{P.14}$$

$$\partial_x K_s(x) = -K_{s-1}(x) - \frac{s}{x} K_s(x)\,. \tag{P.15}$$

If we neglect symmetry breaking effects along the c-axis we have to consider the derivatives with respect to the single parameter $\gamma \equiv \gamma_T$ only. For this, the lattice sum derivatives are easily derived. For the first set we get,

$$\partial_\gamma L^A(s,\gamma) = 2(1-s)A_2(s)\gamma^{1-2s} - 2\gamma^{1-s}A_3(s) \sum_{k,n\in\mathbb{N}} t_{kn}(s) p_{kn} K_s\left(\gamma p_{kn}\right) \tag{P.16}$$

$$\partial_\gamma L^{AA}(s,\gamma) = 2(1-s)A_2(s,r)\gamma^{1-2s} - \gamma^{1-s}A_3(s) \sum_{k\in\mathbb{Z}} \sum_{n\in\mathbb{N}} t_{kn}(s,r) p_{kn}(r) K_s\left(\gamma p_{kn}(r)\right) \tag{P.17}$$

$$\partial_\gamma L^{AB}(s,\gamma) = 2(1-s)A_2(s,r)\gamma^{1-2s} - \gamma^{1-s}A_4(s) \sum_{k\in\mathbb{Z}} \sum_{n\in\mathbb{N}} u_{kn}(s,r) p_{kn}(r) K_s\left(\gamma p_{kn}(r)\right) \tag{P.18}$$

and

$$\partial_\gamma^2 L^A(s,r,\gamma) = (1-2s)\gamma^{-1}\partial_\gamma L^A(s,r,\gamma) + 2\gamma^{1-s}A_3(s) \sum_{k,n\in\mathbb{N}} t_{kn}(s) p_{kn}^2 K_{s-1}\left(\gamma p_{kn}\right) \tag{P.19}$$

$$\partial_\gamma^2 L^{AA}(s,r,\gamma) = (1-2s)\gamma^{-1}\partial_\gamma L^{AA}(s,r,\gamma) + \gamma^{1-s}A_3(s) \sum_{k\in\mathbb{Z}} \sum_{n\in\mathbb{N}} t_{kn}(s,r) p_{kn}^2(r) K_{s-1}\left(\gamma p_{kn}(r)\right) \tag{P.20}$$

$$\partial_\gamma^2 L^{AB}(s,r,\gamma) = (1-2s)\gamma^{-1}\partial_\gamma L^{AB}(s,r,\gamma) + \gamma^{1-s}A_4(s) \sum_{k\in\mathbb{Z}} \sum_{n\in\mathbb{N}} u_{kn}(s,r) p_{kn}^2(r) K_{s-1}\left(\gamma p_{kn}(r)\right) \tag{P.21}$$

For the second set we have,

$$\begin{aligned}\partial_\gamma L^{AA}(\gamma,s) = &-\gamma^{-1}L^{AA}(s,r,\gamma) - (2s-1)\gamma^{-2s-1}B_1(s,r) \\ &+ \gamma^{-(s+\frac{5}{2})}B_3(s) \sum_{k,n\in\mathbb{N}} v_{kn}(s,r) f_{kn} K_{s-\frac{3}{2}}(\gamma^{-1} f_{kn})\end{aligned} \tag{P.22}$$

$$\partial_\gamma L^{AB}(\gamma,s) = -\gamma^{-1}L^{AB}(s,r,\gamma) + \gamma^{-(s+\frac{5}{2})}B_5(s) \sum_{k,n\in\mathbb{N}} w_{kn}(s,r) g_{kn} K_{s-\frac{3}{2}}(\gamma^{-1} g_{kn}) \tag{P.23}$$

and

$$\partial_\gamma^2 L^{AA}(s,r,\gamma) = -2s\gamma^{-2}L^{AA}(\gamma,s) - 2(s+1)\gamma^{-1}\partial_\gamma L^{AA} + \gamma^{-(s+\frac{9}{2})}B_3(s)\sum_{k,n\in\mathbb{N}} v_{kn}(s,r) f_{kn}^2 K_{s-\frac{1}{2}}(\gamma^{-1}f_{kn}) \tag{P.24}$$

$$\partial_\gamma^2 L^{AB}(s,r,\gamma) = -2s\gamma^{-2}L^{AB}(\gamma,s) - 2(s+1)\gamma^{-1}\partial_\gamma L^{AB} + \gamma^{-(s+\frac{9}{2})}B_5(s)\sum_{k,n\in\mathbb{N}} w_{kn}(s,r) g_{kn}^2 K_{s-\frac{1}{2}}(\gamma^{-1}g_{kn}) \tag{P.25}$$

We now extend the lattice sum derivatives to the case where we include symmetry breaking in the location of the hexagonal layers along the main *c*-axis. For the first set of derivatives we use eqs.(P.1)-(P.3) and remember that $\gamma \equiv \gamma_T$ and $r \to r_{k_1k_2} = \gamma^{-1}d_{k_1,k_2}$

$$\partial_{\gamma_j} L^{\mathrm{A}}(s,\{\gamma_i\}) = 2(1-s)\gamma^{1-2s}A_2(s) - 2\gamma^{1-s}A_3(s)\sum_{k,n\in\mathbb{N}} t_{kn}(s)p_{kn}K_s(\gamma p_{kn}) \tag{P.26}$$

$$\partial_{\gamma_j} L^{\mathrm{AA}}(s,\{\gamma_i\}) = \frac{4\pi}{\sqrt{3}}\gamma^{1-2s}\left\{H_-(2s-1,r_{k_1k_2})\left(r_{k_1k_2}-\delta_{j,[k_1k_2-1]}\right) - H_+(2s-2,r_{k_1k_2})\right\} - \gamma^{1-s}A_3(s)\sum_{k\in\mathbb{Z}}\sum_{n\in\mathbb{N}} t_{kn}(s,r_{k_1k_2})p_{kn}(r_{k_1k_2})\left[1-(k+r_{k_1k_2})^{-1}\left(r_{k_1k_2}-\delta_{j,[k_1k_2-1]}\right)\right]K_s(\gamma^{-1}p_{kn}(r_{k_1k_2})) \tag{P.27}$$

$$\partial_{\gamma_j} L^{\mathrm{AB}}(s,\{\gamma_i\}) = \frac{4\pi}{\sqrt{3}}\gamma^{1-2s}\left\{H_-(2s-1,r_{k_1k_2})\left(r_{k_1k_2}-\delta_{j,[k_1k_2-1]}\right) - H_+(2s-2,r_{k_1k_2})\right\} - \gamma^{1-s}A_4(s)\sum_{k\in\mathbb{Z}}\sum_{n\in\mathbb{N}} u_{kn}(s,r_{k_1k_2})p_{kn}(r_{k_1k_2})\left[1-(k+r_{k_1k_2})^{-1}\left(r_{k_1k_2}-\delta_{j,[k_1k_2-1]}\right)\right]K_s(\gamma^{-1}p_{kn}(r_{k_1k_2})) \tag{P.28}$$

and

$$\partial_{\gamma_i}\partial_{\gamma_j}L^{\mathrm{A}}(s,\{\gamma_i\}) = \partial^2_{\gamma_j}L^{A}(s,\{\gamma_i\} = (2s-1)(2s-2)\gamma^{-2s}A_2(s)$$
$$+2(2s-1)\gamma^{-s}A_3(s)\sum_{k,n\in\mathbb{N}}t_{kn}(s)p_{kn}K_s\left(\gamma p_{kn}\right)+2\gamma^{1-s}A_3(s)\sum_{k,n\in\mathbb{N}}t_{kn}(s)p^2_{kn}K_{s-1}\left(\gamma p_{kn}\right) \tag{P.29}$$

$$\partial_{\gamma_i}\partial_{\gamma_j}L^{AA}(s,\{\gamma_i\}) = \frac{4\pi}{\sqrt{3}}\gamma^{-2s}(2s-1)\Big\{H_+(2s-2,r_{k_1k_2})+H_+(2s,r_{k_1k_2})(r_{k_1k_2}-\delta_{i,[k_1k_2-1]})(r_{k_1k_2}-\delta_{j,[k_1k_2-1]})$$
$$-H_-(2s-1,r_{k_1k_2})\left[2r_{k_1k_2}-\delta_{i,[k_1k_2-1]}-\delta_{j,[k_1k_2-1]}\right]\Big\} \tag{P.30}$$
$$+\gamma^{-s}A_3(s)\sum_{k\in\mathbb{Z}}\sum_{n\in\mathbb{N}}t_{kn}(s,r_{k_1k_2})p_{kn}(r_{k_1k_2})\left\{p_{kn}(r_{k_1k_2})K_{s-1}\left(\gamma p_{kn}(r_{k_1k_2})\right)+(2s-1)\gamma K_s\left(\gamma p_{kn}(r_{k_1k_2})\right)\right\}$$
$$\times\left\{1-(k+r_{k_1k_2})^{-1}\left(r_{k_1k_2}-\delta_{i,[k_1,k_2-1]}\right)\right\}\left\{1-(k+r_{k_1k_2})^{-1}\left(r_{k_1k_2}-\delta_{j,[k_1,k_2-1]}\right)\right\}$$

$$\partial_{\gamma_i}\partial_{\gamma_j}L^{\mathrm{AB}}(s,\{\gamma_i\}) = \frac{4\pi}{\sqrt{3}}\gamma^{-2s}(2s-1)\Big\{H_+(2s-2,r_{k_1k_2})+H_+(2s,r_{k_1k_2})(r_{k_1k_2}-\delta_{i,[k_1k_2-1]})(r_{k_1k_2}-\delta_{j,[k_1k_2-1]})$$
$$-H_-(2s-1,r_{k_1k_2})\left[2r_{k_1k_2}-\delta_{i,[k_1k_2-1]}-\delta_{j,[k_1k_2-1]}\right]\Big\} \tag{P.31}$$
$$+\gamma^{-s}A_4(s)\sum_{k\in\mathbb{Z}}\sum_{n\in\mathbb{N}}u_{kn}(s,r_{k_1k_2})p_{kn}(r_{k_1k_2})\left\{p_{kn}(r_{k_1k_2})K_{s-1}\left(\gamma p_{kn}(r_{k_1k_2})\right)+(2s-1)\gamma K_s\left(\gamma p_{kn}(r_{k_1k_2})\right)\right\}$$
$$\times\left\{1-(k+r_{k_1k_2})^{-1}\left(r_{k_1k_2}-\delta_{i,[k_1,k_2-1]}\right)\right\}\left\{1-(k+r_{k_1k_2})^{-1}\left(r_{k_1k_2}-\delta_{j,[k_1,k_2-1]}\right)\right\}$$

Here we used the extension of the Kronecker symbol $\delta_{j,[k_1,k_2-1]} = 1$ if $j \in [k_1, k_2-1]$ and 0 otherwise, and the definition for the Hurwitz sums $H_\pm(s,r_{k_1,k_2}) = \zeta(s,r_{k_1,k_2}) \pm \zeta(s,1-r_{k_1,k_2})$. We see that the first and second derivatives of $L^A(s,\{\gamma_i\})$ with respect to γ_i and γ_j are only dependent of γ.

For the second set we have,

$$\partial_{\gamma_j} L^{\mathrm{AA}}(s,\{\gamma_i\}) = -2s\gamma^{-2s-1}\left[H_+(2s,r_{k_1k_2}) - H_-(2s+1,r_{k_1k_2})\left(r_{k_1k_2}-\delta_{j,[k_1,k_2-1]}\right)\right] - \gamma^{-2}B_2(s)$$
$$+\gamma^{-(s+\frac{3}{2})}B_3(s)\sum_{k,n\in\mathbb{N}} v_{kn}(s,r_{k_1k_2})\left\{(2\pi k)\tan(2\pi k r_{k_1k_2})\left(r_{k_1k_2}-\delta_{j,[k_1,k_2-1]}\right)-2s\right\}K_{s-\frac{1}{2}}\left(\gamma^{-1}f_{kn}\right)$$
$$+\gamma^{-(s+\frac{5}{2})}B_3(s)\sum_{k,n\in\mathbb{N}} v_{kn}(s,r_{k_1k_2})f_{kn}K_{s+\frac{1}{2}}\left(\gamma^{-1}f_{kn}\right) \tag{P.32}$$

$$\partial_{\gamma_j} L^{\mathrm{AB}}(s,\{\gamma_i\}) = -\gamma^{-2}B_4(s) + \gamma^{-(s+\frac{5}{2})}B_5(s)\sum_{k,n\in\mathbb{N}} w_{kn}(s,r_{k_1k_2})g_{kn}K_{s+\frac{1}{2}}\left(\gamma^{-1}g_{kn}\right) \tag{P.33}$$
$$+\gamma^{-(s+\frac{3}{2})}B_5(s)\sum_{k,n\in\mathbb{N}} w_{kn}(s,r_{k_1k_2})\left\{(2\pi k)\tan(2\pi k r_{k_1k_2})\left(r_{k_1k_2}-\delta_{j,[k_1,k_2-1]}\right)-2s\right\}K_{s-\frac{1}{2}}\left(\gamma^{-1}g_{kn}\right)$$

and

$$\partial_{\gamma_i}\partial_{\gamma_j} L^{\mathrm{AA}}(s,\{\gamma_i\}) = 2s(2s+1)\gamma^{-2(s+1)}\Big\{H_+(2s,r_{k_1k_2}) + H_+(2s+2,r_{k_1k_2})\left(r_{k_1k_2}-\delta_{i,[k_1,k_2-1]}\right)\left(r_{k_1k_2}-\delta_{j,[k_1,}$$
$$-H_-(2s+1,r_{k_1k_2})\left(2r_{k_1k_2}-\delta_{i,[k_1,k_2-1]}-\delta_{j,[k_1,k_2-1]}\right)\Big\} + 2\gamma^{-3}B_2(s) \tag{P.34}$$
$$+\gamma^{-(s+\frac{5}{2})}B_3(s)\sum_{k,n\in\mathbb{N}} v_{kn}(s,r_{k_1k_2})C_{kn}(s,k_1,k_2,\gamma)K_{s-\frac{1}{2}}\left(\gamma^{-1}f_{kn}\right)$$
$$+\gamma^{-(s+\frac{7}{2})}B_3(s)\sum_{k,n\in\mathbb{N}} v_{kn}(s,r_{k_1k_2})f_{kn}D_{kn}(s,k_1,k_2,\gamma)K_{s+\frac{1}{2}}\left(\gamma^{-1}f_{kn}\right)$$

$$\partial_{\gamma_i}\partial_{\gamma_j} L^{\mathrm{AB}}(s,\{\gamma_i\}) = 2\gamma^{-3}B_4(s) + \gamma^{-(s+\frac{5}{2})}B_5(s)\sum_{k,n\in\mathbb{N}} w_{kn}(s,r_{k_1k_2})E_{kn}(s,k_1,k_2,\gamma)K_{s-\frac{1}{2}}\left(\gamma^{-1}g_{kn}\right)$$
$$+\gamma^{-(s+\frac{7}{2})}B_5(s)\sum_{k,n\in\mathbb{N}} w_{kn}(s,r_{k_1k_2})g_{kn}D_{kn}(s,k_1,k_2,\gamma)K_{s+\frac{1}{2}}\left(\gamma^{-1}g_{kn}\right) \tag{P.35}$$

Here the coefficients are defined as

$$C_{kn}(s,k_1,k_2,\gamma) = 2s(2s+1) + \gamma^{-2}f_{kn}^2 - (2\pi k)^2\left(r_{k_1k_2}-\delta_{i,[k_1,k_2-1]}\right)\left(r_{k_1k_2}-\delta_{j,[k_1,k_2-1]}\right)$$
$$-2(2s+1)(2\pi k)\tan(2\pi k r_{k_1k_2})\left(2r_{k_1k_2}-\delta_{i,[k_1,k_2-1]}-\delta_{j,[k_1,k_2-1]}\right) \tag{P.36}$$
$$D_{kn}(s,k_1,k_2,\gamma) = -2(2s+1) + (2\pi k)\tan(2\pi k r_{k_1k_2})\left(2r_{k_1k_2}-\delta_{i,[k_1,k_2-1]}-\delta_{j,[k_1,k_2-1]}\right) \tag{P.37}$$
$$E_{kn}(s,k_1,k_2,\gamma) = 2s(2s+1) + \gamma^{-2}g_{kn}^2 - (2\pi k)^2\left(r_{k_1k_2}-\delta_{i,[k_1,k_2-1]}\right)\left(r_{k_1k_2}-\delta_{j,[k_1,k_2-1]}\right) \tag{P.38}$$
$$-2(s+1)(2\pi k)\tan(2\pi k r_{k_1k_2})\left(2r_{k_1k_2}-\delta_{i,[k_1,k_2-1]}-\delta_{j,[k_1,k_2-1]}\right)$$

We see that because of the simple linear dependence of γ on the γ_i for the lattice sums $L^A(s,\{\gamma_i\})$ the first and second derivatives lead to the same functional form compared to eqs.(P.16) and (P.22). However, the derivative for $L^{AA}(s,\{\gamma_i\})$ and $L^{AB}(s,\{\gamma_i\})$ become more complicated. The advantage of the second set of equations is that the Bessel functions are not

dependent on k_1 and k_2 which saves computer time.

Appendix Q

Derivatives from Direct Summation

The derivatives of the lattice sums L^A, L^{AA} and L^{AB} using directly formulas eqs.(11.22), (11.23) and (11.24), respectively, are shown in this section. They become useful for large exponents in the Lennard-Jones potential, i.e. $n \geq 10$. Furthermore, to speed up computer time we can use permutation symmetry between indices when applies. We only consider the more general case here where symmetry breaking for the location of the hexagonal layers along the c-axis is considered. We remember that $\gamma \equiv \gamma_T$. The first lattice sum derivative with respect to to γ_j according to (11.22) becomes,

$$\partial_{\gamma_j} L^A(s,\gamma) = -2s\gamma {\sum_{\vec{i}\in\mathbb{Z}^3}}' i_3^2 S^A(\vec{i},\gamma)^{-(s+1)} \tag{Q.1}$$

and for the second derivative we get

$$\partial^2_{\gamma_j} L^A(s,\gamma) = 2s {\sum_{\vec{i}\in\mathbb{Z}^3}}' \left[2(s+1) i_3^4 \gamma^2 S^A(\vec{i},\gamma)^{-(s+2)} - i_3^2 S^A(\vec{i},\gamma)^{-(s+1)}\right] \tag{Q.2}$$

Note that since $\partial_{\gamma_j}\gamma = 1$, the mixed second derivatives are equal to $\partial^2_{\gamma_j} L^A$. Turning to the lattice sums (11.23) and (11.24) and its derivatives, we need the following relations (remember that $r_{k_1k_2} = \gamma^{-1} d_{k_1k_2}$),

$$\partial_{\gamma_j} r_{k_1k_2} = \gamma^{-1}\left(\chi_j^{[k_1,k_2-1]} - r_{k_1k_2}\right) \tag{Q.3}$$

$$\partial_{\gamma_j} S^{AA}(\vec{i},k_1,k_2,\{\gamma_i\}) = 2\gamma\left(i_3 + r_{k_1k_2}\right)\left[i_3 + \chi_j^{[k_1,k_2-1]}\right] \tag{Q.4}$$

and

$$\partial^2_{\gamma_i\gamma_j} S^{AA}(\vec{i},k_1,k_2,\{\gamma_i\}) = 2\left(i_3 + \chi_i^{[k_1,k_2-1]}\right)^2 \tag{Q.5}$$

where

$$\chi_j^{[k_1,k_2-1]} = \begin{cases} 0 & \text{if } j \notin [k_1,k_2-1] \\ 1 & \text{if } j \in [k_1,k_2-1] \end{cases} \tag{Q.6}$$

where $1 \leq k_1 < k_2$ are the labels of two different layers of the Barlow sequences. The first derivative of L^{AA} becomes,

$$\partial_{\gamma_j} L^{AA} = -2\gamma \sum_{\vec{i}\in\mathbb{Z}^3} s\left(i_3 + r_{k_1k_2}\right) S^{AA}(\vec{i}, k_1, k_2, \{\gamma_i\})^{-(s+1)} \left[i_3 + \chi_j^{[k_1,k_2-1]}\right] \tag{Q.7}$$

and the second derivatives are

$$\begin{aligned}\partial^2_{\gamma_j} L^{AA} = &\sum_{\vec{i}\in\mathbb{Z}^3} 2s(s+1)\gamma\left(i_3 + r_{k_1k_2}\right) S^{AA}(\vec{i}, k_1, k_2, \{\gamma_i\})^{-(s+2)} \left[i_3 + \chi_j^{[k_1,k_2-1]}\right] \\ &- 2sS^{AA}(\vec{i}, k_1, k_2, \{\gamma_i\})^{-(s+1)} \left[i_3 + \chi_j^{k_1,k_2-1}\right]^2\end{aligned} \tag{Q.8}$$

$$\begin{aligned}\partial^2_{\gamma_i\gamma_j} L^{AA} = &\sum_{\vec{i}\in\mathbb{Z}^3} 2s(s+1)\gamma\left(i_3 + r_{k_1k_2}\right) S^{AA}(\vec{i}, k_1, k_2, \{\gamma_i\})^{-(s+2)} \left[i_3 + \chi_j^{[k_1,k_2-1]}\right] \\ &- 2sS^{AA}(\vec{i}, k_1, k_2, \{\gamma_i\})^{-(s+1)} \left[i_3 + \chi_i^{k_1,k_2-1}\right]^2\end{aligned} \tag{Q.9}$$

For the last lattice sum L^{AB} we get similar expressions,

$$\partial_{\gamma_j} L^{AB} = -2\gamma \sum_{\vec{i}\in\mathbb{Z}^3} s\left(i_3 + r_{k_1k_2}\right) S^{AB}(\vec{i}, k_1, k_2, \{\gamma_i\})^{-(s+1)} \left[i_3 + \chi_j^{[k_1,k_2-1]}\right] \tag{Q.10}$$

$$\begin{aligned}\partial^2_{\gamma_j} L^{AB} = &\sum_{\vec{i}\in\mathbb{Z}^3} 2s(s+1)\gamma\left(i_3 + r_{k_1k_2}\right) S^{AB}(\vec{i}, k_1, k_2, \{\gamma_i\})^{-(s+2)} \left[i_3 + \chi_j^{[k_1,k_2-1]}\right] \\ &- 2sS^{AB}(\vec{i}, k_1, k_2, \{\gamma_i\})^{-(s+1)} \left[i_3 + \chi_j^{k_1,k_2-1}\right]^2\end{aligned} \tag{Q.11}$$

$$\begin{aligned}\partial^2_{\gamma_i\gamma_j} L^{AB} = &\sum_{\vec{i}\in\mathbb{Z}^3} 2s(s+1)\gamma\left(i_3 + r_{k_1k_2}\right) S^{AB}(\vec{i}, k_1, k_2, \{\gamma_i\})^{-(s+2)} \left[i_3 + \chi_j^{[k_1,k_2-1]}\right] \\ &- 2sS^{AB}(\vec{i}, k_1, k_2, \{\gamma_i\})^{-(s+1)} \left[i_3 + \chi_i^{k_1,k_2-1}\right]^2\end{aligned} \tag{Q.12}$$

Appendix R

Taylor Expansions Involving Barlow Lattice Sums

In order to discuss the linear trends observed for the properties with respect to the packing fraction, it is convenient to introduce a Taylor expansion for the lattice sum differences. Consider the variable

$$x = \frac{L^{X}(s,\gamma)}{L^{\text{hcp}}(s,\gamma)} - 1 = \frac{\Delta L^{X}(s,\gamma)}{L^{\text{hcp}}(s,\gamma)} \tag{R.1}$$

where $x > 0$ is very small in the range $s \in (1.5, \infty)$ for $\gamma_0 = \sqrt{\frac{2}{3}}$ as pointed out in our first paper[377]. We assume a near linear behavior in the lattice sums, that is

$$\Delta L^{X}(s,\gamma) \approx \alpha^{X}(2)\left(L^{\text{fcc}}(s,\gamma) - L^{\text{hcp}}(s,\gamma)\right) \tag{R.2}$$

with the fcc packing fraction for a specific Barlow packing in the range of $0 \leq \alpha^{\mathbf{X}}(2) \leq 1$. We now introduce the Taylor expansion around $x = 0$ for

$$(1+x)^{q} = 1 + qx + \frac{1}{2}q(q-1)x^{2} + ... \tag{R.3}$$

with $q \in \mathbb{R}$. We apply this first to the minimum lattice constant (11.26) and keep only the first order terms,

$$\begin{aligned}
\Delta a_{\min}^{*\boldsymbol{X}}(n,m,\gamma) &= \left(\frac{L^{\boldsymbol{X}}(\frac{n}{2},\gamma)}{L^{\boldsymbol{X}}(\frac{m}{2},\gamma)}\right)^{\frac{1}{n-m}} - \left(\frac{L^{\mathrm{hcp}}(\frac{n}{2},\gamma)}{L^{\mathrm{hcp}}(\frac{m}{2},\gamma)}\right)^{\frac{1}{n-m}} \\
&= \left(\frac{L^{\mathrm{hcp}}(\frac{n}{2},\gamma)}{L^{\mathrm{hcp}}(\frac{m}{2},\gamma)}\right)^{\frac{1}{n-m}} \left[\left(\frac{\Delta L^{\boldsymbol{X}}(\frac{n}{2},\gamma)}{L^{\mathrm{hcp}}(\frac{n}{2},\gamma)}\right)^{\frac{1}{n-m}} \left(\frac{\Delta L^{\boldsymbol{X}}(\frac{m}{2},\gamma)}{L^{\mathrm{hcp}}(\frac{m}{2},\gamma)}\right)^{-\frac{1}{n-m}} - 1\right] \\
&\approx \frac{1}{n-m}\left(\frac{L^{\mathrm{hcp}}(\frac{n}{2},\gamma)}{L^{\mathrm{hcp}}(\frac{m}{2},\gamma)}\right)^{\frac{1}{n-m}} \left[\frac{\Delta L^{\boldsymbol{X}}(\frac{n}{2},\gamma)}{L^{\mathrm{hcp}}(\frac{n}{2},\gamma)} - \frac{\Delta L^{\boldsymbol{X}}(\frac{m}{2},\gamma)}{L^{\mathrm{hcp}}(\frac{m}{2},\gamma)}\right],
\end{aligned} \tag{R.4}$$

Inserting (R.2) finally gives

$$\begin{aligned}
\Delta a_{\min}^{*\boldsymbol{X}}(n,m,\gamma) &\approx \frac{\alpha^{\boldsymbol{X}}(2)}{n-m}\left(\frac{L^{\mathrm{hcp}}(\frac{n}{2},\gamma)}{L^{\mathrm{hcp}}(\frac{m}{2},\gamma)}\right)^{\frac{1}{n-m}} \left[\frac{L^{\mathrm{fcc}}(\frac{n}{2},\gamma)}{L^{\mathrm{hcp}}(\frac{n}{2},\gamma)} - \frac{L^{\mathrm{fcc}}(\frac{m}{2},\gamma)}{L^{\mathrm{hcp}}(\frac{m}{2},\gamma)}\right] \\
&= \frac{\alpha^{\boldsymbol{X}}(2)}{n-m}\left[\frac{L^{\mathrm{fcc}}(\frac{n}{2},\gamma)}{L^{\mathrm{hcp}}(\frac{n}{2},\gamma)} - \frac{L^{\mathrm{fcc}}(\frac{m}{2},\gamma)}{L^{\mathrm{hcp}}(\frac{m}{2},\gamma)}\right] a_{\min}^{*\mathrm{hcp}}(n,m,\gamma),
\end{aligned} \tag{R.5}$$

Deviations between the two equations (R.4) and (R.5) are smaller than 5×10^{-9}. It is therefore clear that a near linear behavior in $\Delta L^{\mathbf{X}}(s,\gamma)$ with respect to the fcc packing fraction $\alpha(2)$ translates into a near linear behavior in $\Delta a_{\min}^{*\mathbf{X}}(n,m,\gamma)$ because of the small differences between the lattice sums of Barlow packings. We notice that the term $L^{\mathrm{fcc}}(\frac{m}{2},\gamma)/L^{\mathrm{hcp}}(\frac{m}{2},\gamma)$ is close to 1.0 and has a minimum around $m = 7.05$ (or $s = 3.53$). This implies that the term in the square bracket of (R.5) can be positive or negative depending on the (n,m) combination for the LJ potential.

It is straightforward to derive the Taylor expansions to first order for the other properties as

well, e.g. for the cohesive energy

$$
\begin{aligned}
\Delta E_{\mathrm{coh}}^{\boldsymbol{X}\,*}(a^*_{\mathrm{min}},n,m,\gamma) &= -\frac{1}{2}\left[\frac{L^{\boldsymbol{X}}(\frac{m}{2},\gamma)^n}{L^{\boldsymbol{X}}(\frac{n}{2},\gamma)^m}\right]^{\frac{1}{n-m}} + \frac{1}{2}\left[\frac{L^{\mathrm{hcp}}(\frac{m}{2},\gamma)^n}{L^{\mathrm{hcp}}(\frac{n}{2},\gamma)^m}\right]^{\frac{1}{n-m}} \qquad \text{(R.6)}\\
&= \frac{1}{2}\left[\frac{L^{\mathrm{hcp}}(\frac{m}{2},\gamma)^n}{L^{\mathrm{hcp}}(\frac{n}{2},\gamma)^m}\right]^{\frac{1}{n-m}} \left[1-\left(1+\frac{\Delta L^{\boldsymbol{X}}(\frac{m}{2},\gamma)}{L^{\mathrm{hcp}}(\frac{m}{2},\gamma)}\right)^{\frac{n}{n-m}}\left(1+\frac{\Delta L^{\boldsymbol{X}}(\frac{n}{2},\gamma)}{L^{\mathrm{hcp}}(\frac{n}{2},\gamma)}\right)^{-\frac{m}{n-m}}\right]\\
&\approx -\frac{1}{2(n-m)}\left[\frac{L^{\mathrm{hcp}}(\frac{m}{2},\gamma)^n}{L^{\mathrm{hcp}}(\frac{n}{2},\gamma)^m}\right]^{\frac{1}{n-m}} \left[\frac{n\Delta L^{\boldsymbol{X}}(\frac{m}{2},\gamma)}{L^{\mathrm{hcp}}(\frac{m}{2},\gamma)} - \frac{m\Delta L^{\boldsymbol{X}}(\frac{n}{2},\gamma)}{L^{\mathrm{hcp}}(\frac{n}{2},\gamma)}\right]\\
&= -\frac{\alpha^{\boldsymbol{X}}(2)}{2(n-m)}\left[\frac{L^{\mathrm{hcp}}(\frac{m}{2},\gamma)^n}{L^{\mathrm{hcp}}(\frac{n}{2},\gamma)^m}\right]^{\frac{1}{n-m}} \left[\frac{nL^{\mathrm{fcc}}(\frac{m}{2},\gamma)}{L^{\mathrm{hcp}}(\frac{m}{2},\gamma)} - \frac{mL^{\mathrm{fcc}}(\frac{n}{2},\gamma)}{L^{\mathrm{hcp}}(\frac{n}{2},\gamma)} - (n-m)\right]\\
&= \alpha^{\boldsymbol{X}}(2)\left[\frac{n}{(n-m)}\frac{L^{\mathrm{fcc}}(\frac{m}{2},\gamma)}{L^{\mathrm{hcp}}(\frac{m}{2},\gamma)} - \frac{m}{(n-m)}\frac{L^{\mathrm{fcc}}(\frac{n}{2},\gamma)}{L^{\mathrm{hcp}}(\frac{n}{2},\gamma)} - 1\right] E_{\mathrm{coh}}^{\mathrm{hcp}\,*}(a^*_{\mathrm{min}},n,m,\gamma)\ .
\end{aligned}
$$

A similar analysis can be done for the bulk modulus and the Einstein frequency.

Appendix S

Entropy for Crystal Lattices from Statistical Thermodynamics

The equations for the thermodynamic functions of a crystal lattice with atoms interacting through a potential such as the (n,m)-LJ potentials can be obtained from the thermodynamic partition function, Z, in the canonical ensemble. Starting from the Schrödinger equation of a lattice, the first approximation to introduce is the Born-Oppenheimer approximation, enabling us to separate the vibrational, electronic and nuclear degrees of freedom. Then, for a crystal, the total energy is $E = E_{\text{el}} + E_{\text{vib}} + E_{\text{nuc}}$. Since under standard conditions of temperature and pressure the nuclei are in their nuclear ground state, the nuclear energy becomes just an additive constant that drops out when taking energy differences between two crystals of the same composition (here we neglect nuclear spin effects). Hence, we only need to consider the electronic energy defining the potential energy hypersurface $V(\mathbf{R})$ in which the nuclei move, and the energy due to their relative motion by solving the vibrational Schrödinger equation

$$\left[\sum_I \frac{\nabla^2_{\mathbf{R}_I}}{2M_I} + V(\mathbf{R}) - E_{\text{vib}}(\mathbf{R})\right]\chi(\mathbf{R}) = 0 \tag{S.1}$$

with the nuclear coordinates $\mathbf{R}$ and $\chi(\mathbf{R})$ being the wavefunction for the nuclear motion. $V(\mathbf{R})$ can be obtained from first-principles electronic structure methods fit to an empirical potential such as the (m,n)-LJ potential.

All thermodynamic functions for a lattice at finite T can be derived from the partition function[196]

$$Z = \text{Tr}\left(e^{-\beta\hat{H}}\right) = \sum_n g_n e^{-\beta E_n} \tag{S.2}$$

where the Hamiltonian is written in the eigenstate basis, g_n is the degeneracy of the n-th energy level and $\beta = 1/k_B T$. Since the energy is separated into vibrational and electronic contributions (neglecting nuclear contributions), the partition function is written as the product

of $Z = Z_{\text{vib}} Z_{\text{el}}$, with

$$Z_{\text{el}} = \sum_i g_n e^{-\beta E_i} \approx g_1 + g_2 e^{-\beta \Delta E_{12}} \tag{S.3}$$

for well spaced energy levels at lower temperatures, where ΔE_{12} is the energy difference to the 2nd energy level (first excited state) with respect to the ground state which is arbitrarily set to zero. ΔE_{12} is typically in the range of a few eV and the electronic term in the partition function therefore vanishes for relatively low temperatures even for metallic systems where the electronic band gap is zero[127]. Hence, only the first vibrational term is important for us, although we will keep the second term here for completeness.

For the vibrational contribution, let $\phi(r)$ be a two-body potential, such as LJ, describing the energy hypersurface in which the nuclei move. Then, a Taylor expansion around the equilibrium positions of the atoms in a lattice gives

$$V = V_{\text{eq}} + \frac{1}{2} \sum_{\boldsymbol{\ell},\kappa} \sum_{\boldsymbol{\ell}',\kappa'} \left(\frac{\partial^2 \phi_{\kappa\kappa'}(\boldsymbol{\ell}, \boldsymbol{\ell}')}{\partial \mathbf{u}_\kappa(\boldsymbol{\ell}) \partial \mathbf{u}_{\kappa'}(\boldsymbol{\ell}')} \right)_{\mathbf{u}=0} \mathbf{u}_\kappa(\boldsymbol{\ell}) \mathbf{u}_\kappa(\boldsymbol{\ell}) + \dots \tag{S.4}$$

where $\mathbf{u}_\kappa(\boldsymbol{\ell})$ is the displacement from equilibrium of the κ-th atom in the $\boldsymbol{\ell}$-th unit cell. All terms explicitly shown in Eq.(S.4) constitute the harmonic approximation. Higher-order anharmonic corrections become more important at higher temperatures or for weakly interacting systems. In this respect, the atom confinement in a solid makes the vibrations more harmonic compared to a diatomic molecule. From the second derivatives is it possible to find the dynamic matrix and then calculate the (mass-dependent) phonon frequencies by using Eq. (11.37).

The quantum levels (energy eigenvalues) of a crystal within the harmonic approximation are given by

$$E_{\{n_{\mathbf{k}j}\}} = E_{\text{eq}} + \sum_{\mathbf{k},j} \hbar \omega_j(\mathbf{k}) \left(n_{\mathbf{k}j} + \frac{1}{2} \right) \tag{S.5}$$

with the first term being a static contribution to the partition function such as the cohesive energy, i.e. the energy of the lattice in the equilibrium configuration, and the second term being the dynamic contribution. The dynamic part contains all the $3N$ phonon branches at the $\mathbf{k}$ points within the first Brillouin zone for our Barlow packings. Therefore, the vibrational partition function is

$$Z_{\text{vib}} = e^{-\beta E_{\text{eq}}} \prod_{\mathbf{k},j} \frac{e^{-\beta \hbar \omega_j(\mathbf{k})/2}}{1 - e^{-\beta \hbar \omega_j(\mathbf{k})}} \tag{S.6}$$

Consequently, all thermodynamic functions can be written separately into vibrational and electronic contributions. The internal energy of the crystal is given by

$$U = E_{\text{eq}} + \sum_{\mathbf{k},j} \left[\frac{\hbar \omega_j(\mathbf{k})}{2} - \frac{\hbar \omega_j(\mathbf{k})}{1 - e^{\beta \hbar \omega_j(\mathbf{k})}} \right] - \frac{1}{\beta} \left[\frac{1}{\beta} \ln Z_{\text{el}} + \frac{g_2 \Delta E_{12} e^{-\beta \Delta E_{12}}}{Z_{\text{el}}} \right], \tag{S.7}$$

the entropy by

$$S = -k_B \left\{ \sum_{\mathbf{k},j} \left[\frac{\beta\hbar\omega_j(\mathbf{k})}{(1 - e^{\beta\hbar\omega_j(\mathbf{k})})} + \ln\left(1 - e^{-\beta\hbar\omega_j(\mathbf{k})}\right) \right] + T \ln Z_{\text{el}} - \frac{g_2 \Delta E_{12} e^{-\beta\Delta E_{12}}}{Z_{\text{el}}} \right\}, \tag{S.8}$$

and the Helmholtz free energy $F = U - TS$ by

$$F = E_{\text{eq}} + \sum_{\mathbf{k},j} \left[\frac{\hbar\omega_j(\mathbf{k})}{2} - \frac{1}{\beta} \ln\left(1 - e^{-\beta\hbar\omega_j(\mathbf{k})}\right) \right] - \frac{1}{\beta} \ln Z_{\text{el}} \tag{S.9}$$

The vibrational part of eq.(S.8) was used in all our LJ phonon dispersion calculations using the code introduced in Ref. 580 and in our DFT calculations for argon using Phonopy[607].

In CDLT one treats the vibrations in a lattice classically. Within the harmonic approximation, this leads to the following expression for the vibrational entropy (see Ref. 110 for a detailed derivation)

$$\frac{S_{vib}}{N_A k_B} = \frac{3}{2} \ln\left(\frac{2\pi e^2 L^2}{\beta\epsilon\lambda_T^2}\right) - \frac{1}{2N} \sum_{j,\mathbf{k}} \ln\left(\frac{ML^2}{\epsilon}\omega_j^2(\mathbf{k})\right) . \tag{S.10}$$

where $\lambda_T = h/p_T = h/\sqrt{2\pi k_B T}$ the thermal wavelength (p_T the classical thermal momentum coming from the kinetic energy term), N_A the number of atoms, e is Euler's number ($\ln e = 1$), and ϵ and L are an arbitrary energy (e.g. the dissociation energy for a LJ potential) and length (e.g. the equilibrium length r_e or hard-sphere radius σ for a LJ potential) used to render the dynamic matrix dimensionless. The relation to the the quantum formula for the vibrational entropy of a mode is given by the Taylor expansion

$$\frac{S_{vib}}{k_B} = \left(\frac{x}{e^x - 1} - \ln(1 - e^{-x})\right) \approx 1 - \ln(x) = \ln(x/e) \tag{S.11}$$

with $x = \beta\hbar\omega$, where the rhs is the classical result. This relates exactly to the high temperature limit we discussed in the main part of the paper. Therefore, the classical vibrational entropy for very large particle numbers N_A is

$$\begin{aligned} \frac{S_{vib}}{Nk_B} &= 3 \ln\left(\frac{2\pi e}{h\beta}\right) - \frac{1}{2N} \sum_{\lambda,\mathbf{k}} \ln(\omega_\lambda^2(\mathbf{k})) \\ &= \frac{3}{2} \ln\left(\frac{2\pi e^2 L^2}{\beta\lambda\epsilon_T^2}\right) - \frac{1}{2N} \sum_{\lambda,\mathbf{k}} \ln\left(\frac{L^2}{\epsilon} M\omega_\lambda^2(\mathbf{k})\right) \end{aligned} \tag{S.12}$$

and the entropy computed by Eq. (S.11) becomes identical to the one computed by classical statistical mechanics Eq. (S.10). The first term (kinetic term) drops out for entropy differences ΔS_{vib} between different phases at constant temperature and the ΔS_{vib} becomes independent of the temperature T.

The entropy of particles interacting with an inverse power law potential,

$$V(r) = \varepsilon \left(\frac{\sigma}{r}\right)^p \tag{S.13}$$

can be easily derived within CDLT and is given by[110]

$$\frac{S_{vib}}{Nk_B} = \ln\left(\frac{V}{N}\frac{e}{\lambda_T^3}\right) + 3 - \frac{p}{2}\ln(\gamma_p) - b(p)\,, \tag{S.14}$$

where $\gamma_p = \frac{N}{V}\sigma^3\,(\beta\epsilon)^{3/p}$, $\frac{N}{V} = \frac{c_L}{R_{NN}^2}$, R_{NN} is the nearest neighbor particle distance. c_L depends on the particular lattice (fcc or hcp in our case). Using these relations, we get

$$\frac{S_{vib}}{Nk_B} = \ln\left(e^3\left(\frac{\sigma}{\lambda_T^3}\right)^3(\beta\epsilon)^{3/2}\right) + 1 + \ln\left(\left(c_L\left(\frac{\sigma}{R_{NN}}\right)^3\right)^{-\frac{p}{2}+1}\right) - b(p) \tag{S.15}$$

If we choose $L = \sigma$ then Eq. (S.10) (or Eq. (S.12)) becomes

$$\frac{S_{vib}}{Nk_B} = \ln\left(e^3\left(\frac{\sigma}{\lambda_T}\right)^3(2\pi\beta\epsilon)^{3/2}\right) - \frac{1}{2N}\sum_{\lambda,\mathbf{k}}\ln\left(\frac{M\sigma^2\omega_\lambda^2(\mathbf{k})}{\varepsilon}\right) \tag{S.16}$$

For entropy differences at constant T only the last two terms in (S.16) survive. Comparing both formulas we have

$$b(p) = 1 + \ln\left((2\pi)^{-3/2}\left(c_L\left(\frac{\sigma}{R_{NN}}\right)^3\right)^{-\frac{p}{2}+1}\right) + \frac{1}{2N}\sum_{\lambda,\mathbf{k}}\ln\left(\frac{M\sigma^2\omega_\lambda^2(\mathbf{k})}{\varepsilon}\right) \tag{S.17}$$

This function is evaluated by the program HOODLT[110] for inverse power potentials, and provides the values quoted in Table II of Ref. 110. The approximate value chosen in Ref. 110 for the nearest neighbor distance was $R_{NN} = \sigma$. A comparison shows that for the (12,6)-LJ potential we have $\sigma = 2^{-1/6}r_e = 0.8909r_e$ and for the fcc lattice we have $R_{NN} = 0.9713r_e$ evaluated through exact lattice summations. Further, R_{NN} changes due to anharmonicity effects in the zero-point vibrational term and for finite temperatures.

Using HOODLT we get the following entropy differences between the fcc and hcp phases: $\Delta S^{(6,4)} = 4.7131 \times 10^{-3}\,k_B$, $\Delta S^{(12,6)} = 2.8532 \times 10^{-3}\,k_B$, $\Delta S^{(30,12)} = 1.8267 \times 10^{-3}\,k_B$, $\Delta S^{(30,20)} = 1.7436 \times 10^{-3}\,k_B$, and $\Delta S^{(100,25)} = 1.5412 \times 10^{-3}\,k_B$. Our calculated value for the (100,25)-LJ potential is close to the hard-sphere limit of $\Delta S = 1.4754 \times 10^{-3}k_B$ reported in Ref. 110. Beside the difference in magnitude compared to our DFT or LJ results including phonon dispersion, we qualitatively agree with these results, that is fcc is entropically preferred compared to hcp. However, it is clear that the CDLT formalism used in Ref. 110 underestimates the fcc/hcp

entropy differences for the LJ potentials. This can be directly linked through Eq.(11.46) to the difference in the phonon frequencies.

Appendix T

The Iterative Newton-Raphson Algorithm for Barlow Packings

The iterative Newton–Raphson algorithm[481] was used to minimize the cohesive energy with respect to a set of lattice parameters $\{\gamma_i\}$ ($\vec{\gamma} = (\gamma_1, ..., \gamma_N)$),

$$\vec{\gamma}^{(I+1)} = \vec{\gamma}^{(I)} - \lambda \left[(\partial_{\gamma_i} \partial_{\gamma_j}) E^*_{nm}(\{\gamma_i^{(I)}\}) \right]^{-1} \vec{\nabla} E^*_{nm}(\{\gamma_i^{(I)}\}) \,, \tag{T.1}$$

For the Hessian and gradient of the total cohesive energy $E^{\boldsymbol{X}}_{nm}(\{\gamma_i\})$ for a specific periodic Barlow packing with sequence $\boldsymbol{X}$ we require the following derivatives

$$\begin{aligned}
\partial_{\gamma_j} E^{\boldsymbol{X}}_{nm}(\{\gamma_i\}) = \frac{1}{2(n-m)} \Bigg\{ & m \left(\frac{L^{\boldsymbol{X}}(\frac{m}{2}, \{\gamma_i\})}{L^{\boldsymbol{X}}(\frac{n}{2}, \{\gamma_i\})} \right)^{\frac{n}{n-m}} \partial_{\gamma_j} L^{\boldsymbol{X}}(\tfrac{n}{2}, \{\gamma_i\}) \\
& - n \left(\frac{L^{\boldsymbol{X}}(\frac{m}{2}, \{\gamma_i\})}{L^{\boldsymbol{X}}(\frac{n}{2}, \{\gamma_i\})} \right)^{\frac{m}{n-m}} \partial_{\gamma_j} L^{\boldsymbol{X}}(\tfrac{m}{2}, \{\gamma_i\}) \Bigg\}
\end{aligned} \tag{T.2}$$

$$\begin{aligned}
\partial_{\gamma_j} \partial_{\gamma_k} E^{\boldsymbol{X}}_{nm}(\{\gamma_i\}) = & \frac{nm}{2(n-m)^2} \left[\frac{\partial_{\gamma_k} L^{\boldsymbol{X}}(\frac{m}{2}, \{\gamma_i\})}{L^{\boldsymbol{X}}(\frac{m}{2}, \{\gamma_i\})} - \frac{\partial_{\gamma_k} L^{\boldsymbol{X}}(\frac{n}{2}, \{\gamma_i\})}{L^{\boldsymbol{X}}(\frac{n}{2}, \{\gamma_i\})} \right] \\
& \times \left[\left(\frac{L^{\boldsymbol{X}}(\frac{m}{2}, \{\gamma_i\})}{L^{\boldsymbol{X}}(\frac{n}{2}, \{\gamma_i\})} \right)^{\frac{n}{n-m}} \partial_{\gamma_j} L^{\boldsymbol{X}}(\tfrac{n}{2}, \{\gamma_i\}) - \left(\frac{L^{\boldsymbol{X}}(\frac{m}{2}, \{\gamma_i\})}{L^{\boldsymbol{X}}(\frac{n}{2}, \{\gamma_i\})} \right)^{\frac{m}{n-m}} \partial_{\gamma_j} L^{\boldsymbol{X}}(\tfrac{m}{2}, \{\gamma_i\}) \right] \\
& + \frac{1}{2(n-m)} \Bigg\{ m \left(\frac{L^{\boldsymbol{X}}(\frac{m}{2}, \{\gamma_i\})}{L^{\boldsymbol{X}}(\frac{n}{2}, \{\gamma_i\})} \right)^{\frac{n}{n-m}} \partial_{\gamma_k} \partial_{\gamma_j} L^{\boldsymbol{X}}(\tfrac{n}{2}, \{\gamma_i\}) \\
& - n \left(\frac{L^{\boldsymbol{X}}(\frac{m}{2}, \{\gamma_i\})}{L^{\boldsymbol{X}}(\frac{n}{2}, \{\gamma_i\})} \right)^{\frac{m}{n-m}} \partial_{\gamma_k} \partial_{\gamma_j} L^{\boldsymbol{X}}(\tfrac{m}{2}, \{\gamma_i\}) \Bigg\} .
\end{aligned} \tag{T.3}$$

and in general for the Barlow lattice sum derivatives,

$$\partial_{\gamma_k}^{n_1}\partial_{\gamma_j}^{n_2}L^{\mathbf{X}}(s,\{\gamma_i\}) = \left\{\partial_{\gamma_k}^{n_1}\partial_{\gamma_j}^{n_2}L^{A}(s,\{\gamma_i\}) + \frac{2}{N}\sum_{k_1<k_2}^{N}\partial_{\gamma_k}^{n_1}\partial_{\gamma_j}^{n_2}L^{X_{k_1}X_{k_2}}(s,\{\gamma_i\})\right\} \tag{T.4}$$

with $n_1, n_2 \in \{0,1,2\}, n_1+n_2 \leq 2$. This leads to the simple condition for the minimum through the first derivative

$$nL(\tfrac{n}{2},\{\gamma_i\})\partial_{\gamma_j}L(\tfrac{m}{2},\{\gamma_i\}) - mL(\tfrac{m}{2},\{\gamma_i\})\partial_{\gamma_j}L(\tfrac{n}{2},\{\gamma_i\}) = 0\,. \tag{T.5}$$

Here we define $\partial_x f(x) = \partial f(x)/\partial x$. In the case where we do not consider symmetry breaking effects between the hexagonal layers we only consider the derivatives with respect to γ_T. The gradient and Hessian is obtained analytically as discussed in the next section.

Eq.(T.1) is converging very fast. Only few iterations are required to achieve convergence to computer accuracy. For example, we start with $\gamma_i^{(1)} = \sqrt{\frac{2}{3}}$ for all γ_i of the Barlow structures, and for the hcp structure with $\gamma_1 = \gamma_2$ we obtain after the first iteration $\gamma_1^{(2)} = 0.816381646735$ very close to the converged result after 2 iterations with $\gamma_1^{(3)} = 0.81638165246885$.

Appendix U

Tables for Cohesive Energies and Optimized Parameters

Table U.1: Difference in cohesive energies relative to the hcp structure for different Barlow structures and various (n,m)-LJ potentials at fixed $\gamma_i = \sqrt{\frac{2}{3}}$. Notice that $s = n/2$. For the hcp structure the cohesive energy is shown in bold (in reduced units). For the corresponding energy differences at the optimized γ_i values see supporting information.

No.	Stacking	(6,4)	(8,4)	(12,4)	(12,6)	(30,6)	(30,20)
1	AB	**-38.9325305486602**	**-25.0752959432072**	**-18.3098535057780**	**-8.6110697321365**	**-7.5716717703337**	**-6.00928320286815**
2	ABC	-1.672643684e-3	-1.927682096e-4	5.312237310e-4	8.695754328e-4	6.391322107e-4	4.328621270e-5
3	ABAC	-8.361267034e-4	-9.576506098e-5	2.661869698e-4	4.352966307e-4	3.198626830e-4	2.164359436e-5
4	ABABC	-1.003484319e-3	-1.154063871e-4	3.189655319e-4	5.219509746e-4	3.835991612e-4	2.597193729e-5
5	ABABAC	-5.574080672e-4	-6.384034753e-5	1.774586756e-4	2.901987369e-4	2.132423385e-4	1.442906866e-5
6	ABACBC	-1.114955978e-3	-1.280964162e-4	3.545332527e-4	5.800572110e-4	4.262864076e-4	2.885780622e-5
7	ABABABC	-7.167628667e-4	-8.243041752e-5	2.278325291e-4	3.728228336e-4	2.739997973e-4	1.855139134e-5
8	ABABCBC	-7.167176386e-4	-8.225535352e-5	2.279974317e-4	3.729679322e-4	2.740843632e-4	1.855152345e-5
9	ABACABC	-1.194623895e-3	-1.373351599e-4	3.797744533e-4	6.214168958e-4	4.566929165e-4	3.091900854e-5
10	ABABABAC	-4.180527461e-4	-4.787949084e-5	1.330940083e-4	2.176492541e-4	1.599318664e-4	1.082180364e-5
11	ABABACAC	-4.180520536e-4	-4.787876063e-5	1.330945268e-4	2.176495887e-4	1.599320542e-4	1.082180366e-5
12	ABABACBC	-8.362030818e-4	-9.606850383e-5	2.659004636e-4	4.350440465e-4	3.197154429e-4	2.164336327e-5
13	ABABCBAC	-8.361645464e-4	-9.591641730e-5	2.660439760e-4	4.351705059e-4	3.197891564e-4	2.164347883e-5
14	ABABCABC	-1.254413141e-3	-1.444156842e-4	3.985623595e-4	6.523105080e-4	4.794242568e-4	3.246479443e-5
15	ABACBABC	-1.254374610e-3	-1.442635974e-4	3.987058720e-4	6.524369655e-4	4.794979699e-4	3.246490999e-5
16	ABABABABC	-5.574771992e-4	-6.411137373e-5	1.772030807e-4	2.899736212e-4	2.131111247e-4	1.442886320e-5
17	ABABABCBC	-5.574420178e-4	-6.397521224e-5	1.773313386e-4	2.900864763e-4	2.131768984e-4	1.442896595e-5
18	ABABCBCAC	-5.574071464e-4	-6.383937598e-5	1.774593657e-4	2.901991824e-4	2.132425885e-4	1.442906869e-5
19	ABABACABC	-9.291373243e-4	-1.068123280e-4	2.953805980e-4	4.833254002e-4	3.552062442e-4	2.404812685e-5
20	ABABCBABC	-9.291027654e-4	-1.066768168e-4	2.955083939e-4	4.834379566e-4	3.552718505e-4	2.404822958e-5
21	ABABCACBC	-9.291024568e-4	-1.066764916e-4	2.955086248e-4	4.834381056e-4	3.552719341e-4	2.404822959e-5
22	ABACBCABC	-1.300847973e-3	-1.496527692e-4	4.134300799e-4	6.765635216e-4	4.972351413e-4	3.366727759e-5
23	ABABABABAC	-3.344406108e-4	-3.830322317e-5	1.064752074e-4	1.741194999e-4	1.279455471e-4	8.657443938e-5
24	ABABABACAC	-3.344400568e-4	-3.830263900e-5	1.064756222e-4	1.741197676e-4	1.279456974e-4	8.657443958e-5
25	ABABABACBC	-6.689561241e-4	-7.685332484e-5	2.127203740e-4	3.480356232e-4	2.557725701e-4	1.731469472e-5
26	ABABABCBAC	-6.689252934e-4	-7.673165551e-5	2.128351843e-4	3.481367913e-4	2.558315411e-4	1.731478718e-5
27	ABABACACBC	-6.689247409e-4	-7.673107215e-5	2.128355983e-4	3.481370585e-4	2.558316912e-4	1.731478720e-5
28	ABABACABAC	-6.688944643e-4	-7.660998656e-5	2.129499938e-4	3.482379589e-4	2.558905119e-4	1.731487963e-5
29	ABABACBCBC	-6.689555716e-4	-7.685274192e-5	2.127207881e-4	3.480358905e-4	2.557727202e-4	1.731469475e-5
30	ABABCBABAC	-6.688939118e-4	-7.660940363e-5	2.129504078e-4	3.482382262e-4	2.558906619e-4	1.731487964e-5
31	ABABABCABC	-1.003516248e-3	-1.155292204e-4	3.188498951e-4	5.218492734e-4	3.835398908e-4	2.597184480e-5
32	ABABACBABC	-1.003484870e-3	-1.154069688e-4	3.189651187e-4	5.219507077e-4	3.835990114e-4	2.597193727e-5
33	ABABCBCABC	-1.003484593e-3	-1.154066767e-4	3.189653261e-4	5.219508415e-4	3.835990866e-4	2.597193728e-5
34	ABABCBACBC	-1.003453765e-3	-1.152850068e-4	3.190801364e-4	5.220520089e-4	3.836580574e-4	2.597202973e-5
35	ABABCACABC	-1.003484317e-3	-1.154063859e-4	3.189655327e-4	5.219509750e-4	3.835991615e-4	2.597193729e-5
36	ABACABACBC	-1.003423213e-3	-1.151636277e-4	3.191947401e-4	5.221530429e-4	3.837169533e-4	2.597212217e-5
37	ABACABCABC	-1.338027118e-3	-1.539644410e-4	4.252092379e-4	6.958646215e-4	5.114247970e-4	3.462917155e-5
38	ABACBACABC	-1.338026842e-3	-1.539641501e-4	4.252094446e-4	6.958647550e-4	5.114248719e-4	3.462917156e-5
39	ABABABABABC	-4.561150873e-4	-5.245414948e-5	1.449843400e-4	2.372513040e-4	1.743637366e-4	1.180543522e-5
40	ABABABABABAC	-2.786996279e-4	-3.191914736e-5	8.872933992e-5	1.450996370e-4	1.066213193e-4	7.214537187e-6

Table U.2: Difference $\Delta\gamma = \frac{1}{N}\gamma_T^{\mathrm{opt}} - \gamma_0$ values (in units of 10^{-4}) with $\gamma_0 = \sqrt{\frac{2}{3}}$ and corresponding change in the cohesive energy $\Delta E_{\mathrm{coh}} = E_{\mathrm{coh}}(\gamma_T) - E_{\mathrm{coh}}(\gamma_0)$ (in units of 10^{-6}) for case 2 (see main text). For case 3 see supporting information.

		(6,4)		(8,4)		(12,4)		(12,6)		(30,6)		(30,20)	
No.	Stacking	$\Delta\gamma$	ΔE_{coh}	$\Delta\gamma$	ΔE_{coh}	$\Delta\gamma$	ΔE_{coh}	$\Delta\gamma$	ΔE_{coh}	$\Delta\gamma$	ΔE_{coh}	$\Delta\gamma$	ΔE_{coh}
1	AB	1.53893	-2.12134	0.32733	-0.08054	-0.43794	-0.15266	-1.14928	-0.72723	-0.42157	-0.20603	-0.01541	-0.00071
2	ABC	0.00000	0.00000	0.00000	0.00000	0.00000	0.00000	0.00000	0.00000	0.00000	0.00000	0.00000	0.00000
3	ABAC	0.77058	-0.53124	0.16460	-0.02036	-0.21812	-0.03788	-0.57317	-0.18101	-0.21044	-0.05135	-0.00771	-0.00018
4	ABABC	0.61658	-0.34004	0.13135	-0.01296	-0.17480	-0.02433	-0.45888	-0.11604	-0.16846	-0.03291	-0.00617	-0.00011
5	ABABAC	1.02692	-0.94384	0.21886	-0.03600	-0.29138	-0.06759	-0.76511	-0.32247	-0.28080	-0.09143	-0.01028	-0.00032
6	ABACBC	0.51394	-0.23622	0.10975	-0.00905	-0.14540	-0.01683	-0.38201	-0.08043	-0.14028	-0.02282	-0.00514	-0.00008
7	ABABABC	0.88040	-0.69356	0.18737	-0.02638	-0.24997	-0.04975	-0.65601	-0.23709	-0.24076	-0.06721	-0.00881	-0.00023
8	ABABCBC	0.88043	-0.69362	0.18761	-0.02645	-0.24974	-0.04966	-0.65571	-0.23688	-0.24068	-0.06717	-0.00881	-0.00023
9	ABACABC	0.44058	-0.17357	0.09407	-0.00665	-0.12463	-0.01237	-0.32742	-0.05909	-0.12024	-0.01677	-0.00440	-0.00006
10	ABABABAC	1.15500	-1.19421	0.24598	-0.04547	-0.32801	-0.08565	-0.86112	-0.40842	-0.31599	-0.11577	-0.01156	-0.00040
11	ABABACAC	1.15500	-1.19421	0.24599	-0.04547	-0.32801	-0.08565	-0.86111	-0.40842	-0.31599	-0.11577	-0.01156	-0.00040
12	ABABACBC	0.77052	-0.53116	0.16417	-0.02025	-0.21851	-0.03802	-0.57368	-0.18134	-0.21058	-0.05142	-0.00771	-0.00018
13	ABABCBAC	0.77055	-0.53120	0.16438	-0.02030	-0.21832	-0.03795	-0.57343	-0.18118	-0.21051	-0.05139	-0.00771	-0.00018
14	ABABCABC	0.38551	-0.13288	0.08210	-0.00506	-0.10924	-0.00950	-0.28673	-0.04532	-0.10528	-0.01285	-0.00385	-0.00005
15	ABACBABC	0.38554	-0.13290	0.08232	-0.00509	-0.10905	-0.00947	-0.28647	-0.04524	-0.10521	-0.01284	-0.00385	-0.00005
16	ABABABABC	1.02686	-0.94374	0.21848	-0.03587	-0.29173	-0.06775	-0.76557	-0.32285	-0.28093	-0.09151	-0.01028	-0.00032
17	ABABABCBC	1.02689	-0.94379	0.21867	-0.03593	-0.29155	-0.06767	-0.76534	-0.32266	-0.28087	-0.09147	-0.01028	-0.00032
18	ABABCBCAC	1.02692	-0.94384	0.21886	-0.03600	-0.29138	-0.06759	-0.76511	-0.32246	-0.28080	-0.09143	-0.01028	-0.00032
19	ABABACABC	0.68500	-0.41974	0.14594	-0.01600	-0.19423	-0.03004	-0.50990	-0.14327	-0.18718	-0.04063	-0.00685	-0.00014
20	ABABCBABC	0.68503	-0.41978	0.14613	-0.01604	-0.19405	-0.02998	-0.50967	-0.14314	-0.18712	-0.04060	-0.00685	-0.00014
21	ABABCACBC	0.68503	-0.41978	0.14613	-0.01604	-0.19405	-0.02998	-0.50967	-0.14314	-0.18712	-0.04060	-0.00685	-0.00014
22	ABACBCABC	0.34273	-0.10502	0.07317	-0.00402	-0.09693	-0.00748	-0.25463	-0.03574	-0.09351	-0.01014	-0.00342	-0.00004
23	ABABABABAC	1.23183	-1.35852	0.26226	-0.05169	-0.35000	-0.09751	-0.91873	-0.46487	-0.33710	-0.13176	-0.01233	-0.00046
24	ABABABACAC	1.23183	-1.35852	0.26226	-0.05169	-0.35000	-0.09751	-0.91873	-0.46487	-0.33710	-0.13176	-0.01233	-0.00046
25	ABABABACBC	0.92436	-0.76461	0.19681	-0.02911	-0.26239	-0.05481	-0.68873	-0.26133	-0.25277	-0.07409	-0.00925	-0.00026
26	ABABABCBAC	0.92438	-0.76465	0.19698	-0.02916	-0.26223	-0.05475	-0.68853	-0.26117	-0.25271	-0.07405	-0.00925	-0.00026
27	ABABACACBC	0.92439	-0.76465	0.19699	-0.02916	-0.26223	-0.05475	-0.68853	-0.26117	-0.25271	-0.07405	-0.00925	-0.00026
28	ABABACABAC	0.92441	-0.76469	0.19716	-0.02921	-0.26208	-0.05468	-0.68832	-0.26101	-0.25266	-0.07402	-0.00925	-0.00026
29	ABABACBCBC	0.92436	-0.76461	0.19682	-0.02911	-0.26239	-0.05481	-0.68873	-0.26133	-0.25277	-0.07409	-0.00925	-0.00026
30	ABABCBABAC	0.92441	-0.76469	0.19716	-0.02921	-0.26207	-0.05468	-0.68832	-0.26101	-0.25266	-0.07402	-0.00925	-0.00026
31	ABABABCABC	0.61655	-0.34001	0.13118	-0.01293	-0.17496	-0.02437	-0.45908	-0.11614	-0.16851	-0.03293	-0.00617	-0.00011
32	ABABACBABC	0.61658	-0.34003	0.13135	-0.01296	-0.17480	-0.02433	-0.45888	-0.11604	-0.16846	-0.03291	-0.00617	-0.00011
33	ABABCBCABC	0.61658	-0.34004	0.13135	-0.01296	-0.17480	-0.02433	-0.45888	-0.11604	-0.16846	-0.03291	-0.00617	-0.00011
34	ABABCBACBC	0.61660	-0.34006	0.13152	-0.01300	-0.17464	-0.02429	-0.45867	-0.11593	-0.16840	-0.03289	-0.00616	-0.00011
35	ABABCACABC	0.61658	-0.34004	0.13135	-0.01296	-0.17480	-0.02433	-0.45888	-0.11604	-0.16846	-0.03291	-0.00617	-0.00012
36	ABACABACBC	0.61662	-0.34009	0.13169	-0.01303	-0.17449	-0.02424	-0.45847	-0.11583	-0.16834	-0.03286	-0.00616	-0.00011
37	ABACABCABC	0.30847	-0.08507	0.06586	-0.00326	-0.08723	-0.00606	-0.22916	-0.02895	-0.08416	-0.00822	-0.00308	-0.00003
38	ABACBACABC	0.30847	-0.08507	0.06586	-0.00326	-0.08723	-0.00606	-0.22916	-0.02895	-0.08416	-0.00822	-0.00308	-0.00003
39	ABABABABABC	1.12003	-1.12293	0.23828	-0.04267	-0.31831	-0.08066	-0.83530	-0.38431	-0.30650	-0.10892	-0.01121	-0.00038
40	ABABABABABAC	1.28303	-1.47393	0.27310	-0.05606	-0.36465	-0.10585	-0.95715	-0.50453	-0.35118	-0.14299	-0.01284	-0.00050

Bibliography

[1] F. M. Cornford, *Plato's Cosmology: The Timaeus of Plato*, Hackett Publishing Company **1997**.

[2] D. Richeson, *Euler's Gem: The Polyhedron Formula and the Birth of Topology*, Princeton Science Library, Princeton University Press **2019**.

[3] A. Authier, *Early Days of X-ray Crystallography*, International Union of Crystallography Texts on Crystallography, OUP Oxford **2013**.

[4] M. Senechal, *Mathematics Magazine* **1981**, *54*, 227.

[5] B. Grünbaum, *Geombinatorics* **1994**, *4*, 49.

[6] A. Loeb, *Space structures*, Springer Science & Business Media **2012**.

[7] S. I. Tomkeieff, *Mineralogical magazine and journal of the Mineralogical Society* **1942**, *26*, 172.

[8] P. Ball, *Nature* **2011**, *480*, 455.

[9] D. Weaire, T. Aste, *The pursuit of perfect packing*, CRC Press **2008**.

[10] T. C. Hales, *Annals of Mathematics* **2005**, *162*, 1065.

[11] T. Hales, M. Adams, G. Bauer, T. D. Dang, J. Harrison, L. T. Hoang, C. Kaliszyk, V. Magron, S. McLaughlin, T. Nguyen, et al., *Forum of Mathematics, Pi* **2017**, *5*, e2.

[12] D. Hilbert, *Nachrichten von der Königlichen Gesellschaft der Wissenschaften zu Göttingen* **1900**.

[13] J. Limda-de Faria, *Historical Atlas of Crystallography*, Springer Dordrecht **1990**.

[14] R. J. Haüy, *Essai d'une théorie sur la structure des crystaux, appliquée à plusieurs genres de substances crystallisées*, Chez Gogué & Née de la Rochelle **1784**.

[15] R. J. Haüy, *Traité de minéralogie*, Chez Louis **1801**.

[16] F. C. Phillips, *An Introduction to Crystallography*, John Wiley & Sons **1963**.

[17] E. J. W. Whittaker, *Crystallography: An Introduction for Earth Science (and Other Solid State) Students*, Pergammon Press **1981**.

[18] W. Barlow, *Nature* **1884**, *29*.

[19] W. Barlow, *Proceedings of the Physical Society of London* **1897**, *16*, 54.

[20] W. Barlow, W. J. Pope, *Journal of the Chemical Society, Transactions* **1907**, *91*, 1150.

[21] L. Bragg, *The Crystalline State. A General Survey. Vol. I*, G. Bell and Sons Limited **1949**.

[22] P. Tandy, *Proceedings of the Geologists' Association* **2004**, *115*, 77.

[23] S. H. Mauskopf, *Annals of Science* **2015**, *72*, 206.

[24] W. C. Hamilton, *Annual Review of Physical Chemistry* **1962**, *13*, 19.

[25] N. W. Ashcroft, M. N. David, *Solid State Physics*, Thomson Learning, Inc., New York **1976**.

[26] L. A. K. Staveley, *Annual Review of Physical Chemistry* **1962**, *13*, 351.

[27] A. Loidl, *Annual Review of Physical Chemistry* **1989**, *40*, 29.

[28] J. H. Conway, S. N. J. A., *Sphere Packings, Lattices and Groups*, Springer, New York **1999**.

[29] L. Piela, *Ideas of quantum chemistry*, Elsevier **2013**.

[30] P. Drude, *Annalen der Physik* **1900**, *306*, 566.

[31] P. Drude, *Annalen der Physik* **1900**, *308*, 369.

[32] M. H. Müser, S. V. Sukhomlinov, L. Pastewka, *Advances in Physics: X* **2023**, *8*, 2093129.

[33] K. Lejaeghere, V. Van Speybroeck, G. Van Oost, S. Cottenier, *Critical reviews in solid state and materials sciences* **2014**, *39*, 1.

[34] M. Ahlers, *Philosophical Magazine A* **2002**, *82*, 1093.

[35] A. Cuniberti, R. Romero, *Materials Science and Engineering: A* **2003**, *349*, 230.

[36] A. Planes, F.-J. Pérez-Reche, E. Vives, L. Mañosa, *Scripta materialia* **2004**, *50*, 181.

[37] F. J. Pérez-Reche, E. Vives, L. Mañosa, A. Planes, *Physical Review Letters* **2001**, *87*, 195701.

[38] Y. Peng, F. Wang, Z. Wang, A. M. Alsayed, Z. Zhang, A. G. Yodh, Y. Han, *Nature Materials* **2015**, *14*, 101.

[39] J. Thun, L. Seyfarth, J. Senker, R. Dinnebier, J. Breu, *Angewandte Chemie International Edition* **2007**, *46*, 6729.

[40] J.-P. Brog, C.-L. Chanez, A. Crochet, K. M. Fromm, *RSC Advances* **2013**, *3*, 16905.

[41] A. J. Cruz-Cabeza, S. M. Reutzel-Edens, J. Bernstein, *Chemical Society Reviews* **2015**, *44*, 8619.

[42] J. Bauer, S. Spanton, R. Henry, J. Quick, W. Dziki, W. Porter, J. Morris, *Pharmaceutical research* **2001**, *18*, 859.

[43] P. Sacchi, S. E. Wright, P. Neoptolemou, G. I. Lampronti, A. K. Rajagopalan, W. Kras, C. L. Evans, P. Hodgkinson, A. J. Cruz-Cabeza, *Proceedings of the National Academy of Sciences* **2024**, *121*, e2319127121.

[44] T. Ito, H. Ando, T. Suzuki, T. Ogura, K. Hotta, Y. Imamura, Y. Yamaguchi, H. Handa, *Science* **2010**, *327*, 1345.

[45] V. I. Khvorostyanov, J. A. Curry, *The Journal of Physical Chemistry A* **2004**, *108*, 11073.

[46] D. E. Laughlin, K. Hono, *Physical Metallurgy*, Elsevier **2014**.

[47] Liu, Xueyan, Li, Hongwei, Zhan, Mei, *Manufacturing Review* **2018**, *5*, 10.

[48] Q. Wang, L.-M. Wang, M. Z. Ma, S. Binder, T. Volkmann, D. M. Herlach, J. S. Wang, Q. G. Xue, Y. J. Tian, R. P. Liu, *Physical Review B* **2011**, *83*, 014202.

[49] D. M. Herlach, T. Palberg, I. Klassen, S. Klein, R. Kobold, *The Journal of chemical physics* **2016**, *145*.

[50] P. Galenko, V. Ankudinov, K. Reuther, M. Rettenmayr, A. Salhoumi, E. Kharanzhevskiy, *Philosophical Transactions of the Royal Society A* **2019**, *377*, 20180205.

[51] E. Parandi, M. Pero, H. Kiani, *Discover Food* **2022**, *2*, 6.

[52] O. Zheng, L. Zhang, Q. Sun, S. Liu, *Foods* **2024**, *13*, 2773.

[53] D. A. Hanaor, C. C. Sorrell, *Journal of Materials science* **2011**, *46*, 855.

[54] F. Bundy, *The Journal of Chemical Physics* **1963**, *38*, 631.

[55] J. E. Shelby, *Introduction to glass science and technology*, Royal society of chemistry **2020**.

[56] G. Kostorz, *Phase Transformations in Materials*, John Wiley & Sons, Ltd **2001**.

[57] E. Pereloma, D. V. Edmonds, *Phase Transformations in Steels: Fundamentals and Diffusion-Controlled Transformations*, Elsevier **2012**.

[58] E. Pereloma, D. V. Edmonds, *Phase Transformations in Steels: Diffusionless Transformations, High Strength Steels, Modelling and Advanced Analytical Techniques*, Elsevier **2012**.

[59] D. S. Mackenzie, *International Heat Treatment and Surface Engineering* **2008**, *2*, 68.

[60] C. S. Smith, *A history of metallography : the development of ideas on the structure of metals before 1890*, The University of Chicago Press **1960**.

[61] C. S. Smith, *Technology and Culture* **1964**, *5*, 149.

[62] M. Gutnyk, F. Nürnberger, *History of science and technology* **2023**, *13*, 243.

[63] Q. Xing, T. A. Lograsso, M. Ruffoni, C. Azimonte, S. Pascarelli, D. Miller, *Applied Physics Letters* **2010**, *97*.

[64] D. E. Laughlin, *Journal of Phase Equilibria and Diffusion* **2018**, *39*, 274.

[65] G. Krauss, *Steels: processing, structure, and performance*, ASM international **2015**.

[66] H. K. D. H. Bhadeshia, R. W. K. Honeycombe, *Steels: microstructure and properties*, Butterworth-Heinemann **2017**.

[67] J. W. Christian, *Theory of Transformations in Metals and Alloys*, Pergamon Press **1975**.

[68] G. Krauss, *Materials science and engineering: A* **1999**, *273*, 40.

[69] Y. Chen, W. Xiao, K. Jiao, D. Ping, H. Xu, X. Zhao, Y. Wang, *Physical Review Materials* **2018**, *2*, 050601.

[70] G. Nolze, A. Winkelmann, G. Cios, T. Tokarski, *Materials Characterization* **2021**, *175*, 111040.

[71] J. W. Christian, *Proceedings of the Royal Society of London. Series A. Mathematical and Physical Sciences* **1951**, *206*, 51.

[72] R. Johnson Jr, R. Dragsdorf, *Journal of Applied Physics* **1967**, *38*, 618.

[73] P. Tolédano, G. Krexner, M. Prem, H.-P. Weber, V. Dmitriev, *Physical Review B* **2001**, *64*, 144104.

[74] A. Overhauser, *Physical Review Letters* **1984**, *53*, 64.

[75] H. Smith, *Physical Review Letters* **1987**, *58*, 1228.

[76] N. Ashcroft, *Physical Review B* **1989**, *39*, 10552.

[77] W. Schwarz, O. Blaschko, *Physical Review Letters* **1990**, *65*, 3144.

[78] O. Blaschko, V. Dmitriev, G. Krexner, P. Tolédano, *Physical Review B* **1999**, *59*, 9095.

[79] G. J. Ackland, M. Dunuwille, M. Martinez-Canales, I. Loa, R. Zhang, S. Sinogeikin, W. Cai, S. Deemyad, *Science* **2017**, *356*, 1254.

[80] V. Birman, *Applied Mechanics Reviews* **1997**, *50*, 629.

[81] K. Otsuka, C. Wayman, *Shape Memory Materials*, Shape Memory Materials, Cambridge University Press **1999**.

[82] E. Patoor, D. C. Lagoudas, P. B. Entchev, L. C. Brinson, X. Gao, *Mechanics of materials* **2006**, *38*, 391.

[83] J. M. Jani, M. Leary, A. Subic, M. A. Gibson, *Materials & Design (1980-2015)* **2014**, *56*, 1078.

[84] K. Bhattacharya, S. Conti, G. Zanzotto, J. Zimmer, *Nature* **2004**, *428*, 55.

[85] N. Bruno, S. Wang, I. Karaman, Y. Chumlyakov, *Scientific reports* **2017**, *7*, 40434.

[86] A. Ferrari, D. G. Sangiovanni, J. Rogal, R. Drautz, *Physical Review B* **2019**, *99*, 094107.

[87] B. Li, Y. Shen, Q. An, *Acta Materialia* **2020**, *199*, 240.

[88] J. Bowles, J. Mackenzie, *Acta Metallurgica* **1954**, *2*, 129.

[89] J. Mackenzie, u. J. Bowles, *Acta Metallurgica* **1954**, *2*, 138.

[90] C. Wayman, *Metallurgical and Materials Transactions A* **1994**, *25*, 1787.

[91] M. Mamivand, M. A. Zaeem, H. El Kadiri, *Computational Materials Science* **2013**, *77*, 304.

[92] I. Razumov, Y. N. Gornostyrev, M. Katsnelson, *Physics of Metals and Metallography* **2017**, *118*, 362.

[93] A. Yamanaka, *ISIJ International* **2023**, *63*, 395.

[94] R. Meyer, P. Entel, *Physical Review B* **1998**, *57*, 5140.

[95] P. Entel, R. Meyer, K. Kadau, H. Herper, E. Hoffmann, *The European Physical Journal B-Condensed Matter and Complex Systems* **1998**, *5*, 379.

[96] P. Entel, R. Meyer, K. Kadau, *Philosophical Magazine B* **2000**, *80*, 183.

[97] C. Bos, J. Sietsma, B. Thijsse, *Physical Review B* **2006**, *73*, 104117.

[98] P. Entel, K. Kadau, R. Meyer, V. Crisan, H. Ebert, T. C. Germann, P. S. Lomdahl, B. L. Holian, Molecular-dynamics simulations of martensitic transformations, in *Advances in Solid State Physics 40*, pages 345–360, Springer **2007**.

[99] V. A. Yastrebov, M. Fischlschweiger, G. Cailletaud, T. Antretter, *Mechanics Research Communications* **2014**, *56*, 37.

[100] H. Zong, G. Pilania, X. Ding, G. J. Ackland, T. Lookman, *npj Computational Materials* **2018**, *4*, 48.

[101] G. Plummer, M. I. Mendelev, J. W. Lawson, *Physical Review Materials* **2022**, *6*, 123601.

[102] B. Barakat, R. Bacis, F. Carrot, S. Churassy, P. Crozet, F. Martin, J. Verges, *Chemical Physics* **1986**, *102*, 215.

[103] A. Burrows, S. Cooper, P. Schwerdtfeger, *Physical Review E* **2021**, *104*, 035306.

[104] P. Schwerdtfeger, R. Tonner, G. E. Moyano, E. Pahl, *Angewandte Chemie International Edition* **2016**, *55*, 12200.

[105] D. Weaire, *Journal of Physics C: Solid State Physics* **1968**, *1*, 210.

[106] M. Hasegawa, M. Moriyama, M. Watabe, W. H. Young, *Journal of the Physical Society of Japan* **1988**, *57*, 1308.

[107] U. Häussermann, S. Simak, *Physical Review B* **2001**, *64*, 245114.

[108] K. Rościszewski, B. Paulus, P. Fulde, H. Stoll, *Physical Review B* **2000**, *62*, 5482.

[109] G. E. Moyano, P. Schwerdtfeger, K. Rosciszewski, *Physical Review B* **2007**, *75*, 024101.

[110] A. Travesset, *The Journal of Chemical Physics* **2014**, *141*.

[111] J. M. Borwein, *Lattice sums then and now*, 150, Cambridge University Press **2013**.

[112] J. E. Jones, A. E. Ingham, *Proceedings of the Royal Society of London. Series A, Containing Papers of a Mathematical and Physical Character* **1925**, *107*, 636.

[113] P. Epstein, *Mathematische Annalen* **1903**, *56*, 615.

[114] E. C. Titchmarsh, D. R. Heath-Brown, *The theory of the Riemann zeta-function*, Oxford university press **1986**.

[115] E. Madelung, *Physikalische Zeitschrift* **1918**, *19*, 32.

[116] L. Ornstein, F. Zernike, *Proceedings of the Koninklijke Nederlandse Akademie van Wetenschappen (Amsterdam)* **1918**, *21*, 911.

[117] H. A. Bethe, Splitting of terms in crystals, in *Selected Works Of Hans A Bethe: (With Commentary)*, pages 1–72, World Scientific **1997**.

[118] J. Lennard-Jones, B. M. Dent, *Transactions of the Faraday Society* **1928**, *24*, 92.

[119] P. P. Ewald, *Annalen der Physik* **1921**, *369*, 253.

[120] A. Y. Toukmaji, J. A. Board Jr, *Computer Physics Communications* **1996**, *95*, 73.

[121] M. Glasser, *Journal of Mathematical Physics* **1972**, *13*, 1145.

[122] M. Glasser, *Journal of Mathematical Physics* **1973**, *14*, 409.

[123] M. Glasser, *Journal of Mathematical Physics* **1973**, *14*, 701.

[124] I. J. Zucker, *Journal of Physics A: Mathematical, Nuclear and General* **1974**, *7*, 1568.

[125] C. G. J. Jacobi, *Fundamenta nova theoriae functionum ellipticarum*, Cambridge University Press **2012**.

[126] P. Schwerdtfeger, A. Burrows, *The Journal of Physical Chemistry C* **2022**, *126*, 8874.

[127] P. Jerabek, A. Burrows, P. Schwerdtfeger, *Chemical Communications* **2022**, *58*, 13369.

[128] L. Kantorovich, *Quantum Theory of the Solid State: An Introduction*, Springer Science **2004**.

[129] C. Kittel, *Introduction to Solid State Physics*, John Wiley & Sons, Inc., New York **2004**.

[130] H. Wondratschek, U. Müller, *International Tables for Crystallography, Vol. A1*, John Wiley & Sons **2010**.

[131] C. G. Lekkerkerker, Geometry of Numbers **1969**.

[132] T. C. Hales, *Discrete and Computational Geometry* **2001**, *25*, 1.

[133] J. C. Meyer, A. K. Geim, M. I. Katsnelson, K. S. Novoselov, T. J. Booth, S. Roth, *Nature* **2007**, *446*, 60.

[134] T. C. Hales, *The Mathematical Intelligencer* **1994**, *16*, 47.

[135] T. C. Hales, *Discrete and Computational Geometry* **2006**, *36*, 5.

[136] O. Degtyareva, *High Pressure Research* **2010**, *30*, 343.

[137] Y. Sun, L. Zhao, C. J. Pickard, R. J. Hemley, Y. Zheng, M. Miao, *Proceedings of the National Academy of Sciences* **2023**, *120*, e2218405120.

[138] S. Torquato, F. H. Stillinger, *The Journal of Physical Chemistry B* **2001**, *105*, 11849.

[139] S. Torquato, F. H. Stillinger, *Reviews of Modern Physics* **2010**, *82*, 2633.

[140] S. Torquato, et al., *Random heterogeneous materials: microstructure and macroscopic properties*, volume 16, Springer **2002**.

[141] W. Van Saarloos, V. Vitelli, Z. Zeravcic, *Soft Matter: Concepts, Phenomena, and Applications*, Princeton University Press **2024**.

[142] R. J. Ellis, *Trends in Biochemical Sciences* **2001**, *26*, 597.

[143] I. M. Kuznetsova, K. K. Turoverov, V. N. Uversky, *International Journal of Molecular Sciences* **2014**, *15*, 23090.

[144] M. Glazer, G. Burns, A. N. Glazer, *Space groups for solid state scientists*, Elsevier **2012**.

[145] C. Bradley, A. Cracknell, *The mathematical theory of symmetry in solids: representation theory for point groups and space groups*, Oxford University Press **2009**.

[146] S. Melmore, *Nature* **1947**, *159*, 817.

[147] J. H. Conway, N. J. Sloane, *Discrete & computational geometry* **1995**, *13*, 383, this is about defining Barlow packings and the bijection with 3-colorings of the one-dimensional packing (namely ABC, ACB, ABCBC, etc).

[148] M. Pitteri, *International Journal of Plasticity* **1998**, *14*, 139.

[149] M. J. Strutt, *Annalen der Physik* **1928**, *390*, 129.

[150] L. Brillouin, *Journal de Physique et le Radium* **1930**, *1*, 377.

[151] M. Born, R. Oppenheimer, *Annalen der Physik* **1927**, *389*, 457.

[152] F. Jensen, *Introduction to computational chemistry*, John wiley & sons **2017**.

[153] F. Bloch, *Zeitschrift für physik* **1929**, *52*, 555.

[154] P. Hohenberg, W. Kohn, *Physical Review* **1964**, *136*, B864.

[155] W. Kohn, L. J. Sham, *Physical Review* **1965**, *140*, A1133.

[156] R. Peverati, D. G. Truhlar, *Philosophical Transactions of the Royal Society A: Mathematical, Physical and Engineering Sciences* **2014**, *372*, 20120476.

[157] N. Mardirossian, M. Head-Gordon, *Physical Chemistry Chemical Physics* **2014**, *16*, 9904.

[158] P. Fulde, *Electron correlations in molecules and solids*, volume 100, Springer Science & Business Media, Berlin **1995**.

[159] J. Desclaux, P. Pyykkö, *Chemical Physics Letters* **1976**, *39*, 300.

[160] G. Czycholl, Deviations from the Ideal, Three-Dimensional Crystal Structure, in *Solid State Theory, Volume 2: Applications: Non-equilibrium, Behavior in External Fields, Collective Phenomena*, pages 119–158, Springer **2023**.

[161] A. O. Williams, *Physical Review* **1940**, *58*, 723.

[162] N. E. Christensen, B. O. Seraphin, *Physical Review B* **1971**, *4*, 3321.

[163] S. J. Rose, I. P. Grant, N. C. Pyper, *Journal of Physics B: Atomic and Molecular Physics* **1978**, *11*, 1171.

[164] P. Pyykko, *Chemical Reviews* **1988**, *88*, 563.

[165] P. Romaniello, P. L. de Boeij, *The Journal of Chemical Physics* **2005**, *122*, 164303.

[166] F. Calvo, E. Pahl, M. Wormit, P. Schwerdtfeger, *Angewandte Chemie International Edition* **2013**, *52*, 7583.

[167] P. Pyykkö, *Annual Review of Physical Chemistry* **2012**, *63*, 45.

[168] T. Takeda, *Zeitschrift für Physik B Condensed Matter* **1978**, *32*, 43.

[169] M. Reiher, A. Wolf, *Relativistic Quantum Chemistry*, John Wiley and Sons, Ltd **2014**.

[170] R. F. Bader, *Accounts of Chemical Research* **1985**, *18*, 9.

[171] R. F. Bader, *Chemical Reviews* **1991**, *91*, 893.

[172] R. F. Bader, *Monatshefte für Chemie/Chemical Monthly* **2005**, *136*, 819.

[173] R. S. Mulliken, *The Journal of Chemical Physics* **1955**, *23*, 1833.

[174] R. S. Mulliken, *The Journal of Chemical Physics* **1955**, *23*, 1841.

[175] R. Mulliken, *The Journal of Chemical Physics* **1955**, *23*, 2338.

[176] R. Mulliken, *The Journal of Chemical Physics* **1955**, *23*, 2343.

[177] R. Carbó-Dorca, P. Bultinck, *Journal of Mathematical Chemistry* **2004**, *36*, 231.

[178] P.-O. Löwdin, *The Journal of Chemical Physics* **1950**, *18*, 365.

[179] P.-O. Löwdin, On the Nonorthogonality Problem, in *Advances in Quantum Chemistry*, volume 5, pages 185–199, Academic Press **1970**.

[180] I. G. Kaplan, *Intermolecular interactions: physical picture, computational methods and model potentials*, volume 367, Wiley Online Library **2006**.

[181] R. M. Richard, K. U. Lao, J. M. Herbert, *The Journal of Chemical Physics* **2014**, *141*.

[182] K. U. Lao, K.-Y. Liu, R. M. Richard, J. M. Herbert, *The Journal of Chemical Physics* **2016**, *144*.

[183] A. Hermann, R. P. Krawczyk, M. Lein, P. Schwerdtfeger, I. P. Hamilton, J. J. P. Stewart, *Physical Review A* **2007**, *76*, 013202.

[184] K. Szalewicz, R. Bukowski, B. Jeziorski, On the importance of many-body forces in clusters and condensed phase, in *Theory and Applications of Computational Chemistry*, pages 919–962, Elsevier **2005**.

[185] J. P. Heindel, S. S. Xantheas, *Journal of Chemical Theory and Computation* **2020**, *16*, 6843.

[186] J. P. Heindel, S. S. Xantheas, *Journal of Chemical Theory and Computation* **2021**, *17*, 2200.

[187] B. Axilrod, E. Teller, *The Journal of Chemical Physics* **1943**, *11*, 299.

[188] Y. Muto, Force between nonpolar molecules, in *Proceedings of the Physico-Mathematical Society of Japan*, volume 17 **1943** pages 629–631.

[189] B. Axilrod, *The Journal of Chemical Physics* **1949**, *17*, 1349.

[190] B. Axilrod, *The Journal of Chemical Physics* **1951**, *19*, 719.

[191] E. Ermakova, J. Solca, H. Huber, M. Welker, *The Journal of Chemical Physics* **1995**, *102*, 4942.

[192] V. F. Lotrich, K. Szalewicz, *Physical Review Letters* **1997**, *79*, 1301.

[193] H. Huber, A. J. Dyson, B. Kirchner, *Chemical Society Reviews* **1999**, *28*, 121.

[194] J. E. Mayer, E. Montroll, *The Journal of Chemical Physics* **1941**, *9*, 2.

[195] A. Masters, *Journal of Physics: Condensed Matter* **2008**, *20*, 283102.

[196] W. Greiner, L. Neise, H. Stöcker, *Thermodynamics and statistical mechanics*, Springer Science & Business Media **2012**.

[197] H. Margenau, N. R. Kestner, *Theory of Intermolecular Forces: International Series of Monographs in Natural Philosophy*, volume 18, Elsevier **2013**.

[198] J. B. Keller, B. Zumino, *The Journal of Chemical Physics* **1959**, *30*, 1351.

[199] J. Lebowitz, O. Penrose, *Journal of Mathematical Physics* **1964**, *5*, 841.

[200] F. London, *Transactions of the Faraday Society* **1937**, *33*, 8b.

[201] A. Stone, *The theory of intermolecular forces*, Oxford University Press **2013**.

[202] J. D. Jackson, *Classical electrodynamics*, John Wiley & Sons **2021**.

[203] M. Marinescu, J. Babb, A. Dalgarno, *Physical Review A* **1994**, *50*, 3096.

[204] M. Boström, B. E. Sernelius, *Physical Review B* **2000**, *62*, 7523.

[205] G. S. Boltachev, N. Volkov, K. Nagayev, *Journal of Colloid and Interface Science* **2011**, *355*, 417.

[206] M. Kuvakin, E. Karpova, V. Yurasova, J. Colligon, *Radiation Effects and Defects in Solids* **1997**, *140*, 235.

[207] I. Solovyev, K. Terakura, *Physical Review B* **1998**, *58*, 15496.

[208] H.-J. Böhm, R. Ahlrichs, *The Journal of Chemical Physics* **1982**, *77*, 2028.

[209] R. Baxter, *The Journal of Chemical Physics* **1968**, *49*, 2770.

[210] D. Gazzillo, A. Giacometti, *The Journal of Chemical Physics* **2004**, *120*, 4742.

[211] L. Trombach, P. Schwerdtfeger, *Physical Review E* **2018**, *98*, 033311.

[212] G. Chadwick, *Metal Science* **1967**, *1*, 132.

[213] J. Barker, *The Journal of Chemical Physics* **1975**, *63*, 632.

[214] L. V. Woodcock, *Journal of the Chemical Society, Faraday Transactions 2: Molecular and Chemical Physics* **1976**, *72*, 1667.

[215] A. Santos, J. M. Montanero, J. W. Dufty, J. J. Brey, *Physical Review E* **1998**, *57*, 1644.

[216] W. Sutherland, *The London, Edinburgh, and Dublin Philosophical Magazine and Journal of Science* **1893**, *36*, 507.

[217] A. Sherwood, J. Prausnitz, *The Journal of Chemical Physics* **1964**, *41*, 429.

[218] G. Mie, *Annalen der Physik* **1903**, *316*, 657.

[219] E. Grüneisen, *Annalen der Physik* **1912**, *344*, 257.

[220] J. E. Jones, *Proceedings of the Royal Society of London. Series A, containing papers of a mathematical and physical character* **1924**, *106*, 441.

[221] J. E. Jones, *Proceedings of the Royal Society of London. Series A, Containing Papers of a Mathematical and Physical Character* **1924**, *106*, 463.

[222] P. Schwerdtfeger, D. J. Wales, *Journal of Chemical Theory and Computation* **2024**, *20*, 3379.

[223] G. Rutkai, M. Thol, R. Span, J. Vrabec, *Molecular Physics* **2017**, *115*, 1104.

[224] X. Wang, S. Ramírez-Hinestrosa, J. Dobnikar, D. Frenkel, *Physical Chemistry Chemical Physics* **2020**, *22*, 10624.

[225] R. A. Buckingham, *Proceedings of the Royal Society of London. Series A. Mathematical and Physical Sciences* **1938**, *168*, 264.

[226] P. Schwerdtfeger, N. Gaston, R. P. Krawczyk, R. Tonner, G. E. Moyano, *Physical Review B* **2006**, *73*, 064112.

[227] P. Schwerdtfeger, A. Burrows, O. R. Smits, *The Journal of Physical Chemistry A* **2021**, *125*, 3037.

[228] E. Pahl, F. Calvo, L. Koci, P. Schwerdtfeger, *Angewandte Chemie International Edition* **2008**, *47*, 8207.

[229] O. R. Smits, P. Jerabek, E. Pahl, P. Schwerdtfeger, *Angewandte Chemie International Edition* **2018**, *57*, 9961.

[230] O. Smits, P. Jerabek, E. Pahl, P. Schwerdtfeger, *Physical Review B* **2020**, *101*, 104103.

[231] M. Born, K. Huang, *Dynamical Theory of Crystal Lattices*, International series of monographs on physics, Clarendon Press **1988**.

[232] F. Mouhat, F.-X. Coudert, *Physical Review B* **2014**, *90*, 224104.

[233] M. T. Dove, *Introduction to lattice dynamics*, 4, Cambridge university press **1993**.

[234] G. Ackland, M. Warren, S. Clark, *Journal of Physics: Condensed Matter* **1997**, *9*, 7861.

[235] D. C. Gazis, R. F. Wallis, *Physics Review* **1966**, *151*, 578.

[236] I. Pallikara, P. Kayastha, J. M. Skelton, L. D. Whalley, *Electronic Structure* **2022**, *4*, 033002.

[237] C. Lin, S. Poncé, N. Marzari, *npj Computational Materials* **2022**, *8*, 236.

[238] F. Eriksson, E. Fransson, P. Erhart, *Advanced Theory and Simulations* **2019**, *2*, 1800184.

[239] P. N. Keating, *Physical Review* **1966**, *152*, 774.

[240] P. N. Keating, *Physical Review* **1966**, *145*, 637.

[241] D. A. McQuarrie, *Statistical Mechanics*, G - Reference,Information and Interdisciplinary Subjects Series, University Science Books **2000**.

[242] R. D. Levine, *Molecular reaction dynamics*, Cambridge university press **2009**.

[243] G. Jaeger, *Archive for History of Exact Sciences* **1998**, *53*, 51.

[244] B. Cowan, *Topics in statistical mechanics*, World Scientific **2021**.

[245] L. D. Landau, *Zhurnal Eksperimental'noi i Teoreticheskoi Fiziki* **1937**, *11*, 19.

[246] A. Roitburd, Martensitic transformation as a typical phase transformation in solids, in *Solid state physics*, volume 33, pages 317–390, Elsevier **1978**.

[247] M. Wechsler, *Acta Metallurgica* **1959**, *7*, 793.

[248] T. Schneider, G. Srinivasan, C. Enz, *Physical Review A* **1972**, *5*, 1528.

[249] G. Venkataraman, *Bulletin of Materials Science* **1979**, *1*, 129.

[250] R. Cowley, *Integrated Ferroelectrics* **2012**, *133*, 109.

[251] J. Krumhansl, *Solid State Communications* **1992**, *84*, 251.

[252] S. Alexander, J. McTague, *Physical Review Letters* **1978**, *41*, 702.

[253] F. Falk, *Le Journal de Physique Colloques* **1982**, *43*, C4.

[254] B. Rosenstein, D. Li, *Reviews of Modern Physics* **2010**, *82*, 109.

[255] P. Brydon, J. Schmiedt, C. Timm, *Physical Review B* **2011**, *84*, 214510.

[256] E. C. Bain, *Industrial & Engineering Chemistry* **1924**, *16*, 692.

[257] G. Olson, M. Cohen, *Metallurgical Transactions A* **1976**, *7*, 1905.

[258] Z. Nishiyama, *Martensitic transformation*, Academic Press, New York **1978**.

[259] P. Beauchamp, J. Villain, *Journal de Physique* **1983**, *44*, 1117.

[260] L. Sandoval, H. M. Urbassek, P. Entel, *New Journal of Physics* **2009**, *11*, 103027.

[261] T. L. Underwood, G. J. Ackland, *Journal of Physics: Conference Series* **2015**, *640*, 012030.

[262] W. Burgers, *Physica* **1934**, *1*, 561.

[263] G. B. Olson, M. Cohen, *Metallurgica and Materials Transactions A* **1976**, *7*, 1897.

[264] W. Li, T. Wang, *Physical Review B* **1999**, *60*, 11954.

[265] K. J. Caspersen, A. Lew, M. Ortiz, E. A. Carter, *Physical Review Letters* **2004**, *93*, 115501.

[266] D. F. Johnson, E. A. Carter, *The Journal of Chemical Physics* **2008**, *128*, 104703.

[267] H. Cynn, C. S. Yoo, B. Baer, V. Iota-Herbei, A. K. McMahan, M. Nicol, S. Carlson, *Physical Review Letters* **2001**, *86*, 4552.

[268] N. V. Krainyukova, R. E. Boltnev, E. P. Bernard, V. V. Khmelenko, D. M. Lee, V. Kiryukhin, *Physical Review Letters* **2012**, *109*, 245505.

[269] Z. Lu, W. Zhu, T. Lu, W. Wang, *Modelling and Simulation in Materials Science and Engineering* **2014**, *22*, 025007.

[270] K. Burke, *The Journal of Chemical Physics* **2012**, *136*.

[271] H. S. Yu, S. L. Li, D. G. Truhlar, *The Journal of Chemical Physics* **2016**, *145*.

[272] A. D. Becke, *The Journal of Chemical Physics* **2014**, *140*.

[273] A. Pribram-Jones, D. A. Gross, K. Burke, *Annual Review of Physical Chemistry* **2015**, *66*, 283.

[274] R. G. Parr, S. R. Gadre, L. J. Bartolotti, *Proceedings of the National Academy of Sciences* **1979**, *76*, 2522.

[275] R. Parr, Y. Weitao, *Density-Functional Theory of Atoms and Molecules*, International Series of Monographs on Chemistry, Oxford University Press **1989**.

[276] P. Ziesche, S. Kurth, J. P. Perdew, *Computational Materials Science* **1998**, *11*, 122.

[277] D. M. Ceperley, B. J. Alder, *Physical Review Letters* **1980**, *45*, 566.

[278] P. Mori-Sánchez, A. J. Cohen, W. Yang, *Physical Review Letters* **2008**, *100*, 146401.

[279] K. R. Bryenton, A. A. Adeleke, S. G. Dale, E. R. Johnson, *Wiley Interdisciplinary Reviews: Computational Molecular Science* **2023**, *13*, e1631.

[280] J. P. Perdew, K. Burke, M. Ernzerhof, *Physical Review Letters* **1996**, *77*, 3865.

[281] G. I. Csonka, J. P. Perdew, A. Ruzsinszky, P. H. Philipsen, S. Lebègue, J. Paier, O. A. Vydrov, J. G. Ángyán, *Physical Review B* **2009**, *79*, 155107.

[282] J. P. Perdew, K. Schmidt, Jacob's ladder of density functional approximations for the exchange-correlation energy, in *AIP Conference Proceedings*, volume 577, American Institute of Physics **2001** pages 1–20.

[283] J. Sun, A. Ruzsinszky, J. P. Perdew, *Physical Review Letters* **2015**, *115*, 036402.

[284] J. Sun, R. C. Remsing, Y. Zhang, Z. Sun, A. Ruzsinszky, H. Peng, Z. Yang, A. Paul, U. Waghmare, X. Wu, et al., *Nature Chemistry* **2016**, *8*, 831.

[285] A. D. Becke, *Physical Review A* **1988**, *38*, 3098.

[286] M. Marsman, J. Paier, A. Stroppa, G. Kresse, *Journal of Physics: Condensed Matter* **2008**, *20*, 064201.

[287] E. R. Johnson, I. D. Mackie, G. A. DiLabio, *Journal of Physical Organic Chemistry* **2009**, *22*, 1127.

[288] J. Klimeš, A. Michaelides, *The Journal of Chemical Physics* **2012**, *137*.

[289] S. Kristyán, P. Pulay, *Chemical Physics Letters* **1994**, *229*, 175.

[290] J. Pérez-Jordá, A. D. Becke, *Chemical Physics Letters* **1995**, *233*, 134.

[291] S. Grimme, J. Antony, S. Ehrlich, H. Krieg, *The Journal of Chemical Physics* **2010**, *132*.

[292] S. Grimme, S. Ehrlich, L. Goerigk, *Journal of Computational Chemistry* **2011**, *32*, 1456.

[293] L. Goerigk, S. Grimme, *Physical Chemistry Chemical Physics* **2011**, *13*, 6670.

[294] A. Burrows, S. Cooper, P. Schwerdtfeger, *Physical Review E* **2023**, *107*, 065302.

[295] A. Burrows, S. Cooper, E. Pahl, P. Schwerdtfeger, *Journal of Mathematical Physics* **2020**, *61*.

[296] J. E. Jones, *Proceedings of the Royal Society of London. Series A, Containing Papers of a Mathematical and Physical Character* **1924**, *106*, 709.

[297] I. J. Zucker, *Journal of Physics A: Mathematical and General* **1975**, *8*, 1734.

[298] M. Abramowitz, I. Stegun, *Handbook of Mathematical Functions: With Formulas, Graphs, and Mathematical Tables*, Applied mathematics series, Dover Publications **1965**.

[299] A. A. Terras, *Transactions of the American Mathematical Society* **1973**, *183*, 477.

[300] B. M. E. van der Hoff, G. C. Benson, *Canadian Journal of Physics* **1953**, *31*, 1087.

[301] Y. Nesterov, et al., *Lectures on convex optimization*, volume 137, Springer **2018**.

[302] J. Nocedal, S. J. Wright, *Numerical optimization*, Springer **2006**.

[303] R. Garnett, *Bayesian optimization*, Cambridge University Press **2023**.

[304] C. G. Broyden, *IMA Journal of Applied Mathematics* **1970**, *6*, 76.

[305] C. G. Broyden, *IMA Journal of Applied Mathematics* **1970**, *6*, 222.

[306] R. Fletcher, *The Computer Journal* **1970**, *13*, 317.

[307] D. Goldfarb, *Mathematics of Computation* **1970**, *24*, 23.

[308] D. F. Shanno, *Mathematics of Computation* **1970**, *24*, 647.

[309] L. Armijo, *Pacific Journal of Mathematics* **1966**, *16*, 1.

[310] H. J. Kushner, *Journal of Mathematical Analysis and Applications* **1962**, *5*, 150.

[311] D. J. MacKay, *Information theory, inference and learning algorithms*, Cambridge university press **2003**.

[312] D. Malakoff, *Science* **1999**, *286*, 1461.

[313] B. Efron, *Science* **2013**, *340*, 1177.

[314] A. Einstein, *Annalen der Physik* **1907**, *327*, 180.

[315] A.-T. Petit, P.-L. Dulong, *Annales de Chimie et de Physique* **1819**, *10*, 395.

[316] P. Debye, *Annalen der Physik* **1912**, *344*, 789.

[317] M. Yin, M. L. Cohen, *Physical Review B* **1982**, *26*, 3259.

[318] P. Pavone, *Journal of Physics: Condensed Matter* **2001**, *13*, 7593.

[319] G. Kresse, J. Furthmüller, J. Hafner, *Europhysics Letters* **1995**, *32*, 729.

[320] S. Baroni, P. Giannozzi, A. Testa, *Physical Review Letters* **1987**, *58*, 1861.

[321] X. Gonze, C. Lee, *Physical Review B* **1997**, *55*, 10355.

[322] G. Frenking, S. Shaik, *The chemical bond: fundamental aspects of chemical bonding*, volume 1, John Wiley & Sons **2014**.

[323] G. Frenking, S. Shaik, *The Chemical Bond: Chemical Bonding Across the Periodic Table*, volume 2, John Wiley & Sons **2014**.

[324] V. V. Gusev, D. Adamson, A. Deligkas, D. Antypov, C. M. Collins, P. Krysta, I. Potapov, G. R. Darling, M. S. Dyer, P. Spirakis, M. J. Rosseinsky, *Nature* **2023**, *619*, 68.

[325] J. Maddox, *Nature* **1988**, *335*, 201.

[326] N. Tugluoglu, R. H. Mutlu, *Physical Review B* **1996**, *54*, 10253.

[327] A. M. Teale, T. Helgaker, A. Savin, C. Adamo, B. Aradi, A. V. Arbuznikov, P. W. Ayers, E. J. Baerends, V. Barone, P. Calaminici, E. Cancès, E. A. Carter, P. K. Chattaraj, H. Chermette, I. Ciofini, T. D. Crawford, F. De Proft, J. F. Dobson, C. Draxl, T. Frauenheim, E. Fromager, P. Fuentealba, L. Gagliardi, G. Galli, J. Gao, P. Geerlings, N. Gidopoulos, P. M. W. Gill, P. Gori-Giorgi, A. Görling, T. Gould, S. Grimme, O. Gritsenko, H. J. A. Jensen, E. R. Johnson, R. O. Jones, M. Kaupp, A. M. Köster, L. Kronik, A. I. Krylov, S. Kvaal, A. Laestadius, M. Levy, M. Lewin, S. Liu, P.-F. Loos, N. T. Maitra, F. Neese, J. P. Perdew, K. Pernal, P. Pernot, P. Piecuch, E. Rebolini, L. Reining, P. Romaniello, A. Ruzsinszky, D. R. Salahub, M. Scheffler, P. Schwerdtfeger, V. N. Staroverov, J. Sun, E. Tellgren, D. J. Tozer, S. B. Trickey, C. A. Ullrich, A. Vela, G. Vignale, T. A. Wesolowski, X. Xu, W. Yang, *Physical Chemistry Chemical Physics* **2022**, *24*, 28700.

[328] E. Caldeweyher, C. Bannwarth, S. Grimme, *The Journal of Chemical Physics* **2017**, *147*, 034112.

[329] I. S. Lim, M. Pernpointner, M. Seth, J. K. Laerdahl, P. Schwerdtfeger, P. Neogrady, M. Urban, *Physical Review A* **1999**, *60*, 2822.

[330] E. Caldeweyher, J.-M. Mewes, S. Ehlert, S. Grimme, *Physical Chemistry Chemical Physics* **2020**, *22*, 8499.

[331] J. H. Conway, N. J. A. Sloane, *Journal of Number Theory* **1994**, *48*, 373.

[332] R. M. Badger, *The Journal of Chemical Physics* **1934**, *2*, 128.

[333] G. Borelius, *Physica Scripta* **1978**, *18*, 9.

[334] P. Schwerdtfeger, O. R. Smits, P. Pyykkö, *Nature Reviews Chemistry* **2020**, *4*, 359.

[335] N. Takeuchi, C. T. Chan, K. M. Ho, *Physical Review B* **1989**, *40*, 1565.

[336] A. A. Adeleke, E. R. Johnson, *Physical Review B* **2023**, *107*, 064101.

[337] S. Löffelsender, P. Schwerdtfeger, S. Grimme, J.-M. Mewes, *Journal of the American Chemical Society* **2021**, *144*, 485.

[338] G. Kresse, J. Hafner, *Physical Review B* **1993**, *47*, 558.

[339] G. Kresse, J. Hafner, *Physical Review B* **1994**, *49*, 14251.

[340] G. Kresse, J. Furthmüller, *Computational Materials Science* **1996**, *6*, 15.

[341] G. Kresse, J. Furthmüller, *Physical Review B* **1996**, *54*, 11169.

[342] P. E. Blöchl, *Physical Review B* **1994**, *50*, 17953.

[343] G. Kresse, D. Joubert, *Physical Review B* **1999**, *59*, 1758.

[344] P. E. Blöchl, O. Jepsen, O. K. Andersen, *Physical Review B* **1994**, *49*, 16223.

[345] A. Togo, I. Tanaka, *Scripta Materialia* **2015**, *108*, 1.

[346] H. E. Stanley, *Phase transitions and critical phenomena*, volume 7, Clarendon Press, Oxford **1971**.

[347] Y. A. Izyumov, V. M. Laptve, V. N. Syromyatnikov, *Phase Transitions* **1994**, *49*, 1.

[348] G. J. Ackland, A. Jones, R. Noble-Eddy, *Materials Science and Engineering A* **2008**, *481-482*, 11.

[349] G. Grimvall, B. Magyari-Köpe, V. Ozoliņš, K. A. Persson, *Reviews of Modern Physics* **2012**, *84*, 945.

[350] G. Torrents, X. Illa, E. Vives, A. Planes, *Physical Review E* **2017**, *95*, 013001.

[351] D. A. Young, *Phase diagrams of the elements*, University of California Press **1991**.

[352] K. J. Caspersen, E. A. Carter, *Proceedings of the National Academy of Sciences* **2005**, *102*, 6738.

[353] R. Fürth, M. Born, *Proceedings of the Royal Society of London. Series A. Mathematical and Physical Sciences* **1944**, *183*, 87.

[354] F. H. Stillinger, *The Journal of Chemical Physics* **2001**, *115*, 5208.

[355] M. Born, *Mathematical Proceedings of the Cambridge Philosophical Society* **1940**, *36*, 160–172.

[356] R. D. Misra, *Mathematical Proceedings of the Cambridge Philosophical Society* **1940**, *36*, 173–182.

[357] J.-P. Hansen, L. Verlet, *Physical Review* **1969**, *184*, 151.

[358] M. P. Allen, D. J. Tildesley, *Computer Simulations of Liquids*, Oxford Science Publications, New York **1987**.

[359] H. Watanabe, N. Ito, C.-K. Hu, *The Journal of Chemical Physics* **2012**, *136*, 204102.

[360] E. H. Abramson, *High Pressure Research* **2011**, *31*, 549 .

[361] A. Hajibabaei, K. S. Kim, *Physical Review E* **2019**, *99*, 022145.

[362] E. Elizalde, *Journal of Mathematical Physics* **1994**, *35*, 6100.

[363] E. Elizalde, *Journal of Computational and Applied Mathematics* **2000**, *118*, 125.

[364] A. A. Buchheit, J. K. Busse, *arXiv preprint arXiv:2504.11989* **2025**.

[365] D. Borwein, J. Borwein, C. Pinner, *Transactions of the American Mathematical Society* **1998**, *350*, 3131.

[366] P. Attard, *Physical Review A* **1992**, *45*, 5649.

[367] B. Li, G. Qian, A. R. Oganov, S. E. Boulfelfel, R. Faller, *The Journal of Chemical Physics* **2017**, *146*, 214502.

[368] S. Ono, T. Ito, *Physical Review B* **2021**, *103*, 075406.

[369] B. Groh, B. Mulder, *Physical Review E* **1999**, *59*, 5613.

[370] C. Zener, *Physical Review* **1948**, *74*, 639.

[371] J. Rifkin, *Philosophical Magazine A* **1984**, *49*, L31.

[372] D. C. Wallace, J. L. Patrick, *Physical Review* **1965**, *137*, A152.

[373] J. H. Conway, N. J. Sloane, *Advances in Mathematics of Communications* **2007**, *1*, 257.

[374] A. L. Patterson, *Review of Scientific Instruments* **1941**, *12*, 206.

[375] K. L. Fields, *Acta Crystallographica Section A* **1980**, *36*, 194.

[376] S. Torquato, F. H. Stillinger, *Journal of Applied Physics* **2007**, *102*, 093511.

[377] S. Cooper, P. Schwerdtfeger, *SIGMA* **2025**, *21*, 019.

[378] V. Heine, I. J. Robertson, M. C. Payne, J. N. Murrell, J. C. Phillips, D. Weaire, *Philosophical Transactions: Physical Sciences and Engineering* **1991**, *334*, 393.

[379] A. A. Buchheit, J. Busse, R. Gutendorf, *arXiv preprint arXiv:2412.16317* **2024**.

[380] P. Jerabek, O. R. Smits, J.-M. Mewes, K. A. Peterson, P. Schwerdtfeger, *The Journal of Physical Chemistry A* **2019**, *123*, 4201.

[381] O. R. Smits, J.-M. Mewes, P. Jerabek, P. Schwerdtfeger, *Angewandte Chemie International Edition* **2020**, *59*, 23636.

[382] E. Florez, O. R. Smits, J.-M. Mewes, P. Jerabek, P. Schwerdtfeger, *The Journal of Chemical Physics* **2022**, *157*, 064304.

[383] M. G. Duffy, *SIAM Journal on Numerical Analysis* **1982**, *19*, 1260.

[384] Y. Xie, Z. L. Glick, C. D. Sherrill, *The Journal of Chemical Physics* **2023**, *158*, 094110.

[385] I. J. Zucker, M. M. Robertson, *Journal of Physics A: Mathematical and General* **1975**, *8*, 874.

[386] I. J. Zucker, *Symmetry* **2017**, *9*.

[387] W. L. Bade, *The Journal of Chemical Physics* **1957**, *27*, 1280.

[388] E. E. Polymeropoulos, P. Bopp, J. Brickmann, L. Jansen, R. Block, *Physical Review A* **1985**, *31*, 3565.

[389] C. E. Moore, *Atomic energy levels as derived from the analyses of optical spectra*, 467, US Department of Commerce, National Bureau of Standards **1949**.

[390] K. Huber, G. Herzberg, *Molecular Spectra and Molecular Structure Constants of Diatomic Molecules*, Van Nostrand **1979**.

[391] P. Schwerdtfeger, J. K. Nagle, *Molecular Physics* **2019**, *117*, 1200.

[392] F. Milstein, *Journal of Applied Physics* **1973**, *44*, 3825.

[393] P. J. Craievich, J. M. Sanchez, R. E. Watson, M. Weinert, *Physical Review B* **1997**, *55*, 787.

[394] B. W. Kwaadgras, M. W. J. Verdult, M. Dijkstra, R. v. Roij, *The Journal of Chemical Physics* **2013**, *138*, 104308.

[395] E. Ermakova, J. Solca, G. Steinebrunner, H. Huber, *Chemistry - A European Journal* **1998**, *4*, 377.

[396] Y. A. Freiman, S. M. Tretyak, *Low Temperature Physics* **2007**, *33*, 545.

[397] P. Schwerdtfeger, A. Hermann, *Physical Review B* **2009**, *80*, 064106.

[398] J. Zhao, *Multiple Zeta Functions, Multiple Polylogarithms and Their Special Values*, World Scientific, Singapore **2016**.

[399] I. Sanchez-Burgos, E. Sanz, C. Vega, J. R. Espinosa, *Physical Chemistry Chemical Physics* **2021**, *23*, 19611.

[400] A. B. Hopkins, F. H. Stillinger, S. Torquato, *Physical Review E* **2011**, *83*, 011304.

[401] G. Osang, H. Edelsbrunner, M. Saadatfar, *Soft Matter* **2021**, *17*, 9107.

[402] S. Cooper, A. Robles-Navarro, O. R. Smits, P. Schwerdtfeger, *The Journal of Chemical Physics* **2025**, *162*, 014105.

[403] T. C. Hales, *Historical Overview of the Kepler Conjecture*, pages 65–82, Springer New York, New York, NY **2011**.

[404] D. Frenkel, A. J. C. Ladd, *The Journal of Chemical Physics* **1984**, *81*, 3188.

[405] L. V. Woodcock, *Nature* **1997**, *385*, 141.

[406] N. V. Krainyukova, *Low Temperature Physics* **2011**, *37*, 435.

[407] K. Rościszewski, B. Paulus, P. Fulde, H. Stoll, *Physical Review B* **2000**, *62*, 5482.

[408] B. Senger, P. Schaaf, D. S. Corti, R. Bowles, J.-C. Voegel, *The Journal of Chemical Physics* **1999**, *110*, 6421.

[409] R. Lovett, *Reports on Progress in Physics* **2007**, *70*, 195.

[410] K. Lu, Y. Li, *Physical Review Letters* **1998**, *80*, 4474.

[411] A. D. Rosa, G. Garbarino, R. Briggs, V. Svitlyk, G. Morard, M. A. Bouhifd, J. Jacobs, T. Irifune, O. Mathon, S. Pascarelli, *Physical Review B* **2018**, *97*, 094115.

[412] A. Dewaele, A. D. Rosa, N. Guignot, D. Andrault, J. E. F. S. Rodrigues, G. Garbarino, *Scientific Reports* **2021**, *11*, 15192.

[413] A. N. Jackson, A. D. Bruce, G. J. Ackland, *Physical Review E* **2002**, *65*, 036710.

[414] C. Cayron, *Acta Crystallographica Section A* **2013**, *69*, 498.

[415] C. Cayron, *Acta Materialia* **2015**, *96*, 189.

[416] C. Cayron, *Acta Materialia* **2016**, *111*, 417.

[417] H. Cook, *Acta Metallurgica* **1975**, *23*, 1027.

[418] B. Feng, M. Widom, *Physical Review B* **2018**, *98*, 174108.

[419] V. Raghavan, M. Cohen, *Solid-state phase transformations*, Springer, Berlin **1975**.

[420] R. J. Gooding, J. A. Krumhansl, *Physical Review B* **1988**, *38*, 1695.

[421] W. Li, X. Qian, J. Li, *Nature Reviews Materials* **2021**, *6*, 829.

[422] R. Bruinsma, A. Zangwill, *Physical Review Letters* **1985**, *55*, 214.

[423] R. Dovesi, R. Orlando, *Phase Transitions* **1994**, *52*, 151.

[424] X. Liu, P. Müller, P. Kroll, R. Dronskowski, W. Wilsmann, R. Conradt, *ChemPhysChem* **2003**, *4*, 725.

[425] H. Jónsson, G. Mills, K. W. Jacobsen, *Nudged elastic band method for finding minimum energy paths of transitions*, pages 385–404, World Scientific **1998**.

[426] G. Henkelman, B. P. Uberuaga, H. Jónsson, *The Journal of Chemical Physics* **2000**, *113*, 9901.

[427] A. Raju Natarajan, A. Van der Ven, *Chemistry of Materials Journal* **2019**, *31*, 8222.

[428] V. Neuman, P. Wesołowski, K. Bojarski, D. Dewan, M. Schäffler, P. Smardz, D. Wales, *ChemRxiv* **2025**.

[429] S. Cooper, A. Robles-Navarro, O. R. Smits, P. Schwerdtfeger, *The Journal of Physical Chemistry Letters* **2024**, *15*, 8387.

[430] G. Stell, *Journal of Statistical Physics* **1991**, *63*, 1203.

[431] A. Robles-Navarro, S. Cooper, O. R. Smits, P. Schwerdtfeger, *The Journal of Physical Chemistry C* **2025**, *129*, 8389.

[432] H. Eshet, F. Bruneval, M. Parrinello, *The Journal of Chemical Physics* **2008**, *129*, 026101.

[433] A. Robles-Navarro, P. Jerabek, P. Schwerdtfeger, *Angewandte Chemie International Edition* **2024**, *63*, e202313679.

[434] A. Robles-Navarro, S. Cooper, A. A. Buchheit, J. K. Busse, A. Burrows, O. Smits, P. Schwerdtfeger, *The Journal of Chemical Physics* **2025**, *163*, 094104.

[435] T. M. Middlemas, F. H. Stillinger, S. Torquato, *Physical Review E* **2019**, *99*, 022111.

[436] D. Mc Kie, C. Mc Kie, *Essentials of crystallography*, Blackwell Scientific Publications, Palo Alto, CA **1986**.

[437] R. Bell, I. Zucker, *M L Klein and J A Venebles eds., New York: Academic* **1976**.

[438] D. M. Sommerville, *Introduction to the Geometry of N Dimensions*, Courier Dover Publications **2020**.

[439] S.-C. Mau, D. A. Huse, *Physical Review E* **1999**, *59*, 4396.

[440] E. R. Dobbs, G. O. Jones, *Reports on Progress in Physics* **1957**, *20*, 516.

[441] P. Giannozzi, O. Andreussi, T. Brumme, O. Bunau, M. Buongiorno Nardelli, M. Calandra, R. Car, C. Cavazzoni, D. Ceresoli, M. Cococcioni, N. Colonna, I. Carnimeo, A. Dal Corso, S. de Gironcoli, P. Delugas, R. A. DiStasio, A. Ferretti, A. Floris, G. Fratesi, G. Fugallo, R. Gebauer, U. Gerstmann, F. Giustino, T. Gorni, J. Jia, M. Kawamura, H.-Y. Ko, A. Kokalj, E. Küçükbenli, M. Lazzeri, M. Marsili, N. Marzari, F. Mauri, N. L. Nguyen, H.-V. Nguyen, A. Otero-de-la Roza, L. Paulatto, S. Poncé, D. Rocca, R. Sabatini, B. Santra, M. Schlipf, A. P. Seitsonen, A. Smogunov, I. Timrov, T. Thonhauser, P. Umari, N. Vast, X. Wu, S. Baroni, *Journal of Physics: Condensed Matter* **2017**, *29*, 465901.

[442] D. Vanderbilt, *Physical Review B* **1990**, *41*, 7892.

[443] H. Jónsson, G. Mills, K. W. Jacobsen, *Nudged elastic band method for finding minimum energy paths of transitions*, pages 385–404, World Scientific **1998**.

[444] G. Henkelman, H. Jónsson, *The Journal of Chemical Physics* **2000**, *113*, 9978.

[445] G.-R. Qian, X. Dong, X.-F. Zhou, Y. Tian, A. R. Oganov, H.-T. Wang, *Computer Physics Communications* **2013**, *184*, 2111.

[446] K. A. Maerzke, G. Murdachaew, C. J. Mundy, G. K. Schenter, J. I. Siepmann, *The Journal of Physical Chemistry A* **2009**, *113*, 2075.

[447] P. Schwerdtfeger, *ChemPhysChem* **2011**, *12*, 3143.

[448] R. O. Jones, O. Gunnarsson, *Reviews of Modern Physics* **1989**, *61*, 689.

[449] Y. Zhao, D. G. Truhlar, *The Journal of Physical Chemistry A* **2006**, *110*, 5121.

[450] T. Kihara, S. Koba, *Journal of the Physical Society of Japan* **1952**, *7*, 348.

[451] K. Niebel, J. Venables, *Proceedings of the Royal Society of London. Series A. Mathematical and Physical Sciences* **1974**, *336*, 365.

[452] B. W. van de Waal, *Physical Review Letters* **1991**, *67*, 3263.

[453] P. Ehrenfest, *Phasenumwandlungen im ueblichen und erweiterten Sinn, classifiziert nach den entsprechenden Singularitaeten des thermodynamischen Potentiales*, volume 36, NV Noord-Hollandsche Uitgevers Maatschappij **1933**.

[454] G. K. Straub, D. C. Wallace, *Physical Review B* **1971**, *3*, 1234.

[455] W. A. Bassett, E. Huang, *Science* **1987**, *238*, 780.

[456] W. Li, T. Wang, *Physical Review B* **1999**, *60*, 11954.

[457] K. Patkowski, K. Szalewicz, *The Journal of Chemical Physics* **2010**, *133*, 094304.

[458] L. A. Schwalbe, R. K. Crawford, H. H. Chen, R. A. Aziz, *The Journal of Chemical Physics* **1977**, *66*, 4493.

[459] A. J. Cohen, P. Mori-Sánchez, W. Yang, *Chemical Reviews* **2012**, *112*, 289.

[460] R. M. Wentzcovitch, M. L. Cohen, *Physical Review B* **1988**, *37*, 5571.

[461] Y. Chen, K. M. Ho, B. N. Harmon, *Physical Review B* **1988**, *37*, 283.

[462] M. Ekman, B. Sadigh, K. Einarsdotter, P. Blaha, *Physical Review B* **1998**, *58*, 5296.

[463] M. Friák, M. Šob, V. Vitek, *Physical Review B* **2001**, *63*, 052405.

[464] T. Q. Nguyen, K. Sato, Y. Shibutani, *Materials Transactions* **2018**, *59*, 870.

[465] S. Sun, D. Li, C. Yang, L. Fu, D. Kong, Y. Lu, Y. Guo, D. Liu, P. Guan, Z. Zhang, J. Chen, W. Ming, L. Wang, X. Han, *Physical Review Letters* **2022**, *128*, 015701.

[466] J. Zhao, D. Maroudas, F. Milstein, *Physical Review B* **2000**, *62*, 13799.

[467] H. Djohari, F. Milstein, D. Maroudas, *Physical Review B* **2009**, *79*, 174109.

[468] J.-P. Hansen, L. Verlet, *Physical Review* **1969**, *184*, 151.

[469] Y. Chang, S. Chen, F. Zhang, X. Yan, F. Xie, R. Schmid-Fetzer, W. Oates, *Progress in Materials Science* **2004**, *49*, 313.

[470] H. B. Schlegel, *Journal of Computational Chemistry* **2003**, *24*, 1514.

[471] R. J. Bartlett, M. Musiał, *Reviews of Modern Physics* **2007**, *79*, 291.

[472] K. J. Caspersen, E. A. Carter, *Proceedings of the National Academy of Sciences* **2005**, *102*, 6738.

[473] G. A. de Wijs, G. Kresse, M. J. Gillan, *Physical Review B* **1998**, *57*, 8223.

[474] R. Jinnouchi, J. Lahnsteiner, F. Karsai, G. Kresse, M. Bokdam, *Physical Review Letters* **2019**, *122*, 225701.

[475] P. Liu, C. Verdi, F. Karsai, G. Kresse, *Physical Review Materials* **2021**, *5*, 053804.

[476] V. Lobodyuk, E. Estrin, *Martensitic Transformations*, Cambridge International Science Publishing **2014**.

[477] J. A. Venables, *Philosophical Magazine* **1962**, *7*, 35.

[478] R. Bruinsma, A. Zangwill, *Physical Review Letters* **1985**, *55*, 214.

[479] Y. Akahama, M. Nishimura, K. Kinoshita, H. Kawamura, Y. Ohishi, *Physical Review Letters* **2006**, *96*, 045505.

[480] E. K. Gross, R. M. Dreizler, *Density functional theory*, volume 337, Springer Science & Business Media **2013**.

[481] G. Hämmerlin, K.-H. Hoffmann, *Numerical mathematics*, Springer Science & Business Media, Berlin **2012**.

[482] L. Bétermin, L. Šamaj, I. Travěnec, *Studies in Applied Mathematics* **2023**, *150*, 69.

[483] C. L. Guillaume, E. Gregoryanz, O. Degtyareva, M. I. McMahon, M. Hanfland, S. Evans, M. Guthrie, S. V. Sinogeikin, H.-K. Mao, *Nature Physics* **2011**, *7*, 211.

[484] M. Sanati, A. Saxena, T. Lookman, *Physical Review B* **2001**, *64*, 092101.

[485] A. Mujica, A. Rubio, A. Muñoz, R. J. Needs, *Reviews of Modern Physics* **2003**, *75*, 863.

[486] E. Scerri, *Nature Chemistry* **2009**, *1*, 670.

[487] C. F. Liang, P. Paris, R. K. Sheline, *Physical Review C* **2001**, *64*, 034310.

[488] R. W. Gray, W. Ramsay, *Journal of the Chemical Society Transactions* **1909**, *95*, 1073.

[489] E. K. Hyde, *Journal of the American Chemical Society* **1952**, *74*, 4181.

[490] J.-P. Adloff, G. B. Kauffman, *Journal of Chemical Education* **2005**, *10*, 387.

[491] J. E. Sansonetti, *Journal of Physical and Chemical Reference Data* **2007**, *36*, 497.

[492] V. Glasov, V. Koltsov, *Akademiia Nauk SSSR* **1979**, pages 68–75.

[493] A. Lavrukhina, *Radiokhimiya (USSR)* **1979**, *21*, 26.

[494] V. V. Oshchapovskii, *Russian Journal of Inorganic Chemistry* **2014**, *59*, 561.

[495] C. Cao, R. E. Vernon, W. E. Schwarz, J. Li, *Frontiers in Chemistry* **2021**, *8*, 813.

[496] V. A. Dzuba, V. V. Flambaum, O. P. Sushkov, *Journal of Physics B: Atomic, Molecular and Optical Physics* **1984**, *17*, 1953.

[497] A. Landau, E. Eliav, Y. Ishikawa, U. Kaldor, *The Journal of Chemical Physics* **2001**, *115*, 2389.

[498] I. S. Lim, P. Schwerdtfeger, B. Metz, H. Stoll, *The Journal of Chemical Physics* **2005**, *122*, 104103.

[499] M. V. Orna, *Journal of Chemical Education* **2009**, *86*, 1364.

[500] E. Gomez, L. Orozco, G. Sprouse, *Reports on Progress in Physics* **2005**, *69*, 79.

[501] G. Stancari, S. Atutov, R. Calabrese, L. Corradi, A. Dainelli, C. De Mauro, A. Khanbekyan, E. Mariotti, P. Minguzzi, L. Moi, et al., *The European Physical Journal Special Topics* **2007**, *150*, 389.

[502] D. Mukherjee, B. Sahoo, H. S. Nataraj, B. Das, *The Journal of Physical Chemistry A* **2009**, *113*, 12549.

[503] R. Berger, J. Stohner, *Wiley Interdisciplinary Reviews: Computational Molecular Science* **2019**, *9*, e1396.

[504] A. P. Koufos, D. A. Papaconstantopoulos, *International Journal of Quantum Chemistry* **2013**, *113*, 2070.

[505] W. M. Haynes, *CRC handbook of chemistry and physics*, CRC press, Boca Raton **2016**.

[506] C. Barrett, *Acta Crystallographica* **1956**, *9*, 671.

[507] R. Berliner, H. G. Smith, J. R. D. Copley, J. Trivisonno, *Physical Review B* **1992**, *46*, 14436.

[508] H. Stoll, B. Paulus, P. Fulde, *Chemical Physics Letters* **2009**, *469*, 90.

[509] L. Schimka, R. Gaudoin, J. Klimeš, M. Marsman, G. Kresse, *Physical Review B* **2013**, *87*, 214102.

[510] V. Sliwko, P. Mohn, K. Schwarz, P. Blaha, *Journal of Physics: Condensed Matter* **1996**, *8*, 799.

[511] J. E. Jaffe, Z. Lin, A. C. Hess, *Physical Review B* **1998**, *57*, 11834.

[512] N. Christensen, D. Novikov, *Solid State Communications* **2001**, *119*, 477.

[513] J. Upadhyaya, S. Wang, R. Moore, *Canadian Journal of Physics* **1980**, *58*, 905.

[514] E. Arnold, W. Borchers, H. Duong, P. Juncar, J. Lermé, P. Lievens, W. Neu, R. Neugart, M. Pellarin, J. Pinard, et al., *Journal of Physics B: Atomic, Molecular and Optical Physics* **1990**, *23*, 3511.

[515] J.-P. Desclaux, *Atomic Data and Nuclear Data Tables* **1973**, *12*, 311.

[516] P. J. Hasnip, K. Refson, M. I. Probert, J. R. Yates, S. J. Clark, C. J. Pickard, *Philosophical Transactions. Series A, Mathematical, Physical, and Engineering sciences* **2014**, *372*, 20130270.

[517] J. Moellmann, S. Grimme, *The Journal of Physical Chemistry C* **2014**, *118*, 7615.

[518] B. Shahriari, K. Swersky, Z. Wang, R. P. Adams, N. De Freitas, *Proceedings of the IEEE* **2015**, *104*, 148.

[519] P. A. M. Dirac, *Mathematical Proceedings of the Cambridge Philosophical Society* **1930**, *26*, 376–385.

[520] S. H. Vosko, L. Wilk, M. Nusair, *Canadian Journal of Physics* **1980**, *58*, 1200.

[521] J. P. Perdew, A. Ruzsinszky, G. I. Csonka, O. A. Vydrov, G. E. Scuseria, L. A. Constantin, X. Zhou, K. Burke, *Physical Review Letters* **2008**, *100*, 136406.

[522] C. K. Williams, C. E. Rasmussen, *Gaussian processes for machine learning*, volume 2, MIT press Cambridge, MA **2006**.

[523] F. Pedregosa, G. Varoquaux, A. Gramfort, V. Michel, B. Thirion, O. Grisel, M. Blondel, P. Prettenhofer, R. Weiss, V. Dubourg, et al., *Journal of Machine Learning Research* **2011**, *12*, 2825.

[524] J. Mockus, *Towards Global Optimization* **1998**, *2*, 117.

[525] D. R. Jones, M. Schonlau, W. J. Welch, *Journal of Global Optimization* **1998**, *13*, 455.

[526] J. Wilson, F. Hutter, M. Deisenroth, *Advances in Neural Information Processing Systems* **2018**, *31*.

[527] F. Birch, *Physical Review* **1947**, *71*, 809.

[528] F. Birch, *J. Geophys. Res.: Solid Earth* **1978**, *83*, 1257.

[529] J. Hama, K. Suito, *Journal of Physics: Condensed Matter* **1996**, *8*, 67.

[530] V. L. Moruzzi, J. F. Janak, K. Schwarz, *Physical Review B* **1988**, *37*, 790.

[531] R. A. Felice, J. Trivisonno, D. E. Schuele, *Physical Review B* **1977**, *16*, 5173.

[532] M. S. Anderson, C. A. Swenson, *Physical Review B* **1985**, *31*, 668.

[533] C. M. McCarthy, C. W. Tompson, S. A. Werner, *Physical Review B* **1980**, *22*, 574.

[534] R. Berliner, O. Fajen, H. G. Smith, R. L. Hitterman, *Physical Review B* **1989**, *40*, 12086.

[535] K. J. Dunn, A. L. Ruoff, *Physical Review B* **1974**, *10*, 2271.

[536] S. Jana, K. Sharma, P. Samal, *J. Chem. Phys.* **2018**, *149*, 164703.

[537] W. Weickenmeier, U. Diemer, M. Wahl, M. Raab, W. Demtröder, W. Müller, *The Journal of Chemical Physics* **1985**, *82*, 5354.

[538] P. Schwerdtfeger, Relativistic effects in molecular structure of s-and p-block elements, in *Strength from Weakness: Structural Consequences of Weak Interactions in Molecules, Supermolecules, and Crystals*, pages 169–190, Springer **2002**.

[539] C. Thierfelder, P. Schwerdtfeger, A. Koers, A. Borschevsky, B. Fricke, *Physical Review A* **2009**, *80*, 022501.

[540] V. Pershina, A. Borschevsky, J. Anton, *Chemical Physics* **2012**, *395*, 87.

[541] T. Hangele, M. Dolg, P. Schwerdtfeger, *The Journal of Chemical Physics* **2013**, *138*.

[542] A. R. Saetgaraev, L. V. Skripnikov, I. I. Tupitsyn, D. P. Usov, A. V. Oleynichenko, I. M. Savelyev, N. K. Dulaev, V. M. Shabaev, *Physical Review A* **2025**, *112*, 052805.

[543] J. W. Arblaster, *Selected values of the crystallographic properties of elements*, ASM International, Ohio **2018**.

[544] G. G. Szpiro, *Kepler's Conjecture*, John Wiley, New York **2003**.

[545] D. Hilbert, *Bulletin of the American Mathematical Society* **1902**, *8*, 437.

[546] S. Torquato, *The Journal of Chemical Physics* **2018**, *149*.

[547] N. J. Sloane, *Scientific American* **1984**, *250*, 116.

[548] I. Smalley, *Mathematics Magazine* **1963**, *36*, 295.

[549] N. J. Sloane, *Nature* **1998**, *395*, 435.

[550] A. Wells, *Structural Inorganic Chemistry*, 5th Ed., Clarendon Press, Oxford **1984**.

[551] F. Ernst, M. W. Finnis, D. Hofmann, T. Muschik, U. Schönberger, U. Wolf, M. Methfessel, *Physical Review Letters* **1992**, *69*, 620.

[552] C. H. Loach, G. J. Ackland, *Physical Review Letters* **2017**, *119*, 205701.

[553] R. M. Thompson, R. T. Downs, *Structural Science* **2001**, *57*, 766.

[554] A. C. Wilson, *Proceedings of the Royal Society of London. Series A. Mathematical and Physical Sciences* **1942**, *180*, 277.

[555] D. S. Bernstein, O. Kouba, *Aequationes Mathematicae* **2019**, *93*, 1183.

[556] N. J. A. Sloane, *The On-Line Encyclopedia of Integer Sequences*, available at https://oeis.org/ (last accessed 20 May 2024) **2016**.

[557] J. E. Iglesias, *Zeitschrift für Kristallographie-Crystalline Materials* **1981**, *155*, 121.

[558] E. Estevez-Rams, C. Azanza Ricardo, B. Aragón Fernández, *Zeitschrift für Kristallographie-Crystalline Materials* **2005**, *220*, 592.

[559] H. Wiebe, T. L. Underwood, G. J. Ackland, *The Journal of Chemical Physics* **2020**, *153*.

[560] D. J. Wales, J. P. Doye, *The Journal of Physical Chemistry A* **1997**, *101*, 5111.

[561] L. B. Pártay, C. Ortner, A. P. Bartók, C. J. Pickard, G. Csányi, *Physical Chemistry Chemical Physics* **2017**, *19*, 19369.

[562] P. Schwerdtfeger, A. Burrows, Program Jones - A Fortran Program for sc, bcc, fcc, hcp and Barlow Lattice Sums, Massey University, Auckland. Available at http://ctcp.massey.ac.nz (last access: 20 May 2024) **2023**.

[563] J. H. Conway, C. Goodman-Strauss, N. J. Sloane, *Current Developments in Mathematics* **1999**, *1999*, 37.

[564] P. Appell, *Acta Mathematica* **1886**, *8*, 265.

[565] M. Born, A. Landé, *Verhandlungen der Deutschen Physikalischen Gesellschaft* **1918**, *20*, 210.

[566] O. Emersleben, *Mathematische Nachrichten* **1950**, *4*, 468.

[567] A. Buchheit, T. Keßler, P. Schuhmacher, B. Fauseweh, *Bulletin of the American Physical Society* **2023**, *68*.

[568] G. Kane, M. Goeppert-Mayer, *The Journal of Chemical Physics* **1940**, *8*, 642.

[569] T. McLarnan, *Zeitschrift für Kristallographie-Crystalline Materials* **1981**, *155*, 269.

[570] E. A. Lord, S. Ranganathan, A. Subramaniam, *Philosophical Magazine A* **2002**, *82*, 255.

[571] E. Estevez-Rams, C. Azanza-Ricardo, J. Martínez García, B. Aragón-Fernández, *Acta Crystallographica Section A: Foundations of Crystallography* **2005**, *61*, 201.

[572] A. Burrows, S. Cooper, P. Schwerdtfeger, *arXiv preprint arXiv:2202.01392* **2022**.

[573] M. Jaskolski, B. Naskrecki, Z. Dauter, *ChemTexts* **2024**, *11*, 2.

[574] F. Ellinger, W. Zachariasen, *Journal of the American Chemical Society* **1953**, *75*, 5650.

[575] A. Daane, R. Rundle, H. Smith, F. Spedding, *Acta Crystallographica* **1954**, *7*, 532.

[576] L. Warnes, The Structure of Solids, in *Electronic Materials*, pages 1–31, Springer **1990**.

[577] N. Shi, D. Fort, *Journal of the Less Common Metals* **1985**, *113*, 21.

[578] L. Wang, S. Xiang, Y. Tan, W. Shi, Y. Cai, X. Ji, *Materials Science and Engineering: A* **2022**, *853*, 143705.

[579] C. H. Loach, G. J. Ackland, *Physical Review Letters* **2017**, *119*, 205701.

[580] G. E. Moyano, P. Schwerdtfeger, K. Rosciszewski, *Physical Review B* **2007**, *75*, 024101.

[581] S. Grimme, *Wiley Interdisciplinary Reviews: Computational Molecular Science* **2011**, *1*, 211.

[582] R. Howard, *Physics Letters A* **1970**, *32*, 37.

[583] B. Dorner, H. Egger, *Physica Status Solidi (b)* **1971**, *43*, 611.

[584] D. Batchelder, M. Collins, B. Haywood, G. Sidey, *Journal of Physics C: Solid State Physics* **1970**, *3*, 249.

[585] B. Jäger, R. Hellmann, E. Bich, E. Vogel, *Molecular Physics* **2009**, *107*, 2181.

[586] C. Chakrabarti, I. Chakrabarty, *International Journal of Mathematics and Mathematical Sciences* **2005**, *2005*, 2847.

[587] Y. Huang, M. Widom, *Entropy* **2022**, *24*, 618.

[588] J. O. Hirschfelder, C. F. Curtiss, R. B. Bird, *The molecular theory of gases and liquids*, John Wiley & Sons **1964**.

[589] V. Elser, *Physical Review E* **2014**, *89*, 052404.

[590] G. E. Andrews, R. Askey, R. Roy, *Special functions*, volume 71, Cambridge University Press, Cambridge **1999**.

[591] N. M. Temme, *Special functions: An introduction to the classical functions of mathematical physics*, John Wiley & Sons **1996**.

[592] J. M. Borwein, P. B. Borwein, *Transactions of the American Mathematical Society* **1991**, *323*, 691.

[593] S. Cooper, *Ramanujan's theta functions*, Springer, Berlin **2017**.

[594] N. J. A. Sloane, S. Plouffe, *The Encyclopedia of Integer Sequences (online version available at https://oeis.org/)*, Academic Press **1995**.

[595] T. M. Apostol, *Introduction to analytic number theory*, Springer Science & Business Media, Berlin **1998**.

[596] R. E. Crandall, *Manuscript, at https://www.reed.edu/physics/faculty/crandall/papers/epstein.pdf* **1998**.

[597] A. Selberg, S. Chowla, *Journal fur die Reine und Angewandte Mathematik* **1967**, *227*, 87.

[598] P. Bateman, E. Grosswald, *Acta Arithmetica* **1964**, *9*, 365.

[599] P. Schwerdtfeger, B. Assadollahzadeh, A. Hermann, *Physical Review B* **2010**, *82*, 205111.

[600] N. Levinson, R. M. Redheffer, *Complex variables*, Holden-Day **1970**.

[601] L. Glasser, K. T. Kohl, C. Koutschan, V. H. Moll, A. Straub, *Scientia. Series A. Mathematical Sciences. New Series* **2012**, *22*, 129.

[602] G. Fucci, K. Kirsten, *Journal of Physics A: Mathematical and Theoretical* **2015**, *48*, 435203.

[603] M. E. Gurtin, E. Fried, L. Anand, *The mechanics and thermodynamics of continua*, Cambridge University Press **2010**.

[604] R. Abeyaratne, *Lecture Notes on The Mechanics of Elastic Solids* **1998**.

[605] M. Born, R. D. Misra, *Mathematical Proceedings of the Cambridge Philosophical Society* **1940**, *36*, 466.

[606] A. Fletcher, J. C. P. Miller, L. Rosenhead, L. J. Comrie, *An index of mathematical tables*, volume 1, Blackwell **1962**.

[607] A. Togo, L. Chaput, T. Tadano, I. Tanaka, *Journal of Physics: Condensed Matter* **2023**, *35*, 353001.